General Disclaimer

One or more of the Following Statements may affect this Document

- This document has been reproduced from the best copy furnished by the organizational source. It is being released in the interest of making available as much information as possible.

- This document may contain data, which exceeds the sheet parameters. It was furnished in this condition by the organizational source and is the best copy available.

- This document may contain tone-on-tone or color graphs, charts and/or pictures, which have been reproduced in black and white.

- This document is paginated as submitted by the original source.

- Portions of this document are not fully legible due to the historical nature of some of the material. However, it is the best reproduction available from the original submission.

Produced by the NASA Center for Aerospace Information (CASI)

NASA CR-168296-VOL-1

NASA

National Aeronautics and
Space Administration

AEROTHERMAL MODELING

Phase I - Final Report

Volume I - Model Assessment



by
M.J. Kenworthy
S.M. Correa
D.L. Burrus

General Electric Company
Aircraft Engine Group
Advanced Technology Operation

(NASA-CR-168296-Vol-1) AEROTHERMAL MODELING, PHASE 1. VOLUME 1: MODEL ASSESSMENT Final Report (General Electric Co.) 386 p HC A17/MF A01 CSCL 21E

N84-15155

Unclas
G3/07 43298

Prepared for

National Aeronautics and Space Administration

NASA Lewis Research Center
Contract NAS3-23525

1. Report No.	2. Government Accession No.	3. Recipient's Catalog No.
NASA CR-168296-Vol-1		

4. Title and Subtitle	5. Report Date
AEROTHERMAL MODELING, PHASE I FINAL REPORT	November 1983
	6. Performing Organization Code
7. Author(s) M.J. Kenworthy, S.M. Correa, and D.L. Burrus	8. Performing Organization Report No.
	10. Work Unit No.
9. Performing Organization Name and Address General Electric Company Aircraft Engine Business Group Cincinnati, Ohio 45215	11. Contract or Grant No. NAS3-23525
	13. Type of Report and Period Covered Contractor Report Aug 1982-May 1983
12. Sponsoring Agency Name and Address National Aeronautics and Space Administration Washington, D.C. 20546	14. Sponsoring Agency Code

15. Supplementary Notes

Project Manager, Robert R. Tacina, Aerothermodynamics and Fuels Division, NASA Lewis Research Center, Cleveland, Ohio

16. Abstract

The Aerothermal Modeling Program - Phase I was conducted as part of the overall NASA Hot Section Technology (HOST) Program. The purpose of this effort was to determine the predictive accuracy of and the deficiencies within the various analytical modules comprising the overall combustor aerothermal model used at General Electric, as well as to formulate recommendations for improvement were needed.

This effort involved the assembly of a benchmark quality data base from selected available literature, and from General Electric engine and combustor component test data. This data base was supplemented with additional definitive data obtained from an experimental test program conducted as part of the Phase I effort. Using selections from this data base, assessment studies were conducted to evaluate the various modules. Assessment of the internal flow module was conducted using 2-D parabolic and ellipitic, as well as 3-D elliptic internal flow calculations of definitive test data selected from the assembled data base. The 2-D assessment provided methodical examination of the mathematical techniques and the physical submodules, while the 3-D assessment focused on usefulness as a design tool. Calculations of combustor liner metal temperatures, pressure loss performance, and airflow distribution were performed using aerothermal modules which have been in general use for many years at General Electric.

The results of these assessment provided for the identification of deficiencies within the modules. The deficiencies were addressed in some detail providing a foundation on which to formulate a prioritized list of recommendations for improvement.

17. Key Words (Suggested by Author(s))	18. Distribution Statement
Aerothermal Modeling Combustor Modeling Reacting Flow Gas Turbine Combustor	Unclassified - Unlimited

19. Security Classif. (of this report)	20. Security Classif. (of this page)	21. No. of Pages	22. Price*
Unclassified	Unclassified	370	

* For sale by the National Technical Information Service, Springfield, Virginia 22161

NASA-C-168 (Rev. 10-75)

FOREWORD

The program described herein was conducted by the General Electric Company Aircraft Engine Business Group under NASA Contract NAS3-23525. Mr. Robert R. Tacina of the Aerothermodynamics and Fuels Division, NASA Lewis Research Center, was the NASA Project Manager.

Key General Electric Company contributors were: M.J. Kenworthy, Principal Investigator; D.W. Bahr, Technical Program Manager; E.J. Rogala, Program Manager; Dr. S.M Correa with the assistance of Dr. W. Shyy performed the assessment of the axisymmetric program GETREF; D.L. Burrus directed the experimental program, and with the assistance of P.H. Waymeyer, performed the remaining assessments; and W.C. Colley assisted in defining needed computer programming changes in the 3-D elliptic model.

The Final Report is divided into two volumes, with Volume II containing the experimental data obtained under this contract. An Executive Summary report was also prepared.

PRECEDING PAGE BLANK NOT FILMED

PAGE ii INTENTIONALLY BLANK

TABLE OF CONTENTS

Section		Page
1.0	SUMMARY	1
2.0	INTRODUCTION	3
3.0	PROGRAM SCOPE	6
	3.1 Objective	6
	3.2 The General Electric Aerothermal Model	6
	3.3 Data Selected for Comparison with Models	14
	3.4 Program Approach	15
4.0	STRUCTURE OF THE REPORT	17
5.0	AEROTHERMAL MODEL AND BENCHMARK DATA BASE DEFINITION	18
	5.1 Overall Aerothermal Model Description	18
	5.1.1 Preliminary Design Module	20
	5.1.2 Inlet Diffuser Module	20
	5.1.3 Airflow Distribution Module	29
	5.1.4 Combustor Heat Transfer Module	37
	5.1.5 3-D Internal Flow Module	45
	5.1.6 Usefulness of Output Parameters	48
	5.2 Selection of Benchmark Quality Data Base	49
	5.2.1 Available Benchmark Expermiments from the Literature	49
	5.2.2 General Electric Engine and Component Data Base	60
	5.3 Experimental Test Program	74
6.0	FORMAL ANALYSIS OF INTERNAL FLOW MODEL CONCEPTS	99
	6.1 Introduction	99
	6.2 Conservation Equations	100
	6.3 Numerical Methods	103
	6.3.1 Current Method - Hybrid Scheme	104
	6.3.2 Alternative Methods for Three-Dimensional Flows	106
	6.3.3 Numerical Accuracy and Cell Peclet Number	110
	6.3.4 Test Problem I: Boundary Layer Type Flow	114
	6.3.5 Iterative Method	121
	6.3.6 Test Problem II: Flow with Source Term	124
	6.3.7 Test Problem III: Numerical Diffusion Due to Streamline-to-Grid Skewness	132

PAGE IV INTENTIONALLY BLANK

PRECEDING PAGE BLANK NOT FILMED

TABLE OF CONTENTS (Concluded)

Section		Page
	6.3.8 Summary and Conclusions	139
	6.4 Turbulence Closure Models	141
	6.5 Other Two-Equation Turbulence Models	147
	6.6 Turbulence-Chemistry Interaction	147
7.0	ASSESSMENT OF AEROTHERMAL MODEL AGAINST DATA BASE	173
	7.1 Model Assessment Against Definitive Axisymmetric Experiments from the Literature	174
	7.1.1 Turbulent Jet Diffusion Flame	174
	7.1.2 Isothermal Axisymmetric Plenum-Chamber Experiment	188
	7.1.3 Isothermal Co- and Counterswirled Pipe Flow	197
	7.1.4 Bluff Body Stabilized Diffusion Flame	200
	7.2 Assessment of the 3-D Internal Flow Model	239
	7.3 Assessment of Aerothermal Modules in General Use	325
	7.4 Summarized Assessment	346
	7.4.1 Diffuser Module	346
	7.4.2 Flow Distribution Module	346
	7.4.3 Heat Transfer Module	347
	7.4.4 Internal Flow Module	348
8.0	CONCLUDING REMARKS	354
	8.1 Summary	354
	8.2 Prioritized Recommendations	355
REFERENCES		359
APPENDIX - NOMENCLATURE		367

LIST OF ILLUSTRATIONS

Figure		Page
1.	Flow Diagram of Overall General Electric Aerothermal Model.	4
2.	Typical Node Pattern for Liner Heat Transfer Calculations.	8
3.	Velocity Field Calculations Using GETREF Code.	10
4.	Calculated Velocity Field for a Combustor Using 3-D Elliptic Code.	11
5.	Grid Used in 3-D Calculation of Combustor.	12
6.	Calculated Peclet Number in the X-Direction from 3-D Combustor Calculation.	13
7.	Flow Diagram of General Electric Aerothermal Model in General Use.	19
8.	Prediffuser Preliminary Design Layout.	21
9.	Overall Combustor Preliminary Design Layout.	22
10.	Flow Diagram of Preliminary Design Module.	23
11.	Flow Diagram of Inlet Diffuser Design Module.	24
12.	Flow Diagram of Distribution Module.	30
13.	Station Network Layout for Airflow Distribution Module.	32
14.	Airflow Distribution Module Station Matrix and Flow Splits.	33
15.	Airflow Distribution Model Typical Working Station Layout.	38
16.	Relationship of Working Station Layout to Entire Station Matrix.	39
17.	Flow Diagram of Liner Heat Transfer Module.	41
18.	Node Model Showing Heat Transfer Quantities.	43
19.	Typical Calculated Liner Panel Temperature Distribution.	46
20.	E^3 Split Duct Diffuser Model Test Rig.	62
21.	Measured Static Pressure Recovery Levels for E^3 Model Test Rig.	63
22.	Measured Static Pressure Recovery Levels for E^3 Model Test Rig	64
23.	Measured Static Pressure Recovery Levels for E^3 Model Test Rig.	65
24.	Sample of Discharge Coefficients Data for Dilution Holes.	66
25.	Sample of Steady State Liner Metal Temperature.	68
26.	Sample of Transient Liner Metal Temperature Data.	69
27.	Sample of Measured Combustor Exit Gas Temperature Data.	73
28.	Aerothermal Modeling Experimental Test Rig (Unfueled).	76

LIST OF ILLUSTRATIONS (Continued)

Figure		Page
29.	Aerothermal Modeling Experimental Test Rig (Unfueled).	77
30.	Aerothermal Modeling Experimental Test Rig (Unfueled).	78
31.	Aerothermal Modeling Experimental Test Rig (Unfueled).	79
32.	Aerothermal Modeling Experimental Test Rig (Unfueled).	80
33.	Aerothermal Modeling Experimental Test Rig (Fueled).	81
34.	Atmospheric Pressure Radial Patternation Test Stand.	84
35.	Patternation Test Results for Typical CFM56/F101 Fuel Injectors (Atomizing Fuel Nozzle).	86
36.	Patternator Run Using F101 Low Pressure Fuel Injectors.	87
37.	Patternation Test Results for Typical CFM56/F101 Fuel Injectors (Low Pressure Fuel Injector).	88
38.	Patternation Test Results for Typical CFM56/F101 Fuel Injectors (Atomizing Fuel Nozzle).	89
39.	Earlier Patternation Test Results Showing Effects of Eccentricity and Fuel Injector Tip Immersion.	90
40.	Earlier Patternation Test Results Showing Effects of Eccentricity and Fuel Injector Tip Immersion.	91
41.	Earlier Patternation Test Results Showing Effects of Eccentricity and Fuel Injector Tip Immersion.	92
42.	Earlier Patternation Test Results Showing Effects of Eccentricity and Fuel Injector Tip Immersion.	93
43.	Earlier Patternation Test Results Showing Effects of Eccentricity and Fuel Injector Tip Emmersion.	94
44.	Earlier Patternation Test Results Showing Effects of Eccentricity and Fuel Injector Tip Immersion.	95
45.	5 Hole (3-D) Wedge Type Velocity Probe.	96
46.	Wedge Probe Results for GE/F101 Swirl Cup Assembly.	97
47.	Notation Used in a Computational Mesh.	109
48.	Distribution of Source Term in Eq. (52).	126
49.	Numerical Solutions to Test Problem II.	127
50.	Numerical Solutions to Test Problem II.	128
51.	Numerical Solutions to Test Problem II.	129
52.	Numerical Solutions to Test Problem II.	130
53.	Numerical Solutions to Test Problem II.	131

LIST OF ILLUSTRATIONS (Continued)

Figure		Page
54.	Comparison of Accuracy Between First Order Upwind and Skew Upwind Approximations to Eq. (53).	134
55.	Numerical Solutions to Eq. (53) for n = 2.	135
56.	Numerical Solutions to Eq. (53).	137
57.	Numerical Solutions to Eq. (56) at x = 1 - 2Δx.	138
58.	Numerical Solutions to Eq. (56) at x = 1 - 2Δx.	140
59.	No-Fluctuation Model - Frozen Flow.	154
60.	No-Fluctuation Model - Equilibrium Flow.	155
61.	No-Fluctuation Model - Kinetic Flow.	156
62.	No-Fluctuation Model - Frozen Flow.	157
63.	No-Fluctuation Model - Equilibrium Flow.	158
64.	No-Fluctuation Model - Kinetic Flow.	159
65.	No-Fluctuation Model - Equilibrium Flow.	161
66.	No-Fluctuation Model - Kinetic Flow.	162
67.	No-Fluctuation Model - Equilibrium Flow.	163
68.	No-Fluctuation Model - Kinetic Flow.	164
69.	Normalized Decay of CH_4 Along the Centerline of a Round Jet in Still Air.	169
70.	Mean Velocity and Density Profiles in the Self-Similar Region of He and N_2 with Equal Momentum Flux in the Two Streams.	169
71.	Decay of Scalar (CH_4) Fluctuations Along the Centerline of a Round Jet in Still Air.	169
72.	Mean Velocity and Density Profiles in the Self-Similar Region of He and N_2 with Equal Mass Flux in the Two Streams.	169
73.	Burning Turbulent Diffusion Jet with LDV and Pulsed Raman Data.	175
74.	Centerline Profile of Axial Velocity.	177
75.	Radial Profile of Axial Velocity at X/D = 25.	178
76.	Radial Profile of Axial Velocity at X/D = 100.	179
77.	Centerline Profile of Favre-Averaged Mean Mixture Fraction.	180
78.	Radial Profile of Favre-Averaged Mean Mixture Fraction at X/D = 25.	181
79.	Radial Profile of Favre-Averaged Mean Mixture Fraction at X/D = 50.	182
80.	Centerline Profiles of Jet Half-Width Based on Velocity and Favre-Averaged Mean Mixture Fraction.	183

LIST OF ILLUSTRATIONS (Continued)

Figure		Page
81.	Centerline Profile of Turbulence Kinetic Energy.	184
82.	Radial Profile of Turbulence Kinetic Energy at X/D = 25.	185
83.	Centerline Profile of Favre-Averaged Variance of Mixture Fraction.	186
84.	Radial Profile of Favre-Averaged Variance in Mixture Fraction at X/D = 25.	187
85.	Radial Profile of Favre-Averaged Mean Temperature at X/D = 25.	189
86.	Radial Profile of Favre-Averaged Mean Temperature at X/D = 50.	190
87.	Isothermal Slit-Jet Experiment.	191
88.	Radial Profiles of Trubulence Kinetic Energy and Mean Axial Velocity at $x/r_o = -0.61$.	193
89.	Radial Profile of Turbulence Kinetic Energy and Mean Axial Velocity at $x/r_o = 0.37$.	194
90.	Radial Profile of Turbulence Kinetic Energy and Mean Axial Velocity at $x/r_o = 1.20$.	195
91.	Radial Profile of Turbulence Kinetic Energy and Mean Axial Velocity at $x/r_o = 2.77$.	196
92.	Flow Assembly.	199
93.	Centerline Profile of Axial Velocity for Coswirl Flow.	201
94.	Radial Profile of Axial Velocity at $Z/R_i = 3.67$ for Coswirl Flow.	202
95.	Radial Profile of Tangential Velocity at $Z/R_i = 3.67$ for Coswirl Flow.	203
96.	Radial Profile of Turbulence Kinetic Energy at $Z/R_i = 3.67$.	204
97.	Centerline Profile of Axial Velocity for Counterswirl Flow.	205
98.	Radial Profile of Axial Velocity at $Z/R_i = 3.15$ for Counter-swirl Flow.	206
99.	Radial Profile of Tangential Velocity at $Z/R_i = 3.15$ for Counterswirl Flow.	207
100.	Radial Profile of Turbulence Kinetic Energy at $Z/R_i = 3.12$ for Counterswirl Flow.	208
101.	Centerline Profile of Axial Velocity for Counterswirl Flow.	209
102.	Radial Profile of Axial Velocity at $Z/R_i = 3.15$ for Counter-swirl Flow.	210
103.	Radial Profile of Tangential Velocity at $Z/R_i = 3.15$ for Counterswirl Flow.	211

LIST OF ILLUSTRATIONS (Continued)

Figure		Page
104.	Radial Profile of Turbulence Kinetic Energy at Z/R_i = 3.12 for Counterswirl Flow.	212
105.	Centerline Profile of Axial Velocity for Coswirl Flow.	213
106.	Radial Profile of Axial Velocity at Z/R_i = 3.67 for Coswirl Flow.	214
107.	Radial Profile of Tangential Velocity at Z/R_i = 3.67 for Coswirl Flow.	215
108.	Radial Profile of Turbulence Kinetic Energy at Z/R_i = 3.67 for Coswirl Flow.	216
109.	Schematic of AFAPL Combustor Showing Centerline Stagnation Points S1 and S2.	217
110.	Dividing Streamlines from Baseline Simulation.	219
111.	Centerline Axial Velocity.	224
112.	Contours of Turbulence Kinetic Energy.	225
113.	Centerline Turbulence Kinetic Energy.	226
114.	Contours of Mean Mixture Fraction.	228
115.	Contours of Variance in Mixture Fraction.	229
116.	Radial Temperature Profile at X/D = 0.43.	231
117.	Absolute East-West Cell Peclet Numbers.	232
118.	Absolute North-South Cell Peclet Numbers.	233
119.	Location of First Stagnation Point for Higher Jet Velocities.	236
120.	Minimum Centerline Axial Velocity for Higher Jet Velocities.	237
121.	Walker and Kors Experiment Number 67, X/D = 2.	240
122.	Walker and Kors Experiment Number 67, X/D = 4.	241
123.	Walker and Kors Experiment No. 67, X/D = 8.	242
124.	Walker and Kors Experiment No. 67, X/D = 16.	243
125.	Grid 1 (Coarse) 45X 21Y 11Z.	245
126.	Grid 2 (Medium) 50X 21Y 20Z.	246
127.	Grid 3 (Detailed) 50X 26Y 30Z.	247
128.	Calculated Results of Walker and Kors Experiment 67 Using Coarse, Medium, and Detailed Grids, X/D = 2.	249
129.	Calculated Results of Walker and Kors Experiment 67 Using Coarse, Medium, and Detailed Grids, X/D = 4.	250

LIST OF ILLUSTRATIONS (Continued)

Figure		Page
130.	Calculated Results of Walker and Kors Experiment 67 Using Coarse, Medium, and Detailed Grids, X/D = 8.	251
131.	Calculated Results of Walker and Kors Experiment 67 Using Coarse, Medium, and Detailed Grids, X/D = 16.	252
132.	Comparisons of Calculated Jet Penetration with Holdeman Correlation for Walker and Kors Experiment 67.	253
133.	Calculated Results of Walker and Kors Experiment 67 Using Detailed Grid and Optimized Turbulence Inputs, X/D = 2.	255
134.	Calculated Results of Walker and Kors Experiment 67 Using Detailed Grid and Optimized Turbulence Inputs, X/D = 4.	256
135.	Calculated Results of Walker and Kors Experiment 67 Using Detailed Grid and Optimized Turbulence Inputs, X/D = 8.	257
136.	Calculated Results of Walker and Kors Experiment 67 Using Detailed Grid and Optimized Turbulence Inputs, X/D = 16	258
137.	Walker and Kors Experiment No. 69, X/D = 2.	260
138.	Walker and Kors Experiment No. 69, X/D = 4.	261
139.	Walker and Kors Experiment No. 69, X/D = 8.	262
140.	Walker and Kors Experiment No. 69, X/D = 16.	263
141.	Walker and Kors Experiment No. 69 Test Results, X/D = 2.	264
142.	Walker and Kors Experiment 69 Test Results, X/D = 4.	265
143.	Calculated Results of Walker and Kors Experiment 69 Using Medium Grid, X/D = 8	266
144.	Calculated Results of Walker and Kors Experiment 69 Using Medium Grid, X/D = 16.	267
145.	Walker/Kors Experiment 69 Jet Penetration Study Grid.	268
146.	Calculated Results of Grid Sensitivity Investigation for Walker and Kors Experiment 69, X/D = 2.	269
147.	Calculated Results of Grid Sensitivity Investigation for Walker and Kors Experiment 69, X/D = 4.	270
148.	Calculated Results of Grid Sensitivity Investigation for Walker and Kors Experiment 69, X/D = 8.	271
149.	Grid 4D Used to Investigate Sensitivity of Calculated Jet Penetration to Grid Detail Used.	272
150.	Calculated Results of Grid Sensitivity Investigation for Walker and Kors Experiment 69.	274
151.	Calculated Results of Grid Sensitivity Investigation for Walker and Kors Experiment 69.	275

LIST OF ILLUSTRATIONS (Continued)

Figure		Page
152.	Comparison of Calculated Results of Walker and Kors Experiment 69 Obtained from the Northern Research and Garrett Codes, X/D = 2.	276
153.	Comparison of Calculated Results of Walker and Kors Experiment 69 Obtained from the Northern Research and Garrett Codes, X/D = 4.	277
154.	Comparisons of Calculated Results of Walker and Kors Experiment 69 Obtained from the Northern Research and Garrett Codes, X/D = 8.	278
155.	Comparisons of Calculated Results of Walker and Kors Experiment 69 Obtained from the Northern Research and Garrett Codes, X/D = 16.	279
156.	Caomparisons of Calculated Results of Walker and Kors Experiment 69 Obtained from the Northern Research and Garrett Codes.	281
157.	Calculated Turbulence Length Scales for Walker/Kors Experiment 69 AKFAC = 6E-3 ALFAC = 2E-1 AKFAC (JET) = 1.52E-2 Schmidt No. = 0.5.	282
158.	Calculated Results of Walker and Kors Experiment 67 Using Medium Grid with Larger Jet Turbulence Length Scale, X/D = 2.	283
159.	Calculated Results of Walker and Kors Experiment 67 Using Medium Grid with Larger Jet Turbulence Length Scale, X/D = 4.	284
160.	Calculated Results of Walker and Kors Experiment 67 Using Medium Grid with Larger Jet Turbulence Length Scale, X/D = 8.	285
161.	Calculated Results of Walker and Kors Experiment 67 Using Medium Grid with Larger Jet Turbulence Length Scale, X/D = 16.	286
162.	Coarse Grid Selected for Calculations of Experimental Test Configurations.	288
163.	Comparison of Measured and Calculated Results for Experimental Test Configuration 8.	290
164.	Comparison of Measured and Calculated Results for Experimental Test Configuration 8.	291
165.	Comparison of Measured and Calculated Results for Experimental Test Configuration 8.	292
166.	Comparison of Measured and Calculated Results for Experimental Test Configuration 8.	293
167.	Comparison of Measured and Calculated Results for Experimental Test Configuration 4.	294

LIST OF ILLUSTRATIONS (Continued)

Figure		Page
168.	Comparison of Measured and Calculated Results for Experimental Test Configuration 4.	295
169.	Comparison of Measured and Calculated Results for Experimental Test Configuration 4.	296
170.	Comparison of Measured and Calculated Results for Experimental Test Configuration 4.	297
171.	Comparison of Measured and Calculated Results for Experimental Test Configuration 5.	298
172.	Comparison of Measured and Calculated Results for Experimental Test Configuration 5.	299
173.	Comparison of Measured and Calculated Results for Experimental Test Configuration 5.	300
174.	Comparison of Measured and Calculated Results for Experimental Test Configuration 5.	301
175.	Comparison of Measured and Calculated Results for Experimental Test Configuration 6.	303
176.	Comparison of Measured and Calculated Results for Experimental Test Configuration 6.	304
177.	Comparison of Measured and Calculated Results for Experimental Test Configuration 6.	305
178.	Comparison of Measured and Calculated Results for Experimental Test Configuration 7.	306
179.	Comparison of Measured and Calculated Results for Experimental Test Configuration 7.	307
180.	Comparison of Measured and Calculated Results for Experimental Test Configuration 7.	308
181.	Comparison of Measured and Calculated Results for Experimental Test Configuration 7.	309
182.	Comparison of Measured and Calculated Results for Experimental Test Configuration 7.	310
183.	Swirler Input for Test Configuration 13 (Coarse Grid).	311
184.	Comparison of Measured and Calculated Results for Experimental Test Configuration 13.	312
185.	Comparison of Measured and Calculated Results for Experimental Test Configuration 13.	313
186.	Comparison of Measured and Calculated Results for Experimental Test Configuration 13.	314

LIST OF ILLUSTRATIONS (Continued)

Figure		Page
187.	Comparison of Measured and Calculated Results for Experimental Test Configuration 13.	315
188.	F101 Contoured Wall Grid (53X 34Y 23Z).	316
189.	Combustor Calculation with Uniform Inlet (No Fuel).	317
190.	Detailed Grid Selected for Calculations of Experimental Test Configuration 17C.	319
191.	Swirler Input for Test Configuration 17C (Detailed Grid).	320
192.	Detailed Grid Selected for Calculations of Experimental Test Configuration 17C. Contours of the Pattern Factor Parameter.	321
193.	Calculated Peclet Number in the Y Direction from 3-D Combustor Calculation.	323
194.	Calculated Peclet Number in the Y Direction form 3-D Combustor Calculation.	324
195.	Airflow Distribution Module (COBRA) Station Layout for the GE/F101 Combustor.	326
196.	Comparison of Measured to Calculated Pressures and Airflow Distribution.	327
197.	Ratio of Measured to Calculated Airflow Distribution.	328
198.	Comparison of Measured to Calculated Liner Metal Temperatures Using Data from Reference 115.	331
199.	Comparison of Measured to Calculated Liner Metal Temperatures Using Data from Reference 115.	332
200.	Comparison of Measured to Calculated Liner Metal Temperatures	333
201.	Comparison of Measured to Calculated Liner Metal Temperatures.	334
202.	Parallel Versus Perpendicular Thermocouple Installation.	335
203.	Comparison Between Measured Linear Temperature Using Parallel Versus Perpendicular Thermocouple Installation.	336
204.	Comparison of Measured to Calculated Liner Metal Temperatures.	338
205.	Comparison of Measured to Calculated Liner Metal Temperatures.	339
206.	Comparison of Measured to Calculated Liner Metal Temperatures.	341
207.	Detailed Grid Selected to Study Film Slot Treatment in the 3-D Elliptic Codes.	342
208.	Calculated Temperature Profiles from 3-D Calculations Using Coarser Grid.	343
209.	Calculated Temperature Profiles from 3-D Calculations Using Coarser Grid.	344

LIST OF ILLUSTRATIONS (Concluded)

Figure		Page
210.	Calculated Film Effectiveness from 3-D Calculations Using More Detailed Grid.	345

LIST OF TABLES

Table		Page
I.	Predicted Versus Measured Diffuser $\Delta p/p$.	29
II.	Options Available for Types of Stations.	34
III.	Predicted Airflow Distribution Versus Calculated Results from Measured Data, E^3 Double Annular Development Combustor, Mod-I Configuration.	40
IV.	Round Jet in Crossflow.	52
V.	Premixed Combustion.	56
VI.	Experiments from the Literature which were Modeled.	61
VII.	F101 Combustor Performance Stability.	72
VIII.	Summary of Experimental Test Configurations.	83
IX.	Coefficients in Eq. (31) for Approximating Eq. (32).	111
X.	Values of α and β in Eq. (34) by Substituting the Fourier Component Wave Number.	113
XI.	Numerical Solutions to Test Problem I ($p_{e\Delta x} = 0.2$).	116
XII.	Numerical Solutions to Test Problem I ($p_{e\Delta x} = 10.0$).	117
XIII.	Numerical Solutions to Test Problem I ($p_{e\Delta x} = 100$).	118
XIV.	Roots of Eq. (38) Using Four Different Schemes.	120
XV.	Kinetic Scheme for Methane Combustion.	153
XVI.	Stagnation Points from the Data and the Models.	160
XVII.	Flow Parameters and Initial Conditions for Baseline Simulation.	222
XVIII.	Summary of Analysis.	329
XIX.	Sources of Error in 3-D Elliptic Model.	348
XX.	Prioritized Recommendations.	356

1.0 SUMMARY

The Aerothermal Modeling Program - Phase I was conducted as part of the overall Hot Section Technology (HOST) Program, initiated by NASA. The Phase I program was a 9 month effort involving the assembly of a benchmark quality data base from selected available literature and from General Electric's engine and combustor component test data. Additional definitive data were obtained from an experimental test program conducted as part of the Phase I effort. This experimental effort involved the measurement of temperature distributions for a series of combustor-like flows of progressively increasing flow complexity.

Using selections from this assembled data base, assessment studies were conducted to determine the predictive accuracy of, and identify deficiencies within, the various modules comprising the overall aerothermal model used at General Electric. A major need identified was for an internal flow module for improved hot gas side inputs to the heat transfer module. Assessment of the internal flow module was conducted with 2-D parabolic and elliptic, as well as 3-D elliptic internal flow calculations of definitive test data selected from the assembled data base. Calculations of combustor liner metal temperatures, pressure loss performance, and airflow distribution were performed using the aerothermal modules in general use at General Electric. These calculations were compared with test data selected from the data base to assess the predictive capabilities of these modules and identify their deficiencies.

The 2-D axisymmetric assessments provided a methodical examination of the mathematical techniques and the physical submodels, while the 3-D assessments focused on overall usability as a design tool.

The axisymmetric assesments of the mathematical/physical submodels indicated the following:

- For present purposes; the probability density function, pdf, is a satisfactory treatment of the turbulence/chemistry interaction.
- Accurate predictive capabilities require improved accuracy in the numerics by way of an alternate to central-differencing for 3-D combustor problems.
- The K-ε turbulence model is imperfect, but computationally feasible alternatives, except for swirl or streamline curvature corrections, are not available.
- Calculated results are sensitive to the boundary conditions which need to be better defined.

The assessment of the usability of the available 3-D codes showed:

- A variety of difficulties in utilizing the available codes.
- High computer time running costs.

- Some juggling of input parameters, not necessarily consistent with the physics, was often required to match the data.

- The two available codes showed similar penetration and subsequent mixing of diluton jets with the same input parameters, although different levels were calculated for the turbulence throughout the flow field.

- The main feature of the gas exit temperature pattern from a combustor sector was approximately reproduced by the calculations. However, improved methods of defining the initial dome flows and improved numerics are needed before the calculations are sufficiently accurate to be a useful design tool for durability analyses.

2.0 INTRODUCTION

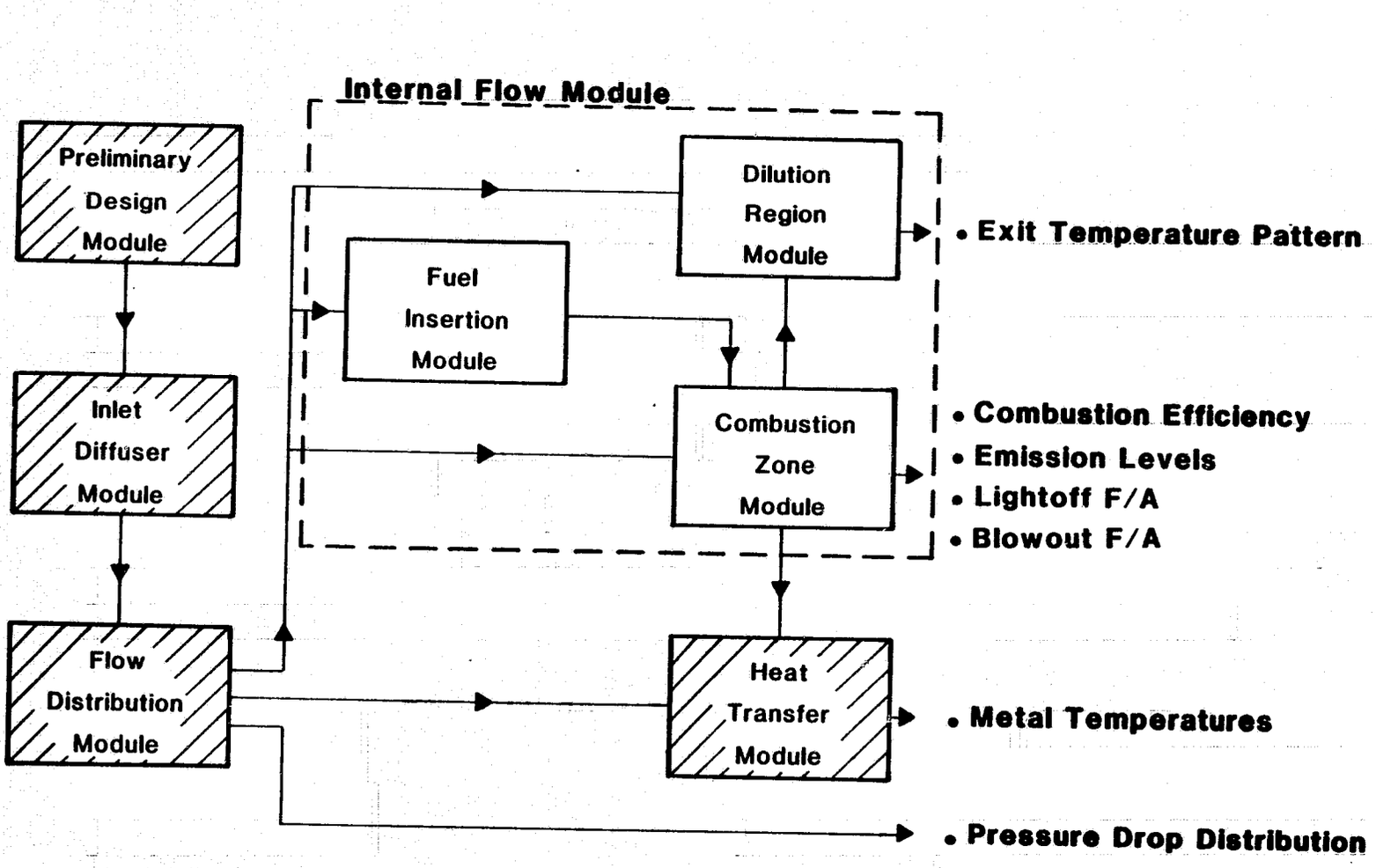
One of the significant ways in which the performance level of aircraft turbine engines has been improved is by the use of advanced materials and cooling concepts that allow a significant increase in turbine inlet temperature level, with attendant thermodynamic cycle benefits. Further cycle improvements have been achieved with higher pressure ratio compressors. The higher turbine inlet temperatures and compressor pressure ratios with corresponding higher temperature cooling air has created a hostile environment for the hot section components. As a result, a major share of the engine maintenance cost is associated with the combustor and the turbine airfoils.

To provide the technology needed to reduce these hot section maintenance costs, NASA has initiated the Hot Section Technology (HOST) program. One key element of this overall program is the Hot Section Technology Aerothermal Modeling Program. The overall objective of this program is to evolve and validate improved analysis methods for use in the design of aircraft turbine engine combustors. The use of such combustor analysis capabilities can be expected to provide significant improvement in the life and durability characteristics of both combustor and turbine components. Another benefit would be a significant reduction in expensive full-scale development testing requirements.

Figure 1 illustrates the overall aerothermal model used at General Electric. Shown in this figure are the separate modules which comprise the overall model. The shaded blocks represent modules already in general use at General Electric, while the unshaded blocks represent components of the detailed internal flow module under development.

Phase I of this modeling program was initiated in 1982. The objectives of the Phase I effort were to assess the current capabilities of combustor aerothermal modules and to identify any significant deficiencies. Three Phase I efforts were sponsored by NASA and were conducted in parallel. The Phase I effort conducted by General Electric is described herein. This effort specifically addressed the combustor aerothermal model currently in use at General Electric.

The Phase I effort conducted by General Electric was comprised of two principal technical tasks. The first task provided a detailed description of the aerothermal model used at General Electric. In addition, a data base of benchmark quality was assembled from General Electric data and from the available literature with which to assess the various components of the overall model. Finally, an experimental testing effort was conducted to provide additional data, specifically of the internal combustor environment to be used in assessing the internal flow module. In the second task, calculations were made using relevant modules of the aerothermal model to predict the flow field and performance parameters identified from the assembled data base. The



- **Shaded boxes are modules in current use in combustor design and development work.**
- **Open boxes are modules in General Electric's aerothermal model planned for use in the future in design and development work after adequate accuracy is demonstrated or developed.**

Figure 1. Flow Diagram of Overall General Electric Aerothermal Model.

accuracy of these calculations was determined through comparisons with the data base. Based on this assessment, specific deficiencies in the generic model were identified, and recommendations for improvement were formulated.

3.0 PROGRAM SCOPE

3.1 OBJECTIVE

The objective of Phase I of the Aerothermal Modeling Program was to identify deficiencies in the aerothermal model that is currently used or planned for use at General Electric in the design of gas turbine engine combustors. This effort was accomplished by assessing the predictions of exising modules with benchmark quality test data. This effort, together with other similar efforts sponsored by NASA, was intended to assess the current state of the art. It was also intended to define Phase II efforts needed to evolve improved and more advanced aerothermal analysis methods, thereby enhancing available capabilities for the design of high performance and durable combustors for advanced aircraft turbine engines.

This Phase I effort was focused on the ability of the existing model to predict or analyze those features associated with durability. These primarily are: (1) the combustor liner metal temperature distribution, and (2) the combustor exit gas temperature patterns, which in turn affects the life of the downstream turbine components. Other features of interest to the combustor designers, such as blowout limits and pollutant emission levels, do not directly affect design for durability.

3.2 THE GENERAL ELECTRIC AEROTHERMAL MODEL

Figure 1 shows schematically General Electric's calculation modules within the overall Aerothermal Model. Except for the internal flow module, the modules are well developed and have been in use for many years. The internal flow module is planned for use in the design process at General Electric after it has been developed and/or demonstrated to have useful accuracy. Thus, assessment of the candidate internal flow modules available at General Electric constitute a major portion of the efforts reported herein.

The model is described in detail in Section 5.0 of this report. Briefly the modules shown in Figure 1 provide the following calculated results. The Preliminary Design Module provides the basic features of the combustor, including its flowpath and the number of fuel nozzles, early in the design process. The Diffuser Module calculates diffuser pressure losses and the three individual pressure levels that feed the inner and outer flowpaths and the dome region. The Flow Distribution Module, using the diffuser exit pressure levels, total airflow, fuel flow, and the combustor aperture areas, and features, calculates the flow and flow angle through each aperture, as well as a one-dimensional internal gas temperature and the overall pressure drop. The program has features to determine effective flow areas from the particular aperture shape and approach flow velocity. A large data base exists at General Electric for providing effective area correlations and new measurements are made on individual apertures whenever needed.

The Heat Transfer Module utilizes the flow distribution, including liner cooling slot flows, the velocities on the cold side of the liner, and some modification of the one-dimensional internal gas temperatures and velocities from the Flow Distribution Module. Through conventional heat transfer equations, together with correlations of cooling film effectiveness based on wind tunnel data, the metal temperatures are calculated throughout the combustor metal structure. Figure 2 illustrates the type of node pattern for which temperatures might be provided for one of the several cooling panels along the length of a combustor liner. This information, together with aerodynamic pressure loading from the Flow Distribution Module, is then used as input to stress and life analysis procedures to provide life estimates or to indicate the life effects of a postulated design change. The input also includes temperature distribution information in the circumferential direction.

Metal temperatures are measured on combustors, but in only a finite number of places. The available stress and life analysis procedures need more than isolated temperature measurements. They need the detailed temperature distribution provided by the Heat Transfer Module. The major source of error in the Heat Transfer Module is in the estimation of the inputs on the hot gas side; the local flow velocities, gas temperatures, and flame radiation levels. If an accurate 3-D elliptic computer code for calculating the internal flow field existed, it could provide substantially better inputs.

At General Electric, the combustor exit gas temperature patterns are measured in detail, typically at seven radial positions and every 1-1/2 degrees around the circumference. This information is of adequate detail for the turbine designers. However, improving or modifying this temperature pattern during the development of the combustor usually involves many cut-and-try test efforts. Changes are often defined with the help of existing data or correlations of simple jet penetration experiments in a cross flow or measurements of flows emerging from the swirl cups surrounding a fuel nozzle in a simple bench experiment. An accurate internal flow module would however be very valuable in providing more detailed and precise inputs and, thus, in reducing total development tests.

Four basic codes for calculating elliptic reacting flows are available at General Electric: (1) the code assembled by the Garrett Turbine Company under the Army-sponsored Combustor Design Validation Program efforts, Mongia et al 1979[1]*; (2) the very similar code assembled by the Northern Research and Engineering Corporation, NREC Report No. 1420[2]; (3) the TEACH code developed initially at Imperial College which uses essentially the same methods as the previous two codes but in a two-dimensional instead of three-dimensional framework; and 4) the two-dimensional (planar or axisymmetric) research code, GETREF (General Electric Turbulent Reactant Flow) developed at General Electric. A parabolic version of this model has also been developed for use in shear flows.

Prior to this effort, plotting routines for the output and some improved flexibility for input had been coupled at General Electric with the three-dimensional elliptic codes and this new format containing both codes was defined as the INTFLOW program. Creation of new programming was not to be part of the scope of effort on this Phase I Aerothermal Modeling program.

*Superscript numbers are reference numbers.

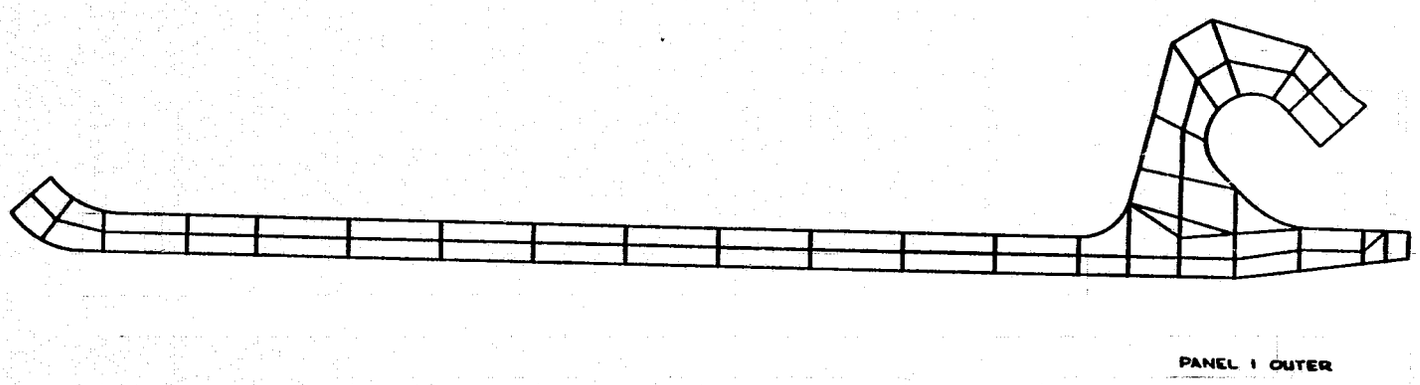


Figure 2. Typical Node Pattern for Liner Heat Transfer Calculations.

The two-dimensional GETREF code provided a valuable addition to the three-dimensional codes because the physical submodels and numerical techniques are more rigorous. Figure 3 is an illustration of a calculation from the GETREF code dealing with the initial swirl cup portion of a combustor where the flows are initially axisymmetric. For a typical full annular combustor, a model of a segment containing one fuel nozzle is modeled. Figure 4 illustrates a calculated flow field. The length of the arrows are proportional to the calculated velocities. Only recently have computer storage capabilities been able to accept a model with this much grid detail, see Figure 5. Little additional grid detail can be introduced at this time due to computer storage limits, but the cost of obtaining a converged solution with more grid could become prohibitive at present computer running time costs.

Some of the immediately obvious limitations of the existing 3-D internal flow codes that were recognized at the outset and influenced the assessments conducted in Phase I were, as follows:

1. With the grid shown in Figure 5 the so called "hybrid" numerics in the program involve the introduction of significant artificial or numerical diffusion. This produces mixing rates greater than specified by the turbulence model. Whenever the individual calculation cells have a Peclet number above 2.0, second order accurate central differencing numerics cannot be used and upwind differencing (first order accurate) is used which introduces significant numerical diffusion. Figure 6 shows that the cell Peclet numbers are below 2.0 in only isolated regions. Thus, without the ability to use much finer grids, the model inherently involves significant numerical diffusion for combustor flows. Claus, 1983[3], showed that even with much more detailed grid for a single dilution hole than possible for a real combustor, analysis inaccuracy results from the numerical diffusion.

2. In order to introduce noncyclindrical combustor walls, the stair-step technique must be used and this involves grid concentration in unneeded regions and crudeness in calculating film-cooled walls.

3. In the existing codes, the geometry-based swirl cup and fuel injection inputs do not correctly produce the initial fuel distribution for all combustors. Swirl cups have been tested at General Electric with minor geometry changes that make major differences in metal hot streaks and exit gas temperature patterns; these geometry changes would not result in any change in the model input unless some knowledge (external to the computer program) of the nature of the flows emerging from the swirl cups was available.

Accordingly, improvements addressing these deficiencies must be evolved before the codes become the effective design and analysis tools suitable for defining combustors with enhanced durability.

ORIGINAL PAGE IS
OF POOR QUALITY

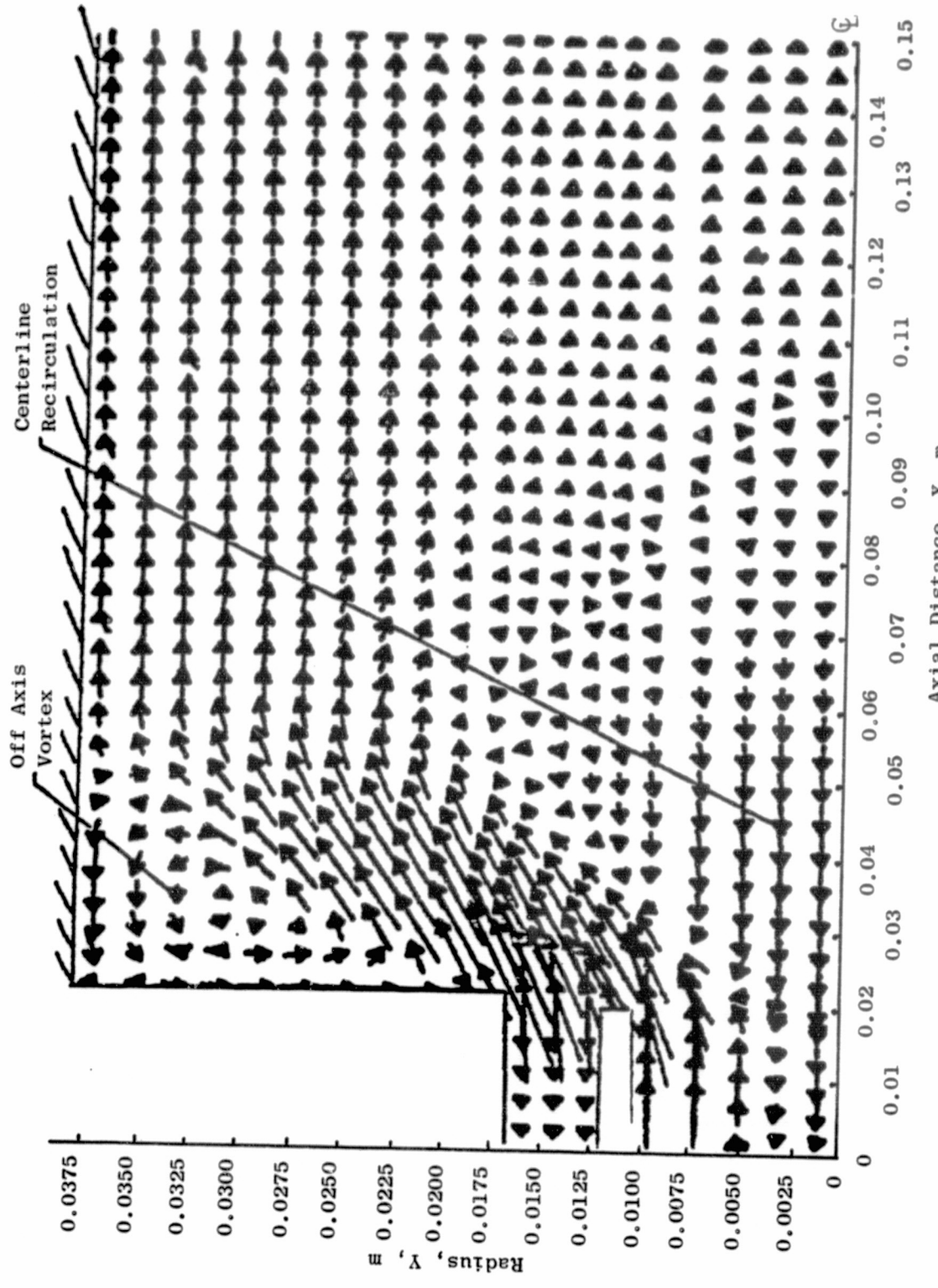


Figure 3. Velocity Field Calculation Using GETREF Code (2-D).

ORIGINAL PAGE IS
OF POOR QUALITY

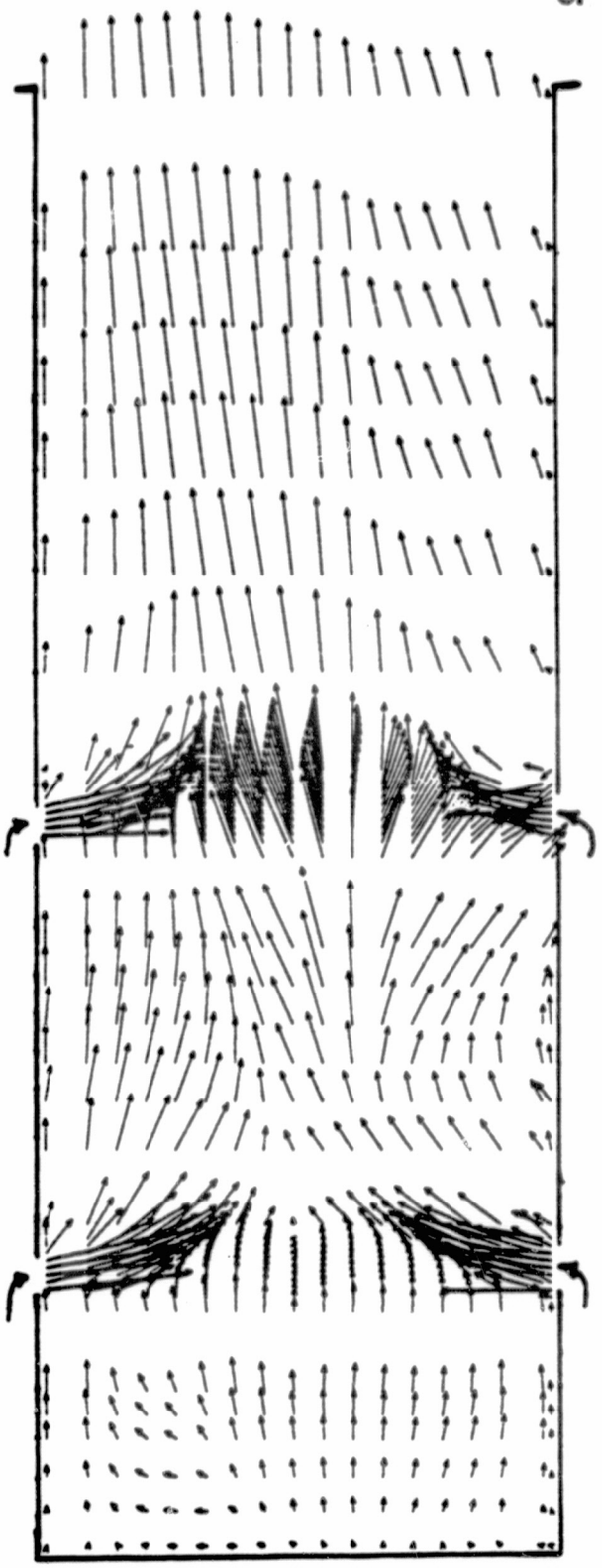
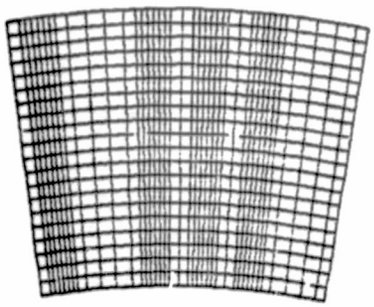
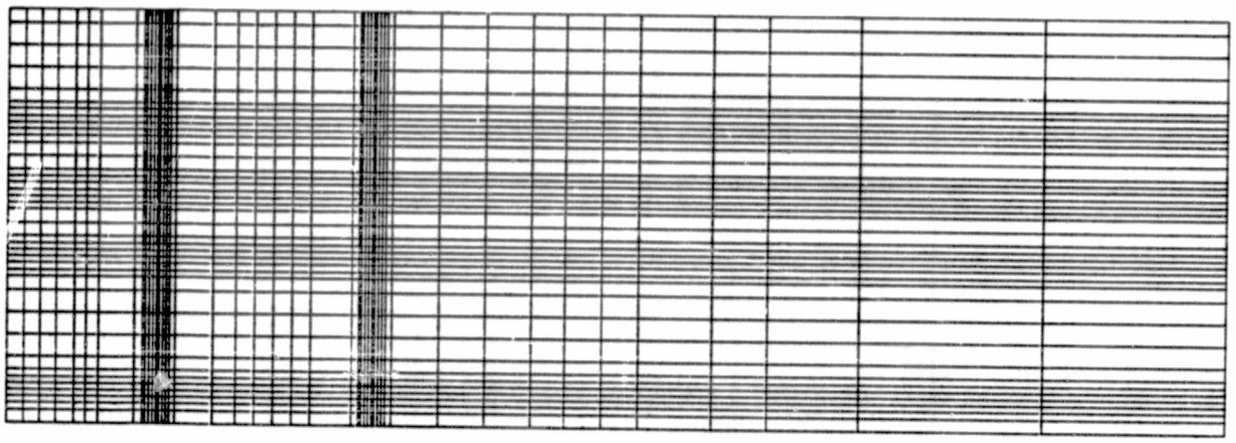


Figure 4. Calculated Velocity Field for a Combustor Using 3-D Elliptic Code (K Plane 15).

ORIGINAL PAGE IS
OF POOR QUALITY



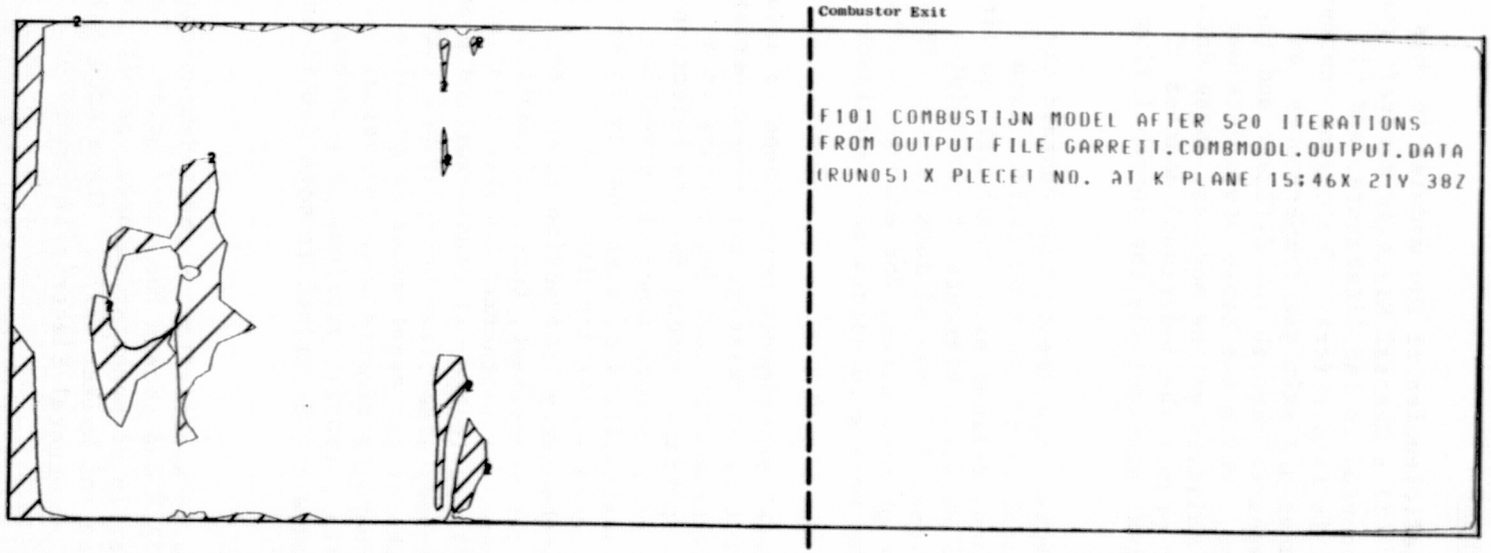
R-Theta Plane



X-Theta Plane (Outer)

Figure 5. Grid Used in 3-D Calculation of Combustor (See Figure 4).

- Shaded Regions Represent X Peclet Numbers Less Than 2



- X Peclet Number Contours in the Calculated Combustor Flow

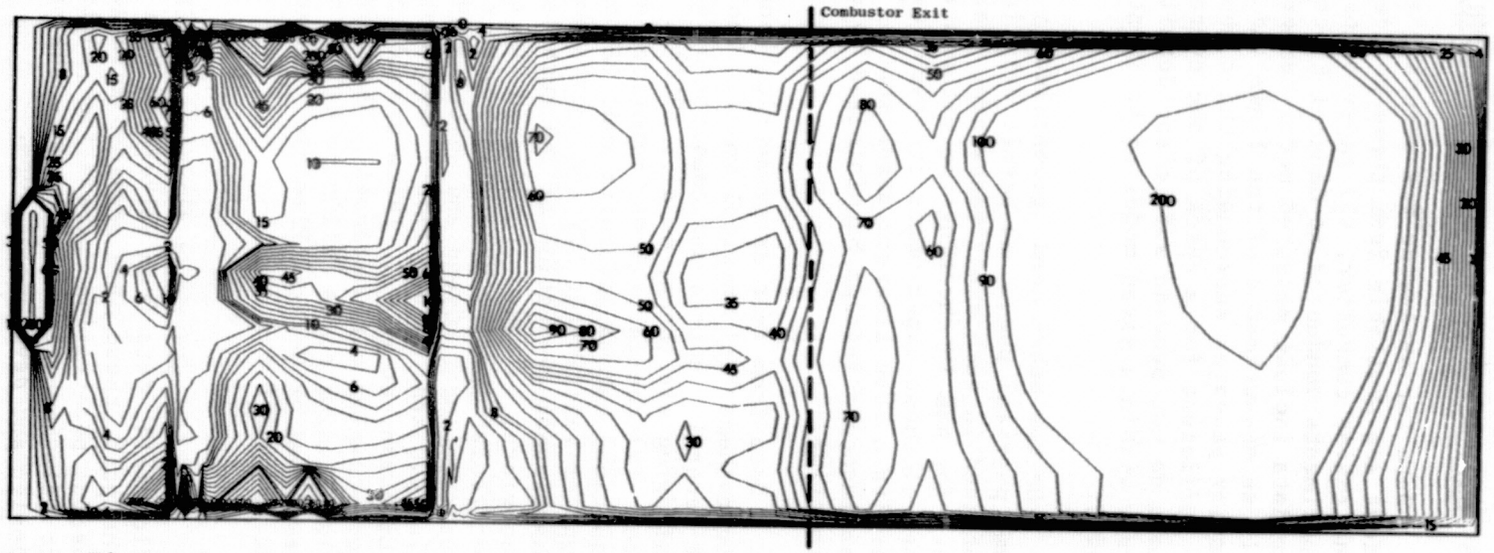


Figure 6. Calculated Peclet Number in the X-Direction from 3-D Combustor Calculation.

ORIGINAL PAGE IS
OF POOR QUALITY

3.3 DATA SELECTED FOR COMPARISON WITH MODELS

Data for assessing the accuracy or deficiencies of the modules in this effort are available from three sources: (1) a General Electric aircraft turbine engine combustor, (2) experiments reported in the literature, and (3) experiments conducted at General Electric in this effort. The engine combustor data include measured metal temperatures and exit gas temperatures, as well as measurements of the flows and pressures through the diffuser and the annular passages surrounding the combustor. While the temperature data may be sufficient for a check of the overall validity of the modules, these data alone do not provide sufficient detail to permit the individual sources of error within a given model to be identified, particularly the internal flow codes.

On the other hand, geometrically simpler experiments that contain the same physical phenomena permit detailed probing of the flow field. Data obtained in such experiments are, therefore, defined as a "benchmark" quality data for use in checking the mathematical physical elements of the modules. Most of these experiments are two-dimensional for ease of data taking. This permits a more accurate assessment of the physics since, for example, numerical inaccuracies can be minimized by using more grid points per coordinate direction.

Data from four axisymmetric "benchmark" experiments were chosen to assess the mathematical physical model. The first is an existing experiment performed at General Electric and consists of an axisymmetric fuel jet burning in a coflowing air (Lapp, et al., 1982[4]). The primary reasons for its selection are: (1) the removal of "numerical diffusion" errors since the governing equations become parabolic and; (2) the availability of high-quality laser doppler velocimeter LDV and spontaneous Raman scattering data. An unambiguous evaluation of the turbulence-chemistry interaction model can, therefore, be made. In addition to the jet experiment, three axisymmetric recirculating flow experiments were chosen: an isothermal annular dilution jet experiment (Green and Whitelaw 1980[5]), an isothermal double-swirled pipe flow (Vu and Golden 1980[6]), and a bluff-body stabilized non-premixed flame (Lightman, et al.[7]). These provide checks of the model under progressively more complex circumstances. The above four experiments were analytically simulated using codes (elliptic GETREF or its parabolic version, as relevent) developed at General Electric. These codes are described in more detail in Sections 6.0 and 7.1.

For simple round dilution jet flows in a crossflow, a three-dimensional flowfield, data from Walker and Kors 1973,[8] was chosen for examination. In the past, these data provided a large matrix of penetration data, permitting useful penetration correlations, Holdeman and Walker 1977[9]. These data and correlations have been used in the past at General Electric in combustor design and development work.

To provide data from more complex flowfields, a series of experiments was devised that involved progressively more complex flows beginning with a row of

jets in a crossflow and followed by opposing jets, alternate jets of different sizes, and a second row of dilution jets with the two row pattern simulating the dilution pattern of one General Electric combustor. These initial tests in the series were conducted with cylindrical inner and outer walls and a flat uniform inlet condition. The two available three-dimensional elliptic computer codes use cylindrical coordinates and, as received at General Electric, did not have capabilities for inputting combustor walls with a converging exit area as is present in actual General Electric combustors. This input capability to the INTFLOW program has been introduced at General Electric along with the ability to input swirler flow in an annular combustor. However, the experiments were devised to progress to provide data, without the complexity of noncylindrical walls and with simple uniform flow simulating the combustor dome flow, first with one row of dilution holes, then with two rows simulating the F101 dilution pattern. Tests with recirculation at the dome location and the two rows of dilution jets were introduced in two steps. First, a nonswirling dome flow was used with flow axisymmetrically diverging from the fuel nozzle position followed by a swirling flow. This last case incorporated a dome with counterrotating swirl cups like those used in a specific General Electric combustor. Then the configuration was tested with the true wall and dome contours of this combustor. All of the above tests were conducted without fuel injection. As in the Walker and Kors[8] data for the simple dilution jet, the approach flow was introduced at a different temperature than the dilution jets and detailed temperature measurements were the primary data. The experiments were then extended to include combustion, first with a gaseous fuel that avoids consideration of fuel drop atomization and vaporization, and then with a liquid fuel. The effect of film slots was introduced in these last tests. The data was supplemented with nonburning data taken on the swirl cup and fuel nozzle by itself.

3.4 PROGRAM APPROACH

The approach for assessing the modules already in general use at General Electric was accompished by relatively straightforward comparisons with available General Electric data.

The approach for assessing the Internal Flow Module was more complex and is discussed in the paragraphs below.

The assessment of the usability of the existing internal flow codes was conducted in two parts. The first part consisted of comparing "benchmark" quality data with the predictions from the axisymmetric elliptic research code (GETREF) and its parabolic version as applicable. These comparisons permit very methodical examinations of the mathematical techniques and the physical submodules. Based on the results, general conclusions regarding future module development were then drawn.

The second aspect of the assessment addressed the usability of the 3-D codes. In these assessments, the methodical assessment of numerical error and the physical submodules as conducted with the axisymmetric code GETREF was not attempted. The assessment approach was more the approach of the eventual

engineer user rather than the original programmer. The objectives, therefore, included observation of the ease of input, convergence rate, computing time, and of the accuracy of the results for a typical user. Primary focus was placed on the ability of the codes in two areas: (1) exit gas temperature prediction and (2) hot gas side inputs to the Heat Transfer Module.

For exit gas temperatures, it was postulated at the outset that, even if the primary combustion zone flow fields were poorly predicted a useful tool could still be develoepd if the dilution jet mixing process could be adequately calculated. An approximately correct dome flow analyses could be input and the subsequent dilution mixing calculation could be used to find the relative effect of some postulated dilution hole change.

In the case of the hot side inputs to the heat transfer calculation, again design usefulness could be expected even with somewhat limited accuracy of the internal flow calculation. First, the protection of the wall by the film cooling could still be dealt with by the present methods which involve the correlation of wind tunnel data for many film slots. Hence, only the hot gas side data just beyond the boundary of the film protection layer would be needed. It was recognized at the outset that the existing codes did not have the capability to predict flame radiation levels better than current estimating methods. The development of this capability and, hence, its evaluation was relegated to some future effort. Again, as in the case of the gas exit temperature patterns, an improved technique for inputting the air swirler and fuel flows into the dome would be needed to obtain this capability.

For real combustors, the basic flow field may be controlled much more by the pressure fields than by the turbulent shear layers prominent in simpler axisymmetric experiments in the literature. For example, the length of a recirculation zone is a critical parameter in the axisymmetric experiments. In a combustor, the recirculation zone length frequently ends just upstream of the first dilution hole location. Its length is predominantly controlled by the pressure field created by dilution holes rather than the turbulent mixing phenomena in the axisymmetric experiments. Thus, it may be possible to calculate reasonable combustor flow fields even though turbulent mixing is not being computed accurately; turbulence models with improved accuracy may not be essential.

In the effort herein it was not presumed that combustor models needed to be as accurate or as detailed in all aspects as was needed for good comparisons with the simplified experiments. Thus, the efforts with the 3-D models were to see if useful results for durability design and development could be achieved even though it was recognized that the node detail available would be inadequate by the standards explored for the axisymmetric experiments. The number of nodes utilized was up to the limits available on General Electric's computer, an IBM 3081D.

4.0 STRUCTURE OF THE REPORT

Section 5.1 describes General Electric's aerothermal model.

Section 5.2 indicates some of the benchmark quality data available in the literature from which four experiments were selected to help assess the model. Comments on modeling from the literature are also included. In addition, a discussion of engine and combustor component test data available at General Electric for assessing the capabilities of the other modules in general use is presented.

Section 5.3 describes the test program conducted at General Electric under this effort to provide additional data.

Section 6.0 discusses the approach in modeling internal flow field at General Electric. The discussions include simple test examples on numeric schemes that are possible alternates to the current hybrid scheme of central differencing and upwind differencing used in many current combustor models. Treatment of the turbulence/chemistry interaction, including the probability density functions, pdf, is included.

Section 7.1 presents results of 2-D model assessment compared to axisymmetric definitive benchmark experiments selected from the literature.

Section 7.2 compares results of the 3-D model assessment with benchmark experiments selected from the literature, and with experimental test data obtained as part of the Phase I program.

Section 7.3 compares results of the assessment of the aerothermal modules in general use at General Electric with selected General Electric test data.

Section 7.4 summarizes the assessments of the aerothermal model.

Section 8.0 discusses the overall conclusions obtained from the various assessment studies conducted. Recommendations for improving current aerothermal models are developed and presented in the form of a prioritized list.

Reference List contains the list of references used in this report.

Volume II contains a complete compilation of all experimental test data obtained as part of the Phase I effort.

5.0 AEROTHERMAL MODEL AND BENCHMARK DATA BASE DEFINITION

This section contains details of the combustor aerothermal model in use at General Electric. Included is a general description, details of the analytical methodology employed, and examples of predictions for each of the key modules comprising the overall model. Also provided in this section is a discussion of the data base assembled for use in assessing the model. The disucssion of the data base addresses experimental data available from the open literature, from General Electric component and engine tests, and from the experimental testing program conducted as part of the overall Phase I program.

5.1 OVERALL AEROTHERMAL MODEL DESCRIPTION

As previously illustrated in Figure 1, the overall combustor aerothermal model is comprised of an analysis model currently in general use and a detailed internal flow model which is still under development.

The analysis model, in general use, features four principle modules:

- Preliminary design module
- Inlet diffuser module
- Combustor flow distribution module
- Liner heat transfer module.

The methods employed in these modules have been highly developed over a long period of time. High sophistication from a fundamental standpoint as well as computerized treatments of empirical and semiempirical data correlations are incorporated into these methods. Because of the great complexity of internal combustor flow, the model in general use does not use detailed 3-D calculations to represent the internal flow field. This represents the model's most significant shortcoming.

In the model's current form, the individual modules are unlinked, and require a sequential stepwise input/output procedure to perform the entire analysis. A flowchart of this anlaysis model is presented in Figure 7.

The following discussion provides the details of the individual modules comprising the model. Contained within this discussion are descriptions of the modules identifying the computer programs involved, a description of the analytical methodology used in the modules, a detailed flowchart of the modules, and, where applicable, the predictive capability of the modules.

ORIGINAL PAGE IS
OF POOR QUALITY

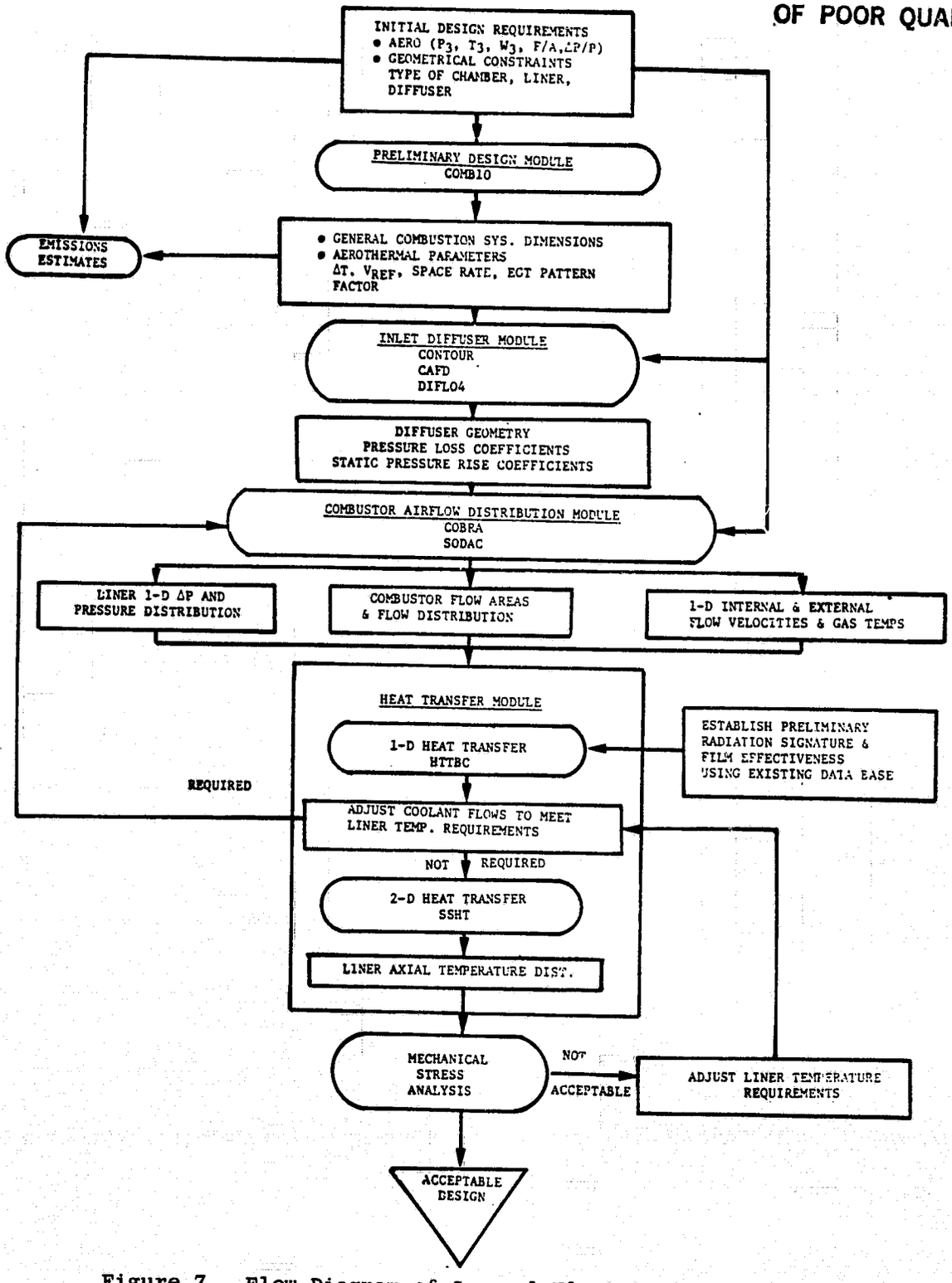


Figure 7. Flow Diagram of General Electric Aerothermal Model in General Use.

5.1.1 Preliminary Design Module

Description

The combustion system preliminary design module (COMBIO), calculates the overall dimensions and preliminary contours of the combustion system flowpath design. This computer program is used to generate the dimensions and coordinates required to calculate the key combustor design parameters and combustor performance estimates (Figures 8 and 9). This preliminary design estimate serves as a starting point for the more detailed design and analysis modules that are used to finalize the combustion system design.

Analytical Methodology

The calculations within the program are based on empirical data correlations that have been in existence at General Electric for many years. In the program values for reference velocity and space rate are varied to provide calculations for an array of design cases. A flowchart of COMBIO, the preliminary design module, is shown in Figure 10.

5.1.2 Inlet Diffuser Module

Description

The inlet diffuser module is comprised of several unlinked computer programs that perform three basic calculations. Prior to entry into the module, the preliminary overall sizing of the diffuser has been determined in the preliminary design module. This information is used along with the aerothermal requirements of the overall combustor design as input into the inlet diffuser module.

The initial calculation step involves generating the diffuser wall contours, and is performed by the CONTOUR program. The next step in the calculation procedure involves determining the streamlime distribution through the diffuser flowpath and potential flow calculations along the streamlines. Computer programs CAFD or STC are used to perform these calculations. The velocity distributions along the diffuser wall contours are obtained as a result of the potential flow calculations. The velocity distributions are used to represent equivalent straight diffusers that in turn are compared with the GE diffuser flow regime criteria to determine the flow separation stall margin of the design. In the final calculation step in the inlet diffuser module, the DIFLO program calculates predictions of the diffuser aerodynamic performance. A flowchart for the Inlet Diffuser Module is provided in Figure 11.

ORIGINAL PAGE IS
OF POOR QUALITY

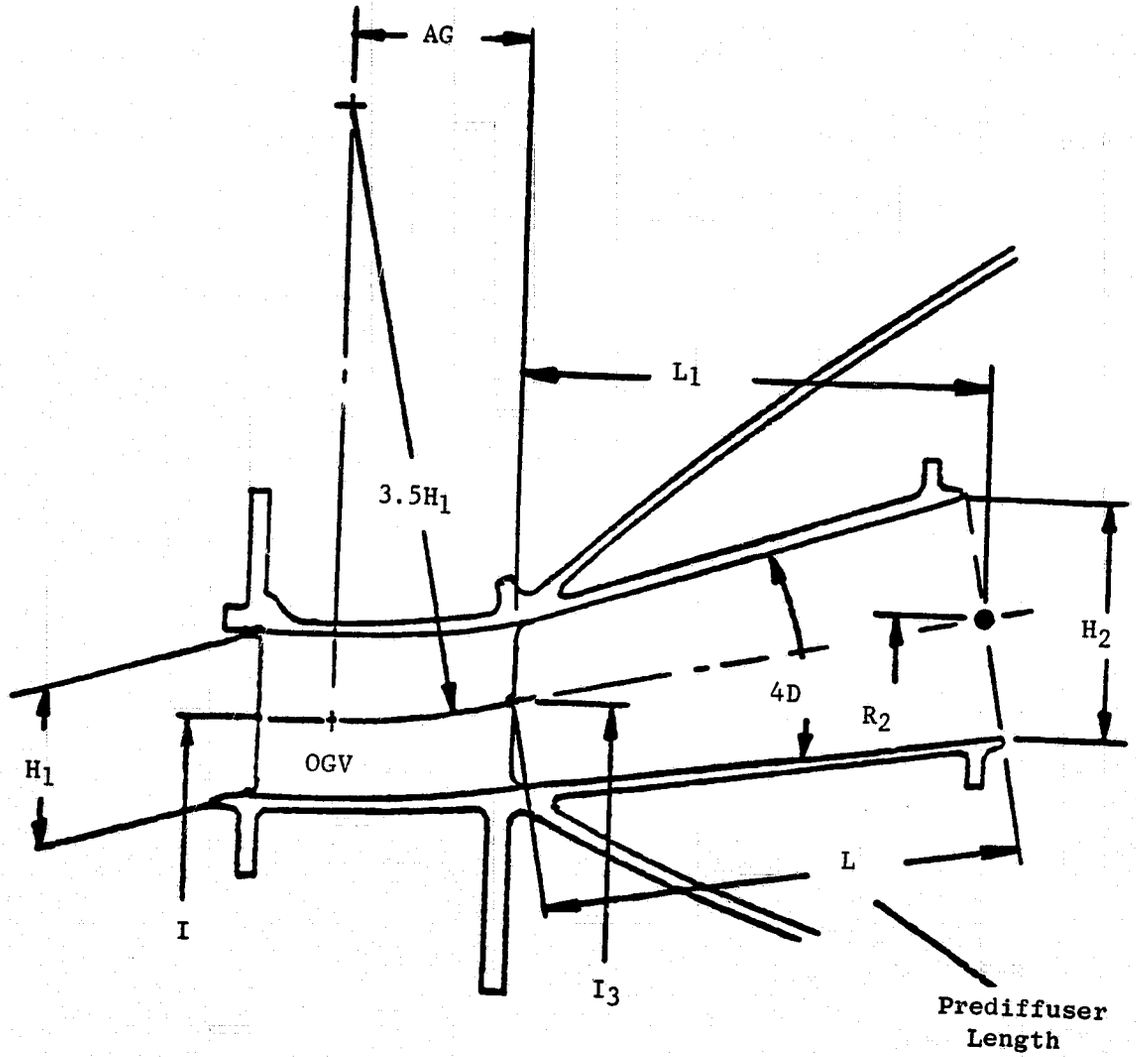


Figure 8. Prediffuser Preliminary Design Layout.

ORIGINAL PAGE IS
OF POOR QUALITY

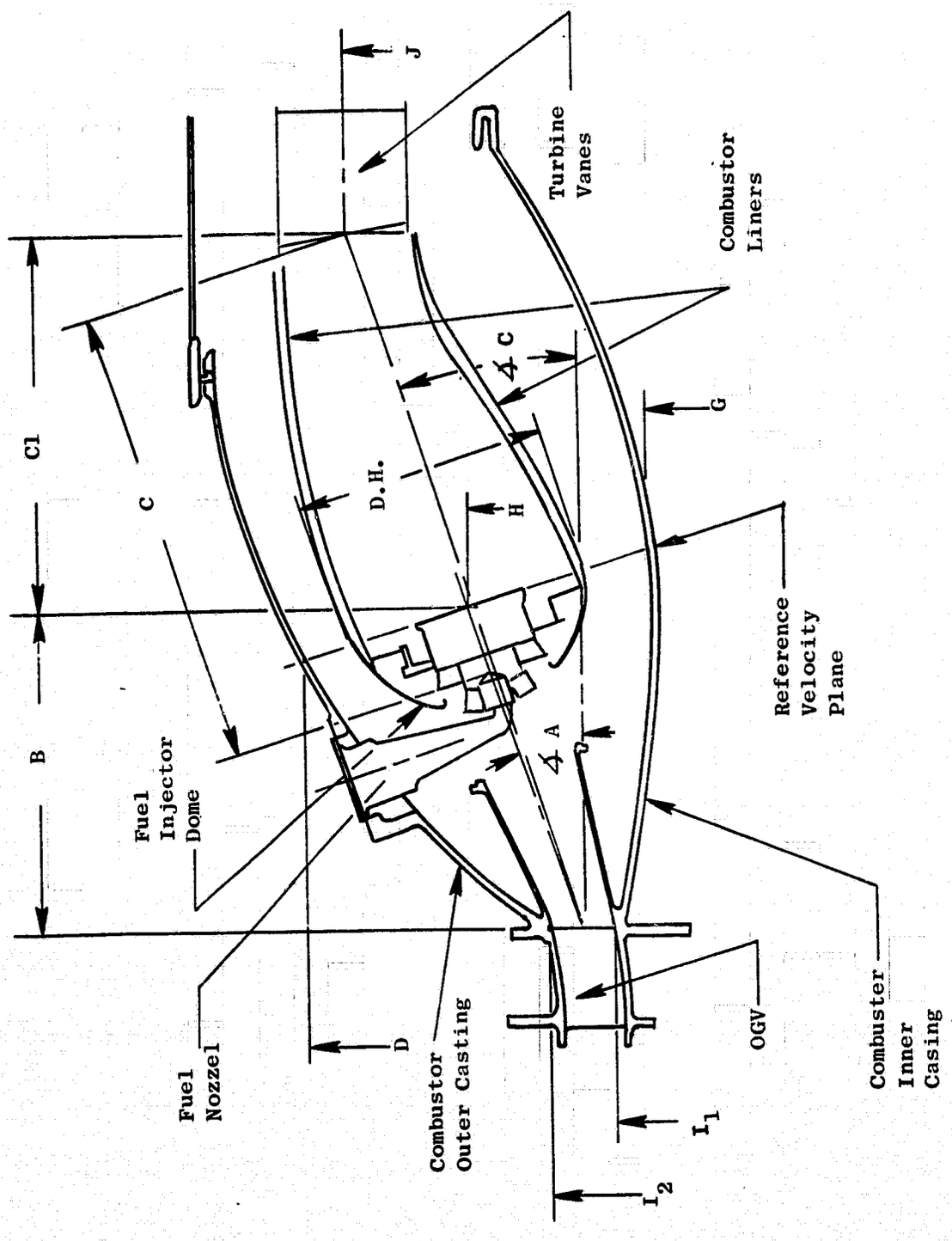


Figure 9. Overall Combustor Preliminary Design Layout.

ORIGINAL PAGE IS
OF POOR QUALITY

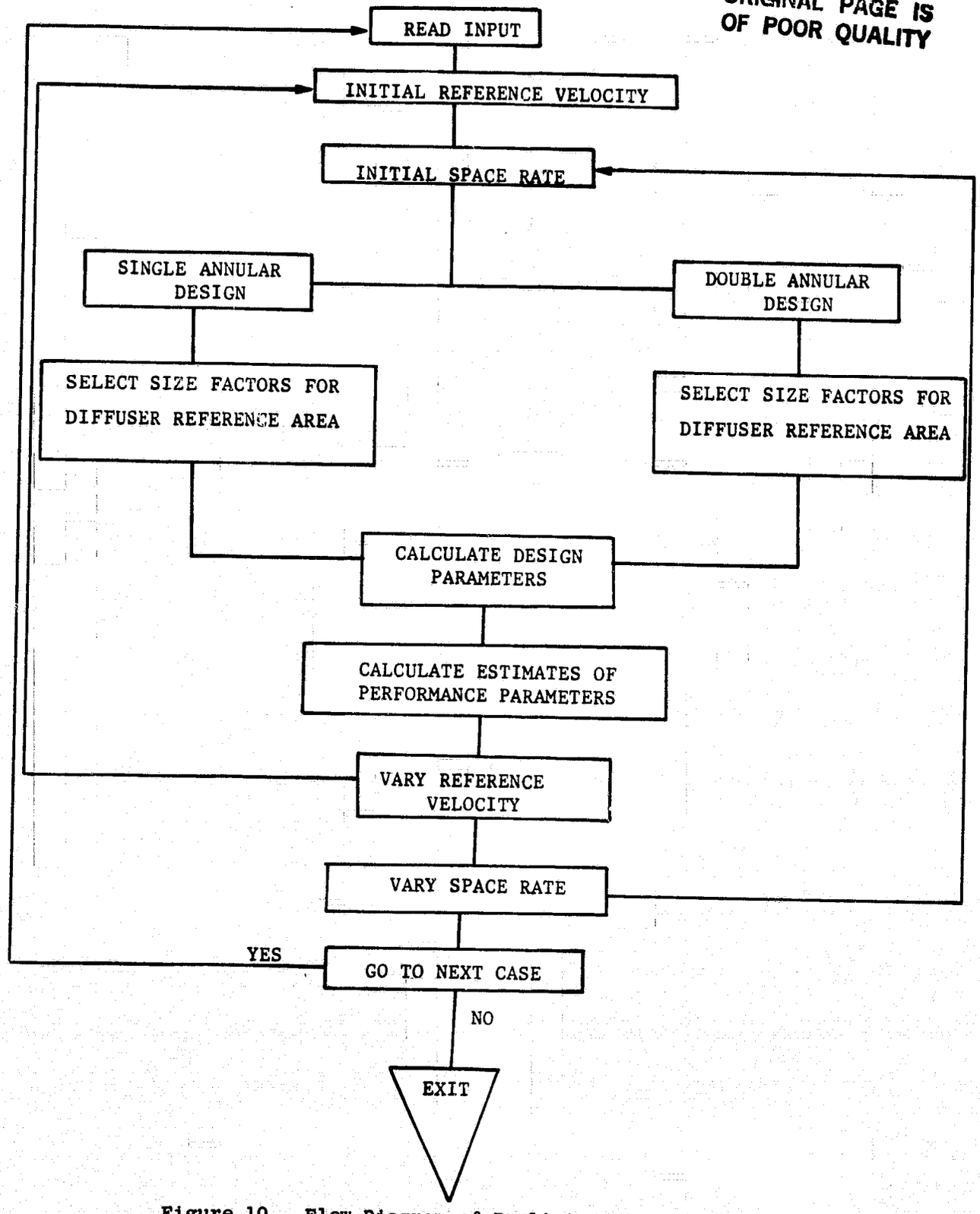


Figure 10. Flow Diagram of Preliminary Design Module.

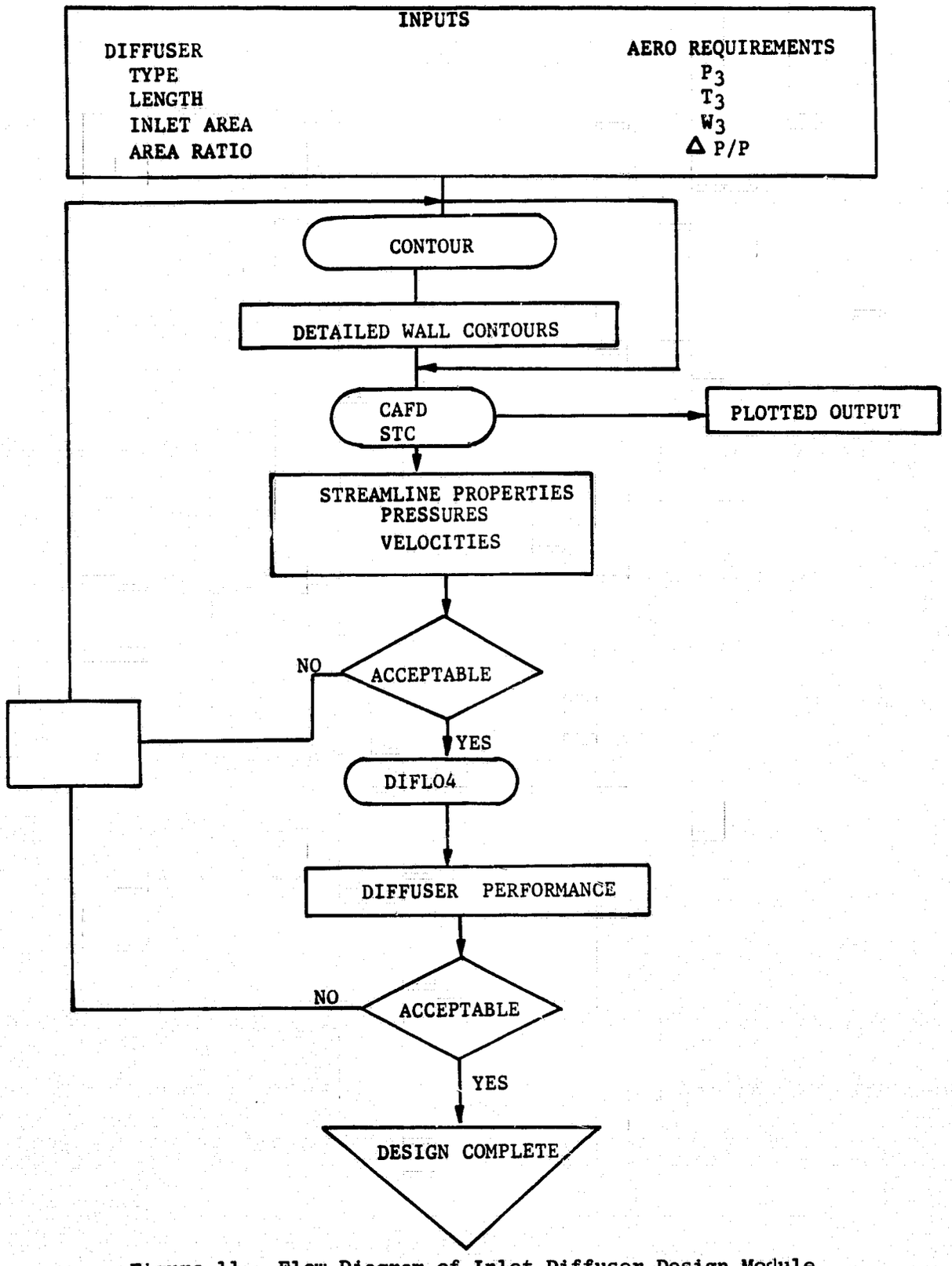


Figure 11. Flow Diagram of Inlet Diffuser Design Module.

Analytical Methodology

The CONTOUR program calculates the coordinates of the centerline of the passage or passages (in the case of multiduct diffuser designs), and, for a selected passage area distributions, it calculates the X and Y coordinates for the passage walls. For a specified number of calculation intervals, this program generates a table of passage centerline coordinates, the distance along the centerline, the centerline area distribution, and outer and inner wall coordinates. The program can handle multipassage diffuser designs.

The passage area distribution is based on a cubic equation with a one parameter shape factor which can vary from 0.500 for an almost linear distribution, to 0.667 for a "bell-shaped" distribution.

These contours can be used as input for the potential flow analysis calculation step with precise definition of the boundaries, which greatly improves the accuracy of the analysis. Also, the output from this program can be used to specify the diffuser wall coordinates for the mechanical design of the diffuser casings.

The CAFD program utilizes the streamline curvature solution technique to compute the circumferentially averaged flow properties. Thermodynamic relations are based on variable gas properties and are consistent with other General Electric data reduction and cycle analysis programs. Axisymmetric force fields and thickness blockage effects are used to represent the effects of struts and vanes. The annulus shape, circumferential vane or strut thickness distribution, and angle distribution are specified. Calculation stations can be arbitrarily shaped. Many options are available for the user to specify the vane row turning and loss. These include design options such as angular momentum and loss coefficient, and analysis type options such as flow angle and loss coefficient.

The cross stream momentum equation is used to calculate velocity gradient as a function of (1) total enthalpy and entropy distribution as determined from "user" input and application of the energy equation, (2) blade force effects determined from blade geometry and work distribution; and (3) local slopes and curvature of the streamlines. The slope and curvature are determined by a curve fit of the assumed streamline positions. This curve fit may be specified as a rotated-spline, or a combination of a spline and a three-point parabola.

An initial set of streamline positions are curve fit to find slopes and curvatures. the cross stream momentum equation and the continuity equation are applied at each calculation station to determine the shift in the streamline positions. These indicated shifts are based on fixed values of slopes and curvatures. Moving the streamlines by the indicated shifts would result in gross overcorrection and the iteration would diverge. Therefore, the actual streamline movements are determined by a second order correction equation. The driving force for this equation is the indicated shifts found

in the flow balance. The actual streamline adjustments, as calculated by the correction equation, are applied without damping. The new positions are used to repeat the above loop. Convergence occurs when the maximum indicated difference is acceptably small. The convergence rate of this system is found to be quite rapid.

The major limitation of the CAFD program, as applied to combustor inlet diffusers, is that constant pressure free streamlines cannot be calculated. Thus, free streamlines downstream of the dumping point of step type diffusers are not accurately simulated.

The STC program (Ferguson and Keith 1975[10]) is a very comprehensive compressible, inviscid, potential flow analysis program developed under NASA sponsorship. Within the program an iterative technique is used to solve planar or axisymmetric flow fields. The method utilized to compute the flow field is the Streamtube Curvature Relaxation technique.

The STC approach utilizes a number of confluent streamtubes, with slightly different properties that are added together to obtain the total flow in the channel. Each streamtube is handled in much the same way as is the one streamtube in the one-dimensional problem. In the limit, as the size of the individual streamtubes approaches zero, the STC method satisfies the inviscid equations of motion exactly.

The solution method is an extension of the streamline curvature method, and is briefly described as follows: First, a crude grid of streamlines and orthogonal lines is assumed. Second, the curvature of the streamlines at each of the grid points is evaluated. Third, the momentum equation is integrated along a line normal to the streamlines to obtain velocity, and the continuity equation is integrated to determine the "correct" streamline positions (for the assumed curvature field). Fourth, an adjustment (Δn) is computed by considering: (1) the difference between the computed and assumed streamline positions and (2) the effect of the implied curvature modification in the integrated momentum equation. Finally, the streamlines are repositioned by the Δn values.

Because the movement of any one grid point alters the velocity at nearby points through a change in curvature, it is highly desirable to account for these interrelating point adjustments simultaneously. The utilization of a simultaneous solution procedure, employed here, is not part of the classical streamline curvature method.

The streamline curvature method is extremely powerful as indicated by the following features:

- No additional complexities arise when the flow is rotational.
- The slip line between an exhaust jet and the external flow can be handled precisely. (The procedure is to consider two coincident streamlines. Their position and pressure are the same; their velocity and stagnation properties may be different.)

- The streamline/orthogonal line grid provides a mapping of the flow field into a rectangular domain. This is helpful from the standpoint of computer program organization.

The STC program has been designed to:

- Handle multiple streams.
- Place grid points at locations in the flow field where they are needed, as determined by local variations of the dependent variables.
- Allow external flow analysis by incorporating matched near field and far field solutions. The far field solutions are obtained analytically utilizing small perturbation theory.

The operations performed by the STC program many be outlined as follows:

1. Define the flow regions and locate (approximately) the "primary" orthogonals and the streamlines which divide the internal and external flows.
2. Refine the grid as required by inserting additional streamlines and orthogonal lines between those already existing.
3. Compute the streamline angle and curvatures.
4. Compute the orthogonal line angles and move the grid points along the streamlines to obtain orthogonality.
5. Compute the velocities on the "far field" boundary.
6. Adjust the flow rates in the exhaust streams, if any, to meet the calculated choking flow rate.
7. Integrate along each orthogonal the momentum and continuity equations.
8. Determine if the streamline positions are within a "rough tolerance". If so, return to Step 2 for additional grid refinement (unless grid refinement limits have already been reached). Otherwise, continue to Step 9.
9. Determine if the streamline positions are within final tolerance. If so, jump to Step 13. Otherwise continue to Step 10.
10. Set up the matrix equation for the streamline correction, Δn.
11. Solve the matrix equation.
12. Modify the streamline positions by Δn, and return to Step 3.

13. Calculate and print the output quantities; then return to Step 1 for the next case, if any.

The first operation includes reading the input for a description of the geometry and flow properties. The first step in the programmed logic is to develop a table for orthogonals or calculation stations for each of the several flow regions. The regions are determined so the calculation can proceed from upstream to downstream. The boundary of each region is defined as a primary orthogonal. The initial grid developed contains only the primary orthogonals and the double streamlines which separate the various streams.

The iterative sequence is to start with a crude grid, as noted above, and to repeat Steps 3 through 12 until the flow balance error is small. This is often accomplished in one or two iterations. The grid is then refined to the next level, and the field reconverged. The refinement/convergence process is continued until the grid refinement criteria is satisfied, or alternately, until storage limits are reached. Greater detail into the analytical methodology used in the STC program can be found in Reference 10.

The DIFLO program calculates total pressure losses and static pressure rise coefficients in each passage of the combustor inlet diffuser. An overall, mass-weighted pressure loss for the diffuser system is also determined. These losses include prediffuser momentum losses, based on General Electric straight annular diffuser test data; flow dumping losses, based on General Electric bench-side test results for simular step configurations; and parasitic drag losses of struts, mounting supports, and fuel nozzle systems. The losses in the prediffuser section are adjusted to account for velocity profile effects. Momentum mixing losses along free streamline boundaries are also included.

Predictions of combustor inlet diffuser pressure losses are based on diffuser test data. A large number of full-scale, full annular diffuser test programs have been conducted by General Electric over the past 25 years for a variety of different combustor inlet diffuser configurations. The extensive data base accumulated from these test programs and from other sources has been used to develop the DIFLO computer program.

Predictive Capabilities

Diffuser performance predictions obtained from the inlet diffuser module are generally in good agreement with measured diffuser test data. The comparison between predicted and measured pressure losses shown in Table I for three current GE combustion systems serves to illustrate the module's performance predictability. Greater accuracy in diffuser pressure loss predictions could be achieved by a more detailed modeling of the loss mechanisms present. Airflow testing of full-scale annular models of the diffuser selected design is still necessary to provide final verfification of the predicted pressure losses and evaluate the effects of distorted inlet velocity

profiles and engine bleed flow requirements which are difficult to accurately analyze with potential flow models.

Table I. Predicted Versus Measured Diffuser Δp/p.

		Outer Passage	Center Passage	Inner Passage
GE29 Single Passage	Predicted	3.11	1.82	2.84
(M_3 = 0.43)	Measured	3.08	1.82	2.85
GE23 Single Passage	Predicted	2.59	0.89	2.45
(M_3 = 0.34)	Measured	2.61	0.74	2.10
CF6-80 Single Passage	Predicted	2.03	0.64	1.22
(M_3 = 0.28)	Measured	2.06	0.29	0.89

5.1.3 Airflow Distribution Module

Description

The airflow distribution module (COBRA), is a computer analysis program that determines the one-dimensional aerothermodynamic characteristics of a jet engine combustor. It provides a quick and economical method for computing the pressure and airflow distributions for a variety of combustor configurations. A flowchart of the COBRA program is presented in Figure 12.

COBRA contains a general building block format which permits application flexibility without regard to the specific configuration of the combustor. COBRA is structured to contain a set of selectable options for the programmer so that, as knowledge of aerothermodynamic systems is obtained, different types of combustor stations, additional types of pressure loss equations, and new types of airflow selections can be inserted rapidly into the existing program files.

COBRA was developed using the GEBOSS Data Management System to take advantage of two of its main features: file storage and file editing. By using GEBOSS, all the source codes, data tables, and construction information are contained on one file called a Program File. This provides the user with a means of editing any of these files and greatly reduces the work of transferring and maintaining COBRA at other installations.

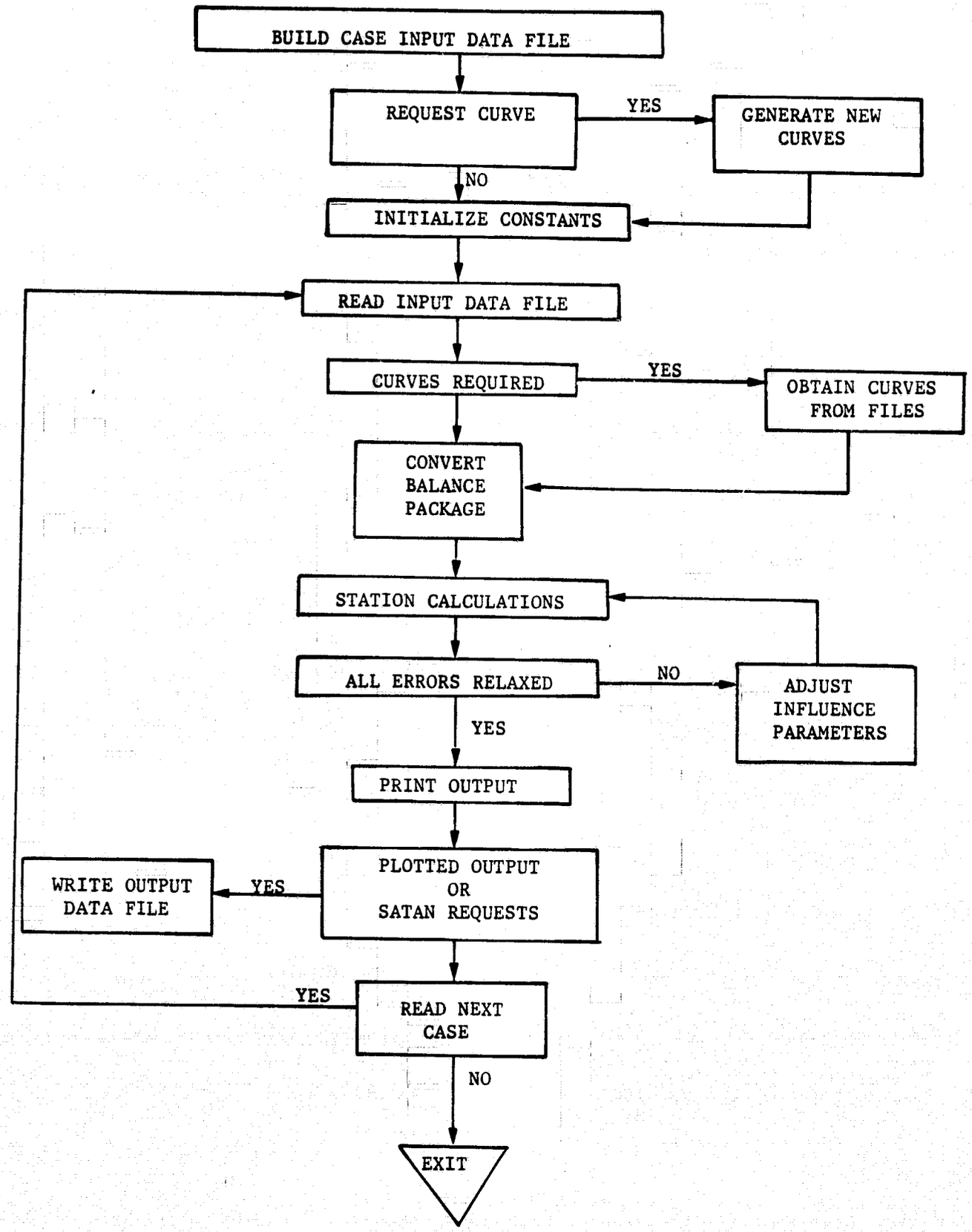


Figure 12. Flow Diagram of Distribution Module.

Analytical Methodology

The COBRA program uses one-dimensional compressible flow relations. The basic procedure for an analysis of a combustor configuration with the COBRA program is characterized by the following steps:

- Obtain a flowpath layout of the combustion system from the flowpath module and establish the station network as shown in Figure 13.

- Identify the station type for each station in the model network. Definition of each station type are provided below:

  - Type 1: Normally used in region of combustor upstream of swirl cup or fuel injection plane. Options in the station allow for airflow selection, pressure drop selection, and hole flow.

  - Type 2: Liner cooling hole flow station designated in a nonburning pathway. Options are hole flow, airflow selection, and pressure drop.

  - Type 3: Flame pathway cooling flow station. Options are airflow selection and pressure drop. Fuel-air ratio and temperature rise are computed automatically.

  - Type 4: Liner dilution hole flow station designated in a nonburning pathway. Options are hole flow, airflow selection, and pressure drop.

  - Type 5: Flame pathway dilution hole station - inserted one slice downstream of companion skirt dilution hole flow station. Options include airflow selection, momentum pressure loss due to dilution flow entering flame passage, and other pressure drops. Fuel-air ratio and temperature rise are computed automatically.

  - Type 6: Liner cooling and dilution hole flow station designated in a nonburning pathway. Options include separate cooling flow and dilution flow hole selections, airflow selection, and pressure drop.

  - Type 7: Flame pathway cooling and dilution - inserted one slice downstream of companion skirt station. Options include airflow selection, momentum pressure loss due to dilution flow entering flame passage and other pressure drops. Fuel-air ratio and temperature rise are computed automatically.

- Determine the required matrix for the stations, splices, and pathways (see Figure 14). These station types are assigned appropriate locations on the flowpath layout and are therefore arranged in a pattern (rows). The program proceeds through the lattice by computing from

ORIGINAL PAGE IS
OF POOR QUALITY

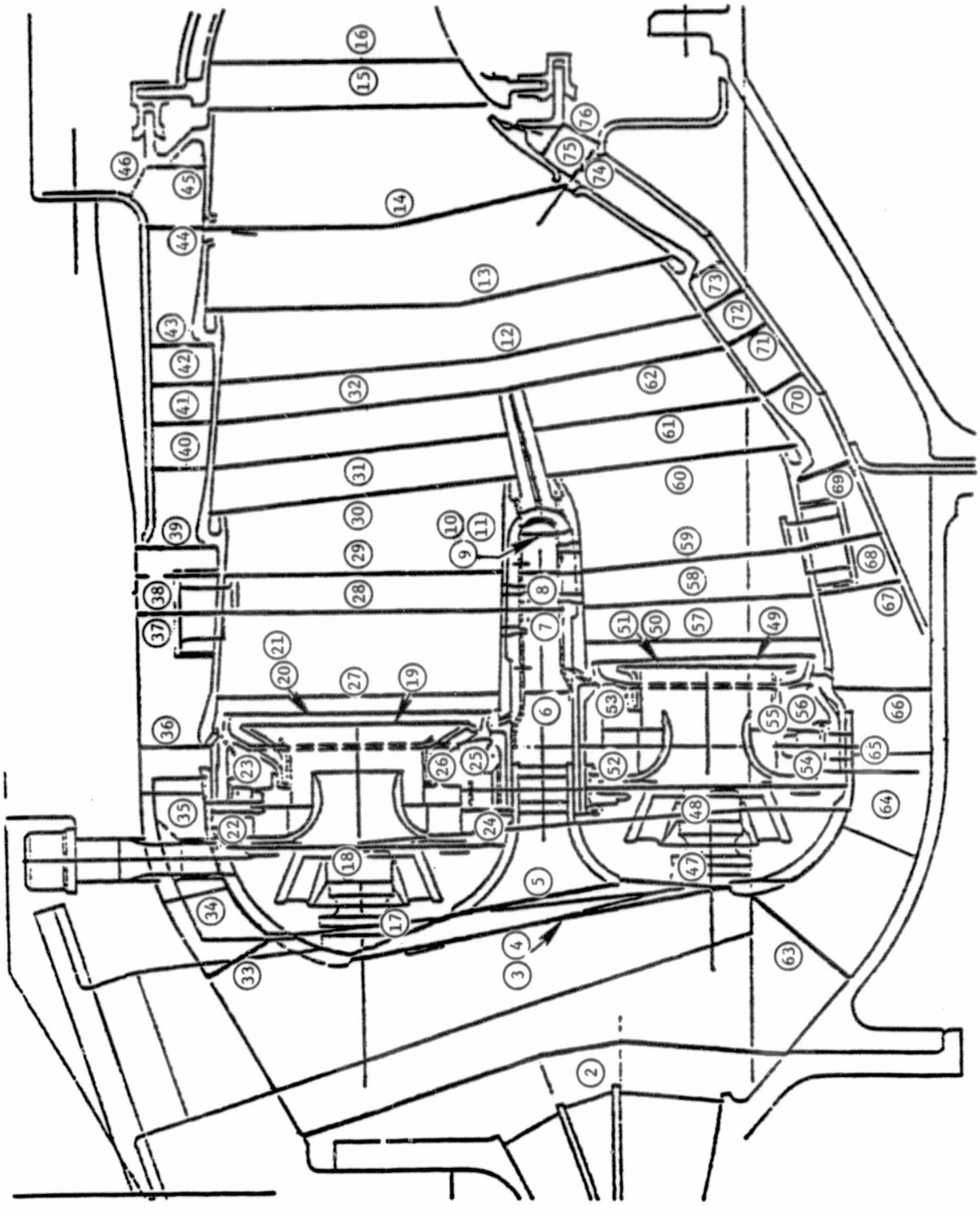


Figure 13. Station Network Layout for Airflow Distribution Module.

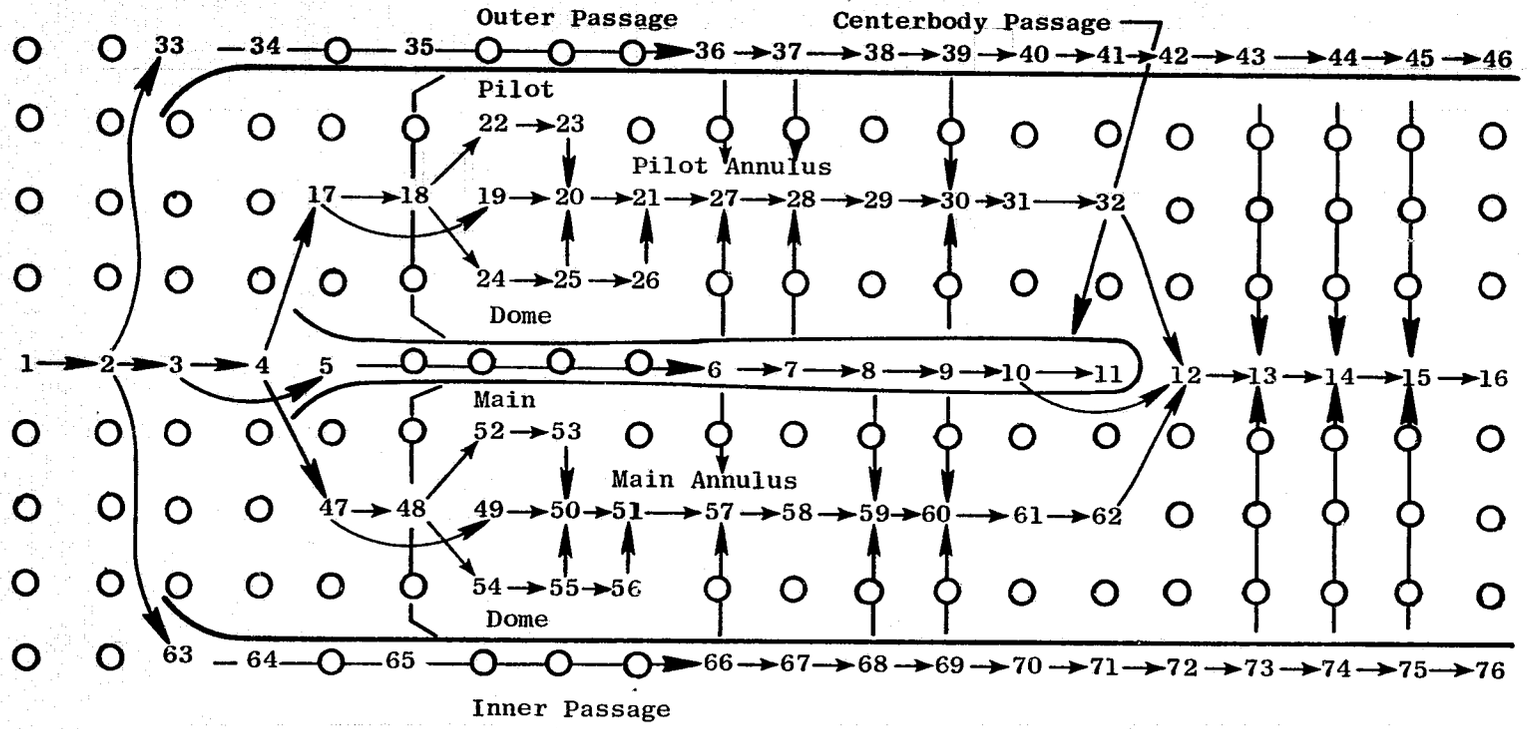


Figure 14. Airflow Distribution Module Station Matrix and Flow Splits.

ORIGINAL PAGE IS
OF POOR QUALITY

ORIGINAL PAGE IS
OF POOR QUALITY

top to bottom on the slices. For program growth purposes, during the initial setup of lattice, slices may be placed through areas of the combustors where cooling or dilution stations may be needed at a future date.

- For each station, select the proper data array options in the program to determine airflow, pressure loss, and airflow splits. Options available for each station type are shown in Table II.

Table II. Options Available for Types of Stations.
(Options Designation Indicated by Circled Number)

Station Type	1	2	3	4	5	6	7
Option Code		1 ΔWC		1 ΔWD		1 ΔWC	
(1)	W	2 W	1 W	2 W	1 W	2 W	1 W
(2)	TTO	3 TTO	2 TTO	3 TTO	2 TTO	3 TTO	2 TTO
(3)	ΔP	4 ΔP	3 ΔP	4 ΔP		4 ΔP	3 ΔP
					3 ΔPM	5 ΔWD	4 ΔPM
						6 ΔP*	
(4)	ΔWF_M	5 ΔWF_M	4 ΔWF_M	5 ΔWF_M	4 ΔWF_M	7 ΔWF_M	5 ΔWF_M
(5)	R_{CHW}	6 R_{CHW}	5 R_{CHW}	6 R_{CHW}	5 R_{CHW}	8 R_{CHW}	6 R_{CHW}
(6)	ΔP_{FN}	7 ΔP_{FN}	6 ΔP_{FN}	7 ΔP_{FN}	6 ΔP_{FN}	9 ΔP_{FN}	7 ΔP_{FN}
(7)	ΔP_{SP}	8 ΔP_{SP}	7 ΔP_{SP}	8 ΔP_{SP}	7 ΔP_{SP}	10 ΔP_{SP}	8 ΔP_{SP}

Definitions:

W	- Weight flow calculation for station.
WC & WD	- Calculation of cooling or dilution hole flow.
TTO	- Total temperature option.
P	- Pressure drop calculation.
PM	- Momentum loss calculation.
WF_M	- Flow through hole, i.e., fuel nozzle hole in a cowl.
R_{CHW}	- Recalculate hole flow (cooling or swirl cup, etc.) when J2 or J6 station is a cooling path station adjacent to initial flame path station. Used only on station located on flame pathway.
P_{FN}	- Passage pressure drop due to a fuel nozzle stem or mounting pin.
P_{SP}	- Passage pressure drop due to an airflow strut in passage, both profile drag and interference drag loss in calculated.

- Other inputs required include geometric data, such as cross sectional area; hole areas; hydraulic diameters; length/hydraulic diameter ratios; compressor discharge conditions; hole flow coefficient curves; and airflow entry angle curves. These curves are obtained from the extensive data base accumulated at General Electric.

- Sufficient boundary conditions must be supplied to direct the program in obtaining the solution. These constraints are applied at stations where major airflow splits occur, specified pressure conditions are to be satisfied, or at the end stations of flowpaths where the airflow is required to be zero. The user must identify those parameters pertinent to his combustor model, and construct, for each of the selected parameters, a constraint equation. He must also associated with each constraint equation a parameter (INFLUENCE PARAMETER) which, when changed, will produce the greatest change in the constraint equation. COBRA allows the user to construct the constraint equation and identify the influence parameters through case input. The program can handle up to 14 constraint equations and their related influence parameters.

There is an option in the program that allows the program to adjust dilution hole area, cooling hole areas or both simultaneously, until the desired pressure loss is obtained. The program accomplishes this by comparing the overall pressure loss of the first balanced case with the desired pressure loss. If the two pressure losses are not the same, then a new case is run using a pressure loss correction.

Runs are repeated until the desired loss is obtained then the final run is printed out along with the new hole areas required.

In the COBRA program it is not necessary to compute and read in changes of temperature level due to the combustion of the fuel. Temperature rise curves based on local fuel-air ratio and compressor discharge temperature are part of the program. In a flame pathway and at each station where fuel-air ratio is computed, the program determines the ideal temperature rise and adds it to compressor discharge temperature. Two sets of curves are available, one set for pressure levels below 20 psia, and one for pressure levels above 20 psia. If combustion efficiency is not put in, a value of 1.0 is used by the program.

An option for calculating penetration at aft dilution holes is also available in the COBRA program. The program uses empirical correlations of momentum ratio versus penetration distance generated from GE test data.

To provide increased insight into COBRA, the following information deals with specific methods for determining airflow and pressure drop.

Airflow is initialized at the starting (compressor discharge) station simply by listing it as an input in the general section of the deck. Thereafter, airflow entering any station is determined as a decimal fraction of

the airflow of any other station or stations. In this way, flow splits can be designated where desired and flow from two or more stations can be consolidated.

When liner cooling or dilution holes occur, the program determines the flow coefficient from an input curve of coefficient versus pressure parameter. Since there is room for a number of these curves, a liner having a number of different types of openings may be analyzed. These curves may be changed or replaced according to the user's discretion.

Pressure loss considerations featured in the COBRA program include internal (one-dimensional) mixing losses due to momentum exchange, parasitic losses, and losses due to heat addition. These losses are represented by subroutines contained within the main program, and are automatically calculated depending on the type of station and option involved. In the case of parasitic losses, drag and area coefficients for the particular obstruction must be included in the input data. In addition to these losses, a number of other pressure loss options are available through option input. These include:

- Diffuser efficiency

$$\Delta P_T = (1-\eta_D)\ (P_{S_2}\ (IDEAL)-P_{S_1}) \qquad (1)$$

- Frictional losses

$$\Delta P_T = 4f\ (L/D)Q \qquad (2)$$

- Coefficient of pressure (Cp). This option is usually used in a model when specific test data is available.

- Percent of J8 total pressure. This option if primarily used to define pressure losses from station to station known from measured test data, but the specific mechanism is not known.

- Turning losses

$$\Delta P_T = Q_2(TURN)\ Q_1 \qquad (3)$$

- Pressure loss due to ram across a carburetor cup

$$P_{T_1} - P_{S_2} = R/2g\ (W_1/Ae)^2\ (T_{S_1}/P_{S_1}) \qquad (4)$$

- Pressure loss due to pressure diferential across a swirl cup

$$\Delta P_S = R/2g\ (W_1/Ae)^2\ (T_{S_1}/P_{S_1})$$

$$P_{T_2} = P_{S_2}\ (T_{T_2}/T_{S_2})^{\gamma/\gamma-1} \qquad (5)$$

- Pressure losses due to screen or profiler placed across the flowpath.

- Percent of any J^{th} station. This option is primarily used to specify a level of pressure at a given station.

In performing the calculations, the program proceeds through the matrix and at each station performs the required calculations. A typical working layouts is shown in Figure 15. The J1 through J8 designations indicate stations adjacent to the working station and represent an important key to the flexibility provided by COBRA (Figure 16). As an option, J1-J8 may be constructed automatically by the program, or this selection may be preempted by the user and arbitrary stations designated.

COBRA uses a special subroutine to achieve the flow balance. This subroutine is a simultaneous, multiparameter iteration technique. The balance package is reduced to a set of independent variables and error terms. The subroutine increments each of the independent variables and calculates the value for each of the error terms. The changes of the errors and independent variables are used to form a matrix of the partial derivatives. This matrix is then used to calculate the variables at the next station.

Prediction Capability

The COBRA analysis program has been used extensively in the development of combustion systems for the CF6 engine family, the CFM56 engine family, and recently in the development of the NASA/GE Energy Efficient Engine (E^3) combustor. Calculated flow parameters from models of these combustors have provided accurate predictions which have been very useful in these development efforts. A comparison between the predicted airflow distribution from a COBRA model of the E^3 double-annular development combustor Mod I configuration, and the airflow distribution calculated from measured data is presented in Table III.

5.1.4 Combustor Heat Transfer Module

Description

The combustor heat transfer module is comprised of two unlinked computer programs: HTTBC and SSHT. Both programs consider only steady-state heat transfer. The preliminary calculations are based on one-dimensional procedures and are performed in HTTBC. This program is used along with the airflow distribution module in an iterative manner until the bulk liner metal temperature requirements are satisfied. Upon completion of this task, two-dimensional calculations are made to provide both maximum and nominal 2-D temperature distributions. This provides the required information to estimate the 3-D circumferential effect which is then input to the stress and life analysis procedures. These 2-D calculations are performed in SSHT. A flowchart of the heat transfer module is provided in Figure 17.

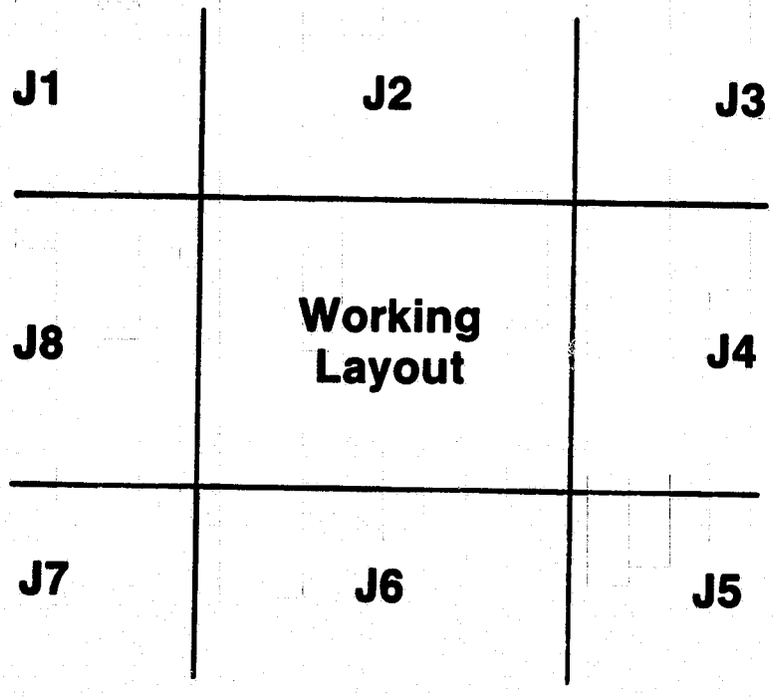


Figure 15. Airflow Distribution Model Typical Working Station Layout.

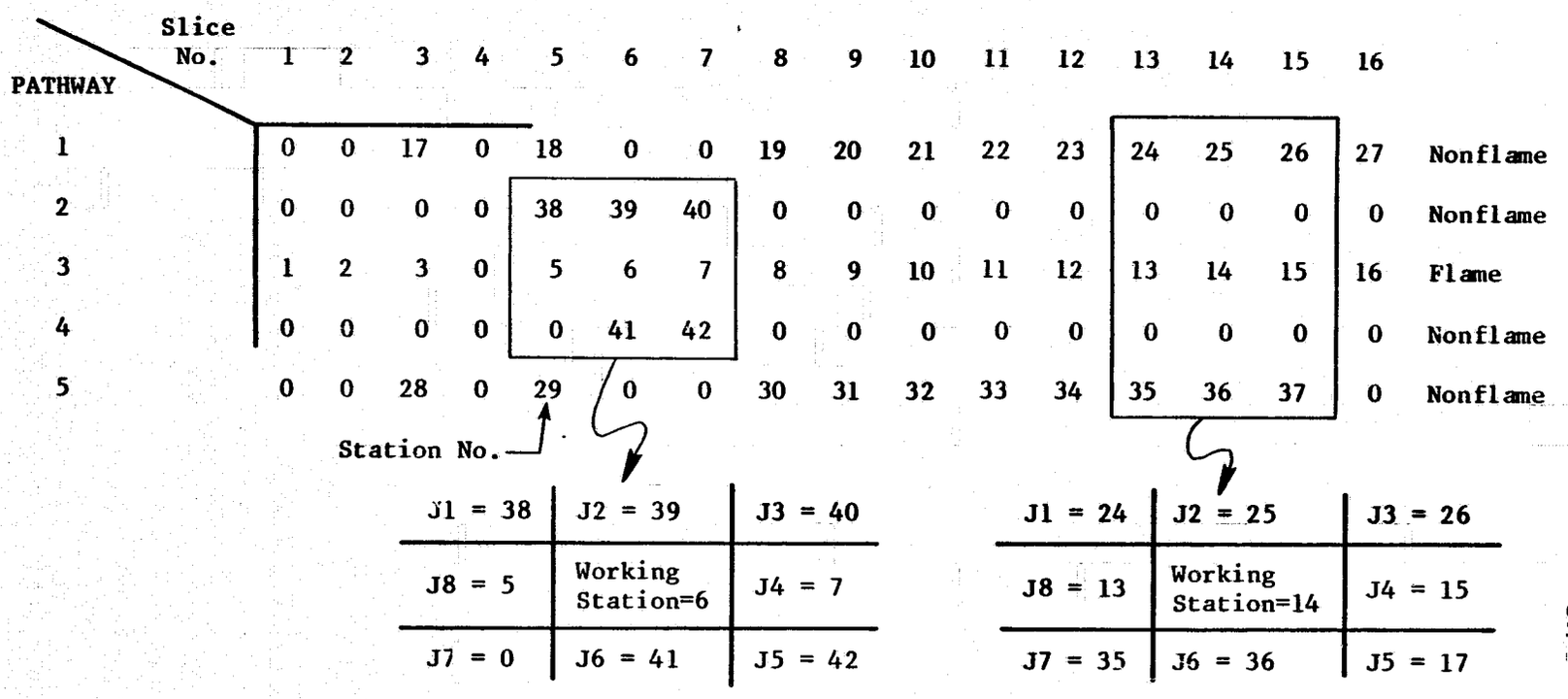


Figure 16. Relationship of Working Station Layout to Entire Station Matrix.

ORIGINAL PAGE IS
OF POOR QUALITY

Table III. Predicted Airflow Distribution Versus Calculated Results from Measured Data, E^3 Double Annular Development Combustor, Mod-I Configuration, Flows Expressed in Terms of %w Combustor.

	Cobra Prediction	From Test Data
Outer Dome	24.8	25.4
Inner Dome	36.8	38.3
Centerbody		
Cooling	5.8	5.7
Dilution	5.9	5.9
Outer Liner		
Cooling	6.7	6.4
Dilution	3.4	3.4
Inner Liner		
Cooling	7.2	6.9
Dilution	9.4	8.0
Overall Total Pressure Drop	5.5%	6.0%

ORIGINAL PAGE IS
OF POOR QUALITY

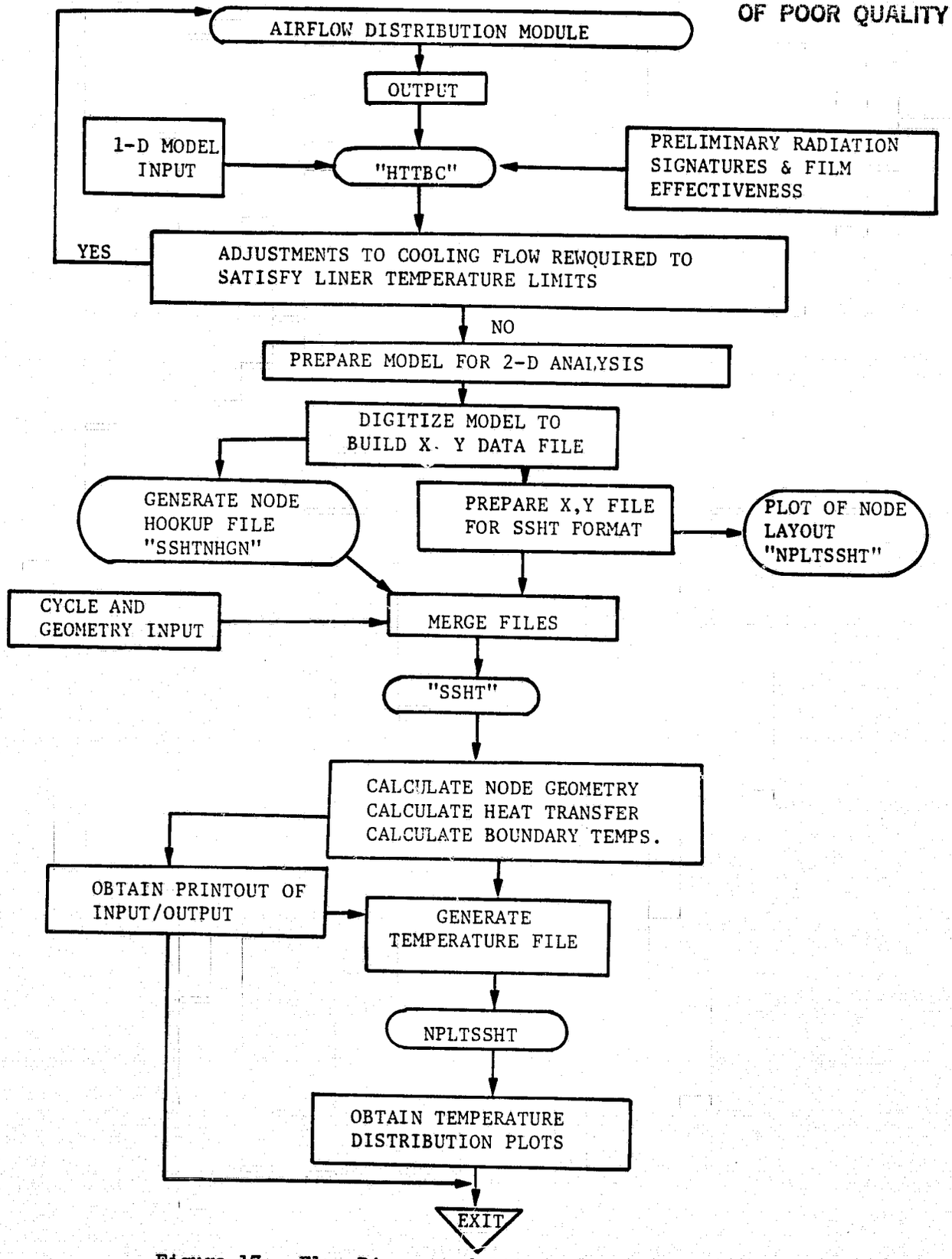


Figure 17. Flow Diagram of Liner Heat Transfer Module.

For transient calculations, the THTD program is used to calculate the time varying temperature distributions. For these transient calculations, heat transfer input parameters must be calculated for selected times in the transient using available test data or cycle deck calcultions. These values are then used as input along with the geometric description of the problem.

The THTD program can perform three-dimensional analyses accounting for geometry, flow, and temperature features in the circumferential direction. The model preparation and calculation of boundary conditions is significantly greater than for two-dimensional analyses; hence, this approach is seldom used. At General Electric it has been established that the three-dimensional effects of the details around coolant slot metering holes on the liner panels can usually be approximated satisfactorily with proper modifications to two-dimensional calculation. It was also determined that cyclic circumferential temperature patterns for thin liners involving one cycle per fuel nozzle, could be adequately calculated with a series of two-dimensional calculations that neglect circumferential conduction. However, thicker liners of the machined ring cooling slot type may have larger circumferential conduction effects which could require three-dimensionl analysis in support of similar stress and life calculations.

Analytical Methodology

The initial total coolant flow and distribution is estimated from the flow required to cool similar or related designs for similar cycle conditions. The parameter used is the coolant flow per unit of cooled surface area per atmosphere of combustor pressure. General Electric has established values of this parameter as part of the combustion system design practice based on years of combustor development. This guide along with the total target coolant flow is used to determine the initial coolant flow distribution. After the initial flow distribution has been selected, the individual panel flows are examined to ensure that the levels are not less than a lower limit which has been established to maintain a protective film over the entire panel length. The flow distribution and combustor information are input to the Flow Distribution Module (COBRA) which calculates the pressure distribution, the local gas velocity, fuel-air ratio, and gas temperature within the combustor. The velocity, fuel-air ratio, and gas temperature values are used in generating the required heat transfer input values.

Both the one-dimensional and two-dimensional heat transfer analysis programs solve for a balance of the heat transfer quantities considered. These include flame radiation in hot side convection, conduction, backside (cold) convection, and radiation out. These heat transfer quantities are illustrated in Figure 18. In the case of the one-dimensional program, only conduction through the material thickness is considered. The results provide the calculated hot side and cold side metal surface temperatures. In the case of the 2-D program, solution to the heat balance is performed at each node of the entire node network defining the liner segment geometry. Since conduction in the axial sense is also considered, the calculation provides the axial

η = Film Effectiveness

$T_{Film} = T_{Gas} - \eta (T_{Gas} - T_{Coolant})$

T_{Gas} = Flame Temperature

$T_{Coolant}$ = Coolant Temperature

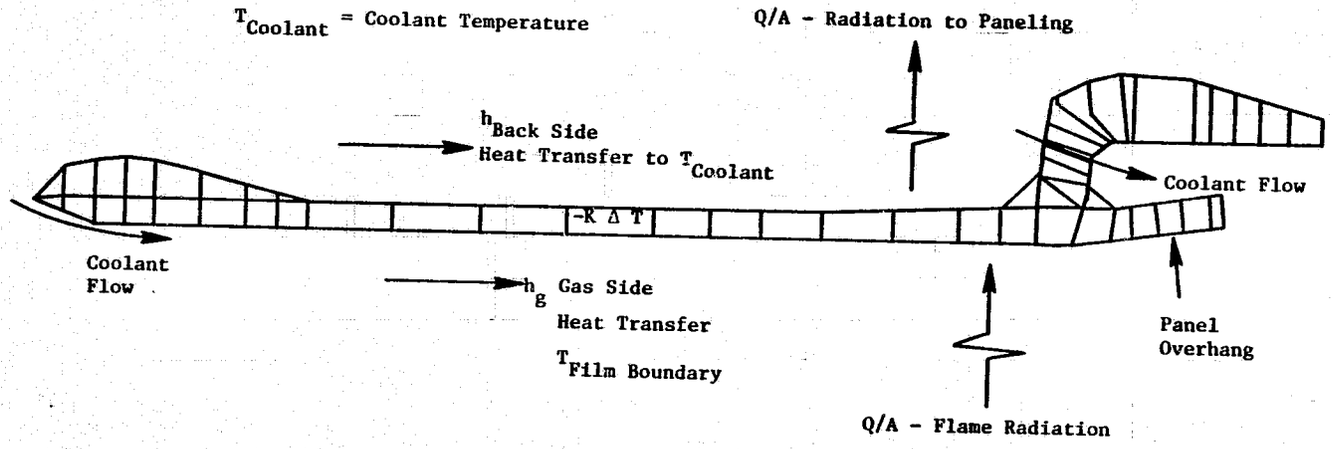


Figure 18. Node Model Showing Heat Transfer Quantities.

ORIGINAL PAGE IS OF POOR QUALITY

temperature distributions as well as temperature distributions through the thickness of the material.

In each of these steady-state programs, correlations for heat transfer coefficients and film effectiveness are incorporated within the programs. However, it is necessary to use the existing General Electric data base as a means of determining which correlations to select as most appropriate to represent the design. The convective heat transfer coefficients are calculated from correlations developed from open literature data, and from wind tunnel test results for specific geometries. In the case of gas-side heat transfer, two correlations are available. One correlation is based on a wall jet flow directly downstream of the film slot and the second is based on a main gas stream correlation where the main stream velocity is relatively high or near the aft end of each panel where the wall jet velocity has decreased. Values are calculated from both correlations and the larger value is used in the analysis. The backside heat transfer coefficients are calculated from a correlation based on the flow of coolant between the liner and the casing or in the case of advanced liners the values are calculated from impingement flow correlations developed from model tests. The overhang is cooled by the impingement of coolant flow and the coefficient is calculated from a correlation based on model tests of the slot configuration.

The film effectiveness data are based on wind tunnel test data of specific film slot designs and on film temperature data derived from combustor tests. In areas where the film is interrupted, such as downstream of dilution holes, the effective film must be back calculated from liner temperature measurements. Normally the film effectiveness is calculated for a single panel and does not account for any film benefit from upstream panels. Hot streaks are simulated in the calculation by assuming circumferential profiles in velocity and temperature.

The flame radiation levels are estimated from measured liner temperature data obtained on similar designs previously operated at similar conditions. This back calculation is done assuming a film effectiveness level and the local gas temperature calculated by the Airflow Distribution Module. The radiation level and film effectiveness combination is then used to analyze the design configuration.

The basic procedure for a heat transfer analysis using the 2-D calculation approach is as follows. The first step is to lay out the node network on a 10 times enlargement of a cross section of the liner and digitize the coordinates. The resulting x, y coordinate file is input to two time-sharing programs. One program (SSHTNHGN) prepares a node hookup file and a second program (NPLTSSHT) prepares the x, y coordinate file in an SSHT main program format. Other options are available in the NPLTSSHT program. One option prepares a plot of coordinate data which serves to check for possible errors in the model. Another option can scale the length of the model so that an existing model can be used for designs where only the panel lengths have been changed. Next, the cycle and combustor geometry data time-sharing files are

prepared. The cycle and geometry files, the node hookup files, and x, y coordinate file are merged to prepare a complete input file for the main program. The output from the main program is in the form of a hard copy of the input/output and a time sharing file of the calculated centroid temperature. The time-sharing file is input to the NPLTSSHT program and prepares the temperature distribution plot.

Predictive Capability

The liner heat transfer module has been applied to the design and analysis of a wide variety of combustor designs for a number of years. These designs have included standard convection/film cooled designs, such as the F101 combustor, and more advanced impingement/film cooled designs. The cooling slot designs have varied from interrupted 360° slots, continuous 360° slots such as the F101 combustor and segmented film liner designs such as the E^3 combustor.

A comparison between predicted axial temperature profiles and some measured metal temperature data for a F101 liner panel is shown in Figure 19. As observed from these comparisons, liner metal temperature predictions generated from the heat transfer module generally reflect the measured levels.

5.1.5 3-D Internal Flow Module

To provide the needed improvement in combustion system design and analysis, the combustor model currently in use at General Electric is being modified to include detailed 3-D internal flow calculations. Since the other modules comprising the overall combustor model have sufficient sophistication and accuracy, the examination of the internal flow module represents the major effort of the Phase I Program.

The internal flow module features three principle parts integrated within a 3-D elliptic computer program. The dilution region module is concerned with the mixing of dilution and film cooling air to guide exit gas temperature pattern development, including the hot streaks along the liners. The fuel insertion module is concerned with the initial specification of fuel droplet size distribution, and velocities of fuel spatial distribution plus the coupling of the fuel spray with the flow field as the drops penetrate and vaporize. The combustion zone module handles heat release and chemical kinetics.

The initial purpose of the internal flow module will be to provide accurate predictions of combustor exit gas temperature pattern trends, and provide detailed liner hot-side aerothermal properties to be used in conjunction with the heat transfer module for improved liner metal temperature predictions. Eventually, the capabilities of the internal flow module would be expanded to provide accurate predictions of exhaust gaseous emissions, plus ignition and blowout characteristics.

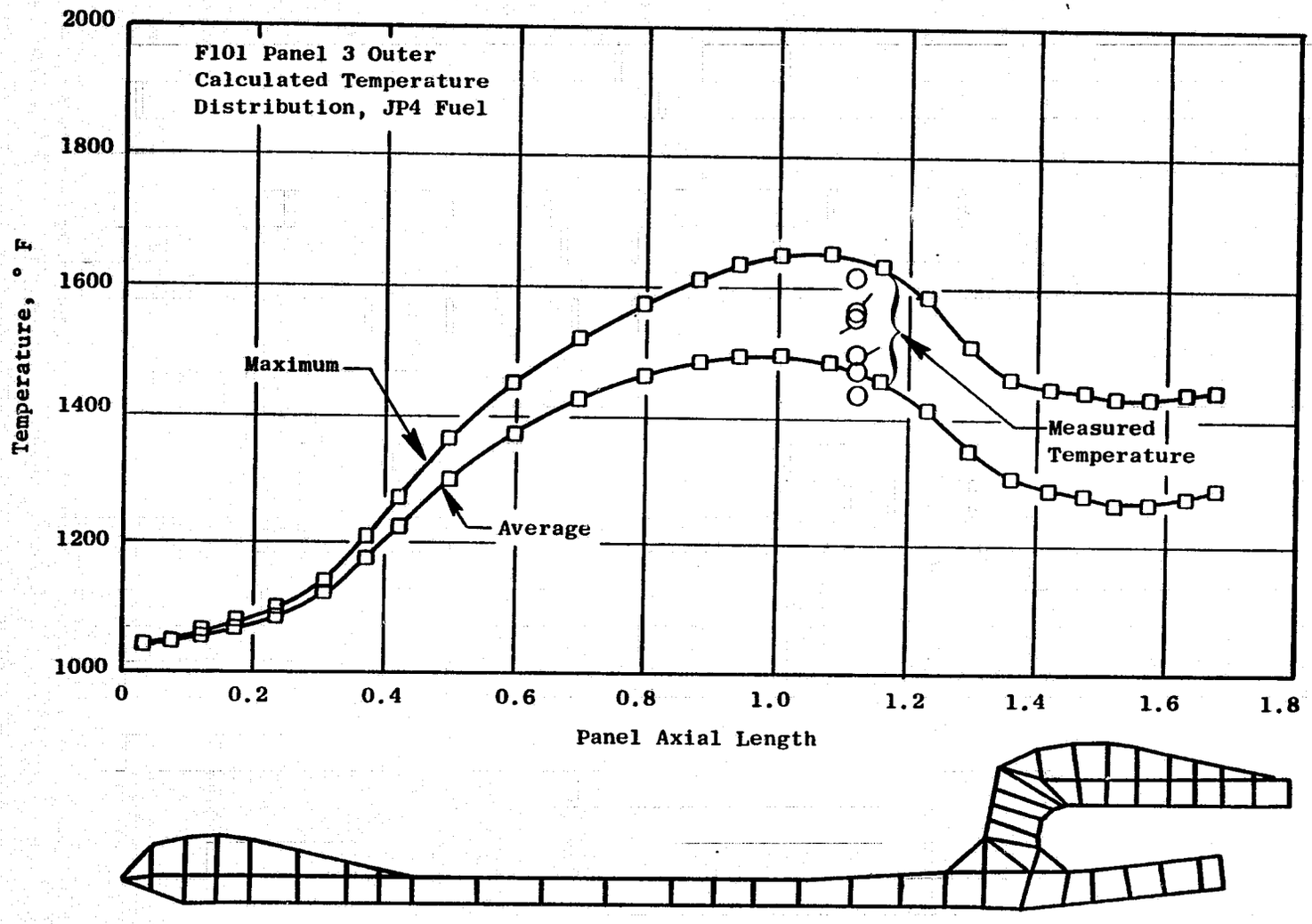


Figure 19. Typical Calculated Liner Panel Temperature Distribution.

ORIGINAL PAGE IS
OF POOR QUALITY

The internal flow module at General Electric features the INTFLOW computer program. It contains two alternate computer programs within its framework, one prepared by The Northern Research and Engineering Corporation, Reference 2 and the second prepared by the Garrett Turbine Company, Reference 1.

Due to the high degree of complexity in the program structure of these internal flow programs, discussions into their analytical methodology, and input/output parameters will be left for the reader to obtain from the references indicated. The analytical predictability of the internal flow module is to be assessed as the major portion of the Phase I Program effort.

Some improvements were developed and incorporated into the 3-D internal flow model. This work was performed as part of an ongoing IR&D program at General Electric. The improvements include:

- Direct individual node treatment of the swirl cup input
- Grid refinement capability
- Stair-step boundary treatment at the front and aft ends of the problem
- Dilution injection on stair-step walls with injection angles
- Simplified dilution injection input.

In addition, an array of plotting programs were developed as part of the same IR&D program to provide visual interpretation of the output generated. Studies have been underway, however, on improved approaches for the basic calculation framework. As these new basic concepts are programmed, General Electric plans to replace the two programs, References 1 and 2, with an improved basic code. It will have features that have been identified in earlier studies at General Electric, from the efforts reported herein, and from the rapidly progressing technology expected to become available in the near future.

2-D Turbulent Reacting Flow Codes

To examine the details of the combusting flow, either experimentally or computationally, a geometrical simplification to two dimensions is required. The complex turbulence and turbulence-chemistry interactions of the fully 3-D case along with the numerical difficulties are still present so that the 2-D studies are very relevant. Furthermore, because fewer data points need to be taken and because the computations can be made on finer grids for the same or less storage and execution time than in 3-D, many more theory-data comparisons and of improved quality are available.

The 2-D research code GETREF had already been developed at General Electric prior to this study. As discussed in Section 6.0, it contains the

single-scalar assumed pdf/equilibrium chemistry/K-ε turbulence model. Favre-averaging of the governing equation is employed exclusively. A parabolic formulation is used to simulate shear flows, for example, a burning jet in coflowing air, and uses a forward-marching solution algorithm. The elliptic version involves a standard relaxation technique: the primary numerical inaccuracy is that caused by convection term discretization. These points are discussed in much greater detail in Section 6.0. In these codes, isothermal flows are simulated by suppressing the combustion aspects; this is facilitated by their modular construction.

5.1.6 Usefulness of Output Parameters

The relative importance of the various modules comprising the overall combustor aerothermal anaysis model are listed in the order of usefulness in General Electric Design procedures below:

Airflow Distribution Module

- Predicted external and internal velocities and pressures
- Predicted pressure drops
- Predicted flow distribution or flow areas.

This output is considered most useful because it is used on a daily basis in the design and development of combustors. The impact of design modifications on airflow distribution and pressure drop can easily be analyzed.

Heat Transfer Module

The metal temperature distribution is used by stress analysis programs for estimating life and is used for evaluating the effect of configuration changes (primarily cooling changes) and postulated changes.

Internal Flow Module

Although not currently in design use, INTFLOW potentially has the ability to predict velocity flow fields near the liner and perhaps hot streaks with improved accuracy that will greatly improve the accuracy of the heat transfer module output. It is also expected to provide useful guidance as a perturbation calculation for dilution hole trimming of pattern factors.

Inlet Diffuser Module

The design technique minimizes development time and provides total pressure levels in each of the passages around the combustor for input into the Airflow Distribution Module.

Preliminary Design Module

Combustor sizing parameters provides envelope that generally remains unchanged throughout development work. Similar information can, however, come from existing correlations from many sources other than this particular computer program.

Light-off, Blowout, Combustion Efficiency and Emissions

These parameters are currently estimated by empirical correlations without using the calculation modules.

5.2 SELECTION OF BENCHMARK QUALITY DATA BASE

One of the specific objectives of the Phase I effort is to identify deficiencies in the aerothermal models currently used in the design and analysis of gas turbine combustors. Towards this purpose, a data base was assembled and studied for selection of benchmark quality test cases used in evaluating each model in the overall combustor aerothermal model. This data base includes data from the available literature, existing General Electric combustor/engine test data, and additional new data obtained from the experimental testing effort conducted as part of the overall Phase I modeling program.

5.2.1 Available Benchmark Experiments from the Literature

The flows which occur in the combustors of gas turbines involve variations of mean properties in three directions with complex turbulence characteristics, combustion which is largely of the diffusion-flame type but may involve some burning of premixed fuel and air, and the evaporation and combustion of liquid droplets. Calculation methods, based on the solution of conservation equations in differential form, require the adoption of models for these physical phenomens as well as schemes to transform the differential equations into finite-difference equations. Thus, even the exact solution to the finite difference equations which are actually solved by approximate iterative procedures) would not exactly represent the flow. The validity of the models can, in principle, be evaluated directly or indirectly. Thus, for example, the components of an effective-viscosity assumption,

$$\overline{u'_i u'_j} = \frac{\mu_{eff}}{\rho}\left(\frac{\partial \bar{u}_i}{\partial x_j} + \frac{\partial \bar{u}_j}{\partial x_i}\right) - \frac{2}{3}\delta_{ij}\, k$$

can all be measured and the value of μ_{eff} can be determined explicitly. In general, however, the direct appraisal of assumptions is not possible and the

merits of all, or most, of the assumptions in a calculation method must be appraised by comparison of calculated and measured results.

While only a few experiments from the literature were selected for comparison with data in this program, a somewhat broader group of experiments were considered. The discussion that follows while not an exhaustive literature survey does indicate many of the available experiments and very briefly presents some of the significant findings from comparisons with models that have been previously emphasized in the literature.

Isothermal Flow

In the past, many experimental and computational investigations have been carried out with two-dimensional flows, that is, those which can be described by two independent spatial variables. The confined-flow measurements of, for example, Pai, et al., 1975[11]; Owen, 1976[12]; and Habib and Whitelaw, 1980[13], come into this category and have allowed calculation methods, such as that of Mongia, 1979[1], to be tested against sudden-expansion configurations and in the presence of swirl. It is clear from the various related computational investigations that the careful location of a large number of grid nodes is required, even in two-dimensional flow, to avoid serious numerical errors. In addition, the advantages and disadvantages of different turbulence-model assumptions have been demonstrated and it can be concluded, for example, that a transport model is necessary to represent recirculating flows and that high degrees of swirl are not well represented by isotropic eddy-viscosity models such as the two-equation forms proposed by Jones and Launder, 1972[14], or Saffman, 1974[15]. At the same time, the use of numerical grids based on, for example, 400 nodes in a two-dimensional solution domain, will usually give rise to cell Reynolds numbers greater than |2| generally leading to first order upwind differencing and numerical diffusion. The introduction of numerical diffusion often nullifies any added benefit which may be gained from the use of Reynolds stress models. Since the problem is even more acute in three-dimensional flows, it is questionable whether higher order closure in turbulence models (such as Reynolds transport) can be justified for use in real combustors. Furthermore, turbulence exerts less control in the jet-in-crossflow arrangement of combustors, where pressure forces are important, than in the sudden-expansion, swirling flows mentioned above. On the other hand, in the future it may prove necessary to further investigate the relative merits of turbulence models in two-dimensional, turbulence-controlled flows; however, with practical calculation methods required in the near future, the present investigation will concentrate on flows which possess features more directly relevant to gas turbines.

The complex geometry of a gas-turbine combustor, even in the absence of combustion, involves the interaction of primary jets, dilution jets, the flow from fueling devices and film-cooling jets in the presence of an annular or cannular confinement. A simplified axisymmetric arrangement was investigated by Green and Whitelaw, 1980[5]. This is one of the experiments selected for comparison with calculations in this program.

The experiment features an axisymmetric form of the crucial dilution jet problem. These data allow examination of the prediction with emphasis on numerical accuracy and the resolution of pressure gradients and without the problems of chemical reaction.

The data of Vu and Gouldin, 1980[6] for a double-annular confined flow with both jets co- or counterswirled are also an excellent data set for comparison. Detailed velocities and turbulence quantities were obtained over a range of swirl numbers. Inlet quantities were clearly measured, thereby providing a benchmark quality data set. This particular data was used in the present efforts to test a modified form of the two-equation model (the algebraic stress model) which directly accounts for the anisotropies of eddy viscosity caused by the streamline curvature.

The round jet in crossflow represents another simple flow used for model testing purposes. It possesses the basic features of one important aspect of combustor flows and permits determination of the influence of node density and distribution particularly in the near jet-exit region. Measurements exist for a range of velocity ratios. Table IV provides a list of the available data. It should be noted that previous computational investigations of the round jet in crossflow have been reported by Patankar, et al. 1973[16]; Jones and McGuirk, 1979[17]; Crabb, 1979,1981[18,19], and White, 1980[20], and provide guidance. Nevertheless, this well-measured flow provides a foundation upon which any calculation development can be based. One particular point of note from previous calculations is the conclusion of White that a greater distribution of nodes than his 25 x 20 x 15 is required to achieve grid independence. A careful analysis of the numerical truncation error, Claus, 1983[21], indicates that at least 75,000 nodes are needed.

The next level of complexity is the row of jets in crossflow and opposed rows of jets in crossflow. In the former case, measurements have been provided by Kamotani and Greber, 1972[22]; Holdeman and Walker, 1977[9]; Crabb, 1979[18]; and Khan and Whitelaw, 1980[23]. The accuracy of measurements made mainly by pitot tube is poorer than that of the single jet data but is more than adequate to assess the calculated mixing of the jets as a function of pitch-to-diameter ratio. It should be noted that the finite and known width of the solution domain renders this flow, in this one sense, easier to represent by a computational mesh than the single jet in crossflow. Again, related calculations have been reported, Khan, et al., 1982[24], and provide useful guidance but in no way obviate the need for further calculations.

The data of Holdeman and Walker 1977[9], and also reported in Walker and Kors 1973[8], were selected for comparisons in this work partly because these data have been previously used at General Electric in guiding combustor design/development efforts.

The flow downstream of opposed jets has been measured by Kamotani and Greber, 1974[25] and Atkinson, et al., 1982[26] and, to date, no related calculations have been reported. The complex structures reported by Atkinson, et al.[26], and created by pressure rather than turbulence forces could provide a

Table IV. Round Jet in Crossflow.

Author	Jet Diameter (mm)	Incident Angle	Jet Velocity Profile	Crossflow Velocity (m/s)	Velocity Ratio	Measured
Callaghan and Ruggeri 1948	6.35, 9.5 12.7, 15.9	90	Orifice	---	---	Penetration Parameters
Ruggeri 1952	6.35, 9.5 12.7, 15.9	30, 45 60, 90	Orifice	72 122	2-8	Correlations Between Parameters
Jordison 1956	12.7 25.4	90	Orifice	---	4, 6, 8	Total Pressures, Flow Directions
Keffer and Baines 1963	9.5	90	Pipe	1.5	4, 6, 8 10	Velocity, Turbulence, Intensity, Entrainments
Bradbury and Wood 1965	25.4	90	Pipe	18.3, 36.6	2, 4, 8 11.3	Static Pressure Distributions
Platten and Keffer 1968	6.35	±15, ±30, ±45, ±90	Pipe	1.6	4, 6, 8	Jet Trajectory Entrainment
Margason and Fearn 1969	25.4	-180, 30, 60 90, 120, 150, 180	Nozzle	---	1.18-10	Trajectory by Photographs
McMahon and Mosher 1969	50.8	90	Pipe	7.6, 15.2	4.12	Wall Static Pressures
Street and Spring 1969	8.4	90	Nozzle	Mach 0.1, 0.2 0.4, 0.6	1.4	Wall Static Pressures
McMahon et al. 1971	50.8	90	Nozzle	15.2	8, 12	Turbulence Measurements in Wake Region
Ramsey and Goldstein 1971	23.5	35, 90	Pipe	30.5, 61	0.1-2	Temperature, Velocity Turbulence Intensity Contours
Thompson 1971	25.4	90	Nozzle	12.2	2, 4, 8, 12,16,20	Wall Static Pressures, Turbulence Intensity Vorticity

ORIGINAL PAGE IS
OF POOR QUALITY

Table IV. Round Jet in Crossflow (Concluded).

Author	Jet Diameter (mm)	Incident Angle	Jet Velocity Profile	Crossflow Velocity (m/s)	Velocity Ratio	Measured
Eriksen 1972	23.5 11.8	35,90	Pipe	30.5, 61	0.1-2.18	Adiabatic Wall Temperature Film Cooling Effectiveness
Kamotani and Greber 1972	6.35	90	Pipe	6-9	2.8-8.5	Velocity and Temperature Distributions
Goldstein et al. 1973	23.5	35, 90	Pipe	30.5 61	0.1-2.0	Adiabatic Wall Temperatures Pitot and Static Pressures
Mikolowsky and McMahon 1973	38.1 76.2	90	Orifice	---	2, 4, 6, 8, 12	Wall Static Pressure Distribution
Shaw and Margason 1973	8.4	90	Nozzle	Mach 0.[illegible], 0.2 0.[illegible], 0.6	Dynamic Pressure Ratio 0 – 1000	Floor Static Pressures
Chassaing et al. 1974	40	90	Pipe	3.[illegible]	2.37, 3.95, 6.35	Velocity Distributions
Fearn and Weston 1974	101.6	90	Orifice	30.[illegible]	53.3	Velocity and Vorticity
Weston 1975	101.6	45, 60, 75 90, 105	Nozzle	30.5 55.3	8	Velocity
Bergeles 1976	19.05	90	Pipe	26	0.046-0.1	Static Pressure, Velocity, Film Cooling Effectiveness
Moussa et al. 1977	23.6	90	Pipe	8.5	3.48	Velocity Vorticity
Rathgeber and Becker 1977			---	Pipe Flow	2-5-12.3	
Crabb et al. 1981	25.4	90	Pipe	12	1.15, 2.3	Velocity, Turbulence and Passive Scalar

ORIGINAL PAGE IS
OF POOR QUALITY

valuable and essential test of the calculation method. In this study, the axisymmetric water-model simulation of Green and Whitelaw 1980[5] was used as isothermal flow benchmark data to provide quantification of the errors brought about by the combination of numerical and turbulence assumptions. These authors have reported accurate representation of internal features such as the length of the primary vortex.

An additional set of measurements that would allow the testing of jet mixing in a cross stream, and at the same time permit the evaluation of the assumption for turbulent heat flux, is that of Norgren and Humenik, 1968[27]. This experiment has the added convenience for numerical methods formulated in cylindrical coordinates of square holes, and, although the results are restricted to values of mean temperature, the intermediate complexity of the geometrical arrangement and the scalar-transport measurements render it a valuable contribution.

Gaseous Combustion

Measurements become more difficult in the presence of high temperatures and, in addition, the meaning of the measurement must be appraised to determine its relationship to density-weighted or unweighted values. Thus, for example, a large diameter thermocouple is likely to measure a value close to

$$\tilde{T} = \langle \rho T \rangle / \langle \rho \rangle \tag{6}$$

rather than to

$$\bar{T} = \langle T \rangle \tag{7}$$

and the difference can amount to several hundred degrees Kelvin. In general, all measurements made with large probes will be close to density-weighted values and, when comparisons are made with calculated results, the latter must also be density-weighted. Fortunately, the conservation equations are readily cast with density-weighted dependent variables (as described for the GETREF code, Section 6.0) and the more difficult problem is usually to calculate the unweighted value.

If the probability density function of a variable ϕ is known, both density-weighted and unweighted values can be obtained from

$$\tilde{\phi} = \int \phi^e(f)\, P(f)\, df, \qquad \bar{\phi} = \bar{\rho} \int \frac{\phi^e(f)}{\rho^e(f)}\, P(f)\, df \tag{8}$$

where P(f) represents the density-weighted probability density distribution of a scalar property f. In the Raman scattering data, Section 7.1, both types of average were derived from the instantaneous data taken.

A very large number of gaseous-flame measurements is available in the literature ranging from open diffusion flames to confined premixed flames and to real combustors. Again, a careful choice was made to concentrate on the confined, nonpremixed configuration. For completeness, however, Table V provides a list of available bluff-body stabilized, premixed gas and air data which may also be used for testing models.

In calculating combustion flows, one must realize that the several models associated with numerical solution techniques, turbulence, heat transfer, and combustion all contribute uncertainties in proportions and with magnitudes that depend on details of the particular flow being investigated. Problems with numerical diffusion due to coarse grids have been discussed, and two-equation turbulence model weaknesses in, for example, recirculation zones have been well documented. Future work calls for continued improvements in these areas as data comparisons are being made. Similar comments can be made regarding more detailed kinetics in the combustion model, the need for handling complex 3-D geometries, and heat transfer models in the vicinity of complex film-cooled combustor liners.

The calculations of Jones, 1979[28] have shown that the hydrogen-diffusion flame of Kent and Bilger, 1973[29] can be represented with fast chemistry assumptions and that different assumed forms of the scslar probability density function can lead to different results. General Electric has just completed a Department of Energy-funded study, Lapp, et al., 1983[4] on turbulent jet diffusion flames. LDV data on mean and fluctuating velocity and Raman data on mean and fluctuating composition and temperature are thus available. This allows direct assessment of the turbulence/chemistry model in a computationally simple flow. These data were selected for comparison, and the results are presented in Section 7.1.

Recirculating diffusion-flame flows include those of Owen, 1976[12]; Elliman, 1977[30], and Elliman, et al., 1978[31]. In both cases, the flow is confined, axisymmetric, and uses a hydrocarbon fuel in a nonpremixed manner. In the case of Elliman,[30,31] for example, nonreacting and reacting flow fields were measured in a duct downstream of an annular baffle with methane flowing through a 10.5 mm diameter central hole and air flowing with 12.5 mm space between the baffle and the confining 150 mm diameter pipe. Measurements of velocity and temperature were obtained with a seven-hole spherical impact probe and an exposed bead thermocouple. The local equivalence ratio was measured with an uncooled sampling probe. The measured values correspond to density-weighted averages and the uncertainties in velocity (outside the region of recirculation), mean temperature, and equivalence ratio are not greater than 10%, 15%, and 20%, respectively.

The flow investigated by Toral and Whitelaw, 1982[32] in a sector rig, introduces the complexities associated with a semicircular combustor head and film-cooling jets which drive the primary vortex in addition to cooling the

Table V. Premixed Combustion.

Authors	Experiment	Findings
Longwell et al., 1949	Flame extinction data as a function of mixture velocity, temperature and pressure and baffle shape and blockage (4% to 23%). Axisymmetric geometry; Re = 1.1 to 22 x 10^6.	Increasing mixture velocity and decreasing temperature narrows stability limits. Influence of pressure small. Streamlined trailing edges an smaller baffles narrow stability limits.
Barrere and Mestre, 1954	Flame extinction data as a function of mixture velocity and temperature for a number of baffle shapes. Plane, two-dimensional geometry; Re = 5 x 10^5.	Increasing mixture velocity and decreasing temperature narrows stability limits. Increasing bluffness and blockage increases limits. Drag of flameholder is less during combustion.
Williams et al., 1949	Flame extinction data as a function of mixture velocity and approach-stream turbulence for rod, multiple rod and gutter baffles. Blockage from 0.5% to 17%. Plane, two-dimensional geometry; Re from 150 to 10^5.	Increasing mixture velocity and increasing approach-stream turbulence narrows statibility limits. Baffle shape unimportant; smaller blockage decreases limits.
DeZubay, 1950	Flame extinction data as a function of mixture velocity and pressure for blockage between 0.8% and 13%. Axisymmetric disks; Re = 90 to 680 x 10^3.	Increasing mixture velocity and decreasing size and pressure narrows stability limits.
Wright, 1959	Recirculation bubble length and width as a function of blockage ratio (< 25%), subsonic Mach number and equivalence ratio. Plane baffles; Re = 8 to 37 x 10^4.	Length decreases with increasing blockage (7 baffle heights at 25% blockage), weakly dependent on Mach number and is shortest at stoichiometric conditions. At blow-off, 'characteristic mechanical time' is independent of blockage. Recirculation length longer for plane than axisymmetric baffles.
Wright and Zukoski, 1962	Flame width as a function of equivalence ratio, approach stream temperature, velocity and fuel type. Circular	Rate of spreading from baffle is independent of equivalence ratio, etc., as long as flame is turbulent and flow is subsonic. Spreading also

ORIGINAL PAGE IS
OF POOR QUALITY

Table V. Premixed Combustion (Continued).

Authors	Experiment	Findings
Bovina, 1958	Residence time as a function of approach stream velocity, turbulence and equivalence ratio. Baffles were 30° apex plane wedges with blockage from 0.22 to 0.66. Re = 1.2 to 9.6 x 10^6.	Residence time is inversely proportional to velocity, increases with turbulence and is independent of equivalence ratio. Time is proportional to baffle blockage.
Winterfeld, 1965	Recirculation length and residence time as a function of approach stream velocity, equivalence ratio, blockage ratio and baffle shape.	Recirculation length increases with velocity, minimum at stoichiometric conditions, decreases with blockage and increases with bluffness (length between 2-1/2 and 3 diameters for 25% blockage). Residence time increases in presence of combustion, decreases with velocity and is independent of blockage.
Crowe, Shipman and Vranos, 1963	Density, velocity and mass fraction profiles for three approach velocities in far-wake. Cylindrical baffle in rectangular duct. Re = 5 to 30 x 10^4; blockage 3.5 and 7%.	Profiles of turbulent mass transfer coefficients and reaction rates. Reaction controlled by flow more than by chemical kinetics.
Lewis and Moss	Power spectral density and probability density function of density gradient, temperature and positive ion current in far-wake. Cylindrical baffle in rectangular duct (blockage 7%). Re = 1 to 3 x 10^4.	Measurements of large scale ordered structures. Findings compatible with description of turbulent flame zone as comprising narrow burning regions embedded in extensive regions of burnt and unburnt gas.
Morrison, 1973, 1974	Measurements of velocity and chemical composition. Annular, 30° vee-gutter mounted in circular duct (28% blockage). Re = 8.3 to 25 x 10^6.	(Cited by Pope, 1976).
Clare et al., 1976	Laser-Doppler velocimetry used and measurements of fluctuating wall pressure and high speed Schlieren photography. Plane, 45° gutter used as baffle: 25% blockage. Re = 7.2 x 10^4.	Recirculation length four gutter heights. Velocity probability density function measured in presence and absence of combustion-induced oscillations. No bimodal distributions found.
Durão and Whitelaw, 1977	Measurements of centerline axial velocity, Reynolds stress and probability density distributions by laser-Doppler velocimetry. Unconfined, disk stabilized premixed and diffusion flames attached to a 50% blockage baffle. Re = 2.9 to 5.3 x 10^3.	Recirculation lengths for isothermal, premixed and diffusion flames are similar at about one baffle diameter. Reynolds stress in flames is smaller than for isothermal flow: diffusion flames result in larger values than premixed flames.

ORIGINAL PAGE IS
OF POOR QUALITY

Table V. Premixed Combustion (Concluded).

Reference	Flow arrangement	Measured Properties	Operating Conditions	Comments
Parks, Sawyer and Ganji 1979 Dit and Daily, 1979 Ganji and Sawyer, 1980	Propane-air flame behind a 2-D backward-facing step	• Spark shadographs • Schlieren photography • Laser Schlieren • LDA and Rayleigh scattering	• Re = 0.5 x 10^4 - 1.5 x 10^4 cm^{-1} • Equivalence ratio of 0.52 - 0.63 • Inlet temperature of 297 and 557 K	• Observed large-coherent structure in both reacting and non reacting flow with discrete frequencies in range 240-450 Hz and at f < 100 Hz. • Freq. influenced by inlet temp. and not by velocity or equivalence ratio
Talyor Whitelaw, 1980	Methane-air flame behind a circular disk in a round tube	• Temperature and velocity by thermocouples and LDA • Stability limits and combustion driven oscillations • Noise characteristics	• Equivalence ratios from 0.7 to 1.6 • Inlet Re = 3.3 x 10^4	• Combustion driven oscillations of high amplitude with frequency natural frequency of duct • Velocity characteristics change with ϕ
Champion, Bray and Mass, 1978 Kalghalgi and Mass 1979	Propane-air flame behind a cylindrical rod in a rectangular duct	• Density gradient field • Mean and rms of temp. fluctuation • Pdf and power spectra of temperature • Spark Schlieren	• Stoichiometric mixture • Inlet velocity = 30 m/s	• Large periodic instabilities f = 890 Hz, invariant with flow rate and stabilizing rod diameter • Shapes of temperature pdf within the flame
Borghi and Movean 1979 Movean, 1978	2-D methane-air flame ignited by a parallel stream of hot gases (τ = 2000° C)	• Velocity (LDA), mean, rms and pdf • Temperature • Gas sampling	• Equivalence ratio of 0.34 • Inlet velocity of two-varied streams	• Concentrates on pdf shapes at different parts of the flame
El Ban Lawey et al., 1978	Propane-air flame	• Mean and ram velocity (LDA) • Sound intensity and frequency	• Equivalence ratios in the range 0.68-1.01	• Sound intensity and frequency change with ϕ • Pms of velocity greatly influenced by combustion-driven oscillations
Smart et al, 1976	Ethylene flame behind a V-gutter	• Pressure transducers • Schlieren movies • Temperature	• Equivalence ratio of 0.75	• Concentrates on the existence of combustion-driven oscillations
Semivjian and Vromes, 1976	Prevaporised jet fuel A-air frame behind a perforated plate	• Concentrations of NO_x, CO, CO_2 and unburned hydrocarbons	• Equivalence ratio of 0.65 • Inlet temp. of 750 K	• Main emphasis on NO_x formation and emission levels

ORIGINAL PAGE IS
OF POOR QUALITY

wall in critical areas. The calculation of this flow requires preliminary steps toward a general geometry package and could provide a very helpful building brick in the development of a method which is generally applicable to practical combustor arrangements. This is particularly so since the data include isothermal measurements and distributions of a passive scalar with and without combustion. Thus, the numerical and turbulence model can be appraised in relation to the isothermal flow velocity results; the heat transfer model can be evaluated in relation to the isothermal flow scalar distributions; and the combustion model can be examined in relation to measurements of velocity, temperature, and the concentrations of unburned hydrocarbon, carbon monoxide, carbon dioxide, and oxygen. It is useful to note that the authors deduce from the measurements that equilibrium or fast chemistry assumptions appear to be justified except in rich regions of their flame.

The axisymmetric bluff body diffusion flame data by Lightman, et al. 1980[7] is another source of detailed velocity data acquired with an LDV system for both nonreacting and reacting flow situations over a broad range of both fuel and air flows. This experiment was modeled in the present study and will be discussed in detail (Section 7.1).

Less detailed results, in combustor geometries which are even closer to practice, have been reported for example by Tuttle, et al., 1973[33]; Vranos and Tabak, 1976[34]; and Noyce, et al., 1981[35].

Droplet Combustion

Models for droplet combustion are usually based on Crowe, 1974[36] and later publications, for example that of Crowe, et al., 1977[37]. They can allow for the separation of the droplet and gaseous velocities by a Lagrangian tracking procedure or can assume no slip between the two phases. Which is more applicable depends on the problem being considered. With the levels of preheat temperature present in many gas turbines and the atomization of the fuel to droplets with Sauter mean diameters of less 50 μm, it is unlikely that the consideration of slip is required, except possibly at idle conditions. In addition, the assumptions necessary in the numerical, turbulence, heat transfer, and combustion models suggest that the droplet model should be as simple as possible. Appropriate assumptions for evaporation and group effects can readily be incorporated as required.

The application of the procedures of Crowe have been reported by, for example, El Banhawy, et al., 1978,[38] and El Banhawy and Whitelaw, 1980[39] and for comparison purposes have made use of the experimental data of Tuttle, et al., 1973[33]; These data correspond to a hollow spray of monodisperse kerosene droplets of around 50 μm with no preheat. It appears from these and similar results that the droplet tracking procedure will only be necessary for the idle condition but further evaluations could be carried out in relation to the above data and to that provided by studies such as those of Botros, et al. 1980[40]; Driscoll and Pelaccio, 1980[41]; and Nicholls, et al., 1980[42].

Experiments Used to Assess Model

Table VI summarizes the experiments selected along with the type of data gathered. Again the two-dimensional elliptic code GETREF and a parabolic version of it were used for the axisymmetric experiments to assess the mathematical/physical model. For the Walker and Kors, 1973[8] data, calculations were accomplished with the 3-D INTFLOW code which provided an overall assessment of the code though with a much less detailed grid and without the error analysis performed for the axisymmetric assessments.

5.2.2 General Electric Engine and Component Data Base

At General Electric, large quantities of measured test data are available on all production and development combustion systems. These data include diffuser performance measurements, combustor airflow distribution/hole flow coefficient data, combustor liner temperature data, and combustor exit gas temperature pattern data. In addition, measured data are available for combustor stability and exhaust emission performance. This extensive data base has been instrumental in the establishment and refinement of combustion systems design guidelines used at General Electric.

Diffuser performance data are routinely obtained from full-scale annular model testing of each new diffuser design. This testing is done as a verification of the design performance predictions obtained from the inlet diffuser module. Detailed pressure measurements are made on numerous positions along the diffuser model flowpath. Such pressure data are obtained over a wide range of operating conditions providing sufficient information to generate performance design curves. These curves become very useful to the designer in predicting changes in diffuser performance at off-design operating conditions. A schematic of a typical model test rig, and performance curves are presented for the NASA/GE Energy Efficient Engine diffuser design in Figures 20 through 23. Because of the finite amount of instrumentation used in these tests, specific details concerning circumferential nonuniformity, boundary layer effects, and wakes downstream of support struts are not well represented. However, the vast amount of design experience accumulated has led to the establishment of design guidelines sufficient to provide diffuser designs that demonstrate excellent performance.

A large volume of data concerning flow coefficients and bulk injection angles for different shaped holes has been accumulated at General Electric over many years. These data were obtained from detailed model wind tunnel tests in which a large array of hole shapes were tested to define the flow coefficient and bulk injection angle. Data of this nature are available for all cooling hole features in all General Electric combustor designs. Much of this dilution hole data have been empirically correlated and introduced into current design methods such as the airflow distribution module. The importance of having this data base readily available is illustrated in Figure 24 by the large variation in hole flow coefficient that occurs as a result of a relatively minor change in the hole shape. These data also take into account

Table VI. Experiments From the Literature Which Were Modeled.

Isothermal Combustor-Like Flows

1. A. Green and J.H. Whitelaw, Measurements and Calculations of Isothermal Flow in Axisymmetric Models of Combustor Geometries, Journal Mech. Eng. Sci., Vol. 22, No. 3, 1980. (LDV Measurements of Mean Velocity and Turbulence in Slit-Jet/Plenum Chamber Geometry).

2. B.T. Vu and F. Gouldin, Flow Measurements in a Model Swirl Combustor, AIAA Paper No. 80-007, 1980. (Axisymmetric double-annular flow geometry where both flows were independently swirled. Mean velocity and turbulence measurements.)

Combustion Flows

1. M. Lapp, M.C. Drake, C.M. Penney, R.W. Pitz and S.M. Correa, "Turbulent Combustion Experiments and Modeling." Final report DoE contract DE-AC04-78 ET 13146. (Turbulent CO/H2/N2 jet diffusion flame in coflowing air. LDV and Pulsed Raman data for mean and fluctuating components of velocity, concentrations and temperature. Pdf's directly measured.)

2. A.J. Lightman, et al, "Velocity Measurements in a Bluff-Body Diffusion Flame." AIAA Paper No. 80-1544. (Non-premixed axisymmetric bluff-body stabilized propane flame. LDV measurements for mean and fluctuating axial velocities. Thermocouple measurements for temperature.

3-D Dilution Jets

1. R.E. Walker and D.L. Kors, "Multiple Jet Study Final Report". NASA CR-121217. Three-dimensional dilution jet experiments. Thermocouple measurements of jet penetration and mixing.

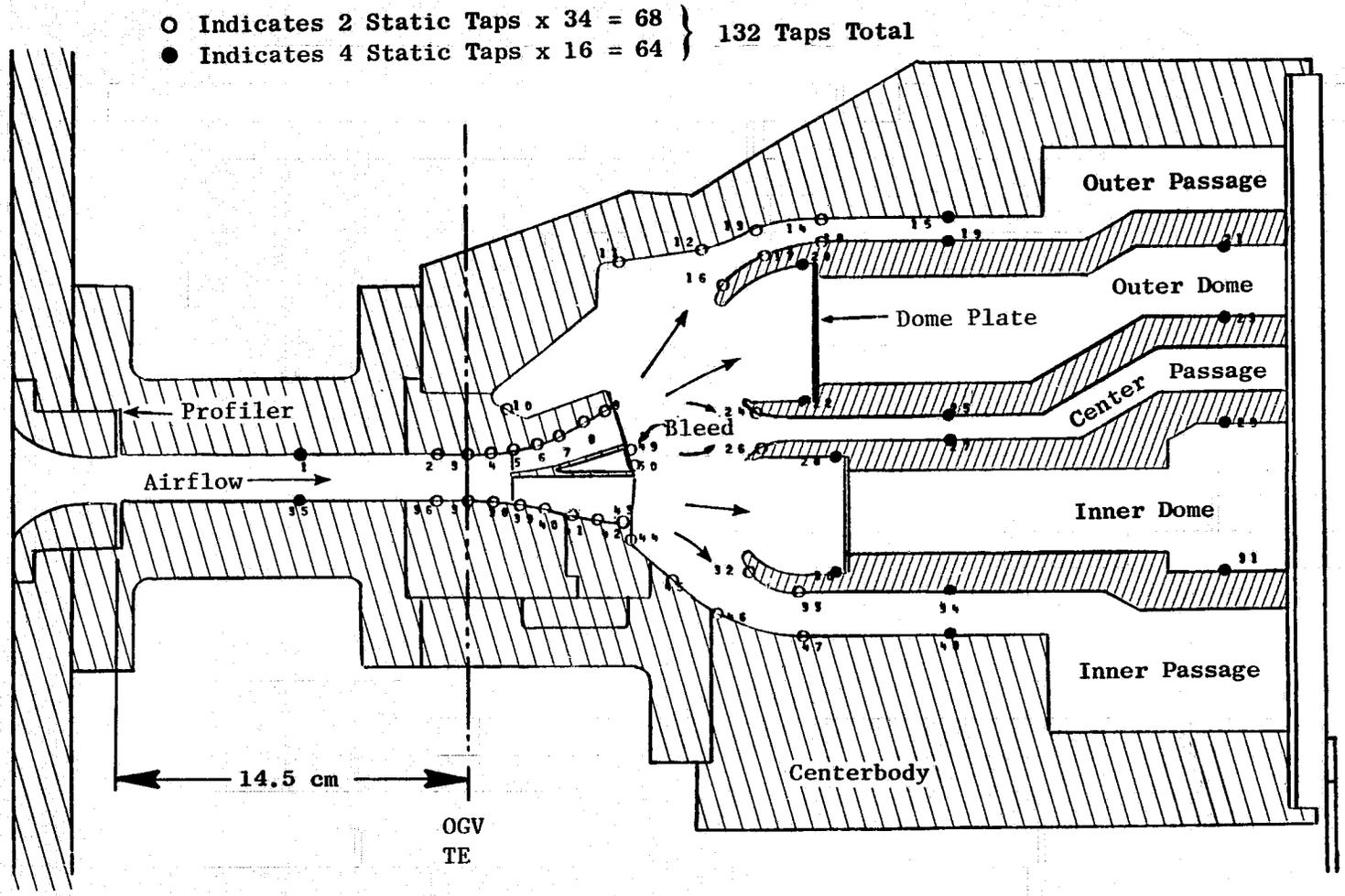


Figure 20. E^3 Split Duct Diffuser Model Test Rig.

ORIGINAL PAGE IS
OF POOR QUALITY

ORIGINAL PAGE IS
OF POOR QUALITY

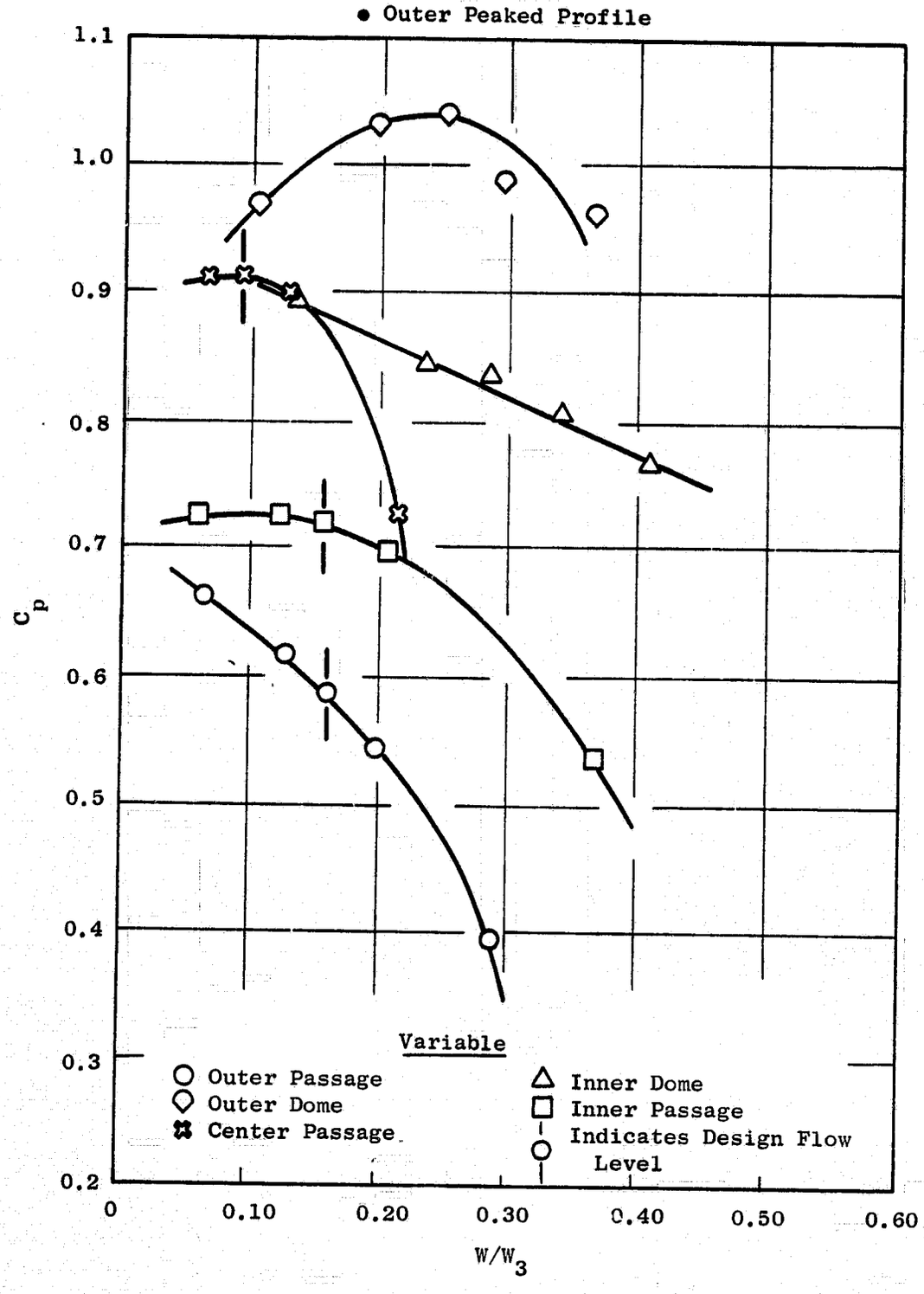


Figure 21. Measured Static Pressure Recovery Levels for E^3 Model Test Rig.

ORIGINAL PAGE IS
OF POOR QUALITY

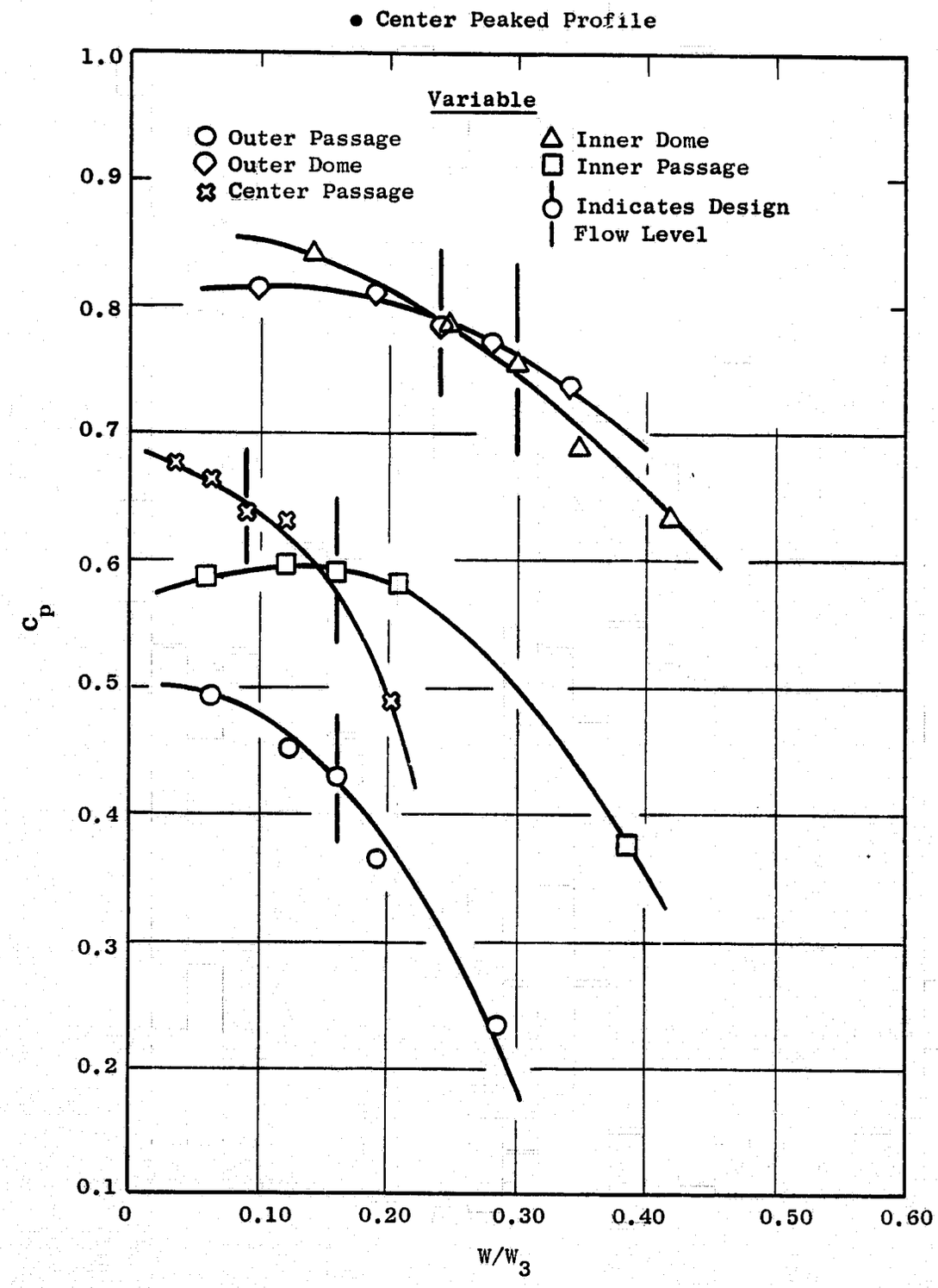


Figure 22. Measured Static Pressure Recovery Levels for E^3 Model Test Rig.

ORIGINAL PAGE IS
OF POOR QUALITY

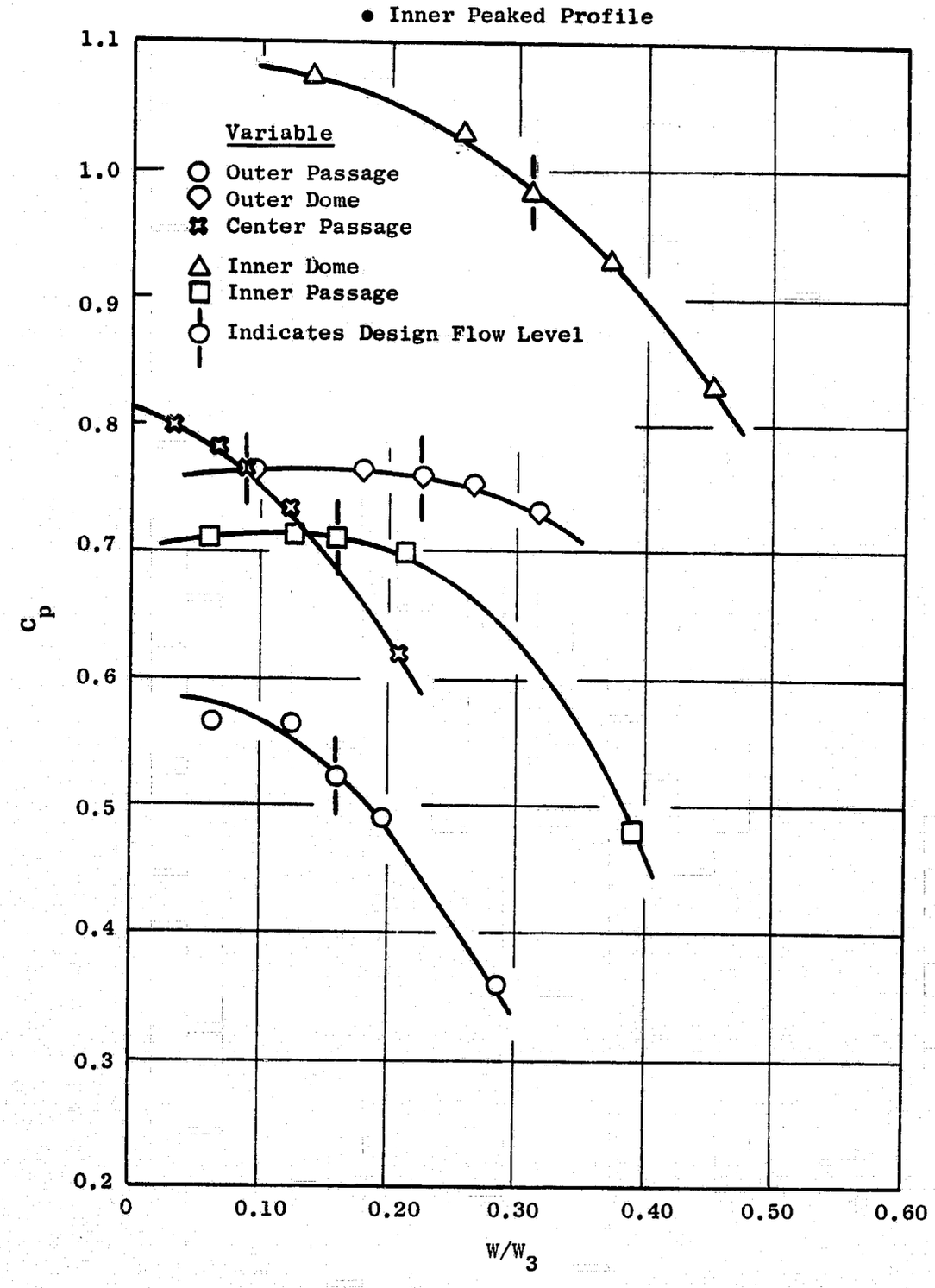


Figure 23. Measured Static Pressure Recovery Levels for E^3 Model Test Rig.

ORIGINAL PAGE IS
OF POOR QUALITY

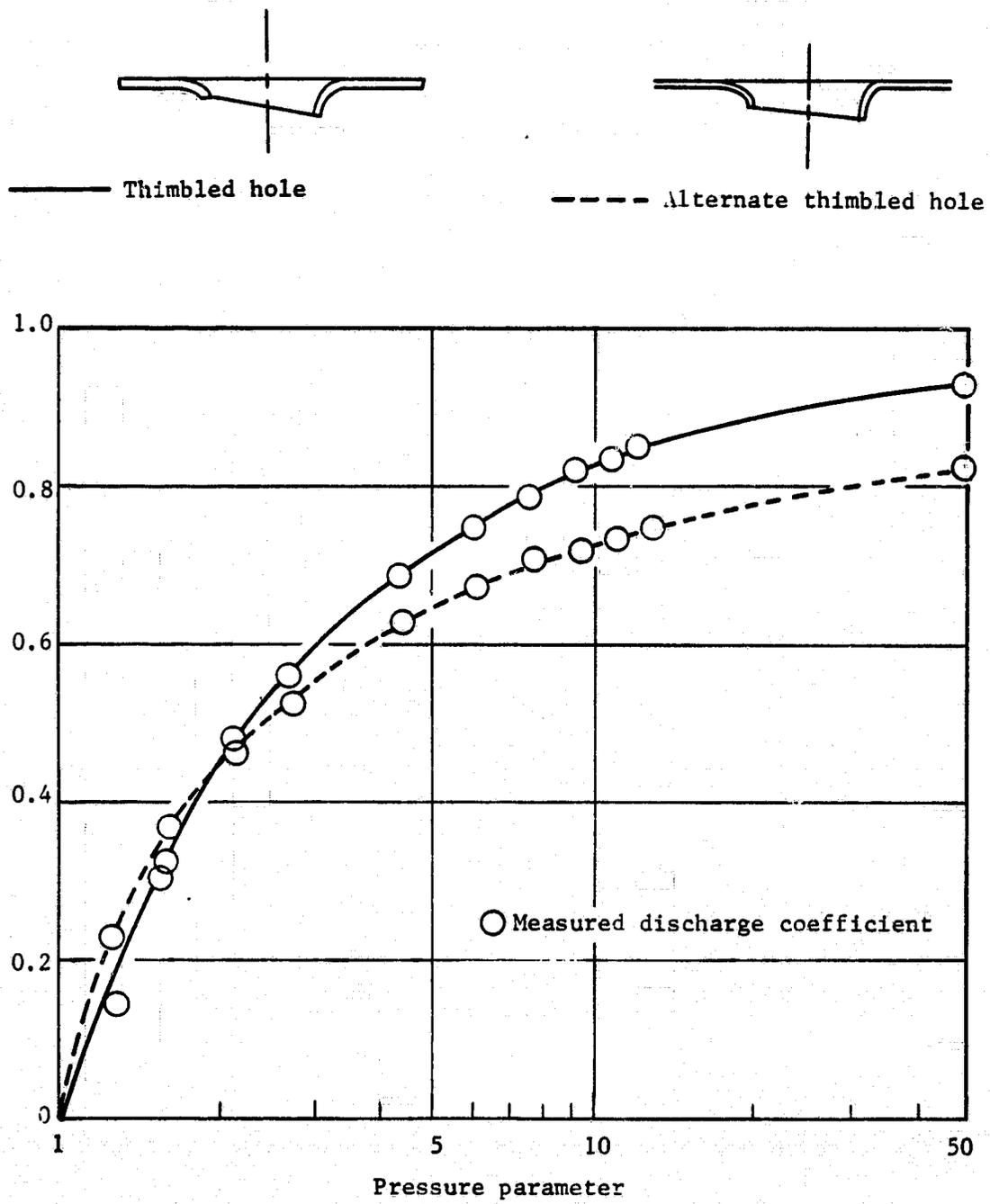


Figure 24. Sample of Discharge Coefficient Data for Dilution Holes.

the effect of back side velocity and pressure drop on the flow coefficient and the bulk injection angle. As a verification, the flow areas of the individual flow features of combustors are periodically measured in an atmospheric calibrated flow stand. Despite the extent of the data base, there is a lack of data concerning turbulence levels in and around the penetrating jet, metastable jet characteristics, and details within the jet such as velocity and injection angle variation across the jet as a result of the nonuniform pressure fields surrounding the jet. These are not so important for the gross analysis conducted using the airflow distribution module. However, their importance is evident when attempting accurate detailed internal flow calculations.

Measured combustor liner temperature data have been accumulated at General Electric for a variety of designs, both production and devleopment. These include conventional convection-cooled designs, impingement-cooled designs, and designs featuring convection and impingement cooling. This extensive data base includes the effects of fuel type, inlet pressure, inlet temperature, and fuel/air ratio. A typical example of these data is provided in Figure 25. The majority of these data have been obtained from component testing in which test conditions are set to simulated actual engine operations. Component testing provides the advantages of using large quantities of thermocouple instrumentation, plus the ability to investigate a wide range of operating conditions, both on cycle and off cycle. Additional temperature data are obtained from actual engine tests. The increased complexities of engine testing requires the use of significantly less instrumentation, plus the inability to set operating conditions very far off the engine operating line. The advantages of obtaining liner temperature data from engine testing is that actual engine cycle conditions are set at high power settings, plus one has the ability of obtaining transient data during throttle movements. Figure 26 provides an example of the transient liner temperature data base, these data still represent finite discrete measurements. As such, this lacks the ability to provide detailed information on axial and circumferential temperature variation and detailed information concerning liner temperature patterns around dilution holes. At General Electric, it has been established that cyclic circumferential temperature patterns for thin liner shells involving one cycle per fuel nozzle can be adequately represented using this data base along with a series of two dimensional calculations. However, liner designs with thicker shells may have larger circumferential conduction effects which may require three dimensional treatment.

In addition to liner temperature data, a substantial amount of cooling slot film effectiveness data exists at General Electric. These data are based on wind tunnel testing of models of various cooling slot designs, and on film temperature data derived from combustor tests. These wind tunnel model tests cannot simulate combustion conditions such as swirling and recirculating flows, but are very useful in separating design features of various slots. These features include:

- Feed hole spacing to diameter ratios.
- Feed hole orientation.

ORIGINAL PAGE IS
OF POOR QUALITY

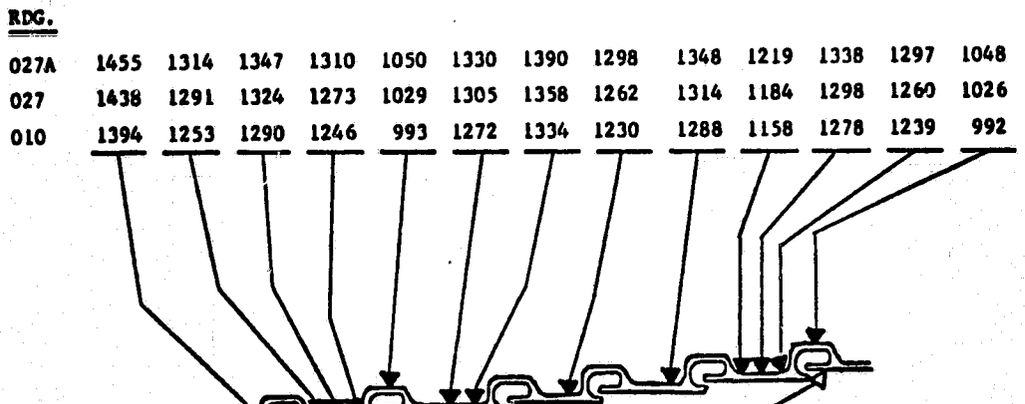


Figure 25. Sample of Steady State Liner Metal Temperature.

ORIGINAL PAGE IS
OF POOR QUALITY

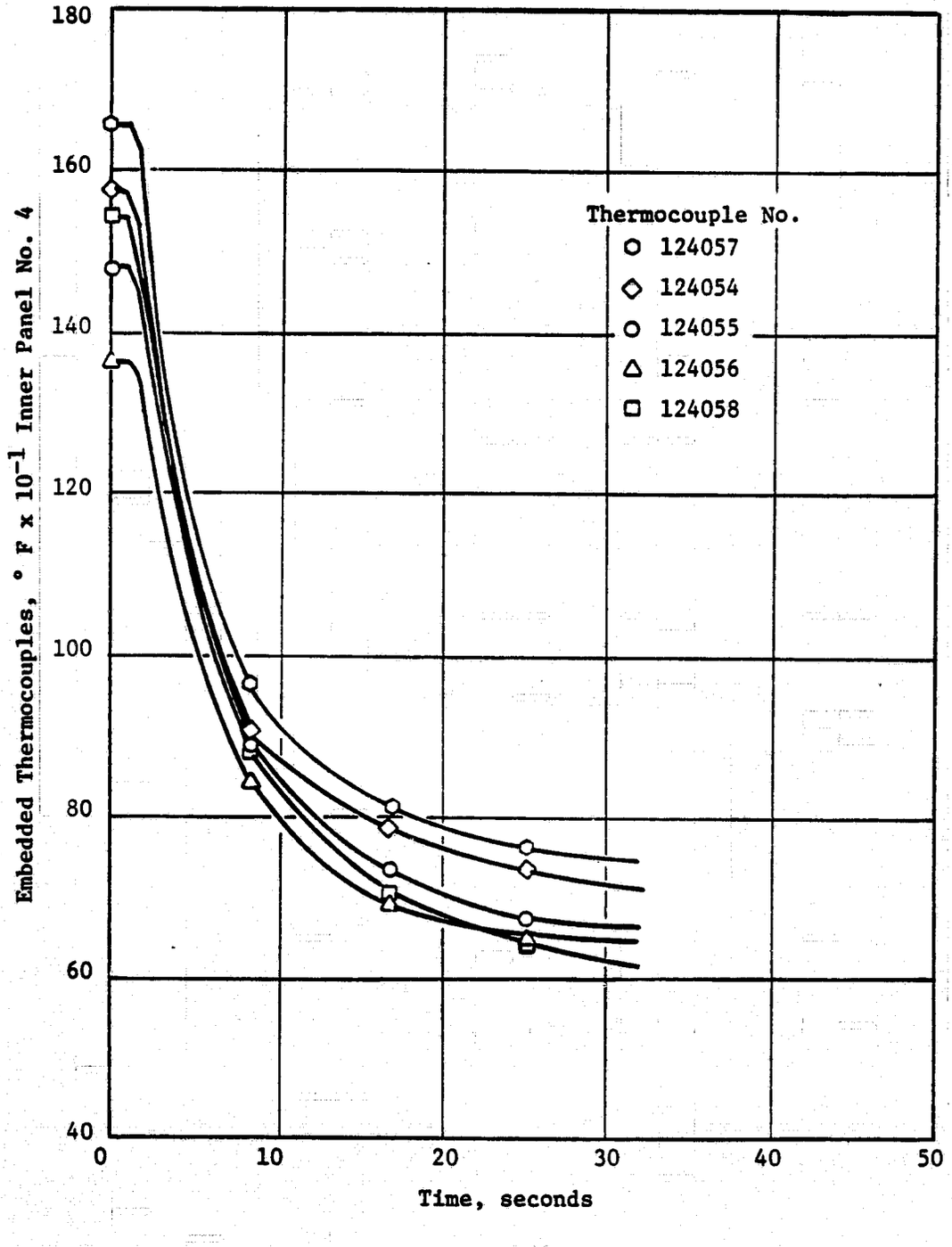


Figure 26. Sample of Transient Liner Metal Temperature Data.

- Cooling slot overhang length.
- Overhang thickness to slot height ratio.
- Slot flow to mainstream flow ratio.
- Slot plenum volume.

Film effectiveness levels in actual combustor environments are derived from component or engine test data. These levels are derived either by back calculations from measured metal temperature data or from direct measurement of cooling film temperatures.

The General Electric Company has long recognized the importance of developing combustion systems which demonstrate low levels of pattern factors and averaged profiles. The pattern factor parameter is defined as:

$$\frac{T_{MAX\ 4} - T_3}{T_{AVG\ 4} - T_3} \qquad (9)$$

where;

$T_{MAX\ 4}$ is the highest temperature anywhere in the exit plane.

$T_{AVG\ 4}$ is the average temperature in the exit plane.

T_3 is the compressor discharge temperature.

The average profile is defined by:

$$\frac{T_{LOCAL}}{T_{AVG}} \qquad (10)$$

where;

$T_{LOCAL} = T_{AVG\ 4}$ (at one radial location) $- T_{AVG\ 4}$

$T_{AVG} = T_{AVG\ 4} - T_3$

The pattern factor defines the magnitude of the highest temperature level in the combustor exhaust stream, and is of concern to the structural integrity of the stationary turbine hardware, particularly the turbine inlet nozzle hardware. The averaged profile is a measure of the circumferentially averaged radial temperature profile, and is of concern to the turbine rotating hardware. In support of these concerns, a substantial amount of exit gas temperature data have been obtained at General Electric. The majority of the data are acquired through detailed exit gas temperature measurements of full annular combustors.

Some additional data are provided from exit gas temperature measurements of sector combustors. Sector data are cheaper to obtain, but can suffer end wall effects. In all current as well as in past production programs, it has been the practice to measure exit gas temperature patterns on production combustors on a sampling basis. This is done to ensure that profile and pattern factor levels are being maintained in the production engines. A significant amount of additional exit gas temperature data are obtained from combustor designs in the development phase. This is done to ensure that the hardware design release for production satisfies the design intent. So extensive is this data base, that empirical design information has been generated for all production combustors which can be used to predict the impact on the profile and pattern factor from changes in airflow distribution, changes in dilution patterns, changes in fuel type and injection hardware, as well as the impact of combustor hardware deterioration. Table VII summarizes the results obtained from F101 and CFM56 combustors subjected to various hours of rigorous endurance testing. In a production situation some variation in the measured profile and pattern factor can be encountered due to the mechanical tolerances allowed on the various combustor flow features and leakage. Sufficient data exist to provide a statistical experience range for the measured profile and pattern factor. An example of this is shown in the following tabulation of data for a member of CFM56 combustors of the same design configuration.

No. of Combustors	Pattern Factor
1	1.24
3	1.22
1	1.21
1	1.18
1	1.17

The exit gas temperature data base also serves to illustrate another point. Typically there is a considerable amount of nonuniformity in the exit gas temperature pattern around the exit annulus of a combustor. Figure 27 shows contours of the pattern factor parameter calculated from measured exit gas temperature data obtained from a typical F101 combustor. It is observed from this figure that similarities exist from cup to cup. However, the variations in levels from cup to cup serve to illustrate the degree of nonuniformity. This is of particular interest when considering three dimensional internal flow calculations. Current aerothermal models of this type typicallly feature cyclic boundary conditions. This essentially states that the combustor section modeled is exactly identical to all other sections comprising the entire combustor. With current grid limitations, models typically represent single cup sections of the entire combustor in order to

Table VII. F101 Combustor Performance Stability.

Combustor Type	Pre-engine Pattern Factor	Post-engine Pattern Factor	Test Hours	Comment
Pre-PFRT	1.173	1.180	10	Slight Damage
PFRT	1.215	1.230	162	No Damage
PFRT Development	1.218	1.255	480	Slight Damage
PV	1.220	1.220	390	Slight Damage
Development	1.265	1.263	349	Very Damaged
PV	1.200	1.210	373	Some Damage
Development	1.230	1.200	119	Some Damage
Development	1.230	1.260	392	Minor Damage
Initial Product	1.220	1.200	522	Minor Damage

ORIGINAL PAGE IS
OF POOR QUALITY

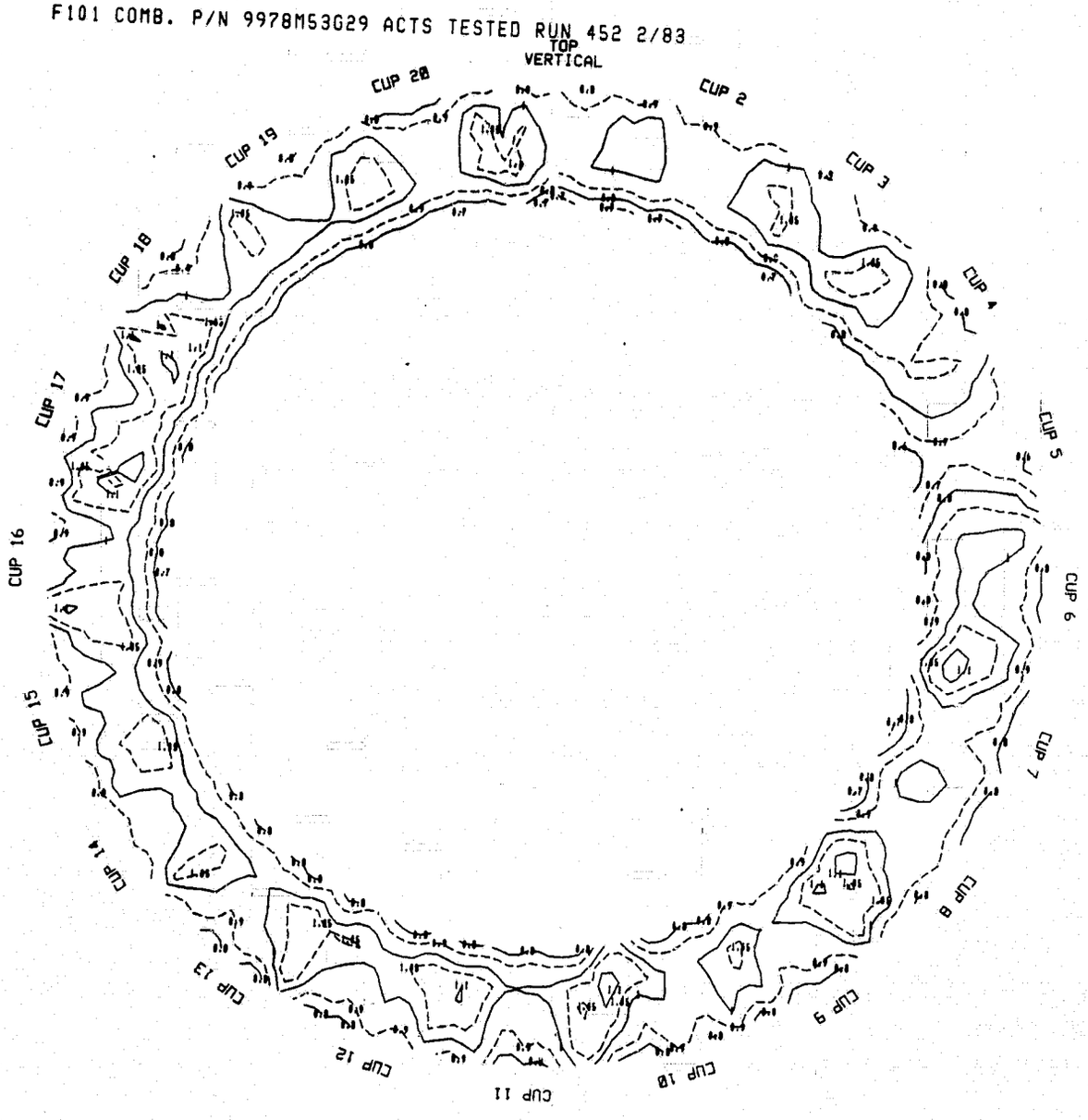


Figure 27. Sample of Measured Combustor Exit Gas Temperature Data.

provide the grid detail necessary for accurate flow calculations. Thus, the current aerothermal model cannot address the circumferential nonuniformity issue. This represents a significant limitation in the application of the model for predictions of pattern factor.

As previously mentioned, additional test data concerning combustor stability and gaseous and particulate emissions are also available at General Electric. Because they are not of significance in the scope of the Phase I effort, no further discussions about these data will be made.

In selecting which sets of data to use as the benchmark test case for comparison with calculations from the General Electric aerothermal model in general use, consideration was given to a number of items. First, the combustion system represented by the data had to be of advanced, modern design. Additional considerations included the amount, quality, and availability of the test data, as well as the range of operating conditions represented in the data. Consideration was also given to the availability of wind tunnel model test data to document hole flow coefficients, and film effectiveness and heat transfer coefficient data. From these considerations, the data base for the GE/F101 combustor was selected as the benchmark test case.

5.3 EXPERIMENTAL TEST PROGRAM

As part of the Phase I Aerothermal Modeling Program, an experimental test program was conducted at General Electric. The purpose of this effort was to obtain additional definitive data with respect to the internal flow field of a combustor from which to assess the capabilities of the 3-D elliptic detailed internal flow model. A total of 18 configurations were tested using two available test rigs. Each test rig represented a 90° sector of a full annulus combustor.

The majority of the experimental testing was conducted in a rig representing a simple combustor design. This rig featured a flat uncooled dome inlet, and parallel cylindrical uncooled liner walls. The geometry of this rig was well within the geometrical constraints of the 3-D elliptic model. The dome section was interchangable to allow various dome configurations to be tested. In this testing effort four dome inlet configurations were tested in this rig. These configurations were:

- Low pressure drop uniform/parallel flow inlet using a wire mesh
- High pressure drop uniform/parallel flow inlet using a perforated plate
- Nonswirl air injector cups
- Actual GE/F101 swirl cup hardware.

The liner walls featured two rows of dilution holes patterned after the GE/F101 combustor. The hole sizes could be varied or entirely blocked off depending

on the desired configuration. Since this rig was totally uncooled, only two-temperature trace experimental testing was conducted using this rig.

The parallel wall test rig was designed with three separate flow control systems to independently set conditions feeding the dome inlet, the outer dilution holes, and the inner dilution holes. This provided the capability for two-temperature trace testing.

Data were obtained by using a rake with 21 equally (radial) spaced thermocouple elements mounted onto a traversing arm designed to allow axial as well as circumferential movement of the rake. During a typical test run, the rake was moved from -18° from top center to +18° from top center at 1° increments at 4 axial planes downstream of the aftmost dilution injection point. This provided an array of 777 temperature measurements within the 36° section at each axial plane. In addition to the thermocouples, 11 equally (radial) spaced impact pressure probes were initially mounted onto the rake. These pressures were used to map out the inlet velocity profiles in the rig when using the uniform/parallel flow dome inlet configurations. All data obtained was sent through a data logger system and loaded onto a cassett tape for posttest processing.

A schematic of the parallel wall test rig is shown in Figure 28. An overall view of the test rig hardware and closeups views of various features of the rig are shown in the photographs in Figures 29 through 32.

The other test rig used in the experimental test effort was a 90° sector of an actual GE/F101 combustor. The F101 combustor features a conical dome with 20 equally spaced counterrotating swirl cup assemblies. The liners are a machined ring type featuring 6 film cooling slots in the outer liner, and 5 film cooling slots in the inner liner. The liners are contoured resulting in a converging internal flowpath. Each liner has 2 rows of dilution holes. Corresponding rows on each liner feature opposed holes of equal size. The primary injection row features 40 holes equally spaced around the circumference, one hole directly in line with the cup center, and one hole between cup centers. The holes in line have a diameter of 0.84 cm (0.33 inch), while the holes between are larger with a diameter 1.04 cm (0.41 inch). The secondary injection row features 60 holes equally spaced around the circumference. The holes are offset 3° from the cup centers. All 60 holes have diameter of 0.91 cm (0.36 inch).

With this test rig, data were obtained by using a rake with 13 equally (radial) spaced thermocouple elements. The rake was mounted onto a traversing arm that permitted movement only in the circumferential sense. Thus temperature measurements in this rig were made only at the discharge plane. During a typical test run the rake was moved from -36° from top center to +36° from top center in 1.5° increments. This provided an array of 637 temperature measurements within the 72° section of the discharge plane. All data obtained were sent through a data logger system and loaded onto cassett tapes for posttest processing. An illustration of the F101 sector combustor test rig is shown in Figure 33.

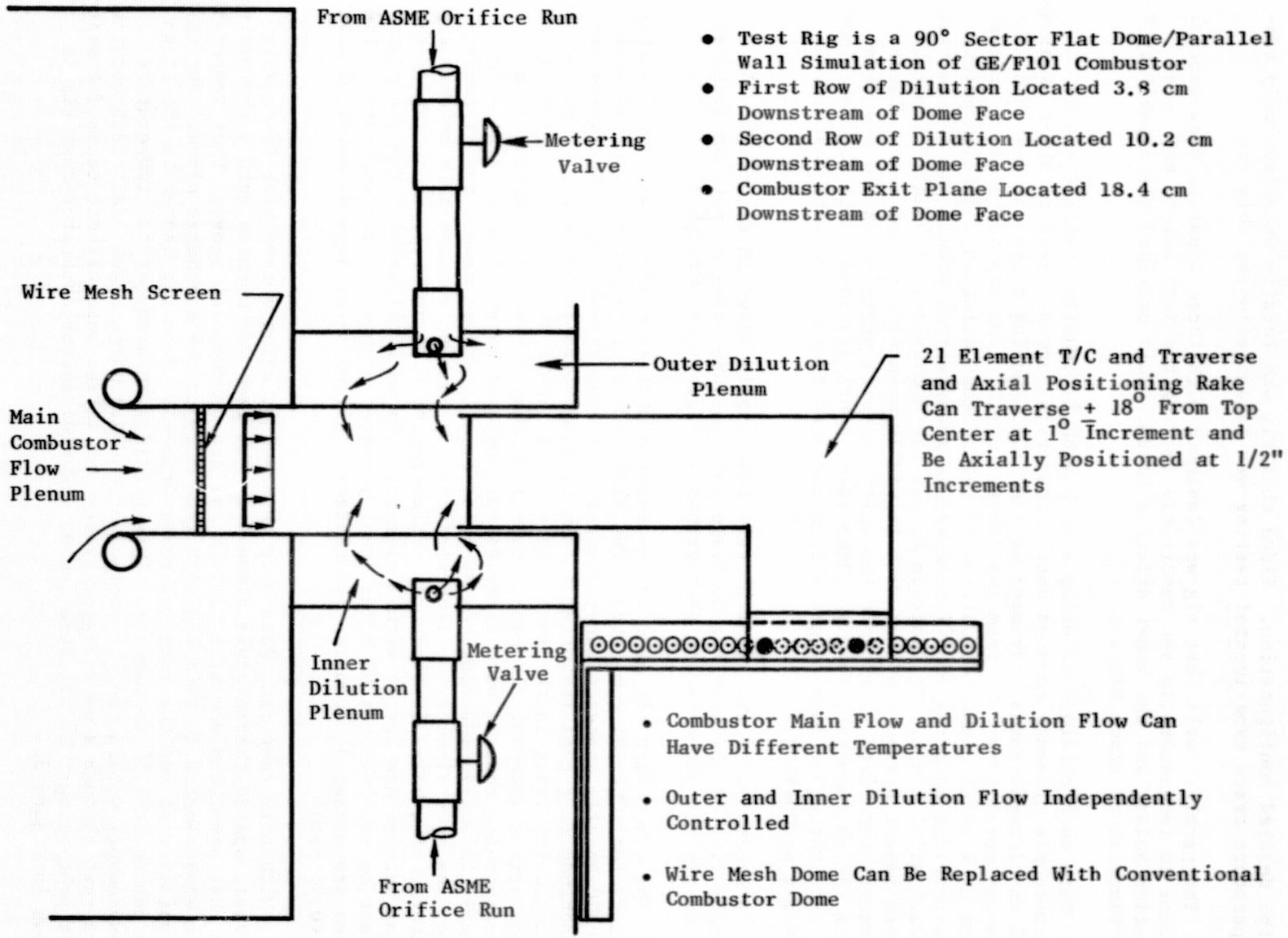


Figure 28. Aerothermal Modeling Experimental Test Rig (Unfueled).

ORIGINAL PAGE IS
OF POOR QUALITY

ORIGINAL PAGE IS
OF POOR QUALITY

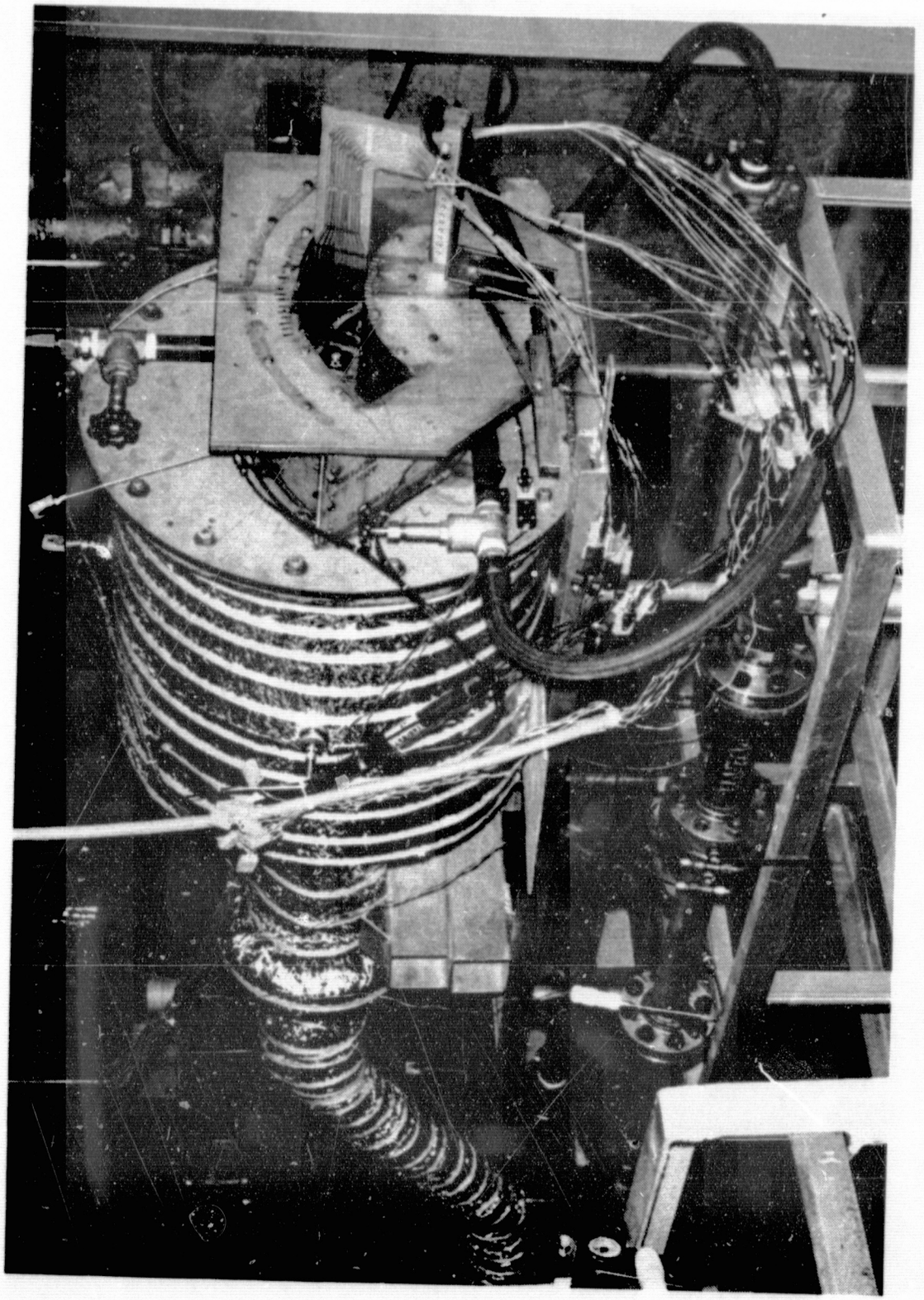


Figure 29. Aerothermal Modeling Experimental Test Rig (Unfueled).

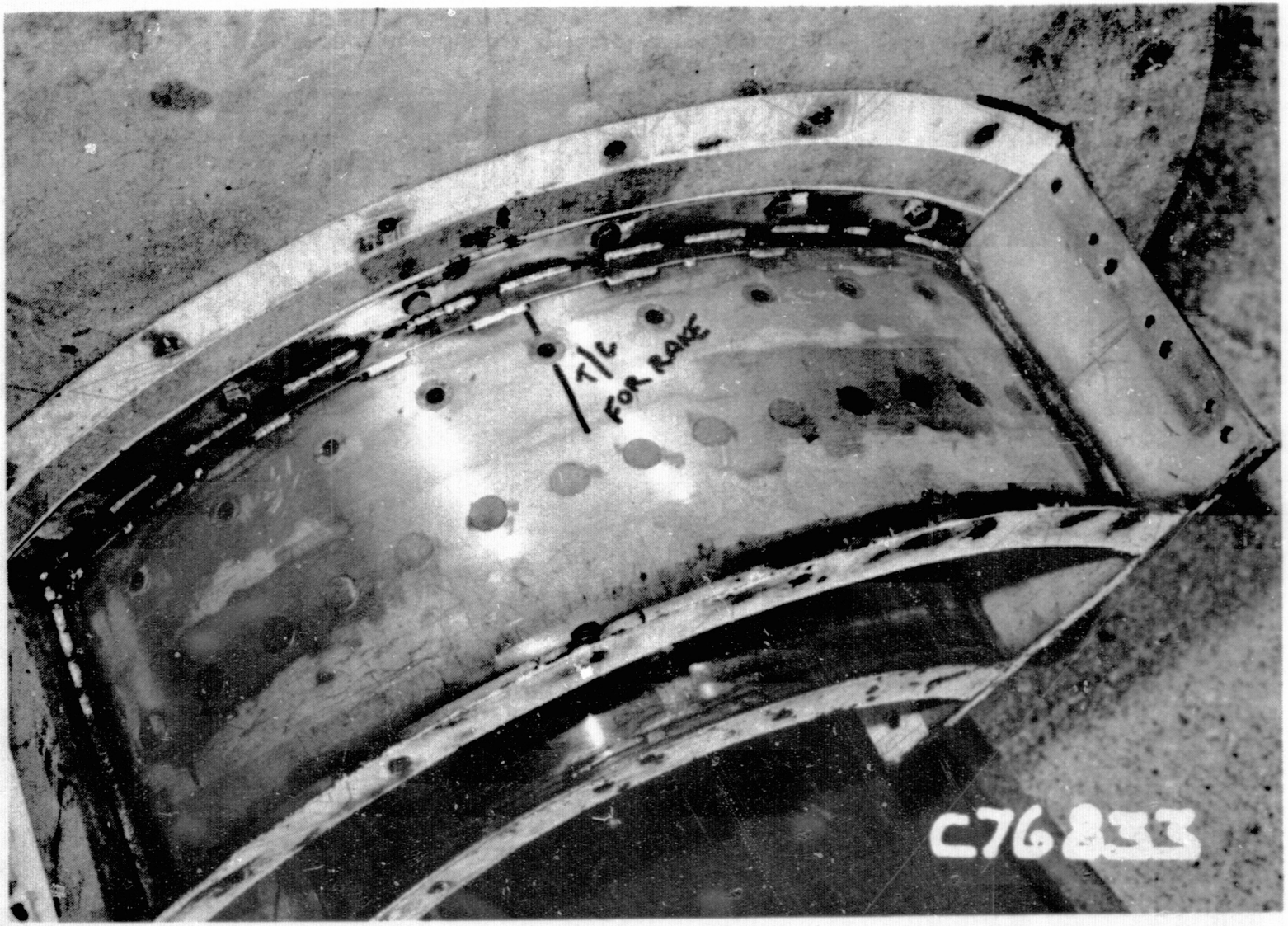


Figure 30. Aerothermal Modeling Experimental Test Rig (Unfueled).

ORIGINAL PAGE IS
OF POOR QUALITY

ORIGINAL PAGE IS
OF POOR QUALITY

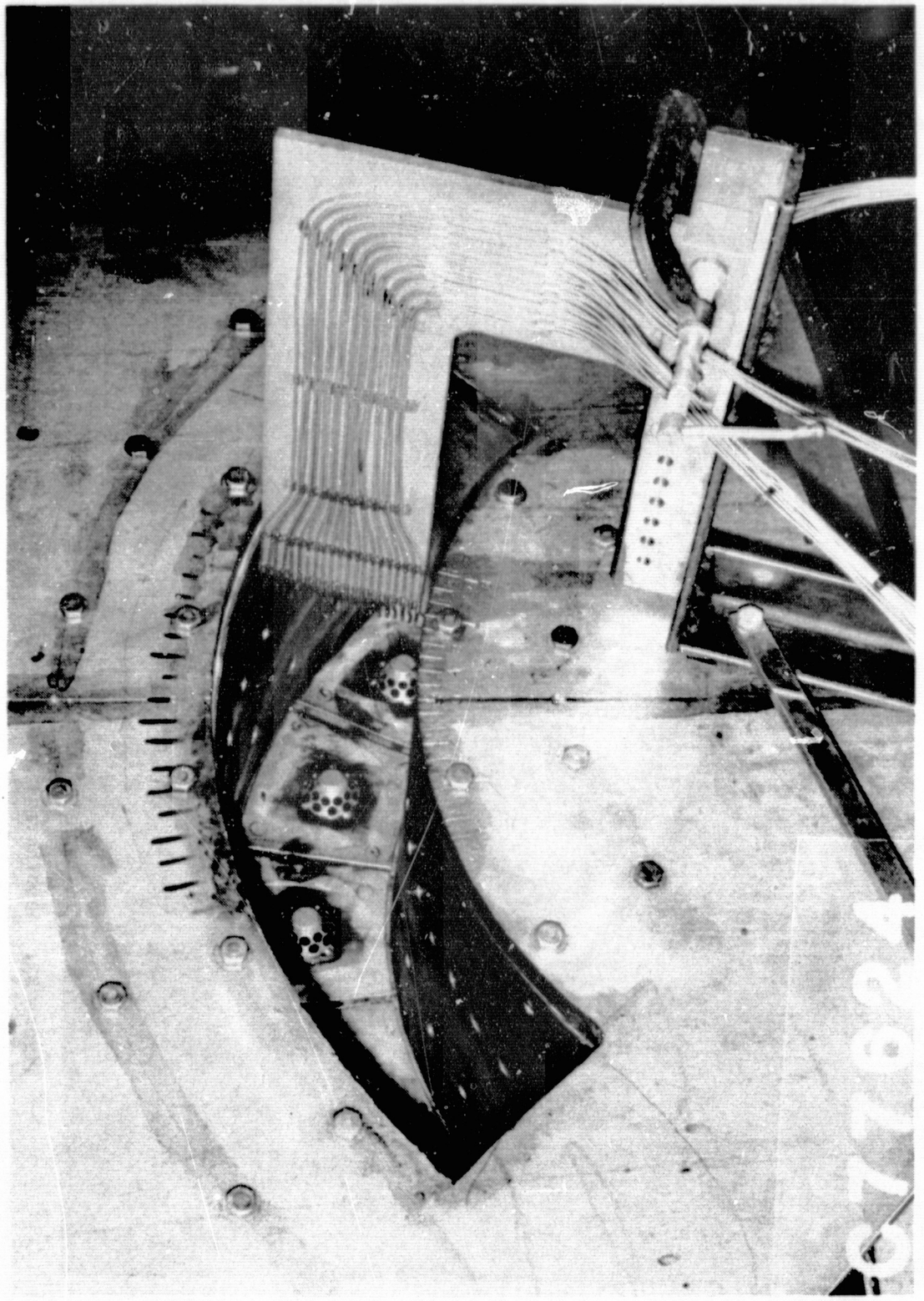


Figure 31. Aerothermal Modeling Experimental Test Rig (Unfueled).

ORIGINAL PAGE IS
OF POOR QUALITY

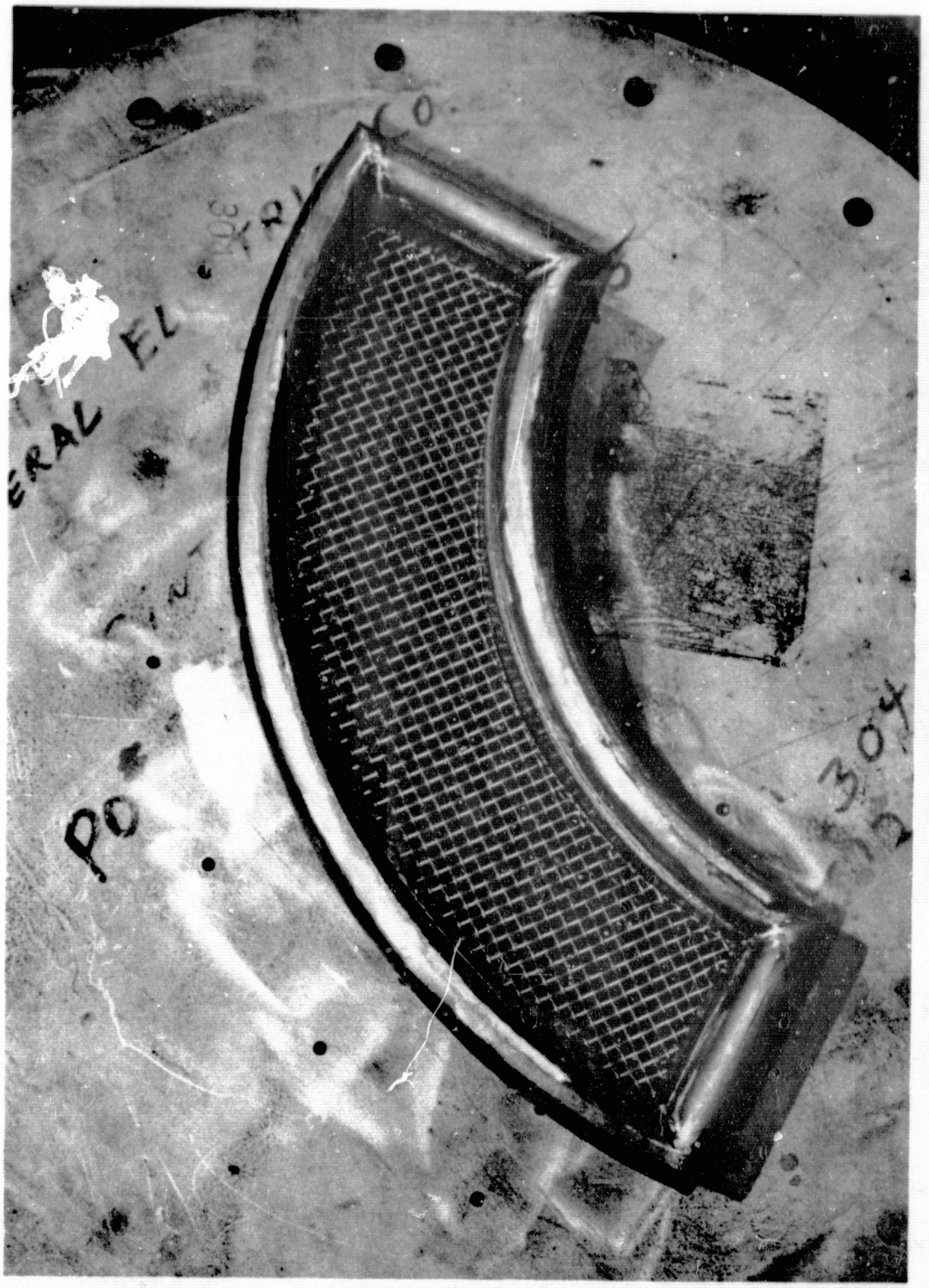


Figure 32. Aerothermal Modeling Experimental Test Rig (Unfueled).

ORIGINAL PAGE IS
OF POOR QUALITY

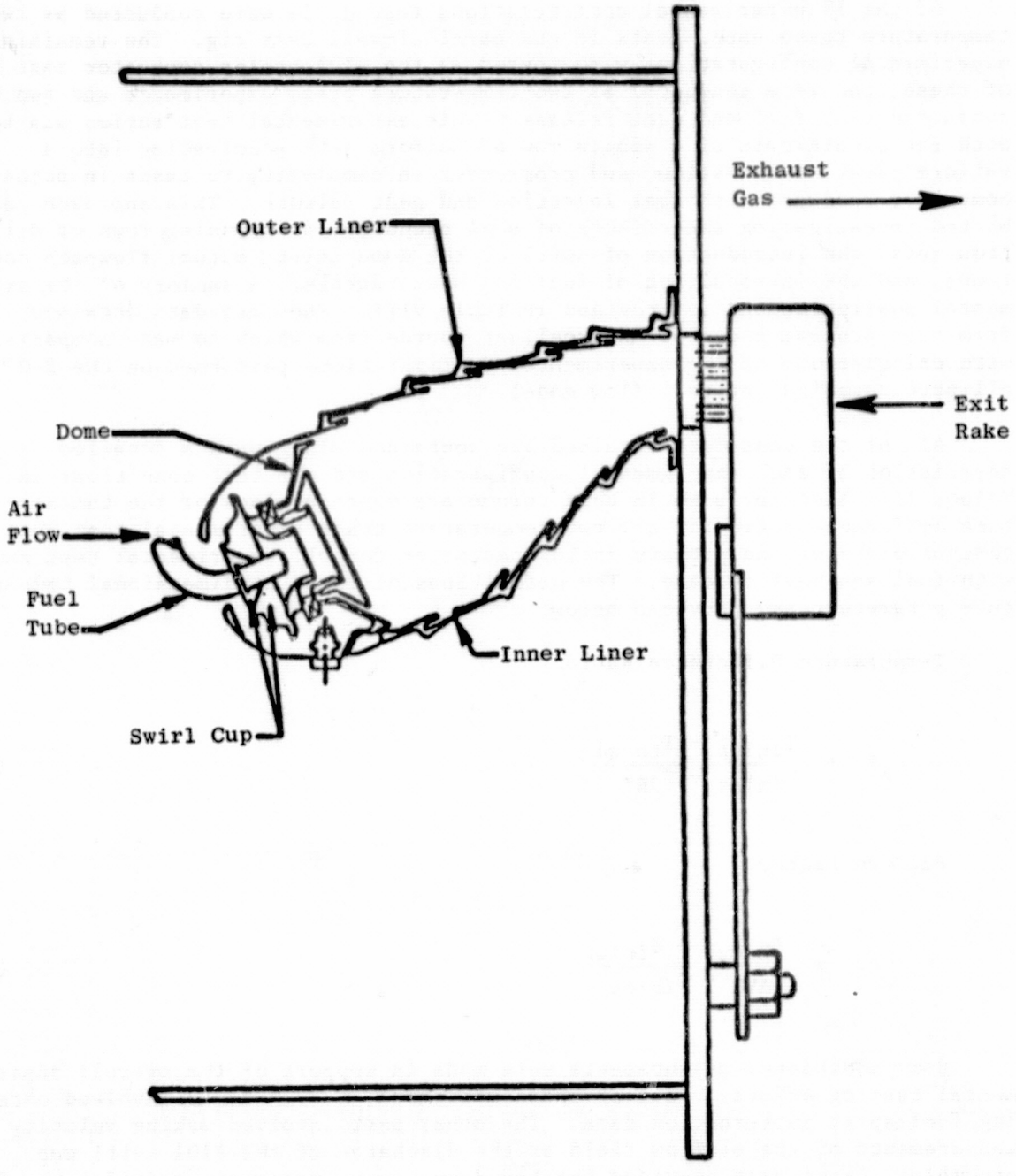


Figure 33. Aerothermal Modeling Experimental Test Rig (Fueled).

Of the 18 experimental configurations tested, 14 were conducted as two-temperature trace experiments in the parallel-wall test rig. The remaining 4 experimental configurations were tested in the F101 sector combustor test rig. Of these, two were conducted as two-temperature trace experiments and two were conducted with fuel and heat release. This experimental test series started with the simple case of a single row of uniform jets penetrating into a uniform/parallel crossflow, and progressed in complexity to cases in actual combustor hardware with fuel injection and heat release. This approach permitted investigating the effects of such phenomena as opposing rows of dilution jets, the introduction of swirl at the dome inlet, actual flowpath contours, and the introduction of fuel and heat release. A summary of the experimental configurations is provided in Table VIII. The test data obtained from this program provided an excellent source from which to make comparisons with calculations of the experimental configurations performed on the 3-D elliptic detailed internal flow model.

All of the test data obtained are contained along with a detailed description of each experimental configuration and the test conditions in Volume II. Also included in this volume are contour plots of the temperature difference ratio for all two-temperature trace experimental test runs, and contour plots of the pattern factor parameter for all experimental test runs with fuel and heat release. The definitions of these nondimensional temperature parameters are provided below.

Temperature Difference Ratio:

$$\theta = \frac{T_{Inlet} - T_{Local}}{T_{Inlet} - T_{JET}} \tag{11}$$

Pattern Factor

$$P_f = \frac{T_{Local} - T_{Inlet}}{T_{AVG} - T_{Inlet}} \tag{12}$$

Some additional measurements were made in support of the overall experimental testing effort. Part of these additional measurements involved obtaining fuel spray patternation data. The other part involved making velocity measurements of the airflow field at the discharge of the F101 swirl cup assembly. These data provided the boundary inputs necessary to model the dome inlet conditions for experimental test configurations featuring this hardware.

The fuel spray patternation data were obtained in the radial patternation test stand at General Electric. This test stand is shown in Figure 34. In

C-2

Of the 18 experimental configurations tested, 14 were conducted as two-temperature trace experiments in the parallel-wall test rig. The remaining 4 experimental configurations were tested in the F101 sector combustor test rig. Of these, two were conducted as two-temperature trace experiments and two were conducted with fuel and heat release. This experimental test series started with the simple case of a single row of uniform jets penetrating into a uniform/parallel crossflow, and progressed in complexity to cases in actual combustor hardware with fuel injection and heat release. This approach permitted investigating the effects of such phenomena as opposing rows of dilution jets, the introduction of swirl at the dome inlet, actual flowpath contours, and the introduction of fuel and heat release. A summary of the experimental configurations is provided in Table VIII. The test data obtained from this program provided an excellent source from which to make comparisons with calculations of the experimental configurations performed on the 3-D elliptic detailed internal flow model.

All of the test data obtained are contained along with a detailed description of each experimental configuration and the test conditions in Volume II. Also included in this volume are contour plots of the temperature difference ratio for all two-temperature trace experimental test runs, and contour plots of the pattern factor parameter for all experimental test runs with fuel and heat release. The definitions of these nondimensional temperature parameters are provided below.

Temperature Difference Ratio:

$$\theta = \frac{T_{Inlet} - T_{Local}}{T_{Inlet} - T_{JET}} \tag{11}$$

Pattern Factor

$$P_f = \frac{T_{Local} - T_{Inlet}}{T_{AVG} - T_{Inlet}} \tag{12}$$

Some additional measurements were made in support of the overall experimental testing effort. Part of these additional measurements involved obtaining fuel spray patternation data. The other part involved making velocity measurements of the airflow field at the discharge of the F101 swirl cup assembly. These data provided the boundary inputs necessary to model the dome inlet conditions for experimental test configurations featuring this hardware.

The fuel spray patternation data were obtained in the radial patternation test stand at General Electric. This test stand is shown in Figure 34. In

C-2

Table VIII. Summary of Experimental Test Configurations.

Configuration	Outer Wall 1st Dilution Row	Inner Wall 1st Dilution Row	Outer Wall 2nd Dilution Row	Inner Wall 2nd Dilution Row	Dome Type	Wall Type	Fuel Type	Momentum Ratio
1	0.794 CM Diameter Spacing Every 9° From Top	None	None	None	Low AP Screen	Cylindrical - Uncoled	None	13
2		0.794 CM Diameter Spacing Every 9° From Top						12
3		None	0.794 CM Diameter Spacing Every 6° From 3° CW					15
4	0.794 CM Diameter 0°, 18°, 36° 1.032 CM Diameter 9°, 27°, 45°	0.794 CM Diameter 0°, 18°, 36° 1.032 CM Diameter 9°, 27°, 45°	None					10
5								50
6		0.794 CM Diameter 0°, 18°, 36° 1.032 CM Diameter 9°, 27°, 45°	0.913 CM Diameter Spacing Every 6° From 3° CW	0.913 CM Diameter Spacing Every 6° From 3° CW				10
7								50
8		None	None	None				50
9		0.794 CM Diameter 0°, 18°, 36° 1.032 CM Diameter 9°, 27°, 45°	0.913 CM Diameter Spacing Every 6° From 3° CW	0.913 CM Diameter Spacing Every 6° From 3° CW	Perforated Plate 5% AP			50
10			None	None	Nonswirl Air Injectors			50
11			0.913 CM Diameter Spacing Every 6° From 3° CW	0.913 CM Diameter Spacing Every 6° From 3° CW				50
12			None	None	Counterrotating Swirl Cup			50
13			0.913 CM Diameter Spacing Every 6° From 3° CW	0.913 CM Diameter Spacing Every 6° From 3° CW				50
14					Nonswirl Air Injectors			770
15 (GE/F101 Sector)	Standard Configuration (Equivalent Areas) 0.794 CM Diameter 0°, 18°, 36° 1.032 CM Diameter 9°, 27°, 45°	Standard Configuration (Equivalent Areas) 0.794 CM Diameter 0°, 18°, 36° 1.032 CM Diameter 9°, 27°, 45°	Standard Configuration (Equivalent Areas) 0.93 CM Diameter Spacing Every 6° From 3° CW	Standard Configuration (Equivalent Areas) 0.93 CM Diameter Spacing Every 6° From 3° CW	Standard Configuration	Standard Configuration		Injection 52 M/Sec
16A (GE/F101 Sector)					Without Dome Cooling			Injection 44 M/Sec
16B (GE/F101 Sector)								Injection 29 M/Sec
17A (GE/F101 Sector)						Without Liner Cooling		Injection 44 M/Sec
17B (GE/F101 Sector)								Injection 29 M/Sec
17C (GE/F101 Sector)							JP-5 Low AP Injectors f/a = 0.016	Injection 160 M/Sec
17D (GE/F101 Sector)							JP-5 High AP Injectors f/a = 0.016	Injection 233 M/Sec
18A (GE/F101 Sector)					Standard Configuration	Standard Configuration	JP-5 Low AP Injectors f/a = 0.020	5% Pressure Drop
18B (GE/F101 Sector)							City Gas Low AP Injectors f/a = 0.012	5% Pressure Drop
18C (GE/F101 Sector)							JP-5 High AP Injectors f/a = 0.020	5% Pressure Drop
18D (GE/F101 Sector)							JP-5 High AP Injectors f/a = 0.012	5% Pressure Drop

ORIGINAL PAGE IS
OF POOR QUALITY

ORIGINAL PAGE IS
OF POOR QUALITY

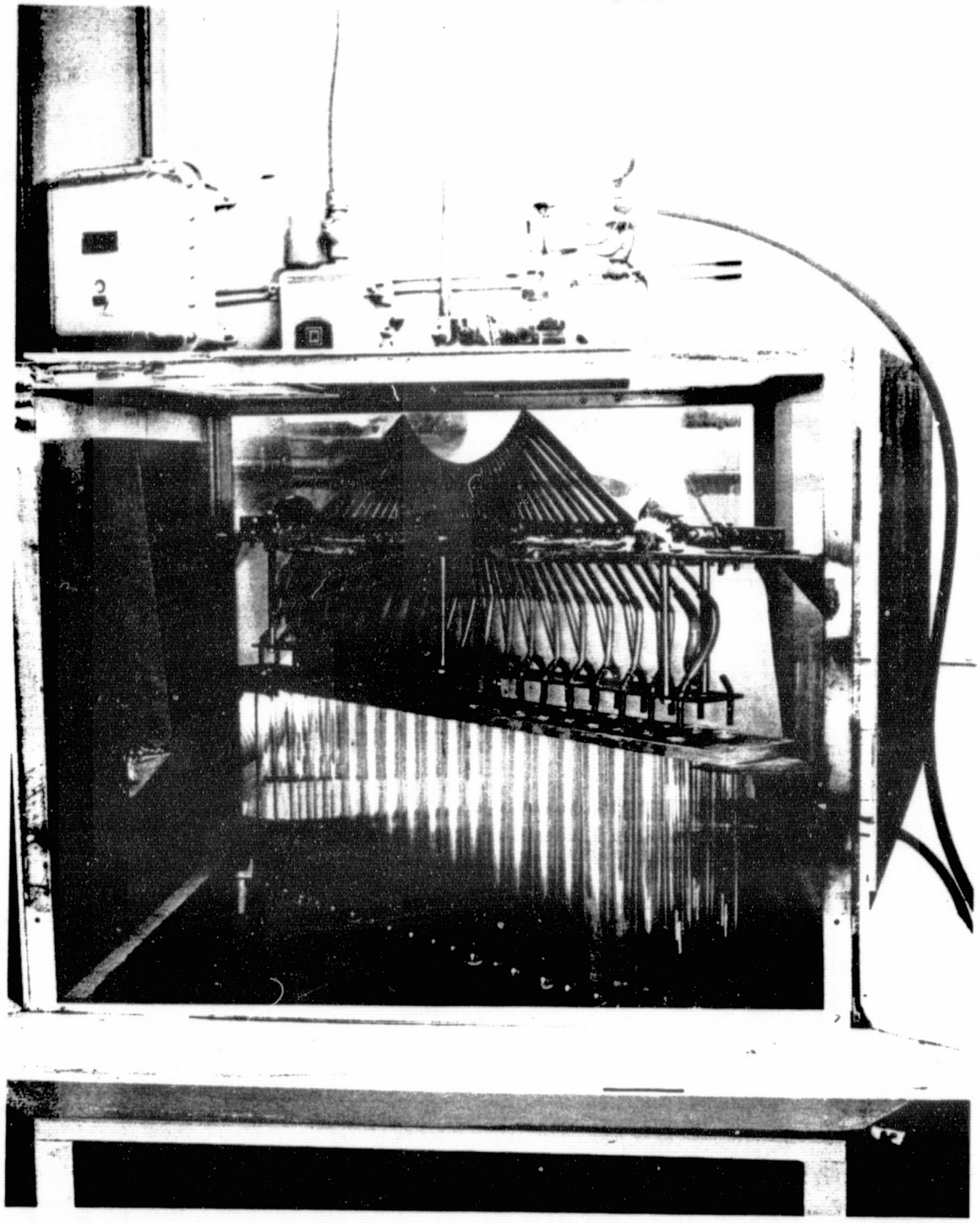


Figure 34. Atmospheric Pressure Radial Patternation Test Stand.

this test stand, the swirl cup - fuel injector assembly is mounted centrally above a multitude collector rake. The tubes in this rake are arranged along a radial arc and serve to collect fuel over a predetermined run time. The plate onto which the swirl cup is mounted can be rotated with respect to the rake allowing measurements of radial fuel distributions at any circumferential position. Test runs are conducted at atmospheric pressure and ambient temperature. The swirl cup and fuel injector pressure drops can be set to simulate the desired test rig or engine operating conditions. Radial patternations were performed on the F101 swirl cup and splashplate assembly featuring the standard low pressure fuel injector, and the high pressure atomizing fuel nozzle. Both configurations were featured in some of the experimental test configurations. In each case care was taken so that the axisymmetric parts were concentric about the swirl cup axis. The splashplate assembly is asymmetric. The data obtained from these measurements are presented in Figures 35 and 36. Graphic 3-D presentations of the data are shown in Figures 37 and 38. It is evident from these data that the fuel distributions are not axisymmetric. In both cases the greatest concentration of fuel lies in the region from 180° to 360° clockwise aft looking forward. These results are in agreement with past results obtained on this swirl cup design. They point out the need for considerable detail in modeling the dome inlet if accuracy is to be achieved with analytical calculations. Some additional patternation data is presented in Figures 39 through 44. These are results from a similar swirl cup design illustrating the effects of eccentricity among the axisymmetric parts, and of the fuel nozzle tip immersion through the face of the primary swirler. Neither of these effects were present in the experimental rig testing conducted as part of this program. However in a real engine, each swirl cup around the annulus can suffer from different degrees of eccentricity and fuel injector tip immersion. The resulting circumferential nonuniformity can have a significant impact on the measured combustor liner and turbine inlet gas temperature patterns.

Airflow velocity measurements at the discharge plane of the F101 swirl cup assembly were made using a five-hole (3-dimensional), wedge probe. An illustration of this probe is shown in Figure 45. In this test stand the swirl cup test piece is mounted onto a plate at the end of a 10.2-cm (4-inch) air supply pipe section. Air is supplied to the swirl cup through this pipe section at ambient temperature and atmospheric pressure. The wedge probe is positioned using a device which allows axial, vertical, and horizontal movement as well as rotation about the axis of the probe. Pressures from all five probe orifices are read on a bank of water manometers. The axial, radial, and tangential velocity components are calculated from these pressure measurements using a set of calibration curves generated for the five-hole wedge probe. The results of the wedge probe measurements made on the F101 swirl cup assembly are shown in Figure 46. The probe was initially positioned at the swirl cup centerline at a distance of 0.25-cm (0.10-inch) downstream of the discharge plane. Measurements were made by moving the probe horizontally along the cup diameter away from the cup center at 0.13-cm (0.05-inch) increments. As observed from the results, at this measurement plane the swirl cup exhibits a recirculation zone extending radially outward 1.14-cm (0.45-inch) from the

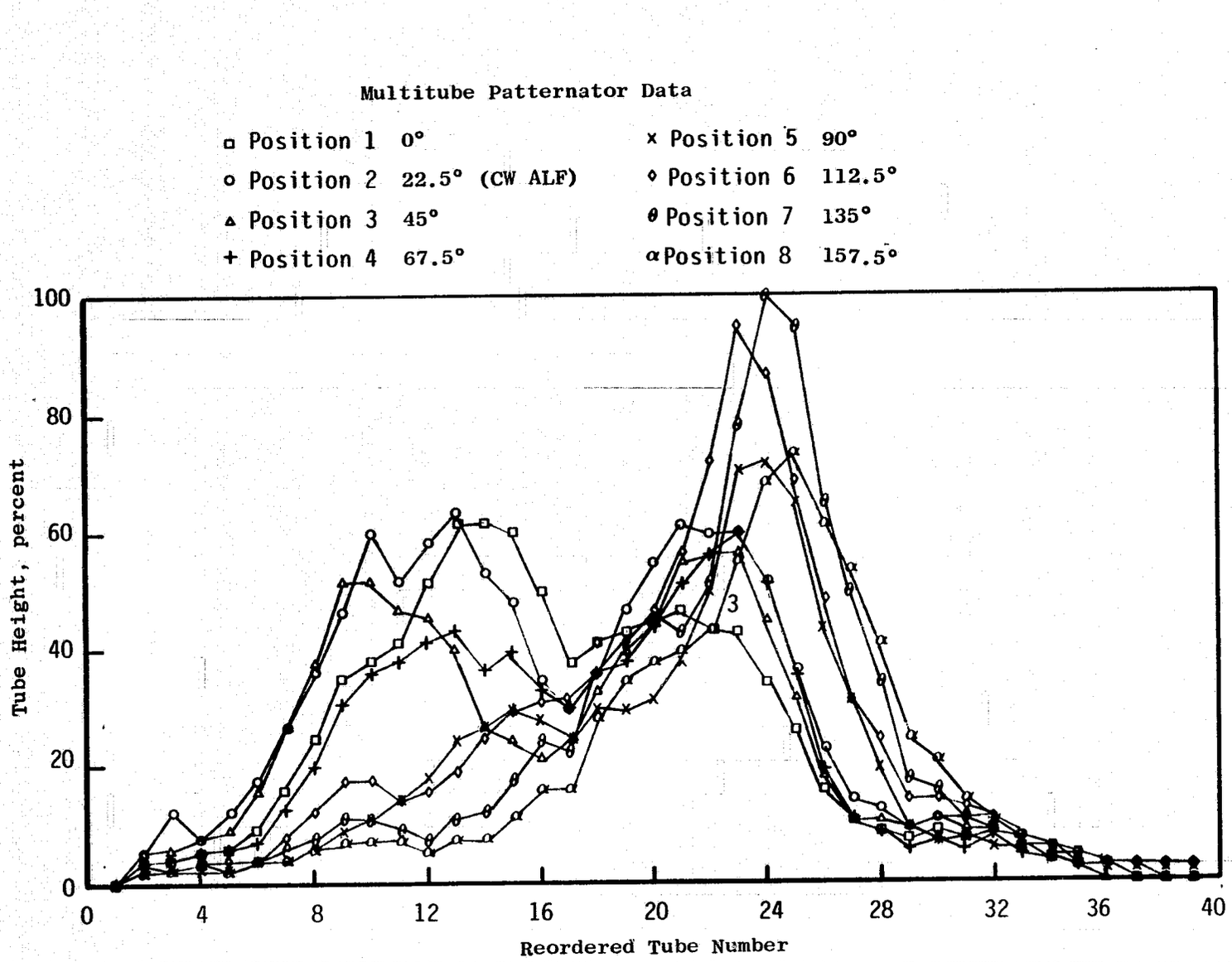
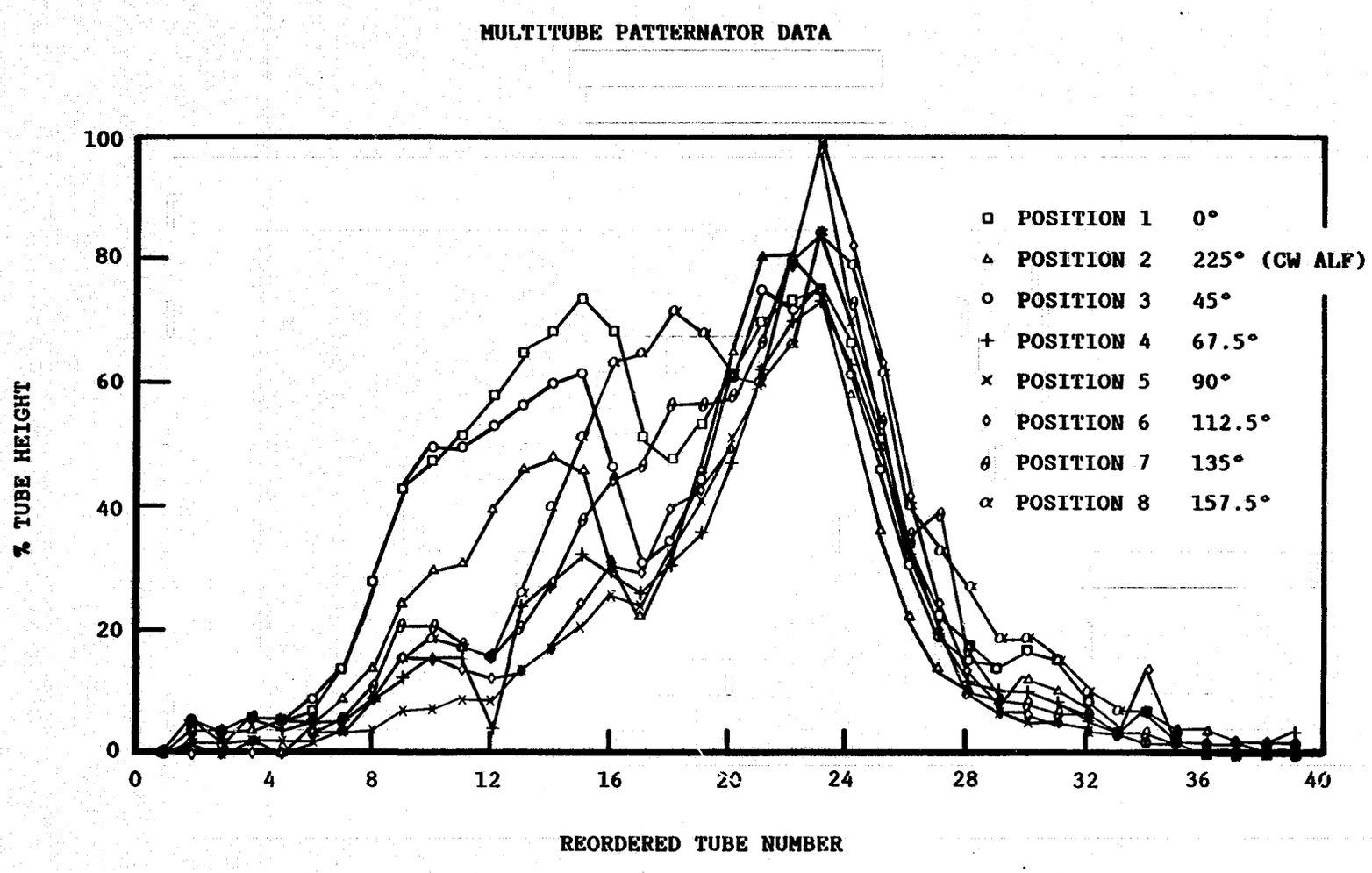


Figure 35. Patternation Test Results for Typical CFM56/F101 Fuel Injectors (Atomizing Fuel Nozzle).

ORIGINAL PAGE IS
OF POOR QUALITY



ORIGINAL PAGE IS
OF POOR QUALITY

Figure 36. Patternator Run Using F101 Low Pressure Fuel Injectors.
Patternation Test Results for Typical CFM56/F101 Fuel Injectors
(Low Pressure Fuel Injectors)

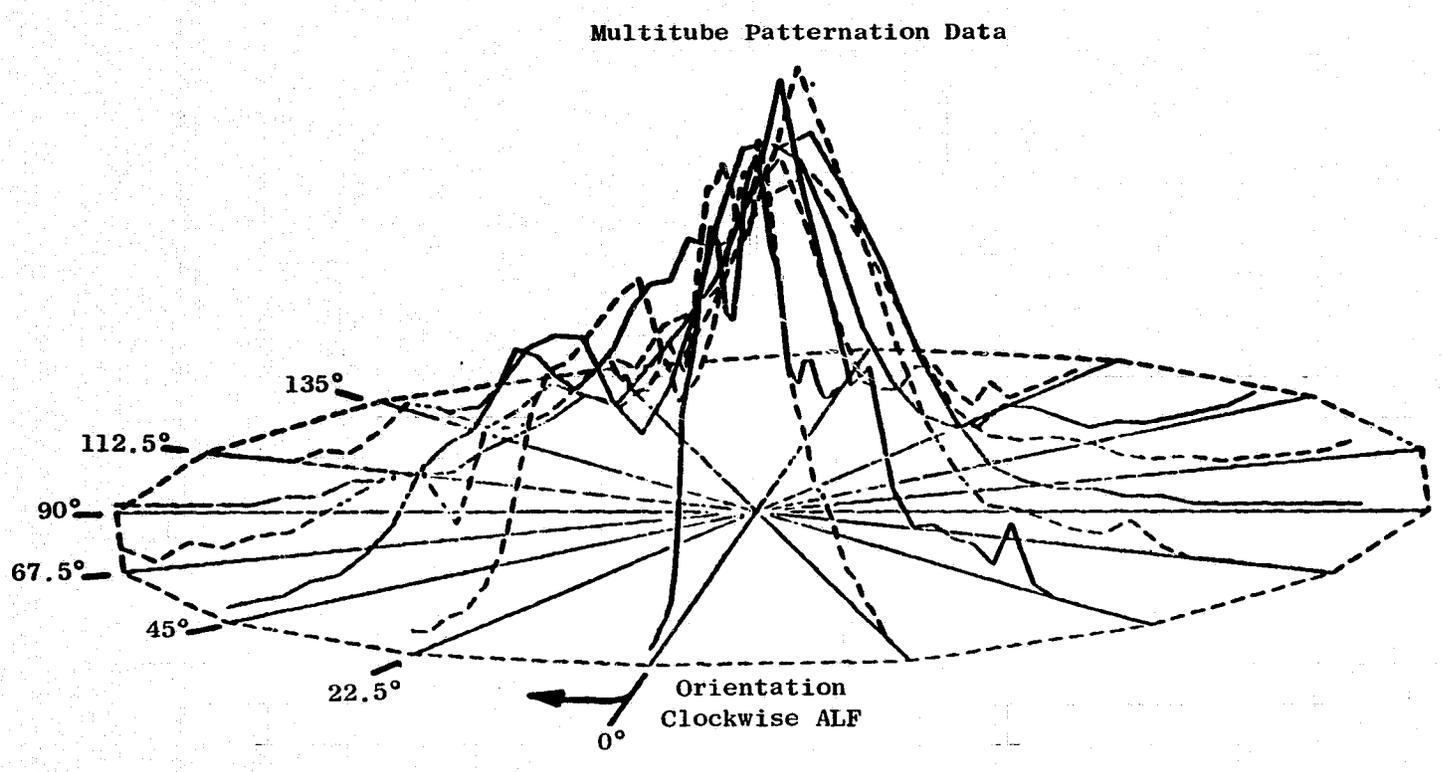
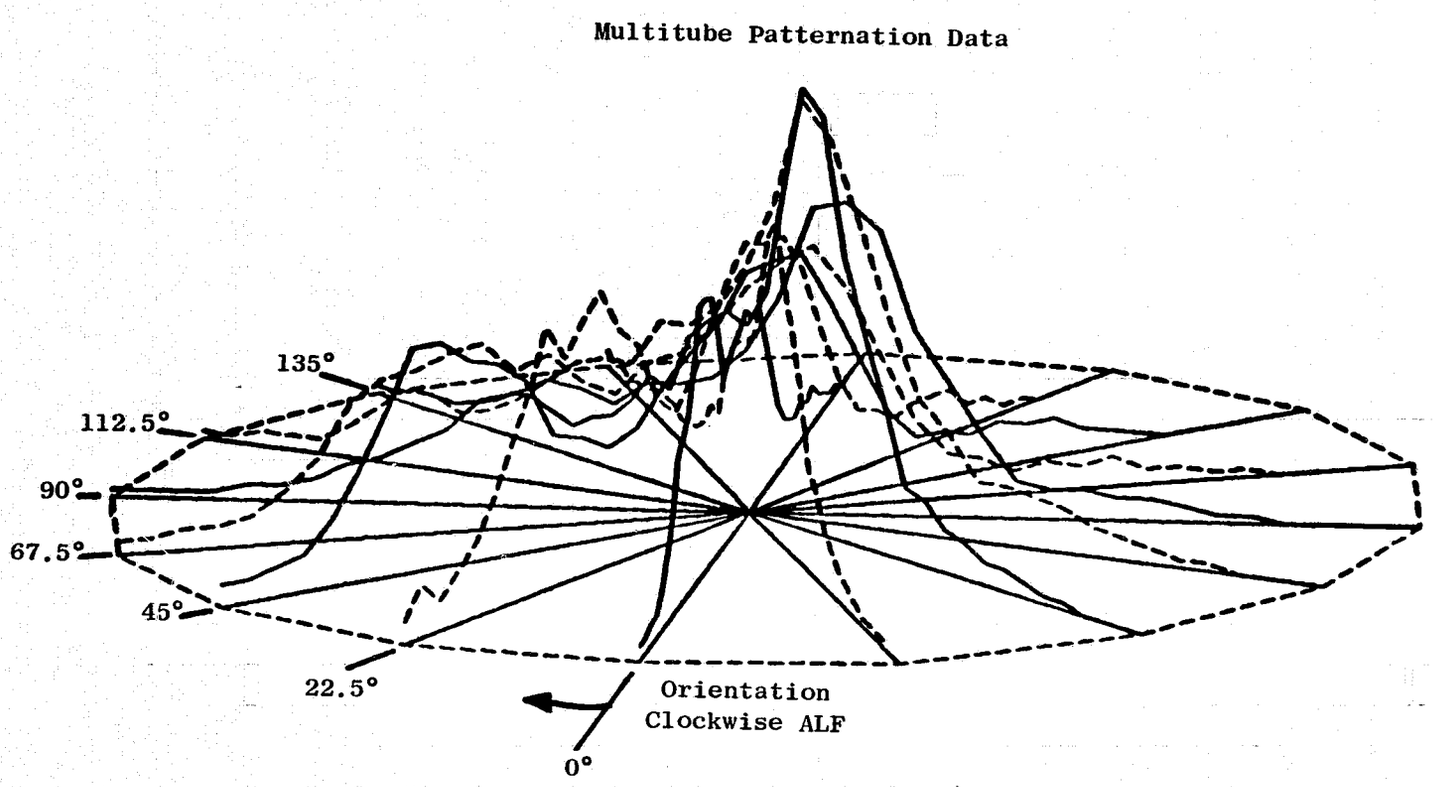


Figure 37. Patternation Test Results for Typical CFM56/F101 Fuel Injectors (Low Pressure Fuel Injector).

ORIGINAL PAGE IS
OF POOR QUALITY



ORIGINAL PAGE IS
OF POOR QUALITY

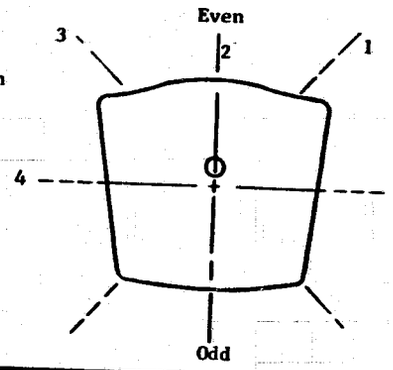
Figure 38. Patternation Test Results for Typical CFM56/F101 Fuel Injectors (Atomizing Fuel Nozzle).

F101 Rich Dome

AB11P04
VENTURI VIII
Std. Secondary Swirler
Sleeve P/N 202P12
Std. Fuel Tube Tip, Immersion - Std.
Pri. Swirler Moved Radially Out 0.10 In.
Run 2

Wf = 20 PPH
Dome ΔP = 21" H_2O

Orientation



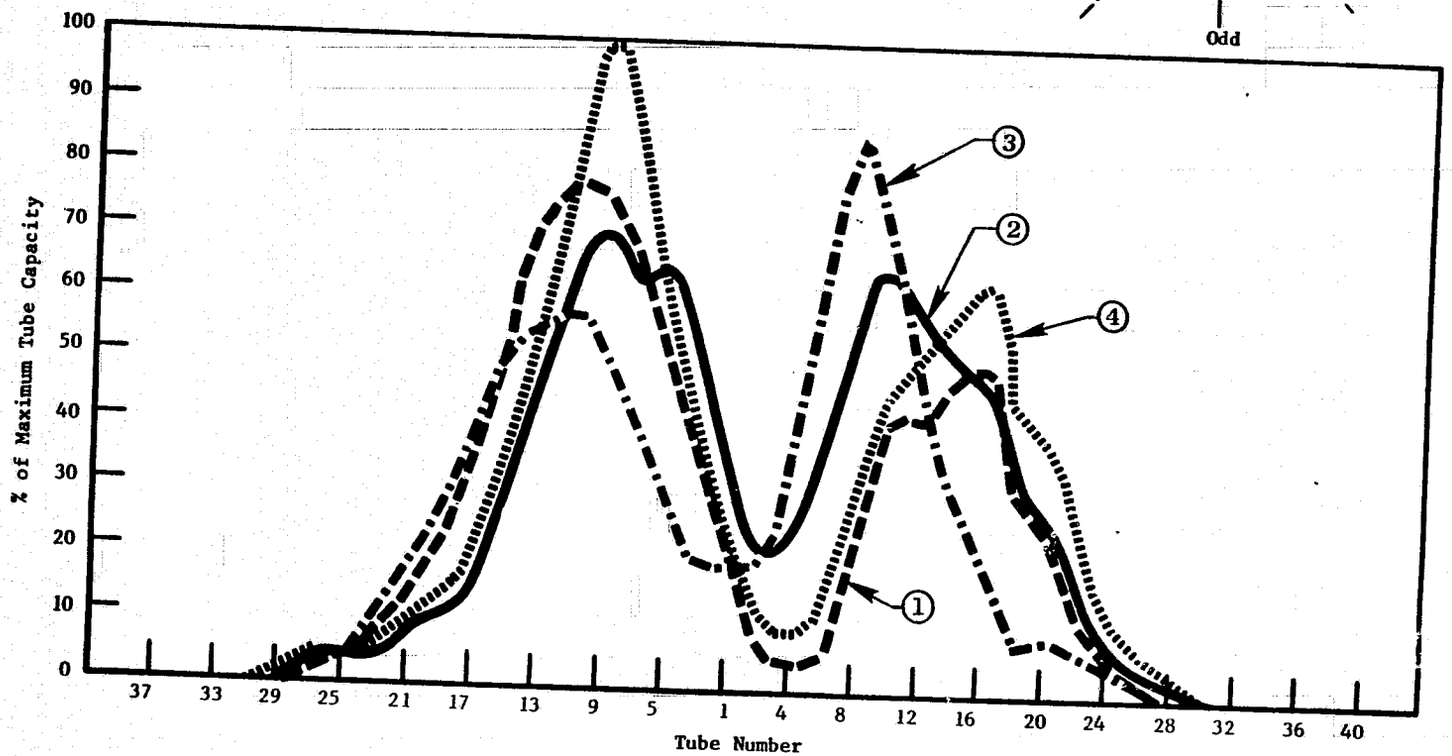


Figure 39. Earlier Patternation Test Results Showing Effects of Eccentricity and Fuel Injector Tip Immersion.

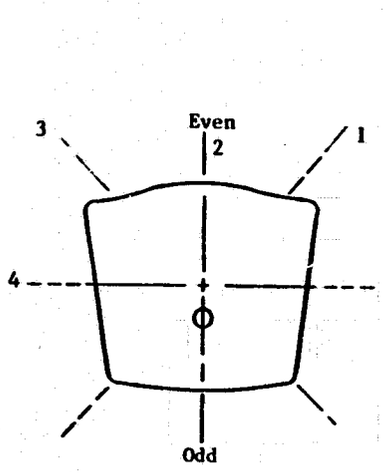
ORIGINAL PAGE IS
OF POOR QUALITY

F101 Rich Dome

AB11P04
VENTURI VIII
Std. Secondary Swirler
Sleeve P/N 202P12
Std. Fuel Tube tip, Immersion - Std.
Pri. Swirler Moved Radially in 0.10 In.
Run 3

Wf = 20 PPH
Dome ΔP = 21" H_2O

Orientation



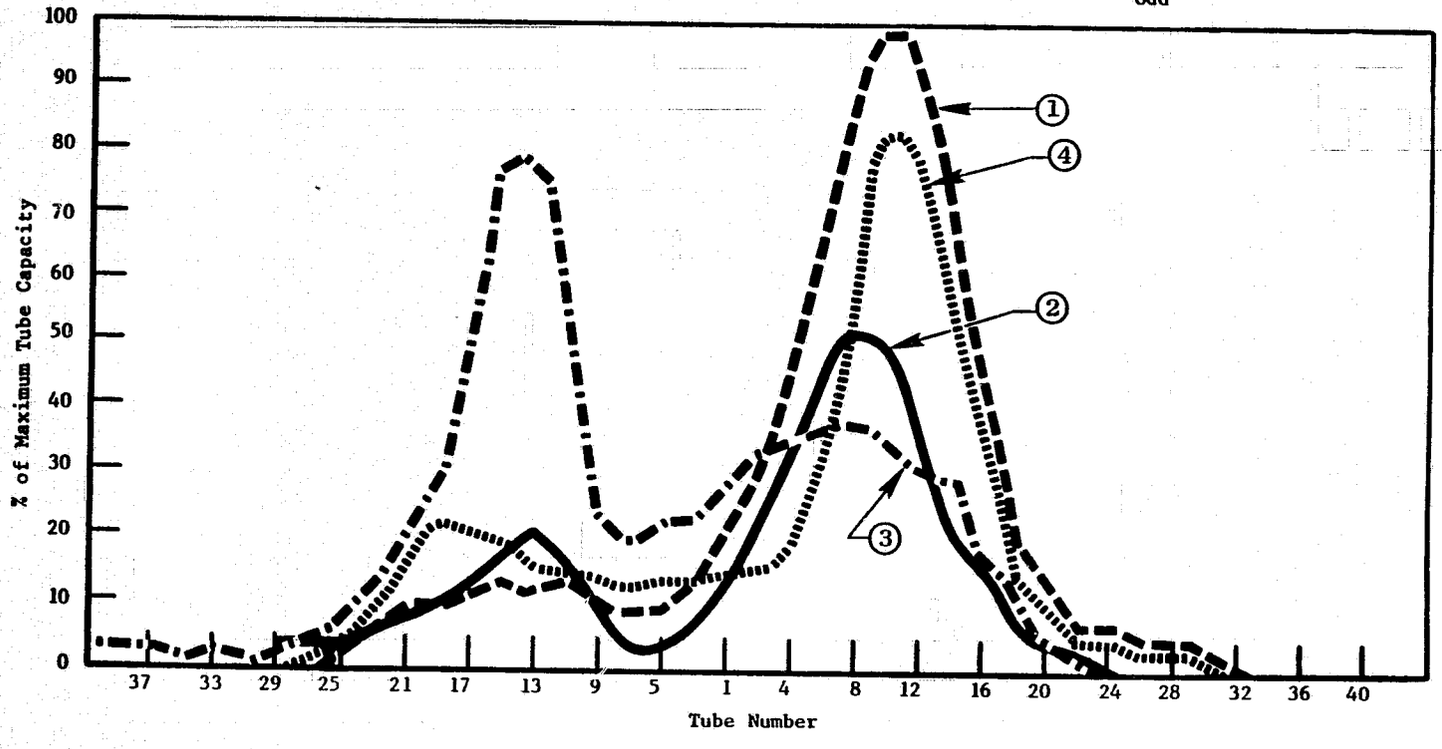


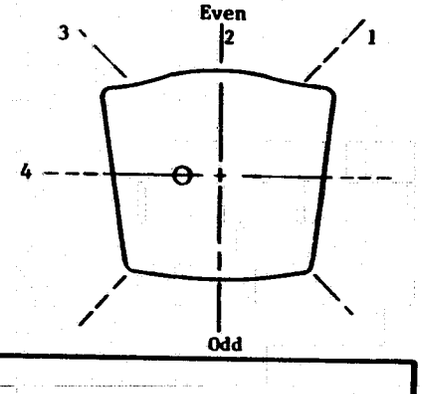
Figure 40. Earlier Patternation Test Results Showing Effects of Eccentricity and Fuel Injector Tip Immersion.

ORIGINAL PAGE IS
OF POOR QUALITY

F101 Rich Dome

AB11P04
VENTURI VIII
Std. Secondary Swirler
Sleeve P/N 202P12
Std. Fuel Tube Tip, Immersion - Std.
Pri. Swirler Moved Circumferentially
0.1 Inch in the 270° Direction
Run 4

W_f = 20 PPH
Dome ΔP = 21" H_2O



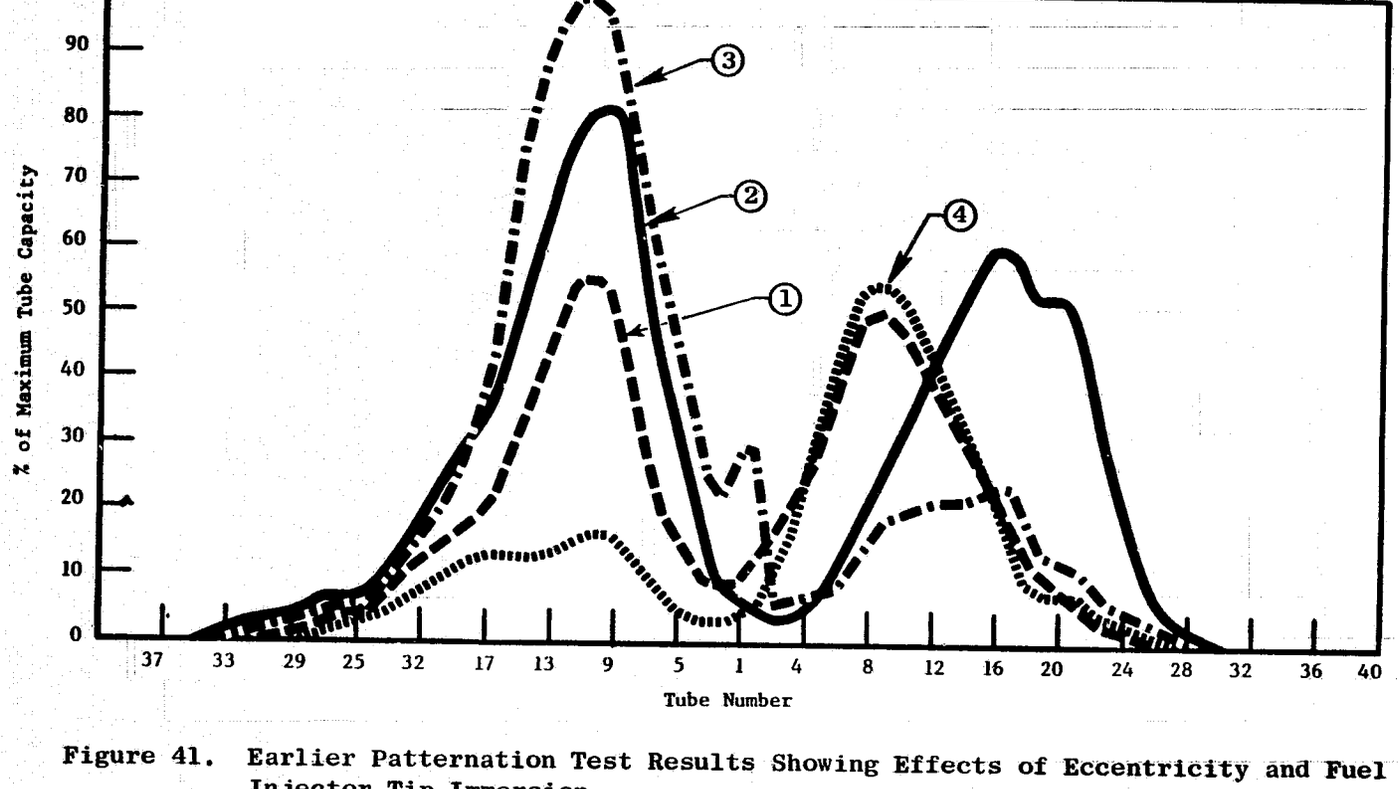
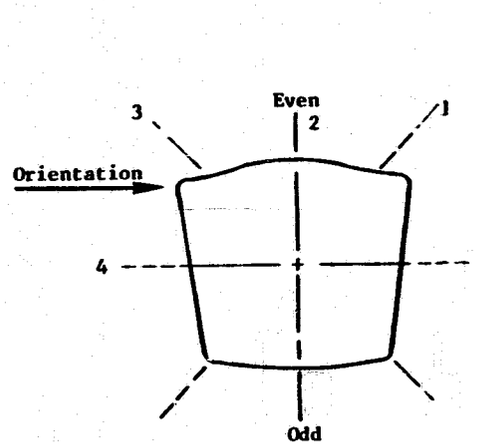


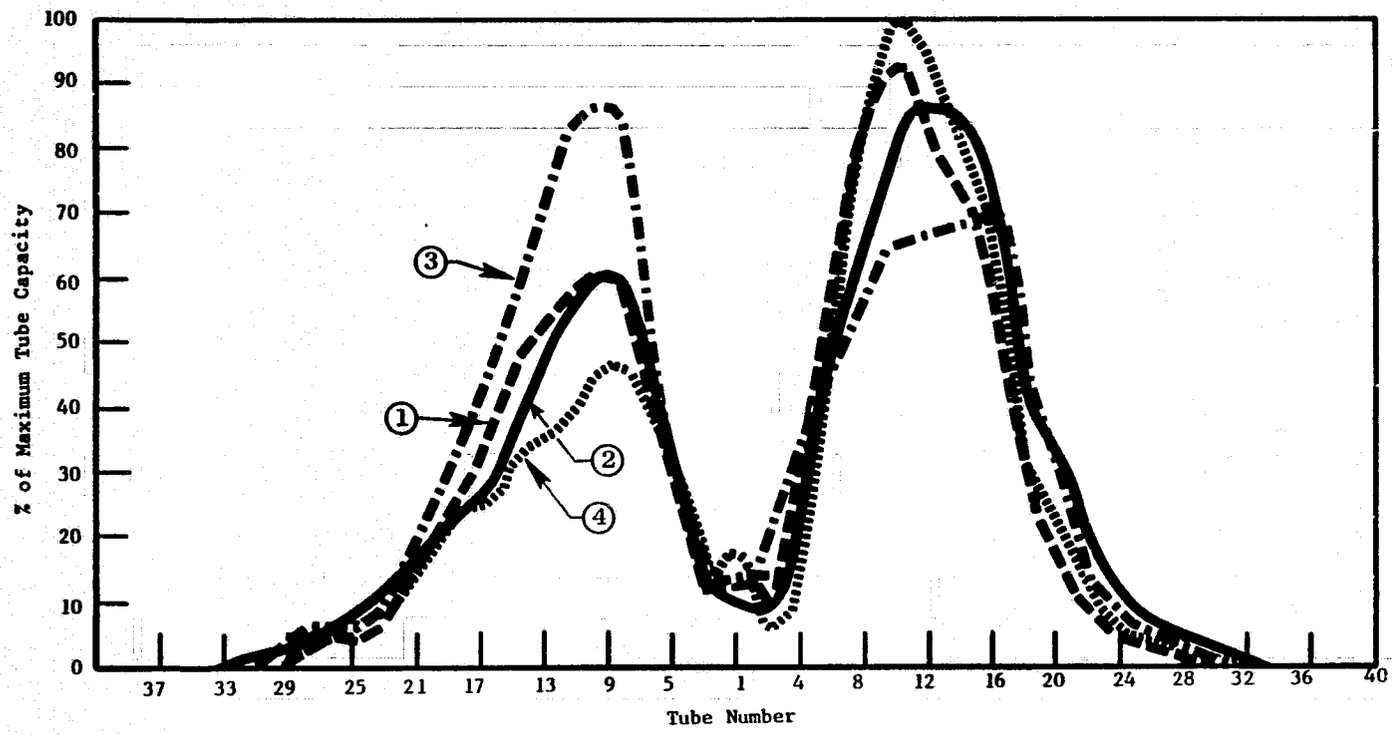
Figure 41. Earlier Patternation Test Results Showing Effects of Eccentricity and Fuel Injector Tip Immersion.

ORIGINAL PAGE IS
OF POOR QUALITY

F101 Rich Dome

AB11P04 — Wf = 20 PPH
VENTURI VIII — Dome ΔP = 21" H_2O
Std. Secondary Swirler
Sleeve P/N 202P12
Std. Fuel Tube Tip, Immersion - Std.
Run 1





ORIGINAL PAGE IS
OF POOR QUALITY

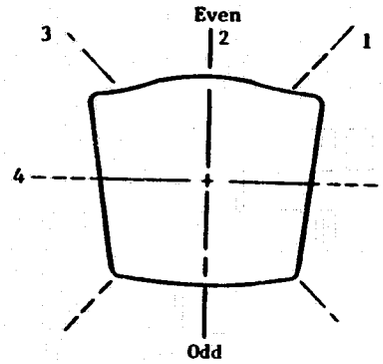
Figure 42. Earlier Patternation Test Results Showing Effects of Eccentricity and Fuel Injector Tip Immersion.

F101 Rich Dome

AB11P04
VENTURI VIII
Std. Secondary Swirler
Sleeve P/N 202P12
Std. Fuel Tube Tip, Immersion - 0.15, Minimum
Run 5A

Wf = 20 PPH
Dome Δp = 21" H_2O

Orientation



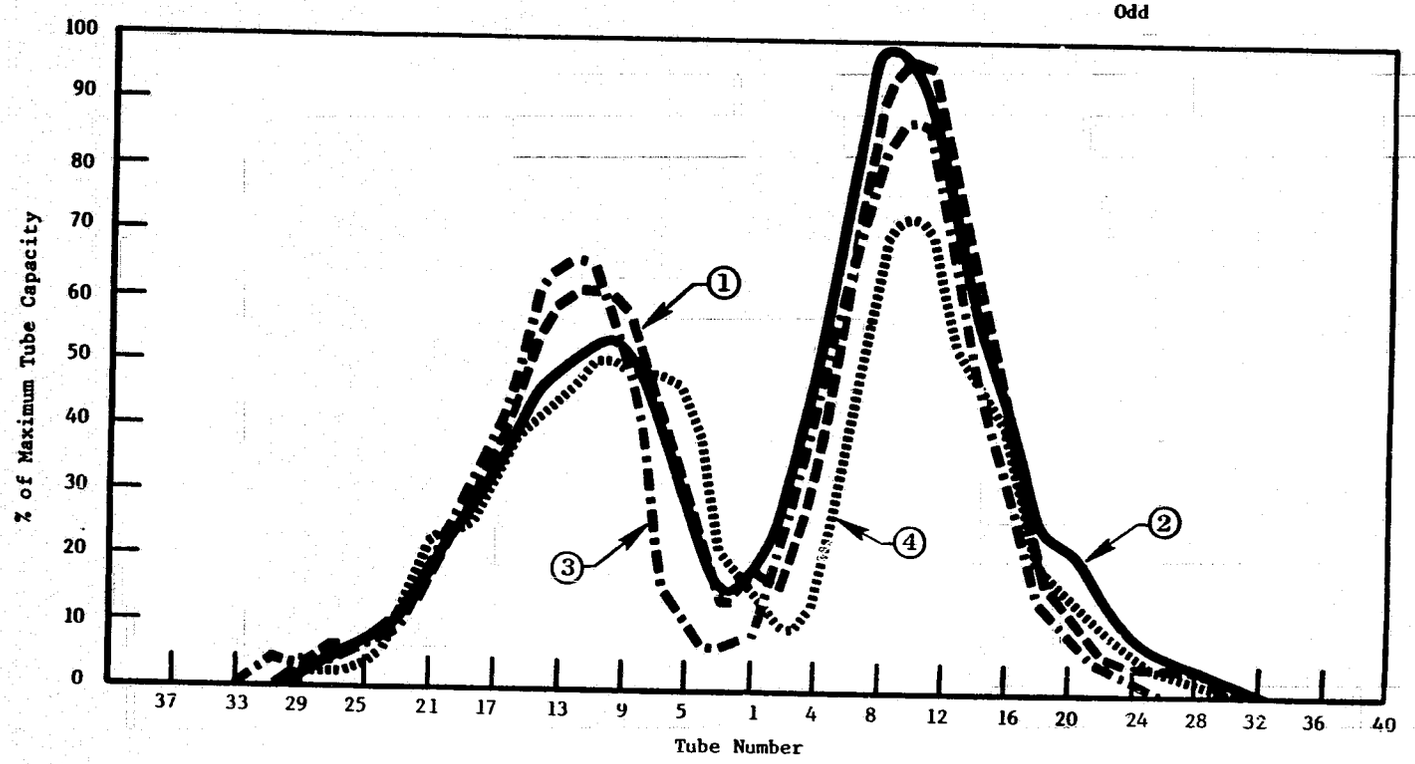
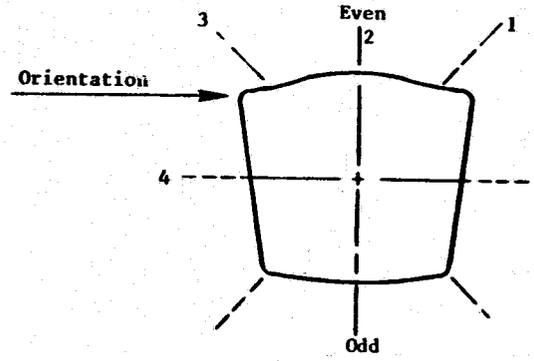


Figure 43. Earlier Patternation Test Results Showing Effects of Eccentricity and Fuel Injector Tip Immersion.

ORIGINAL PAGE IS
OF POOR QUALITY

F101 Rich Dome

AB11P04 Wf - 20 PPH
VENTURI VIII Dome ΔP = 21" H_2O
Std. Secondary Swirler
Sleeve P/N 202P12
Std. Fuel Tube Tip, Immersion - 0.45
Run 5C



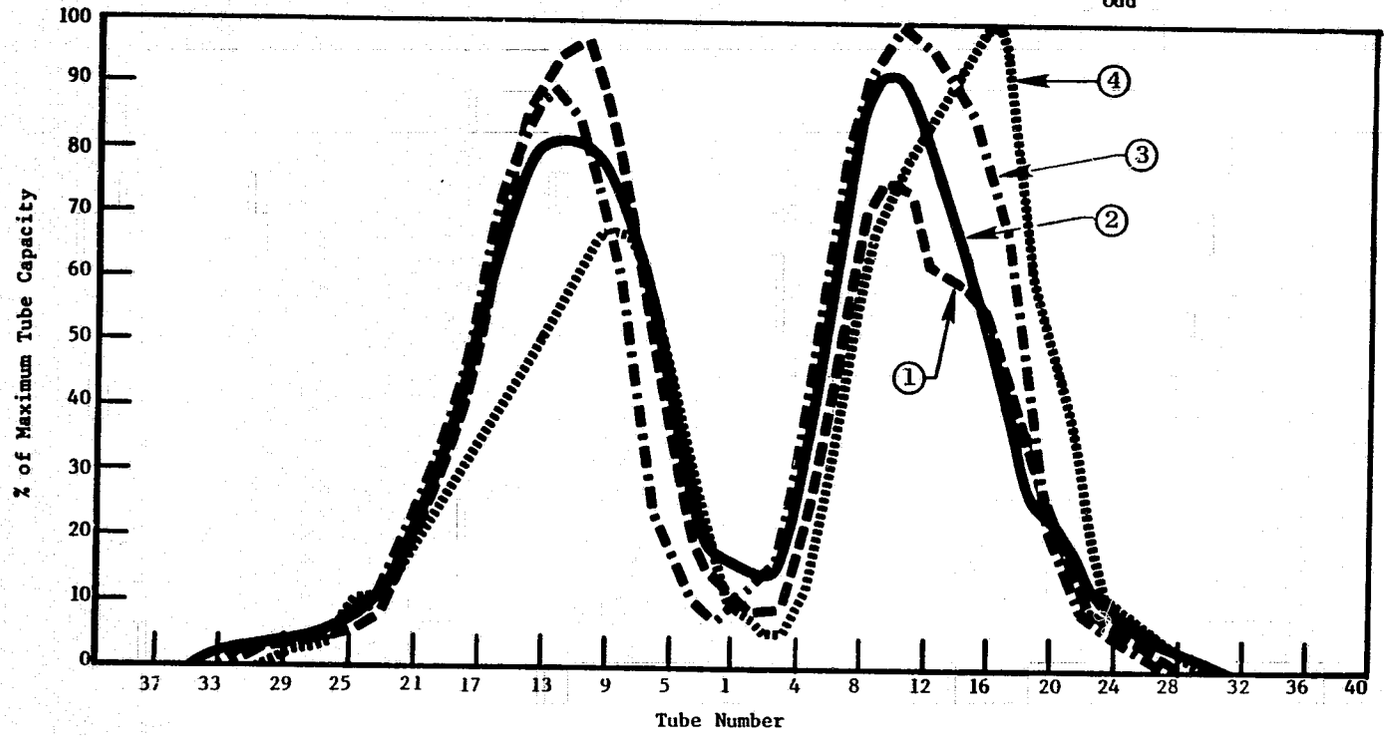


Figure 44. Earlier Patternation Test Results Showing Effects of Eccentricity and Fuel Injector Tip Immersion.

ORIGINAL PAGE IS
OF POOR QUALITY

ORIGINAL PAGE IS
OF POOR QUALITY

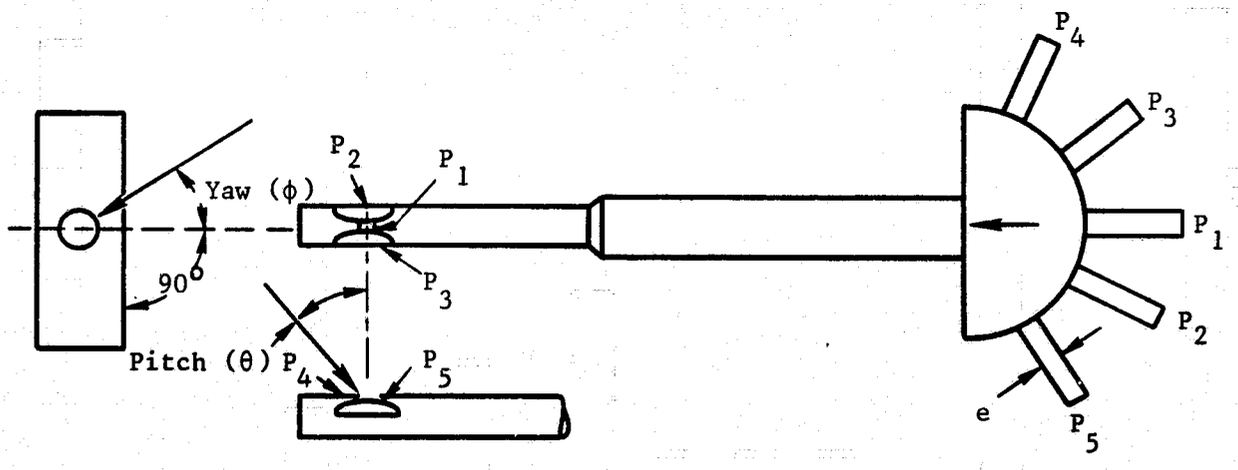


Figure 45. 5 Hole (3-D) Wedge type Velocity Probe.

ORIGINAL PAGE IS
OF POOR QUALITY

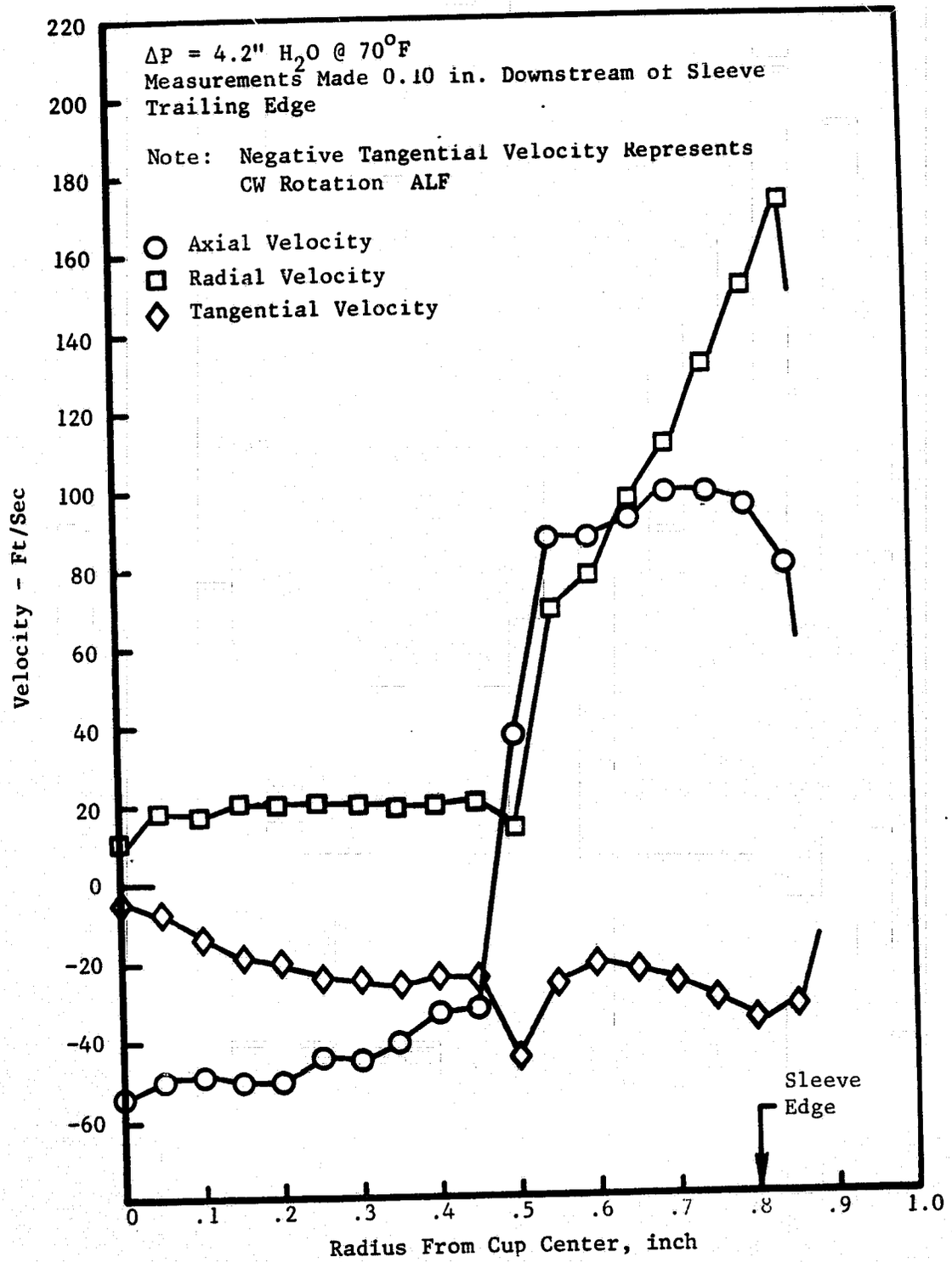


Figure 46. Wedge Probe Results for GE/F101 Swirl Cup Assembly.

center. The low tangential velocities reflect the offsetting effects of the counterrotation feature of this swirl cup design. At the center some small radial and tangential velocities were measured. The fact that these are not exactly zero may indicate that the probe was not exactly centered, and, or interference to the flow field was caused by the presence of the probe body. Although this type of intrusive measurement suffers from inaccuracies caused by the probe body interference, it is considerably faster and cheaper to perform than more sophisticated laser velocimeter techniques. The results of these measurements were easily modeled into the 3-D elliptic detailed internal flow model through the use of special swirler inputs incorporated in the coding.

6.0 FORMAL ANALYSIS OF INTERNAL FLOW MODEL CONCEPTS

6.1 INTRODUCTION

Comprehensive three-dimensional computer codes have been developed for the analysis of gas turbine combustors. The code prepared by the Garrett Turbine Company contains models for each of the relevant aspects of combustor flows. Northern Research and Engineering Corporation has assembled a model very similar to the Garrett model. These two models are incorporated in General Electric's internal flow module, INTFLOW. Another similar model named PACE developed at Rolls Royce has often been cited in the literature but is not available at General Electric.

These programs represent major accomplishments in establishing the feasibility of computer programs which, at least in an approximate sense, include and codify physical submodels for a description of a practical gas turbine combustor. Many of the submodels, however, are inadequate and require major rethinking of both the relevant physics and the numerical algorithms. Hence, the simulation of the axisymmetric benchmark flows performed in this study utilized another code developed at General Electric, a versatile two-dimensional research code GETREF (General Electric Turbulent Reacting Flow), which is discussed in detail in this section of the report.

Considerable efforts over the last 3 years have been made at the General Electric Company to improve the mathematical techniques and the physical submodels. This inhouse work, demonstrated in this section, starts with a careful formulation of the overall conservation equations employing density-weighted averaging to obtain the mean equations. The appearance of additional terms in these equations compared to constant density flows is discussed. Alternative combustion submodels were developed accounting for either finite rate chemistry or equilibrium chemistry first with fluctuations of the chemical source terms ("unmixedness") neglected. An equilibrium model accounting for these fluctuations by using an assumed probability density function (pdf) was developed and compared to the earlier submodels. Furthermore, improved turbulence submodels which account for anisotropies due to streamline curvature and swirl have been developed. The influence of density variations on the turbulence submodels was also considered. Means to reduce the numerical truncation errors, which influence (to some degree) all finite difference solutions, have been incorporated into the computer codes. The proposed methods have been included in programs which treat only axisymmetric geometries, since the majority of the important physics can be incorporated and developed in 2-D computer analyses with a diminished complexity and cost compared to fully 3-D codes. Furthermore, most of the available benchmark quality flows are axisymmetric.

The current generic mathematical techniques and physical models used for computation of turbulent combusting flows are analyzed and/or discussed in this section, while the application of GETREF to the selected axisymmetric benchmark flows is presented in Section 7.1.

ORIGINAL PAGE IS
OF POOR QUALITY

6.2 CONSERVATION EQUATIONS

The general equations which describe turbulent reacting flows are given below using Cartesian tensor notation for brevity. These equations are for the instantaneous flow field, Libby and Williams, 1980[43]. (Repeated indices imply summation over that index.)

Overall Mass Conservation

$$\frac{\partial \rho}{\partial t} + \frac{\partial}{\partial x_i} (\rho u_i) = 0 \tag{13}$$

Conservation of Momentum

$$\frac{\partial}{\partial t} (\rho u_i) + \frac{\partial}{\partial x_j} (\rho u_i u_j) = - \frac{\partial p}{\partial x_i} + \rho g_i + \frac{\partial}{\partial x_j} \tau_{ij} \tag{14}$$

Conservation of Energy (N Species)

$$\frac{\partial}{\partial t} (\rho h) + \frac{\partial}{\partial x_i} (\rho u_i h) = \frac{\partial p}{\partial t} + \frac{\partial}{\partial x_i} \left[\frac{\mu}{Pr} \frac{\partial h}{\partial x_i} + \mu \left(\frac{1}{Sc} - \frac{1}{Pr}\right) \sum_{j=1}^{N} h_j \frac{\partial Y_j}{\partial x_i}\right] \tag{15}$$

Species Conservation

$$\frac{\partial}{\partial t} (\rho Y_j) + \frac{\partial}{\partial x_i} (\rho u_i Y_j) = \frac{\partial}{\partial x_i} \left(\rho D \frac{\partial Y_j}{\partial x_i}\right) + \dot{w}_j \tag{16}$$

ORIGINAL PAGE IS
OF POOR QUALITY

The mixture enthalpy h is related to the temperature in terms of the species enthalpies:

$$h = \sum_{i=1}^{N} Y_i \, h_i \tag{17a}$$

$$h_i = \int_{T_r}^{T} C_{p_i} \, dT + h_i^0 \, , h_i^0 = \text{ heat of formation of species i} \tag{17b}$$

The equation of state for an ideal gas is given by

$$\rho = \frac{P}{R_0 \, T \sum_{i=1}^{N} (Y_i / M_i)} \tag{18}$$

Further discussion of the enthalpy and species conservation equations will follow.

In combustor flows of interest, the term $\partial p/\partial t$ in the enthalpy equation is neglected on the basis that the Mach numbers in gas turbine combustors are low.

In turbulent combustion systems, the time and length scales vary over such a wide range and the exact solutions (if available) would be so sensitive to initial and boundary conditions that it is not feasible to seek an exact analytical or even a direct numerical solution of the above equations. For the high Reynolds number of interest in practical systems, the scales of the fluctuations are several orders of magnitude greater than those associated with molecular processes (diffusion). Turbulence reduces the scales of the fluctuations ultimately to a microscale range where molecular diffusion (viscous dissipation) becomes important, but this is an inertially controlled process. The models which follow, therefore, do not account for molecular effects, but rather assume the turbulence is inertially dominated.

The standard approach to this problem is to decompose each independent variable (u_i, h, Y_i, etc.) into a mean plus fluctuating part, e.g.,

$$u = \overline{U} + u' ; \; \overline{U} = \lim_{\tau \to \infty} \frac{1}{\tau} \int_{t_o}^{t_o+\tau} u \, dt \text{ and } \overline{u'} = 0 \, . \tag{19}$$

ORIGINAL PAGE IS
OF POOR QUALITY

This decomposition is carried out for each variable and then substitution is made into the governing equations, with the resulting equations averaged in an ensemble sense (equivalent to time averaging for stationary flows). The averaging process, especially because of the nonlinear convective terms and the chemical source terms in each species conservation equation, results in loss of detailed information and closure problems such as $u'_i\, u'_j$ are introduced, Hinze, 1959[44]. Determination of such correlations is the essence of turbulence modeling. If conventional time averaging is adopted for variable density flows, correlations (including the Reynolds stresses) such as $\rho' u'_j$ and $\rho'\, u'_i\, u'_j$ arise. At the present time, insufficient data is available to accurately evaluate such terms. Instead, if density-weighted, or Favre-averaging, is utilized, viz,

$$u = \tilde{u} + u''; \quad \tilde{u} = \lim_{\tau\to\infty} \frac{1}{\bar{\rho}} \frac{1}{\tau} \int_{t_o}^{t_o+\tau} \rho\, u\, dt \quad \text{and} \quad u^{\tau\prime\prime} = 0 \,, \tag{20}$$

major simplifications in the form of the equations results. For example, the convection flux term in the momentum equations may be written

$$\overline{\rho u_i u_j} = \bar{\rho}\, u_i \tilde{u}_j$$

$$= \bar{\rho}\, \bar{u}_i\, \bar{u}_j + \bar{\rho}\, \overline{u'_i u'_j} + \bar{u}_j\, \overline{\rho' u'_i} + \bar{u}_i\, \overline{\rho' u'_j} + \overline{\rho' u'_i u'_j} \tag{21}$$

$$= \bar{\rho}\, [\tilde{u}_i \tilde{u}_j + \tilde{u''}_i \tilde{u''}_j]$$

Obviously, the use of Favre-averaging simplifies the resulting expressions.

The choice of either time-averaging or density-weighted averaging is not simply a matter of choice. Many investigators who have used time-averaging have neglected correlations including e' due to insufficient information. If that is done, or if Favre-averaging is used, equations arise which superficially look like constant density equations where ($\bar{}$) correlations are replaced by ($\tilde{}$) correlations. Additional terms areise in the modeled turbulence equations when correctly Favre-averaged that do not arise if e' correlations are neglected.

Favre-averaging provides a consistent framework to consider variable density effects. Firstly, the density weighting results in equations describing the variation of the mean values of the conserved quantities Jones and Whitelaw, 1981[45]. In the momentum equation, what arises is the mean momentum $\overline{\rho u_i} = \bar{\rho}_u \tilde{u}_i = \bar{\rho}\, \bar{u}_i$. Secondly, as will be discussed below, the turbulence modeling of the Reynolds stress $u''_i\, u''_j$ at present can most directly be

ORIGINAL PAGE IS
OF POOR QUALITY

carried over from constant density models which have been most severely tested. In essence, this is done with the "hope" that no significant errors result, Jones, 1979[28], despite the evidence of the necessity for density ratio effects in turbulence models, Libby and Bray, 1977[46], for premixed flames. Lastly, if density-weighted averages are compared with experiments, one must take care how the measurements were taken before comparing data with calculations, especially noting $\tilde{\phi} - \overline{\phi} = 1\overline{\rho'\phi'}/\overline{\rho}$, where ϕ is any variable of interest. Thus if conventional and Favre-averaged quantities are significantly different, the density fluctuation correlations are clearly important.

The Favre-averaged form of the Equations (13), (14), (15), and (16) are given (for steady flows) by

$$\frac{\partial}{\partial x_i}(\overline{\rho}\,\tilde{u}_i) = 0 \tag{22}$$

$$\frac{\partial}{\partial x_j}(\overline{\rho}\,\tilde{u}_i\,\tilde{u}_j) = -\frac{\partial \overline{P}}{\partial x_i} + \overline{\rho} g_i - \frac{\partial}{\partial x_j}(\overline{\rho}\,\widetilde{u''_i u''_j}) \tag{23}$$

$$\frac{\partial}{\partial x_i}(\overline{\rho}\,\tilde{u}_i\,\tilde{\phi}) = -\frac{\partial}{\partial x_i}(\overline{\rho}\,\widetilde{u''_i \phi''}) + S_\phi(\tilde{\phi}) \tag{24}$$

where ϕ is any scalar variable (h, Y_i, $i = 1, \ldots, N$) and S_ϕ is the related source term. Note that the molecular diffusion terms are ignored herein, under the assumption that the Reynolds number is sufficiently high. Also in any modeling it is assumed that Sc = Pr (in Equation (11), i.e., the Lewis number is unity.)

The means of handling the unknown velocity correlations $\overline{\rho u''_i u''_j}$ (i.e., the Favre-averaged Reynolds stresses), the velocity-scalar correlations $\overline{\rho u''_i \phi''}$, and the chemical source terms are discussed in detail in the following sections on turbulence and combustion modeling. The equation set (22) - (24) represents the mean flow equations of interest.

6.3 NUMERICAL METHODS

This section discusses the basic features of the numerical algorithms used to solve the elliptic equations required to describe recirculating combustor flows; discretization of the convection term is emphasized. The need

for elliptic solvers arises since real gas turbine combustors employ flame-stabilizing recirculation zones including swirl flows as well as large three-dimensional dilution air jets. In particular, general studies for reducing reducing numerical diffusion effects are discussed in detail, and results are shown to demonstrate the improvements gained.

6.3.1 Current Method - Hybrid Scheme

The basic numerical algorithm commonly used is based on the TEACH elliptic finite difference program, Gosman and Pun, 1974[47] developed at Imperial College London. This method is well documented in the open literature, and has been the basis of most of the elliptic flow computations applied to gas turbine combustor flows, Mongia, et al., 1979[1], Syed and Sturgess, 1980[48], Bozsan et al., 1981[49], and Lilley, 1979[50]. Details of the method are available in the literature. A good introduction to the method is given in Patankar, 1980[51].

The turbulence and turbulence/chemistry interaction modeling aspects will be discussed in the next section. In essence, all of the equations can be written (now using an axisymmetric x-r coordinate system) in the standard form

$$\frac{\partial}{\partial x}(\bar{\rho}\,\tilde{u}\,\tilde{\phi}) + \frac{1}{r}\frac{\partial}{\partial r}(r\,\bar{\rho}\,\tilde{v}\,\tilde{\phi}) = \frac{\partial}{\partial x}\left(\frac{\mu_t}{\sigma_\phi}\frac{\partial\tilde{\phi}}{\partial x}\right) + \frac{1}{r}\frac{\partial}{\partial r}\left(\frac{\mu_t}{\sigma_\phi}\frac{\partial\tilde{\phi}}{\partial r}\right) + S_\phi \qquad (25)$$

for $\tilde{\phi} = \tilde{u},\tilde{v},\tilde{w}$ (swirl), $\tilde{h}$, $\tilde{y}_i$. The equations are discretized by requiring each conservation equation to be balanced for any computational cell. This is a finite volume, as opposed to strictly finite difference, approach. The pressure is calculated by using the overall mass continuity equation, coupled with the momentum equations, to derive a pressure correction equation, the so-called SIMPLE (Semi-Implicit Method for Pressure-Linked Equations) algorithm, Patankar, 1980[51]. The procedure necessarily uses a staggered velocity and scalar grid system to stabilize the pressure calculation. For high Mach number flows the pressure-correction equation can then be replaced by the equation-of-state with attendant savings in storage, since a nonstaggered grid can then be used. At low Mach numbers this is not possible because the continuity equation cannot be solved accurately enough for nearly incompressible flows.

The procedure works iteratively, based on initial guesses for each dependent variable. The conservation equation for each variable is successively solved, using the most recent values of all the dependent variables. An implicit line-by-line relaxation technique is used in solving the equations, coupled with the standard tri-diagonal matrix algorithm (TDMA) to solve along each line. Within each iteration cycle (i.e., solution for each dependent variable), several line sweeps are made for each variable in order to update the values of that particular dependent variable. This is necessary as non-linear terms, for example u^2, are written as u*u, where * denotes the value from a prior sweep or iteration. This form of linearization is stable, but

requires many line sweeps and iteration cycles to reach convergence. Convergence is usually judged to be reached when the sum over the entire computational field of the absolute values of the residual error at each computation cell is reduced below some prescribed limit. For example, the sum total of mass continuity residuals is generally required to be less than 0.001 times the total inlet mass flux. The other residuals are also monitored. In 3-D flows some authors have targeted for a mass continuity residual of 0.01.

Boundary conditions are satisfied using the wall function method, Launder and Spalding, 1972[52]. The viscous boundary conditions are satisified using the no slip condition at the wall and the law-of-the-wall to calculate the wall shear stress.

The source terms S_ϕ are linearized in the finite difference form for the hydrodynamic variables according to $S_\phi = S_u - S_{p\phi}$, where $S_p \geq 0$, S_p and S_u can be functions of the coordinate and any dependent variable (based on a prior iteration). The source terms for the species conservation equations cannot be so linearized and, therefore, pose special problems and treatments. This topic will be treated more fully in the following section on chemical kinetics.

The finite difference approximation employs so-called hybrid differencing, i.e., second order central differencing is used for cell Peclet numbers (absolute value), $e|u|\Delta x/u_t$, less than two; otherwise first order upwind differencing is applied. This methodology is required since second order central differencing of the convective terms for cell Peclet number greater than two results in oscillatory solutions, and often in divergence of the iterations if a standard Gauss-Seidel procedure is applied. The result of this unwinding is that a numerical viscosity with magnitude $e|u|\Delta x/2$ is added to the turbulent eddy viscosity u_t, resulting in excessive artificial or numerical diffusion in the flow field. This diffusional effect may exceed the physical turbulent diffusion and so plague the accuracy of the numerical simulations. For example, in the pioneering work by Allen and Southwell, 1955[53], the first order upwind approximation was employed in a vorticity-stream function solution to the Navier-Stokes equations for viscous flow around a cylinder. The results show that the downstream eddies are too short and they vary only slightly between R = 100 and 1000 on a coarse mesh.

Furthermore, de Vahl Davis and Mallinson, 1976[54] pointed out that when the velocity vector is more than marginally skewed relative to the computational grid lines, and the cell Peclet number significantly exceeds unity in regions where diffusive transport normal to the flow direction is important, the error due to numerical diffusion may become so dominant as to obscure the effects of physical diffusivity on the flow. Also, Castro, 1979[55] showed that in regions of complex flow, particularly near sharp corners, the size of the truncation error associated with the first order upwind scheme cannot easily be reduced to insignificance, but it can be simply convected downstream leading to bad predictions over the rest of the flow field. In addition, Raithby, 1976[56] and Leonard 1979[57] have shown that in the presence of source terms, large errors may result from the first order upwind solutions for a convection dominated flow.

Most of the published calculations for elliptic flows demonstrate various levels of agreement with experimental data. Often authors cite the need for a more sophisticated turbulence model to improve the quality of the calculation. However, in most instances, the amount of numerical error has not been ascertained. It is necessary to determine, for example, whether numerical diffusion has "smeared" the results in regions of high gradient. McGuirk, Taylor and Whitelaw, 1981[58] have published results for the calculation of the axisymmetric flow behind a bluff plate within a circular pipe. Grid refinement was carried out by examining for a given mesh the error due to false diffusion and then refining the mesh until such error was minimized. This is a laborious task, but one that should in some sense be automated to quantify the numerical errors involved. With three-dimensional calculations, the ability to demonstrate either grid independence of solutions or their degree of error, as suggested above, is severely limited. Coupled with the additional equations required for combusting flows, numerical testing for errors will be expensive and difficult, if not impossible, for three dimensional flows, Jones and Whitelaw, 1981[45]. Without combustion, some of these difficulties have been demonstrated by Green and Whitelaw, 1980[4] and Green, 1981[59].

The difficulty of a numerical simulation is further compounded by the fact that for the cell Reynolds Number (Re = global Reynolds number, Δx = nondimensional mesh spacing) greater than unity, difference schemes of higher order formal accuracy do not necessarily promise smaller total error. Chen and Shubin, 1978[60] studied the one-dimensional, steady-state Burgers equation. They found that the error in computational results with formally second order accurate algorithms and coarse meshes varies widely, and does not increase as Δx^2 or $(Re\Delta x)^2$. Furthermore, the first order accurate algorithm can provide essentially the same solutions as do some of the second order algorithms; such results can be either better or worse than those offered by other formally second order schemes. Thus, they concluded that the formal order of accuracy of a difference algorithm may not reflect the magnitude of computational errors for large $Re\Delta x$. Stubley, et al., 1980[61] demonstrated that it is not just the error introduced in the approximation of local function values or gradients by a particular discretization scheme which is important, but also the nature of the way this local error is propagated by the discretized version of the convection and diffusion terms in the differential equation.

6.3.2 Alternative Methods for Three-Dimensional Flows

Most of the numerical simulations done for the axisymmetric benchmark experiments employ the hybrid scheme since for two-dimensional flows the grid refinements, which make the cell Peclet always less than two (so that the second order central differencing is applicable), are possible within current computer capacities. For the three-dimensional flows of practical interest such grid densification in each coordinate direction is currently impractical so that the second order accuracy of central differencing cannot be realized. Stability considerations dictate the use of first order upwinding; however, this is now seen to be too diffusive to be of practical use. Clearly, a second order accurate scheme with an expanded stable range of Peclet numbers is

needed. This has been studied at General Electric, Shyy, 1983[62] and the results are presented below. Generally, all the alternatives to the hybrid scheme are necessarily more complex. Several potentially useful schemes are currently available. One such method, proposed by Raithby, 1976[63], is termed skew upwind differencing. The skew upwind differencing scheme, although like the conventional upwind scheme formally only first-order accurate, yields a significant reduction in numerical diffusion by taking the direction of the velocity vector into account. Another method, proposed by Leonard, 1979[57] is called QUICK (Quadratic Upstream Interpolation for Convective Kinematics). The QUICK scheme is based on the use of upstream-shifted parabolic interpolation for every control volume surface on the computational grid and is free from (second order) numerical diffusion. Both skew upwind and QUICK have been examined by Leschziner, 1980[64], and by Leschziner and Rodi, 1981[65] for some idealized cases as well as for unconfined recirculating flows. The schemes are found to be superior to the conventional upwind simulation for the cases studied. Both formulations have been shown, however, to involve boundedness problems by under- and over-shoots in the solutions. It should also be noted that the skew upwind scheme does not resolve the difficulties associated with the source term when applying the first order upwind approximations; Leonard, 1979[57] has shown that QUICK does give good resolution in the presence of the source term. On the other hand, however, if an iterative method such as Gauss-Seidel is adopted for the solution procedure, Han, et al., 1981[66] reported that special care must be taken for the QUICK scheme to guarantee convergence.

Another finite difference approximation which has attracted comparatively little attention was the one used by Atias, et al., 1977[67]. They studied a second order upwind scheme for discretizing the convection terms in the vorticity transport equation and found that it has the potential of yielding sufficient accuracy. No systematic study has been made for this scheme as yet; but Gupta and Manohar, 1978[68] pointed out the restriction of numerical stability imposed by the von Neumann type of analysis.

In the study conducted at General Electric, Shyy, 1983[62], attempts have been made to clarify some of these ambiguities associated with the numerical simulation of a high cell Peclet number flow as well as to find a comparatively accurate finite difference scheme and an effective procedure to get the solution to the discretized equation. The restraints set by the size of the cell Peclet number on the effectiveness of a given finite difference scheme are studied at first. The accuracy of a finite difference approximation to an idealized flow problem in the presence of a source term is then analyzed. Comparisons are made by studying the solutions by different schemes for several test problems. The effects of numerical diffusion due to the inclination of the computational grid lines in a multi-dimensional flow field are also compared among different schemes. The influences of different boundary conditions on the mathematical accuracy and on the physical reality of the numerical solutions are examined. One objective here is to shed some light on the relative merits of several schemes and to contrast their performances under both "mild" and "stringent" flow conditions. Five different finite difference schemes approximating the convection terms are analyzed: the first order upwind, the skew upwind, the second order central differencing, the second

ORIGINAL PAGE IS
OF POOR QUALITY

order upwind, and the QUICK scheme. Test cases are chosen to be simple but relevant. A stable iterative procedure is constructed to give convergent solutions for all the schemes considered.

In what follows, exclusive use of the second order central differencing will be adopted to approximate the diffusion terms in the governing equation, e.g.,

$$\left.\frac{\partial^2 \phi}{\partial x^2}\right|_{i,j} = \frac{\phi_{i+1,j} - 2\phi_{i,j} + \phi_{i-1,j}}{\Delta x^2} + T_d \qquad (26)$$

where T_d is the truncation error resulting from replacing the diffusion term with the finite difference approximation; the notation used in Equation (26) is shown in Figure 47.

For the finite difference approximation to the convection terms, the following schemes will be considered and tested:

a) first order upwind

$$\left.\frac{\partial(u\phi)}{\partial x}\right|_{i,j} = \begin{cases} \dfrac{u_{i,j}\phi_{i,j} - u_{i-1,j}\phi_{i-1,j}}{\Delta x} + T_c, \text{for } u > 0 \\ \dfrac{u_{i+1,j}\phi_{i+1,j} - u_{i,j}\phi_{i,j}}{\Delta x} + T_c, \text{for } u < 0 \end{cases} \qquad (27)$$

where T_c is the truncation error inherent in replacing the convection term with the finite difference approximation.

b) second order central differencing

$$\left.\frac{\partial(u\phi)}{\partial x}\right|_{i,j} = \frac{u_{i+1,j}\phi_{i+1,j} - u_{i-1,j}\phi_{i-1,j}}{2\Delta x} + T_c \qquad (28)$$

ORIGINAL PAGE IS
OF POOR QUALITY

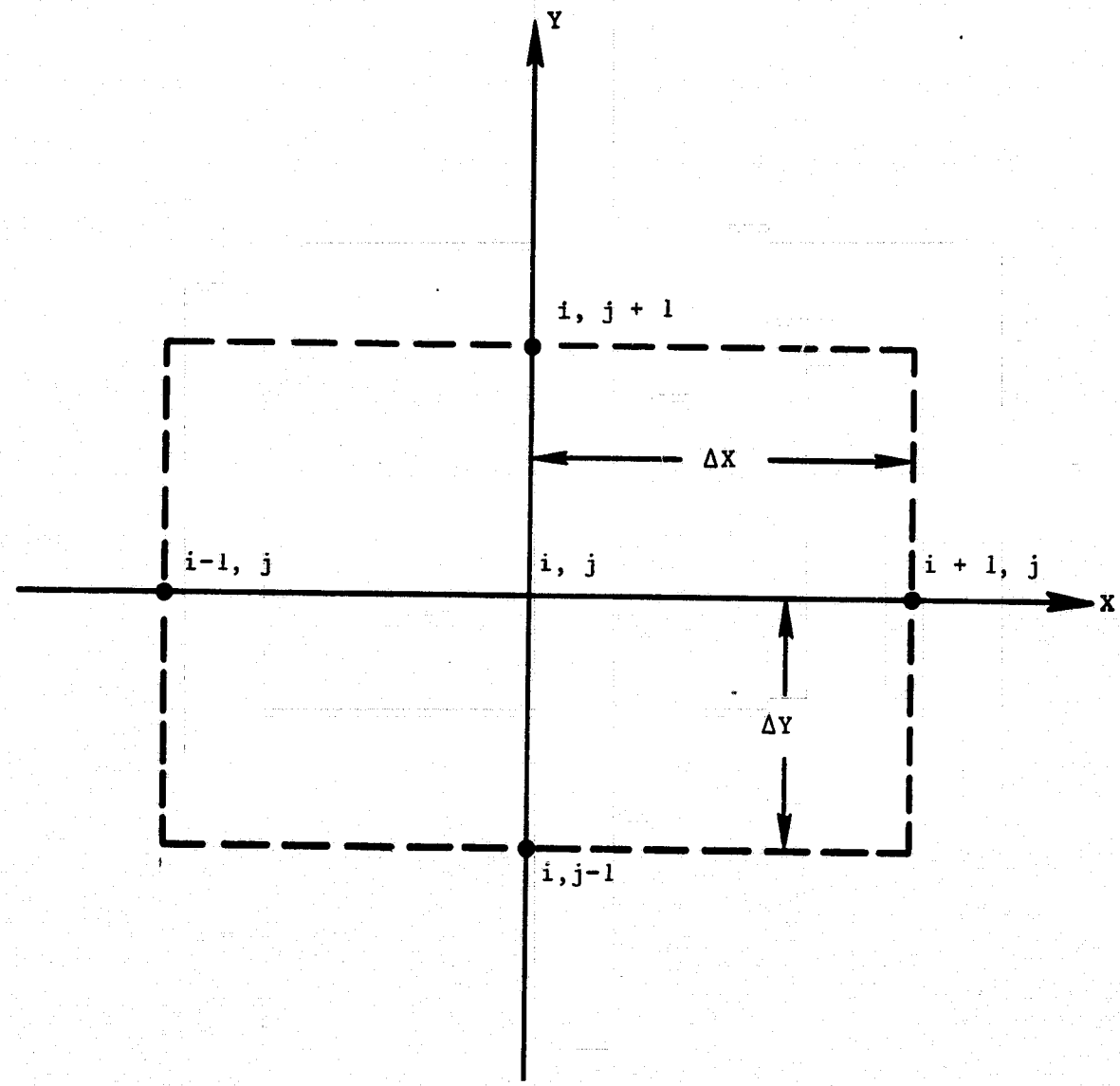


Figure 47. Notation Used in a Computational Mesh.

ORIGINAL PAGE IS
OF POOR QUALITY

c) second order upwind

$$\frac{\partial(u\phi)}{\partial x}\Big|_{i,j} = \begin{cases} \frac{1}{2\Delta x}\left(3u_{i,j}\phi_{i,j} - 4u_{i-1,j}\phi_{i-1,j} + u_{i-2,j}\phi_{i-2,j}\right) + T_c & \text{for } u > 0 \\ \frac{1}{2\Delta x}\left(-u_{i+2,j}\phi_{i+2,j} + 4u_{i+1,j}\phi_{i+1,j} - 3u_{i,j}\phi_{i,j}\right) + T_c & \text{for } u < 0 \end{cases} \tag{29}$$

d) QUICK

$$\frac{\partial(u\phi)}{\partial x}\Big|_{i,j} = \begin{cases} \frac{1}{\Delta x}\left(\frac{3}{8}u_{i+1,j}\phi_{i+1,j} + \frac{3}{8}u_{i,j}\phi_{i,j} - \frac{7}{8}u_{i-1,j}\phi_{i-1,j} + \frac{1}{8}u_{i-2,j}\phi_{i-2,j}\right) + T_c & \text{for } u > 0 \\ \frac{1}{\Delta x}\left(-\frac{1}{8}u_{i+2,j}\phi_{i+2,j} + \frac{7}{8}u_{i+1,j}\phi_{i+1,j} - \frac{3}{8}u_{i,j}\phi_{i,j} - \frac{3}{8}u_{i-1,j}\phi_{i-1,j}\right) + T_c & \text{for } u < 0 \end{cases} \tag{30}$$

Skew upwind differencing is similar to the original first order upwind scheme for a one-dimensional problem. For a multidimensional flow problem, it can reduce numerical diffusion by taking the direction of the velocity vector into account as will be described later in this report.

6.3.3 Numerical Accuracy and Cell Peclet Number

It is well known by now that numerical schemes (to any finite degree of accuracy) introduce numerical diffusion and dispersion in roughly the same way as physical diffusion and dispersion in the phenomena of fluid flow, Richtmyer and Morton, 1967[69], Chu, 1978[70]. This can be examined by expanding the finite difference equation in a Taylor series, to get the original differential equation plus higher order terms which represent the truncation errors introduced in the course of approximation. The resulting equation is called the modified equation. Table IX shows the coefficients of the first six derivatives in the modified equation

Table IX. Coefficients in Eq. (31) for approximating Eq. (32) by Four Different Schemes.

Method	a	q	r	d	e	f
first order upwind	u	$\frac{u\Delta x^2}{6}$	$\frac{u\Delta x^4}{120}$	$\nu + \frac{u\Delta x}{2}$	$\frac{\nu\Delta x^2}{12}\left(\frac{p_e\Delta x}{2} + 1\right)$	$\frac{\nu\Delta x^4}{360}\left(\frac{p_e\Delta x}{2} + 1\right)$
second order upwind	u	$-\frac{u\Delta x^2}{3}$	$-\frac{7u\Delta x^4}{60}$	ν	$\frac{\nu\Delta x^2}{12}\left(-3p_{e\Delta x} + 1\right)$	$\frac{\nu\Delta x^4}{360}\left(-15p_{e\Delta x} + 1\right)$
second order central	u	$\frac{u\Delta x^2}{6}$	$\frac{u\Delta x^4}{120}$	ν	$\frac{\nu\Delta x^2}{12}$	$\frac{\nu\Delta x^4}{360}$
QUICK	u	$\frac{u\Delta x^2}{24}$	$\frac{11u\Delta x^4}{480}$	ν	$\frac{\nu\Delta x^2}{12}\left(-\frac{3p_e\Delta x}{4} + 1\right)$	$\frac{\nu\Delta x^4}{360}\left(\frac{-15}{4}p_{e\Delta x} + 1\right)$

ORIGINAL PAGE IS
OF POOR QUALITY

ORIGINAL PAGE IS
OF POOR QUALITY

$$u\phi_x + q\phi_{xxx} + r\phi_x^{(5)} = d\phi_{xx} + e\phi_x^{(4)} + f\phi_x^{(6)} + HOT \tag{31}$$

where HOT represents the higher order terms in Taylor series, derived by the combination of one of the finite difference approximations discussed in Eqs. (27) to (30) to the convection term and Eq. (26) to the diffusion term of the one-dimensional, steady state linear Burgers equation (source free)

$$u\phi_x = \nu\phi_{xx}, \quad u, \nu = \text{constants} > 0 \tag{32}$$

If we expand the dependent variable ϕ in Eq. (31) as a Fourier series in the x-direction we obtain

$$\phi = \sum_{j=-\infty}^{\infty} a_j e^{ik_j x} \tag{33}$$

The Fourier component of the shortest wavelength resolved by a finite difference mesh is of wavelength $l = 2\Delta x$. The corresponding wave number is $k_{max} = \pi/\Delta x$. The longest wavelength is $l_{max} = L$, which is the total length spanned by the mesh. The corresponding minimum wave number is $k_{min} = 2\pi/L$. If one substitutes a Fourier component $\phi_j = a_j e^{i k_j x}$ into Eq. (13), then one can easily find that all the schemes in Table IX except the first order upwind give good approximations to Eq. (32) for $k = k_{min}$ with the errors proportional to $1/N^2$ ($L = N\Delta x$). On the other hand, as $k = k_{max}$, no scheme can yield reasonably accurate approximations. This can be seen from Table X which shows the values of α and β for the Fourier components with $k = k_{max}$, for the various schemes, where

$$\alpha = \frac{q\phi_{xxx} + r\phi_x^{(5)}}{u\phi_x} \tag{34a}$$

$$\beta = \frac{(d-\nu)\phi_{xx} + e\phi_x^{(4)} + f\phi_x^{(6)}}{\nu\phi_{xx}} \tag{34b}$$

ORIGINAL PAGE IS
OF POOR QUALITY

Table X. Values of α and β in Eq. (34) by Substituting the Fourier Component of Wave Number $k = \pi/\Delta x$.

Method	α	β
first order upwind	-0.83	$0.23\ p_{e\Delta x} - 0.55$
second order upwind	-8.07	$-1.59\ p_{e\Delta x} - 0.55$
second order central	-0.83	-0.55
QUICK	1.82	$-0.40\ p_{e\Delta x} - 0.55$

All the values of α and β are at least of the order of unity; in the region where those high wave number Fourier components are important for the solution, the numerical diffusion and dispersion are by no means negligible even though all the schemes studied here, except the first order upwind, make exact approximations to the first and the second derivatives in Eq. (32). Furthermore, this difficulty cannot be resolved by using a formally higher order scheme.

For a high Peclet number flow problem, the convection terms are dominant in the main part of the flow domain; the real solution might vary rapidly in some thin regions where the convection terms are balanced by the diffusion terms due to, for example, the restraint imposed by the boundary conditions. Hence, in a numerical viscous flow simulation the mesh size should be fine enough so that the ratio of $u\phi_x/(\nu\phi_{xx})$ in Eq. (32) is of the order of unity, at least at the highest resolvable wave number, $k = k_{max} = \pi/\Delta x$. If the ratio is much larger than one, then the convection term can never be balanced by the viscous term in all the numerically resolvable scales. If a Fourier component $\phi_j = a_j e^{ikjx}$ is substituted into $u\phi_x/(\nu\phi_{xx})$ and $k_j = k_{max}$ is used, then as pointed out by MacCormack and Lomax, 1979[71], the condition for a unity ratio between the convection and the diffusion terms is

$$P_{e\Delta x} = \frac{u\Delta x}{\nu} = O(1) \tag{35}$$

At high Peclet numbers, the mesh size cannot, with present computers, be made fine enough to fulfill this condition. The viscous diffusion at wave numbers higher than those resolved by the numerical approximation must be accounted for through modeling. Hence, a suitable finite difference scheme for a high Peclet number flow should be the one that maintains good accuracy in the convection dominated region; in the regions where the convection terms and the viscous terms in the original differential equation must balance each other, but numerically this cannot be done exactly, the truncation error should enhance the weight of the viscous terms. By doing this, though the fine structure of the real solutions cannot be resolved due to the large error introduced in high wave number component part, the results obtained from the numerical approximation are, in general, physically correct and useful; the disturbances arising from an inaccurate numerical simulation in a thin layer can be damped out without propagating into the main region. As will be shown later, the truncation error of a given finite difference scheme may or may not be able to increase the viscous effects where needed. Hence, a formally higher order scheme does not necessarily perform better for the high cell Peclet number problems, due to the inadequate resolution of the rapidly varying solution in the thin layers.

6.3.4 Test Problem I: Boundary Layer Type Flow

Eq. (32) with the boundary conditions $\phi = 0$ at $x = 0$, and $\phi = 1$ at $x = 1$ is considered here. The exact solution of this problem is

ORIGINAL PAGE IS
OF POOR QUALITY

$$\phi(x) = \frac{1-e^{p_e x}}{1-e^{p_e}} \tag{36}$$

where $p_e = ul/\nu$ is a Peclet number. For small to moderate p_e, $\phi(x)$ displays a soulution which varies smoothly throughout the entire domain. However, as is increased much larger beyond unity, the solution becomes one of a boundary layer type in that $\phi(x)$ is virtually zero except in the region near x = 1 within a thin layer of thickness $\delta \simeq 1/p_e$ wherein the entire variation in the solution is contained. Upstream of this boundary layer, the flow is entirely convection dominated. The numerical solutions to this test problem by the combination of Eq. (26) and one of the schemes described in Eq. (27) to Eq. (30) for different values of cell Peclet number are contained in Tables XI through XIII. For $p_{e\Delta x} = u\Delta x/\nu = 0.2$ the soulutions by QUICK and the second order central differencing are the most accurate while that by the second order upwind is also very acceptable. For $p_{e\Delta x}$ less than 1, the Fourier components with the wave number equal to or larger than k_{max} are not crucial for ϕ in Eq. (36), and the leading truncation error term of a finite difference approximation is representative of the order of total numerical error. In Table XI the first order upwind yields the solution with the largest error due to the introduction of the numerical viscosity (see Table IX) to the second derivative term in Eq. (32). It is noted that among the four different schemes described in Eqs. (27) to (30), only the first order upwind always gives a diagonally dominant coefficient matrix for the set of difference equations. For $p_{e\Delta x} = 10$ and 100, both QUICK and the second order central differencing show solutions with wiggles; the magnitudes of this spurious oscillation in the solution by the second order central differencing are generally much larger than those by QUICK. Yet, throughout the whole range of $p_{e\Delta x}$, the solutions by both the first order upwind and the second order upwind are wiggle free. This can be analyzed by studying the roots of the characteristic equation associated with a specific scheme. For example, if QUICK is used, the resulting finite difference equation for Eq. (32) at the grid point i is

$$\frac{p_{e\Delta x}}{8}\phi_{i-2} - \left(1 + \frac{7}{8}p_{e\Delta x}\right)\phi_{i-1} + \left(2 + \frac{3}{8}p_{e\Delta x}\right)\phi_i - \left(1 - \frac{3}{8}p_{e\Delta x}\right)\phi_{i+1} = 0 \tag{37}$$

The exact solution of Eq. (37) is given by Dahlquist and Björck, 1974[72]

$$\phi_i = \gamma_1 Z_1^{i-1} + \gamma_2 Z_2^{i-1} + \gamma_3 Z_3^{i-1} \tag{38}$$

Table XI. Numerical Solutions to Test Problem I.
(Number of Grid Points = N + 1 = 11, $P_{e\Delta x} = 0.2$)

Method	ϕ_1	ϕ_2	ϕ_3	ϕ_4	ϕ_5	ϕ_6	ϕ_7	ϕ_8	ϕ_9	ϕ_{10}	ϕ_{11}
Eq. (26)	0	3.47 E-2	7.70 E-2	0.129	0.192	0.269	0.363	0.478	0.619	0.790	1.00
First order upwind	0	3.85 E-2	8.48 E-2	0.140	0.207	0.287	0.383	0.498	0.636	0.801	1.00
Second order upwind	0	3.58 E-2	7.88 E-2	0.131	0.195	0.272	0.367	0.482	0.622	0.792	1.00
Second order central	0	3.45 E-2	7.67 E-2	0.128	0.191	0.268	0.362	0.477	0.618	0.790	1.00
QUICK	0	3.53 E-2	7.77 E-2	0.129	0.193	0.270	0.364	0.479	0.619	0.791	1.00

ORIGINAL PAGE IS
OF POOR QUALITY

Table XII. Numerical Solutions to Test Problem I (11 Grid Points, $P_{e\Delta x} = 10.0$)

Method	ϕ_1	ϕ_2	ϕ_3	ϕ_4	ϕ_5	ϕ_6	ϕ_7	ϕ_8	ϕ_9	ϕ_{10}	ϕ_{11}
Eq. (26)	0	8.19 E-40	1.80 E-35	3.98 E-31	8.76 E-27	1.93 E-22	4.25 E-18	9.36 E-14	2.06 E-9	4.54 E-5	1.00
First order upwind	0	3.90 E-10	4.65 E-9	5.12 E-8	5.64 E-7	6.21 E-6	6.83 E-5	7.51 E-4	8.26 E-3	9.09 E-2	1.00
Second order upwind	0	-3.46 E-10	-3.57 E-10	3.34 E-9	6.59 E-8	1.05 E-6	1.65 E-5	2.59 E-4	4.07 E-3	6.38 E-2	1.00
Second order central	0	-4.41 E-2	2.21 E-2	-7.72 E-2	7.17 E-2	-1.52 E-1	1.83 E-1	-3.19 E-1	4.35 E-1	-6.96 E-1	1.00
QUICK	0	1.06 E-5	1.27 E-4	-2.28 E-4	9.22 E-4	-2.79 E-3	9.21 E-3	-2.96 E-2	9.58 E-2	-3.09 E-1	1.00

ORIGINAL PAGE IS
OF POOR QUALITY

Table XIII. Numerical Solutions to Test Problem I (11 Grid Points, $P_{e\Delta x} = 100$)

Method	ϕ_1	ϕ_2	ϕ_3	ϕ_4	ϕ_5	ϕ_6	ϕ_7	ϕ_8	ϕ_9	ϕ_{10}	ϕ_{11}
Eq. (26)	0	0	0	0	0	0	0	0	0	0	1.00
First order upwind	0	1.05 E-16	1.01 E-15	3.19 E-15	1.45 E-12	9.69 E-11	9.61 E-9	9.71 E-7	9.80 E-5	9.90 E-3	1.00
Second order upwind	0	-5.05 E-11	-9.06 E-11	-1.40 E-10	-2.11 E-10	-3.03 E-10	1.47 E-9	2.92 E-7	4.41 E-5	6.64 E-3	1.00
Second order central	0	-4.15	1.69 E-1	-4.32	3.53 E-1	-4.52	5.52 E-1	-4.72	7.67 E-1	-4.95	1.00
QUICK	0	2.46 E-5	2.51 E-3	-2.65 E-3	8.94 E-3	-1.70 E-2	4.09 E-2	-8.85 E-2	2.01 E-1	-4.46 E-1	1.00

ORIGINAL PAGE IS
OF POOR QUALITY

ORIGINAL PAGE IS
OF POOR QUALITY

where Z_1, Z_2, and Z_3 are zeros of the characteristic equation

$$\frac{P_{e\Delta x}}{8} - (1 + \frac{7}{8}P_{e\Delta x})\, Z + (2 + \frac{3}{8}\, P_{e\Delta x})Z^2 - (1 - \frac{3}{8}P_{e\Delta x})Z^3 = 0 \qquad (39)$$

These zeros are

$$Z_1 = 1,\ Z_{2,3} = \frac{(1 + \frac{3}{4}\, P_{e\Delta x}) \pm \sqrt{(1 + \frac{3}{4}\, P_{e\Delta x})^2 - \frac{P_{e\Delta x}}{2}(1 - \frac{3}{8}\, P_{e\Delta x})}}{2\,(1 - \frac{3}{8}\, P_{e\Delta x})}$$

The constants γ_1, γ_2, and γ_3 are determined by the two boundary conditions $\phi_1 = 0, d_{N+1} = 1$, and the value of ϕ_2 which is calculated by a starting calculation method. Here, the first order upwind may be used for both QUICK and the second order upwind schemes; it is found that, for this specific problem, the solutions obtained in this way are comparable with other more accurate strategies such as the one that will be discussed later on for the flow problem with a source term. Eq. (39) indicates that, for the problem considered, QUICK gives a solution with wiggles for $P_{e\Delta x} > 8/3$; this is because one of the roots in Eq. (40) has a negative sign for $P_{e\Delta x} > 8/3$. Hence $P_{e\Delta x} = 8/3$ is called the critical cell Peclet number for QUICK. Table XIV shows the roots of the characteristic equations and the values of the critical cell Peclet number associated with the various schemes for the test problem I. Those roots of both the first order upwind and the second order upwind are always positive; the solutions for the model problem by the two schemes are wiggle free. The critical cell Peclet number for second order central differencing is, as is well known, 2. As $P_{e\Delta x}$ is far longer than unity the two characteristic roots of the second order central differencing are very close to each other in magnitude. Hence, as was shown by Gresho and Lee, 1979[73], the magnitudes of the oscillation in the solution are dependent upon whether the total number of mesh points is even or odd. Nevertheless, it is clear that, for this model problem, with high values of $P_{e\Delta x}$, both the second order central differencing and QUICK will not be very satisfactory; the higher order terms in the modified equations cannot increase the weight of the diffusion term adequately to balance the convection term in the boundary layer without letting the disturbances propagate into the main region, therefore, the numerical solutions oscillate. On the other hand, the solutions by both the first order upwind and the second order upwind are wiggle free and acceptable: the second order upwind derives more accurate simulations than the first order one for the whole range of $P_{e\Delta x}$. Hence, the truncation errors in these two schemes are able to help damp out the disturbances where needed more effectively than those in QUICK and the second order central differencing. By examaning the performance of the three second order accurate schemes, it is clear that the formal order of accuracy loses its meaning if a boundary layer exists in a high $P_{e\Delta x}$ problem since the leading truncation error term no longer represents the real size of the error introduced by the numerical approximation. But for a low $P_{e\Delta x}$ flow, the formal order of accuracy is still a good basis by which to judge the relative accuracy

Table XIV. Roots of Eq. (38) Using Four Different Schemes.

Scheme	Roots	Critical Value of $p_{e\Delta x}$
First Order Upwind	$1 + p_{e\Delta x}$ 1	∞
Second Order Upwind	$\dfrac{\left(1 + \frac{3p_{e\Delta x}}{2}\right) \pm \sqrt{\left(1 + \frac{3p_{e\Delta x}}{2}\right)^2 - 2p_{e\Delta x}}}{2}$ 1	∞
Second Order Central	$\dfrac{1 + \frac{p_{e\Delta x}}{2}}{1 - \frac{p_{e\Delta x}}{2}}$ 1	2
QUICK	$\dfrac{\left(1 + \frac{3p_{e\Delta x}}{4}\right) \pm \sqrt{\left(1 + \frac{3p_{e\Delta x}}{4}\right)^2 - \frac{p_{e\Delta x}}{2}\left(1 - \frac{3p_{e\Delta x}}{8}\right)}}{2\left(1 - \frac{3}{8}p_{e\Delta x}\right)}$ 1	$\frac{8}{3}$

ORIGINAL PAGE IS
OF POOR QUALITY

between two schemes with different order, e.g., the first order upwind and QUICK.

Another aspect concerning the validity of the numerical solutions with the large values of the cell Peclet number which is worth commenting on is that no scheme is accurate if a quantity such as ϕ_x is to be calculated at the right hand boundary point for this model problem. This is, again, due to the fact that the high wave number Fourier components, which are important at right hand boundary for high $p_{e\Delta x}$ flow, cannot be evaluated accurately in the course of the numerical approximations by a finite difference scheme. Here, $\phi_{N+1} = 1$ and the smallest value of ϕ_N that one would like to see is zero (otherwise the wiggles start to appear). Hence, the numerical calculation for ϕ_x at $x = 1$ is, at best, $(\phi_{N+1} - \phi_N)/\Delta x = 1/\Delta x$. This result is independent of the Peclet number, in contrast to that which was obtained from the analytical solution which increases directly with $p_{e\Delta x}$.

6.3.5 Iterative Method

The numerical procedures suitable to get the solution of the finite difference equations approximating the large $p_{e\Delta x}$ flows are discussed. For test problem I, if the standard SOR procedure is applied, it is learned that a convergent solution for any large values of $p_{e\Delta x}$ can be guaranteed only for the first order upwind scheme; all the other three schemes fail to provide convergent solutions if $p_{e\Delta x}$ is larger than some values. The reason is as follows. For a system of real linear equations $\vec{A}\phi = \vec{b}$, in which the matrix A can be written as A=I-L-U, where L is the strictly lower triangular matrix, U is the strictly upper triangular matrix, and I is the identity matrix, the Jacobi matrix G_J and the SOR matrix G_ω, corresponding to the relaxation factor ω, can be written as

$$G_J = L + U \tag{41a}$$

$$G_\omega = (I - \omega L)^{-1} [(1 - \omega)I + \omega U] \tag{41b}$$

If the matrix A is consistently ordered, then the following relation exists between the eigenvalues μ of G_J and the eigenvalues λ of G_ω, Varga, 1962[74]

$$(\lambda + \omega - 1)^2 = \omega^2 \mu^2 \lambda \tag{42}$$

ORIGINAL PAGE IS
OF POOR QUALITY

Young, 1971[75] showed that an iterative method is convergent if and only if $0 < \omega_{max}$, where

$$\omega_{max} = \frac{2}{[1 + \mu_I (1 - \mu_R^2)^{-\frac{1}{2}}]} \tag{43a}$$

$$\mu = \mu_R + \sqrt{-1}\mu_I \tag{43b}$$

Furthermore, if either $\mu_R = 0$ or $\mu_I = 0$ and $|\mu_R| < |$, then the following formula is available to determine the optimum value of the relaxation factor, ω_{opt} Varga, 1962[74]

$$\omega_{opt} = \frac{2}{1 + (1-\mu^2)^{\frac{1}{2}}} \tag{44}$$

We now compare the eigenvalues of G_J from the second order central differencing scheme with those from the first order upwind scheme for the test problem I. The central differencing approximation for Eq. (32) at the point i is

$$\phi_i = \frac{1}{2}\left[\left(1 + \frac{p_e \Delta x}{2}\right) \phi_{i-1} + \left(1 - \frac{p_e \Delta x}{2}\right)\phi_{i+1}\right] \tag{45}$$

The first order upwind approximation for Eq. (32) at the point i is

$$\phi_i = \frac{1}{2 + p_{e\Delta x}} \left[(1 + p_{e\Delta x})\, \phi_{i-1} + \phi_{i+1}\right] \tag{46}$$

The eigenvalules μ of the Jacobi matrix for both schemes are:

Central Differencing

$$(\mu)_{central} = \sqrt{1 - \left(\frac{p_e \Delta x}{2}\right)^2} \cos \frac{k\pi}{N+1}, \quad k = 1, \ldots, N \tag{47}$$

ORIGINAL PAGE IS
OF POOR QUALITY

First Order Upwind

$$(\mu)_{Fu} = 2\sqrt{\frac{1+p_{e\Delta x}}{(2+p_{e\Delta x})^2}}\cos\frac{k\pi}{N+1}, \quad k = 1, \ldots, N \tag{48}$$

Since all $(\mu)_{Fu}$ in Eq. (48) are always real and less than one in magnitude, it is known from Eq. (43a) that any value of the relaxation factor ranging from 0 to 2 is allowed to give the convergent solution. For the second order central differencing scheme, all $(\mu)_{central}$ in Eq. (47) are real and less than one in magnitude for $p_{e\Delta x} < 2$; they become purely imaginary for $p_{e\Delta x} > 2$. Hence, one learns from Eq. (43a) that, for the second order central differencing scheme, ω_{max} is 2 for $p_{e\Delta x} < 2$ and ω_{max} is less than 2 for $p_{e\Delta x}$ 2. Furthermore, if $p_{e\Delta x} >> 1$, then Eq. (44) indicates that the optimum value of the relaxation factor is

$$(\omega_{opt})_{central} \cong (\omega_{max})_{central} \cong \frac{2}{(1+\frac{p_{e\Delta x}}{2})} \tag{49}$$

which is a very small number. The eigenvalues of G_J from the second order upwind and from QUICK are not known analytically. But it is proposed here that a relaxation factor ω, analogous to that in Eq. (49) of the form

$$\omega = \frac{1}{\sigma} \tag{50}$$

be used for the iterative process to get the solutions of the various schemes considered here. σ is the sum of the absolute values of all off-diagonal elements in the i^{th} equation (normalized with respect to the absolute sum of the diagonal elements) if the i^{th} point is to be calculated. For example, the value of $(1 + 0.5\ p_{e\Delta x})$, $(2 + 2.5\ p_{e\Delta x})/(2 + 1.5\ p_{e\Delta x})$, and $(2 + 11\ p_{e\Delta x}/8)/(2 + 3\ p_{e\Delta x}/8)$ is used for the second order central differencing, the second order upwind, and QUICK, respectively in the test Problem I. The iterative method with those under-relaxation factors has produced convergent solutions by all the schemes for all the test problems studied here. Of course, for the first order upwind scheme, the standard SOR procedure is always effective in giving convergent solutions; SOR should still be used for the first order upwind.

No attempt is made here to compare in detail the computing time needed to get the final solutions for those finite difference equations using the relaxation factor just described. But for all the problems with high $p_{e\Delta x}$ tested in his study, including the one-dimensional convection diffusion flow, the multidimensional flow, and the flow with a source term, the second order upwind

scheme and QUICK require almost the same number of iterations which are slightly more than those needed for the first order upwind but are less than those for the second order central differencing. This is contrary to the findings of Atias, et al., 1977[67] who applied the Gauss-Seidel method to solve the two-dimensional vorticity transport equation and reported that the second order upwind is always somewhat less efficient than central differencing. For the problem they solved, whether the present iterative method will show the same relative efficiency between the two schemes or not is open to further investigation. Nevertheless, in the study by Atias, et al., upper limits exist for the cell Peclet number for both schemes using the Gauss-Seidel method, as just explained. Another aspect worth commenting on is that the numerical stability restraint (in von Neumann sense) of an explicit scheme for the time-dependent problem is not equivalent to that of an iterative scheme for the steady-state problem. Hence, the criticism by Gupta and Manohar, 1978[68] regarding the stringent stability limit of the second order upwind scheme for the time-dependent equation is not applicable here. An illuminating comparative study for the various iterative methods applied to large problems with the convection terms approximated by the second order central differencing scheme was given by Botta and Veldman, 1982[76].

6.3.6 Test Problem II: Flow with Source Term

Leonard, 1979[57] chose the model problem

$$u\phi_x = \nu\phi_{xx} + S(x),\ u,\ \nu = \text{constants} > 0 \tag{51a}$$

$$\phi(0) = 0 \tag{51b}$$

$$(\phi_x)_{x=L} = 0 \tag{51c}$$

to study the accuracy of the finite difference approximation to high $Pe_{\Delta x}$ flow in the presence of a source term. Further investigation is proposed for the same problem by varying the distribution of S(x) to set up the limit of an adequate numerical simulation as well as comparing the performances among different schemes. The basic form of S(x) used here is

ORIGINAL PAGE IS
OF POOR QUALITY

$$S(x) = \begin{cases} ax + b, & 0 \le x \le x_1 \\ -\dfrac{(ax_1 + b)}{x_2}\, x + \dfrac{(x_1 + x_2)}{x_2}\,(ax_1 + b), & x_1 \le x \le x_1 + x_2 \end{cases} \tag{52}$$

as shown in Figure 48.

For the extreme case of $P_{e\Delta x} \to \infty$, Leonard, 1979[57] has shown that the solutions given by QUICK are much better than those by the first order upwind which follow closely the exact solution of $P_{e\Delta x} = 2$, and those by the second order central differencing which are more susceptible to the changes of the downstream boundary condition; here we concentrate on the comparisons between the solutions by the second order upwind and by QUICK for $P_{e\Delta x} = 10^8$. For a source spanning several mesh lengths, both schemes can give accurate solutions for $P_{e\Delta x} \to \infty$; the only complicating issue is the strategy for the starting calculation. Figure 49 shows the solutions calculated by both schemes using the first order upwind scheme to calculate the first unknown value of the dependent variable, ϕ_2. Figure 50 shows the solutions by both schemes putting the left hand boundary point, $x = 0$, at the mid-point of the first numerical mesh, and assigning the value of ϕ at the first grid point, ϕ_1, by linearly extrapolating the values of ϕ_2 (which is located at $x = \Delta x/2$ and the boundary value at $x = 0$. Here, $\phi = 0$ at $x = 0$, hence $\phi_1 = -\phi_2$. The solutions calculated in this way, as suggested by Leonard, 1979[57], are more accurate than those shown in Figure 49 for both schemes. Also, in both Figures 49 and 50, the accuracy of the solutions by the two schemes are comparable. Figure 51 shows what changes can be made for the numerical results if $\phi = 0$, not $\phi_x = 0$, is used as the downstream boundary condition. For this example, the solution by the second order upwind scheme is more satisfactory than that by QUICK. The restraint imposed by the downstream boundary condition forces the QUICK solution to show oscillations because the higher order terms in the modified equation fail to help damp out the disturbances in that thin layer. Figure 52 compares the two numerical solutions with the exact solution for a more rapid varying source term spanning two mesh lengths. Neither of the two numerical solutions is totally accurate for all grid points but the one by second order upwind is better. Figure 53 shows the numerical solutions by the two schemes against the exact solution for a more stringent source distribution. For this problem the Fourier components with the wave number equal to or higher than $\pi/\Delta x$ are important to the exact solution, and, as was discussed previously, they cannot be resolved satisfactorily by the finite difference approximations; the solutions by both schemes carry unacceptably large errors even though the exact value of ϕ_2 is assigned to eliminate any error involved in the starting calculation method. This demonstrates the fact that any attempt to accurately simulate a flow with the length scale $2\Delta x$ (or less) is out of the question; a more refined mesh must

ORIGINAL PAGE IS
OF POOR QUALITY

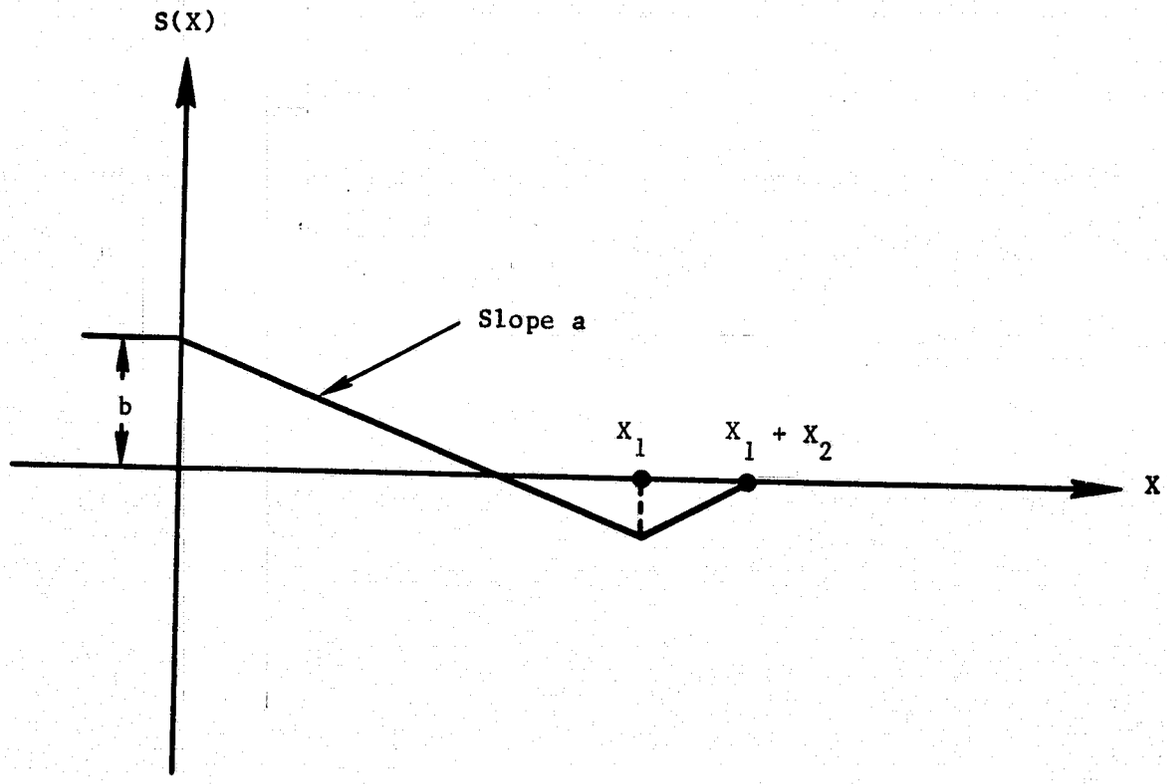


Figure 48. Distribution of Source Term in Eq. (52).

ORIGINAL PAGE IS
OF POOR QUALITY

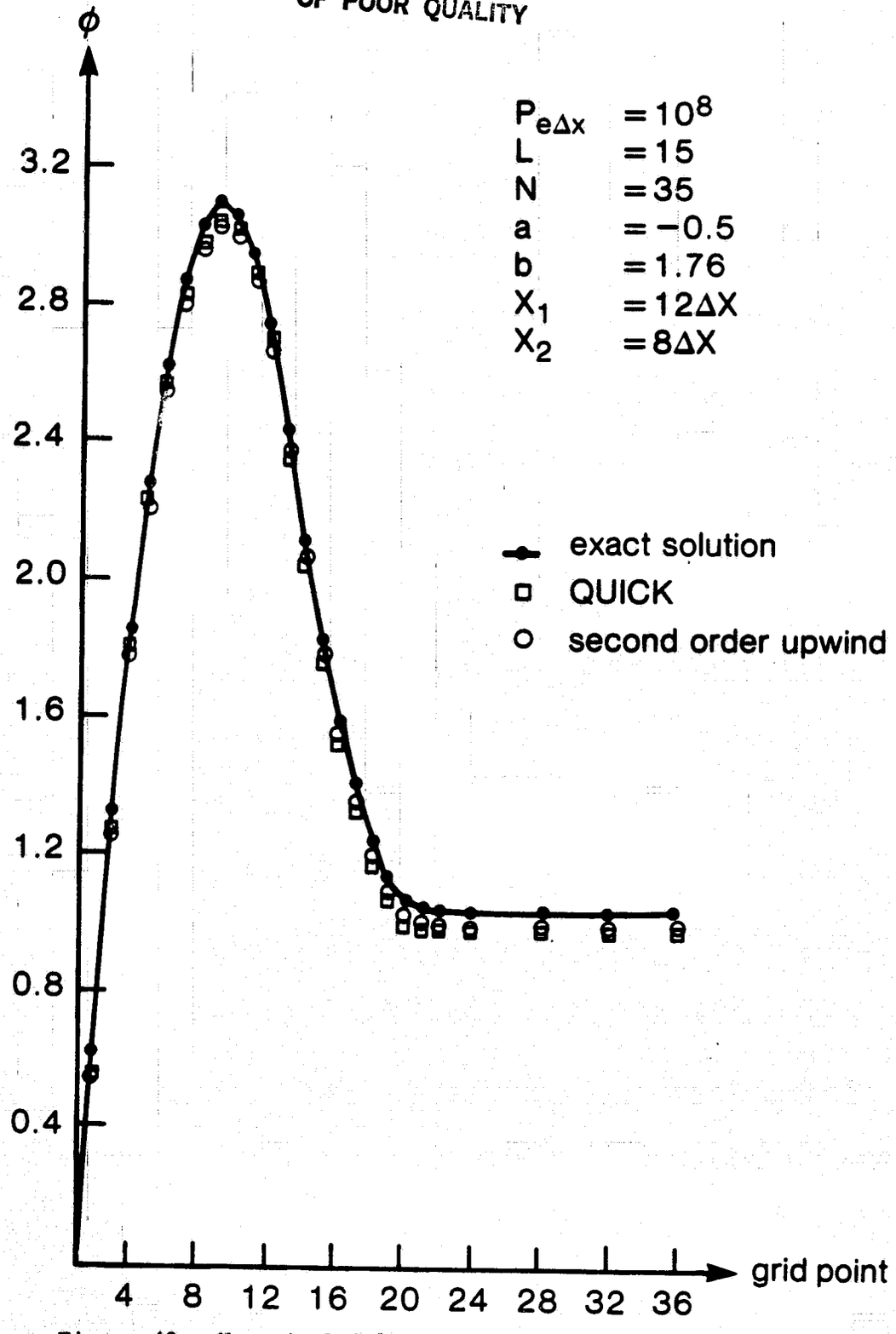


Figure 49. Numerical Solutions to Test Problem II (Downstream Boundary Condition: d ϕ/d x = 0) Starting Calculation Method: ϕ_1 (0) = 0, ϕ_2: by First Order Upwind.

ORIGINAL PAGE IS
OF POOR QUALITY

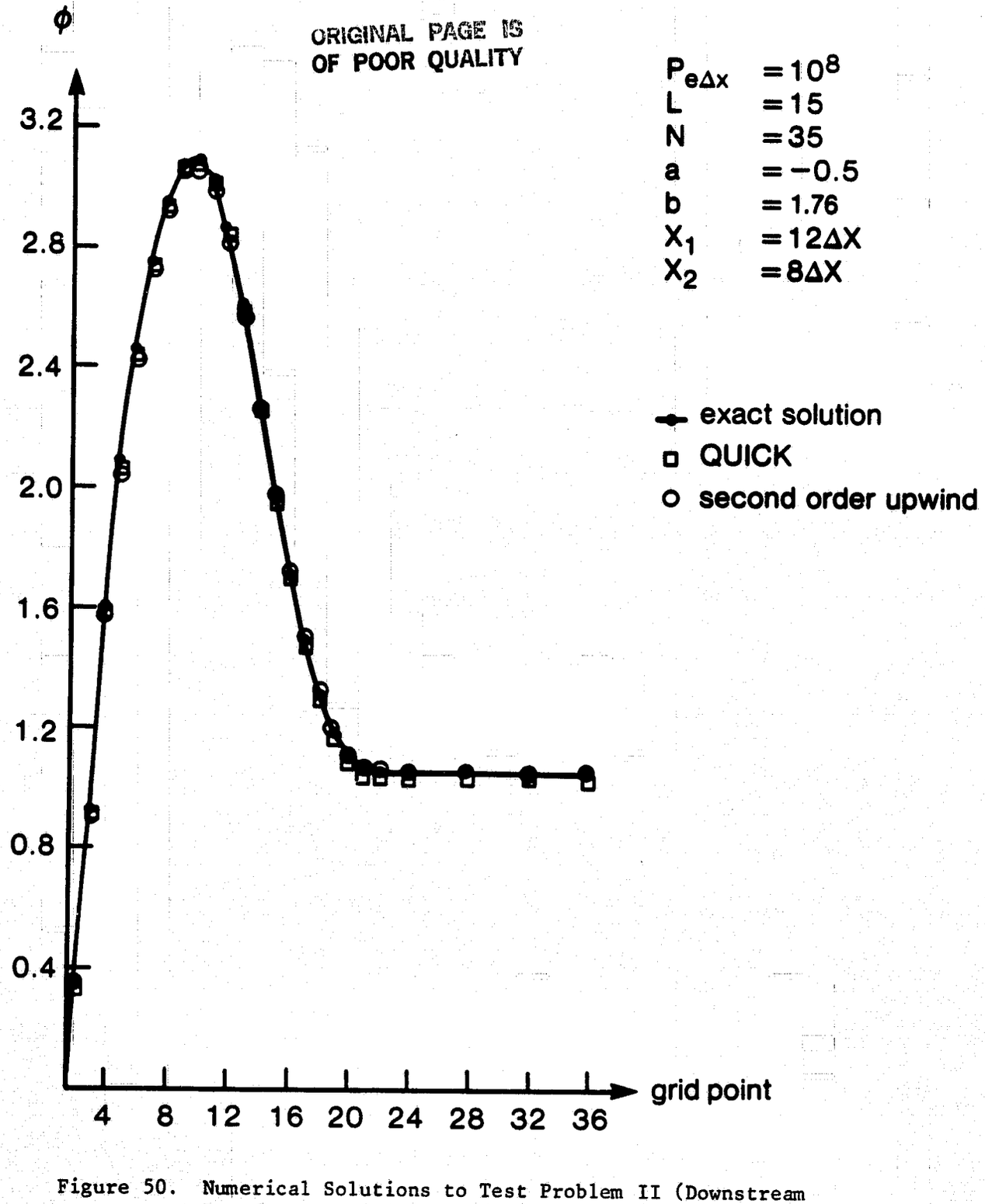


Figure 50. Numerical Solutions to Test Problem II (Downstream Boundary Condition: d ϕ/d x = 0) Starting Calculation Method: $\phi_1 = \phi\ (-\Delta X/2) = -\phi_2$ ϕ_2: by first order upwind.

ORIGINAL PAGE IS
OF POOR QUALITY

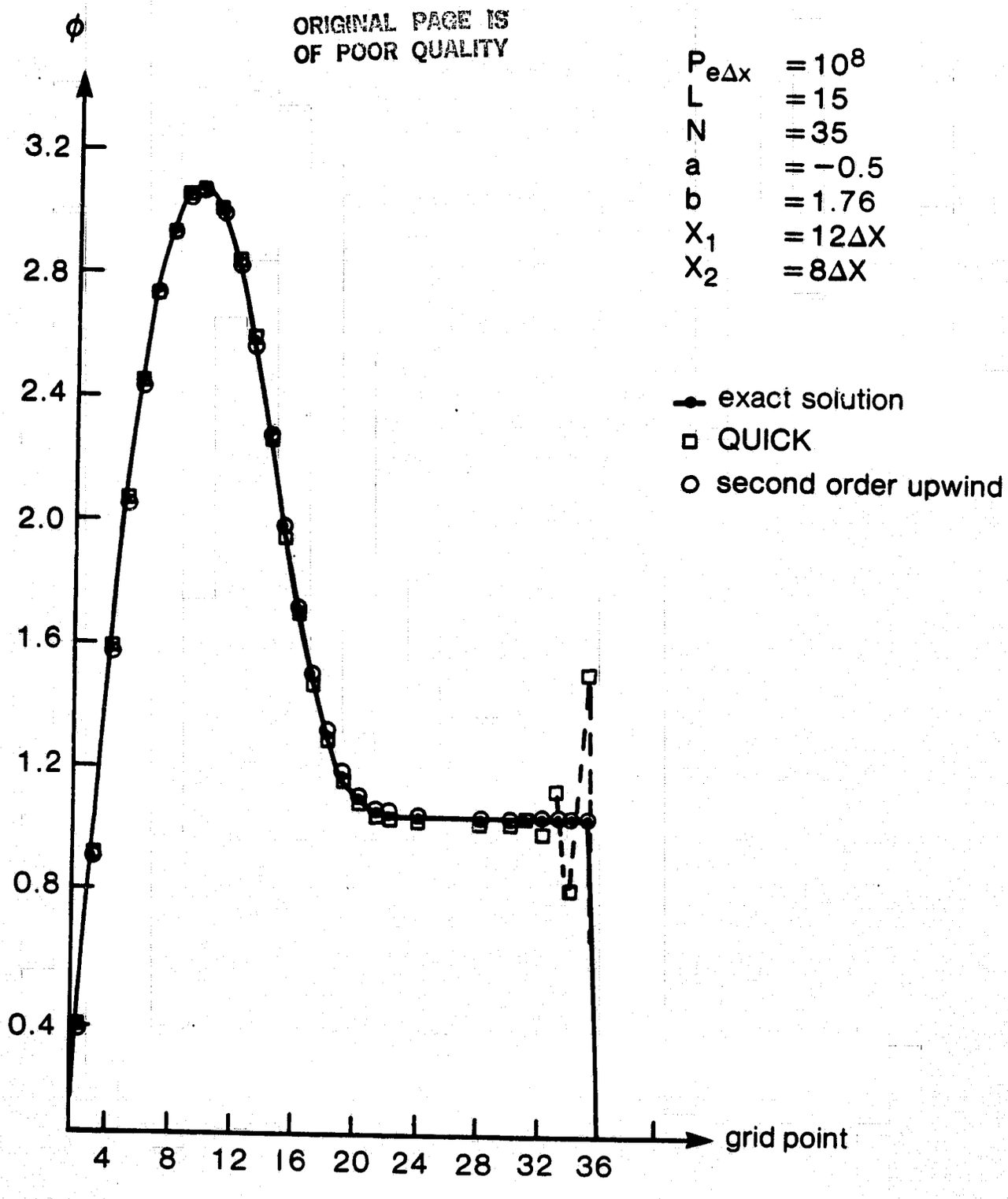


Figure 51. Numerical Solutions to Test Problem II (Downsteam Boundary Condition: $\phi = 0$) Starting Calculation Method: $\phi_1 = \phi(-\Delta x/2) = -\phi_2$, ϕ_2: by First Upwind.

ORIGINAL PAGE IS
OF POOR QUALITY

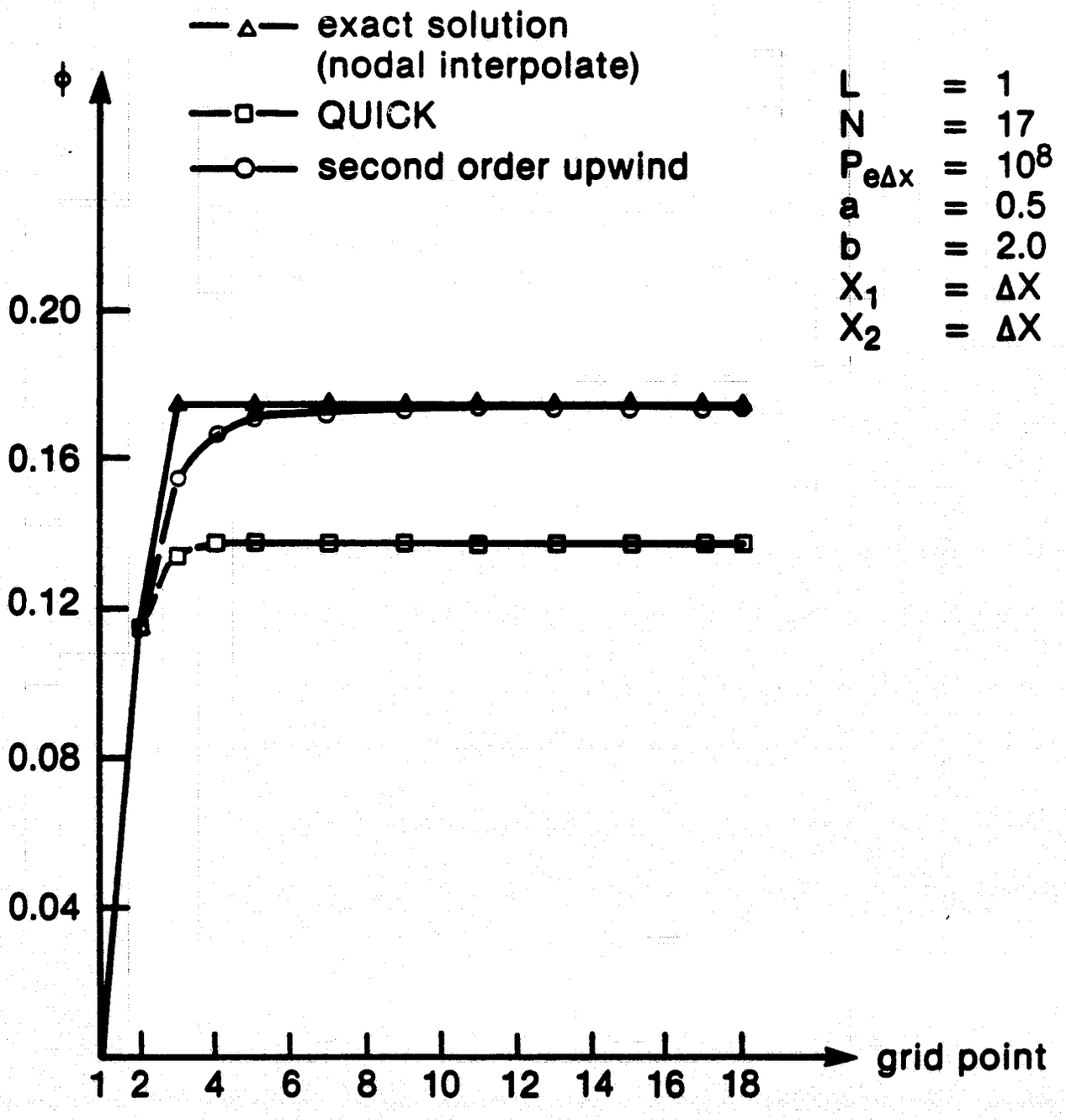


Figure 52. Numerical Solutions to Test Problem II (Downsteam Boundary Condition: d ϕ/d x=0) Starting Calculation Method: $\phi_1=\phi(0)=0$, ϕ_2 by First Order Upwind.

ORIGINAL PAGE IS
OF POOR QUALITY

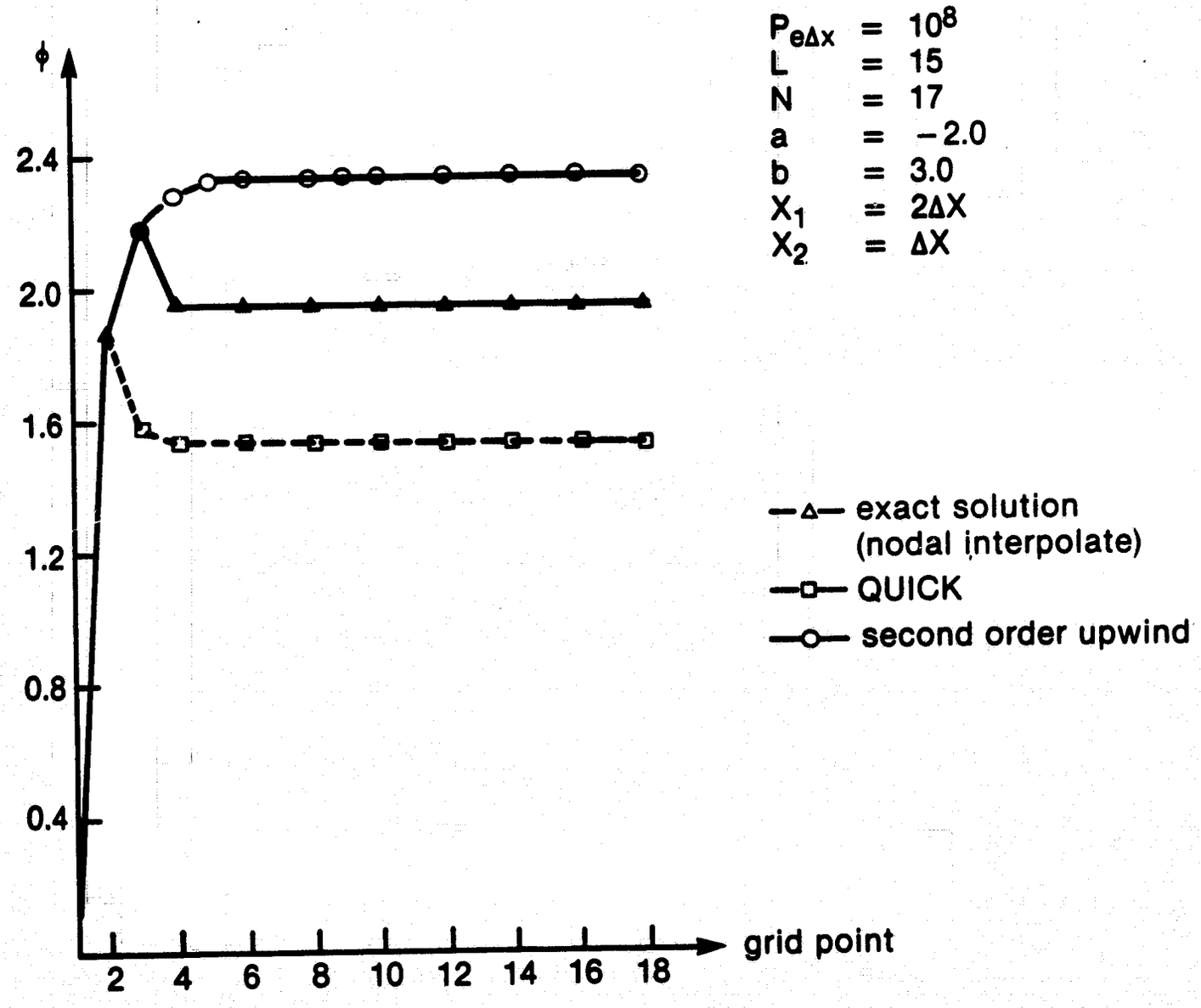


Figure 53. Numerical Solutions to Test Problem II (Downstream Boundary Condition: ϕ_x=0) Starting Calcualtion Method: ϕ_1=ϕ(0)=0, ϕ_2=ϕ(ΔX)= Exact Solution.

ORIGINAL PAGE IS
OF POOR QUALITY

be used for all schemes considered here. On the other hand, for a problem with a mild source distribution and downstream boundary condition such as that shown in Figure 50, an accurate numerical approximation is possible for large $Pe\Delta x$ because the diffusion term in Eq. (51a) plays no important role in the whole flow region.

6.3.7 Test Problem III: Numerical Diffusion Due to Streamline-to-Grid Skewness

To study the problem of numerical diffusion in a multidimensional flow, the following idealized case is considered at first:

$$u\phi_x + v\phi_y = 0 \ , \ 0 \leq x \leq 1, \quad 0 \leq y \leq 1 \tag{53a}$$

$$\phi(0, y) = 100y^n, \quad 0 \leq y \leq 1 \tag{53b}$$

$$\phi(x, 0) = 100\left(\frac{x}{\cot\theta}\right)^n, \quad 0 \leq x \leq 1 \tag{53c}$$

where cot θ = u/v, and u and v are positive constants. The difference between the first order upwind and the skew upwind schemes is analyzed here to show some basic characteristics of numerical diffusion. The first order upwind approximation to Eq. (53a) at the grid point (i, j) can be written as follows:

$$\phi_{i,j} = \phi_{i-1,j} + \frac{a}{1+a}\left(\phi_{i,j-1} - \phi_{i-1,j}\right) \tag{54a}$$

where

$$a = \frac{v}{u}\frac{\Delta x}{\Delta y} \tag{54b}$$

Eq. (54a) shows how ϕ_{ij} is calculated by linearly interpolating between ϕ_{i-1} and $\phi_{i,j-1}$ at the point where the straight line connecting the grid points (i-1, j) and (i, j-1) intersects the velocity vector at the point (i,j). It is known that when convection dominates in establishing the spatial distribution of the quantity ϕ, the gradient in ϕ in the streamwise direction vanishes, and the cross-flow gradient depends on the upstream boundary conditions. From Eq. (54b) it is clear that the first order upwind gives the exact solution if the exponent n in Eqs. (53b, c) is unity; otherwise, the error resulting from the linear interpolation in Eq. (54a) will cause numerical diffusion in the

ORIGINAL PAGE IS
OF POOR QUALITY

cross stream direction. Recognizing this, Raithby, 1976[63] devised the following scheme to approximate Eq. (53a) more closely:

$$u\frac{\phi_{i+\frac{1}{2},j} - \phi_{i-\frac{1}{2},j}}{\Delta x} + v\frac{\phi_{i,j+\frac{1}{2}} - \phi_{i,j-\frac{1}{2}}}{\Delta y} = 0 \qquad (55a)$$

where

$$\phi_{i+\frac{1}{2},j} = \phi_{i,j} - (\phi_{i,j} - \phi_{i,j-1})\frac{a}{2} \qquad (55b)$$

$$\phi_{i-\frac{1}{2},j} = \phi_{i-1,j} - (\phi_{i-1,j} - \phi_{i-1,j-1})\frac{a}{2} \qquad (55c)$$

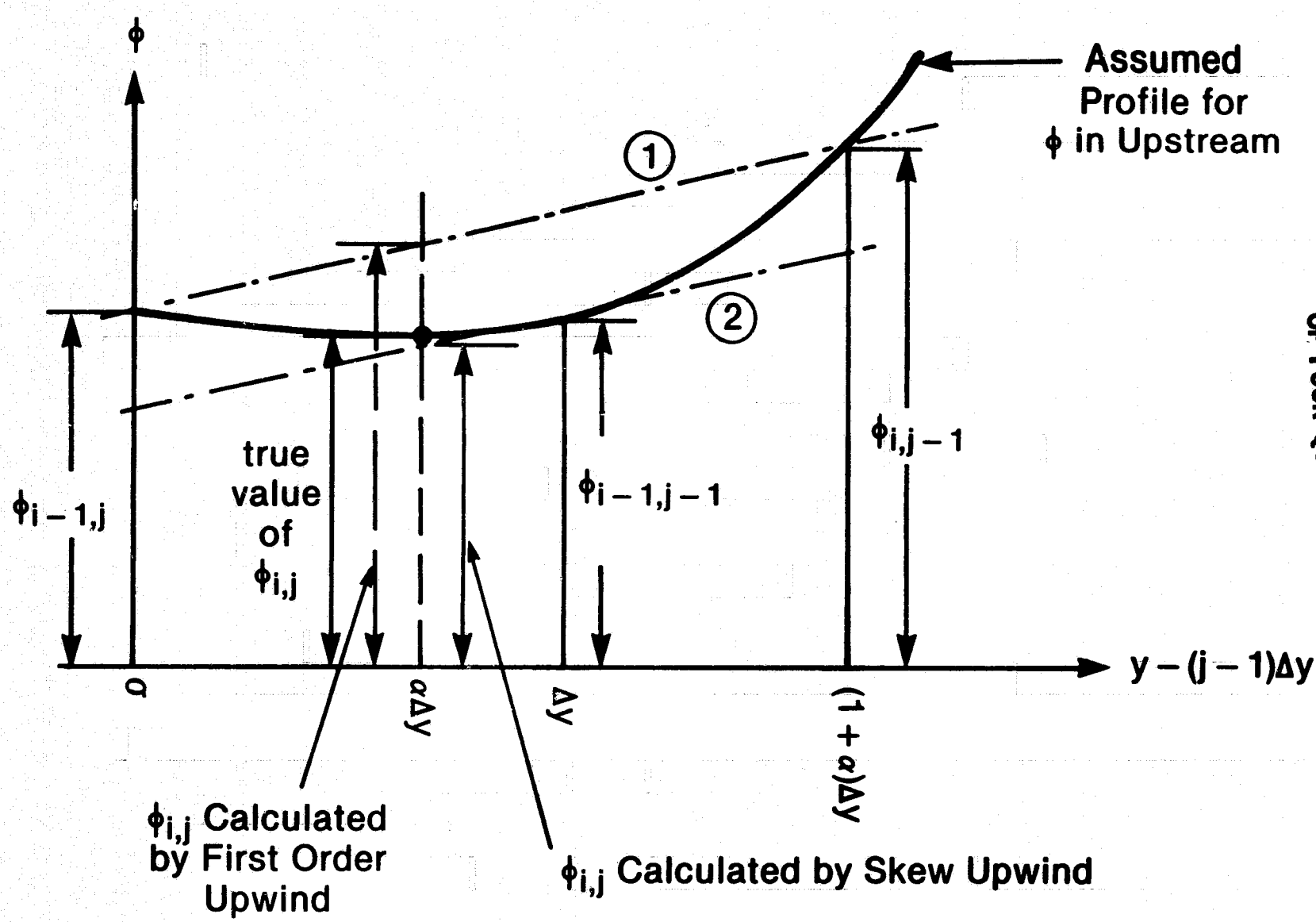
$$\phi_{i,j+\frac{1}{2}} = \phi_{i,j} - (\phi_{i,j} - \phi_{i-1,j})\frac{1}{2a} \qquad (55d)$$

$$\phi_{i,j-\frac{1}{2}} = \phi_{i,j-1} - (\phi_{i,j-1} - \phi_{i-1,j-1})\frac{1}{2a} \qquad (55e)$$

Eq. (55a) can be rewritten as follows:

$$\phi_{i,j} = \phi_{i-1,j-1} + \frac{1-a}{1+a}(\phi_{i-1,j} - \phi_{i,j-1}) \qquad (56)$$

Figure 54 compares the way to calculate $\phi_{i,j}$ by the first order upwind and that by the skew upwind. It can be seen that, although both schemes are formally exact only to a linear variation of ϕ profile in the cross-stream direction, the $\phi_{i,j}$ calculated by the skew upwind can be improved substantially compared with that by the first order upwind. As for the second order upwind and QUICK, both are exact to the quadratic profile of ϕ in the cross-stream direction. Figure 55 shows the numerical solutions to Eqs. (55) by the four schemes: first order upwind, skew upwind, second order upwind, and QUICK, for m=2 and Cot θ=2. The skew upwind is used to calculate the first unknowns from



ORIGINAL PAGE IS
OF POOR QUALITY

Figure 54. Comparison of Accuracy Between First Order Upwind and Skew Upwind Approximations to Eq. (53): Lines 1 and 2 are Parrell.

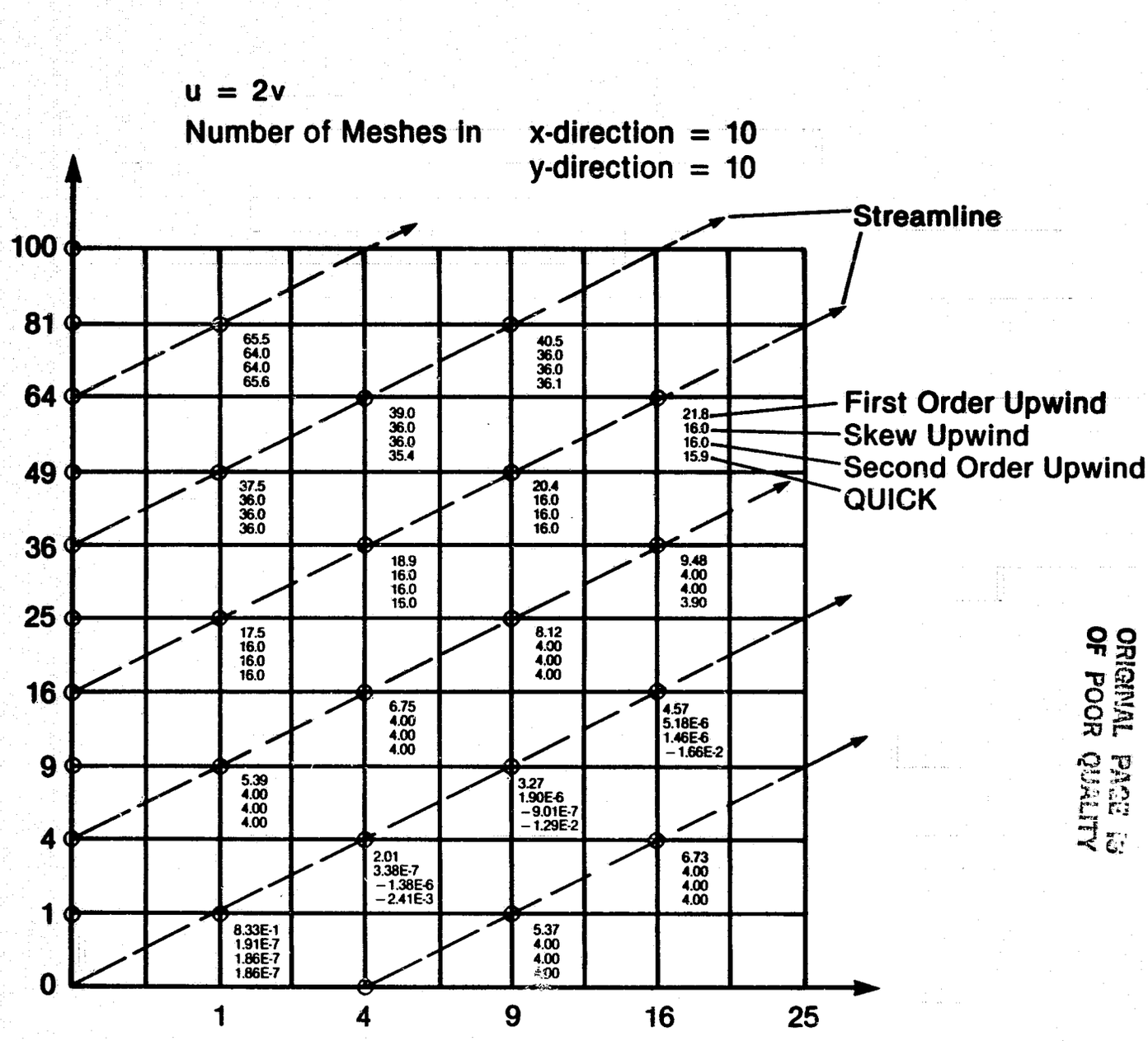


Figure 55. Numerical Solutions to Eq. (53) for n = 2.

ORIGINAL PAGE IS
OF POOR QUALITY

the upstream boundaries for both the second order upwind and QUICK. In addition, the downstream boundary conditions are also needed by QUICK, and the skew upwind is also used there. In Figure 55, the grid points connected by any single streamline should possess the same value of ϕ. While the first order upwind gives the solutions with some noticeable numerical cross-stream diffusion, all other three schemes give very good approximations. It is noted that the small errors appearing in the solution by QUICK are caused by the calculation for the downstream boundary values. Figure 55 demonstrates that the first order skew upwind differencing can reduce the cross-stream numerical diffusion substantially. Figure 56 shows the numerical solutions by the four schemes for the same equation but with a more stringent upstream boundary condition; a step function, instead of a n-th power polynomial, is used. Here, again, because of the importance of the high wave number Fourier components to the real solution, no scheme is able to give a very accurate approximation; the sharp variation in the real solution is smeared out due to the numerical diffusion. Also, the solutions by the skew upwind, by the second order upwind, and by QUICK all exhibit overshoots; the solution by QUICK also exhibits undershoots. Globally speaking, QUICK and the second order upwind perform better here.

After examining the possible error caused by the numerical approximations to the convection terms, a two-dimensional flow problem including both the convection and the diffusion terms, as stated in the following, is considered next.

$$u\phi_x + v\phi_y = \nu(\phi_{xx} + \phi_{yy}), 0 \leq x \leq 1, \quad 0 \leq y \leq 1 \tag{57a}$$

$$\phi(0, y) = 100, \quad 0 < y \leq 1 \tag{57b}$$

$$\phi(x, 0) = 0, \quad 0 \leq x \leq 1 \tag{57c}$$

where u and v are positive constants; u/v = 2, and the cell Peclet number based on $u\Delta x/v = 40$ are used in the study. Two different downstream conditions are investigated: The periodic values of ϕ along a streamline, or the zero value of ϕ. Five numerical schemes, first order upwind, skew upwind, second order central differencing, second order upwind, and QUICK, are compared in this test problem. For the first of the downstream boundary condition, i.e., the periodic values along a streamline, a typical profile of ϕ, plotted as a function of y at $x = 1 - 2\Delta x$, given by the numerical approximations are shown in Figure 57. The profile by the first order upwind is the smoothest one due to the excessive numerical diffusion. The solution by the second order central differencing, on the other hand, shows the wiggles in the flow region. The other three schemes all produce the solutions with some limited extent of overshoots near the downstream boundary. Among them, the solutions by QUICK and by the second order

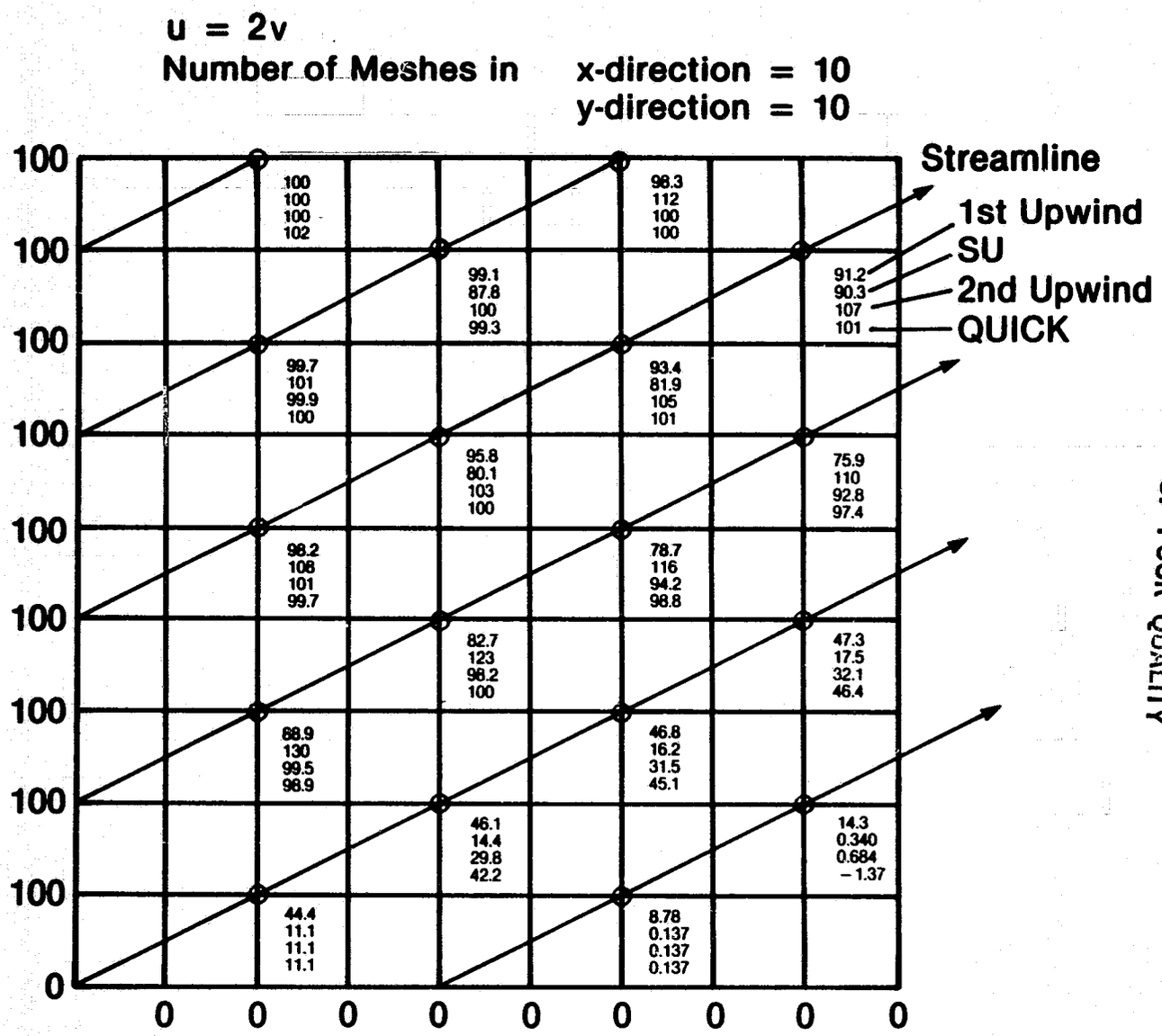


Figure 56. Numerical Solutions to Eq. (53) (Upstream Boundary Conditions: $\phi(0,y) = 100$ $0 \leq y \leq 1$, $\phi(x,0) = 0$, $0 \leq x \leq 1$).

ORIGINAL PAGE IS
OF POOR QUALITY

ORIGINAL PAGE IS
OF POOR QUALITY

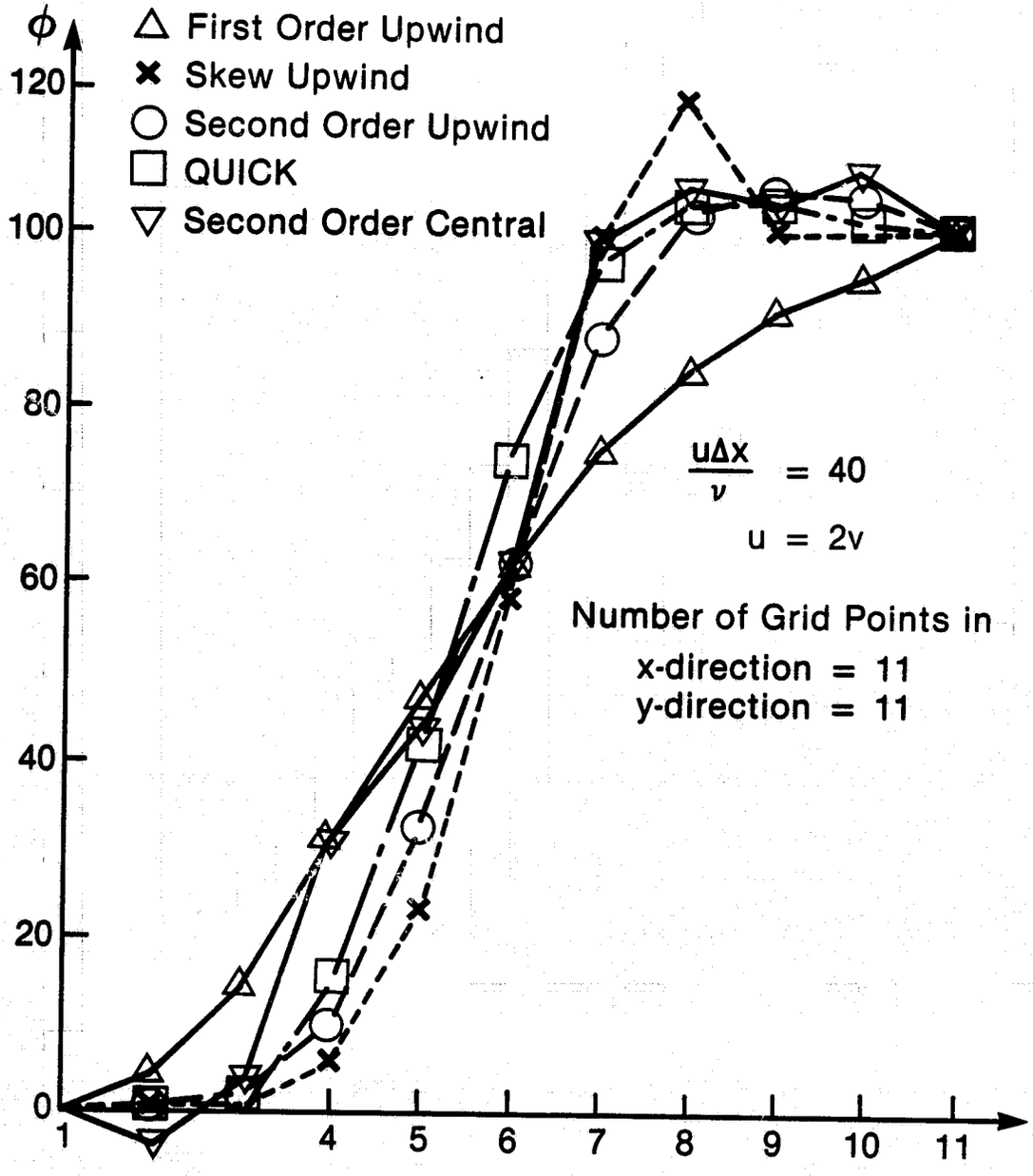


Figure 57. Numerical Solutions to Eq. (56) at x = 1 - 2Δ x (Down Stream Boundary Conditions: Gradient of ϕ = 0 in Streamwise Direction).

upwind are the more satisfactory. Compared with the true solution for the first kind of boundary condition, the true solution for the second kind of downstream boundary conditions, i.e., $\phi = 0$, and high $p_{e\Delta x}$ flow should be of the character that a boundary layer region is formed in the vicinity of the downstream boundary with the solution in the main region of the flow field virtually unaffected. The solutions by the five numerical schemes for this problem are compared in Figure 58. Those by the second order central differencing and by QUICK show unacceptably large magnitudes of oscillation. The solutions by the three upwind schemes are, compared to those in Figure 57, unaffected by the change of the boundary condition except for the points far downstream. In this case, the best scheme is the second order upwind which shows a reasonable compromise between an accurate simulation in the convection dominated region and an effective enhancement to the diffusion term in the boundary layer region which prevents the disturbances from propagating.

6.3.8 Summary and Conclusions

Five different finite difference schemes: first order upwind, skew upwind, second order upwind, second order central differencing, and QUICK, approximating the convection terms in the equation governing fluid motion have been studied. It is shown that in a finite difference simulation with large cell Peclet number, the high wave number Fourier components of the real solutions cannot be evaluated accurately. As a result of this, in a convection dominated flow, if the viscous terms are required to balance the convection terms in a thin layer close to the downstream boundary due to, for example, a Dirichlet type boundary condition being applied there, a finite difference approximation can, at best, use the truncation errors of the approximations to help damp out the disturbances in that thin layer. The detailed structure of the real solution is unresolved. Even this may or may not be accomplished by a given scheme, and hence for a high cell Peclet number flow the formal order of accuracy is a poor criterion to judge the performances among different schemes. Among the five schemes examined in this study, the second order upwind scheme gives the most satisfactory results for the particular test cases in this study. It still, however, exhibits overshoots in the solution to a limited extent. On the other hand, although both the second order central differencing and QUICK are formally of the same order of accuracy as the second order upwind, they fail to enhance the viscous terms properly, in the region where needed, for a high cell Peclet number flow problem, and noticeable spurious oscillations appear in the numerical solutions. It should be noted that the magnitudes of those spurious oscillations in the solutions by QUICK are generally less serious than those by the second order central differencing. Furthermore, if no boundary layer type of region exists in the real solution, the accuracy of the approximating solutions given by QUICK and by second order upwind are comparable. As for the first order upwind, it is free from producing the unphysical over- and under-shoots in the solutions for all the test problems, but fails to give accurate approximations in the presence of a source term and shows too much numerical diffusion in the convection dominated region for a multi-dimensional flow. The skew upwind is able to reduce numerical diffusion by the first order in the cross-stream direction substantially, but it

ORIGINAL PAGE IS
OF POOR QUALITY

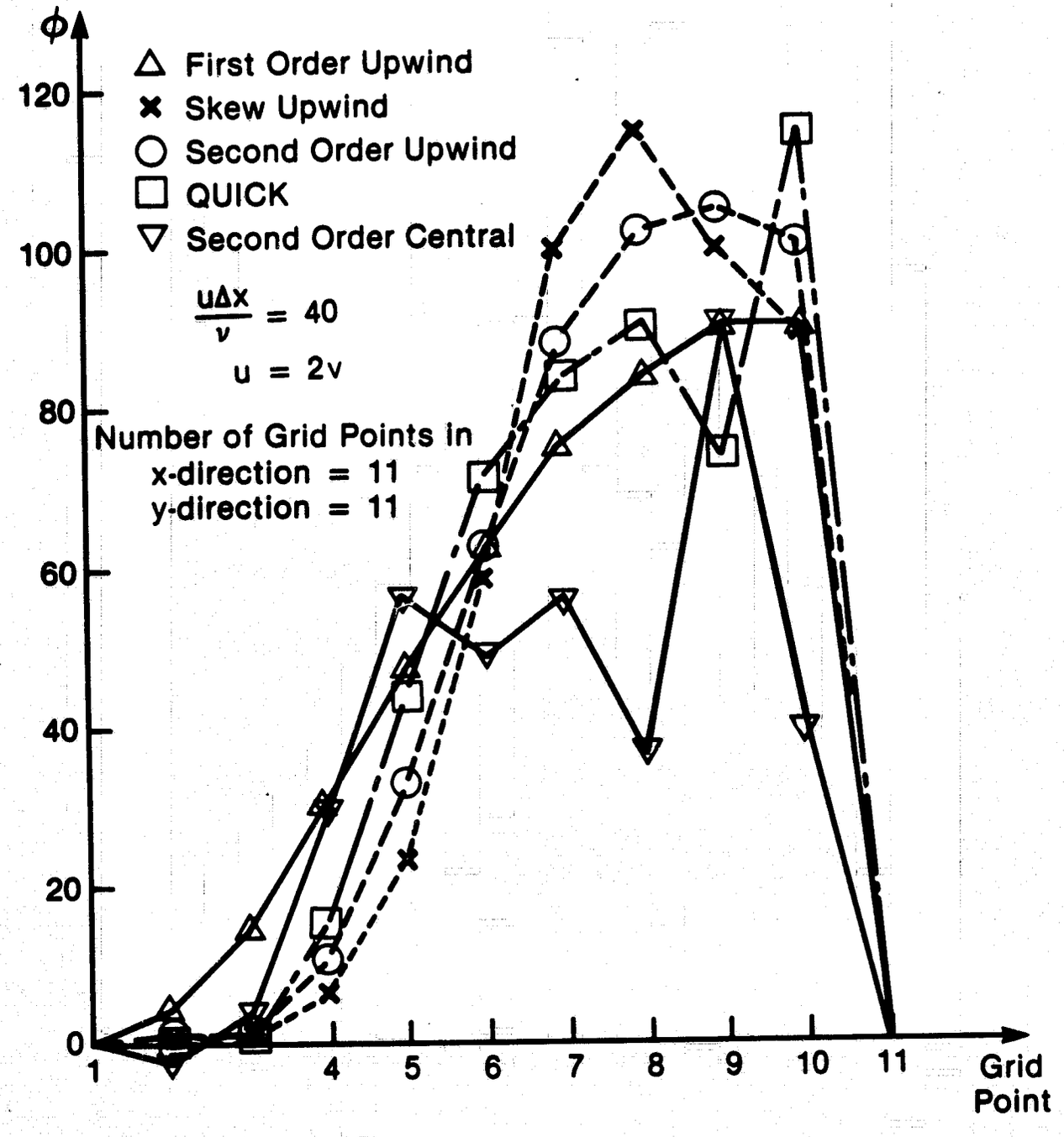


Figure 58. Numerical Solutions to Eq. (56) at x = 1 - 2Δ x
(Downstream Boundary Conditions: ϕ = 0).

is found to be less satisfactory compared with the second order upwind. The skew upwind scheme also fails to to give accurate solutions in the presence of the source terms, Raithby, 1976[63]. For all the formally second order accurate schemes studied here, the standard SOR technique cannot be applied for large values of $P_e\Delta x$; a modified relaxation factor yields convergent solutions for all cases considered.

6.4 TURBULENCE CLOSURE MODELS

This section discusses the general features as well as some specific points in the field of turbulence modeling.

The one point correlations, $u''_i u''_j$ and $u''_i \phi''$, which appear in the mean flow equations (23) and (24) require further description to provide determination of their local values. This situation is the classical "closure problem" which arises from averaging of the instantaneous governing equations, (13) to (18), which are believed to contain all of the relevant physics. The loss of information in the averaging process necessitates "modeling" of certain resulting terms, e.g., $u''_i u''_j$, in the mean flow equations. In this section, the general problem is described followed by discussion of two-equation turbulence models, variable density effects, and anisotropies due to streamline curvature and swirl which can be corrected by algebraic stress models.

The Reynolds stresses $\bar{\rho} u''_i u''_j$ appearing in equation (23) can be found as a solution of the following transport equation, Jones, 1979[28].

$$\bar{\rho}\tilde{U}_k \frac{\partial}{\partial x_k}\widetilde{(u''_i u''_j)} = -\frac{\partial}{\partial x_k}\widetilde{(\bar{\rho} u''_i u''_j u''_k)} - \overline{(u''_i \frac{\partial \bar{p}}{\partial x_j} + u''_j \frac{\partial \bar{p}}{\partial x_i})}$$
$$- \overline{(u''_j \frac{\partial p'}{\partial x_j} + u''_i \frac{\partial p'}{\partial x_j})} - \bar{\rho}\widetilde{(u''_i u''_k \frac{\partial \tilde{U}_j}{\partial x_k} + u''_j u''_k \frac{\partial \tilde{U}_i}{\partial x_k})} - \bar{\rho}\varepsilon_{ij} \qquad (58)$$

In these equations, higher order (third order) correlations appear, which have to be related to lower order (usually second) in order to close this set. Certain key assumptions regarding the convection [left side of (58)] and diffusion term [first term on right side of (58)], reduce these equations to algebraic forms which can include important effects of streamline curvature and swirl, which introduce significant anisotropies in the Reynolds stresses, as might appear in practical combustors. Before presenting recent GE results with these so-called algebraic stress models, the standard two-equation eddy viscosity turbulence modeling approach is considered first. The deficiencies of this approach are recognized at the outset, but it is the appropriate basis for comparisons for inclusion of variable density effects important in combustion, as well as the above-mentioned anisotropic effects. Libby and Williams, 1981[77] have indicated many of the difficulties of this approach.

ORIGINAL PAGE IS
OF POOR QUALITY

Following Jones and Launder, 1972[14], the Reynolds stresses are assumed to be linearly related to the rate of strain according to

$$\overline{\rho}\,\widetilde{u''_i\,u''_j} = -\mu_t\left(\frac{\partial \tilde{U}_i}{\partial x_j} + \frac{\partial \tilde{U}_j}{\partial x_i}\right) + \frac{2}{3}\delta_{ij}\left(\overline{\rho}\tilde{k} + \mu_t\frac{\partial \tilde{U}_k}{\partial x_k}\right) \qquad (59)$$

where $\tilde{k}$ is the mass-averaged turbulent kinetic energy, $1/2\ \widetilde{u''_i\,u''_j}$. Similarly the turbulent flux of each scalar quantity is related to the mean flow gradient according to

$$\overline{\rho}\,\widetilde{u''_j\,\phi''} = -\frac{\mu_t}{\sigma_\phi}\frac{\partial \tilde{\phi}}{\partial x_j} \qquad (60)$$

where σ_ϕ is the appropriate (constant) turbulent Prandtl-Schmidt number for each scalar ϕ, which must be chosen by "optimization" with use of comparisons with appropriate experimental data.

There is an implicit assumption of a unique length scale leading to the effective eddy viscosity μ_t. From the exact transport equations for the Reynolds stresses, Tennekes and Lumley, 1972[78] have shown that this assumption is valid if the vorticity of eddies involved in cross stream momentum transfer scales with the cross stream vorticity of the mean flow. Furthermore, the shear stress has to scale with any components of the Reynolds stress tensor. This can occur only if there is a unique length-scale and time-scale in the flow. Simple shear flows fall into this category.

A recirculating flow such as that behind the bluff-body described in Section 7.1, has several characteristic length scales: the jet diameter, the annulus height, the thickness of the boundary layer on the bluff-body and the recirculation zone length. Then zero stress may not coincide with zero strain, Durao and Whitelaw, 1978[79]. Thus the assumption of an effective eddy viscosity is questionable in recirculating flows unless the turbulence is dominated by mean pressure gradients.

The isotropic eddy viscosity is given by

$$\mu_t = C_\mu\,\overline{\rho}\,\tilde{k}^2/\tilde{\varepsilon}$$

where $\tilde{\varepsilon}$ is the rate of dissipation of turbulent kinetic energy. For Favre-averaged $\tilde{k}$ and $\tilde{\varepsilon}$, the following equations are solved

ORIGINAL PAGE IS
OF POOR QUALITY

$$\bar{\rho}\,\tilde{U}_i \frac{\partial \tilde{k}}{\partial x_i} = \frac{\partial}{\partial x_i}\left(\frac{\mu_t}{\sigma_k}\frac{\partial \tilde{k}}{\partial x_i}\right) - \bar{\rho}\,\widetilde{u''_i u''_j}\frac{\partial \tilde{U}_i}{\partial x_j} + \frac{\overline{\rho' u''_i}}{\bar{\rho}}\frac{\partial \bar{p}}{\partial x_i} - \bar{\rho}\tilde{\varepsilon}$$

$$\bar{\rho}\,\tilde{U}_i \frac{\partial \tilde{\varepsilon}}{\partial x_i} = \frac{\partial}{\partial x_i}\left(\frac{\mu_t}{\sigma_\varepsilon}\frac{\partial \tilde{\varepsilon}}{\partial x_i}\right) - C_1\,\bar{\rho}\,\frac{\tilde{\varepsilon}}{\tilde{k}}\left[\widetilde{u''_i u''_j}\frac{\partial \tilde{U}_i}{\partial x_j} + \frac{\overline{\rho' u''_i}}{\bar{\rho}}\frac{\partial \bar{p}}{\partial x_i}\right] \tag{61}$$

$$- C_2\,\bar{\rho}\,\frac{\tilde{\varepsilon}^2}{\tilde{k}} + \bar{\rho}\,\tilde{\varepsilon}\frac{\partial \tilde{U}_i}{\partial x_i}\Big] \tag{62}$$

Note that in these equations, the divergence of the mean flow field, $\partial\tilde{U}_i/\partial x_i$, explicity appears. From equation (22),

$$\frac{\partial \tilde{U}_i}{\partial x_i} = -\frac{U_i}{\bar{\rho}}\frac{\partial \bar{\rho}}{\partial x_i} \tag{63}$$

which is zero only in constant (mean) density flows.

The derivation and discussion of these equations have been discussed by Jones and Launder, 1972[14], and many others. The constants chosen are C_μ = 0.09, C_1 = 1.44, C_2 = 1.92, σ_k = 1.0, σ_ε = 1.0, and σ_t = 0.7. These equations, (42) through (47), are, in fact, the variable density version through inclusion of both the $\rho\,\partial\tilde{u}_i/\partial x_i$ terms and through the $\overline{\rho' u''_i}$ correlations. These latter correlations pose a major modeling problem, as the above equation set has been carried over (except for the specific variable density terms) directly from turbulence modeling in constant density flows (including the constants given above). The use of the above $\tilde{k}$-$\tilde{\varepsilon}$ model in practical combustion systems, i.e., with major recirculation zones and with large dilution jet penetration, where the flows are largely pressure, rather than turbulence controlled as in the decay of wakes, can be expected to yield realistic results. Details regarding the length of recirculation zones and effects of high swirl can be refined with proposed algebraic stress models.

The correlations $\overline{\rho' u''_i}$ in equations (61) and (62) can have a significant influence, Libby and Bray, 1977[46], Libby and Williams, 1981[77], and Bilger, 1980[80]. Various models have been proposed in the literature, Jones, 1979[28], but at the present the gradient flux model has been assumed in the General Electric combustion models, viz,

$$\overline{\rho' u''_i} = -\frac{\mu_t}{\sigma_t}\frac{\partial \bar{\rho}}{\partial x_i} \qquad (64)$$

This is expected to show particularly strong effects in confined flows where strong pressure fields exist, including dilution or swirl-dominated flow fields. Significant work is required as these $\overline{\rho' u''_i}$ correlations are coupled to the mean pressure gradients in (61) and (62) and can be expected to have significant effects in the pressure-dominated flows in gas turbine combustors.

These terms, as well as the $\partial \tilde{U}_i / \partial x_i$ terms, have generally been neglected by many authors, Mongia, et al., 1981[1]; Syed and Sturgess, 1980[48]; and Bozsan, et al., 1981[49], despite its apparent importance for combusting flows with non-zero pressure gradients. Furthermore, Borghi and Dutoya, 1979[81] and Schefer, et al., 1982[82] suggest that the conventional gradient transport expression, Eq. (64), may predict the wrong sign of the turbulent transport flux, i.e., that countergradient diffusion may occur. It is thus obvious that the role of $\overline{\rho' u''_i}$ in prediction of turbulent, recirculating flows needs considerable attention to provide more appropriate modeling and testing with detailed comparisons with experimental data. Alternates to (64), including the solution of transport equations for $\overline{\rho' u''_i}$, have been proposed (e.g., Jones, 1979[28]). The complexity of this approach requires further development and study, and the General Electric models presently use the simple model given by equation (64).

In addition to the above-cited density-velocity fluctuation correlations which couple to the mean pressure gradient, questions regarding flame generated turbulence need further study. Many investigators, e.g. Bray, 1979[83]; Libby and Williams, 1981[77]; and Bilger, 1980[80], have raised this issue and proposed alternate models for limited application (with simple diffusion or premixed jet flames). For example, Libby and Bray, 1978[46] multiply the eddy viscosity by a density ratio $(\bar{\rho}/\rho_{initial})^{\alpha}$ and show certain turbulence effects can be so correlated at least in premixed flames. Bilger, 1980[80] also pointed out the possibility of important direct effects of density on turbulence properties which alters the rate of generation of turbulent kinetic energy due to mean flow gradients. In an interesting study, Borghi and Dutoya, 1979[81] suggested that, due to the chemical reactions, the eddy diffusion coefficient on the fresh gas side of the flame should be increased, and the eddy diffusion coefficient on the burned gas side should be decreased significantly. This implies that the turbulent Schmidt number may vary significantly because of the combustion.

As was stressed in the previous section, the problem of inadequate turbulence modeling is further compounded by the fact that the numerical accuracy is not always satisfactory in a simulation process. For example, the measurements of the flow in an annular jet, made by Durao and Whitelaw, 1978[79], have been used for the evaluation of various turbulence models, e.g., Pope and Whitelaw, 1976[84]; Taylor, 1981[85]; and Leschziner and Rodi, 1981[65], and finite differencing schemes; e.g., Leschziner and Rodi, 1981[65]; and Rastogi, 1980[86]. A general conclusion for computational studies of separted flows is that the

use of finer numerical grids than most of those reported in the literature is necessary. The calculations done by Taylor, 1981[85], using the standard k-ε model and extensive grid refinements, for the turbulent flows behind bluff bodies show that the recirculation length is only one tenth too small compared with the measurements, whereas Pope and Whitelaw, 1976[84] reported a discrepancy of one third. Hence, care must be taken in judging the validity of a turbulence model.

The two-equation ($\tilde{k}$ and $\tilde{\varepsilon}$) turbulence models such as the one described by equations (59) to (62) suffer other weaknesses. The assumption that the one-point, two-variable correlations in (59) and (60) are directly proportional to the mean gradients implies that the eddy viscosity is isotropic. In flows with significant body forces such as highly buoyant, curved, and swirled flows, experimental evidence shows, for example, that the ratio of turbulent Reynolds stress to mean flow gradient is not isotropic. Such effects have been accounted for in atmospheric turbulence (buoyance) problems and for flows over curved surfaces (e.g., turbine blade boundary layer flow and heat transfer). In addition, many numerical studies have shown that the recirculation zone, either in a backward-facing step or due to high swirl, is underpredicted significantly when the turbulence model does not account for streamline curvature and swirl properly. The following discussion will be mainly concerned with the representation of curvature effects on this class of turbulence closure scheme, as demonstrated with axisymmetric elliptic flow computations.

Leschziner and Rodi, 1981[65] and Hah and Lakshminarayana, 1980[87] have proposed algebraic Reynolds closure models for the curved turbulent flows. Leschziner and Rodi derived the relationship between strain and stress for the curved turbulent flow based on rather unrealistic assumptions such as:

$$\frac{U_r}{r} = \frac{\partial U_n}{\partial n} = \frac{\partial U_s}{\partial s} = 0 \tag{65}$$

where U_s, U_n, U_r are streamwise (s), normal (n), and radial (r) velocity components. Also they include the effects of curvature on only one Reynolds stress component as follows:

$$-\overline{U'_s U'_n} = \frac{-k_1 k_2}{[1 + 8k_1^2\, k^2/\varepsilon^2\, (\partial U_s/\partial n + U_c/R_c)\, U_c/R_c]} \frac{k^2}{\varepsilon} \left(\frac{\partial U_s}{\partial n} - \frac{U_s}{R_c}\right) \tag{66}$$

and the resulting coefficient for the effective eddy viscosity

$$C_\mu = \frac{-k_1 k_2}{[1 + 8k_1^2\, k^2/\varepsilon^2\, (\partial U_s/\partial n + U_c/R_c)\, U_c/R_c]} \tag{67}$$

ORIGINAL PAGE IS
OF POOR QUALITY

where

$$k_1 = 1 - \frac{\beta}{\alpha}$$

$$k_2 = \frac{2}{3}\frac{(1 - \alpha - \beta)}{\alpha}$$

$$\alpha = 1.5$$

$$\beta = 0.6$$

is made dependent on the local curvature through the term

$$\left(\frac{\partial U_s}{\partial n} + \frac{U_s}{R_c}\right)\frac{U_c}{R_c} \quad . \tag{68}$$

The formulation of equation (66) is inconsistent with the standard k-ε model because higher effective eddy viscosity is predicted if k_1K_2 is not arbitrarily readjusted. Furthermore, the estimation of U_s, U_e, R_c for effective eddy viscosity is very difficult and nearly impossible for many complicated flows; the formulation is restricted to two-dimensional flows with one component of the streamline curvature. The three-dimensional turbulent flow in a combustion chamber often contains swirling velocity components and the curvature has more than one component. Consequently many Reynolds stress components (like the normal stress along the radius of the curvature) should be handled more carefully. Hah and Lakshminarayana, 1980[87] showed that the use of turbulence kinetic energy production as a primary source term in the turbulence energy equation [see equation (69)] makes the turbulence closure scheme insensitive to the streamline curvature.

$$U_i \frac{\partial \varepsilon}{\partial x_i} = \frac{\partial}{\partial x_i}\left(\frac{\nu_{eff}}{\sigma_\varepsilon}\frac{\partial \varepsilon}{\partial x^i}\right) + C_{\varepsilon 1}\left(\frac{\varepsilon}{k}\right) P - C_{\varepsilon 2}\frac{\varepsilon^2}{k} \tag{69}$$

where

$$P = -\overline{u_i u_j}\, U_{i,j}.$$

They proposed to use the following exact form of the source term which does not include mean strain rate in the energy dissipation,

$$S = C_\varepsilon \frac{\varepsilon^2}{k^3} (u_i u_j - \tfrac{2}{3} k \delta_{ij}) (u_j u_i - \tfrac{2}{3} k \delta_{ij}) \quad . \tag{70}$$

The non-zero Reynolds stress components are estimated using the following modeled Reynolds stress equation

$$\begin{aligned} 0 = {} & (1 + C_1) (- u_k u_j U_{,k_i} - u_k u_i U_{,k_j}) (1 - \gamma) - 2 (\varepsilon_{ilm} \Omega_l u_m u_j \\ & + \varepsilon_{jlm} \Omega_l u_m u_i - \tfrac{2}{3} \delta_{ij} \varepsilon (1 - \gamma) - C_{\phi 1} (\tfrac{\varepsilon}{k}) (u_i u_j - \tfrac{2}{3} \delta_{ij} k) \end{aligned} \tag{71}$$

The above model is tensor-invariant and can be used for the general three-dimensional flow. The model has been incorporated into General Electric elliptic flow codes and tested for a wide range of two- and three-dimensional flows demonstrating that the curvature effects are well represented.

6.5 OTHER TWO-EQUATION TURBULENCE MODELS

There are other formulations of the two-equation type of turbulence model. While they all retain k as one of the dependent variables, the choice of the second variable differs. In the k-ε model it is the dissipation rate ε, in the k-L model it is the length-scale of turbulence L, and in the k-w model it is a measure of the fluctuating vorticity w. Since they all represent the turbulence by two scalar quantities and therefore have only one characteristic time and length scale, they all necessarily lead to the eddy viscosity concept on dimensional grounds. Because it is the very concept of eddy viscosity which is limiting, there is nothing fundamental to differentiate between the three models. On the other hand since the k-ε model has been the most widely tested with respect to the "constants", it is logical to recommend it over the other two for future use.

Another criterion which would help to pick between the three models would be whether or not the modeled quantities could be measured. The turbulence kinetic energy k can indeed be measured (e.g., by single-point LDV) but all the second scalars (ε, L, or w) are more difficult to measure. Typically, two-point LDV would be required. Thus even on experimental grounds there is little to choose between the models.

6.6 TURBULENCE-CHEMISTRY INTERACTION

In a turbulent reacting flow, the interaction between turbulence and chemistry is of critical importance. Three general regimes may be identified.

If the fluid mechanical time scale τ_f is much smaller than the kinetic time scale τ_c, the flow is "micromixed" and kinetically limited. If on the other hand $\tau_c \ll \tau_f$ the flow is instantaneously in equilibrium. Finally, if $\tau_f \sim \tau_c$ both turbulent mixing and chemical kinetics must be accounted for. In this section several approaches to this problem are discussed leading up to the most appropriate. The preferred approach is the assumed shape pdf for scalar(s) with local moments from transport equations solved simultaneously with the hydrodynamic equations. Eddy Break-Up, ESCIMO, and Monte-Carlo models are also discussed.

In a chemically reacting flow, the individual species mass-fractions obey the conservation law, equation (16)

$$\frac{\partial}{\partial t}(\rho Y_i) + \frac{\partial}{\partial x_k}(\rho u_k Y_i) = \frac{\partial}{\partial x_k}\left(\rho D \frac{\partial Y_i}{\partial x_k}\right) + \dot{w}_i \tag{72}$$

Averaging, whether conventional or density weighted, necessitates closure assumptions, including special treatment of the highly nonlinear chemical production term.

For demonstrative purposes, the elementary reaction between species M_1 and M_2 at rate k_f

$$M_1 + M_2 \rightarrow M_3 \tag{73}$$

may be considered. The instantaneous production (consumption) rate ($\dot{w}_1$) of species 1 is then

$$-\dot{w}_1 = \rho^2 k_f Y_1 Y_2 \tag{74}$$

Under Favre (density) averaging, the mean rate of production is

$$-\langle\dot{w}_1\rangle = \rho k_f (\bar{\rho} \tilde{Y}_1 \tilde{Y}_2 + \overline{\rho Y''_1 Y''_2})$$
$$+ \overline{\rho(\rho k_f)'' Y''_2}\,\tilde{Y}_1 + \overline{\rho(\rho k_f)'' Y''_1}\,\tilde{Y}_2 + \overline{\rho(\rho k_f)'' Y''_1 Y''_2} \tag{75}$$

The rate constant k_f which is a function of temperature T may be written simply as

$$k_f = B\, e^{-T_a/T} \tag{76}$$

ORIGINAL PAGE IS
OF POOR QUALITY

where B is the Arrhenius preexponential factor and T_a is the activation temperature. A direct approach to expanding this function is to replace T by its mean and fluctuating components

$$k_f = B\, e^{-T_a/T} \left[1 + \frac{T_a}{T^2} T'' + \left(\frac{T_a^2}{2T^4} - \frac{T_a}{T^3}\right) T''^2 + \ldots\right] \tag{77}$$

and Favre average to obtain

$$\tilde{k}_f = B\, e^{-T_a/\tilde{T}} \left[1 + \frac{T_a^2}{2T^4} \frac{\overline{\rho T''^2}}{\bar{\rho}} + \ldots\right] \tag{78}$$

where

$$\frac{T_a}{T^3} \ll \frac{T_a^2}{2T^4}$$

since typically,

$$T \ll T_a$$

However the higher order terms are negligible only if

$$\frac{T_a\, T''}{T^2} \ll 1$$

which is not true in practical flows where the temperature fluctuations are very large.

In general, then

$$\langle \dot{w}_1 (T) \rangle = \dot{w}_1 (\langle T \rangle) \, [1 + F] \tag{79}$$

where F is an expansion involving corrections between means, means and fluctuations, and fluctuations and fluctuations.

Hence the mean production rate is not the production rate evaluated at the mean temperature. Direct closure methods for the expansion series are generally restricted by the large activation energy

$$T_a/T \gg 1$$

except in near isothermal flows or in systems with small activation energies. The more general closure method is based on probability density functions. Various models discussed below account for this "unmixedness" effect in turbulent reacting flows.

Chemical Kinetics

A chemically reacting system contains the initial reactants, the products and the various intermediate species produced in the course of the overall reaction sequence. The species conservation equations contain $\dot{w}_i$, the mass production rate of species i per unit volume. A general chemical kinetic scheme comprised of N species and R reaction steps may be written in the form

$$\sum_{i=1}^{N} \nu'_{ij} M_i \rightarrow \sum_{i=1}^{N} \nu''_{ij} M_i \qquad j = 1, 2, \ldots R \tag{80}$$

where ν'_{ij} and ν''_{ij} are the stoichiometric reactant and product coefficients for species i and reaction j. The chemical source term $\dot{w}_i$ is given by

$$\dot{w}_i = \sum_{j=1}^{R} \dot{w}_{ij} \tag{81}$$

where $\dot{w}_{ij}$ is the contribution of reaction j to the net rate

$$\dot{w}_{ij} = (\nu''_{ij} - \nu'_{ij})\, k_{fj} \cdot \rho^{m_j} \prod_{i=1}^{N} Y_i^{\nu'_{ij}} \cdot \left(1 - \frac{k_{bj}}{k_{fj}} \rho^{n_j - m_j} \prod_{i=1}^{N} Y_i^{(\nu''_{ij} - \nu'_{ij})}\right) \tag{82}$$

and k_{fj} is the forward Arrhenius rate of reaction j (the backward rate k_{bj} depends on k_{fi} and the equilibrium constant), including a possible temperature dependence in the preexponential.

$$k_{fj} = B_j T^{\alpha_j} e^{-Ta_j/T} \tag{83}$$

In the event that the reactions are very fast compared with the smallest time scale in the flow, the system may be regarded as being in equilibrium at all times. The production rate per unit volume, w_i, is then not explicitly calculated. Instead, the instantaneous configuration of the thermochemical system is more efficiently solved by minimization of Gibbs free energy.

In practical combustors, the short hydrodynamic time scales ultimately necessitate a treatment of chemical kinetics ($\tau_f << \tau_c$). For example, the existence of CO in the liner region of a gas turbine combustor, Wolters, 1973[88], is due to thermal quenching; the oxidation rate is greatly reduced near the relatively cool liner while the CO in the core burns out. Similarly, ignition delay times cause a shift in the location of heat releasing zones. Various intermediate and pollutant species, for example, O and NO_x, cannot be properly accounted for with equilibrium chemistry. Furthermore, the highly turbulent flow field is very significant in affecting the exact value of these important kinetically limited species.

(i) Closure at Mean Temperature

A first strategy used at General Electric to account for full chemical kinetics consists of solving the hydrodynamic equations (for example, equations (22), (23), (61) and (62) for conservation of mass, momentum, turbulence kinetic energy and dissipation rate, respectively) using the elliptic solver discussed in the earlier section on Numerical Methods. The local convection-diffusion coefficients for each computational cell are thus obtained. After scaling with appropriate generalized Prandtl numbers, the species and enthalpy conservation equation in Newton-Raphson correction form are solved by pivotal Gaussian elimination, Pratt and Wormeck, 1976[89]. Thus the local species mass fractions Y_i (i = 1, N) and temperature are also obtained. The new field values of mass density obtained from the equation of state are then used to redetermine the hydrodynamic solutions. This "superiteration" between hydrodynamic and thermochemical fields is repeated until pointwise (at each node) convergence on temperature is achieved. The chemical source term in each Y_i equation is calculated in this procedure at the mean temperature. The method knowingly ignores effects of fluctuations on this source term in order to demonstrate finite rate kinetic effects compared with equilibrium chemistry.

This solution of the thermochemical system is restricted to ideal gases. The optimal algorithm for the thermochemical equations (with strongly linked, nonlinear source terms) and the optimal algorithm for the hydrodynamic equations (with weakly linked source terms) combine to provide a rapidly converging code.

By way of a demonstration, the model has been applied to an axisymmetric, gaseous fuel, bluff-body stabilized combustor, Roquemore, et. al., 1980[90]. The hydrodynamic aspect of the flow was treated by solving the equations for conservation of mass and momentum and utilizing the k-ϵ model for the eddy viscosity. The thermochemical aspect of the flow involved 15 chemical species and 17 reactions including NO_x chemistry (Table XV).

It must be emphasized that this demonstrative calculation employed a relatively coarse grid (30 x 27) without an assessment of numerical error. The objective was to demonstrate the qualitative differences between the equilibrium and kinetic flow fields; also, unmixedness is explicitly ignored. A more rigorous simulation of this flow is presented in Section 7.1.

The flow fields for equilibrium and kinetic flow are partially shown in Figures 59 through 61 and magnified in Figures 62 through 64. The flow rate of propane is 11.66 Kg/hr, corresponding to a jet exit velocity of about 100 m/s. Stagnation points from the data and the models are shown in Table XVI.

A comparison of the location of the stagnation points from the data and the models shows the jet penetration to be somewhat underpredicted. Despite this quantitative discrepancy, which could be addressed through more exact turbulence and turbulence-chemistry interaction modeling, and refined numerics, several qualitative points emerge:

1. Both theory and data show that the effect of combustion is to increase the jet penetration.

2. The flow field predicted by the equilibrium model shows stagnation points, while the kinetic model (in agreement with the data which shows penetration for $m \geq 8$Kg/hr) predicts penetration. This emphasizes the consequences of approximating the combustion chemistry with an equilibrium model based on the mean temperature above. Similarly the frozen flow prediction shows two stagnation points in agreement with the data for $m \leq 14$ Kg/hr.

3. Temperature profiles immediately downstream of the jet exit, Figures 65 and 66 and 0.020 m downstream, Figures 67 and 68 show that the equilibrium flame is narrower than the kinetic flame. The peak temperature of the equilibrium flame is also higher by about 300 K. These temperature overpredictions result in low densities at the nodes, which then lead to erroneous flow field calculations. Thus, the finite rates of the major heat releasing reactions cannot be neglected. The kinetic temperature profile agree qualitatively with the data. It is interesting to note that the effect of random compositional fluctuations on the equilibrium flow is also to smear out the peaks. (This is the more likely phenomena as shown in Section 7.1.)

It is repeated that this demonstrative calculation cannot be used to quantitatively assess the submodels. A methodical study of this particular flow is reported below and the critical appraisal is then made.

ORIGINAL PAGE IS
OF POOR QUALITY

Table XV. Kinetic Scheme for Methane Combustion.

$$k_f = 10^{B_j} T^{N_j} \exp(-Ta_j/T) \quad (m^3/kg-mol-s)$$

j							B	N	T_a	
1	CH_4	O_2		CO	H_2		11.5	0.0	12200	GLOBAL
2	CO	OH		CO_2	H		6.602	0.5	0.0	WALD7/74
3	CO_2		M	CO	O	M	12.000	0.0	50353	WALD7/74
4	H	OH		H_2	O		6.903	1.0	3525	WALD7/74
5	H_2O		M	OH	H	M	12.477	0.0	52870	WALD7/74
6	H	HO_2		OH	OH		11.3981	0.0	957	WALD7/74
7	OH	H_2		H	H_2O		10.3980	0.0	2618	WALD7/74
8	H	O	M	OH		M	9.903	0.0	0.0	WALD7/74
9	OH	O		H	O_2		10.398	0.0	0.0	WALD7/74
10	H	O_2	M	HO_2		M	9.176	0.0	503.5	WALD7/74
11	OH	OH		H_2O	O		9.778	0.0	503.5	WALD7/74
12	OH	N		H	NO		8.778	0.5	4028	WALD7/74
13	H	N_2O		OH	N_2		10.903	0.0	7553	WALD7/74
14	N	NO		N_2	O		10.1760	0.0	0.0	WALD7/74
15	N	O_2		NO	O		6.778	1.0	3172	WALD7/74
16	N_2O	O		NO	NO		11.000	0.0	15000	WALD7/74
17	N_2O		M	N_2	O	M	11.000	0.0	25176	WALD7/74

Chemical Species

CH_4	CO	CO_2	H	H_2	H_2O	HO_2	N
NO	NO_2	N_2	N_2O	O	OH	O_2	

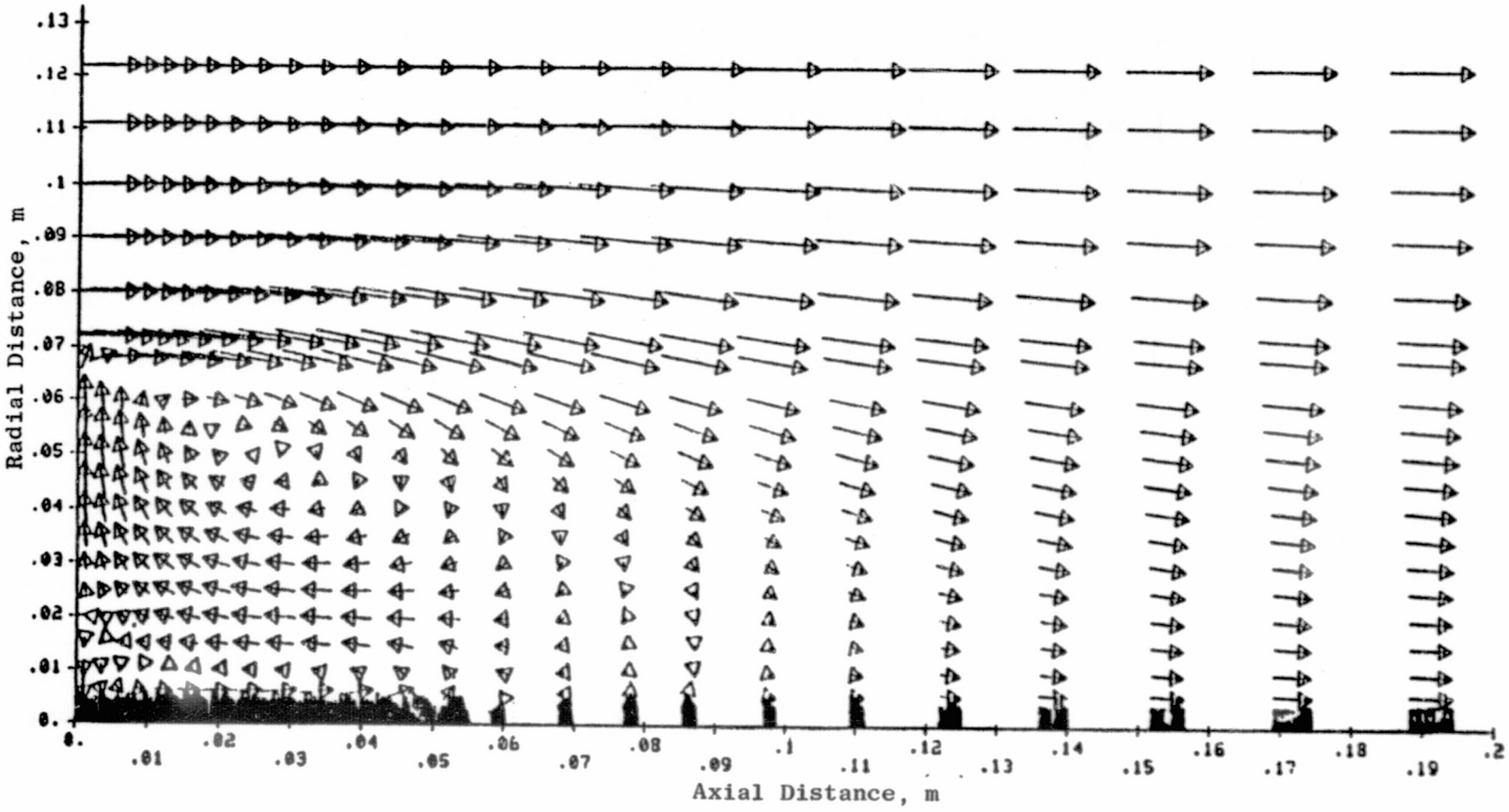


Figure 59. No-Fluctuation Model - Frozen Flow.

ORIGINAL PAGE IS
OF POOR QUALITY

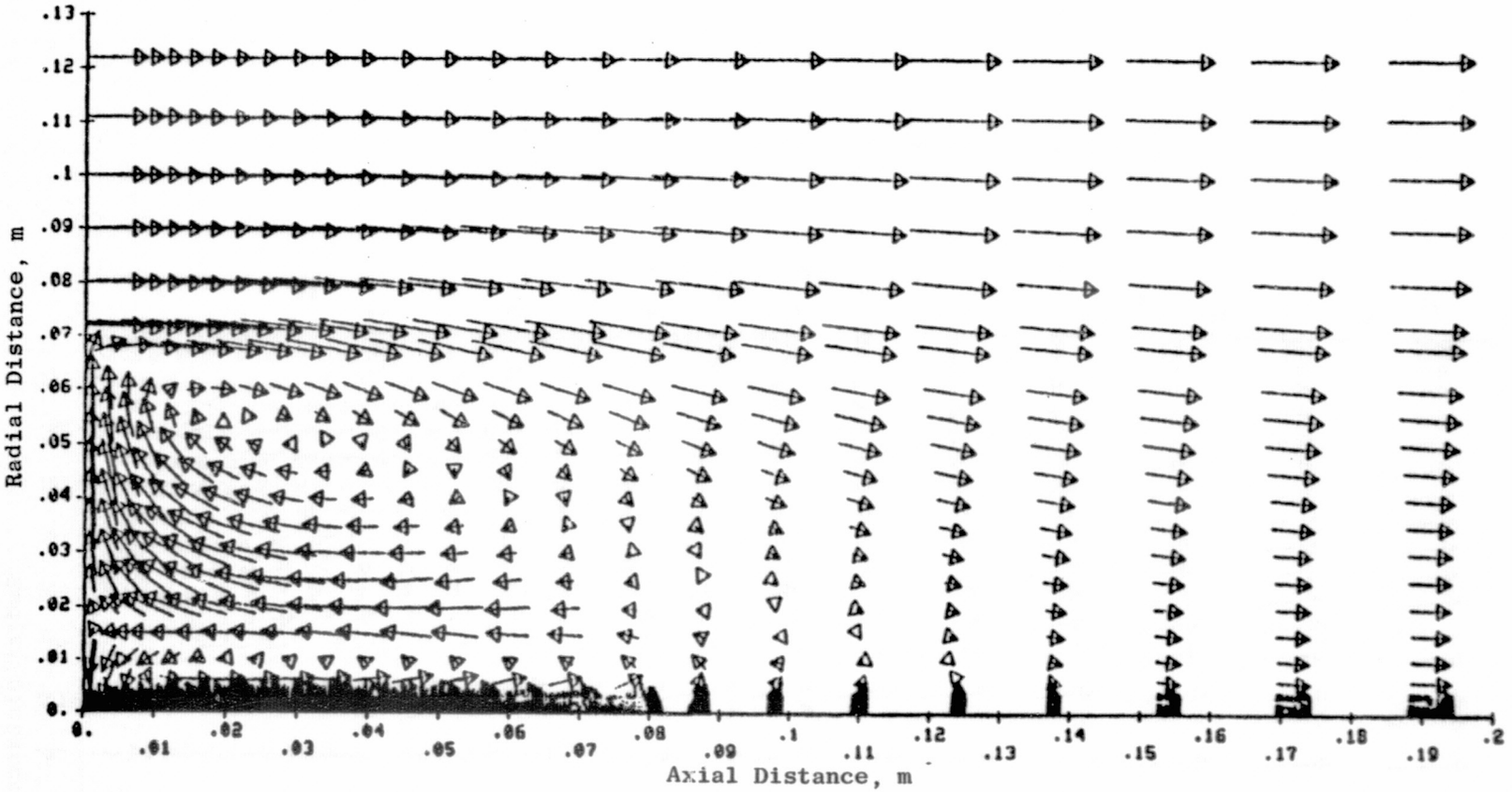
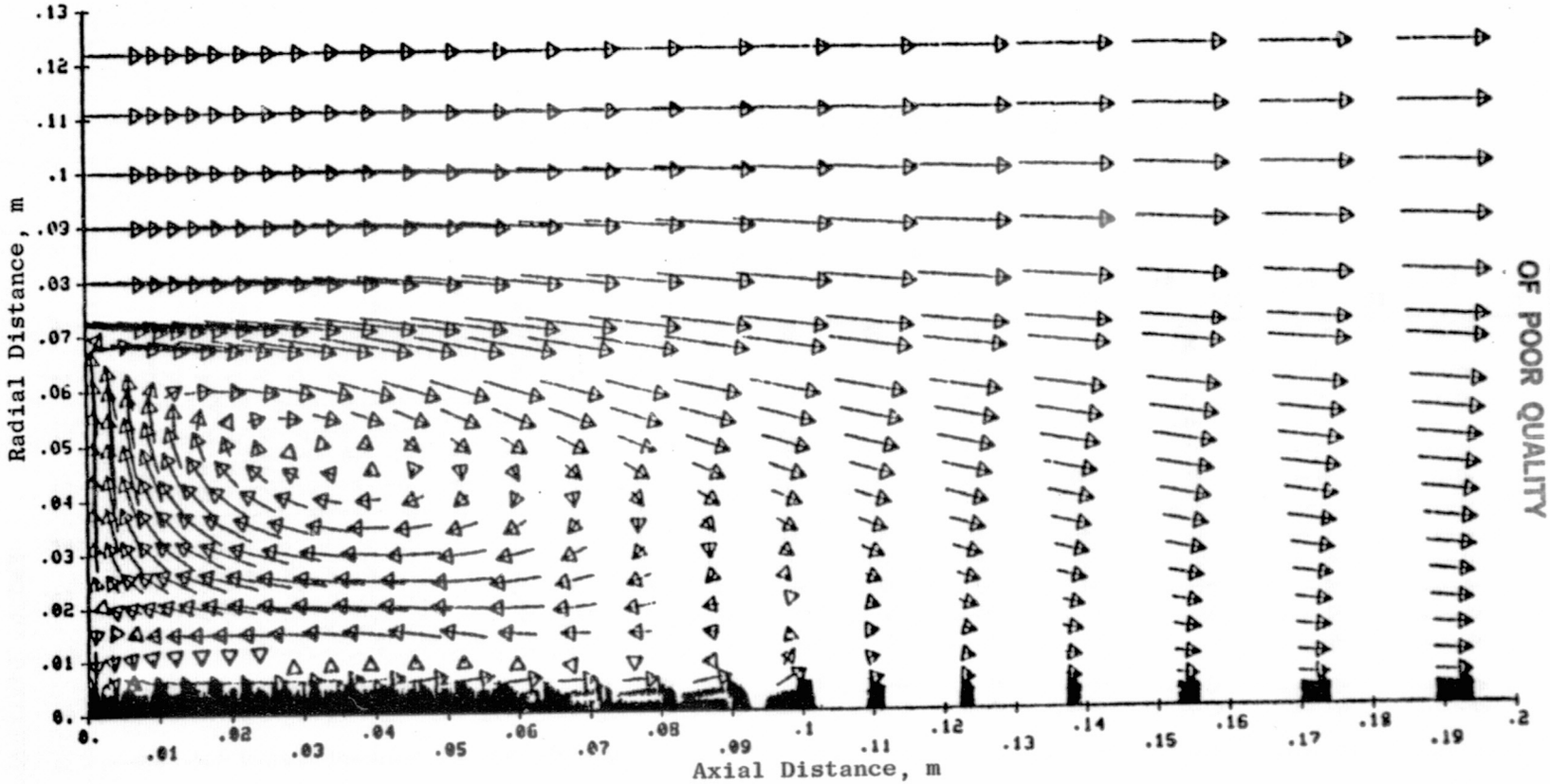


Figure 60. No-Fluctuation Model - Equilibrium Flow.

ORIGINAL PAGE IS
OF POOR QUALITY



ORIGINAL PAGE IS
OF POOR QUALITY

Figure 61. No-Fluctuation Model - Kinetic Flow.

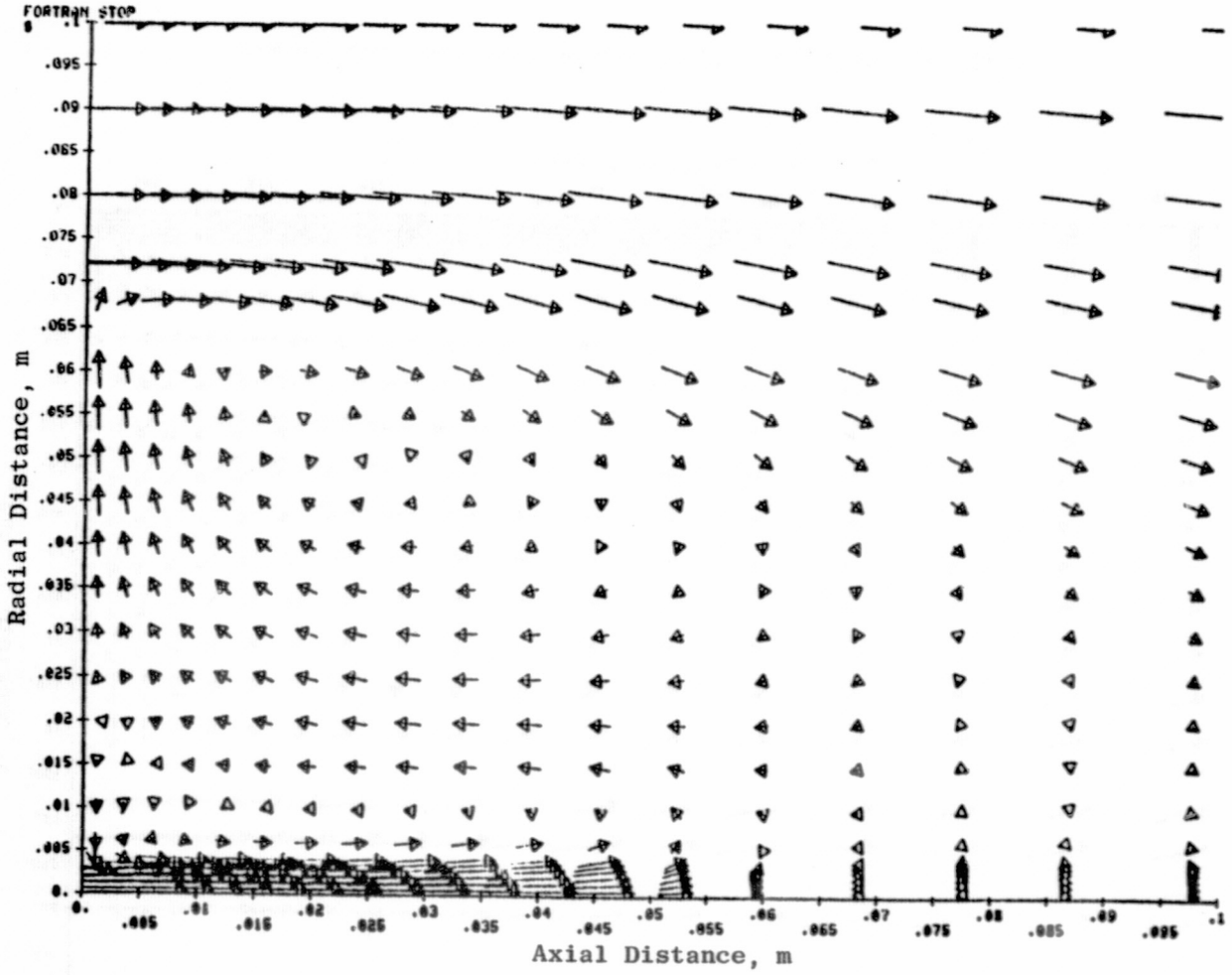
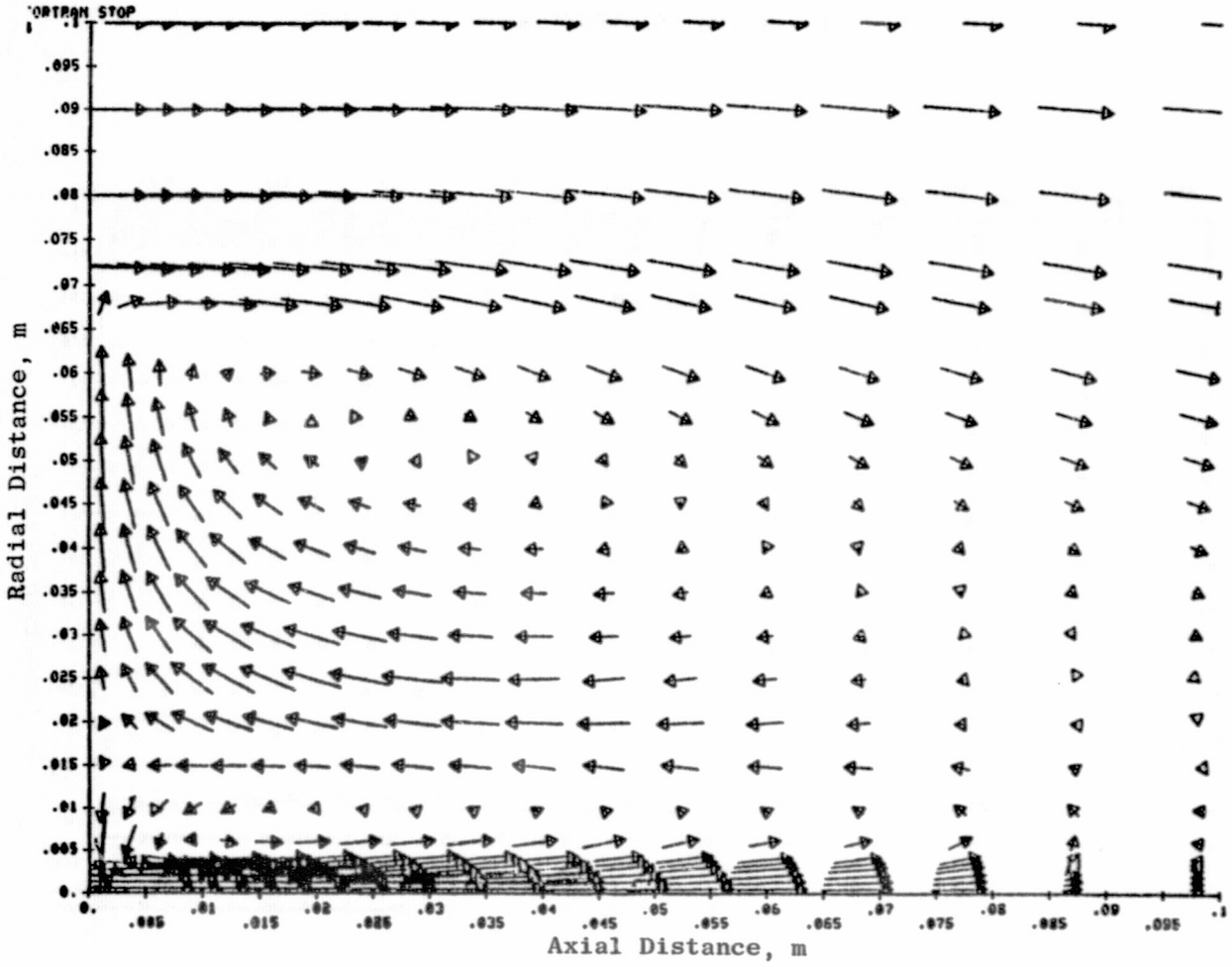


Figure 62. No-Fluctuation Model - Frozen Flow.

ORIGINAL PAGE IS
OF POOR QUALITY



ORIGINAL PAGE IS
OF POOR QUALITY

Figure 63. No-Fluctuation Model - Equilibrium Flow.

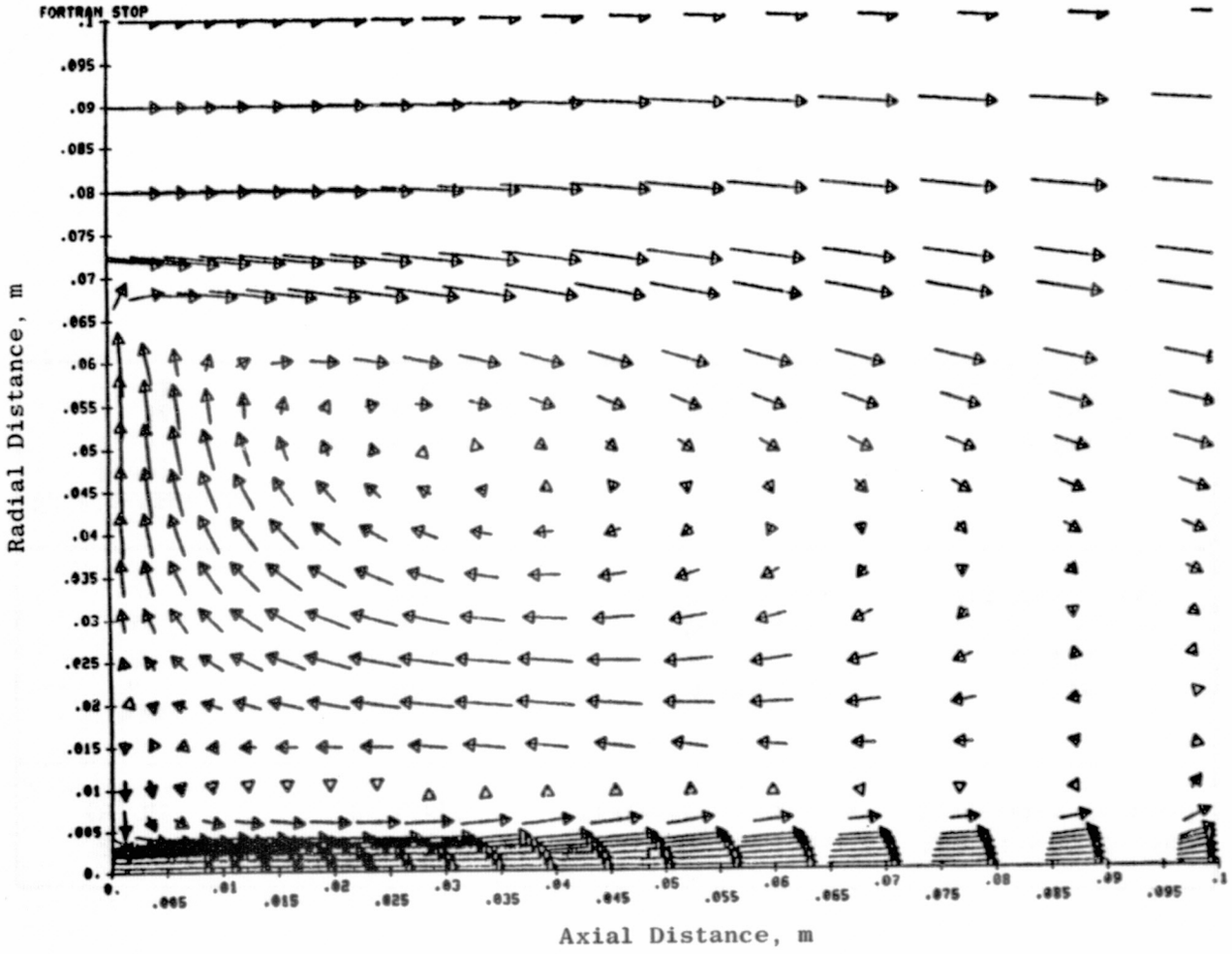


Figure 64. No-Fluctuation Model - Kinetic Flow.

ORIGINAL PAGE IS
OF POOR QUALITY

Table XVI. Stagnation Points from the Data and the Models.

$\dot{m}$ jet (kg/hr)	Burning?	Location of First Stagnation Point (m)	Location of Second Stagnation Point(m)
Data			
8	No	0.070	0.126
12	No	0.102	0.126
$\geq$14	No	Jet Penetrates	Jet Penetrates
$\geq$8	Yes	Jet Penetrates	Jet Penetrates
No Fluctuation Model			
11.66	No (Frozen)	0.06	0.083
11.66	Yes (Equilibrium)	0.093	0.133
11.66	Yes (Kinetic)	Jet Penetrates	Jet Penetrates

ORIGINAL PAGE IS
OF POOR QUALITY

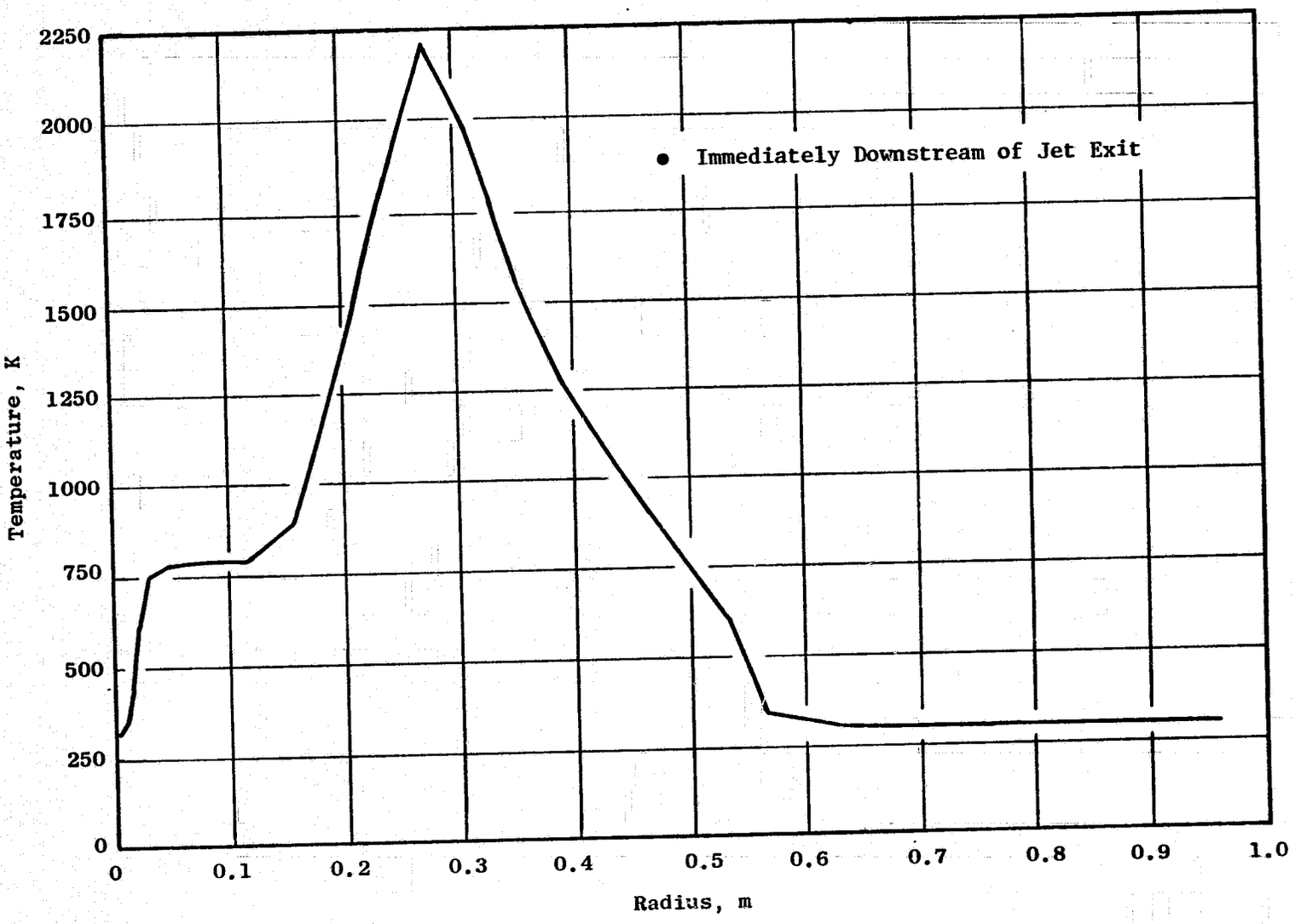
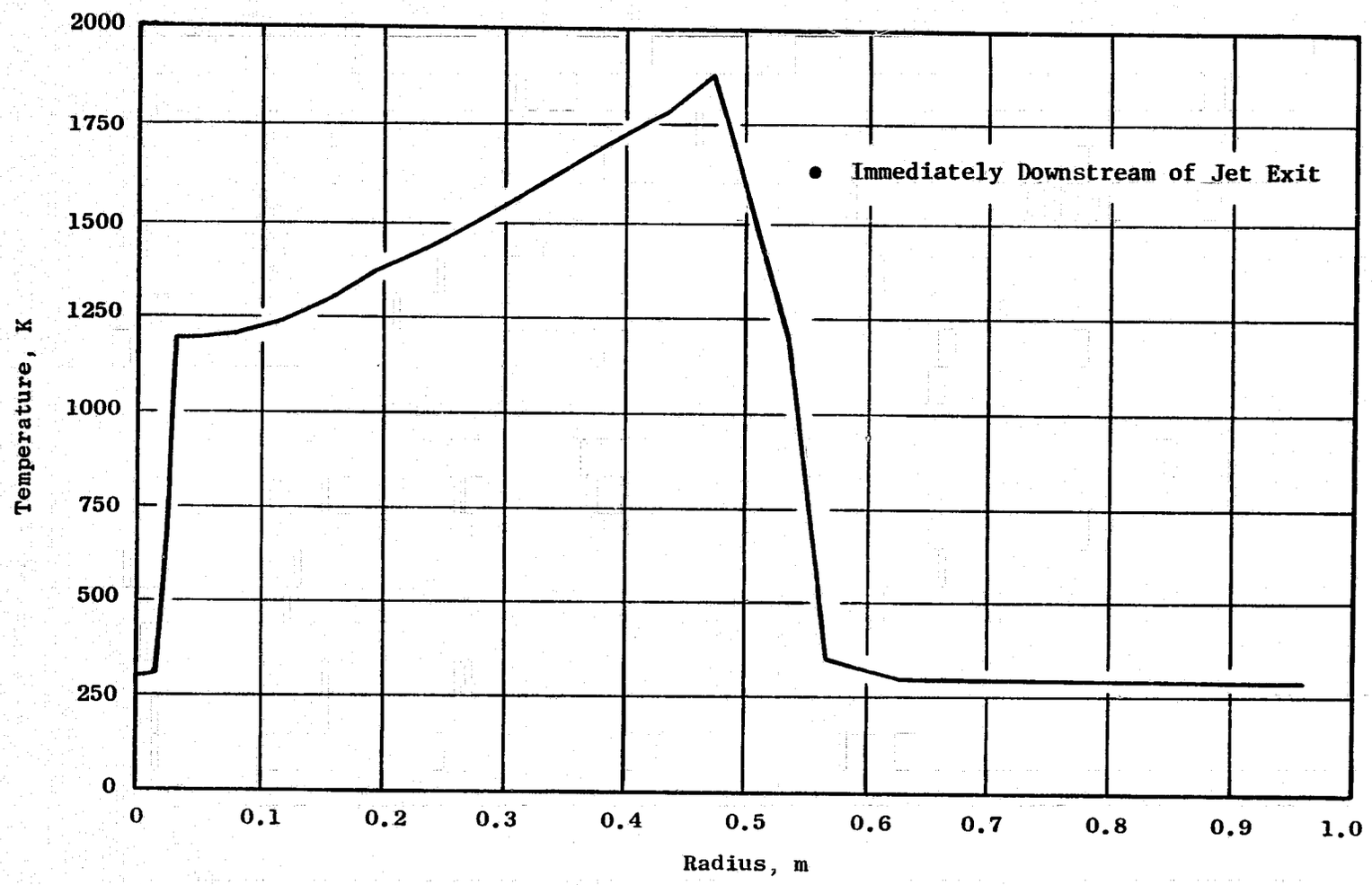


Figure 65. No-Fluctuation Model - Equilibrium Flow.

ORIGINAL PAGE IS
OF POOR QUALITY



ORIGINAL PAGE IS
OF POOR QUALITY

Figure 66. No-Fluctuation Model - Kinetic Flow.

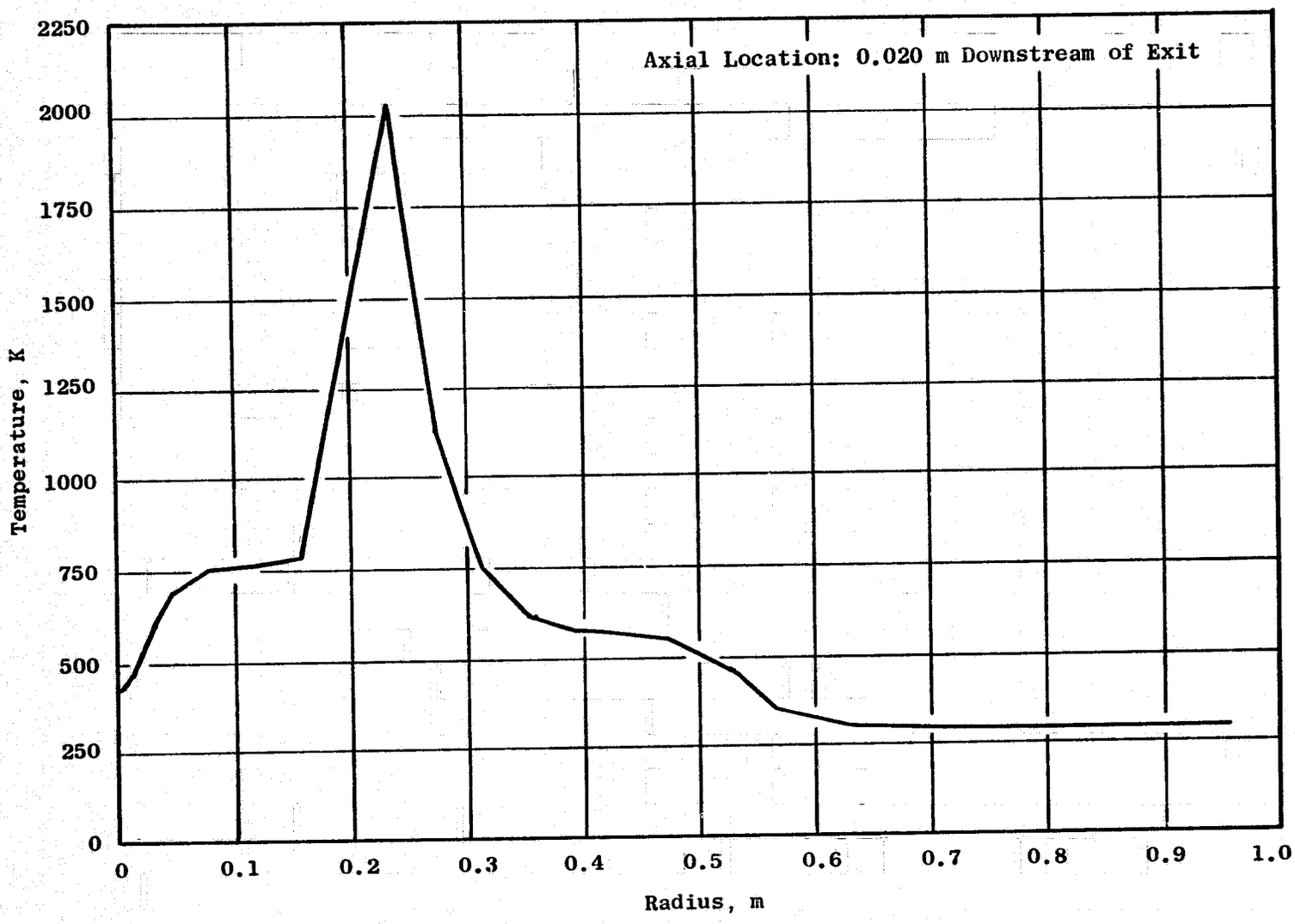


Figure 67. No-Fluctuation Model - Equilibrium Flow.

ORIGINAL PAGE IS
OF POOR QUALITY

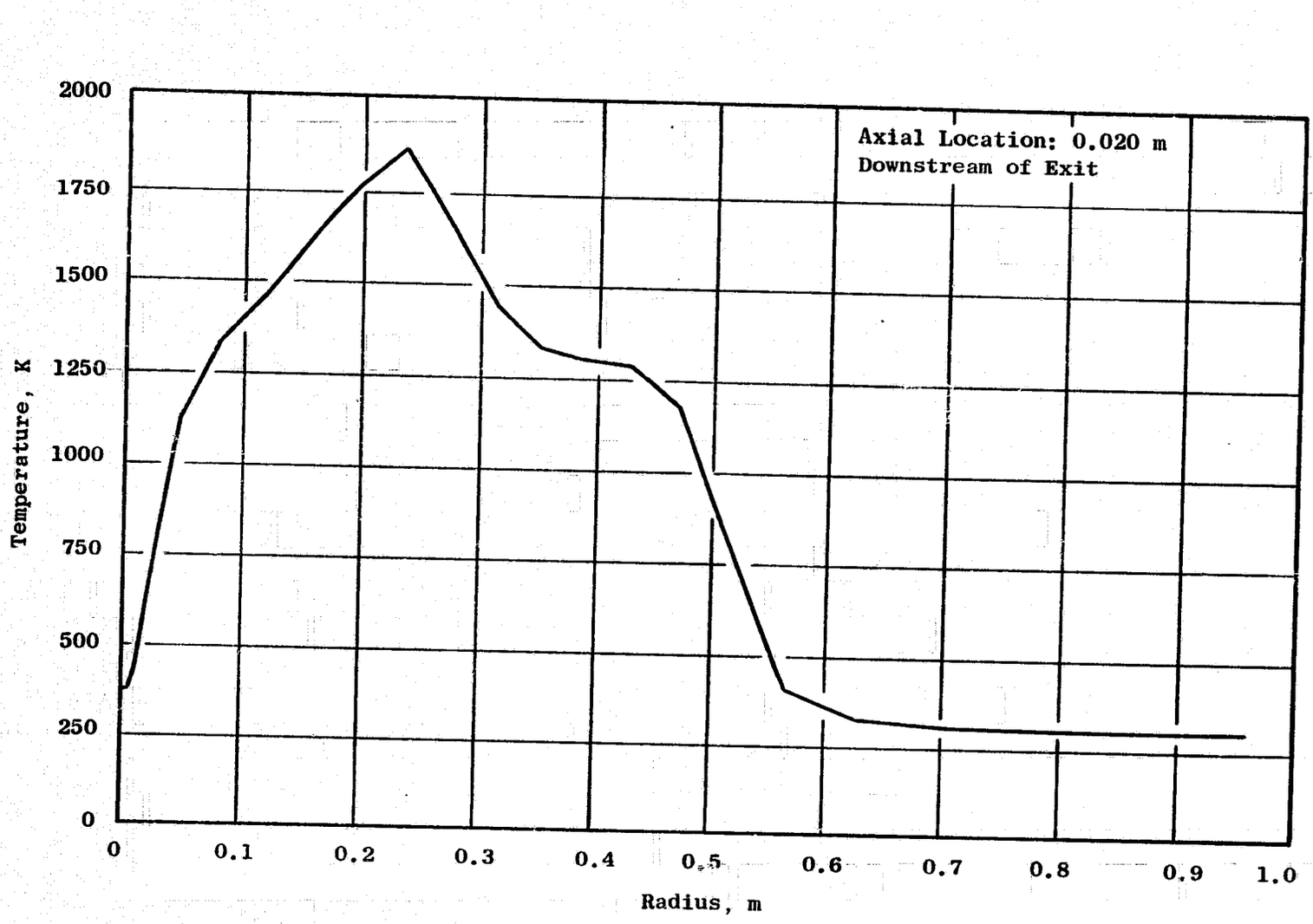


Figure 68. No-Fluctuation Model - Kinetic Flow.

ORIGINAL PAGE IS
OF POOR QUALITY

(ii) Assumed PDF Model

The turbulent reacting flow model described above ignores the effects of local fluctuations on the flow, thus implicitly evaluating chemical source terms at the mean local temperature. In some situations, the kinetics are very rapid compared with characteristic flow times; the effect of the fluctuations then becomes more pronounced than the effect of kinetics, i.e., the effect of unmixedness becomes important, Hawthorne, et. al., 1949[91]. A model accounting for this regime of behavior has been constructed.

The approach is based on obtaining at each point the probability density function (pdf) for the minimum number of dependent variables $\vec{\xi}$ needed to characterize the instantaneous state of the fluid. Then the local average of any quantity Q is

$$\overline{Q(\vec{x})} = \int \ldots \int Q(\vec{\xi})\ P\ (\vec{\xi};\ \vec{x})\ d\vec{\xi} \tag{84}$$

where $Q\ (\vec{\xi})$ is the instantaneous value of the quantity e.g., density or temperature, and $P\ (\vec{\xi};\ \vec{x})$ is the probability density function at $\vec{x}$ for the scalar set $\vec{\xi}$. Notice that the mean value of Q at $\vec{x}$ is <u>not</u> the value of Q at the mean local $\vec{\xi}$:

$$\overline{Q(\vec{x})} \neq Q(\overline{\vec{\xi}\ (\vec{x})}) \tag{85}$$

The first approach to obtaining $P\ (\vec{\xi};\ \vec{x})$ is the assumed shape model described next.

Instead of writing equations for the conservation of species, the elemental mass fractions may be treated directly. As elements are neither created nor destroyed in chemical reactions, their conservation equations are homogeneous. With the assumption of a unity Lewis number, the element mass fractions and the total (chemical plus sensible) enthalpy may be linked to a single conserved (since the conservation equatons are homogeneous) scalar, the mixture fraction ξ which will be sufficient to describe the state of the fluid in equilibrium. ξ varies between zero in one stream (the air stream) and unity in the other, Bilger, 1976[92]. The transport equation for this conserved scalar is then used to derive separate transport equations for the mean $(\tilde{\xi})$ and the variance $(\widetilde{\xi})$, Spalding, 1971[93], which are solved by the same algorithm as the fluid mechanical conservation equations. These equations are

ORIGINAL PAGE IS
OF POOR QUALITY

$$\bar{\rho}\,\tilde{U}_j \frac{\partial \tilde{\xi}}{\partial x_j} = \frac{\partial}{\partial x_j}\left(\frac{\mu_t}{\sigma_t}\frac{\partial \tilde{\xi}}{\partial x_j}\right)$$

$$\bar{\rho}\,\tilde{U}_j \frac{\partial \tilde{\xi''^2}}{\partial x_j} = \frac{\partial}{\partial x_j}\left(\frac{\mu_t}{\sigma_t}\frac{\partial \tilde{\xi''^2}}{\partial x_j}\right) + 2\frac{\mu_t}{\sigma_t}\left(\frac{\partial \tilde{\xi}}{\partial x_j}\right)^2 - \frac{2\bar{\rho}\tilde{\varepsilon}}{\tilde{k}}\tilde{\xi''^2} \qquad (86)$$

where $\sigma_t = 0.7$, and μ_t is the eddy viscosity calculated from the k-ε turbulence model. Thus the first two moments of the pdf for scalar ξ are known at each point in the flow.

Experimental evidence shows that the temporal fluctuations in ξ are representable by the β-probability density function (β-pdf) Rhodes, 1975[94]:

$$P(\xi) = \frac{\xi^{a-1}\,(1-\xi)^{b-1}}{\int_0^1 \xi^{a-1}\,(1-\xi)^{b-1}\,d\xi} \qquad (87)$$

where a and b are given by the local moments

$$a = \tilde{\xi}\left[\frac{(1-\tilde{\xi})\,\tilde{\xi}}{\tilde{\xi''^2}} - 1\right], \quad b = \frac{1-\tilde{\xi}}{\tilde{\xi}}a \qquad (88)$$

Realizability constraints on the fluctuations at each point $\vec{x}$

$$0 \leq \tilde{\xi''^2} \leq \tilde{\xi}\,(1-\tilde{\xi})$$

i.e., the variance cannot be greater than that due to alternating pure air and fuel "eddies" leads to $a \geq 0$. However, $a < 1$ or $b < 1$ cause singularities at $\xi = 0$ and $\xi = 1$ which were analytically removed before numerical convolution of any quantity with the pdf.

The assumed shape pdf model does not necessarily require equilibrium chemistry. If chemical kinetics are important additional scalar(s) such as the reaction progress variable can be used to formulate a joint pdf. The number of moment transport equations to be solved goes up but the principle of obtaining local moments, assuming a parametric shape, deriving the local joint pdf and convoluting to obtain local means remains the same.

(iii) Monte-Carlo Model for Joint Velocity-Scalars PDF

The assumed shape pdf model is obtained from a finite number (two) of its moments and an assumption regarding its shape (β-pdf). Furthermore, it describes the pdf for scalar fluctuations only so that correlations with velocity are not known. Thus, gradient diffusion and a separate turbulence model (k-ε) are required. All of these restrictions can be removed by formulating a transport equation for the joint pdf itself in the phase space $(\vec{v}, \vec{\xi}; \vec{x}, t)$ where $\vec{v}$ is the velocity and $\vec{\xi}$ is the scalar(s) set.

This approach is under active development Pope, 1981[95] but is currently far from application to recirculating flows, primarily because of a step-by-step validation for shear flows which is now in progress partly with General Electric collaboration. The details will not be discussed here but important features will be highlighted.

The transport equation for the joint pdf P can be obtained from its definition and the Navier-Stokes and species conservation equations. The transport equation has large dimensionality so that finite difference solution is intractable. Hence, the Monte-Carlo technique is used, in a form optimized for computational efficiency. In the transport equation the highly nonlinear reaction source terms appear in closed form. Notice that this is true also for the scalar(s) only pdf which is discussed next. However, in the joint pdf model, the convection terms both for mean and fluctuating velocities also appear in closed form. Thus there is no need to postulate gradient diffusion, which has recently been faulted on both experimental and theoretical grounds Schefer, et al., 1982[82]. Closure approximations are needed for the fluctuating pressure terms and the viscous and diffusive mixing. These are analogous to those used in Reynolds stress models, Pope, 1981[95].

The joint pdf described here is still a one-point pdf, i.e., it describes the probability of various combinations of velocities and scalars occurring simultaneously at a single point. Because it is a one-point pdf, it carries no length-scale information. Multi-point pdf transport equations can be formulated but their solution would be a formidable task. Hence the one-point pdf model requires, for example, the ε (dissipation) equation or some combination (k/ε) to provide a length-scale.

(iv) Monte-Carlo Model for Scalars Only

If only the scalar(s) pdf transport equation is sought a simpler transport equation results. However, the solution algorithm is still Monte-Carlo.

As a demonstration, scalar transport in two dimensional and axisymmetric turbulent shear flows is calculated by means of a hybrid scheme. The aerodynamic flow field is determined from a solution of the mean mass and momentum equations, closed for simplicity with a one-equation model for the viscosity (transport equation for turbulence kinetic energy, prescribed length scale). Other turbulence models could easily be substituted.

Knowing the aerodynamic flow field, a scalar transport model is used to create ensembles of scalar elements in the downstream locations. The coalescence/dispersion model of Curl, 1963[96] is then used to calculate the turbulent mixing of the ensembles. This approach does not require a turbulent Prandtl-Schmidt number assumption as the species (scalar) transport equations are not solved simultaneously with the flow equations. However, a unity Lewis number approximation is implicit in the reactive flow modeling.

The micromixing of reacting chemical species is described by the coalescence and dispersion of a large number of identifiable elements comprising the fluid at each location in the flow. Pairs of elements are selected at random and assumed to: (1) coalesce (mix instantaneously at the molecular level), (2) remain in contact for a micromixing time, t_s, and (3) disperse (separate into two elements of identical properties). During the micromixing time, t_s, either equilibrium or finite rate chemistry may be assumed to occur; however, in view of the large number of elements at each point in the flow, special kinetic algorithms are needed to reduce the calculation time. Such an algorithm has been developed by Pratt, 1979[97] and can be used if finite rate chemistry is to be considered.

The coalescence/dispersion model for scalar transport has been applied by General Electric to a number of mixing layer and jet experiments reported in the literature. Results for the free round jet experiment of Birch, et. al., 1978[98] (methane jet in air, density ratio = 0.55) and the Roshko, 1976[99] mixing layer (helium and neon, density ratio = 7) are presented in Figures 69 through 72. Five hundred scalar elements in each ensemble were used. The results are generally good with only the variance of the scalar fluctuations being in some error. This discrepancy has been traced to the relatively simple turbulence models used to close the mean flow equations.

Criticism of the coalescence-dispersion model is possible at several levels. Pope, 1981[95] has shown that the simple Curl model does not properly predict Gaussians in the limit of decaying turbulence and has suggested sophisticated biasing techniques to correct this. Perhaps more significantly, the Monte-Carlo scalar(s) only pdf can be questioned on the basis of what <u>it</u> contributes that the moment transport model does <u>not</u>: higher (than second) moments of the scalar(s) pdf. Whether these higher moments are really necessary and are worth the computational expense is debatable. Furthermore, one of the main advantages of the joint velocity-scalar(s) pdf is lost; i.e. the ability to directly handle velocity correlations so that gradient diffusion assumptions and a separate turbulence model, e.g., k-ε model, are not needed. For these reasons the scalar(s) only pdf approach appears unattractive.

(v) Spalding's ESCIMO Model

The Eulerian approach to computing turbulent reacting flows has been criticized by Spalding, 1978[100] as being incapable of directly treating fluctuations in species concentrations and temperature. The pdf transport models are claimed to be restricted to simple kinetic schemes for the combustion chemistry; furthermore, recent observations of coherent structures in several classes of flows cannot be properly described in an Eulerian reference frame.

ORIGINAL PAGE IS
OF POOR QUALITY

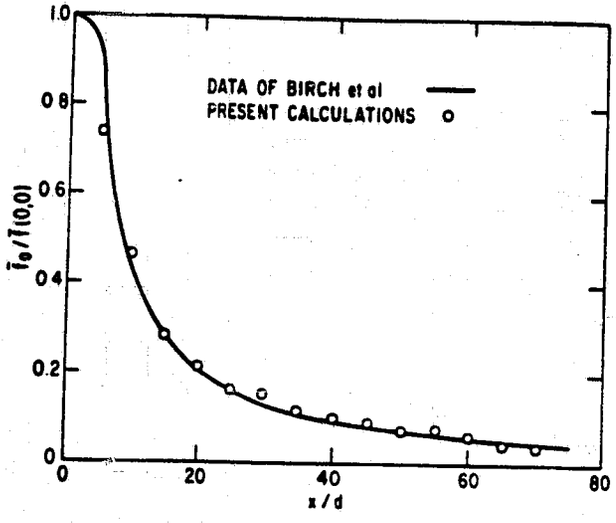


Figure 69. The Normalized Decay of CH_4 Along the Centerline of a Round Jet In Still Air.

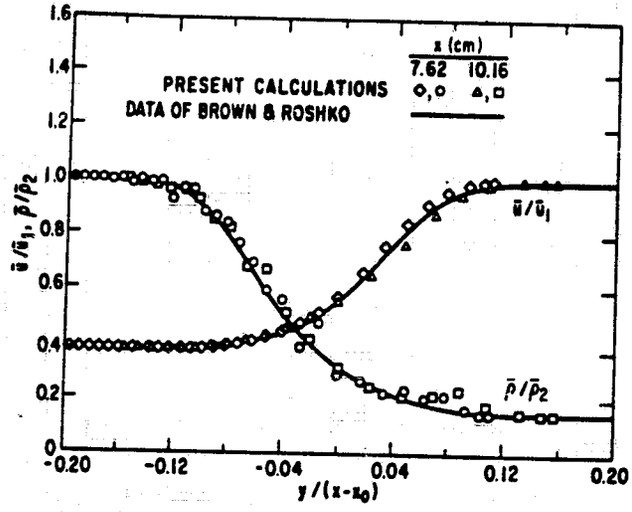


Figure 70. The Mean Velocity and Density Profiles in the Self-Similar Region of He and N_2 With Equal Momentum Flux in the Two Streams.

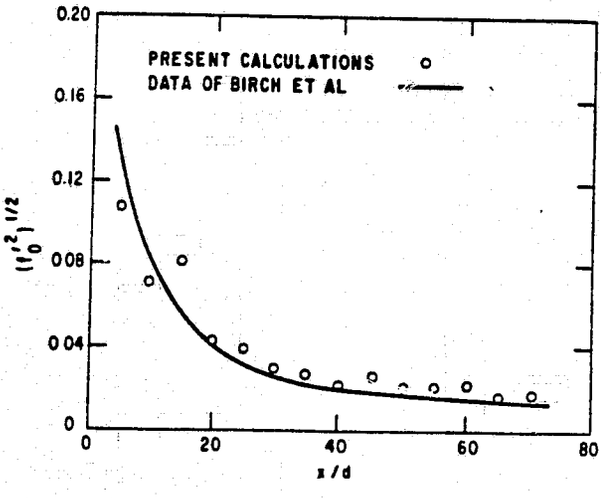


Figure 71. Decay of Scalar (CH_4) Fluctuations Along the Centerline of a Round Jet In Still Air.

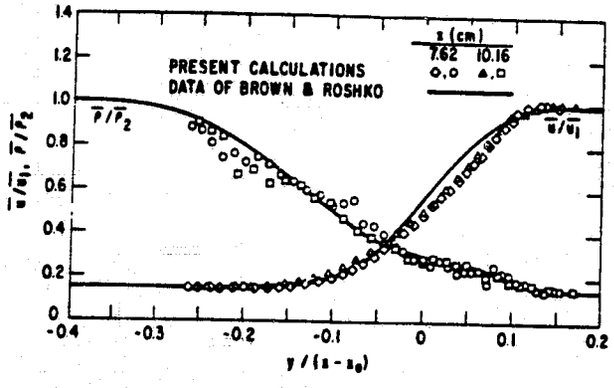


Figure 72. The Mean Velocity and Density Profiles in the Self-Similar Region of He and N_2 With Equal Mass Flux in the Two Streams.

To make up for these perceived deficiencies, Spalding, 1978[100] has proposed his Engulfment, Stretching, Coherence, Interdiffusion, Moving Observer (ESCIMO) model. This model combines the Eulerian and Lagrangian approaches to describing the flow field evolution. The model is highly intuitive and quantitative and supporting evidence would be difficult to generate. However, the conceptual grounds for the model appear to be well founded.

Tongues of fluid from a turbulent jet are envisioned as "engulfing" freestream fluid into a jet interior. The interleaved elements of jet and freestream fluid are steadily stretched by the mean shear and by turbulent fluctuations so that the thickness continuously decreases. This "sandwich" of jet and freestream fluid can never be separated; the material is imagined to cohere as it flows downstream.

Within the sandwich, the laminar processes of diffusion and chemical reaction can occur ("interdiffusion"). These processes are analyzed in a moving reference frame attached to the sandwich. The processes are thus one dimensional and transient and can be described by parabolic differential equations.

Thus the ESCIMO theory consists of an Eulerian (or "demographical") aspect in which the "birth rate", transport, envirommment and "death rate" of the "sandwiches" are described and a Lagrangian (or "biographical") aspect, which treats the one dimensional transient details of the "life". The results of the theory could then be expressed in terms of pdf's. Although this theory may never be detailed enough for implementation in an elliptic flow model, preliminary applications to simple flows such as stirred reactors is encouraging. The model has many significant physical features which can be calibrated (by empirical coefficients) as required.. However, there is insufficient direct evidence to quantitatively justify many of the key assumptions in the model.

(vi) Eddy-Break Up Models

Another semiempirical model for turbulent combustion has been postulated by Spalding, 1971[93]. This so-called "Eddy Break Up" (EBU) model has application in situations where the local turbulence state has a dominant influence on the local reaction rate. The EBU model is easy to implement and has been used in combustor performance codes with some success, Mongia, et al., 1979[1].

The EBU model was first formulated to predict certain features of turbulent premixed flames. The plane flame behind a rod-shaped flame holder exhibits a constant spreading angle for a variety of mixture ratios, approach velocities, and turbulence levels and temperatures of the inlet stream, Howe, 1963[101]. Direct solution of the governing parabolic partial differential equations (applicable downstream of the recirculation zone) under the assumptions of Arrhenius bimolecular kinetics with mean concentrations and temperatures gave flame spread rates which were of the right order of magnitude. However, the predicted results were far more sensitive to the flow conditions than were the experiments.

To overcome this difficulty, an alternative to the Arrhenius burning rate was sought. The gas is imagined to be composed of discrete parcels of composition ranging from the unburned (reactedness $\tau = 0$) to the fully burned state ($\tau = 1$). Then rates up to the maximum reaction rate (maximized with respect to τ) $\dot{m}_{max}$ can occur at the interface between parcels or eddies. The rate at which eddies are broken up -- to form new interfaces -- is obtained by analogy with the rate of decay of turbulence, $0.35\ \rho\ k\ \partial u/\partial y$ (ρ = density, k = local turbulence kinetic energy, $\partial u/\partial y$ = local velocity gradient). This analogy is made for the equilibrium state (turbulence generation and decay rates are equal).

Two alternative rates are now available, the Arrhenius rate ($\dot{m}_{Arr}$) and the eddy break up rate ($\dot{m}_{EBU}$). The EBU model caters to the simultaneous influence of each effect by actually using the hybrid rate

$$\dot{m} = [\ \dot{m}_{Arr}^{-1} + \dot{m}_{EBU}^{-1}\ ]^{-1} \qquad (88)$$

The model then predicts the rod stabilized premixed flame more accurately than if $\dot{m} = \dot{m}_{Arr}$ were used. Spalding, 1971[93] also points out various other effects, such as Reynolds number influence and proposes empirical formulae to account for them. Further developments, Spalding, 1976[102], were also reported, reflecting a shift towards the ESCIMO (combined Eulerian-Lagrangian) model discussed earlier. However, the drawback of the EBU model is that although difficulties with Arrhenius kinetics at mean conditions have been identified, the proposed alternative approach is too empirical to implement in an overall computational scheme that is to be composed of "fundamental" physical submodels. In fact, Pope, 1977[103] has demonstrated that the predictions are multiple-valued.

Conclusion

In this section several modeling approaches to turbulence-chemistry interaction have been discussed:

1. Closure at mean temperature.
2. Assumed-shape scalar(s) pdf from finite number of moments.
3. Joint velocity-scalar(s) pdf: Monte-Carlo.
4. Scalar(s) only pdf: Monte-Carlo and the empirical approaches.
5. ESCIMO.
6. Eddy break up.

It is concluded that (2) is the most tractable and accounts for the important physics. In the long run if computational efficiency and several detailed algorithms are improved the joint velocity-scalar(s) Monte-Carlo model may be practicable and should in principle be more accurate on physical grounds. The procedure outlined in (2) was used in the code GETREF and the results are described next.

7.0 ASSESSMENT OF AEROTHERMAL MODEL AGAINST DATA BASE

The assessment procedure for evaluating General Electric's computation modules against the selected test cases is outlined below.

Assessments were made against 2D axisymmetric experiments reported in the literature. These assessments were made with the 2D parabolic or elliptic flow code. To help assess errors or inaccuracies within the model, it is possible to examine specific features such as the differencing scheme, modified turbulence models for flow curvature (swirl), chemical kinetics, and unmixedness, in more detail and with reasonable computation times in the 2D codes. It should be emphasized that this rigorous formulation and analysis could not be done for the 3D code.

For an advanced, modern General Electric combustor design, calculations using the four basic aerothermal computation modules (diffuser module, flow distribution module, heat transfer module, and the internal flow module) were generated and compared with General Electric's measured data on the features treated by these individual modules. Since the first three of these modules are based on methods that have been in use for many years, their accuracy and weaknesses are already reasonably well known. The principal source of inaccuracy in the modules for computing combustor durability or life has been the inputs to the heat transfer module based on the combustor internal flow field. Since the internal flow module is a newer, less proven module, the major part of the assessment efforts were devoted to this module.

Since the original form of the available 3D codes for the internal flow field treat accurately only combustor walls that are aligned with rectangular or cylindrical coordinates, assessment against geometrically suitable experiments were chosen for the more detailed studies. Specifically, this included data obtained from a GE/F101-type combustor with a flat dome and parallel combustor walls without the usual curved wall contraction at the aft end and data from the available literature involving dilution jet injection into a parallel flow rectangular duct. First used was data on the strictly fluid dynamic flow of a dilution pattern simulating that of the equivalent real engine combustor, but without the presence of chemical reactions. This included data an a simple straight-through dome flow as well as data with swirl cup flows to separate this latter effect, and included different degrees of dilution hole complexity. The comparison including chemical reaction was done first with a gaseous fuel and then with liquid atomized fuel to isolate the treatment of these two effects.

Through the above assessment approach, those modules responsible for inaccuracies in the predictions and the analytical and/or numerical methods within the modules that are inaccurate or in error were identified, permitting recommendations for specific needs for future work.

7.1 MODEL ASSESSMENT AGAINST DEFINITIVE AXISYMMETRIC EXPERIMENTS FROM THE LITERATURE

The various submodels and techniques that are available have been analyzed in Section 6.0 of this report. Here predictions for four axisymmetric experimental turbulent flows, two nonreacting and two reacting, will be presented. The codes used are axisymmetric parabolic or elliptic (as required) formulations of the recommended physical models as discussed above.

The assessment against "benchmark" data was originally intended to address only the three recirculating flows in Table VI. However, during this contract period relevant modeling and experimental work on a turbulent jet diffusion flame was performed (DoE Contract DE-AC04-78 ET 13146). Since shear flows allow evaluation of physical submodels with minimum ambiguities due to numerical error, and since the spectroscopic data gathered is not available for recirculating flows, the theory-data comparisons from the DoE report, Lapp, et al., 1983[4], will be cited here.

The experiments which were simulated are, in the order of the discussion to follow:

1. Turbulent jet diffusion flame: Lapp, et al., 1983[4]
2. Axisymmetric isothermal slit-jet plenum/chamber: Green and Whitelaw, 1980
3. Co- and counterswirled pipe flow: Vu and Gouldin, 1980[6],
4. Bluff-body stabilized diffusion flame: Roquemore, et al., 1980[90].

7.1.1 Turbulent Jet Diffusion Flame

The turbulent jet diffusion flame allows assessment of an important feature of more general flows, viz., the interaction between turbulence and chemistry. Two major complicating issues, turbulence and numerical truncation error, are minimized. The turbulence is simpler to model because it is generated by strong cross-stream shear; in fact, most turbulence model constants are derived from shear flow simulations. Furthermore, the very large radial gradients increase the accuracy of the gradient transport assumption. The issue of differencing is also simpler: being convection-dominated in the axial direction the governing equations are in parabolic form and axial diffusion is negligible. Thus, upwinding in the axial direction is acceptable so that in the radial direction grid nodes can be closely spaced. Finally, a forward marching solution algorithm may be used so that iteration is not required.

The experiment simulated here is a 40% CO, 30% H_2, 30% N_2 "syngas" jet burning in coflowing air in a tunnel. The fuel tube is 3.2 mm in diameter (Figure 73). Optical access was arranged by virtue of two 0.9 m quartz windows. Data was obtained by Laser Doppler velocimetry, pulsed Raman scattering

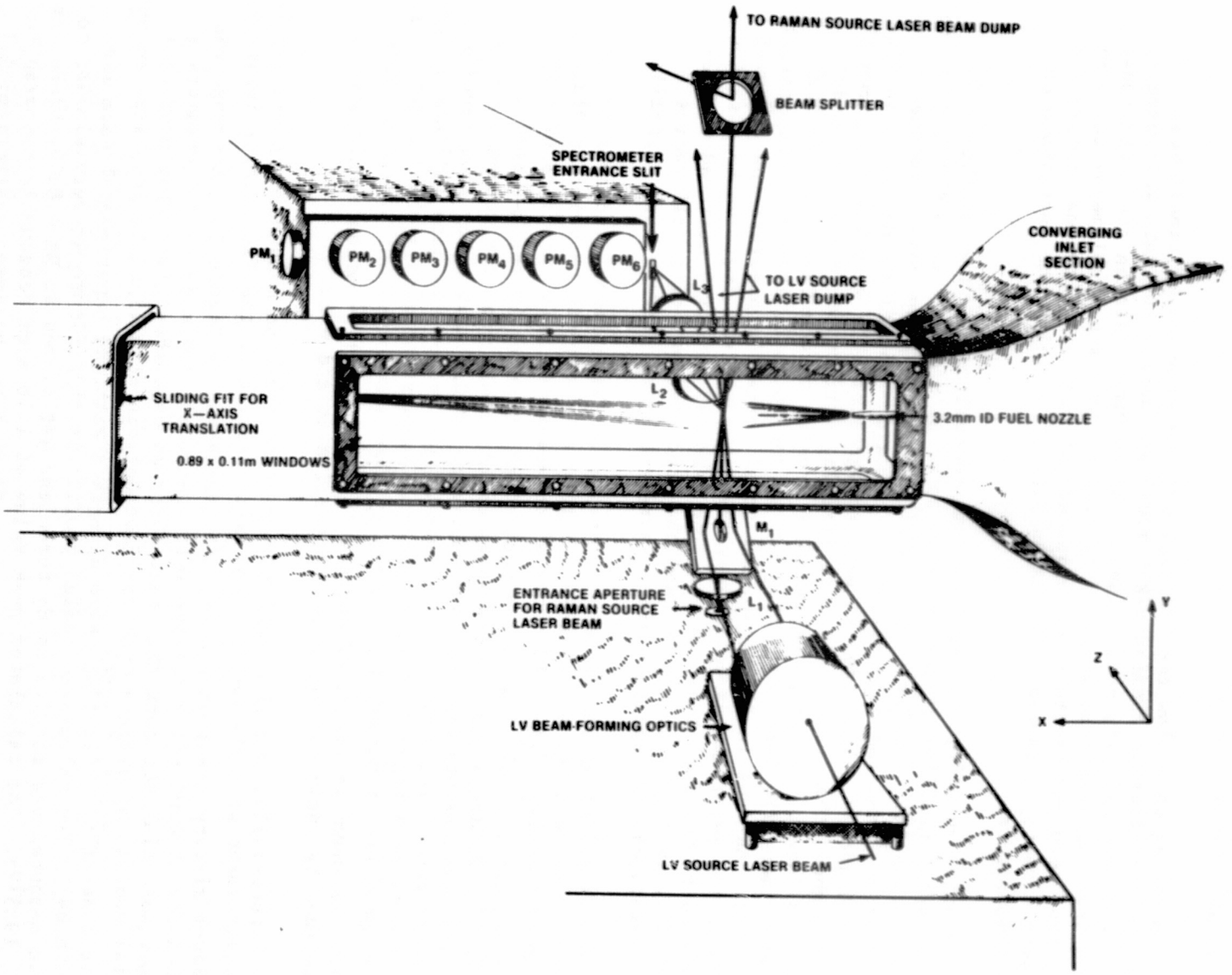


Figure 73. Burning Turbulent Diffusion Jet with LDV and Pulsed Raman Data.

ORIGINAL PAGE IS
OF POOR QUALITY

and, for thermal NO, from sample probes. Further details may be found in Lapp, et al., 1983[4]

In modeling this flow the "parabolized" Favre-averaged single-scalar assumed pdf/equilibrium chemistry/k-ε model was used. LDV data were used to compare with the velocity predictions. Pulsed Raman data on the instantaneous mixture fraction were statistically treated to generate local means and variances; thus mean and fluctuating components of both velocity and mixture fraction were directly compared. The Raman data also yields the instantaneous local temperature.

The axial velocity $\tilde{u}$ along the flame centerline is shown in Figure 74 and the radial profiles of the axial velocity at x/d = 25 and 100 are shown in Figures 75 and 76. Similarly, the axial variation of the Favre-averaged mixture fraction $\tilde{\xi}$ and radial profiles of $\tilde{\xi}$ at x/d = 25 and 50 are shown in Figures 77, 78 and 79. The model is seen to agree closely with the experimental data throughout the flame. The most striking difference is that the model predicts a longer laminar potential core (region of constant $\tilde{u}$ and $\tilde{\xi}$) than that experimentally observed. This may be due to small errors in the initial conditions. As seen in Figure 80, the model correctly predicts the observed spread in the jet flame as defined by the Favre mixture fraction half-radius normalized by the fuel tube radius. The measured velocity half-radius (conventionally-averaged) is larger than the predicted velocity half-radius (Favre-averaged) as expected, since Favre averaging narrows such a profile.

The excellent agreement between theory and experiment displayed for average values of velocity and mixture fraction also extends to velocity fluctuation measurements. Figure 81 shows a comparison of axial profiles of turbulence intensity $(\overline{u'^2})^{1/2}$ with the equivalent quantity in the k-ε model, $(2k/3)^{1/2}$. Although small differences might result from the conventionally-averaged measurements and the Favre-averaged predictions, they show excellent agreement beyond x/d = 20. In the initial jet region the data indicate a faster rise in turbulence intensity, which is consistent with a shorter jet core. Radial profiles of turbulence intensity also show excellent agreement with theory, as shown in Figure 82 where $(\overline{u'^2})^{1/2}$ and $(\tilde{k})^{1/2}$ measurements are normalized by their values on the centerline at x/d = 25.

Surprisingly, the fluctuation of mixture fraction measurements are not in good agreement with the model. The axial profile of the fluctuation intensity of Favre mixture fraction $[(\tilde{\xi}''^2)^{1/2}/\tilde{\xi}]$ are shown in Figure 83. Although the values downstream (x/d > 40) are well predicted, the model again predicts a longer potential jet core than that observed experimentally. The predicted radial profile of mixture fraction fluctuations normalized by its value on the centerline $(\xi''^2)^{1/2}/(\tilde{\xi}''^2)^{1/2}_{c1}$ also disagrees with the experimental data (see Figure 84). The calculated radial profile in this figure is very similar to those measured and modeled in H_2 turbulent jet flames at Re = 8500, Drake, et al., 1983[104]. The calculated peak value of 1.16 seem reasonable compared to values of 1.2 measured in the H_2 (Re = 8500) flame by Raman scattering; 1.1

ORIGINAL PAGE IS
OF POOR QUALITY

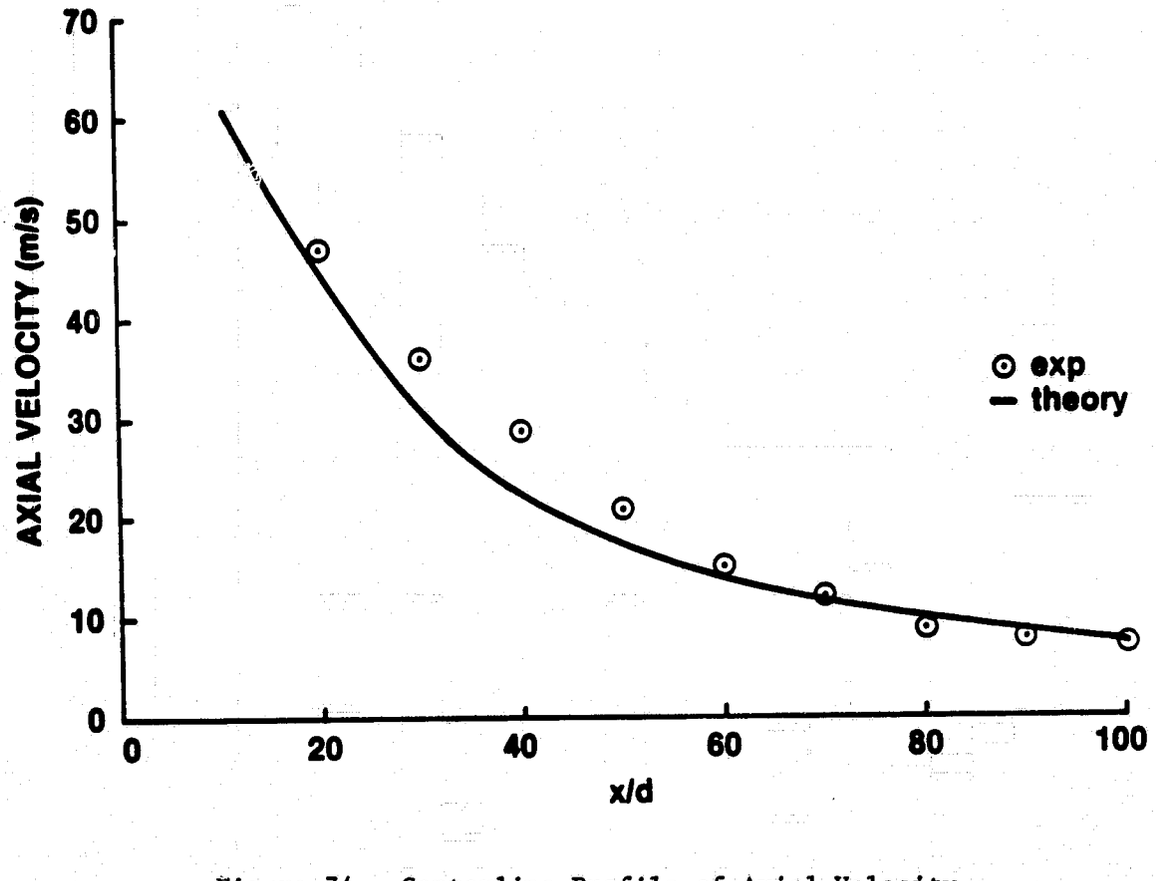


Figure 74. Centerline Profile of Axial Velocity.

ORIGINAL PAGE IS
OF POOR QUALITY

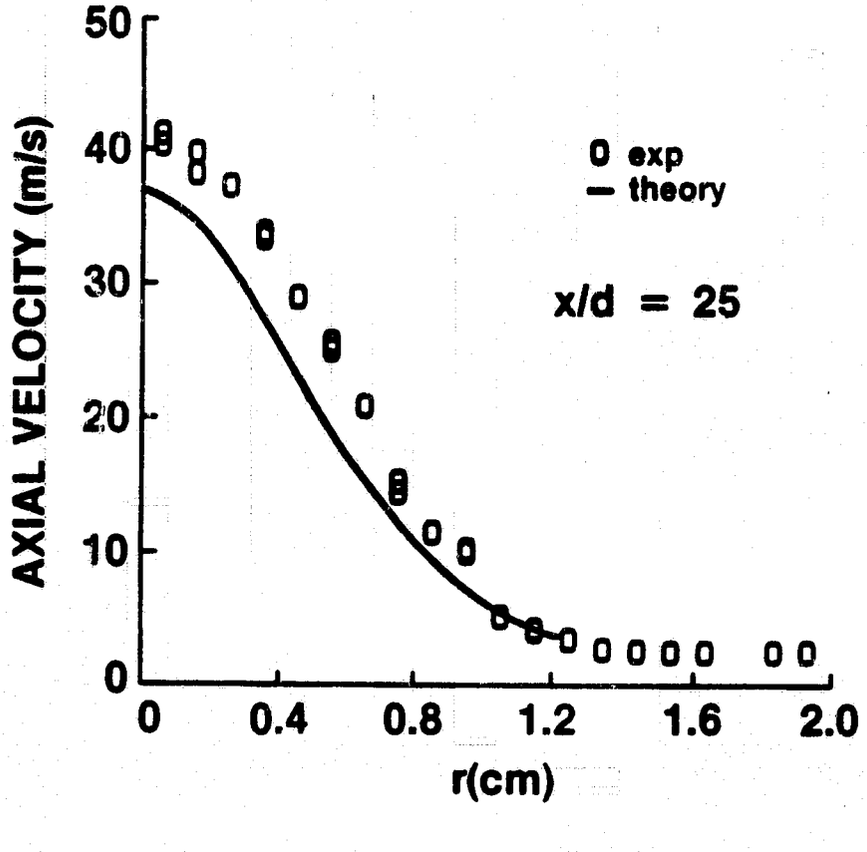


Figure 75. Radial Profile of Axial Velocity at X/D = 25.

ORIGINAL PAGE IS
OF POOR QUALITY

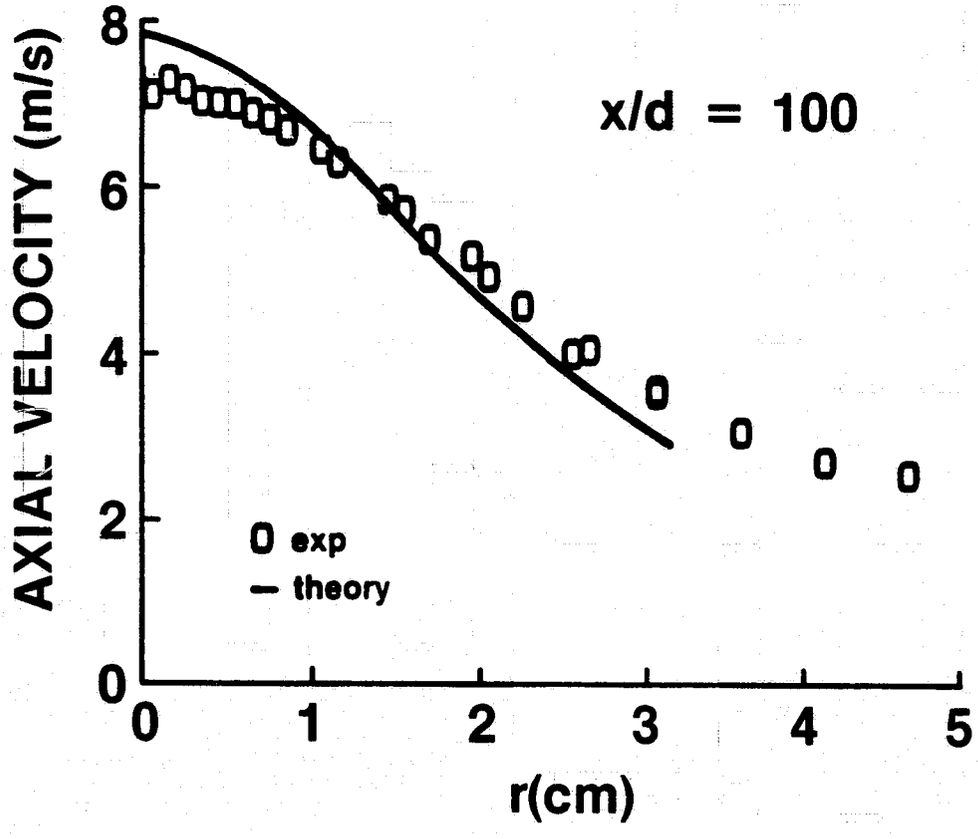


Figure 76. Radial Profile of Axial Velocity at X/D = 100.

C-3

ORIGINAL PAGE IS
OF POOR QUALITY

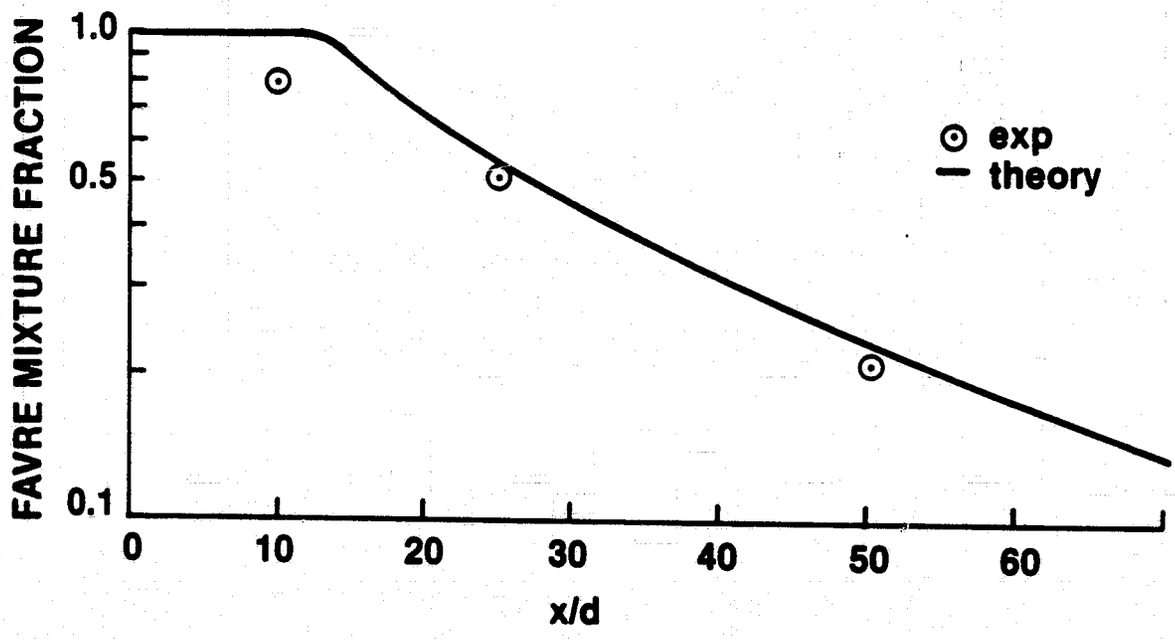


Figure 77. Centerline Profile of Favre-Averaged Mean Mixture Fraction.

ORIGINAL PAGE IS
OF POOR QUALITY

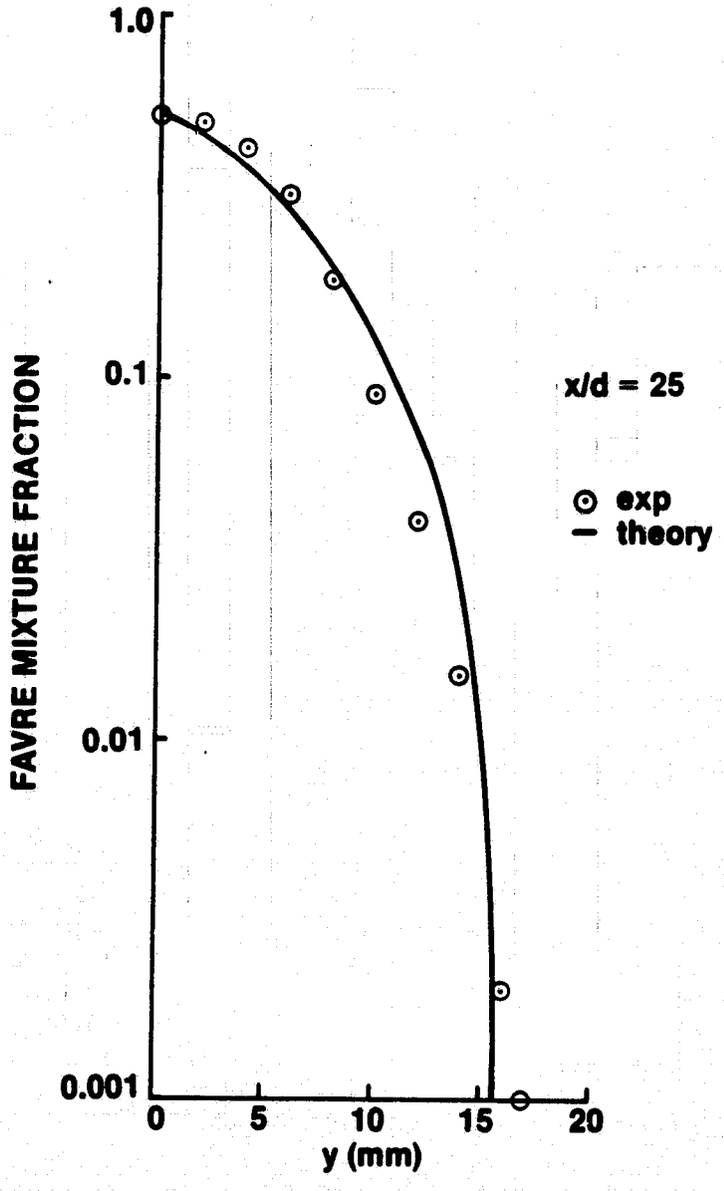


Figure 78. Radial Profile of Favre-Averaged Mean Mixture Fraction at X/D = 25.

ORIGINAL PAGE IS
OF POOR QUALITY

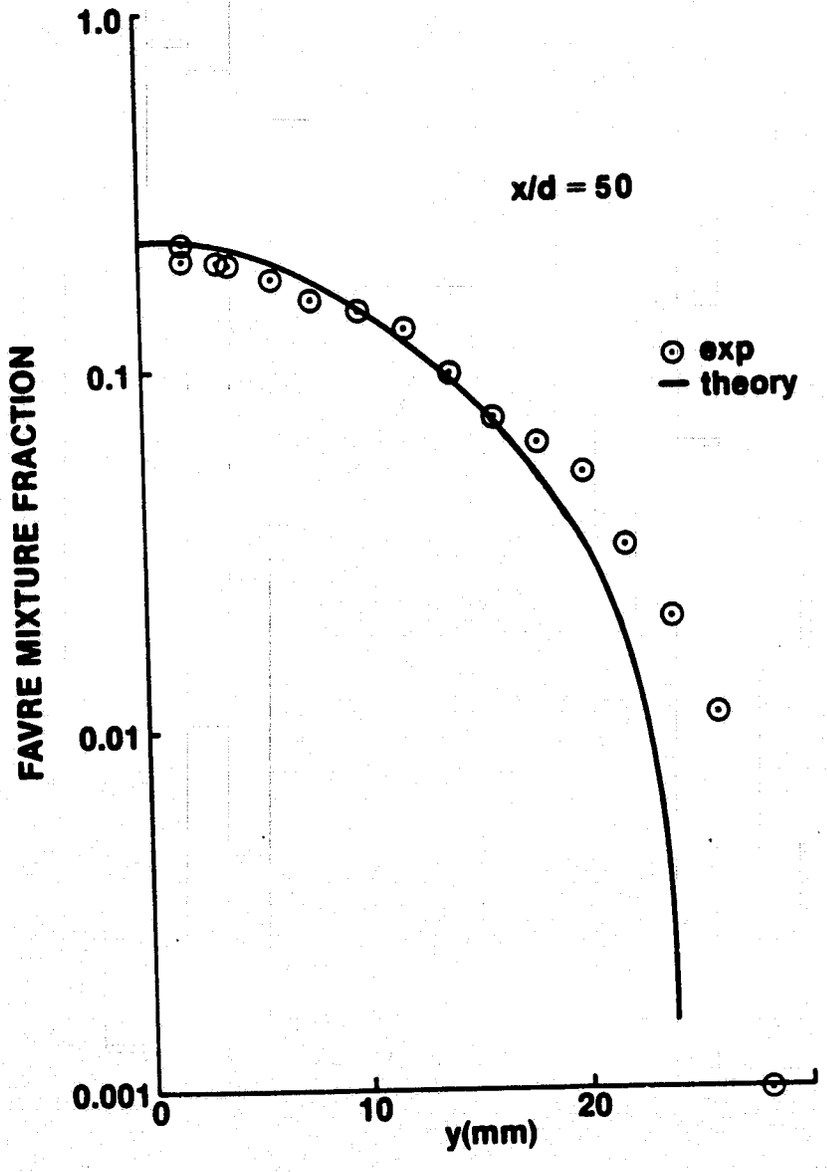
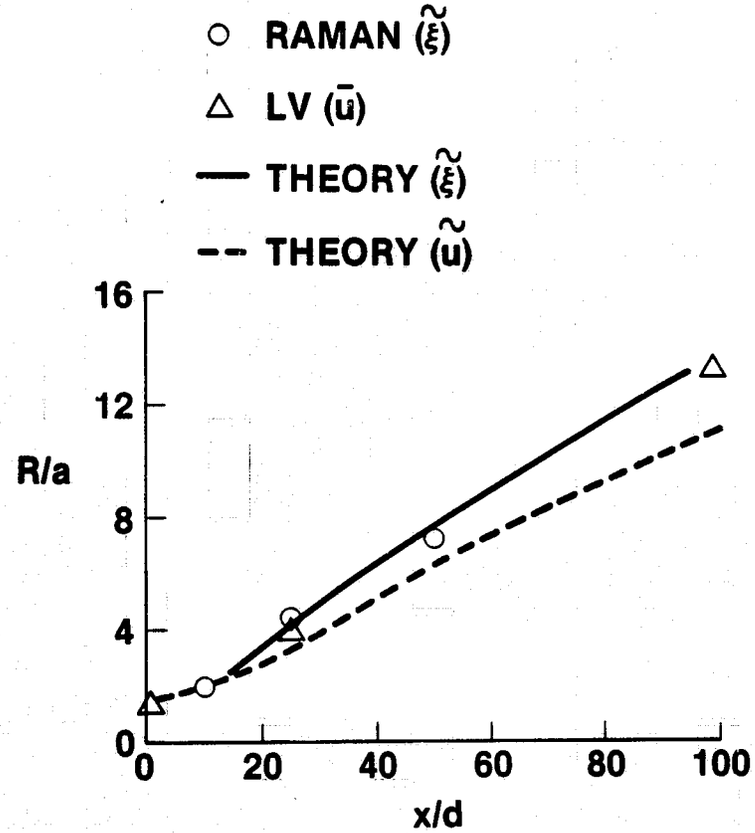


Figure 79. Radial Profile of Favre-Averaged Mean Mixture Fraction at X/D = 50.

ORIGINAL PAGE IS
OF POOR QUALITY



Jet Half Width Normalized to Initial Jet Radius Verses Axial Length Normalized to Jet Diameter.

Figure 80. Centerline Profiles of Jet Half-Width Based on Velocity (LV) and Favre - Averaged Mean Mixture Fraction (Raman).

ORIGINAL PAGE IS
OF POOR QUALITY

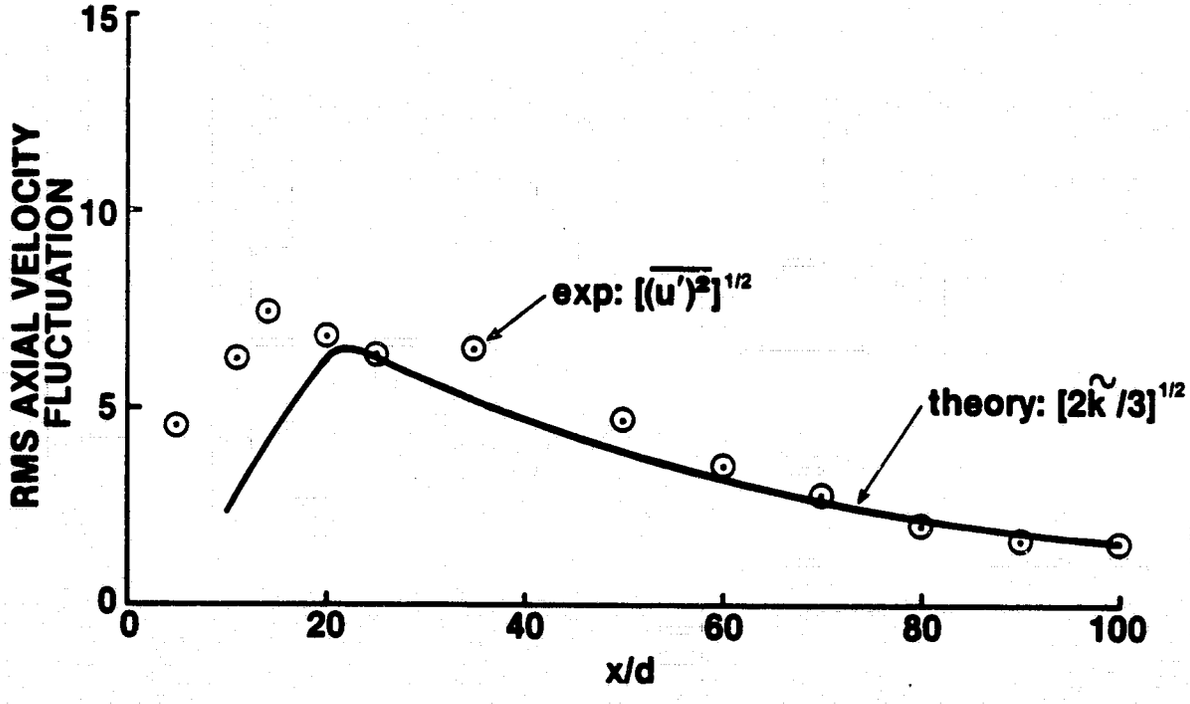


Figure 81. Centerline Profile of Turbulence Kinetic Energy.

ORIGINAL PAGE IS
OF POOR QUALITY

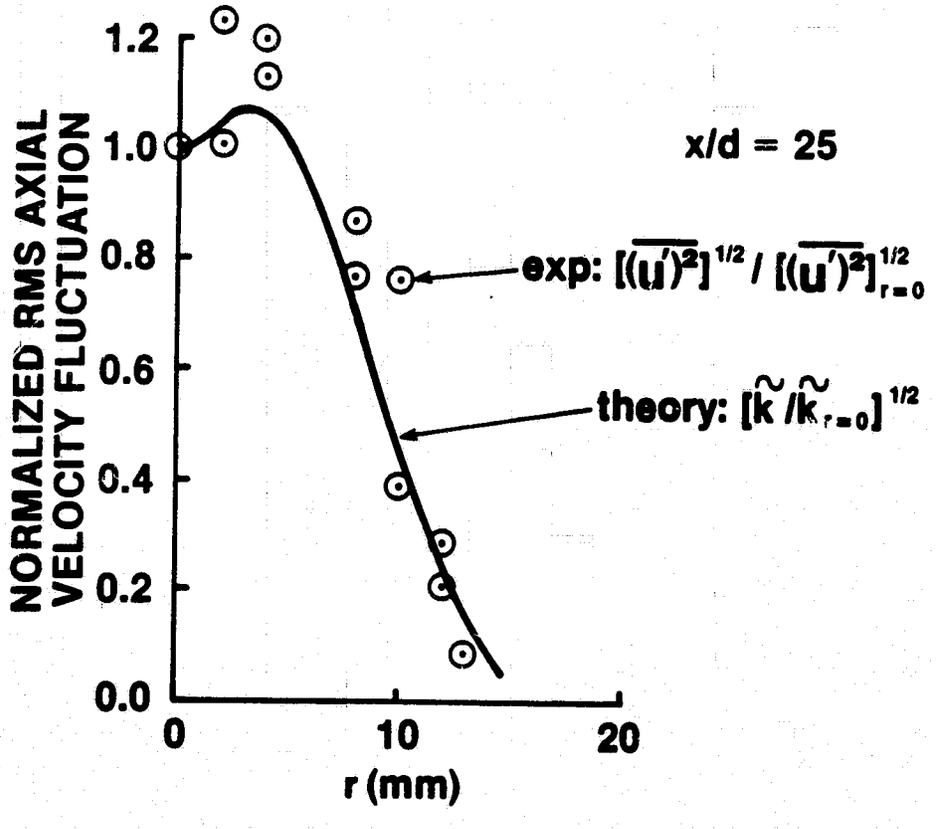
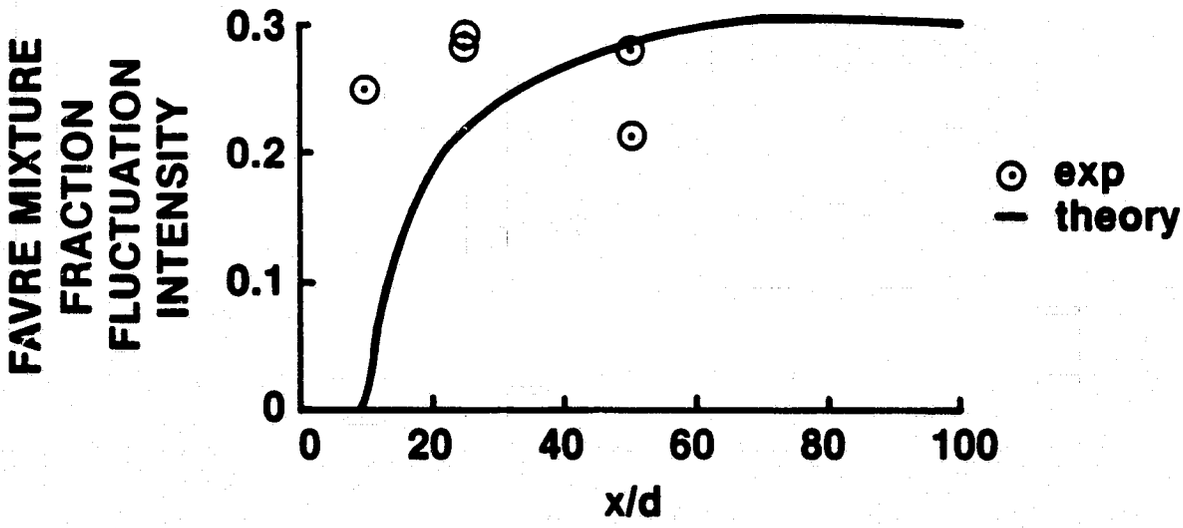


Figure 82. Radial Profile of Turbulence Kinetic Energy at X/D = 25.

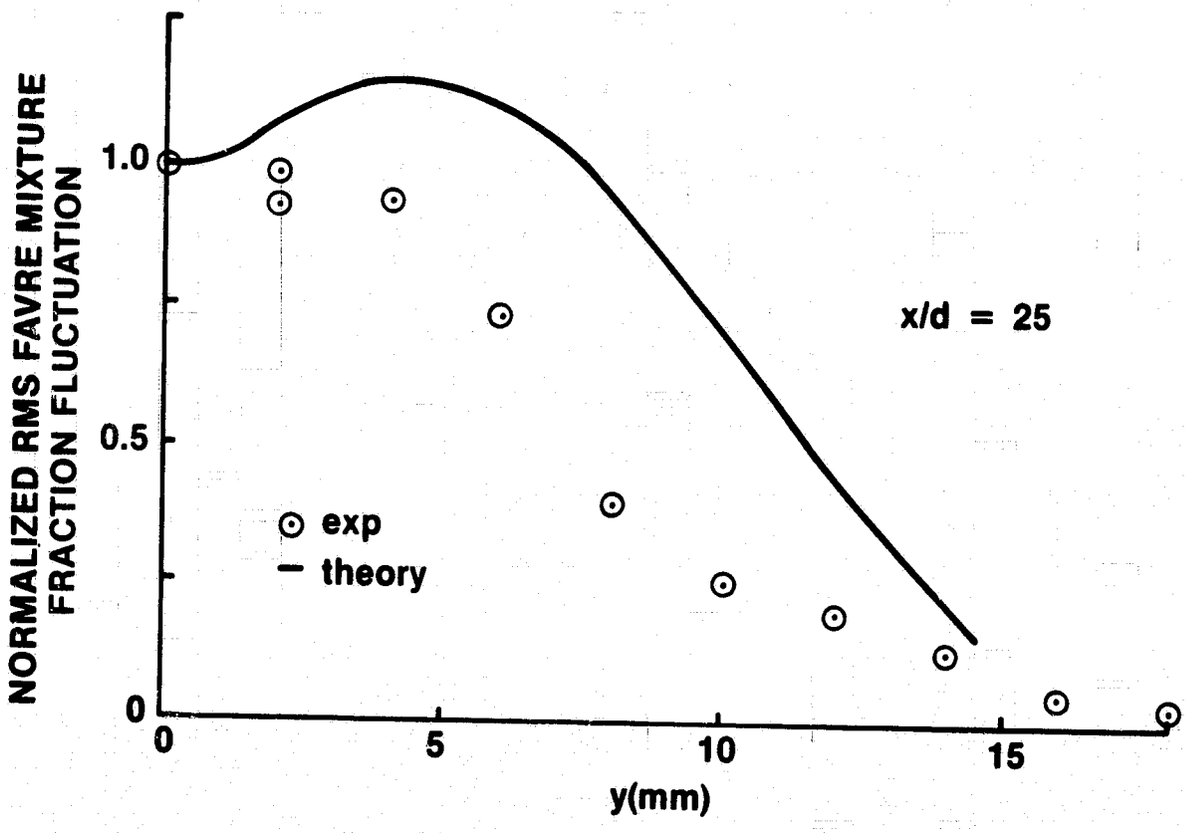
ORIGINAL PAGE IS
OF POOR QUALITY



$[(\tilde{\xi}''^2)^{1/2}/\tilde{\xi}$ Versus Normalized Axial Length]

Figure 83. Centerline Profile of Favre-Averaged Variance of Mixture Fraction.

ORIGINAL PAGE IS
OF POOR QUALITY



$[(\tilde{\xi}''^2)/(\tilde{\xi}''^2)^{1/2}_{\text{At Centerline}}]$ Versus Height Above Centerline

Figure 84. Radial Profile of Favre-Averaged Variance in Mixture Fraction at X/D = 25.

measured in a cold jet into still air, Becker, et al., 1967[105]; 1.3 in a slightly heated jet, Antonia and Bilger, 1976[106]; and 1.2 measured by Mie scattering in an Re = 11,200 H_2 flame, Kennedy and Kent, 1981[107]. The measurements shown in Figure 84, however, do not show an off-axis peak, which was expected in light of the presence of an off-axis peak in the velocity fluctuations (Figure 82). This may indicate a problem with the data rather than with the model and is under further study.

Radial profiles of conventionally-averaged values of temperature are shown in Figures 85 and 86 at x/d=25 and 50, respectively. Compared to the profiles of $\tilde{u}$ and $\tilde{\xi}$ which were in excellent agreement with the experimental data, the modeling of temperature shows significantly larger departures. This is undoubtedly related to the fact that velocity and mixture fraction are explicit variables followed in the model while temperatures and species concentrations are calculated by a further convolution with the assumed shape mixture fraction pdf. The mixture fraction pdf at any point in the flow is modeled using only two parameters $\tilde{u}$ and $(\tilde{\xi}''^2)^{1/2}$ and assuming a clipped Gaussian form for the turbulent part of the pdf and a correlation for the nonturbulent intermittent part. This is because intermittency is an important feature of shear flows. Since the model and experimental values of $(\tilde{\xi}''^2)^{1/2}$ are not in perfect agreement, it is not surprising that values for temperature differ as well.

This experiment offers the highest possible caliber of experimental data for a case where the numerics and turbulence aspects of the modeling are greatly simplified. The good agreement between the data and the prediction validates the model for turbulence/chemistry interactions. Further simulations including thermal and fuel-bound-nitrogen formation, Lapp et al., 1983[3], provide more evidence but will not be discussed here.

7.1.2 Isothermal Axisymmetric Plenum-Chamber Experiment

Several complicated flow phenomena are simultaneously present in the gas turbine combustor. To predict such a flow therefore involves models for turbulence, combustion, vaporization, radiation, etc., as well as approximations inherent in the numerics. The benchmark experiment of Green and Whitelaw 1980[5] addresses a "combustion-chamber-like" flow including the plenum but which is isothermal. Comparison with the predictions therefore provides a test of the turbulence model and the numerical accuracy.

Two experiments were performed: one involved round jets while the other had a circumferential slit which linked the plenum with the chamber. The second flow is axisymmetric and is therefore computationally more convenient. The model was run for the axisymmetric case.

The experimental apparatus is shown in Figure 87. Water from a constant-head tank enters the plenum and flows into the chamber through the slit. Laser Doppler Velocimetry was used to determine the mean velocity and turbulence.

ORIGINAL PAGE IS
OF POOR QUALITY

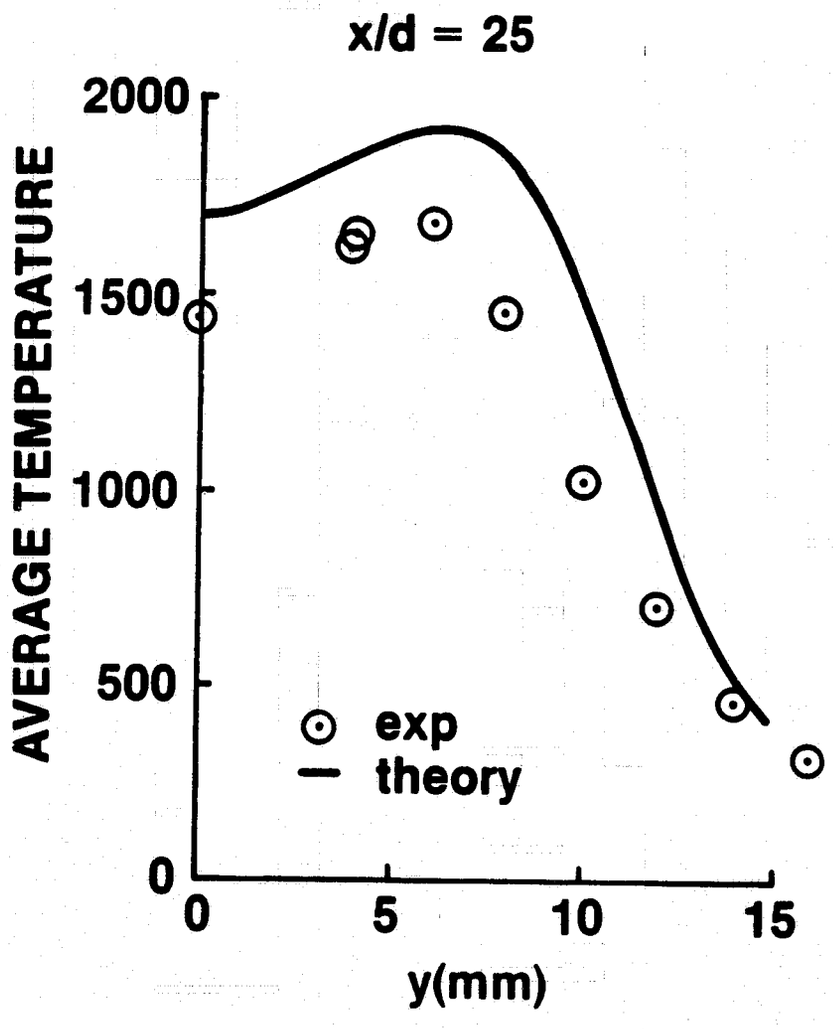


Figure 85. Radial Profile of Favre-Averaged Mean Temperature at X/D = 25.

ORIGINAL PAGE IS
OF POOR QUALITY

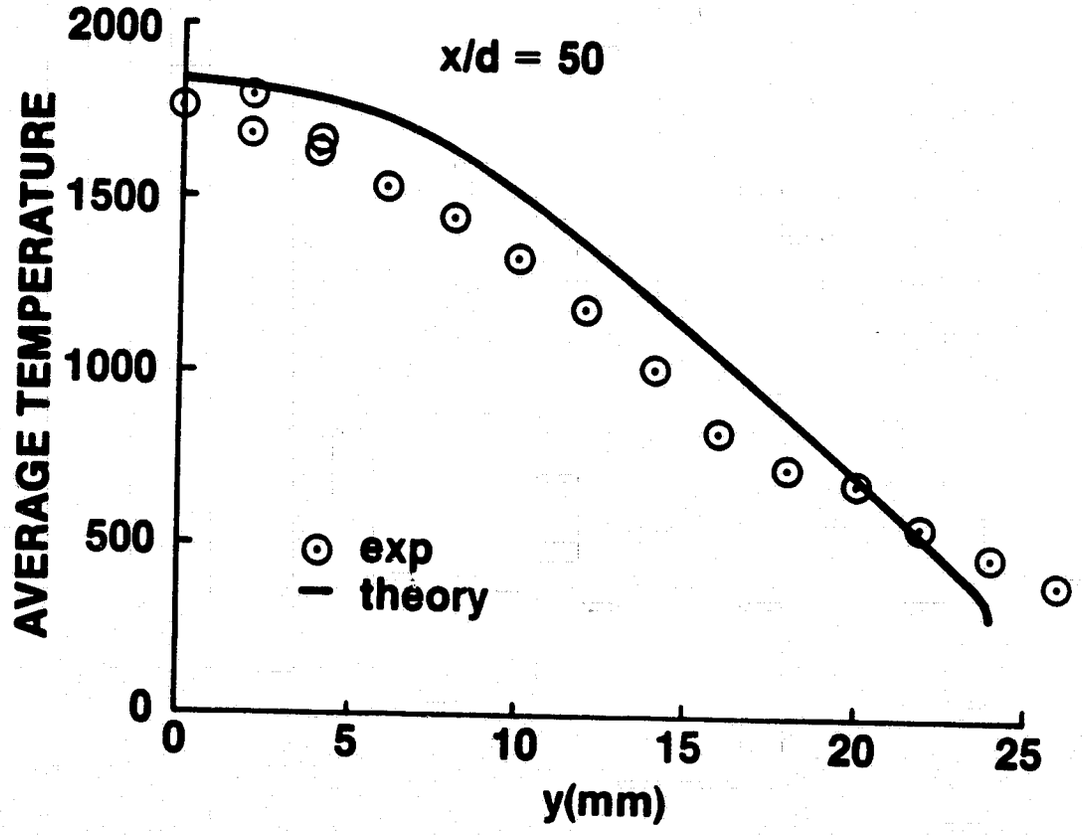


Figure 86. Radial Profile of Favre-Averaged Mean Temperature at X/D = 50.

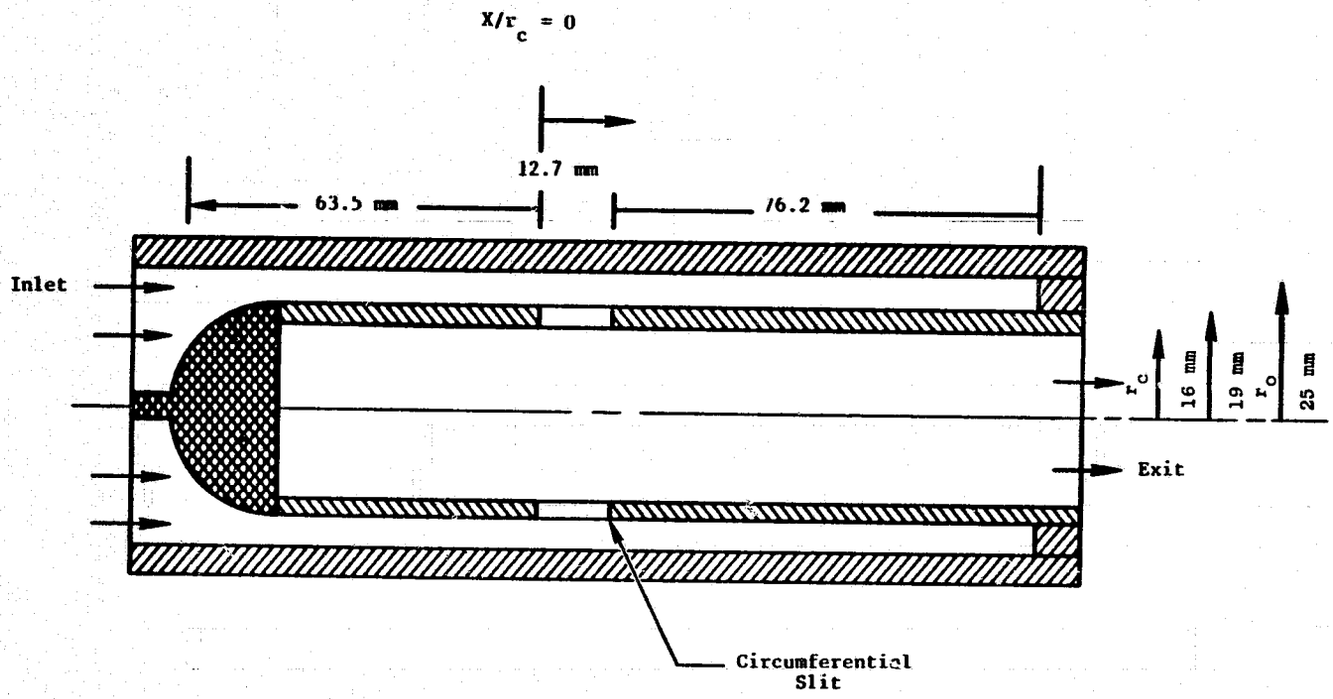


Figure 87. Isothermal Slit-Jet Experiment.

ORIGINAL PAGE IS
OF POOR QUALITY

The equations to be solved are those for mean continuity, axial and radial mean velocity, and turbulence kinetic energy and dissipation rate. The standard (isotropic eddy viscosity) k-ε turbulence model was used. Boundary conditions were taken as symmetry about the centerline, zero normal velocity and logarithmic law-of-the-wall at all solid surfaces, and zero axial gradient of all dependent variables far downstream. This downstream boundary was located approximately three inner tube diameters downstream of the gap and did not affect the results. The inlet boundary condition for axial velocity was measured and this profile was used in the calculation. Inlet conditions for turbulence kinetic energy and dissipation rate were obtained from assumptions regarding the intensity and length-scale of inlet turbulence. For example, the initial length-scale was taken as 3% of the annulus height. The grid was arrived at after successive refinements, as discussed below, and comprised 74 (axial) x 38 (radial) nodes.

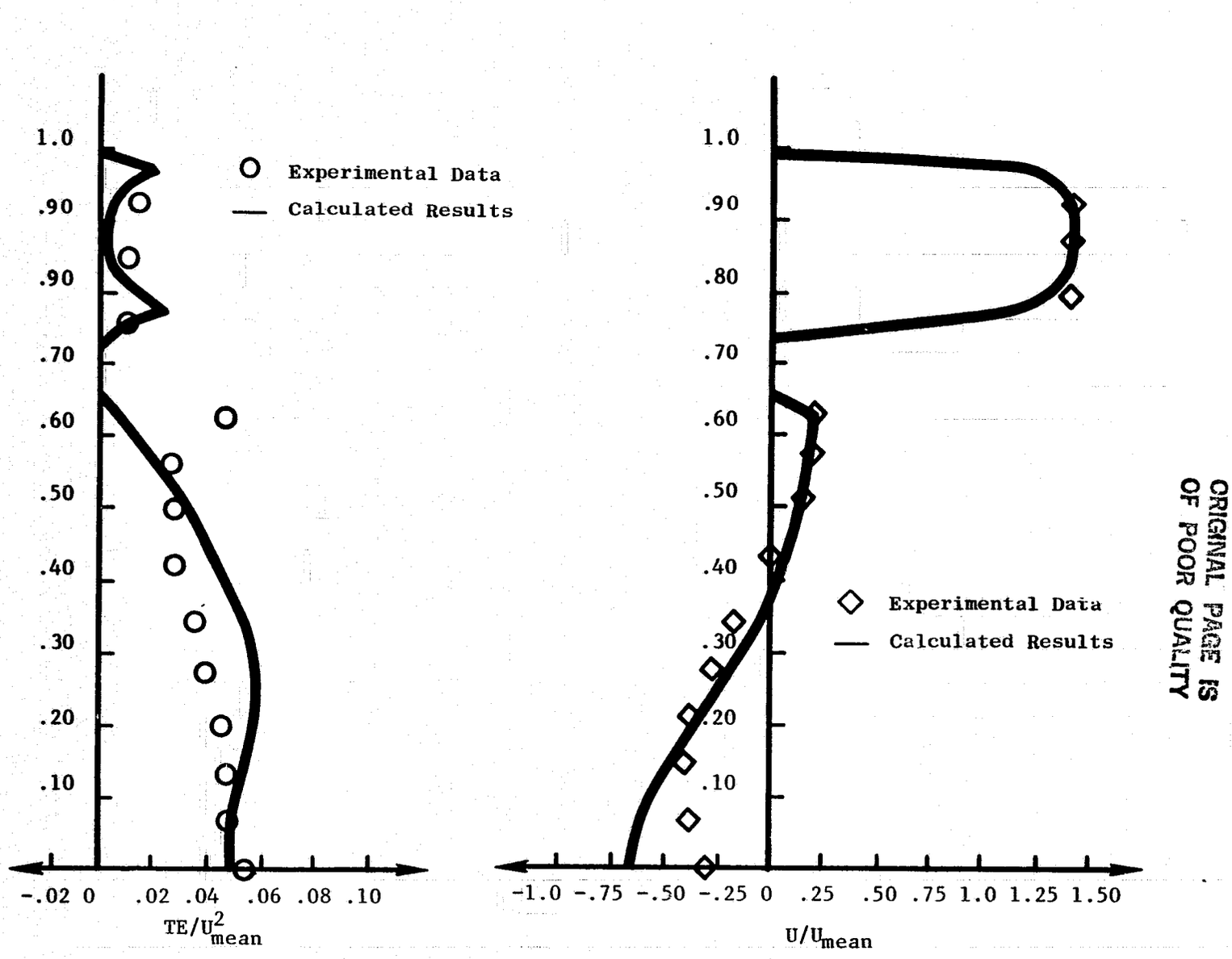
Predicted profiles of the turbulence kinetic energy (TKE) and the mean axial velocity are shown (Figures 88 to 91) at four different axial locations. The measured data are also shown. A first inspection of these results shows a striking feature of this flow: the agreement on the mean axial velocity is significantly better than that on TKE. This implies that in the mean momentum equations the turbulent diffusion was not a dominant term.

Errors in this calculation could stem from inaccurate boundary conditions, turbulence modeling or the discretization scheme. It is interesting to note that Green and Whitelaw 1980[5] tried to distinguish between these sources of error. They studied the terms in the axial momentum equation and found that turbulent and numerical diffusion were comparable in the gap region. However, these terms were dominated by convection and mean pressure gradient. By refining the grid to resolve steep pressure gradients in the gap, the vortex formed downstream of the slit was predicted. From this, the flow was labeled as being "pressure dominated".

In this study a 47 x 27 grid was first used. The vortex downstream of the slit was not reproduced and the profiles of turbulence kinetic energy showed even larger disagreement with the data particularly downstream near the inner wall where the experimentally observed upstream separation was important. Successive refinements of the grid were made without sacrificing nodes elsewhere, i.e., the later grids were nested so that prior nodes did not change. The vortex was then predicted. The 74 x 38 node grid used eventually is far more detailed than the 30 x 28 grid used by Green and Whitelaw 1980[5].

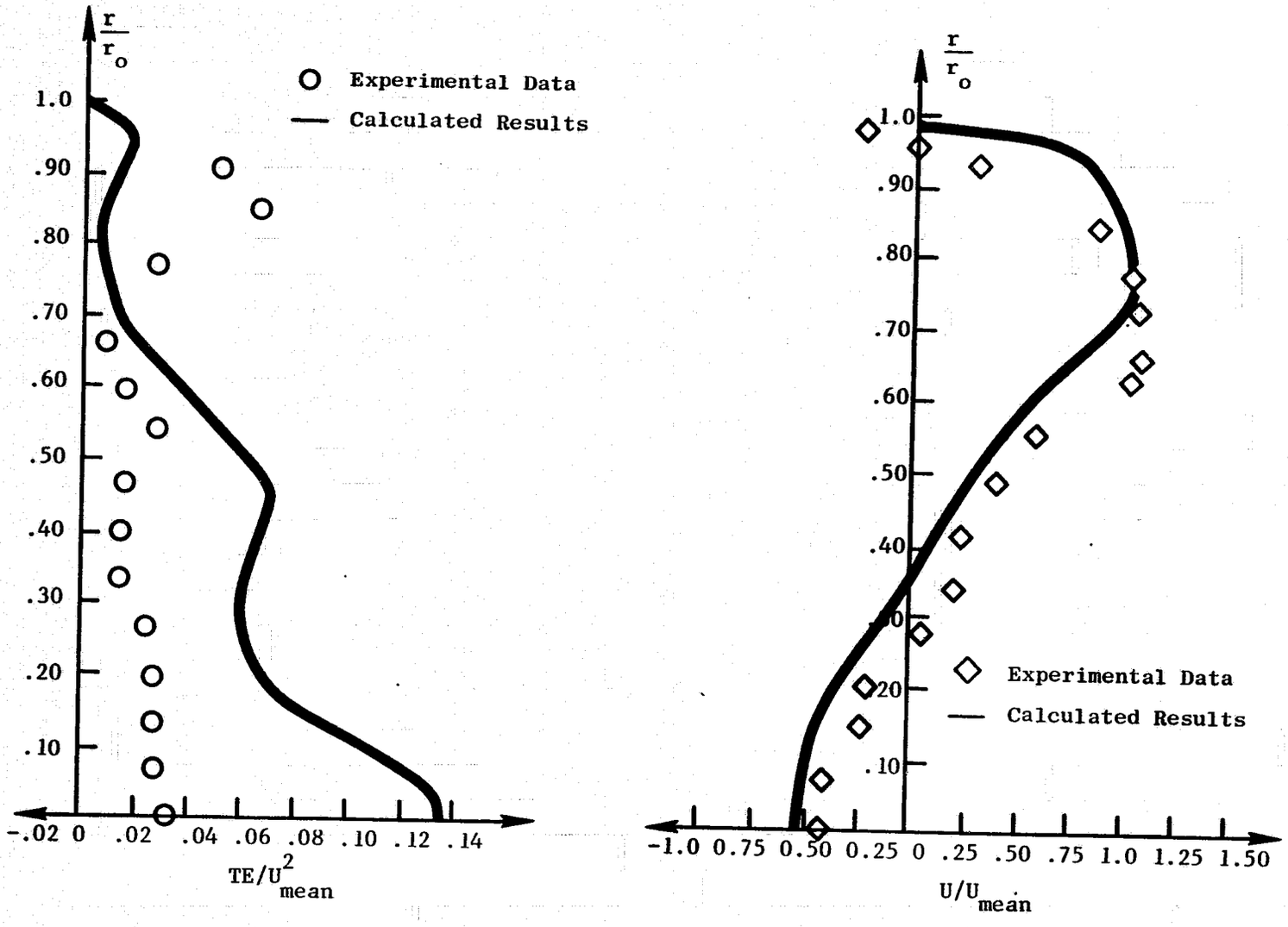
The occurrence of the vortex is an important feature of this flow which perhaps would not be realized a priori. Therefore it is important to adequately resolve regions of steep pressure gradient in any calculation. This requires either the time-consuming process of repeated runs or a dynamic remeshing.

Although it appears that the mean flow agreement is satisfactory, the reasons for the discrepancy in TKE must be addressed. These errors are pronounced in the inner chamber although far downstream the agreement improves.



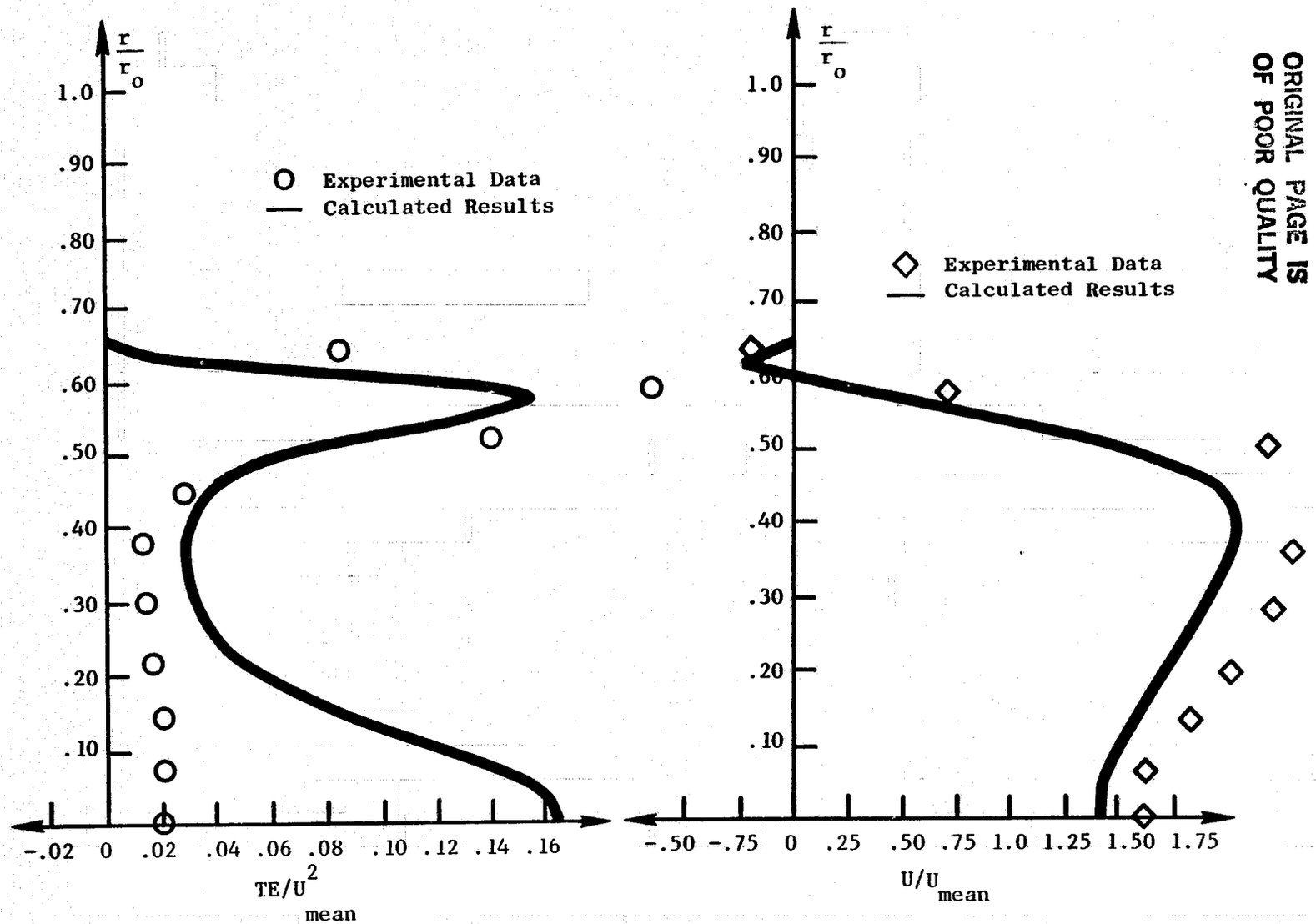
ORIGINAL PAGE IS
OF POOR QUALITY

Figure 88. Radial Profiles of Turbulence Kinetic Energy and Mean Axial Velocity at $x/r_o = -0.61$.



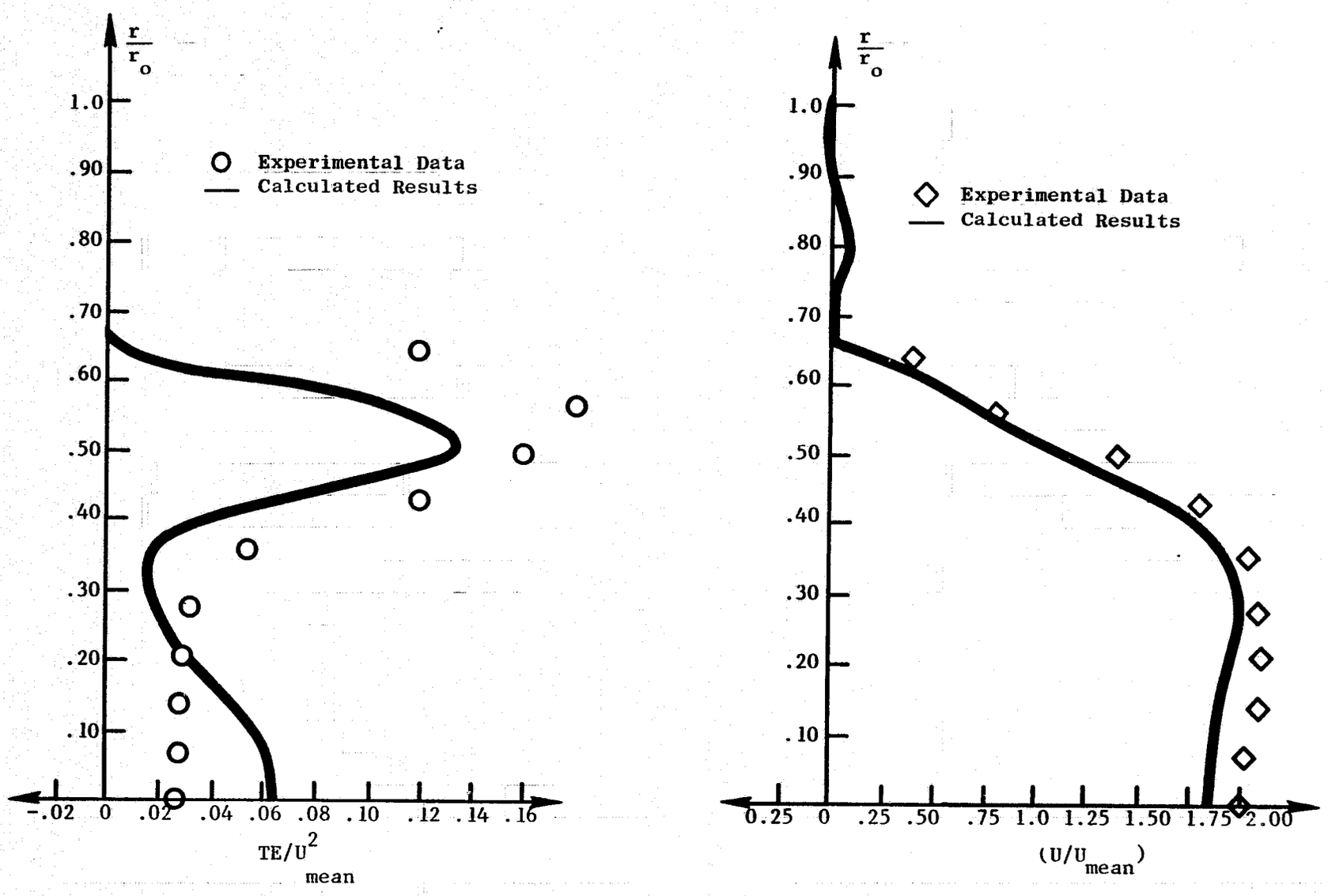
ORIGINAL PAGE IS
OF POOR QUALITY

Figure 89. Radial Profile of Turbulence Kinetic Energy and Mean Axial Velocity at $x/r_o = 0.37$.



ORIGINAL PAGE IS
OF POOR QUALITY

Figure 90. Radial Profile of Turbulence Kinetic Energy and Mean Axial Velocity at $x/r_o = 1.20$.



ORIGINAL PAGE IS
OF POOR QUALITY

Figure 91. Radial Profile of Turbulence Kinetic Energy and Mean Axial Velocity at $x/r_o = 2.77$.

The assumptions in the k-ε model and their contribution to the total error have already been discussed for turbulent flows in general. In this flow, two particular features make the model even less accurate: the importance of the inner wall boundary layer and the presence of a free stagnation point. Generation of TKE in the layer and the matching of the high Reynolds number flow solutions to the law-of-the-wall region are thus significant. In addition, the free stagnation point along the centerline represents a region where assumptions such as gradient diffusion and inaccurate normal-stress normal-strain interaction are significant. The effect of streamline curvature on the isotropy of stresses, and the fact that in multiple length-scale flows the use of an effective viscosity is not entirely justifiable also contribute to the total error.

The major conclusion to be drawn, however, is that in the isothermal flow mean pressure gradients can dominate turbulence in determining the mean flow. In a combusting flow, however, the turbulence is intimately connected with the combustion so that any errors affect the heat release and therefore the mean flow. Thus, although the mean pressure gradient emerges as an importnat aspect of a flow, it is not necessarily as dominating as in the present slit-jet/plenum/chamber flow.

7.1.3 Isothermal Co- and Counterswirled Pipe Flow

This simulation was performed to demonstrate an improved turbulence model. In the k-ε model for turbulence, a turbulence relation between turbulent stresses and rate of strain is assumed to exist. In constant density flow this means

$$\overline{u'_i u'_j} = \frac{2}{3}\delta_{ij}\left[k + \nu_t \frac{\partial \overline{U}_k}{\partial x_k}\right] - \nu_t\left[\frac{\partial \overline{U}_i}{\partial x_j} + \frac{\partial \overline{U}_j}{\partial x_i}\right] \qquad (89)$$

The kinematic eddy viscosity ν_t which appears is obtained from the solution of transport equations for k and ε:

$$\nu_t = c_\mu k^2/\varepsilon \qquad (90)$$

where c_μ is a constant (0.09) obtained from matching the model with shear flow data. The eddy viscosity is thus isotropic.

In flows with significant curvature of the mean streamlines experimental evidence indicates that the turbulent stresses are highly anisotropic. The experiment of Vu and Gouldin, 1982[6] provides benchmark quality data for the

mean velocity and the turbulence field in such a flow. In the present study, the numerical model was run with the standard (isotropic eddy viscosity) k-ε turbulence model and also with the algebraic stress model described in Section 6.4. Predictions from the former model are not even qualitatively correct while the improved model agrees closely with the data.

The improved model is thus very significant for gas turbine combustors since they are characterized by large swirl components. It may be noted that a previous study, Srinivasan and Mongia, 1980[108], of this flow also identified weaknesses of the standard k-ε model and demonstrated an improvement based on a Richardson number correction. However, the current algebraic stress model represents a more universal approach which has now been applied to several flows with marked success.

The experimental apparatus consists of two swirl generators feeding an inner pipe and a concentrically arranged outer pipe (Figure 92). The inner and annulus flows may have co-, zero, or counterswirl. The mixing region test section is a clear acrylic pipe. Separate blowers and plenums are used for the two streams. Swirl is imparted by means of vanes and is defined by the swirl number S

$$S = \frac{\text{axial flux of angular momentum}}{[\text{ axial flux of axial momentum }]\, R} \qquad (91)$$

where $R = R_1$ and $R = R_o$ are used for the inner and outer flows, respectively.

Measurements of the mean flow were made with a directional five-hole pitot probe and of the turbulence by hot-wire anemometry. Qualitative dissipation data were obtained by analog time differentiation. Further details regarding the experimental apparatus, the instrumentation and the experimental errors involved may be found in Vu and Gouldin, 1980[6]. This report will focus on the model used here and the level of agreement with the data. An important feature of the present study is the effort to reduce truncation errors in the convection term finite-difference representation so that turbulent diffusion is not masked by numerical error.

Two flow cases were studied in detail, the first corresponding to co-swirl and the second to maximum counterswirl. In the experiment the counter-swirled flow produced a recirculation zone extending approximately from the inlet to 1.5 inner pipe diameters downstream. The occurrence of this recirculation zone provides a stringent and (in view of the gas turbine combustor being swirl-stabilized) necessary test of the turbulence model.

The model was applied to this flow, first using k-ε closure and then the algebraic Reynolds stress model described above. The computational domain, again chosen so as not to affect the results, extended 8.5 inner pipe radii downstream of the inlet plane. After repeated runs in which numerical diffusion errors were assessed a grid of 65 (axial) x 39 nodes was adopted for all the calculations. This detailed grid allows an accurate assessment of the turbulence model.

ORIGINAL PAGE IS
OF POOR QUALITY

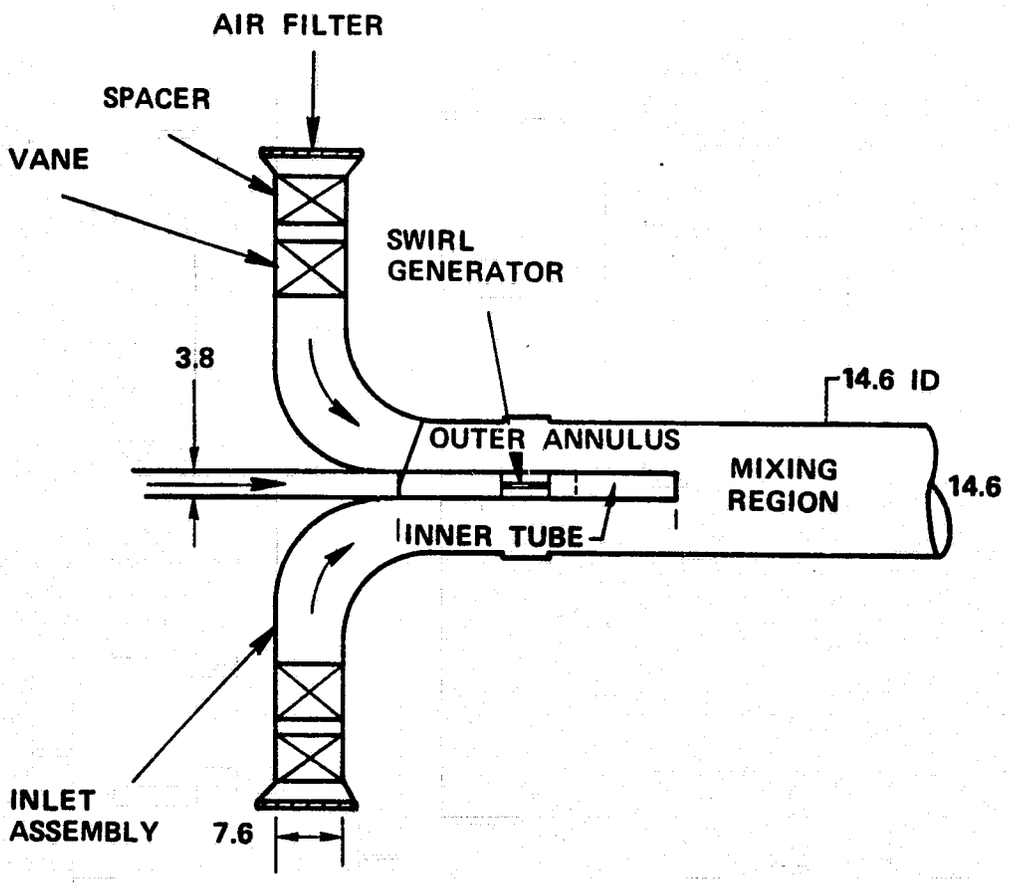


Figure 92. Flow Assembly (from Srinvasan and Mongia, 1980).

Predictions using the k-ε model with isotropic eddy-viscosity are compared with the measured data for the coswirl case (Figures 93 to 95) and the counter-swirl case (Figures 97 to 100). The failure to predict the co-swirl case is clear from the centerline axial velocity plot which shows the measured decay to be much slower than predicted. The effects of the swirl on the lateral turbulent diffusion of momentum are not accounted for. In the counter-swirl case the effect is even more dramatic since the observed center-line reverse flow region is simply not predicted. This is in agreement with previous applications of the k-ε model to this flow, Srinivasan and Mongia, 1980[108].

In situations where anisotropic eddy viscosity is clearly to blame for the failure of the model, several researches have developed modified two-equation models. These models, however, are based on somewhat empirical arguments and do not carry over to general flows. In this study a more universal model was used. This model has already been discribed (Section 6.4) and has been validated in two- and three-dimensional swirling and nonswirling flows.

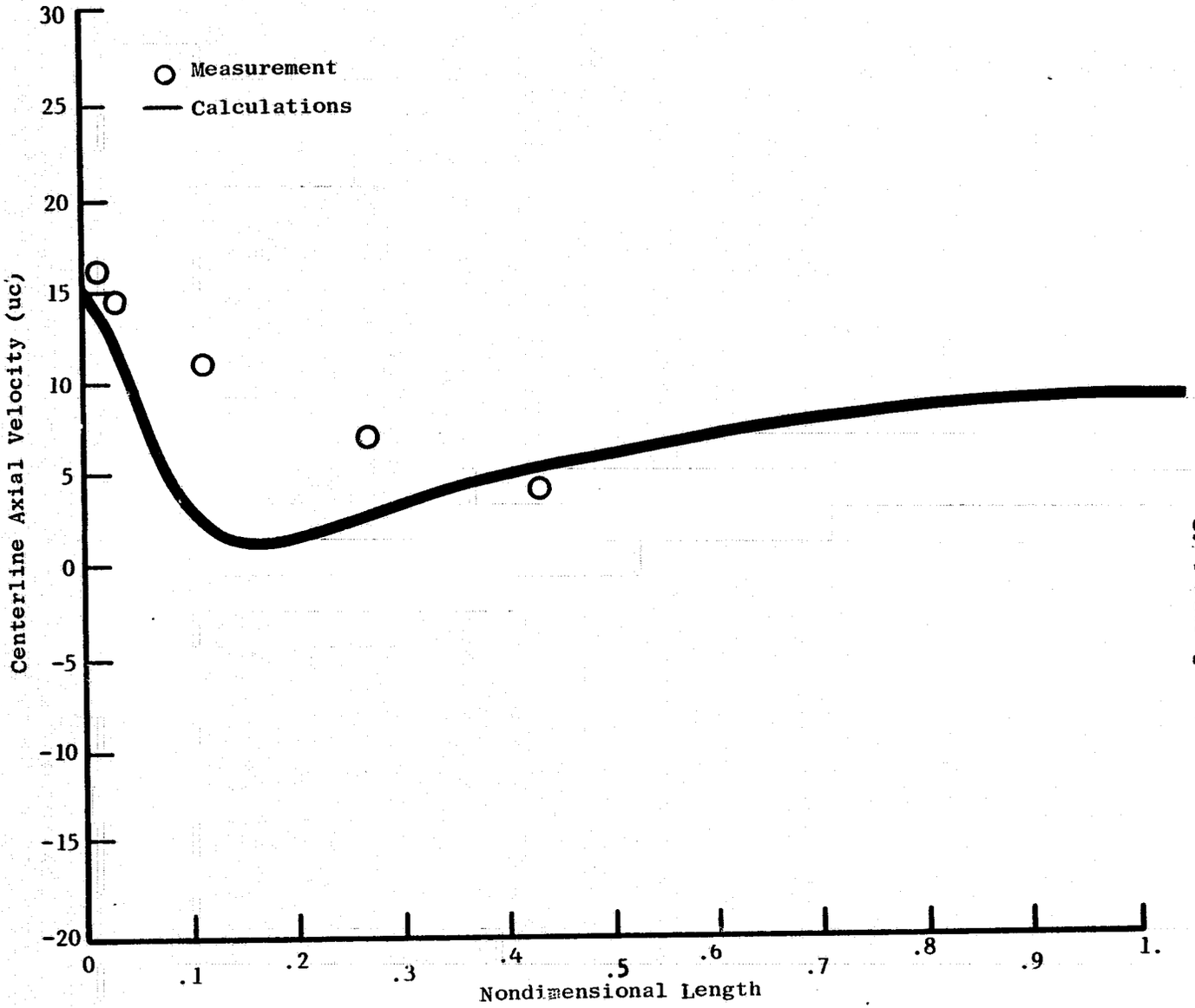
The predictions using this algebraic Reynolds stress model (Figures 101 to 108) show that the critical recirculation zone for the counterswirling case is indeed predicted. The maximum reverse velocity and the downstream recovery rate are not exactly in agreement but the recirculation zone length is very close. It is repeated that this calculation is on a fine grid so that numerical errors are minimized.

A recent study by Sturgess, et al., 1983[109] indicates the role of inlet boundary conditions in this flow, performance of the k-ε and derivative two-equation models will certainly be affected by the boundary conditions but the general conclusions stand. From this simulation it is evident at least qualitatively that the k-ε model could be unusable in the eventual aerothermal model. The proposed alternative, which retains the computationally attractive two-equation format, has been tested without modification in a wide variety of flows including the present case. The success of this algebraic stress model suggests that it should be used henceforth.

7.1.4 Bluff Body Stabilized Diffusion Flame

A bluff body stabilized diffusion flame combustor has been developed at the Air Force Aeronautical Propulsion Laboratory (AFAPL). This experimental facility was designed to provide benchmark quality data to the modeling community. Isothermal as well as combusting flows have been studied for a range of fuel and airflow rates. In this section, the experiment is described, modeling results are presented, and the implications of the level of agreement obtained are discussed. Simulations were made with the code GETREF, which is an elliptic formulation of the Favre-averaged single-scalar assumed pdf/equilibrium chemistry/k-ε model.

The bluff body stabilized combustor (Figure 109) represents an important step towards the "real" problem. Stabilization of the flame by recirculation of the hot products in the wake of the bluff body allows larger flow rates



ORIGINAL PAGE IS
OF POOR QUALITY

Figure 93. Centerline Profile of Axial Velocity for Coswirl Flow, k-ε Model.

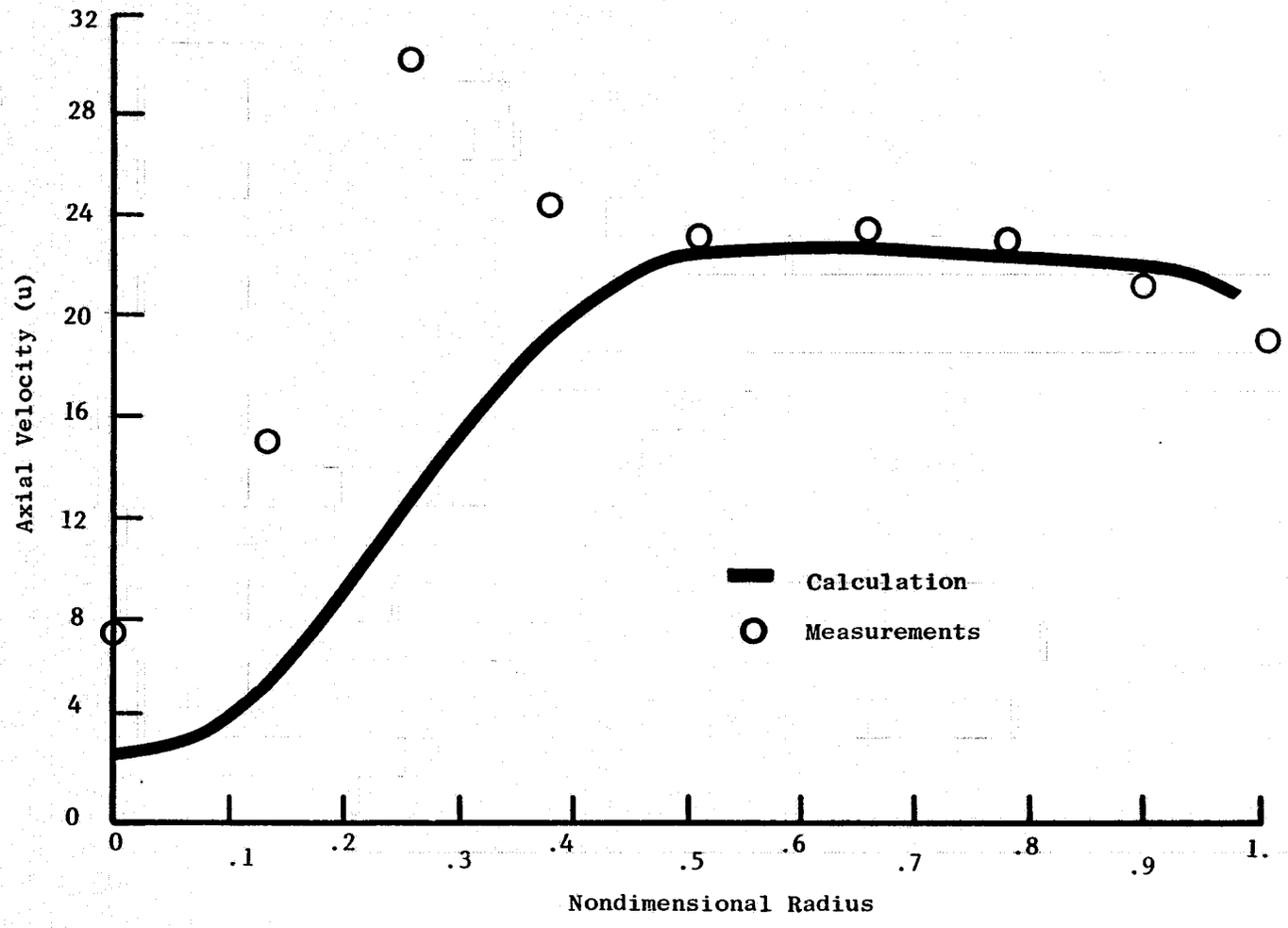
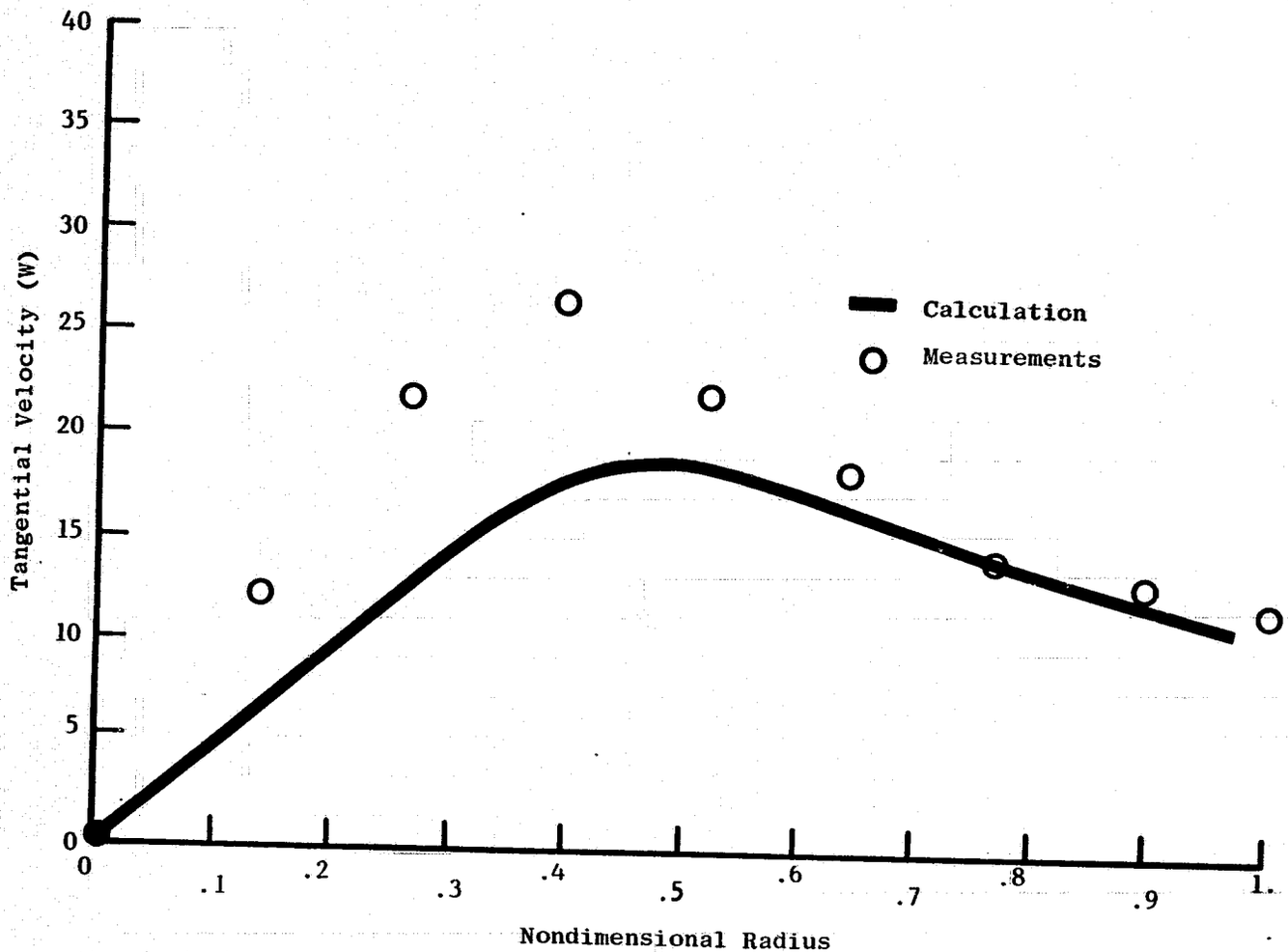


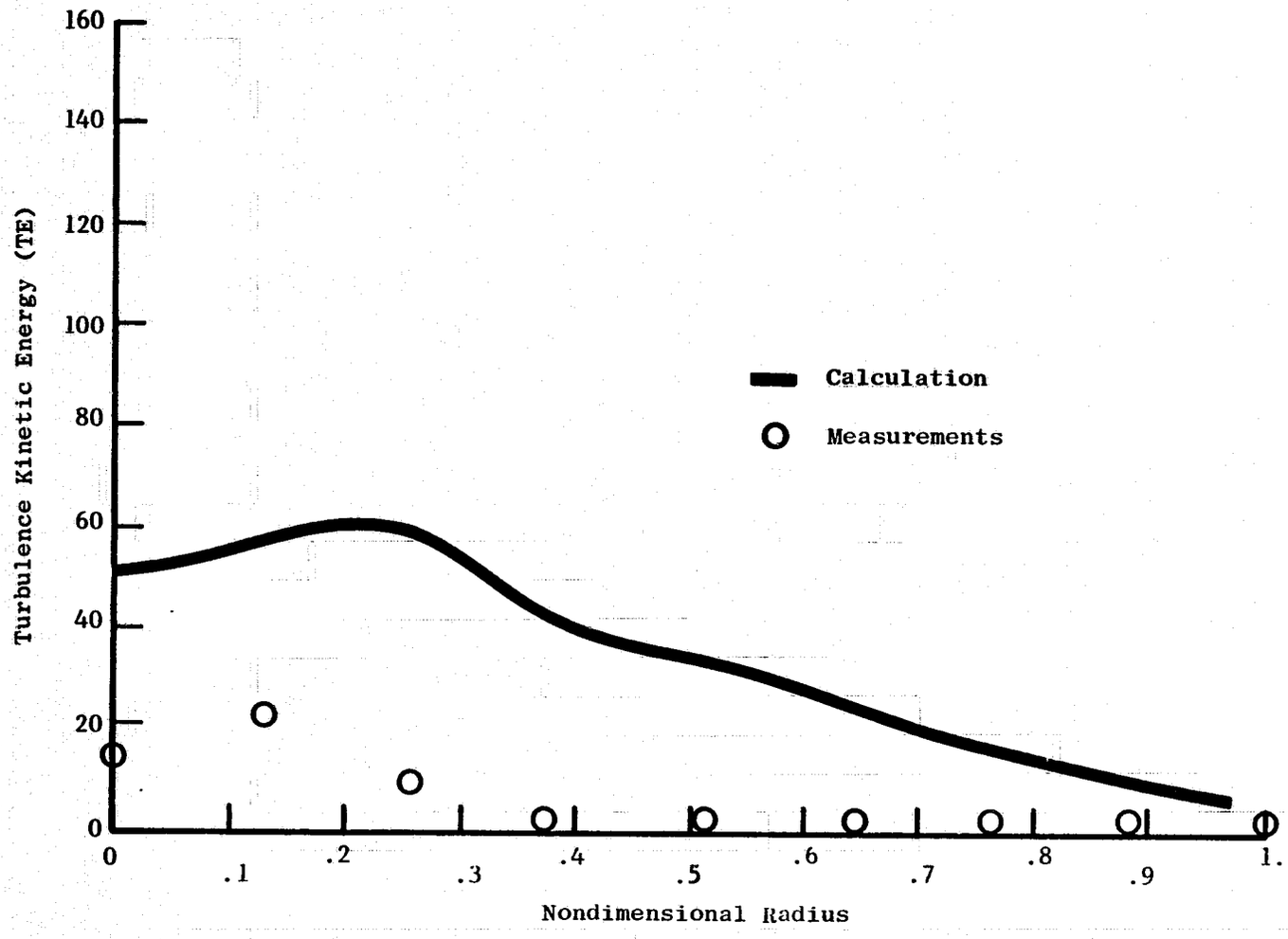
Figure 94. Radial Profile of Axial Velocity at Z/R_i = 3.67 for Coswirl Flow, k-ε Model.

ORIGINAL PAGE IS
OF POOR QUALITY



ORIGINAL PAGE IS
OF POOR QUALITY

Figure 95. Radial Profile of Tangential Velocity at $Z/R_1 = 3.67$ for Coswirl Flow, k-ε Model.



ORIGINAL PAGE IS
OF POOR QUALITY

Figure 96. Radial Profile of Turbulence Kinetic Energy at Z/R_i = 3.67, k-ε Model.

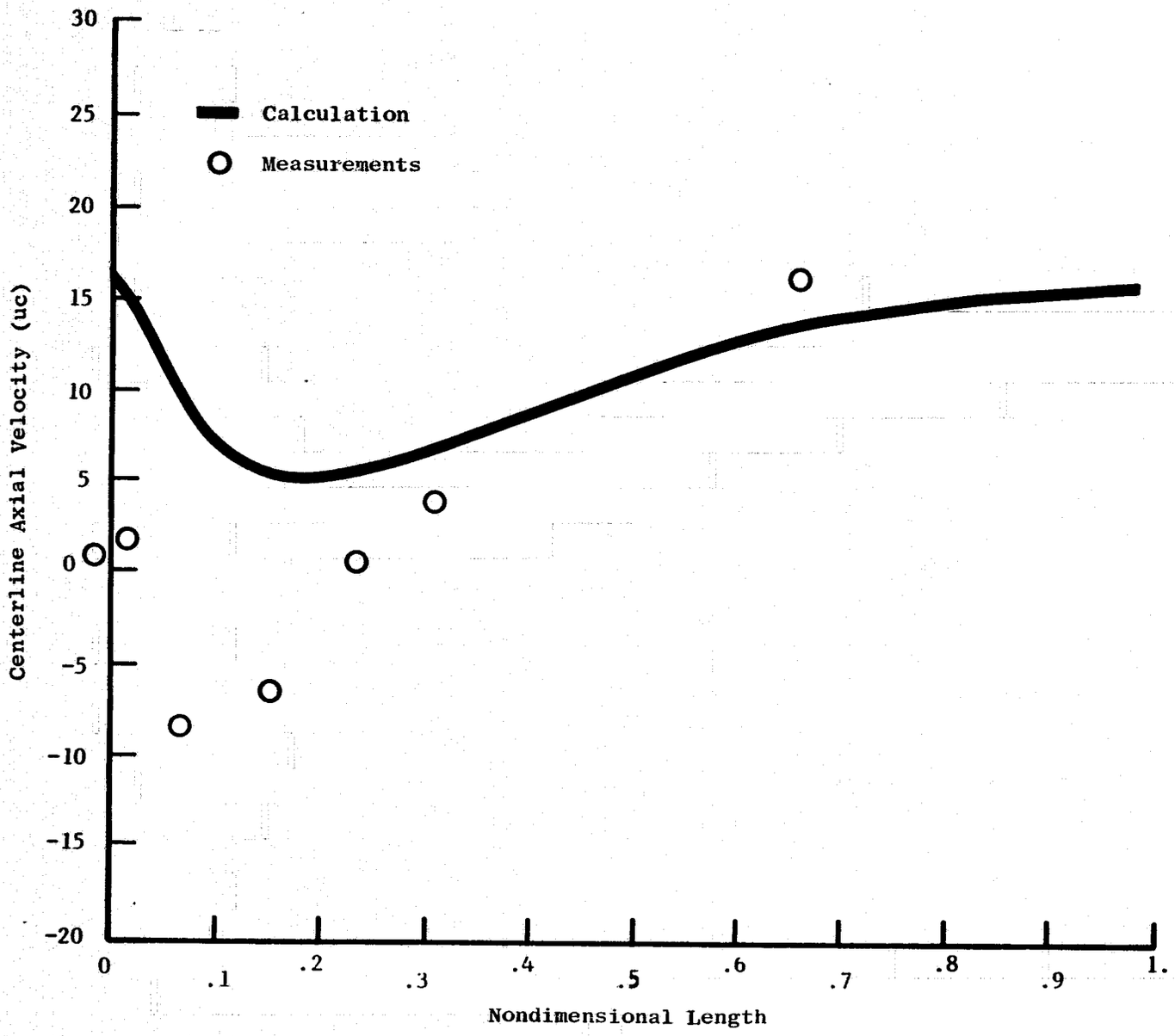
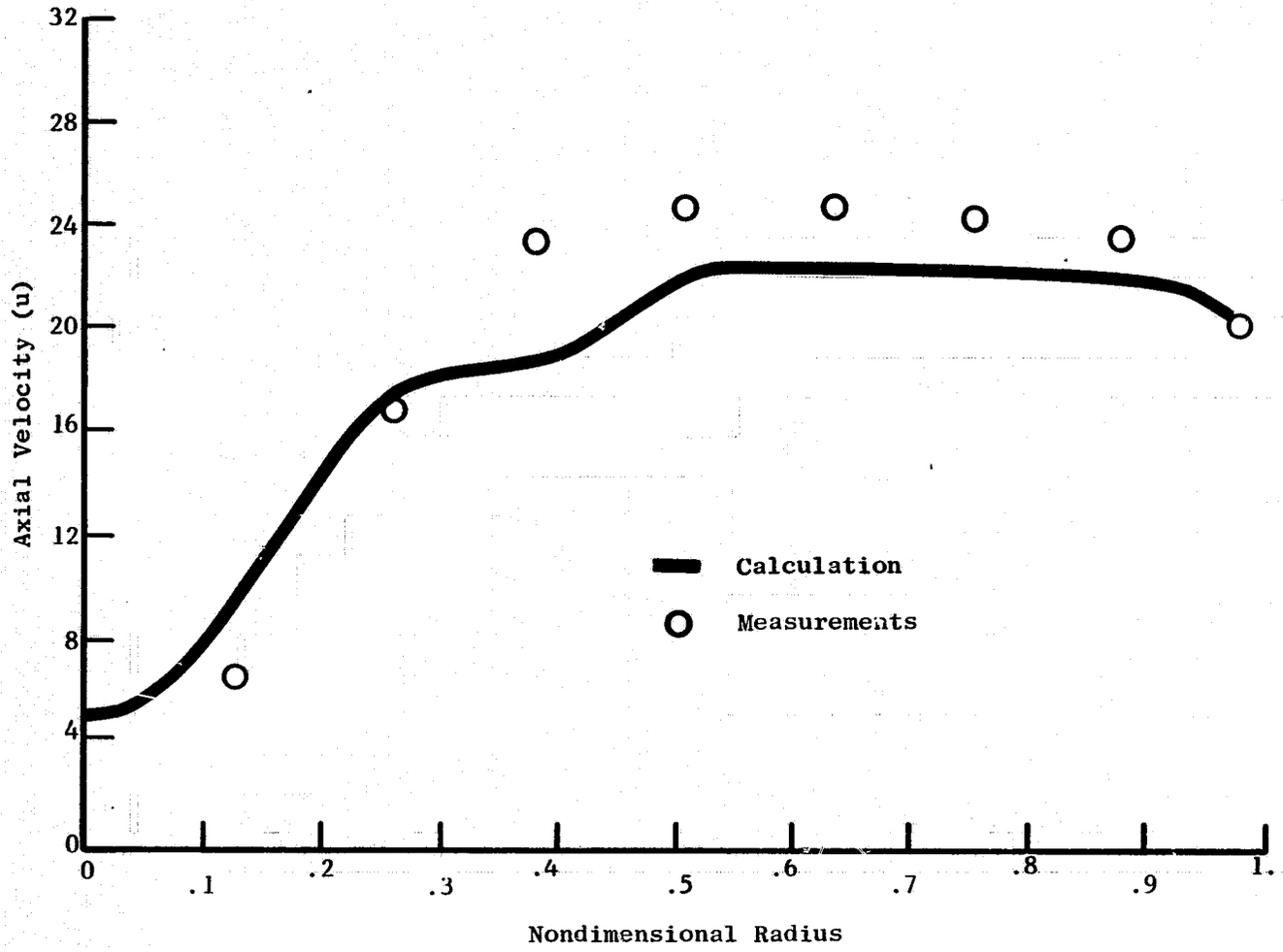


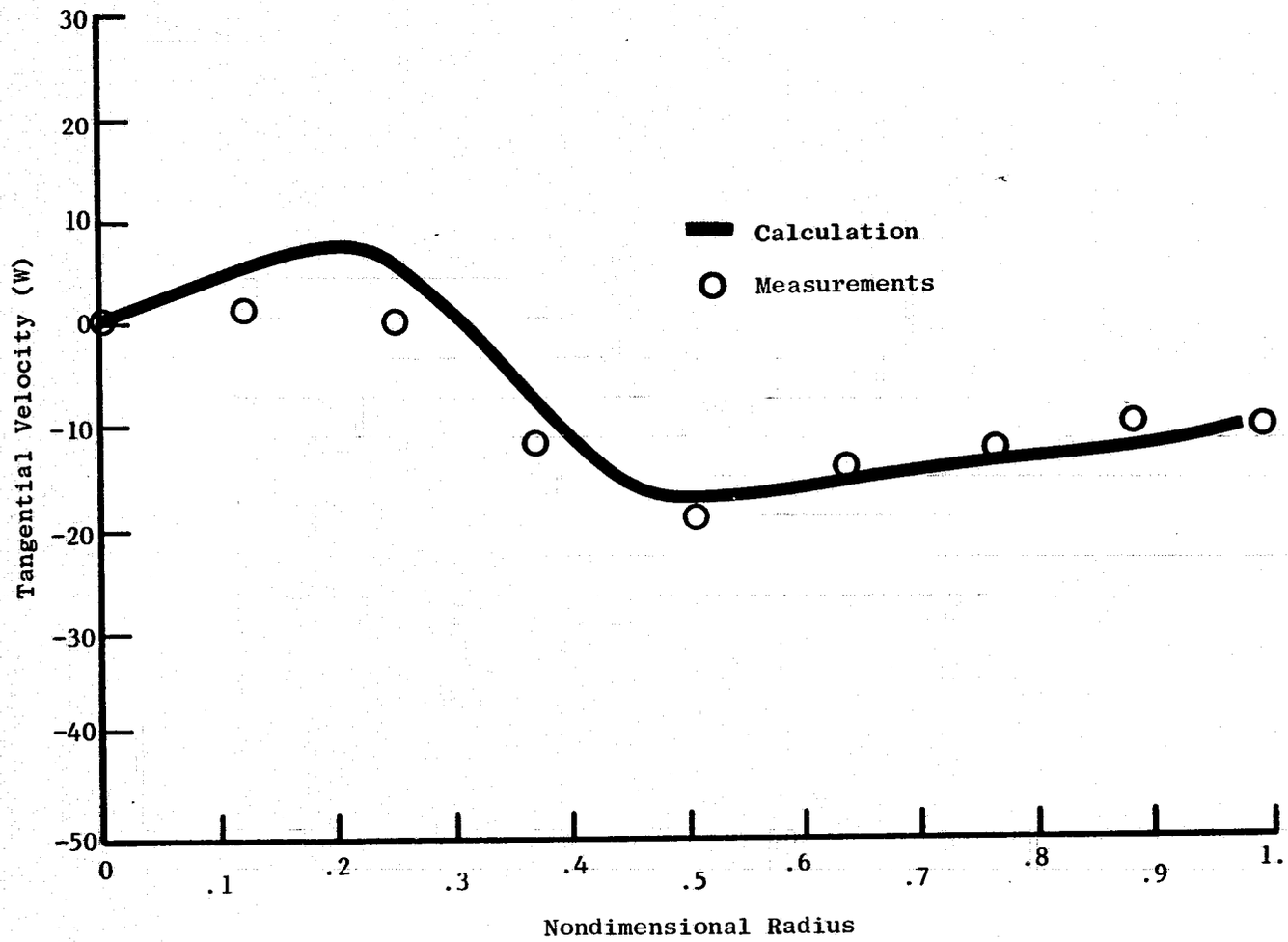
Figure 97. Centerline Profile of Axial Velocity for Counterswirl Flow, k-ε Model.

ORIGINAL PAGE IS
OF POOR QUALITY



ORIGINAL PAGE IS
OF POOR QUALITY

Figure 98. Radial Profile of Axial Velocity at Z/R_i = 3.15 for Counterswirl Flow, k-ε Model.



ORIGINAL PAGE IS
OF POOR QUALITY

Figure 99. Radial Profile of Tangential Velocity at Z/R_i = 3.15 for Counterswirl Flow, k-ε Model.

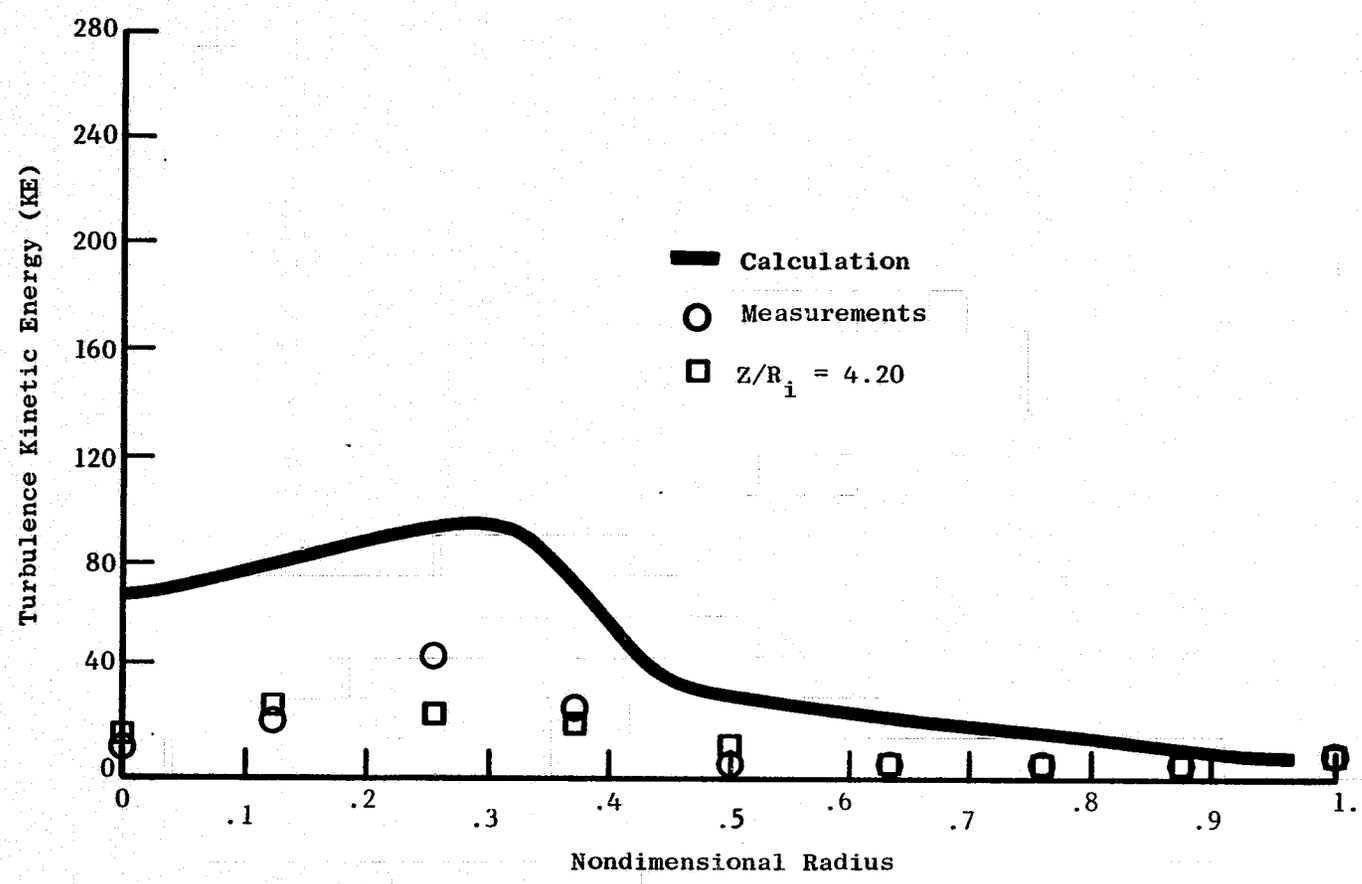


Figure 100. Radial Profile of Turbulence Kinetic Energy at $Z/R_i = 3.12$ for Counterswirl Flow, k-ε Model.

ORIGINAL PAGE IS
OF POOR QUALITY

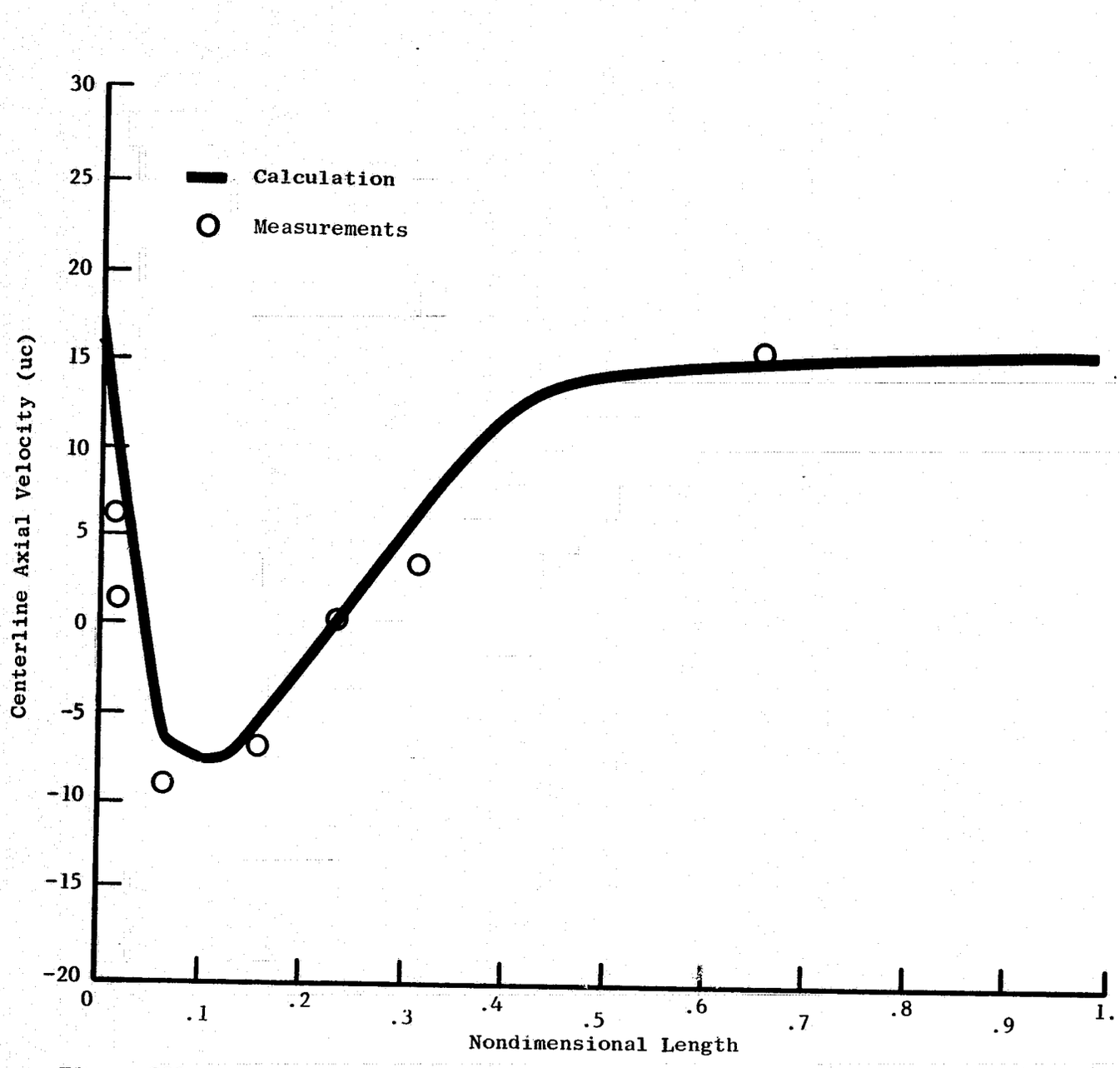


Figure 101. Centerline Profile of Axial Velocity for Counterswirl Flow, Algebraic Stress Model.

ORIGINAL PAGE IS
OF POOR QUALITY

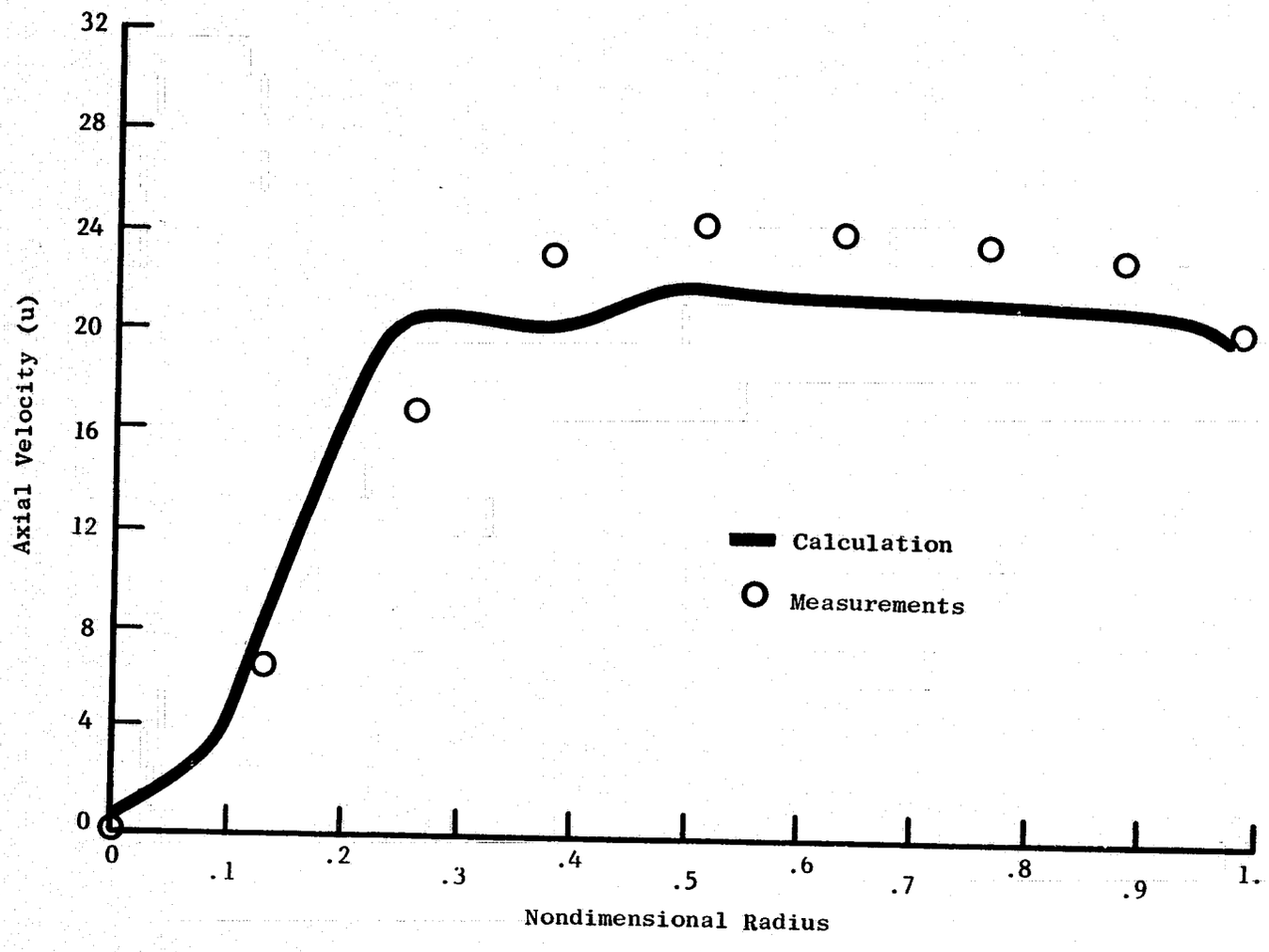
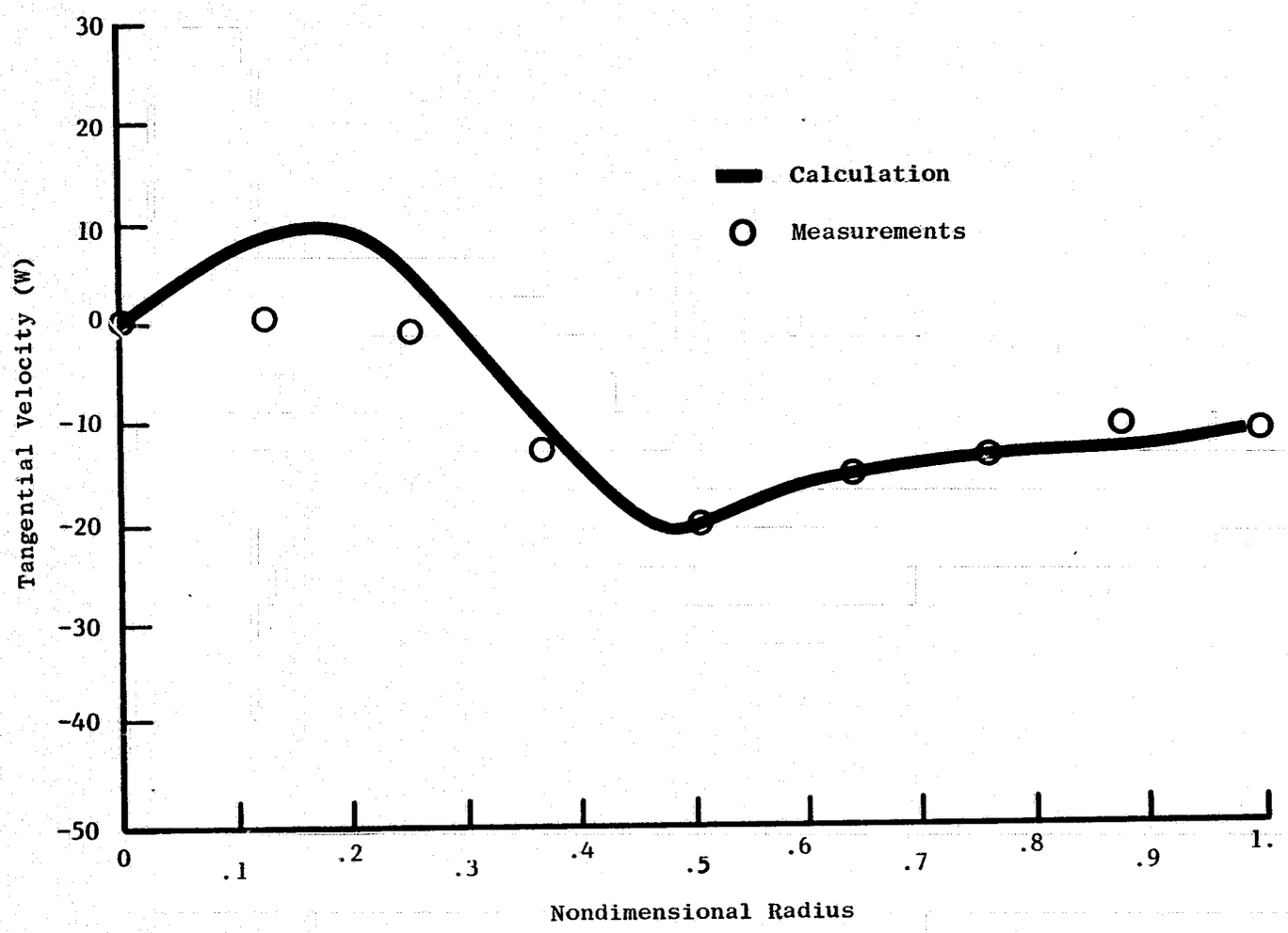


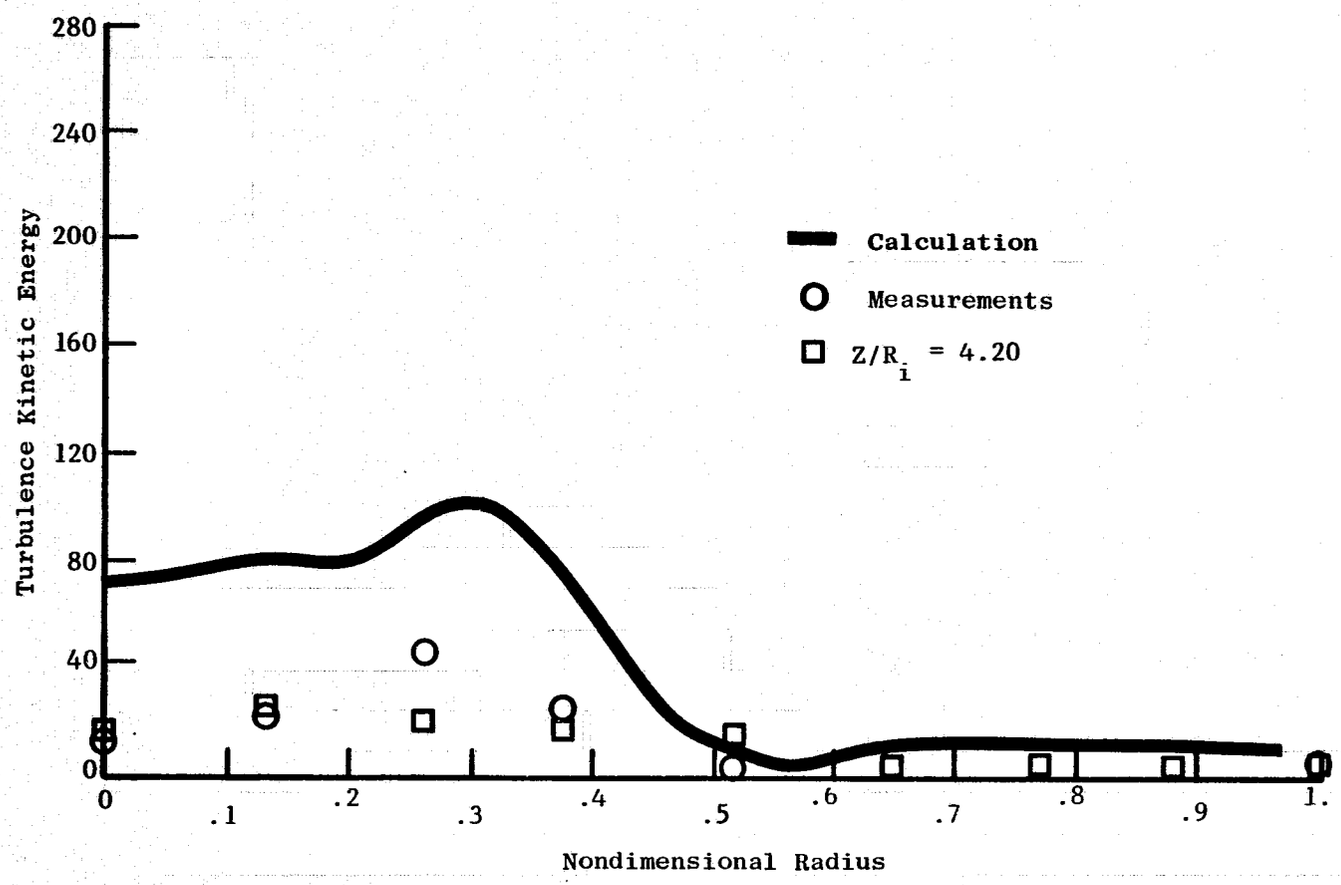
Figure 102. Radial Profile of Axial Velocity at Z/R_i = 3.15 for Counterswirl Flow, Algebraic Stress Model.

ORIGINAL PAGE IS
OF POOR QUALITY



ORIGINAL PAGE IS
OF POOR QUALITY

Figure 103. Radial Profile of Tangential Velocity at $Z/R_i = 3.15$ for Counterswirl Flow, Algebraic Stress Model.



ORIGINAL PAGE IS
OF POOR QUALITY

Figure 104. Radial Profile of Turbulence Kinetic Energy at Z/R_i = 3.12 for Counterswirl Flow, Alegebraic Stress Model.

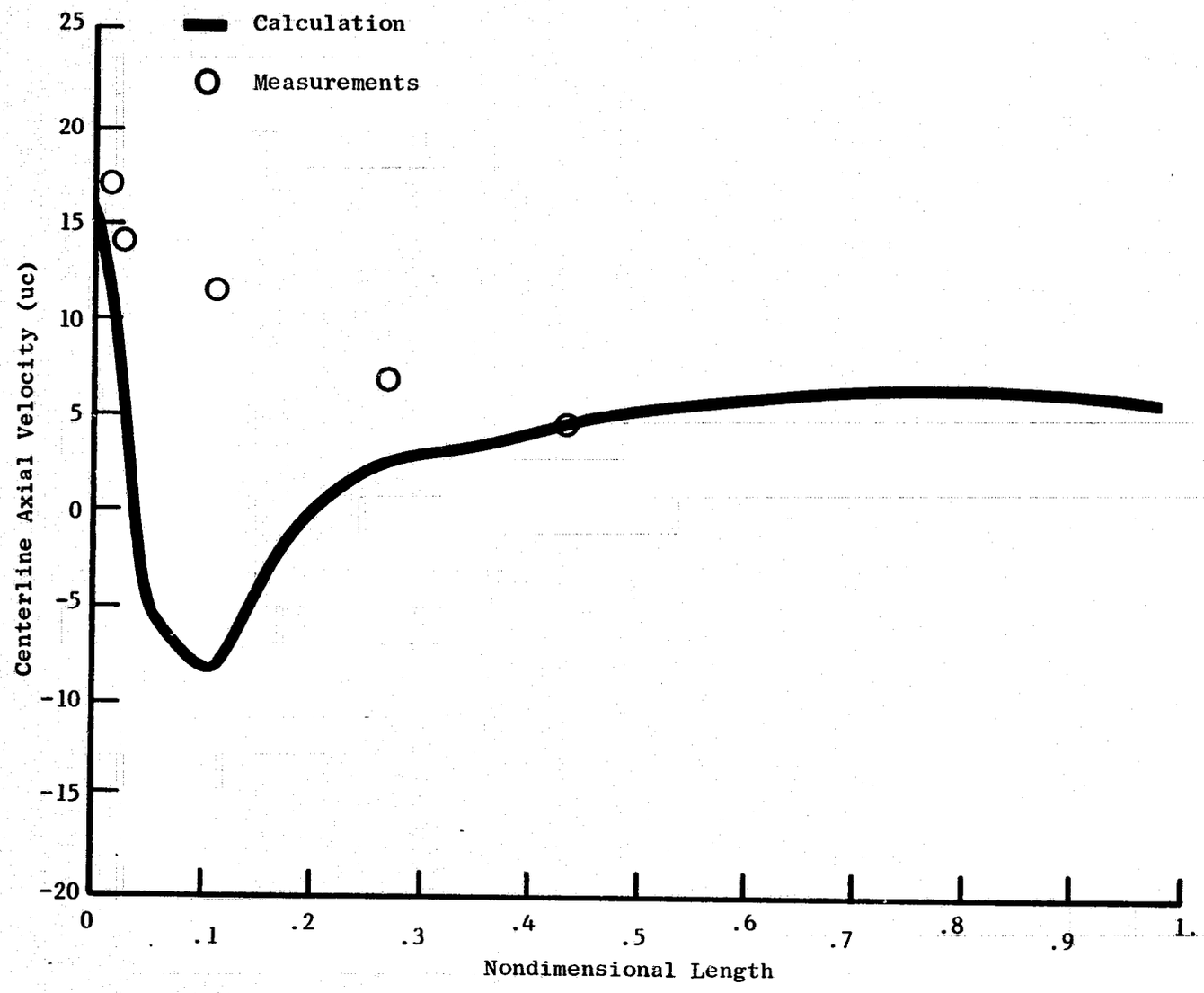


Figure 105. Centerline Profile of Axial Velocity for Coswirl Flow, Algebraic Stress Model.

ORIGINAL PAGE IS
OF POOR QUALITY

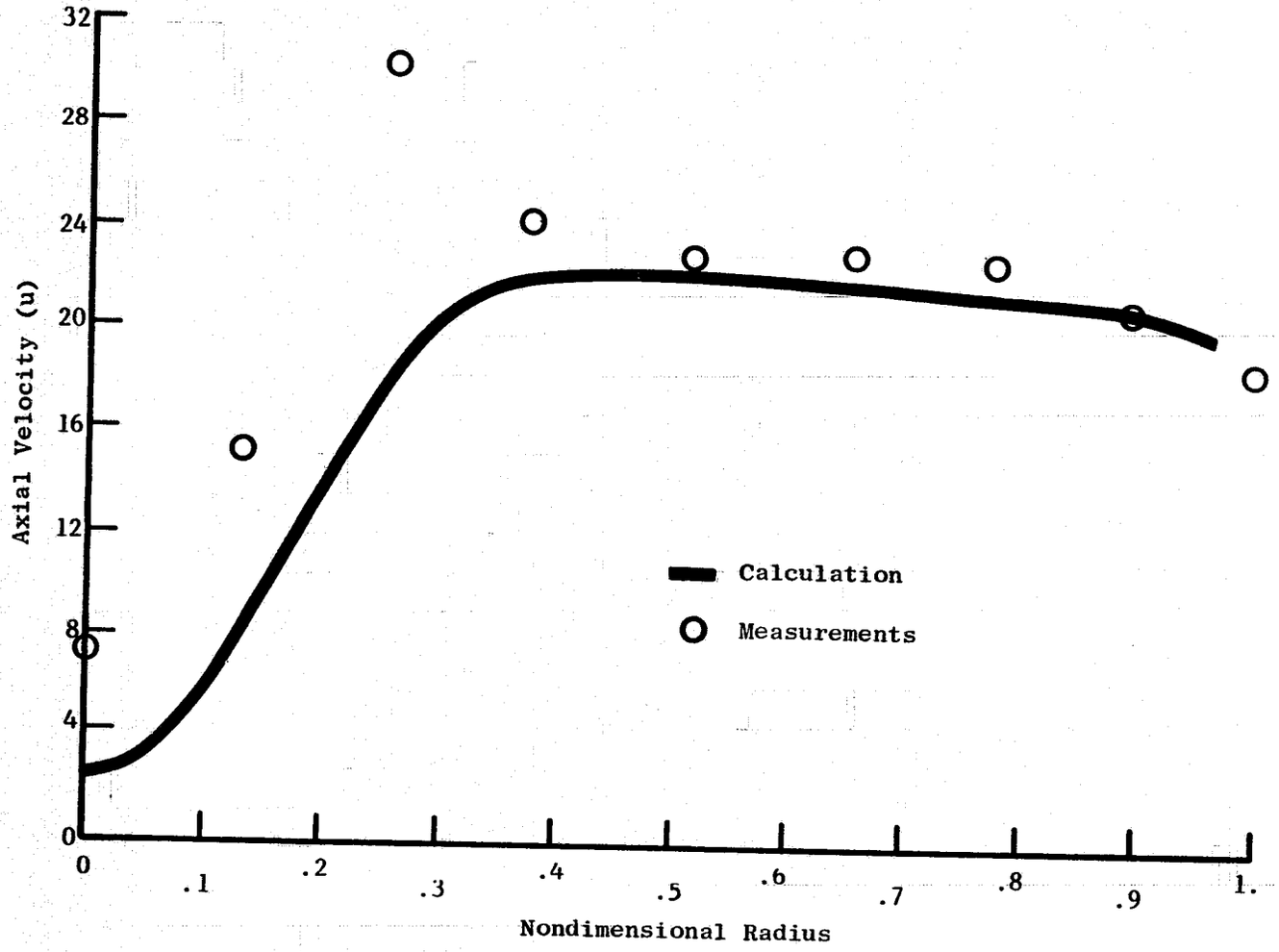


Figure 106. Radial Profile of Axial Velocity at Z/R_i = 3.67 for Coswirl Flow, Algebraic Stress Model.

ORIGINAL PAGE IS
OF POOR QUALITY

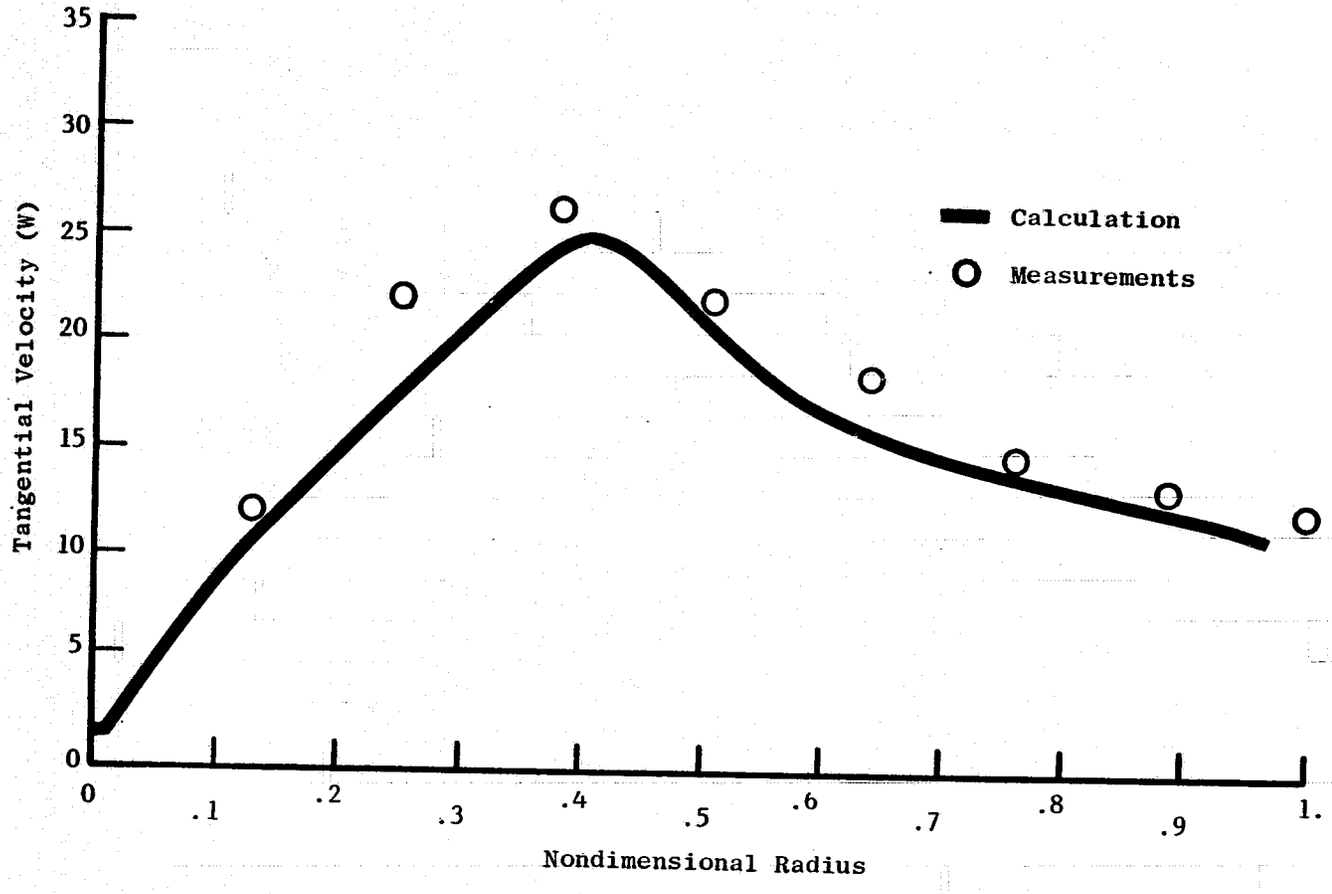


Figure 107. Radial Profile of Tangential Velocity at Z/R_i = 3.67 for Coswril Flow, Algebraic Stress Model.

ORIGINAL PAGE IS
OF POOR QUALITY

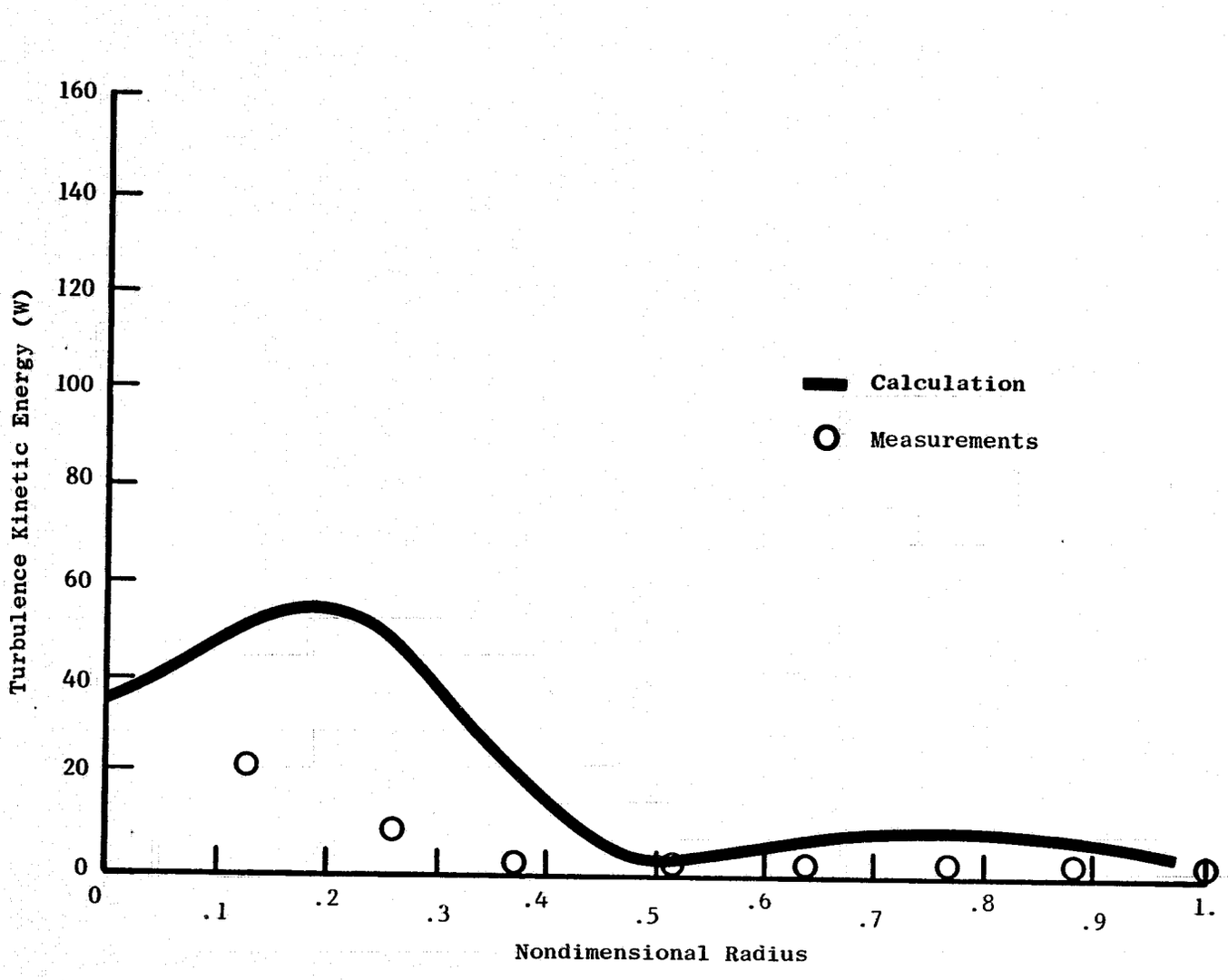


Figure 108. Radial Profile of Turbulence Kinetic Energy at Z/R_i = 3.67 for Coswirl Flow, Algebraic Stress Model.

ORIGINAL PAGE IS
OF POOR QUALITY

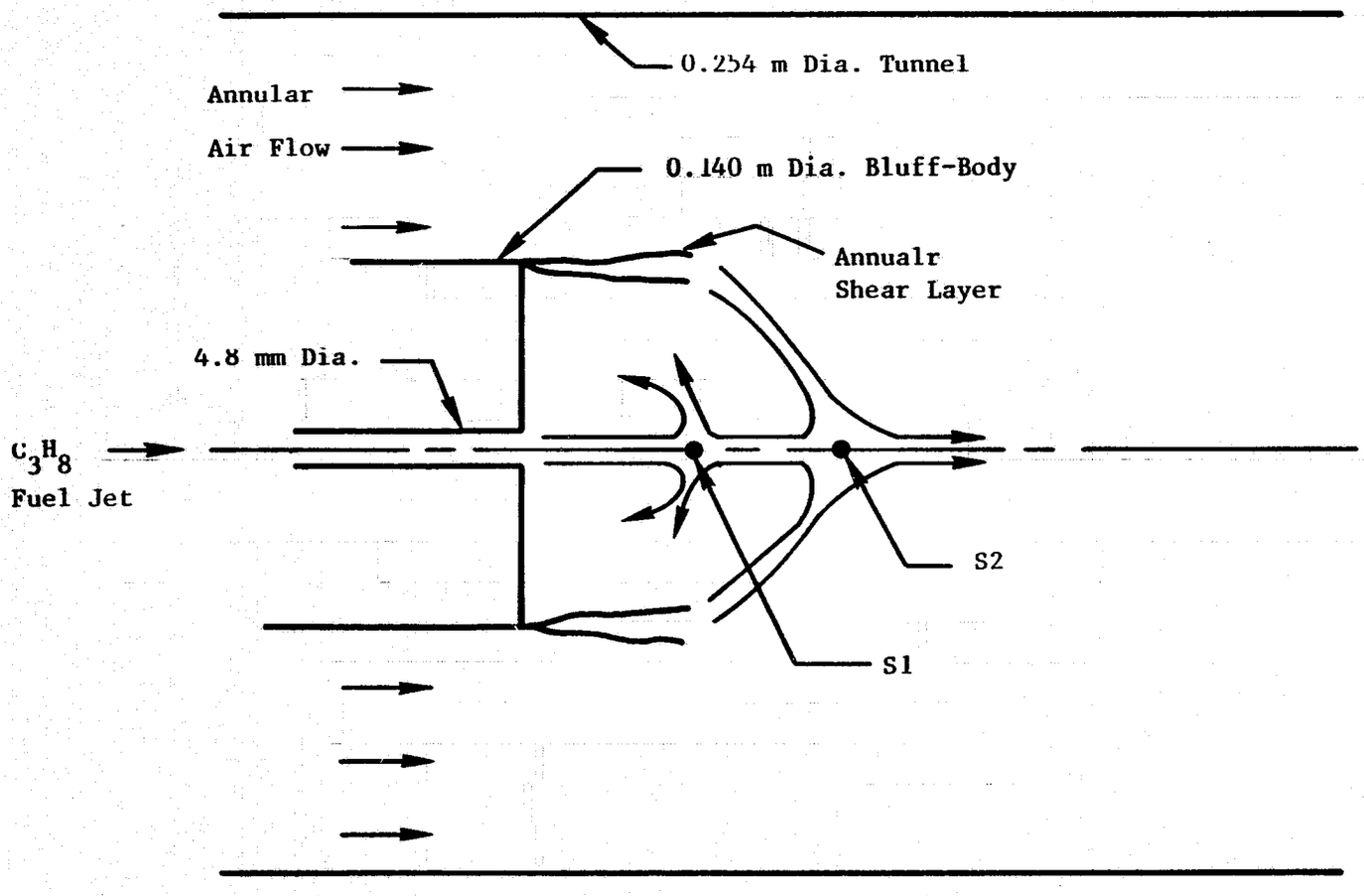


Figure 109. Schematic of AFAPL Combustor Showing Centerline Stagnation Points S1 and S2.

ORIGINAL PAGE IS
OF POOR QUALITY

(and so Reynolds numbers) to be attained. The recirculation itself is an important aerodynamic feature of the gas turbine combustor. Turbulence is complicated due to the presence of several length-scales and the fact that there is no strong gradient that predominates, unlike in a shear flow. Turbulence-chemistry interactions typical of a gas turbine combustor occur because of the hydrocarbon fuel used. Thus important physical aspects of the gas turbine combustor are duplicated.

The AFAPL combustor was run at a variety of annular airflow rates and central fuel jet flow rates. The fuel used was propane except for isothermal flow studies when CO_2 was substituted. LDV data on the mean and fluctuating components of velocity as well as thermocouple data on temperature are available. Coherent anti-Raman scattering data for mean and fluctuating species concentrations and temperatures were to have been taken but are still not available. This is very unfortunate because it prevents direct assessment of conserved scalar transport predictions which are key to the temperature and density predictions; the density field of course affects the entire flow field.

The qualitative nature of the flow has been discussed extensively in the literature, Roquemore, et al., 1980[90]. Briefly, three flow regimes were identified.

1. An annulus dominated regime (Figure 110) in which the annular airflow velocity (u_a) is large relative to the fuel jet velocity (u_f). The recirculation zone produced behind the bluff body is then strong enough to produce two on-axis stagnation points. The forward point S1 corresponds to the jet while the downstream point S2 coresponds to the air stream. In this flow regime an ellipsoidal flame is formed.

2. A transitional regime in which neither the annular flow nor the central jet dominated.

3. A jet-dominated flow in which there were no stagnation points along the axis. The flame appeared similar to a jet flame though the spread rate was large. In the last two regimes unsteady effects were very pronounced.

The bluff body stabilized diffusion flame is characterized by a narrow fuel jet, an annular shear layer and the lack of radial jets. These features are direct consequences of the desire for a simple, axisymmetric geometry and a nonpremixed flame. However, entirely aside from all concerns regarding unsteadiness, these simplifications introduce certain sensitivities atypical of gas turbine combustors. Development of the annular shear layer is of par- amount importance in the length of the recirculation zone. On the other hand, in a practical combustor the primary zone is terminated by the strong radial jets. This is another manifeststion of the difference between turbulence-dominated and pressure-dominated flows. Furthermore, the shear layer in the AFAPL combustor could contain large-scale structures important in that flow but not necessarily relevant to practical combustor flows.

ORIGINAL PAGE IS
OF POOR QUALITY

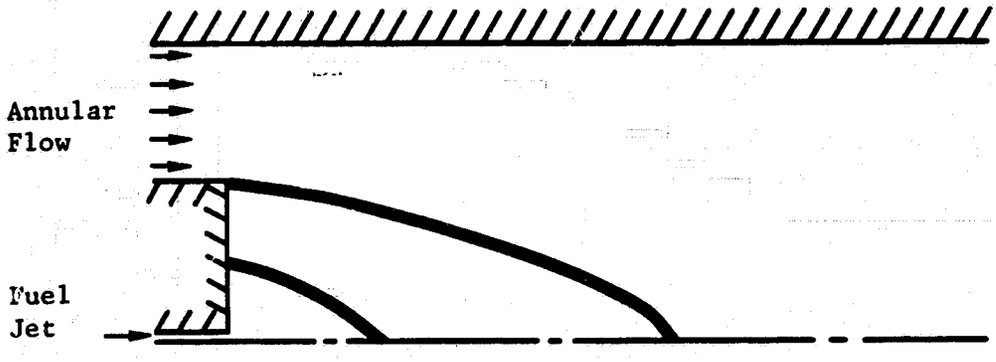


Figure 110. Dividing Streamlines from Baseline Simulation.

Another distinctive feature of the AFAPL combustor is the central fuel jet and its importance in determining the entire flow field. In itself the spread rate of round free jets requires a major modification of standard turbulence models to account for the hoop-stretching of vorticity and the consequential influence on the energy dissipation rate, Pope, 1978[110]. This heuristic modification cannot be implemented in a general recirculating flow. Thus one of the most important elements of the AFAPL flow -- the jet -- cannot be properly modeled. Of course, in the wake of the bluff body it is conceivable that the free jet physics are completely overwhelmed by other phenomena.

The central fuel jet has another modeling difficulty. Because its diameter is small compared with the tunnel, a highly non-uniform grid in the radial direction is required. For reasons of numerical accuracy a small expansion ratio in cell-to-cell dimension should be retained. This entails a large number of nodes. In the axial direction an increasing cell size is used so that the downstream boundary condition is far enough downstream. Thus, high downstream cell aspect ratios result, particularly along the centerline and in the shear layer. On the other hand, because of the two-dimensionality of the mean flow, it is possible to have a large number of nodes. The gas turbine combustor would be characterized by a more uniform grid with fewer nodes per dimension. One other feature of the jet is that it remains very fuel rich up to the stagnation point and so may not be in chemical equilibrium.

Finally, the instrumentation used in the AFAPL combustor can be questioned. The LDV technique is fairly reliable if seeding levels are uniform in both streams, otherwise, these biases affect the predictions. This is particularly important for predicting the location of the on-axis stagnation points. These locations are an important aspect of assessing the predictions. Thermocouple data for the mean temperature suffers from a problem discussed earlier in this report: the ambiguity between Favre-averaged and conventionally-averaged temperature. Furthermore, temperature is an indirect measure of the model since the primary dependent variables are mean and variance of mixture fraction. Temperature is obtained after a further assumption of the pdf shape. Thus, the temperature comparison is ambiguous (as to which average the data represents) and is a simultaneous assessment of the assumption of pdf shape, of the assumption of equilibrium and of the accuracy of calculated moments. It would be highly desirable to directly compare these ingredient assumptions and variables directly as was done for the turbulent jet diffusion flame, (Section 7.1.1).

Despite many reservations, the bluff body stabilized diffusion flame is an important benchmark flow on the way to reliable gas turbine combustor models. The AFAPL experiment is well-documented and the available and future data are geared towards modeling needs. Hence although some doubts remain, this flow was selected as perhaps the only such flow which could be modeled.

Computational Domain and Boundary Conditions

The governing equations for recirculating flow are mathematically elliptic so that downstream boundary conditions are required; these were taken to

be a pipe-flow, i.e., zero axial gradients of all dependent variables. The length of the computational domain thus becomes very important: if it is too short the premature tendency to attain pipe flow will affect the results. If it is too long then the extra nodes are essentially wasted in computing the flow. In this calculation the length of the domain was adopted as the shortest length which did not affect the calculated results (approximately 5-6 bluff body diameters).

The number and distribution of nodes in this domain were arrived at after an analysis of the numerical truncation error as described below. In the axial direction 51 nodes were used with a gradually increasing cell size. The lengths of successive cells increased in a geometric progression with a ratio of 1.05. In the radial direction, 36 nodes were used, clustered in the central jet and in the annular shear layer. This grid was held constant as a parametric study of the flow was made.

The choice of inlet conditions and a parametric study of their influence are included in following discussions of the AFAPL experiment.

Comparison of Predictions With Data

The numerical model was run for a baseline case consisting of an annular airflow rate of 2 kg/s and a central jet flow rate of 4 kg/hr. The predicted results were compared with the available data. For this simulation a baseline set of initial conditions was used as described below.

With the same flow rates a sensitivity analysis of the predictions to the initial conditions was then performed. These predictions in some cases showed improved agreement with the data but should not be used in any sense as the "optimal" runs.

Finally, with the baseline initial conditions, the central jet fuel flow rate was increased. Several runs were made until the predicted jet flow penetrated the recirculation zone. As discussed above, these runs encompass the unsteady flow regime and so detailed studies of the influence of initial conditions were not performed.

Baseline Case

Inlet conditions for the baseline simulation are shown in Table XVII. The jet flow is taken to be a turbulent pipe flow with an average exit velocity of about 46 m/s corresponding to the flow rate of 4 kg/hr. Turbulence kinetic energy in the jet exit plane is taken as 3% of the mean velocity squared while the dissipation rate is obtained from the inlet length scale, 3% of the tube diameter. The mean of mixture fraction is, by definition, unity while the variance is zero.

Table XVII. Flow Parameters and Initial Conditions for Baseline Simulation.

Jet	
Mass Flow Rate (Propane)	4 kg/hr
Temperature	400 K
Average Exit Velocity, $\overline{U}_f$	46.2 m/s
Turbulence Kinetic Energy	3% $\overline{U}^2$
Length Scale of Turbulence	3% Tube Diameter
Mean of Mixture Fraction	1
Variance of Mixture Fraction	0
Annulus	
Mass Flow Rate (Air)	2 kg/s
Temperature	300 K
Average Exit Velocity, $\overline{U}_a$	47.2 m/s
Turbulence Kinetic Energy	Measured Function of Radial Position
Lenght Scale of Turbulence	3% of Annulus Height
Mean of Mixture Fraction	0
Variance of Misture Fraction	0

Measured axial velocity and turbulence kinetic energy profiles are used as the initial conditions in the annulus. The dissipation rate again follows from an assumption of the length scale of approaching turbulence, taken as 3% of the annulus height. Finally, by definition, the mean and variance of mixture fraction are both zero in the annular gap.

The recirculation zone formed in the wake of the bluff body is evident from Figure 111. When centerline mean axial velocity is compared with LDV data, the predicted first stagnation point (S1) is too near the bluff body while the second (S2) is too far. Compared with the isothermal case, the predicted stagnation points are further downstream, which agrees with the experimentally observed trend.

Contours of turbulence kinetic energy (Figure 112) show that the turbulence is generated at the edge of the jet and in the annular shear layer. The peak occurs well downstream of the edge of the bluff body. Data are not available for the AFAPL experiment but a downstream shift between isothermal and combusting flow was observed by Taylor, 1981[85] in a series of disk- and cone-stabilized flows. A comparison along the centerline (Figure 113) correctly shows the higher levels of turbulent kinetic energy that were found in the combusting experiments compared with the nonreacting experiments, but there is no peak at the location of the first stagnation point. Notice that the model predicts Favre-averaged velocity and turbulence kinetic energy while the LDV data as presented gives the unweighted average.

The discrepancies between the data and the predicted mean velocity and turbulence fields are due to several different reasons. Some of these apply to the isothermal flow as well, where also the predicted centerline reverse flow region is larger than measured, Sturgess and Syed, 1982[111].

An important feature of this flow is the central jet and the rate at which it spreads. This spread rate clearly affects the location of the first stagnation point S1. However, the spread rate of even a free axisymmetric jet is a notoriously difficult modeling problem. Although the two-equation turbulence model can correctly predict the plane shear flow, it predicts that the spread rate of a round jet is higher than for the plane jet. The opposite trend is observed experimentally. Pope, 1978[110] has speculated that the difference between the two flows is the hoop stretching of vorticity in the axisymmetric case. This vortex stretching coupled with the conservation of angular momentum decreases the width of the vortex. Thus, the round jet has a greater scale reduction which leads to an enhanced spectral energy transfer and so augments the rate of dissipation. Modification of the k-ε model to account for this process results in the correct spread rate. However, Taylor, 1981[85] has pointed out that the model cannot be employed in recirculating flows because there the constraint of realizability may be violated. Realizability demands that

$$\frac{D\varepsilon}{Dt} \rightarrow 0 \quad \text{as} \quad \varepsilon \rightarrow 0 \tag{92}$$

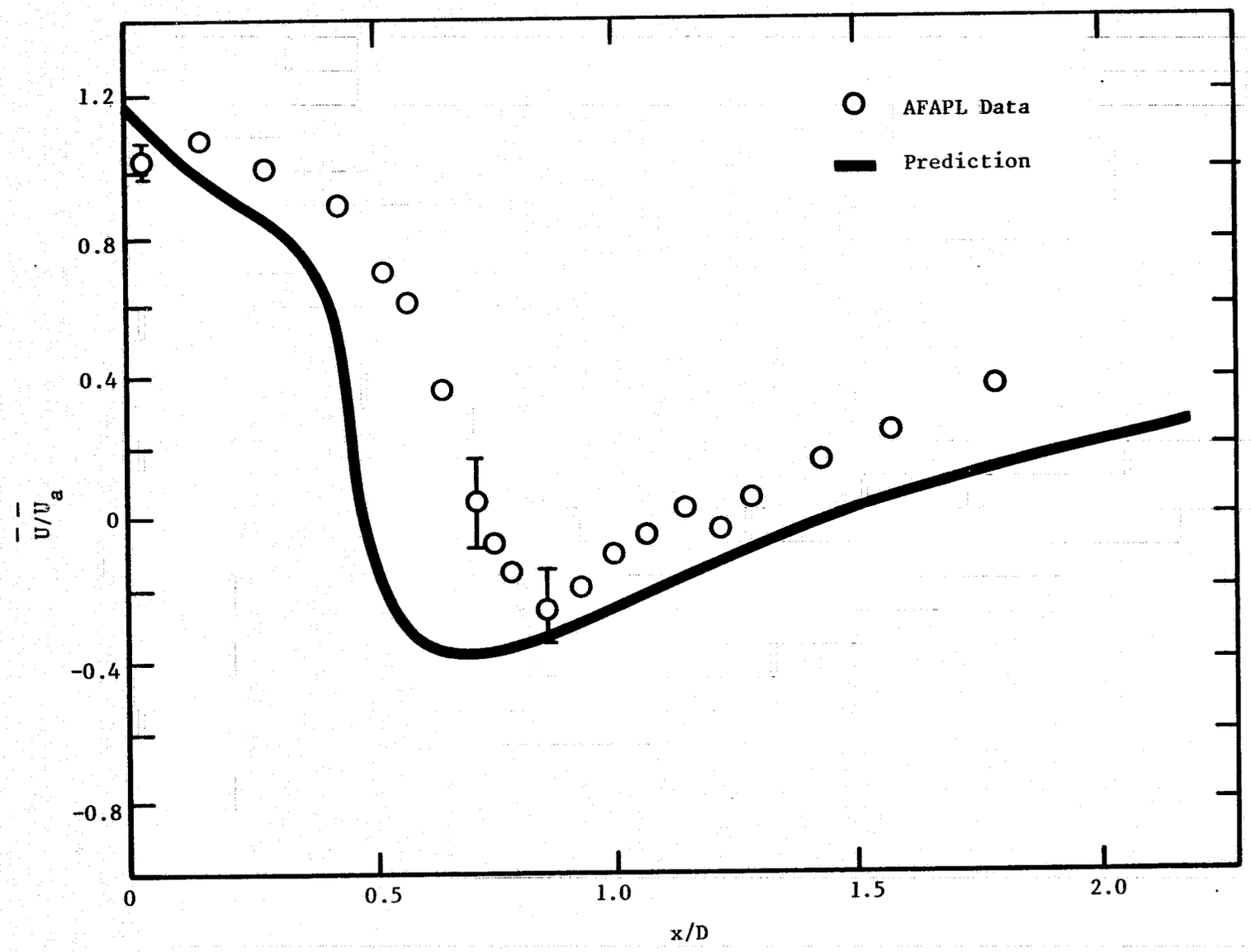


Figure 111. Centerline Axial Velocity.

ORIGINAL PAGE IS
OF POOR QUALITY

ORIGINAL PAGE IS
OF POOR QUALITY

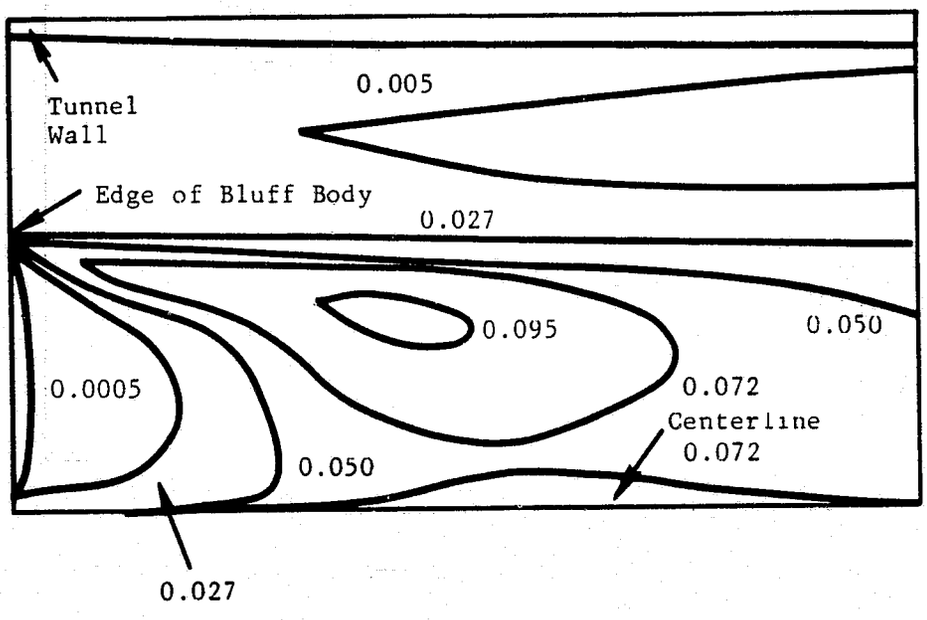


Figure 112. Contours of Turbulence Kinetic Energy ($k/\bar{u}_a^2$).

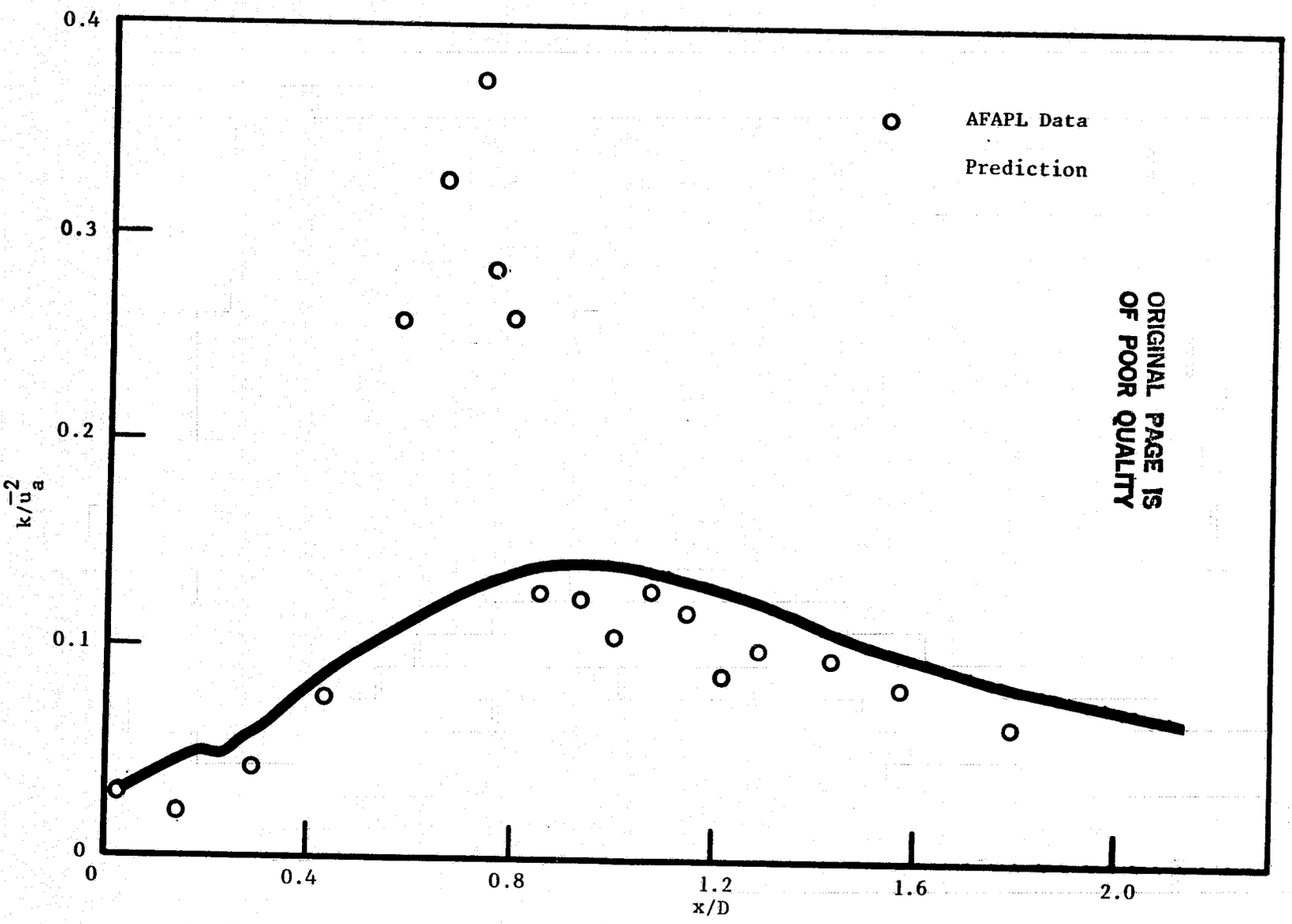


Figure 113. Centerline Turbulence Kinetic Energy.

However, the additional source term has the factor v/ε which does not go to zero with ε. If the radial velocity is negative (which does not occur in the jet) this will result in nonphysical negative dissipation rates.

Thus, although the spread rate of the jet has a significant influence on the entire flow, the preferred model for the free jet cannot be implemented. This possible source of error therefore remains in the model and can be removed only if the geometry of the combustor is changed. It may be noted that the process of vortex stretching described above is not expected to be as significant in the gas turbine combustor.

Other sources of error in the turbulence model which contribute to the total error include:

a. The failure to correctly account for normal stresses and the normal stress-normal strain generation of turbulence kinetic energy known to be important at free stagnation points

b. The assumption of isotropic eddy viscosity

c. The implicit assumption that turbulence at any location has a single length-scale

d. The assumption of local equilibrium of turbulence

e. The assumption that the isothermal turbulence model closures can directly be used in the density-weighted model

f. The failure to account for convection of Reynolds stresses

g. The gradient diffusion closure for turbulent correlations.

These points have been discussed at greater length in the formal analysis of the turbulence model.

In isothermal confined flows, the effect of inaccurate turbulence modeling is often dominated by the mean pressure gradient in the momentum equations. However, in a combusting flow the time scale for dissipation of compositional fluctuations and the diffusivity of mean ($\tilde{\xi}$) and variance ($\tilde{\xi}''^2$) are obtained from the k and ε equations. Furthermore, $\tilde{\xi}$ and $\tilde{\xi}''^2$ are used to generate the density field which "drives" all the equations. The turbulence model is therefore more consequential in the combusting flow.

Contours of mean and variance (Figures 114 and 115) show that the flame forms a closed ellipsoidal shape as observed. The stoichiometric contour ($\tilde{\xi} = \xi_s \approx 0.06$) gives the time-mean position of the flame which is bounded by those locations where approximately

ORIGINAL PAGE IS
OF POOR QUALITY

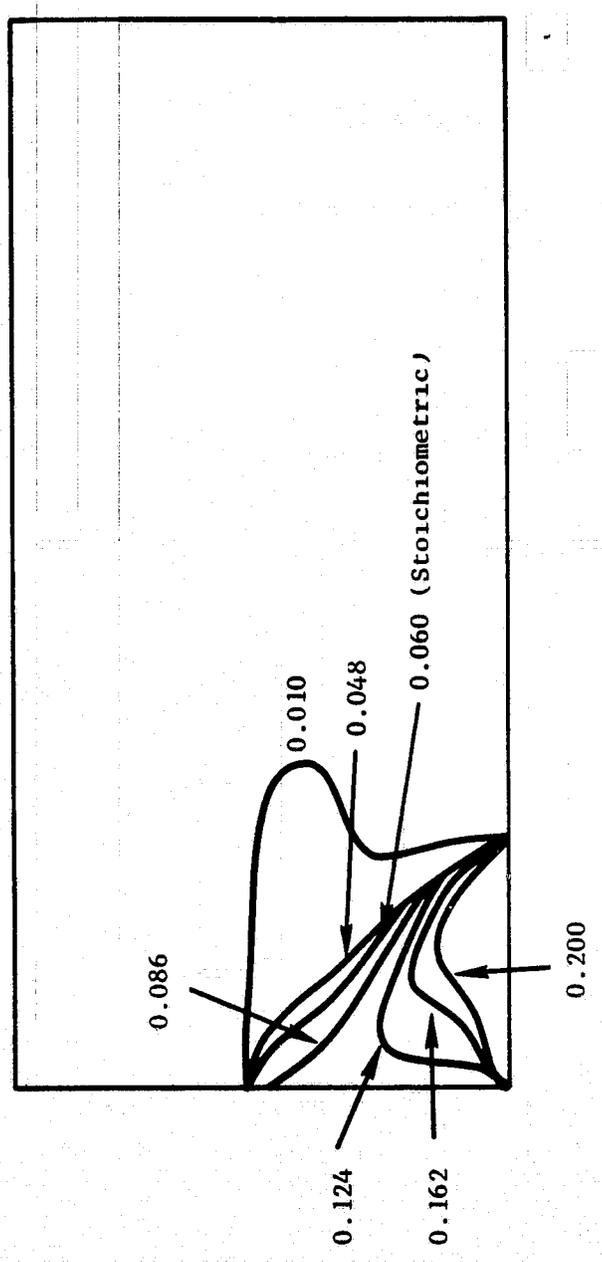


Figure 114. Contours of Mean Mixture Fraction.

ORIGINAL PAGE IS
OF POOR QUALITY

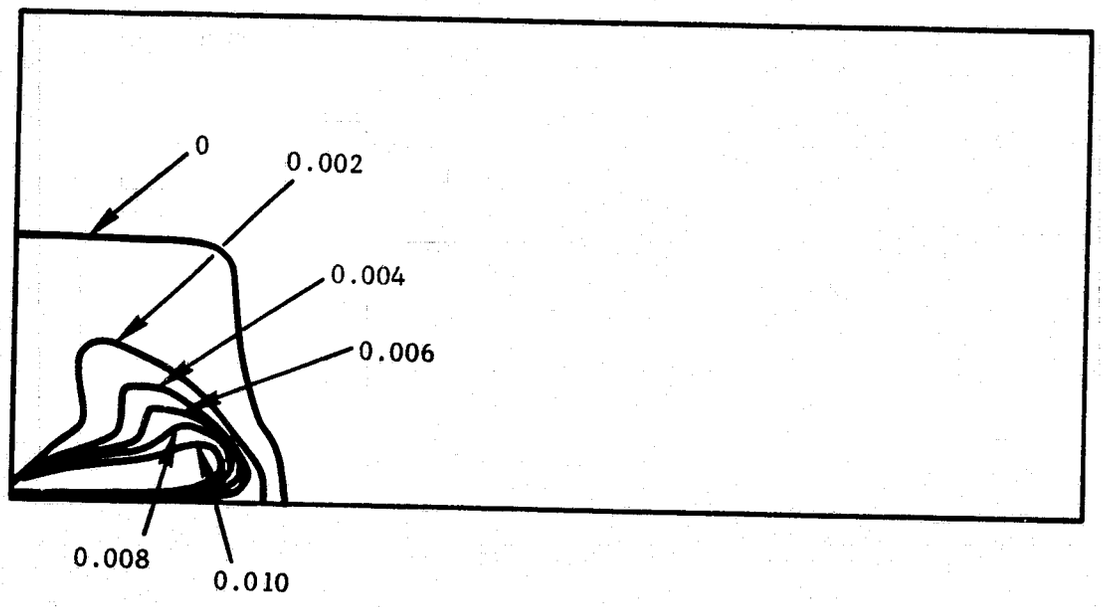


Figure 115. Contours of Variance in Mixture Fraction.

$$\tilde{\xi} + 3(\tilde{\xi}''^2)^{1/2} \geq \xi_{lean}$$

$$\tilde{\xi} - 3(\tilde{\xi}''^2)^{1/2} \leq \xi_{rich}$$

Notice that this is just a physical interpretation of the results; the model actually has a continuous variation of $\tilde{\xi}$, $\tilde{\xi}''^2$ and so of temperature T. The "flame" is just an a posteriori concept.

Since no data for mean and variance are available in this flow the contours cannot be assessed in any detail. Such data would indicate among other things the validity of the gradient diffusion assumption and the influence of pressure-gradient correlations in the recirculating flow.

A radial density-weighted temperature profile in the recirculation zone shows general agreement with thermocouple data (Figure 116). As explained earlier in this report, the temperature is a derived quality which involves assuming the shape of the pdf, taken here as a β function. Intermittency is known to cause "spikes" in the pdf; the spikes are located at $\xi = 0$ near the air stream and at $\xi = 1$ near the fuel stream. In the annular shear layer this might explain why the predicted temperature gradient is steeper than measured. Intermittency has been recognized in free combustion jets, Drake, et al., 1983[104], by assuming that the total pdf is composed of a delta-function plus a continuous part which represents the turbulent flow. The relative contributions were empirically based on free jet data and so could not be used here. Near the jet, intermittency is less significant; near stoichiometric, values of ξ (0.06) are not expected to occur, and so the temperature fluctuations will not be as large. The overprediction of centerline temperature may be due to assuming instantaneous chemical equilibrium. The fuel-rich and, therefore, relatively cool jet is probable kinetically limited. This finding that fast chemistry is appropriate except in rich regions agrees with results from the three-dimensional sector combustor of Toral and Whitelaw, 1982[32].

Another potentially significant source of error in the calculation is the use of first-order upwind differencing in the regions where the absolute cell Peclet number exceeds two. As explained earlier, this is done to preserve diagonal dominance in the coefficient matrices. For lower Peclet numbers central differencing, which is second-order accurate, is used. Thus, numerical diffusion errors must be suspected in the regions indicated in Figures 117 and 118. However, $(Pe) \geq 2$ merely indicates that first-order upwinding is being used and not that the truncation error is large. For example, the east-west Peclet numbers are large in the jet, in a lobe within the recirculation zone, and again outside the recirculation zone. In the jet region first-order upwinding in the axial direction is perfectly acceptable because the jet is in fact convection-dominated. Therefore, the magnitude of the truncation error must be assessed, not merely the fact that it exists.

ORIGINAL PAGE IS
OF POOR QUALITY

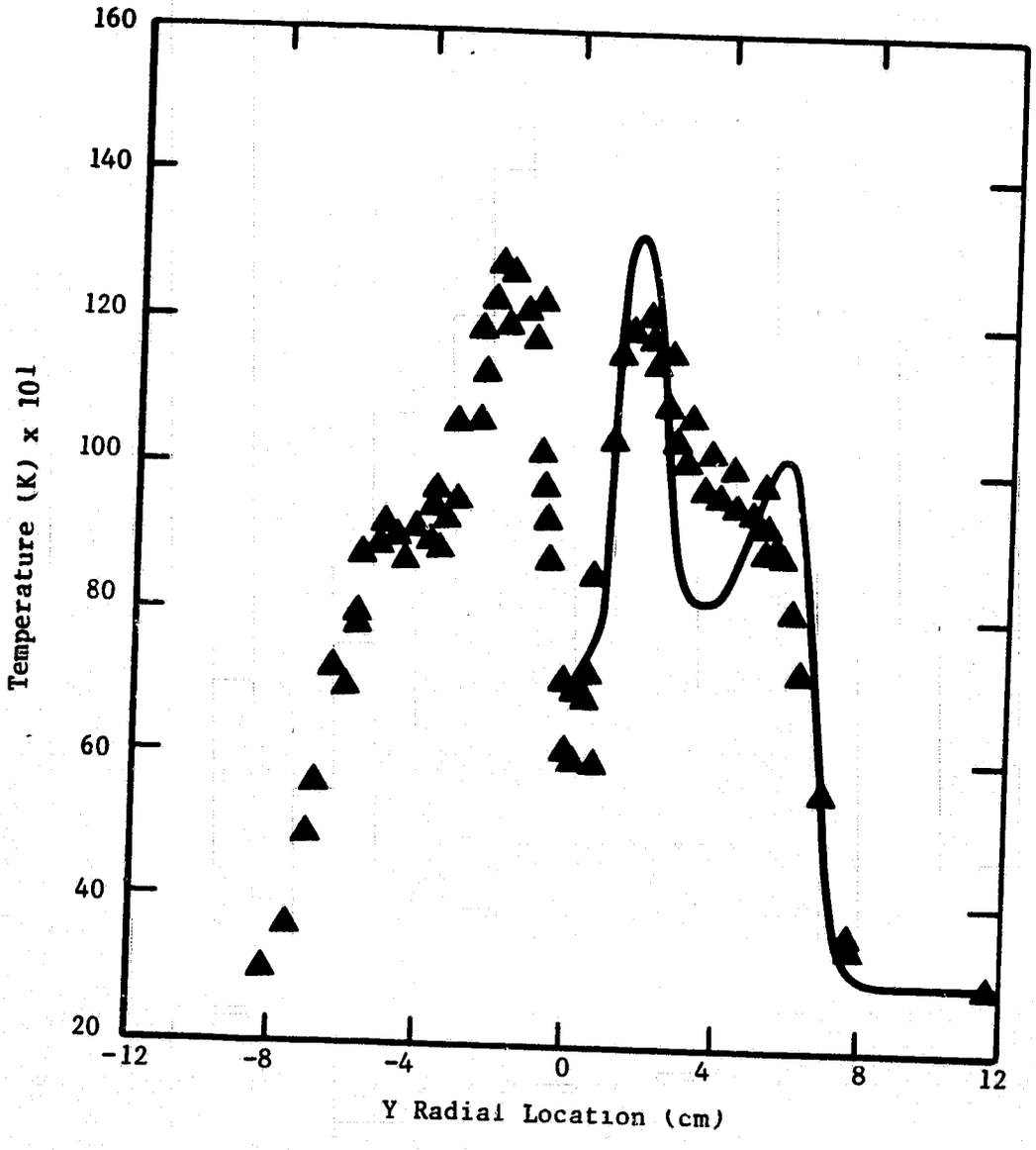


Figure 116. Radial Temperature Profile at X/D = 0.43.

ORIGINAL PAGE IS
OF POOR QUALITY

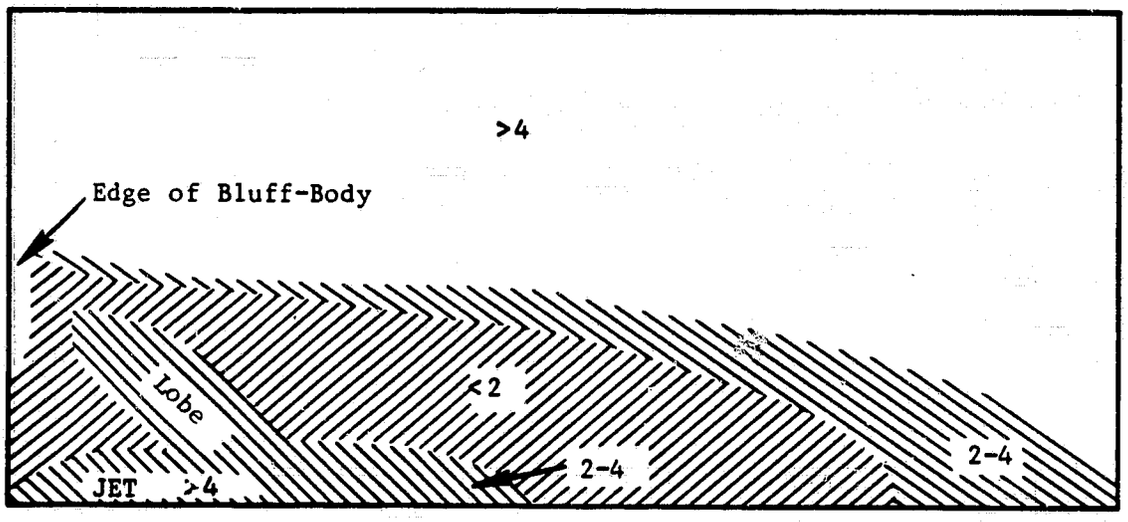


Figure 117. Absolute East-West Cell Peclet Numbers.

ORIGINAL PAGE IS
OF POOR QUALITY

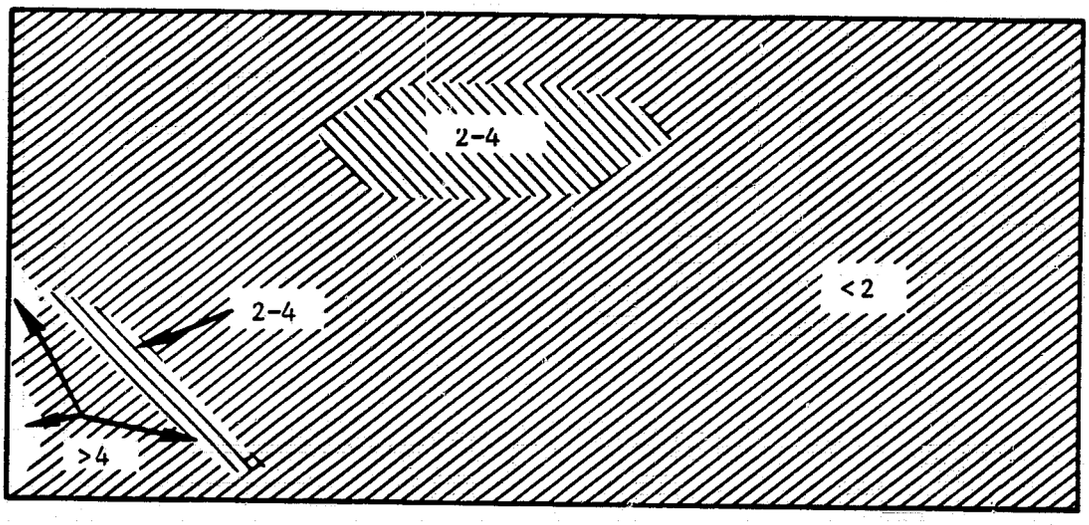


Figure 118. Absolute North-South Cell Peclet Numbers.

There are two ways to quantify the truncation error. The first is due to de Vahl Davis and Mallinson, 1976[54] who showed that both the cell size (δx by δr) and grid-to-streamline skewness (angle α) contributions to the error are given by

$$\mu_{numerical} = |\vec{V}|\delta x\ \delta r \frac{|\sin 2\alpha|}{4(\delta r|\sin^3\alpha| + \delta x|\cos^3\alpha|)} \qquad (93)$$

where $\vec{V}$ is the velocity. This analysis showed that the largest errors occurred in the lobe region where the skewness is a maximum. It should be noted that the analysis only compares numerical viscosity to turbulent viscosity. It cannot assess whether the turbulent viscosity itself is important at any point in the flow.

A more sophisticated analysis following McGuirk, et al., 1981[58] compares the various terms in the finite difference equation with the second-order truncation error. This analysis also indicated that the numerical diffusion error was insignificant except in the lobe. To increase the accuracy of the calculation, the well-known QUICK scheme, Leonard, 1979[57], was applied, first in the momentum equations only and then in all the equations.

The QUICK scheme has been described and analyzed earlier in this report. When it was applied to the momentum equations there was virtually no change in the predicted results. This is because the initial calculation itself was largely free from the second-order errors. Many previous users of the QUICK scheme have been restricted to the momentum equations. However, McGuirk, et al., 1981[58] have shown that numerical diffusion errors can occur in the k and ε equations as well. Furthermore, the ξ equation is homogeneous and so numerical diffusion will certainly affect the solution. This is true also for the ξ''^2 equation though in some regions the source terms for variance are large (depending on the gradient of the mean). However, attempts to use the QUICK scheme in these equations also lead to oscillations in the solutions and to nonphysical values for denpendent variables, e.g., negative variance.

Although in this calculation selective grid densification ensured that numerical diffusion was not a major source of error, the same will not be true for a general three-dimensional flow. Refined grids, truncation error analysis, and repeated runs will be too time-consuming and costly. Thus, a stable and accurate differencing scheme for the convection term will be required.

Variation of the Boundary Conditions

Annulus and jet exit velocity, turbulence kinetic energy, and dissipation rate are required inputs for the model. Although measurements or reasonable guesses are available for most of these, it is worthwhile to study their influence on the predictions.

In the baseline simulation there was no radial component to the annulus inlet flow. When this condition is modified by taking the radial velocity to be

$$\overline{v} = -5\% \, \overline{u} \tag{94}$$

the second stagnation point moves about 6% closer to the bluff body while the first stagnation point is unaffected. This causes better agreement with the data but cannot be used to replace the baseline simulation unless radial components are in fact measured. The levels of TKE are unaffected except on the bluff body face so that the extra strain appears insignificant.

When the inlet turbulence length-scale in the annulus is halved to 1.5% of the annulus height, both the stagnation points move away from the bluff body. Because the inlet dissipation rate is effectively doubled, the upstream levels of TKE are reduced, leading to less radial transport across the annular shear layer. By about 1.5 bluff body diameters downstream, the radial TKE profiles are about the same as in the baseline case. This sensitivity is unfortunate because length-scale boundary conditions will entail two-point or autocorrelative measurements in the annulus.

Varying the inlet turbulence level in the jet does not alter the predicted stagnation points. The shear-generated turbulence at the edge of the jet essentially dominates the initial condition.

Higher Fuel-Flow Rates:

On increasing the jet exit velocity the stagnation points S1 and S2 were observed to move away from the bluff body until at a flow rate of about 8 kg/hr the jet penetrates along the centerline. The model, with the baseline initial conditions, was used to study these higher fuel-flow rates. The stagnation points do move outward although the underprediction of S1 remains (Figure 119). By monitoring the minimum centerline axial velocity as a function of the jet exit velocity (Figure 120), the breakthrough point can be estimated. The predicted breakthrough flow-rate of about 12 kg/hr is much higher than the observed 7-8 kg/hr.

The agreement between theory and data deteriorates as the jet velocity increases. In the transitional regime where neither the jet nor the annulus flow dominates, unsteady effects due to acoustic resonance, inflow perturbations or heat-release feedback phenomena may make the predictions very inaccurate. For the higher central jet velocities, the flow indeed does exhibit distinct axial slugs of flame, named "turbules, Roquemore, et al., 1982[112], which convect downstream. The axial velocity in the turbules, which were present about 74% of the time, is much greater than in the intervening nonluminous regions, Magill, et al., 1982[113]. The flow is, therefore, unsteady with the possibility of intermittent jet penetration.

ORIGINAL PAGE IS
OF POOR QUALITY

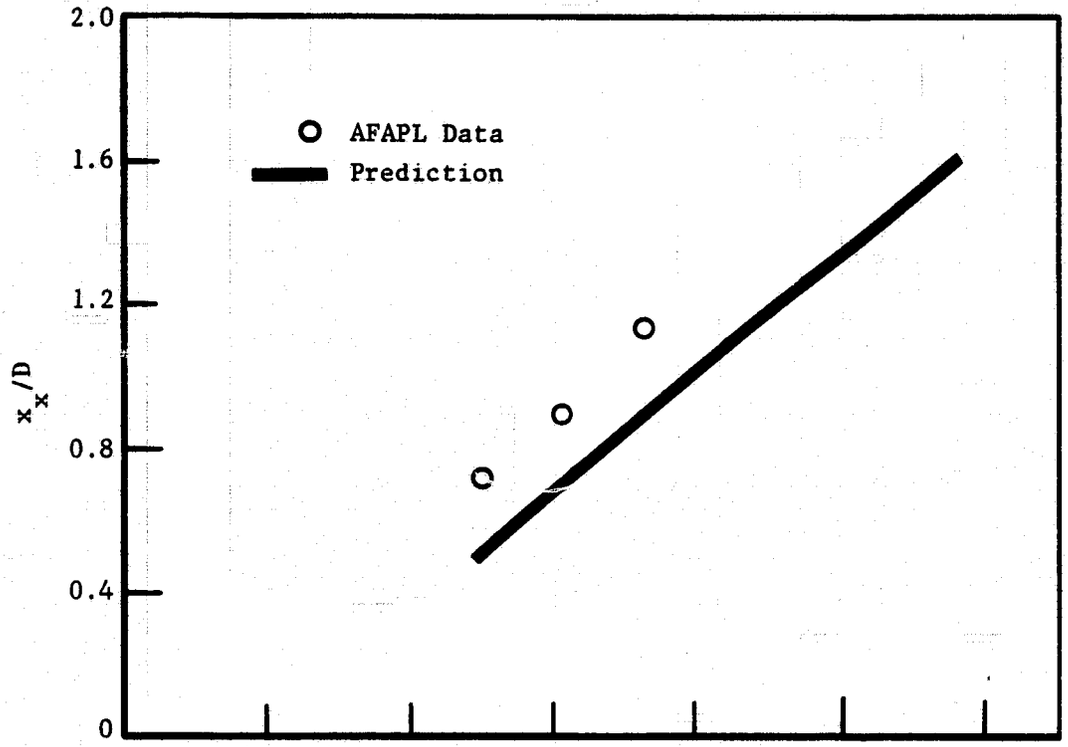


Figure 119. Location of First Stagnation Point for Higher Jet Velocities

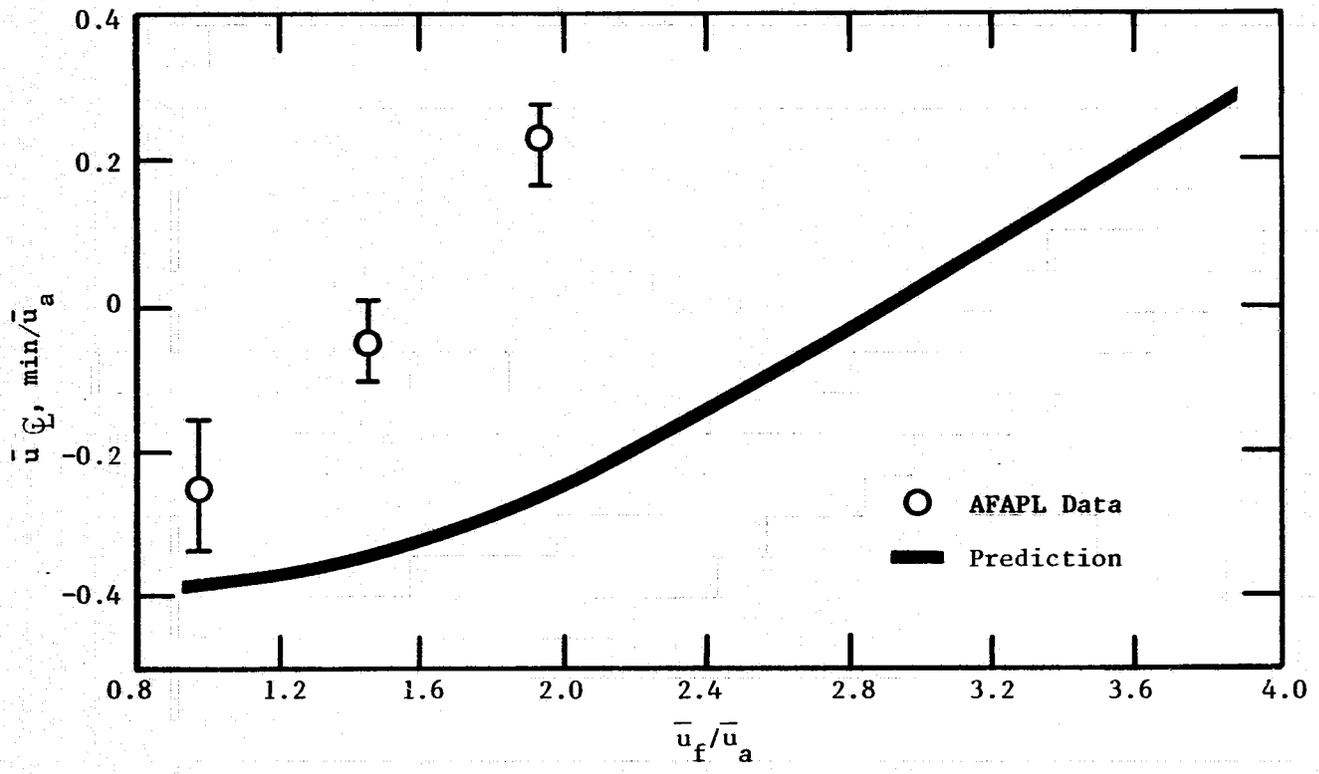


Figure 120. Minimum Centerline Axial Velocity for Higher Jet Velocities

ORIGINAL PAGE IS
OF POOR QUALITY

While the current model accounts for random fluctuations in velocity and concentrations, periodicity is not addressed. Any "coherent" structures in the flow thus compromise the accuracy of the predictions. Such structures can be acoustically excited in the annular shear layer, Corres and Pitz, 1982[114], and change the structure of the flow. Whether they are significant in practical combustors and must therefore be included in numerical models is not entirely clear at present.

Conclusions

Modeling the AFAPL combustor permits certain aspects of an eventual gas turbine combustor model to be assessed. Although general agreement with the measurements is obtained, there are some significant discrepancies. These may be divided into two categories: some are particular to this flow field while the others are of general significance.

Flame stability in the AFAPL experiment is obtained by the recirculation of hot combustion products in the wake of the axisymmetric bluff body. Simplification of the geometry, however, makes the entire flow very sensitive to the development of the annular shear layer. Periodic behavior and intermittency in the shear layer will affect the local temperatures and densities and the overall recirculation zone length. Another atypical aspect of the combustor is the sensitivity to the fuel jet. Proper prediction of the spread rate of round free jets is known to require a modification to the k-ε model. In the AFAPL combustor, an error in the jet spread affects the stagnation points and therefore the entire flow field.

On the other hand, some general conclusions regarding the model may be drawn:

1. The k-ε model performs about as well as in isothermal flows. The predictions show that the peak levels of TKE occur further downstream than in the isothermal flow which is supported by data from another experiment.

2. Contours of mean and variance of scalar fluctuations show that the flame has a closed, ellipsoidal shape as observed. Together with the predicted temperature field, this emphasizes the appropriateness of the turbulence-chemistry interaction model.

3. Radial temperature profile predictions are perhaps affected by neglect of intermittency in the annular shear layer.

4. Numerical diffusion errors have largely been avoided by concentrating the grid near the bluff body. In a three-dimensional flow with radial jets, the entire computational domain would have to be centrally-differenced to obtain results of equivalent quality, which does not currently appear practical. Thus a reliable, i.e., "wiggle-free", numerical scheme is desired as an alternative to first order upwind differencing.

5. The importance of having the boundary conditions in order to assess the performance of the numerical model is reiterated. In practical gas-turbine combustor flows, this involves the fuel swirl-cup exit flow and the dilution jet flows.

6. Theory-data discrepancies are larger for the higher jet exit velocities. The unsteadiness observed in the jet-dominated flow regime becomes increasingly significant. This effect of periodicity is not accounted for.

7.2 ASSESSMENT OF THE 3-D INTERNAL FLOW MODEL

Assessment studies of the usability of the 3-D elliptic internal flow model were conducted using calculations of experimental test results selected from the available literature, and generated as part of the overall Phase I program. The general purpose of these studies was to learn how to apply the model, assess its capabilities, and identify deficiencies in the model which limit its application as a combustor design tool. Detailed studies of the numerics and physical submodels of the kind performed with the 2-D codes were not done here. The majority of this effort involved calculations of dilution in a crossflow. For these calculations, the data selected for comparison included the Walker and Kors experiments, (Reference 8), and data from experimental configurations tested as part of this program. These sets of experimental data represented relatively simple flowfields of progressively increasing complexity. The remaining effort involved calculations which featured the added complexity of inlet swirl, fuel injection with heat release, and contour flowpath walls. The capability to use complex inlet swirler flows, and wall contours along the entire length of the combustor was incorporated into the model as part of an ongoing IR&D program. The data selected for comparison in these calculations included several of the experimental configurations tested as part of this program.

The initial assessment studies were conducted using data from experiment 67 of the Walker and Kors experiments. This set of data represented a two-temperature trace experiment involving a single row of dilution jets injected into a crossflow at a momentum ratio of about 6. This set of data was specifically selected because the dilution hole size and spacing characteristics were similar to many conventional combustor designs. Specific details concerning these data can be found in the reference. From these data, plots of temperature difference ratio contours were generated for each measurement plane downstream of the injection point. These plotted data, shown in Figures 121 through 124, represent averaged values over the span of two adjacent holes, and provide a visual presentation of the jet penetration, jet shape, and jet temperature dissipation.

In the first of this series of studies, an evaluation of three different grid networks was conducted. Each grid represented a different number of total nodes, but more importantly, a different number of nodes was used to represent the dilution hole. In each of the three grids, the (X) grid lines

ORIGINAL PAGE IS
OF POOR QUALITY

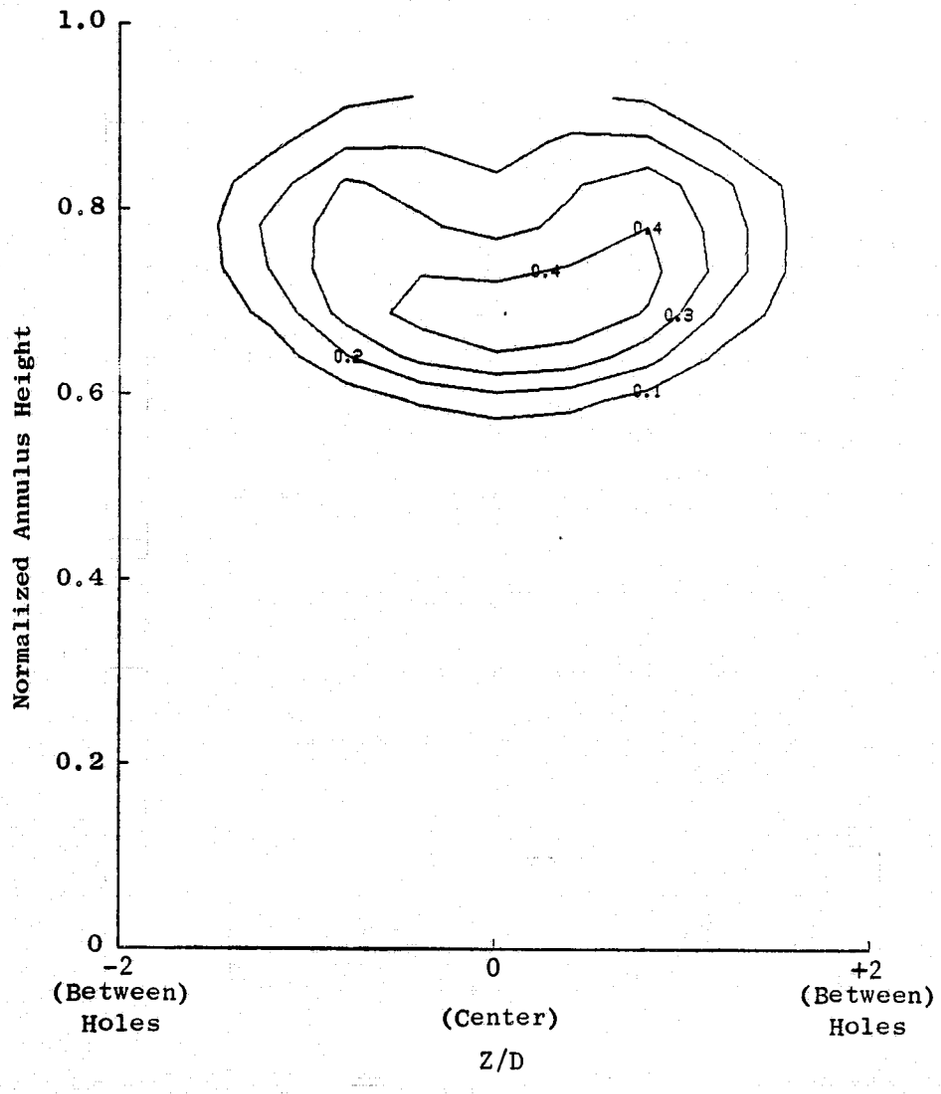


Figure 121. Walker and Kors Experiment Number 67, X/D = 2.
Contours of $\frac{T_{Inlet} - T_{Local}}{T_{Inlet} - T_{Jet}}$

ORIGINAL PAGE IS
OF POOR QUALITY

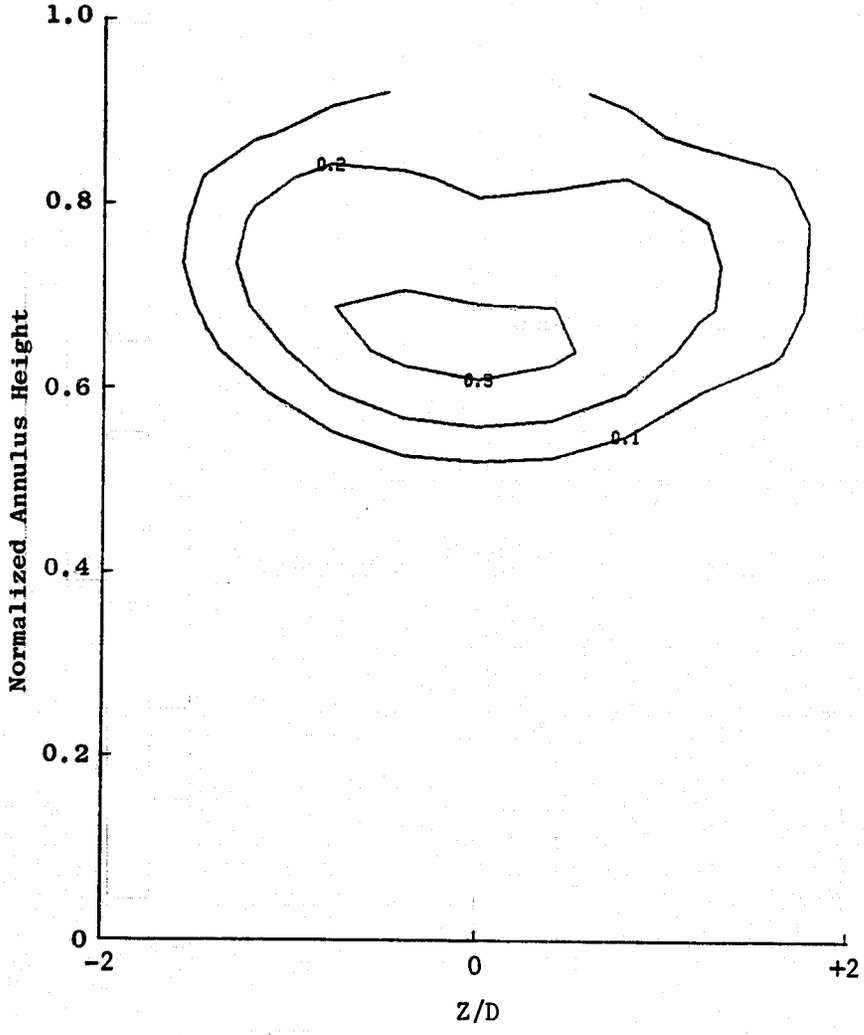


Figure 122. Walker and Kors Experiment No. 67, X/D = 4.

Contours of $\frac{T_{Inlet} - T_{Local}}{T_{Inlet} - T_{Jet}}$

ORIGINAL PAGE IS
OF POOR QUALITY

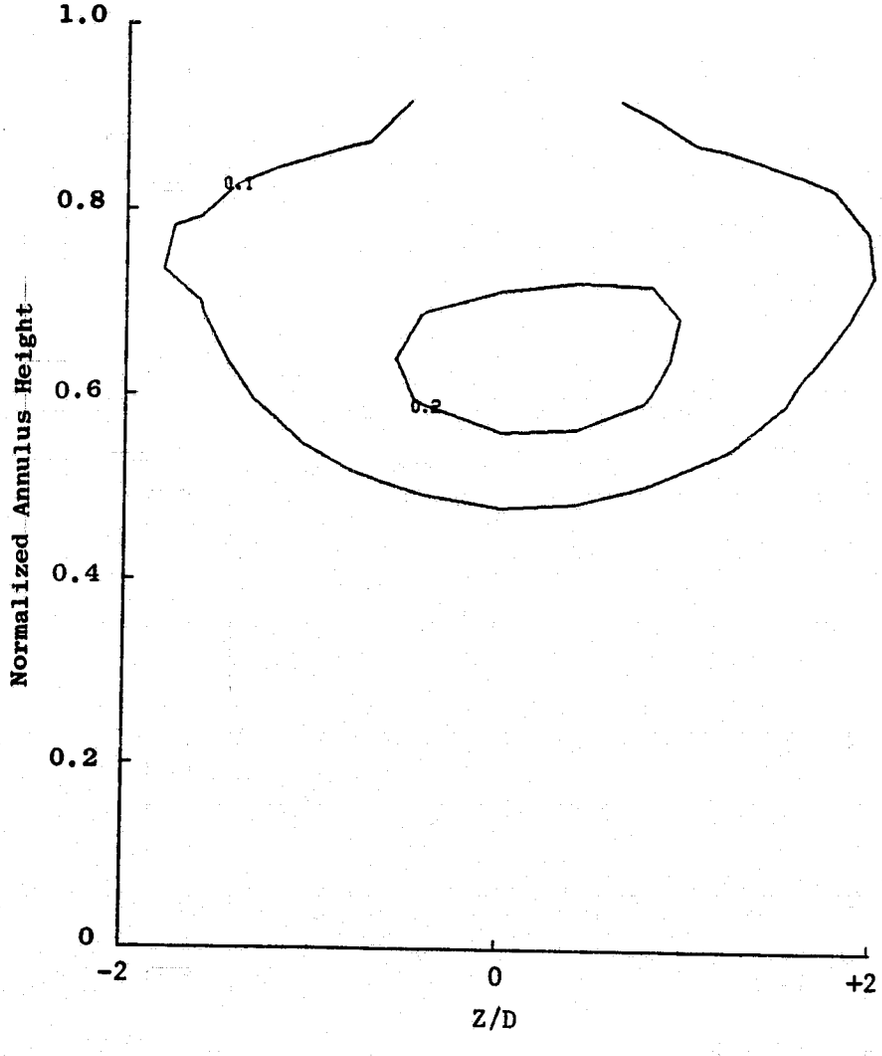


Figure 123. Walker and Kors Experiment No. 67, X/D = 8.

Contours of $\frac{T_{Inlet} - T_{Local}}{T_{Inlet} - T_{Jet}}$

ORIGINAL PAGE IS
OF POOR QUALITY

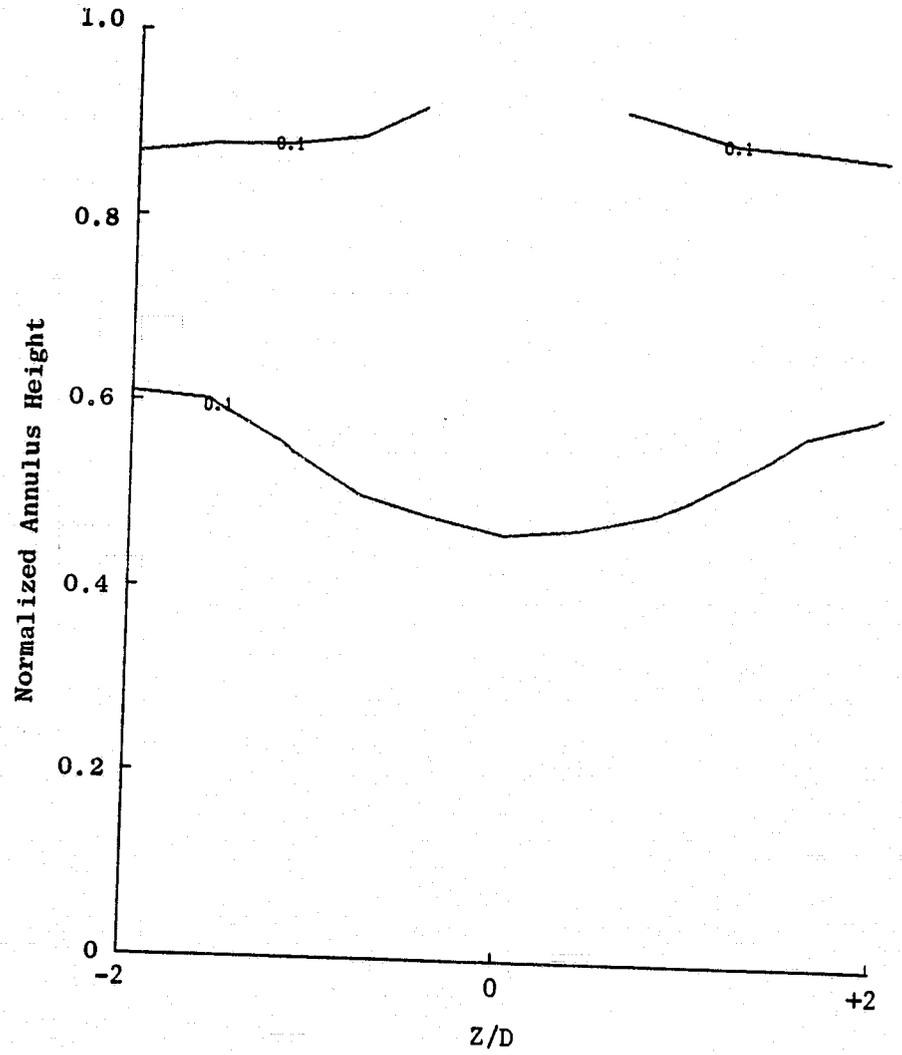


Figure 124. Walker and Kors Experiment No. 67, X/D = 16. Contours of $\frac{T_{Inlet} - T_{Local}}{T_{Inlet} \quad T_{Jet}}$

near the aft-end boundary were compressed to more closely achieve $\Delta x/\Delta y \approx 1$. This grid technique had earlier demonstrated improvement in reducing the mass residuals by up to 20% for the same number of interations.

The first grid network was coarse, containing 10,395 total nodes of which four arranged in a square pattern were used to represent the dilution hole. An illustration of this grid network is presented in Figure 125. In this figure, it appears as though the dilution hole is not properly centered. This results from the necessity to incorporate an extra (Z) grid line in the network to satisfy the cyclic boundary treatment featured in the code.

The second grid network evaluated contained 21,000 total nodes of which 25 arranged in a square pattern were used to represent the dilution hole (Figure 126). The only difference between this grid and the first grid lies in the extra detail used to represent the dilution hole.

The third grid network evaluated contained 41,600 total nodes of which 57 were used to represent the dilution hole. Instead of using a square arrangement, the dilution hole nodes were arranged in a more circular pattern. Due to the rectangular nature of the grid, a round hole shape must be approximated. An illustration of this detailed grid is presented in Figure 127. The storage requirements for this particular grid approaches the storage capacity currently available on the IBM 3081D system at General Electric.

Each of the three grids were run on the Northern Research 3-D code using the same turbulence energy, length scale, and turbulent Schmidt number input values.

Turbulence Energy Parameter (AKFAC)	3×10^{-3}
Inlet Turbulence Length Scale Parameter (ALFAC)	2×10^{-2}
Turbulent Schmidt Number	0.9

In the Northern Research code, the jet turbulent length scale is not an input, but is derived as a fraction of the effective diameter of the individual nodes comprising the dilution jet. In these studies this fraction was 3 percent. These values were selected from the program sample case provided. The cases for the first two grids were run until reasonably converged. Relative convergence was determined by examining changes in the solution parameters after each subsequent restart run. For the first grid (coarse), 200 iterations were run, while for the second grid (medium), 300 iterations were run. In the third grid (detailed), only 200 iterations were run; it was not fully converged. However, the excessive expense of running the model with this grid led to the decision not to run additional iterations. The convergence of the solution was determined by comparing calculated results after successive restarts. The sum of the error on mass continuity as calculated was not used as a measure of convergence. Earlier investigations had shown it to be an unreliable measure of the convergence of the solution. The tablulation below shows the approximate amount of CPU (Central Processing) time and cost per iteration for each of these three grids.

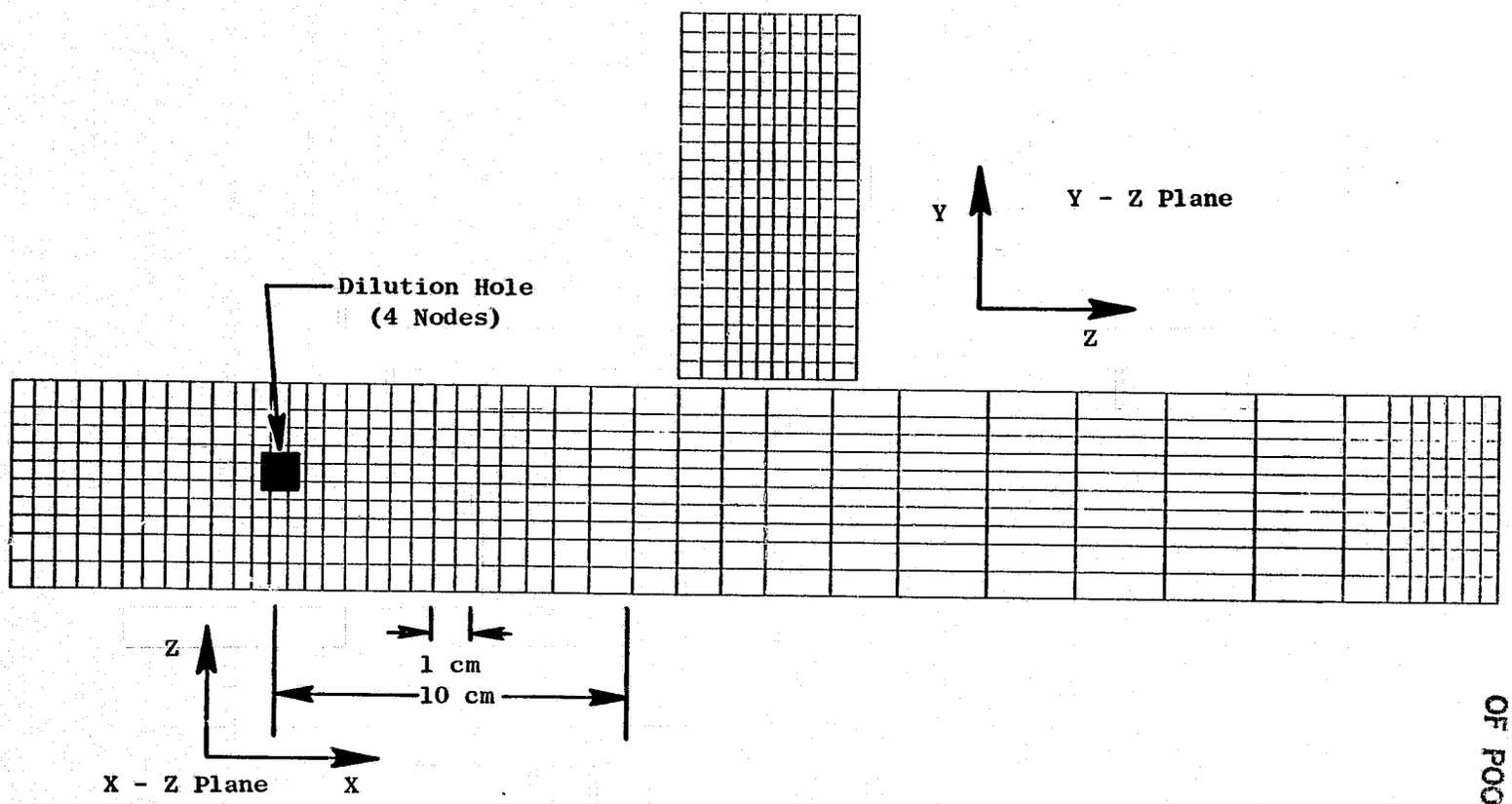


Figure 125. Grid 1 (Coarse) 45X 21Y 11Z.

ORIGINAL PAGE IS
OF POOR QUALITY

Figure 126. Grid 2 (Medium) 50X 21Y 20Z.

ORIGINAL PAGE IS
OF POOR QUALITY

Figure 127. Grid 3 (Detailed) 50X 26Y 32Z.

ORIGINAL PAGE IS
OF POOR QUALITY

	Per Iteration CPU Time (Min.)	Costs ($)
Grid No. 1 (10395)	0.27	2.50
Grid No. 2 (21000)	0.64	5.62
Grid No. 3 (41600)	1.28	13.12

Plotted results from these calculations in the form of temperature difference ratio contours are shown in Figures 128 through 131. These figures are to be compared with the Walker and Kors data shown in Figures 121 through 124. The observed lack of symmetry evident in some of the calculated results at the jet core represents minor imperfections in the convergence of the calculated solution coupled with the interpolating technique employed in the contour plotting routine. The jet penetration calculated with each of the grids is compared with that calculated from the Holdeman correlations (Reference 9) in Figure 132. The Holdeman correlations were derived from the Walker and Kors studies of dilution jet penetration and mixing.

As observed from this figure, the less detailed grids (1 and 2), after 200 or 300 iterations produced jet penetration levels generally in good agreement with the Walker and Kors data. The more detailed grid, (3), would require significantly more iterations to achieve reasonable convergence, but may be approaching the correlation. The shape of the jet as determined by the outline of the temperature difference ratio contours appears to improve with added grid detail. The impact of the grid of the calculated spreading of the jets is evident from Figure 131. The calculated jet temperature dissipation is considerably slower than observed from the test data. The more detailed the grid, the worse the problem becomes for $X/D<4$. Grid 2 shows more rapid dissipation than Grid 1 for $X/D<4$. Further improvement would be expected with Grid 3 if run to convergence. Increasing the energy level and the scale of the input turbulence would go in the direction of generating more rapid mixing, thus increasing the dissipation rate of the jet.

In the next study conducted with the data from Walker and Kors experiment 67, the impact of the turbulence energy, turbulence length scale, and the Schmidt number inputs was investigated. The intent of this study was to determine values for these input parameters which would produce calculated results that closely matched the test data in terms of jet penetration, shape, and jet temperature dissipation. It is recognized that searching for input turbulence parameters that provide agreement may be little more than finding a fudge factor. However, identifying the sensitivity of the results to these parameters may be of help in understanding the modeling problem. In any case, such calculations were made and are presented in this section. To conduct this study, a single grid was selected. The grid selected was the medium grid used in the initial study, (21,000 nodes). The values through which each of these three input parameters are varied are shown below.

Turbulence Energy/Velocity^2 (AKFAC)	6×10^{-3} to 1×10^{-1}
Inlet Turbulent Length Scale/Characteristic Dimension (ALFAK)	2×10^{-2} to 2×10^{-1}

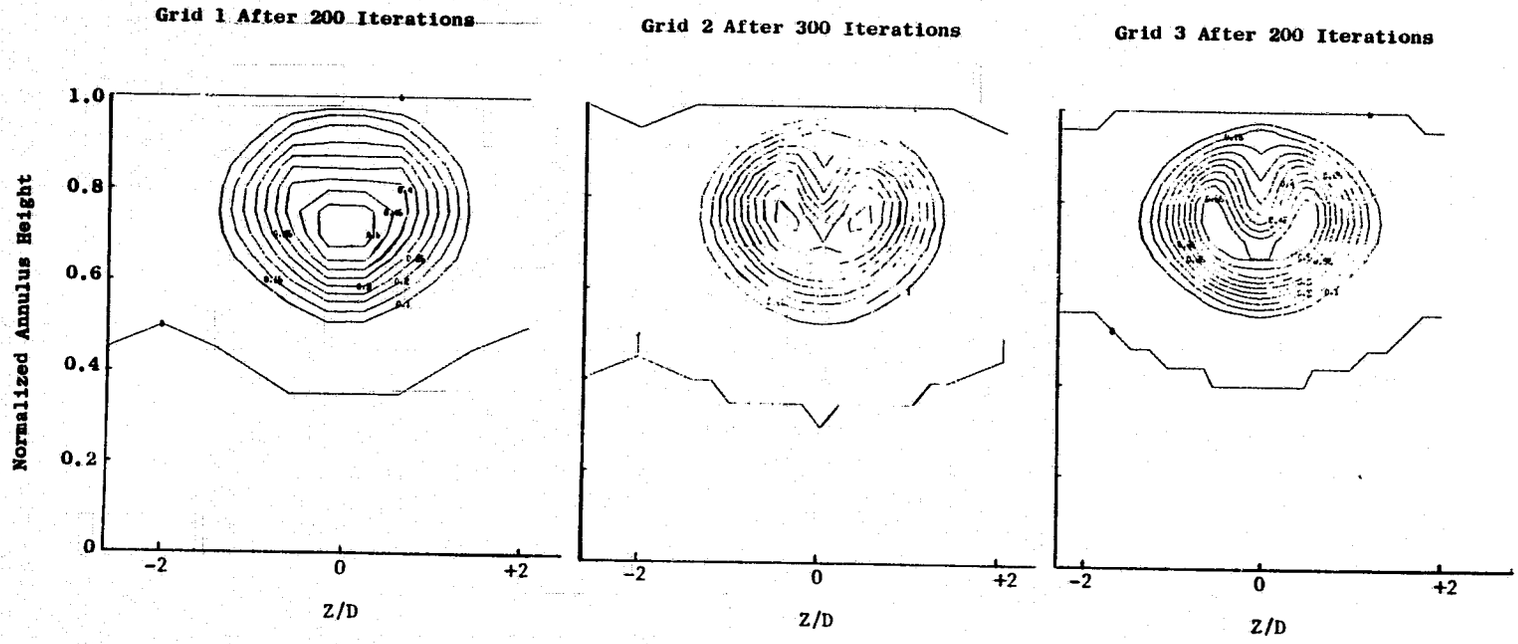
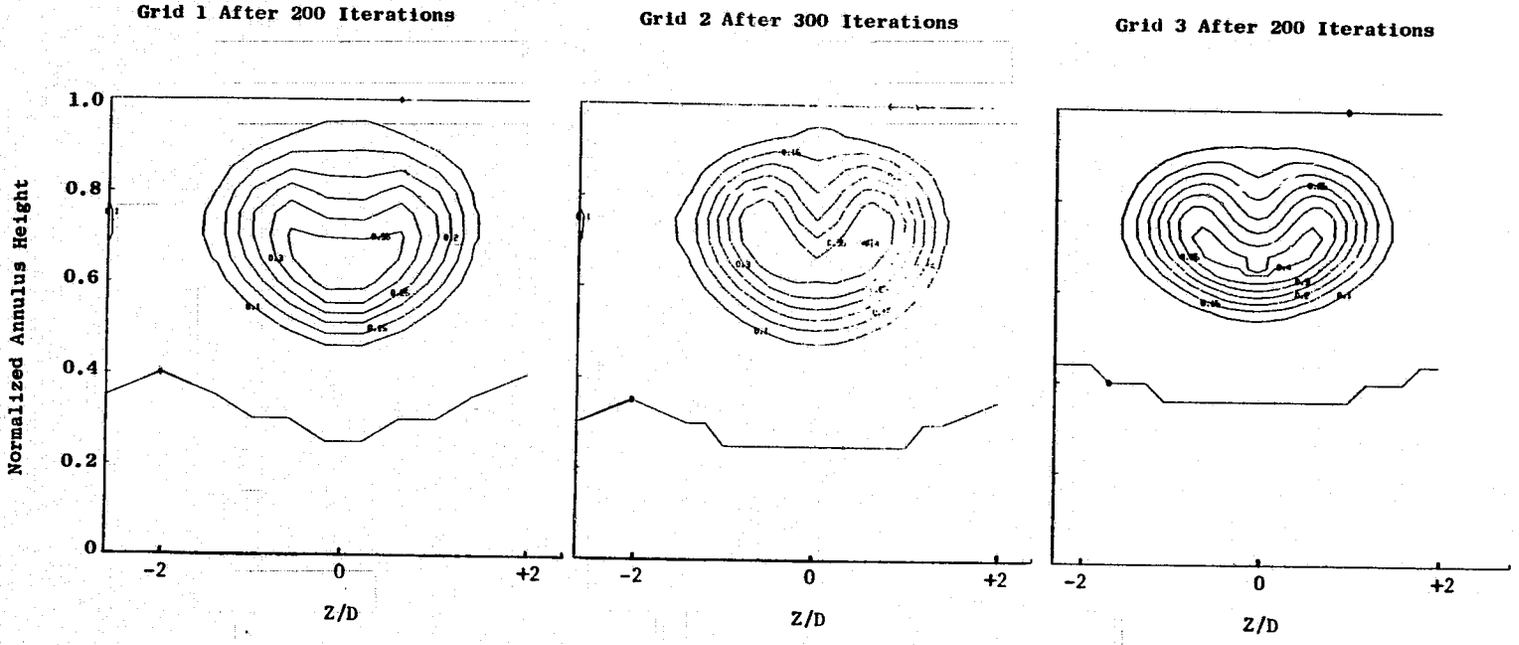


Figure 128. Calculated Results of Walker and Kors Experiment 67 Using Coarse, Medium, and Detailed Grids, X/D = 2.

Contours of $\frac{T_{Inlet} - T_{Local}}{T_{Inlet} - T_{Jet}}$

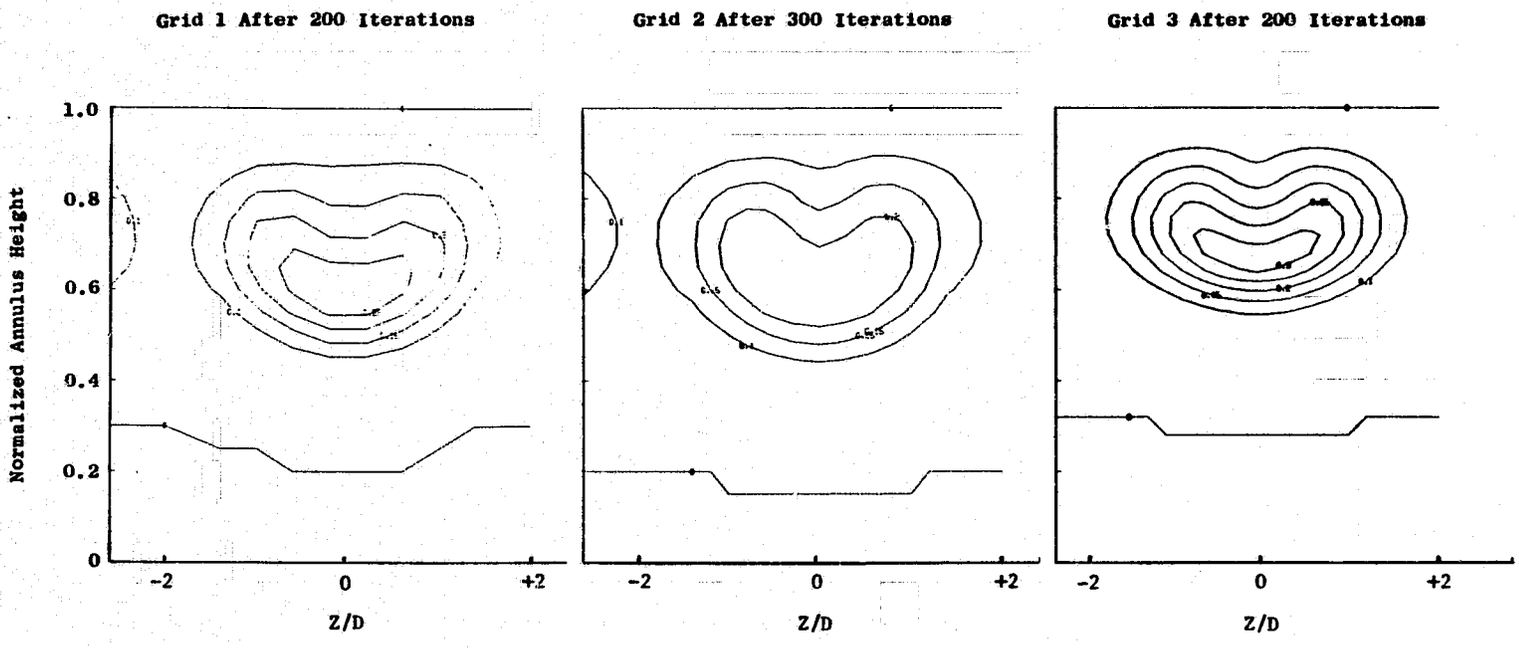
ORIGINAL PAGE IS
OF POOR QUALITY



ORIGINAL PAGE IS
OF POOR QUALITY

Figure 129. Calculated Results of Walker and Kors Experiment 67 Using Coarse, Medium, and Detailed Grids, X/D = 4.

Contours of $\frac{T_{Inlet} - T_{Local}}{T_{Inlet} - T_{Jet}}$



ORIGINAL PAGE IS
OF POOR QUALITY

Figure 130. Calculated Results of Walker and Kors Experiment 67 Using Coarse, Medium, and Detailed Grids, X/D = 8.

Contours of $\frac{T_{Inlet} - T_{Local}}{T_{Inlet} - T_{Jet}}$

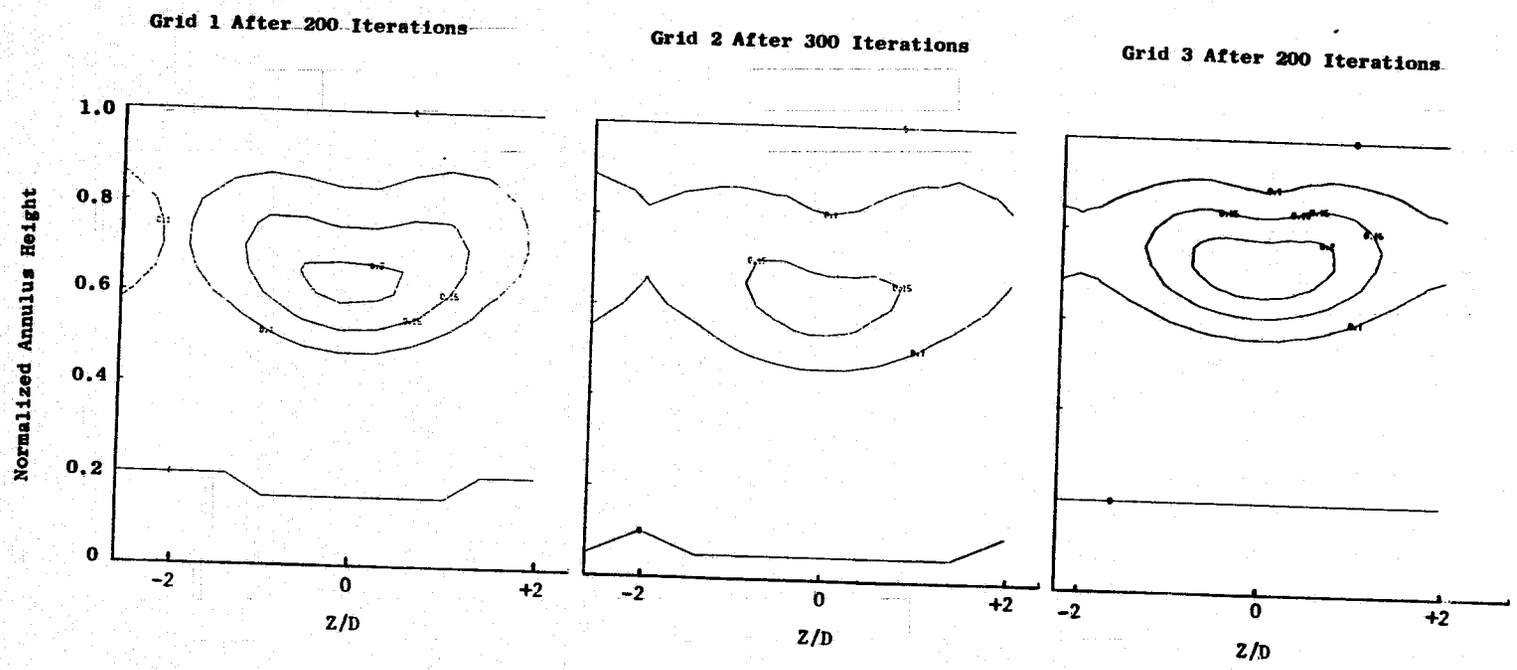


Figure 131. Calculated Results of Walker and Kors Experiment 67 Using Coarse, Medium, and Detailed Grids, X/D = 16.
Contours of $\frac{T_{Inlet} - T_{Local}}{T_{Inlet} - T_{Jet}}$

ORIGINAL PAGE IS
OF POOR QUALITY

ORIGINAL PAGE IS
OF POOR QUALITY

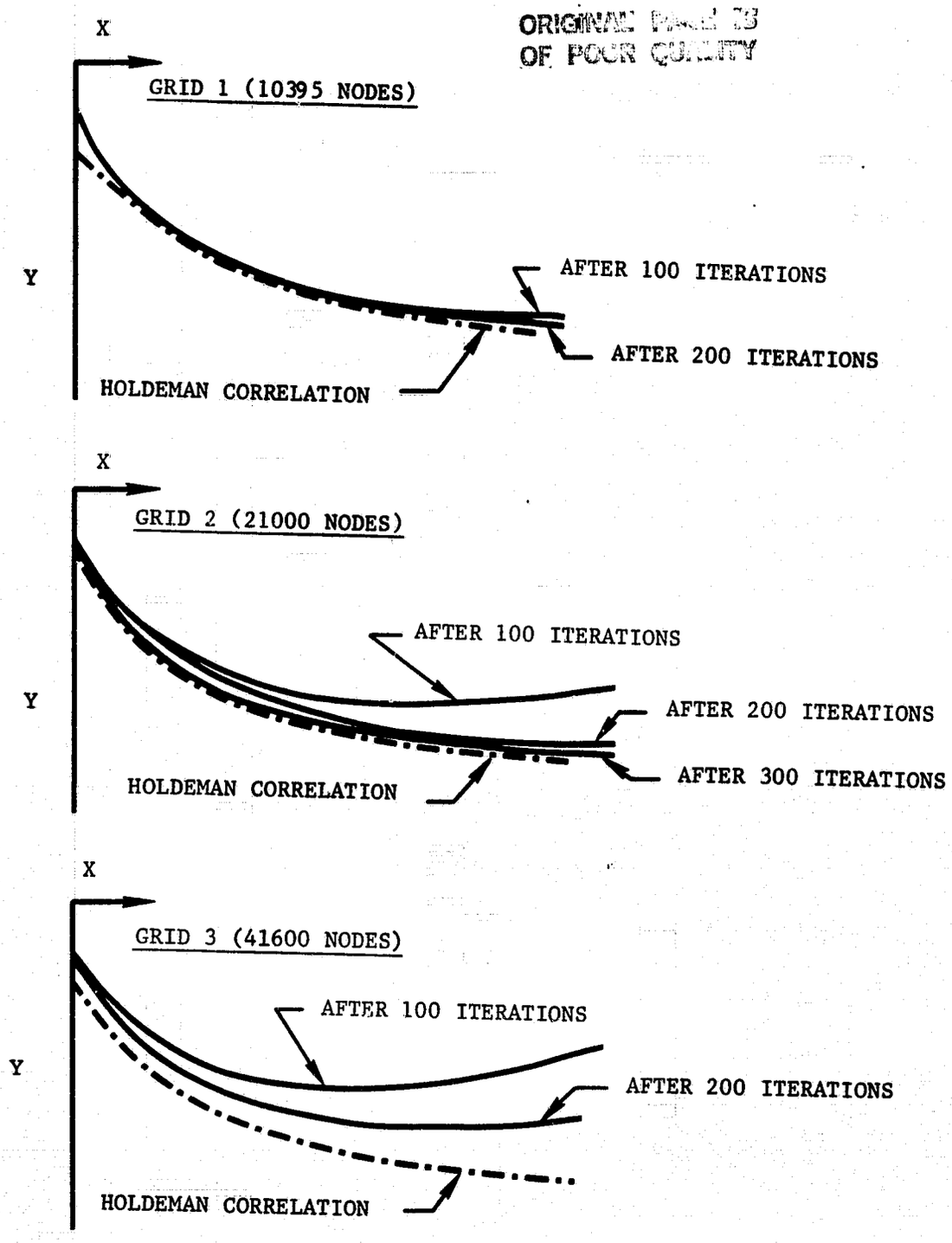


Figure 132. Comparisons of Calculated Jet Penetration with Holdeman Correlation for Walker and Kors Experiment 67.

Turbulent Schmidt Number	0.5 to 0.9

The jet turbulent length scale remained at about 3 percent of the node effective diameter.

It was determined from the results of this study that the inlet length scale parameter had the greatest impact on the calculated turbulence levels, and the jet temperature dissipation rate. Of the range of values investigated, the best results were achieved using 2×10^{-1}. Varying the turbulence energy parameter within the range of values investigated produced an insignificant impact on both the calculated turbulence levels and jet temperature dissipation rate. No best value was determined. Varying the turbulent Schmidt number within the range of values investigated produced generally minor changes in the calculated turbulence levels, but a moderate impact on the jet temperature dissipation. The best results were achieved using a turbulent Schmidt number of 0.5.

Using the values of these input parameters which produced the best results with the medium grid, calculations of the experiment 67 data were made using the most detailed grid, (41,600 nodes). The values selected for these three input parameters were:

Turbulence Energy/Velocity^2 (AKFAC)	6×10^{-3}
Turbulence Length Scale/Characteristic Dimension (ALFAC)	2×10^{-1}
Turbulent Schmidt Number	0.5

By using the detailed grid along with the selected input parameters, it was intended to demonstrate that with sufficient iterations the proper jet penetration, shape and temperature dissipation could be calculated. The model, using the detailed grid, was run for 400 iterations consuming over 500 minutes processor time. The results of these calculations are compared with the Walker and Kors experiment 67 test data in Figures 133 through 136.

In general, the agreement was quite good. The jet shape resembles the reference test data. However, the calculated results produce a shape which is too "round" at X/D = 2. The jet temperature dissipation for $X/D \geq 2$ matched well with the data. The results still showed problems near the injection point ($X/D \leq 2$). The calculated jet penetration is a little less than observed from the reference test data. Even after 400 iterations, the solution was not entirely converged. Improvement would be anticipated with additional iterations. Because of cost concerns, no additional iterations were run. The calculated results after 400 iterations predict the results from this test data selection reasonably well. However, the calculated results suggest the need to use detailed grids at the expense of large storage requirements and excessive run times. This would severely limit the use of such 3-D codes for general use in combustor design problems.

Following the satisfactory results obtained from Walker and Kors experiment 67 test data, 3-D calculations were performed on the Walker and Kors

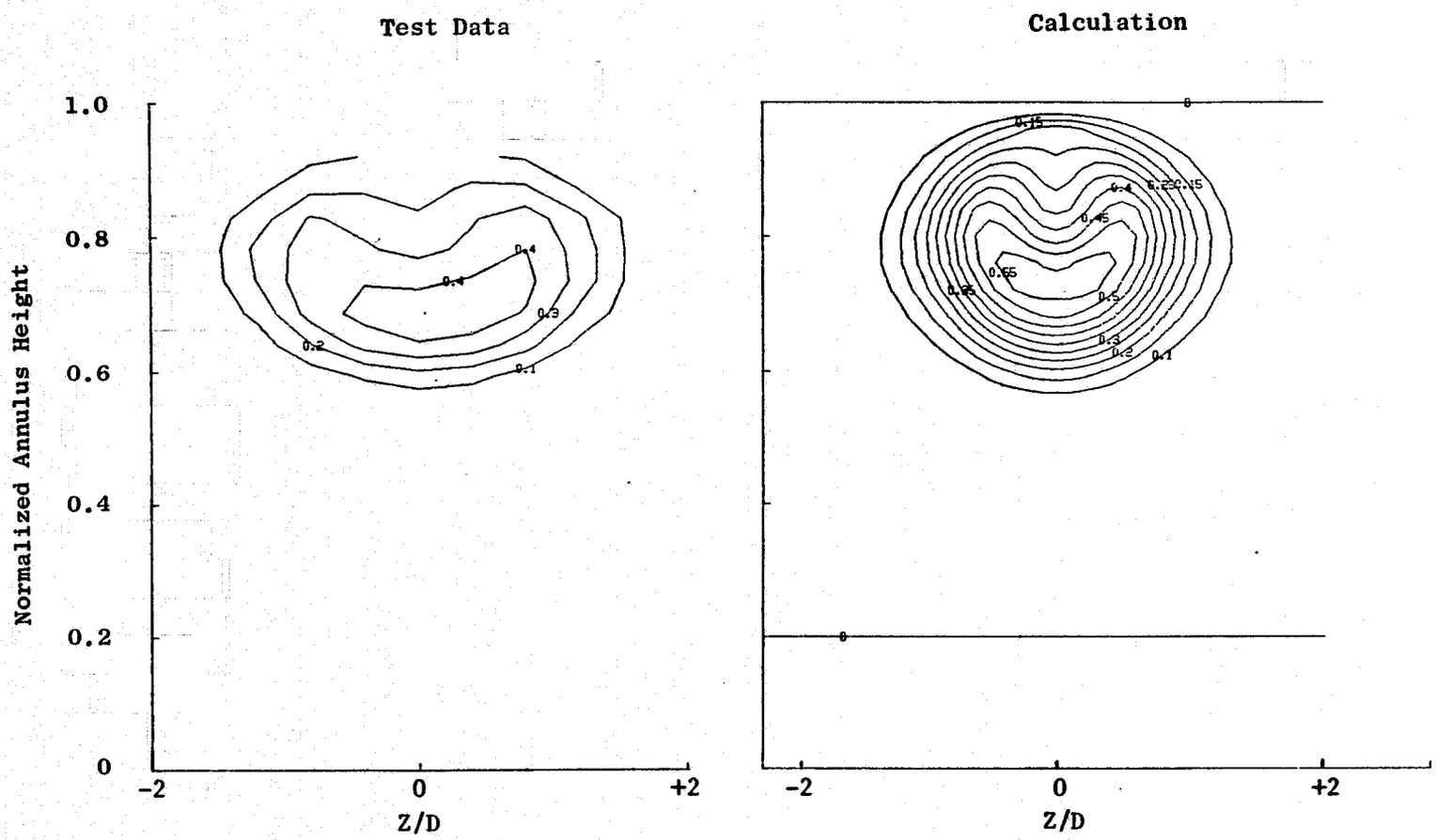


Figure 133. Calculated Results of Walker and Kors Experiment 67 Using Detailed Grid and Optimized Turbulence Inputs, X/D = 2.

Contours of $\frac{T_{Inlet} - T_{Local}}{T_{Inlet} - T_{Jet}}$

ORIGINAL PAGE IS
OF POOR QUALITY

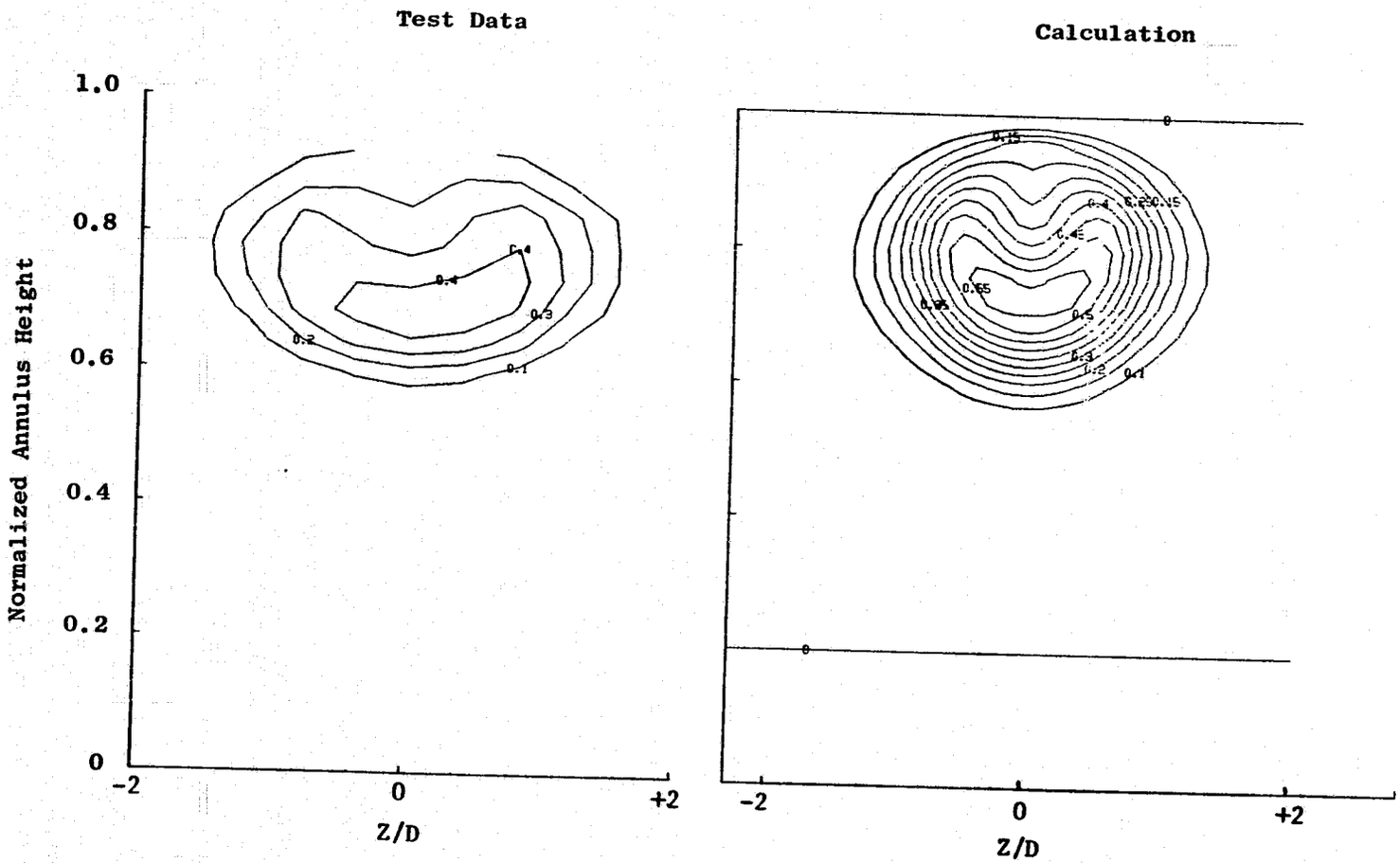


Figure 134. Calculated Results of Walker and Kors Experiment 67 Using Detailed Grid and Optimized Turbulence Inputs, X/D = 4.

Contours of $\frac{T_{Inlet} - T_{Local}}{T_{Inlet} - T_{Jet}}$

ORIGINAL PAGE IS
OF POOR QUALITY

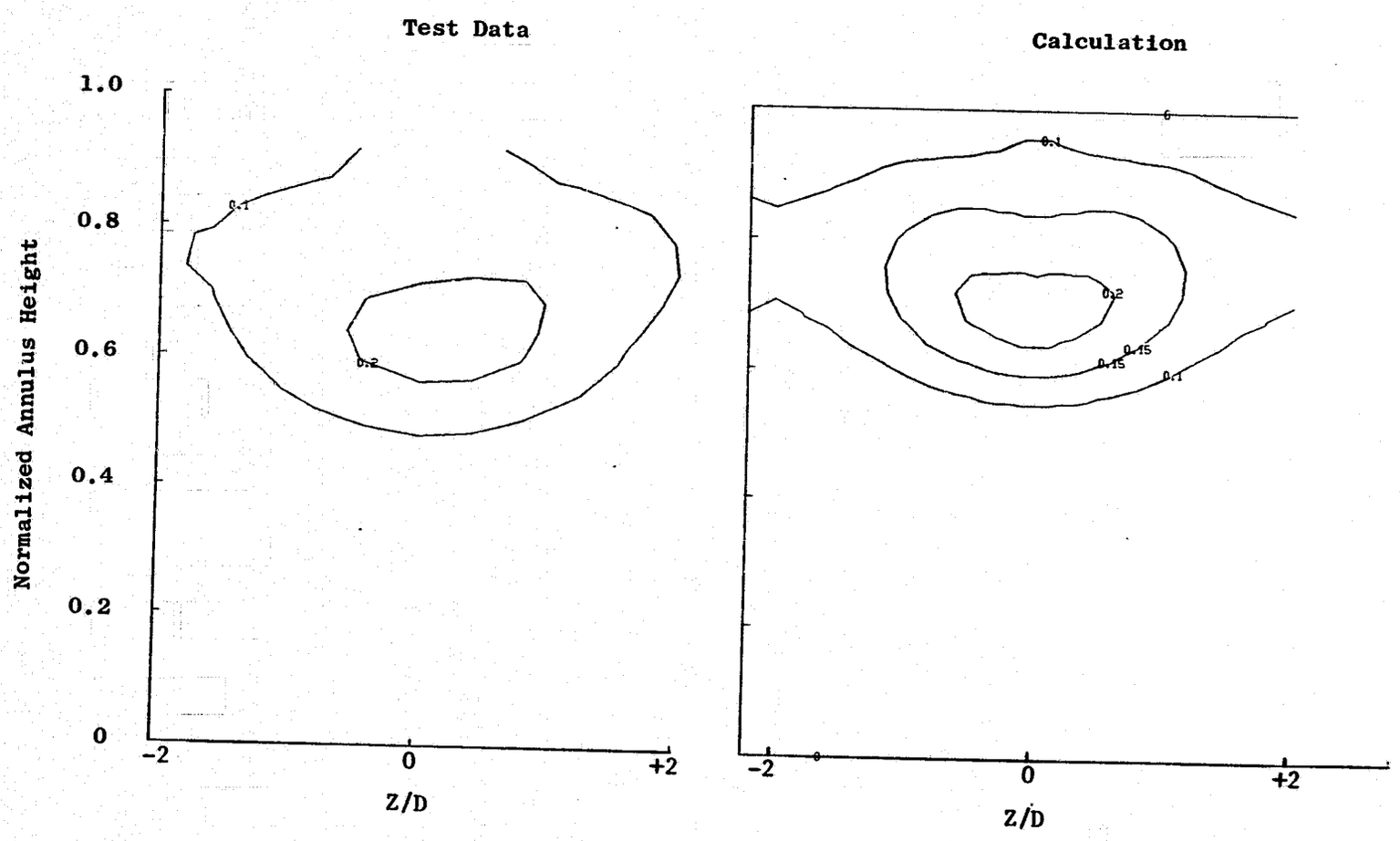


Figure 135. Calculated Results of Walker and Kors Experiment 67 Using Detailed Grid and Optimized Turbulence Inputs, X/D = 8.

Contours of $\frac{T_{Inlet} - T_{Local}}{T_{Inlet} \quad T_{Jet}}$

ORIGINAL PAGE IS
OF POOR QUALITY

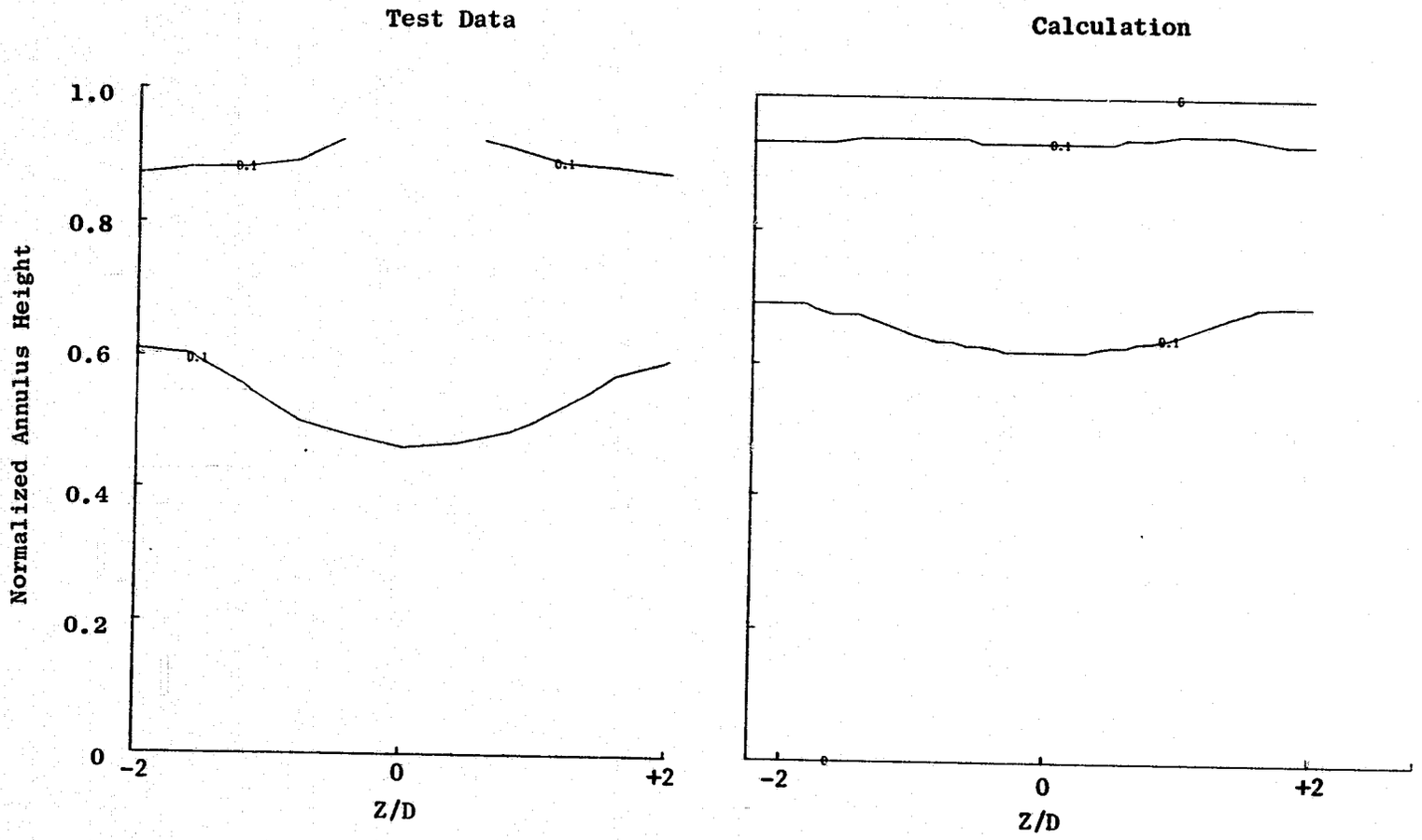


Figure 136. Calculated Results of Walker and Kors Experiment 67 Using Detailed Grid and Optimized Turbulence Inputs, X/D = 16.

Contours of $\frac{T_{Inlet} - T_{Local}}{T_{Inlet} - T_{Jet}}$

ORIGINAL PAGE IS
OF POOR QUALITY

experiment 69 test data. This data set was selected because it represented the same dilution pattern featured in the experiment 67 data. However, the jet injection momentum ratio was greater, approximately 27 compared to approximately 6 in the case of experiment 67. The higher momentum ratio is more representative of actual combustor conditions, particularly at the first dilution hole or primary hole row. The test data in the form of plots of temperature difference ratio contours is shown in Figures 137 through 140. These plots represent averaged values over the span of two adjacent holes. The grid selected for use in the initial calculations of these data was the medium grid (21,000 nodes). The calculation was run for 400 iterations using the Northern Research code. The same turbulence and Schmidt number inputs selected from the studies of the experiment 67 test data were used. The jet turbulence length scale represented approximately 3 percent of the effective diameter of the 25 individual nodes comprising the jet.

The calculated results are presented in Figures 141 through 144. Comparisons between these calculated results and the measured test data reveal that the calculated jet penetration is considerably greater than is observed from the test data. The calculated jet temperature dissipation is considerably slower than observed from the test data. Adjustments to the inlet and jet turbulence level and inlet turbulence length scale failed to provide any improvement. Results obtained from calculations of the experiment 67 test data had also shown insensitivity of the solution to the turbulence kinetic energy input parameter. One possible explanation was thought to be related to grid dependence.

To investigate the grid dependence, calculations of Walker and Kors experiment 69 test data were performed using a grid network in which the Y grid was refined; the X and Z grid were fixed. In this grid, the dilution hole was represented by nine nodes arranged in a square pattern. An illustration of this grid showing the variations in Y grid detail is presented in Figure 145. In the (A) version of this grid, 11 Y grid lines are featured; in the (B) version, 21 Y grid lines are featured; and the (C) version, 41 Y grid lines are featured. This overall refinement produced nearly a fourfold increase in the number of Y grid lines. Calculations using the (A) grid were run for 100 iterations. Calculations using the (B) and (C) grids were run for 200 iterations. The extra iterations were run to achieve convergence levels at least as good as the (A) after 100 iterations. Results of the calcuations performed using these grids are compared with the experiment 69 test data in Figures 146 through 148. Surprisingly, very little change in calculated jet penetration is observed for the increase in Y grid. There is a slight trend toward improvement in the calculated jet penetration with increasing Y grid. One additional calculation was made using a modification to the (B) grid. The modification involved increasing the number of Z grid lines from 14 to 23, while maintaining the X and Y grid. The dilution hole characteristics remained unchanged, nine nodes arranged in a square pattern. Figure 149 presents an illustration of the (D) grid network. Calculations using this grid were intended to determine if the anticipated increase in tangential spreading of the jet would result in a decrease in the jet penetration. This calculation was also run for 200 iterations. The results are compared to

ORIGINAL PAGE IS
OF POOR QUALITY

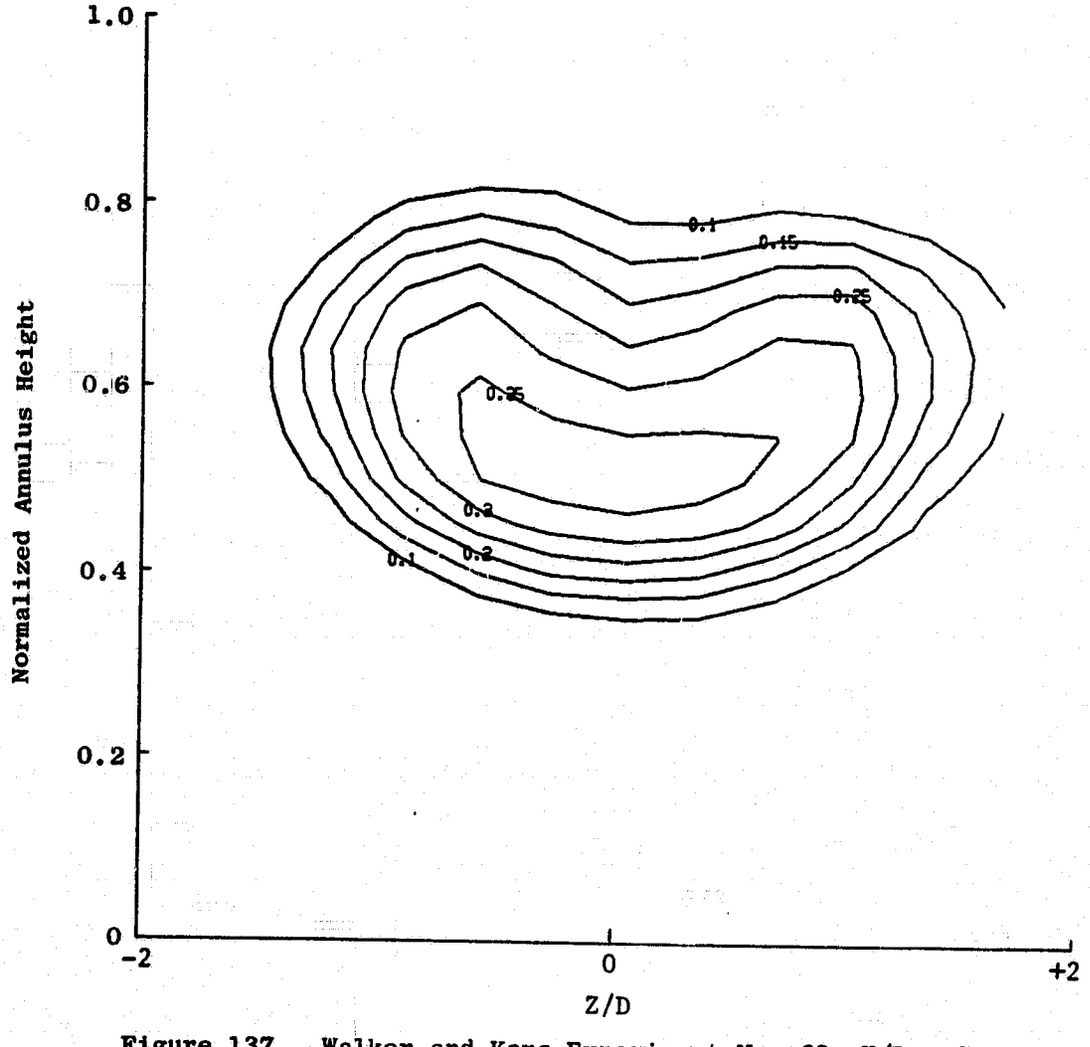


Figure 137. Walker and Kors Experiment No. 69, X/D = 2.
Contours of $\frac{T_{Inlet} - T_{Local}}{T_{Inlet} - T_{Jet}}$

ORIGINAL PAGE IS
OF POOR QUALITY

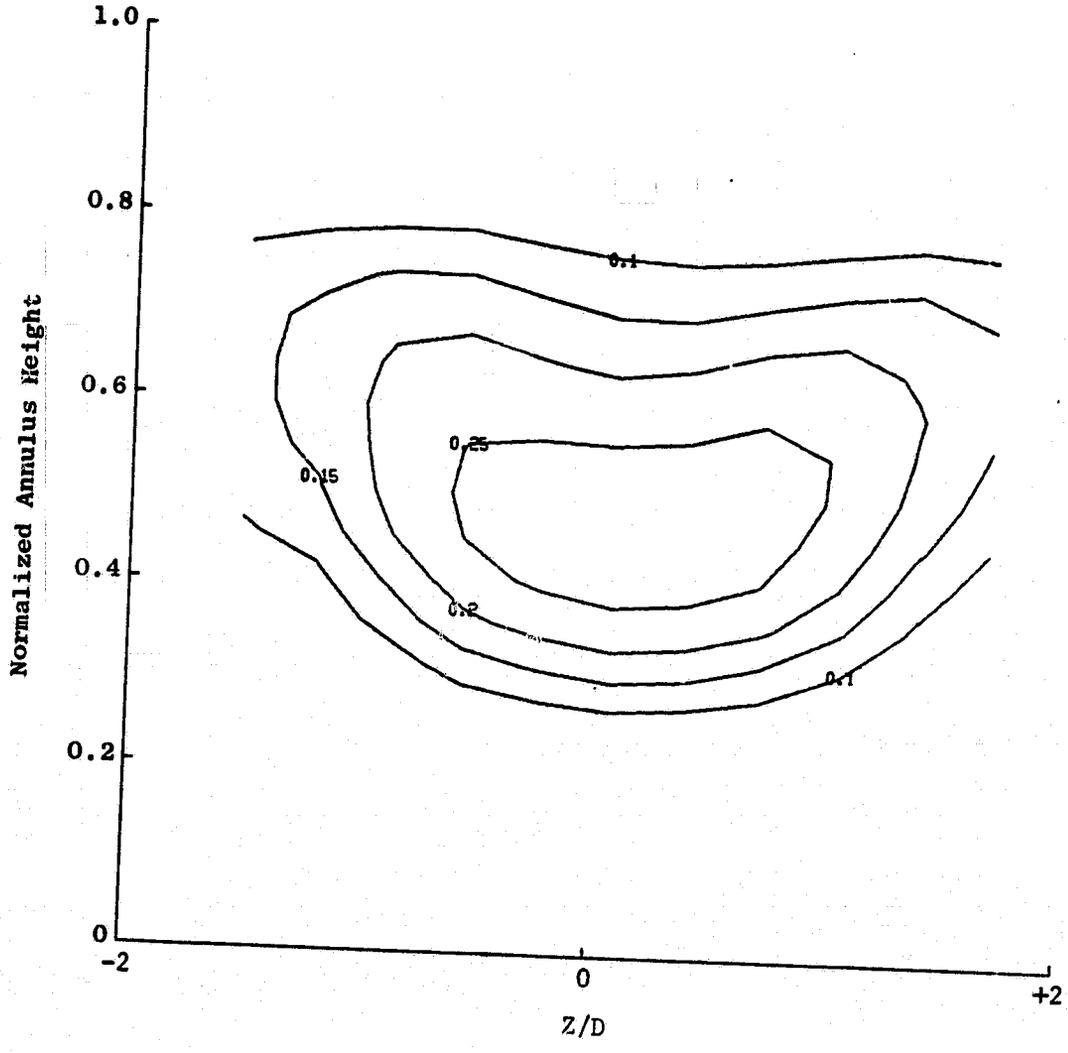


Figure 138. Walker and Kors Experiment No. 69, X/D = 4. Contours of $\frac{T_{Inlet} - T_{Local}}{T_{Inlet} \quad T_{Jet}}$

ORIGINAL PAGE IS
OF POOR QUALITY

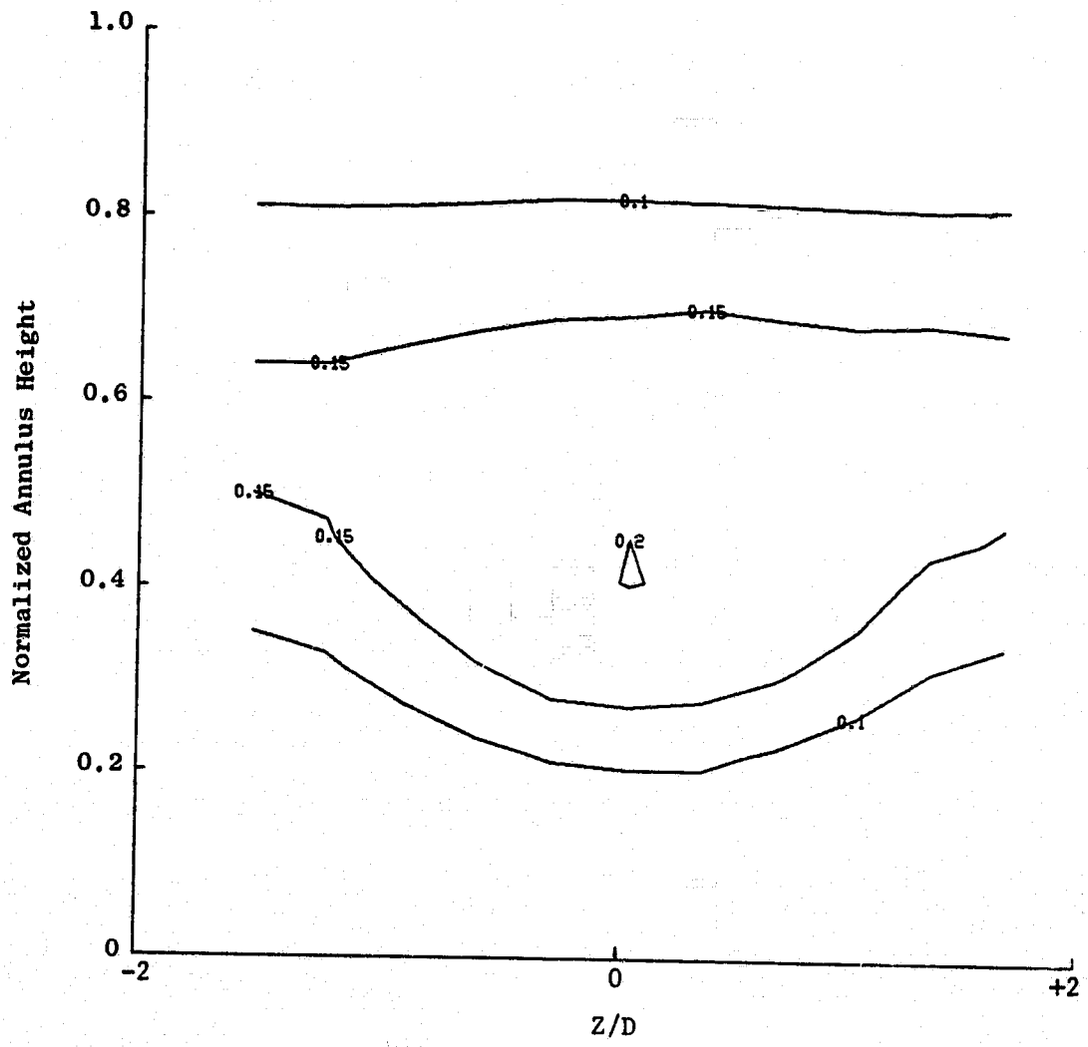


Figure 139. Walker and Kors Experiment No. 69, X/D = 8. Contours of $\frac{T_{Inlet} - T_{Local}}{T_{Inlet} - T_{Jet}}$

ORIGINAL PAGE IS
OF POOR QUALITY

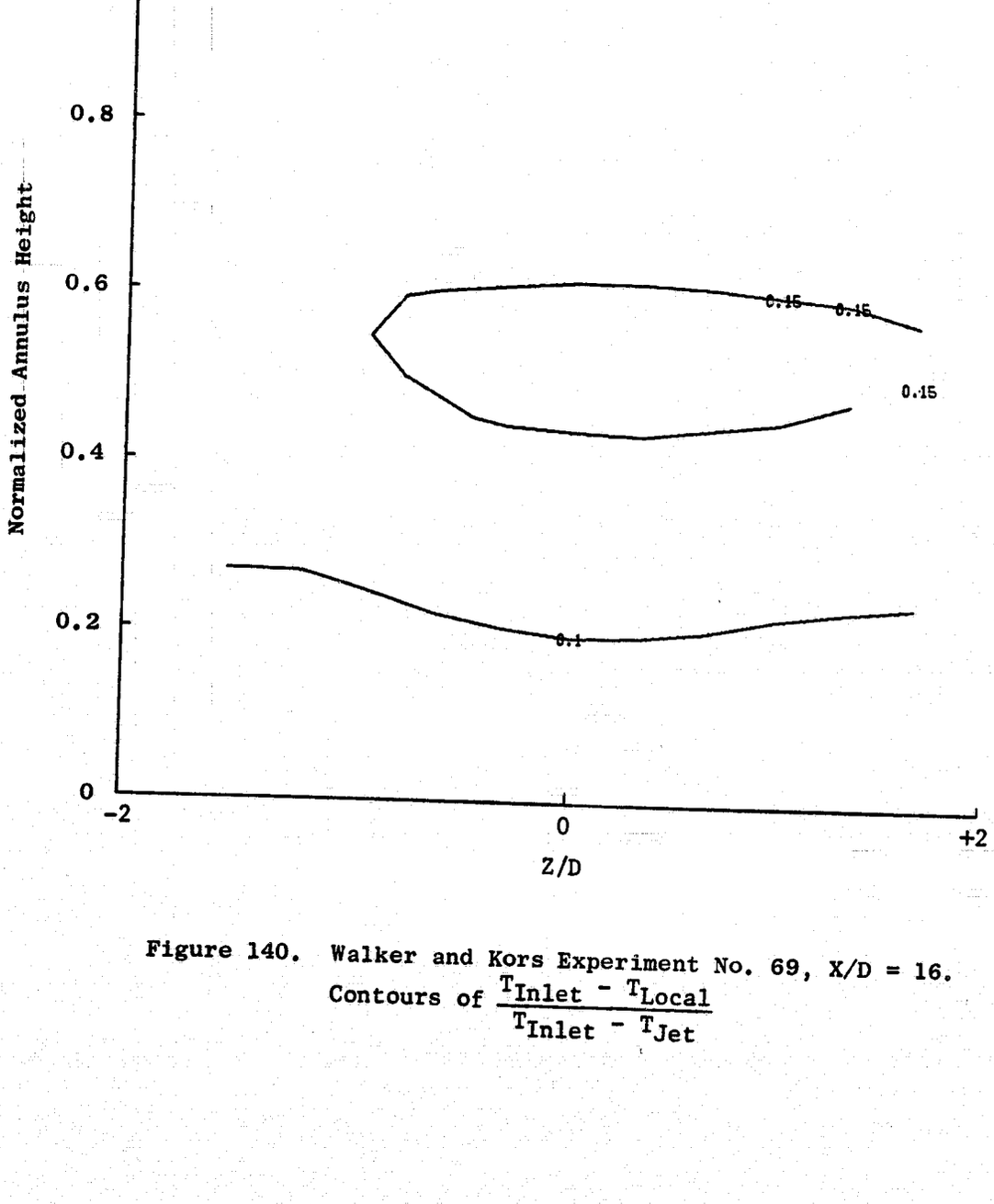
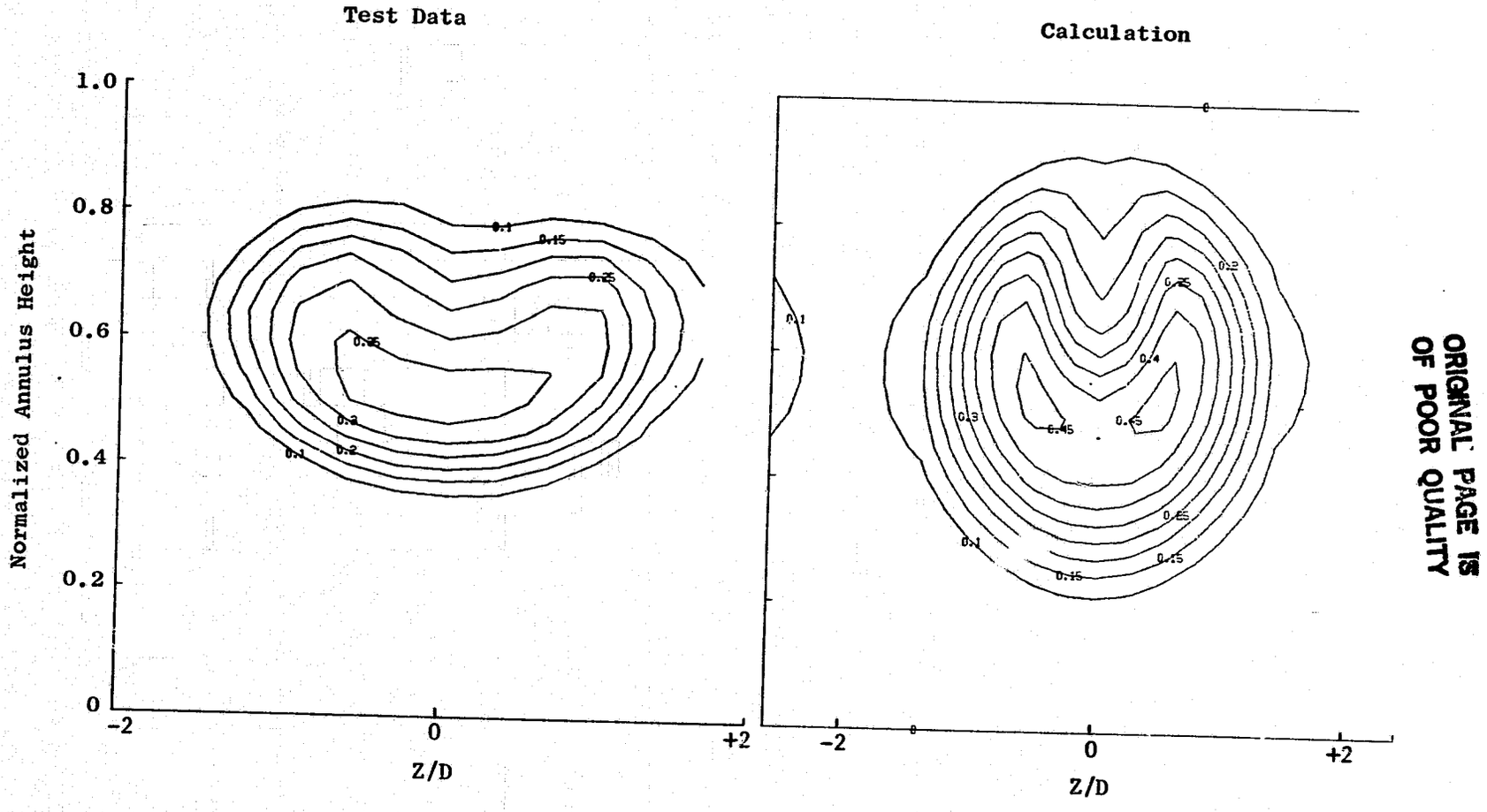


Figure 140. Walker and Kors Experiment No. 69, X/D = 16.
Contours of $\frac{T_{Inlet} - T_{Local}}{T_{Inlet} - T_{Jet}}$



ORIGINAL PAGE IS
OF POOR QUALITY

Figure 141. Walker and Kors Experiment 69 Test Results, X/D = 2.
Contours of $\frac{T_{Inlet} - T_{Local}}{T_{Inlet} - T_{Jet}}$

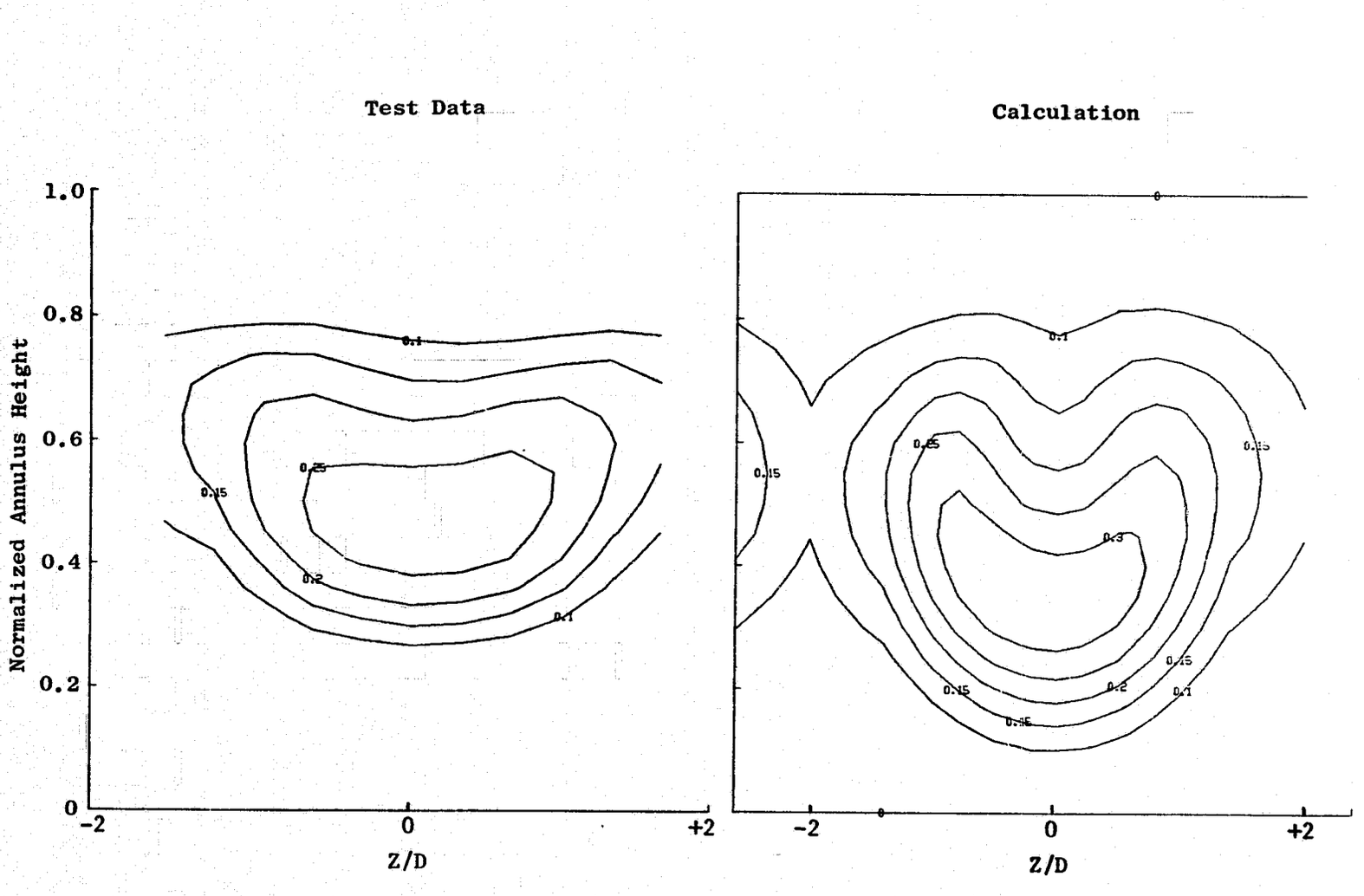


Figure 142. Walker and Kors Experiment 69 Test Results, X/D = 4.
Contours of $\frac{T_{Inlet} - T_{Local}}{T_{Inlet} - T_{Jet}}$

ORIGINAL PAGE IS
OF POOR QUALITY

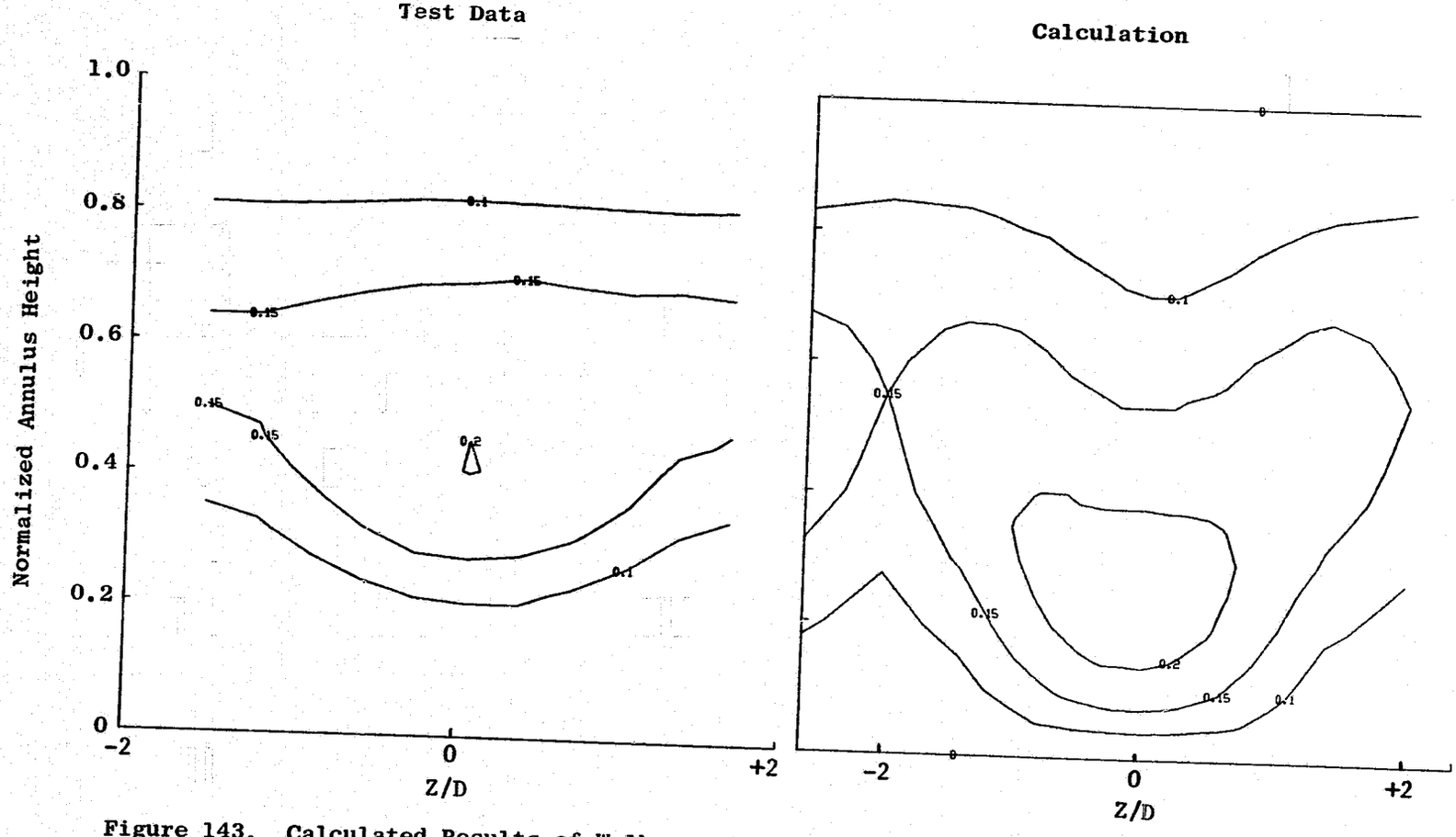
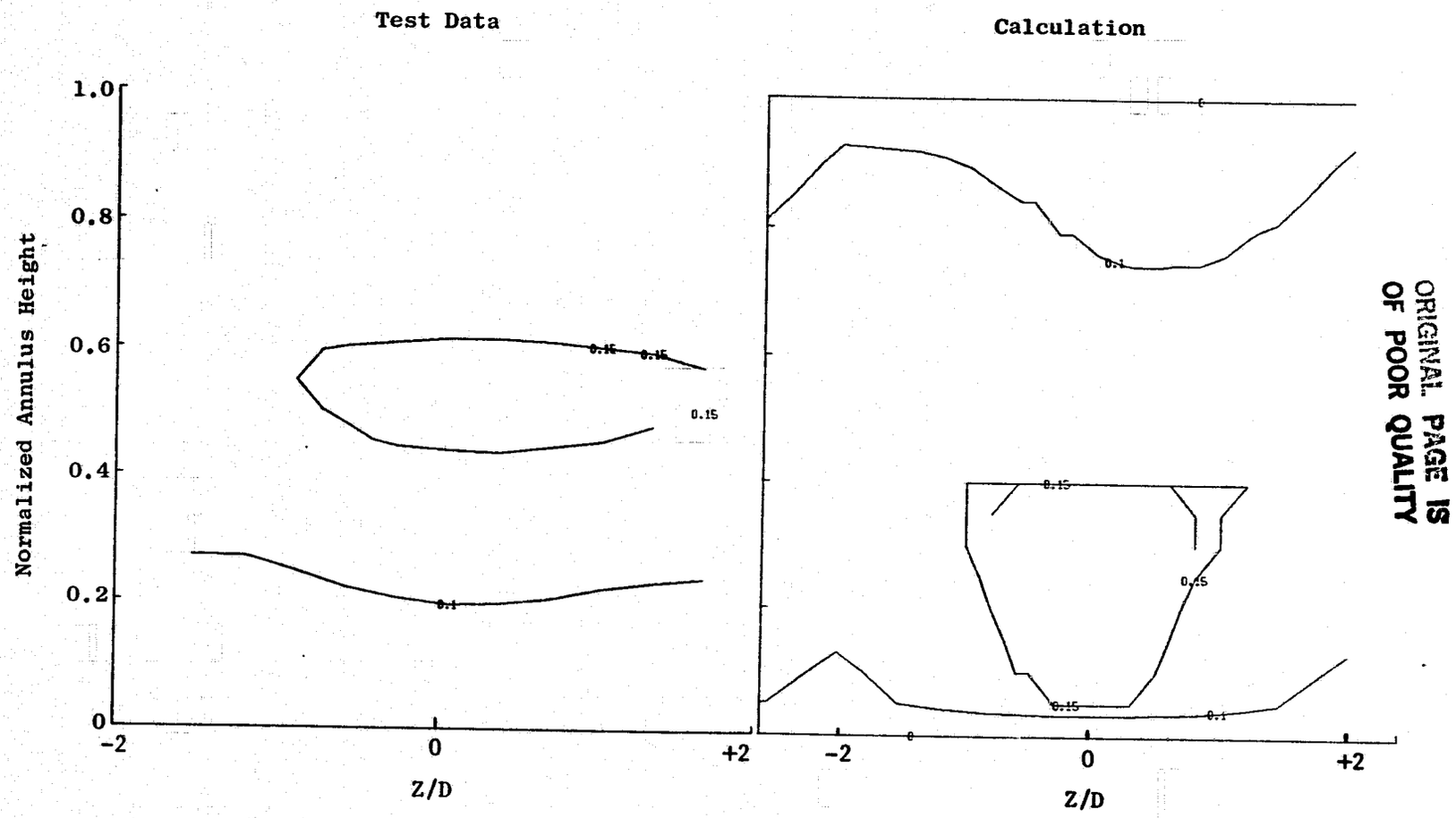


Figure 143. Calculated Results of Walker and Kors Experiment 69 Using Medium Grid, X/D = 8. Contours of $\frac{T_{Inlet} - T_{Local}}{T_{Inlet} - T_{Jet}}$

ORIGINAL PAGE IS
OF POOR QUALITY



ORIGINAL PAGE IS
OF POOR QUALITY

Figure 144. Calculated Results of Walker and Kors Experiment 69 Using Medium Grid, X/D = 16. Contours of $\frac{T_{Inlet} - T_{Local}}{T_{Inlet} - T_{Jet}}$

ORIGINAL PAGE IS
OF POOR QUALITY

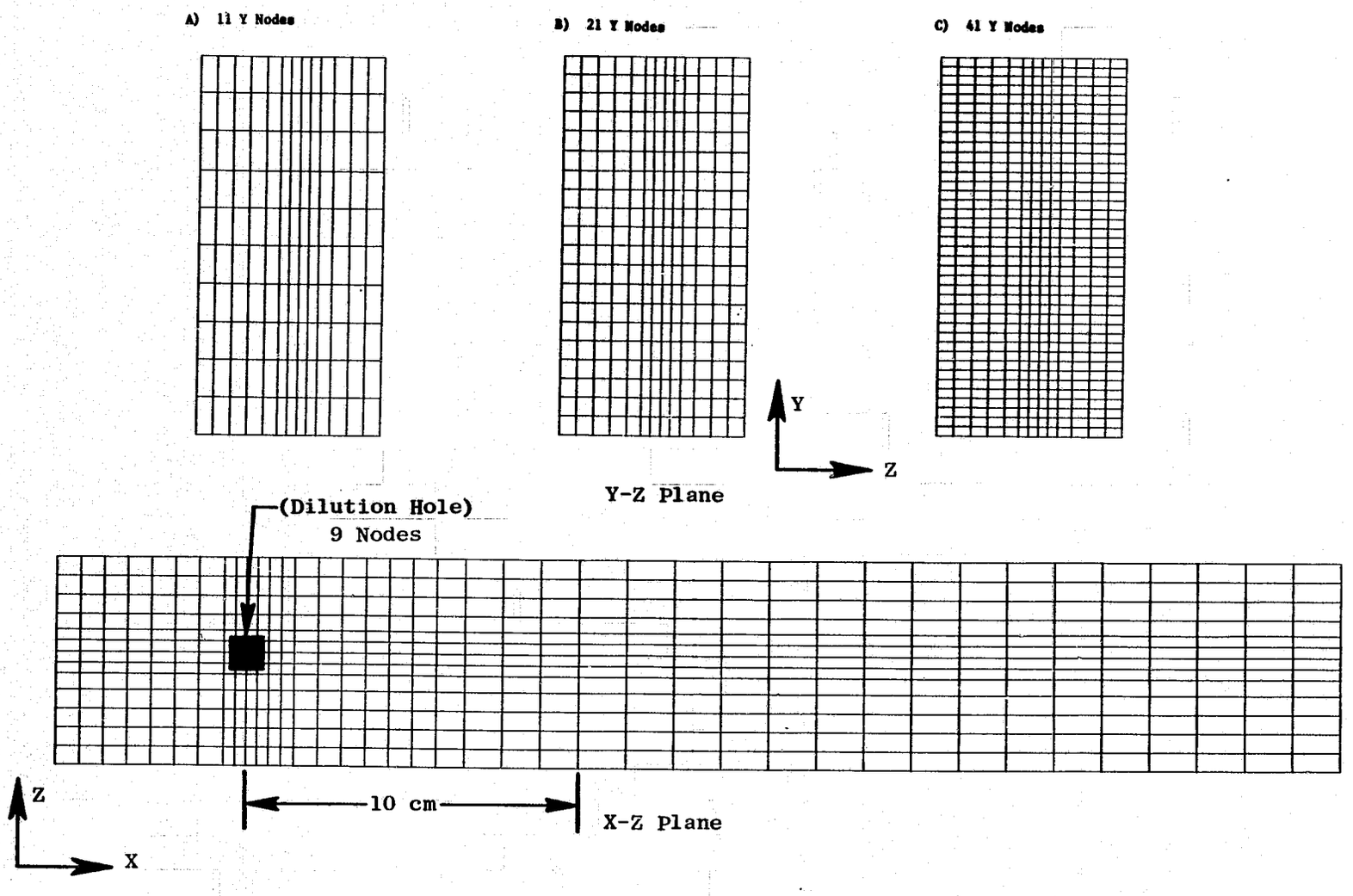


Figure 145. Walker/Kors Experiment 69 Jet Penetration Study Grid.

ORIGINAL PAGE IS
OF POOR QUALITY

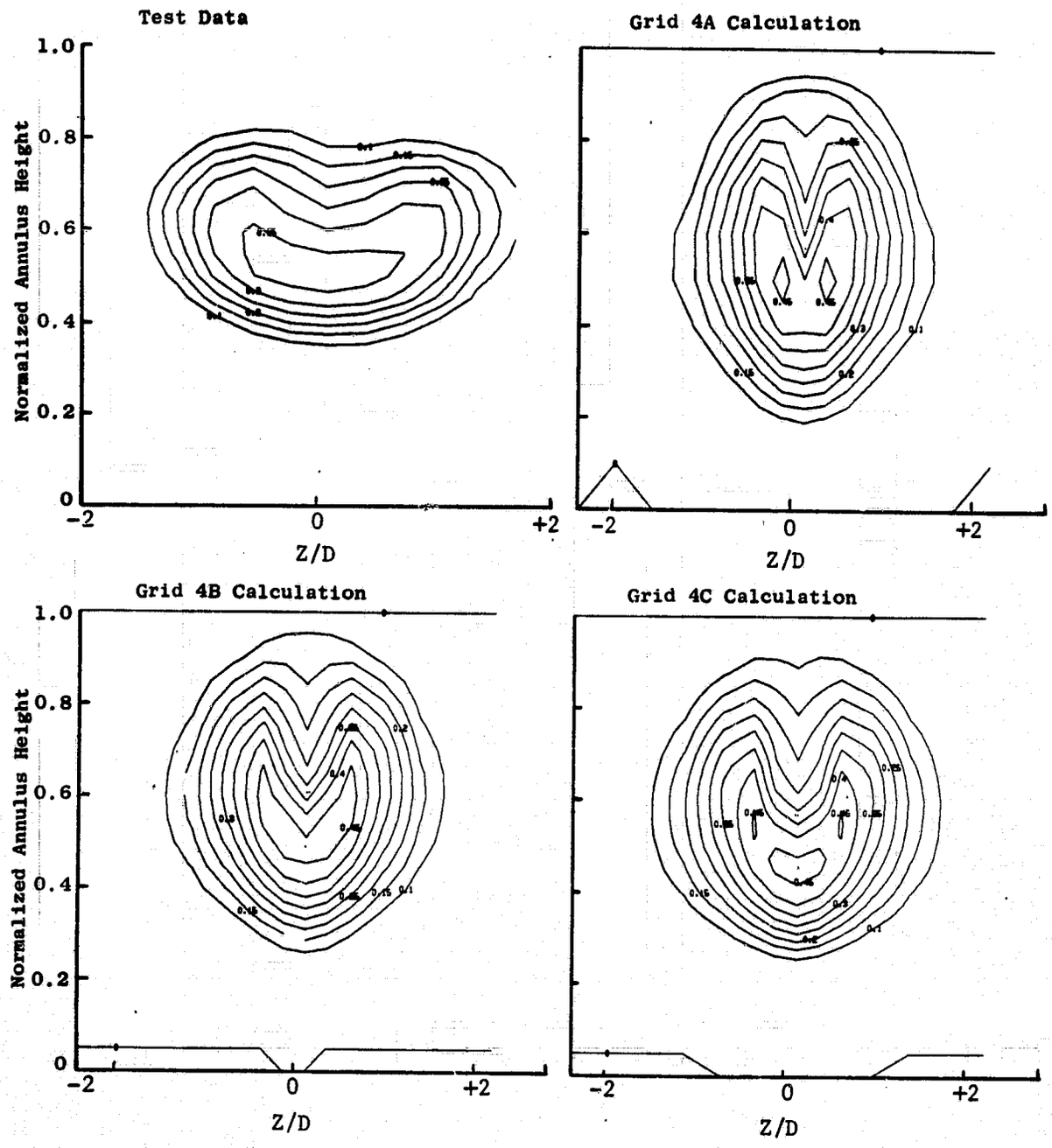


Figure 146. Calculated Results of Grid Sensitivity Investigation for Walker and Kors Experiment 69, X/D = 2.
Contours of $\frac{T_{Inlet} - T_{Local}}{T_{Inlet} - T_{Jet}}$

ORIGINAL PAGE IS
OF POOR QUALITY

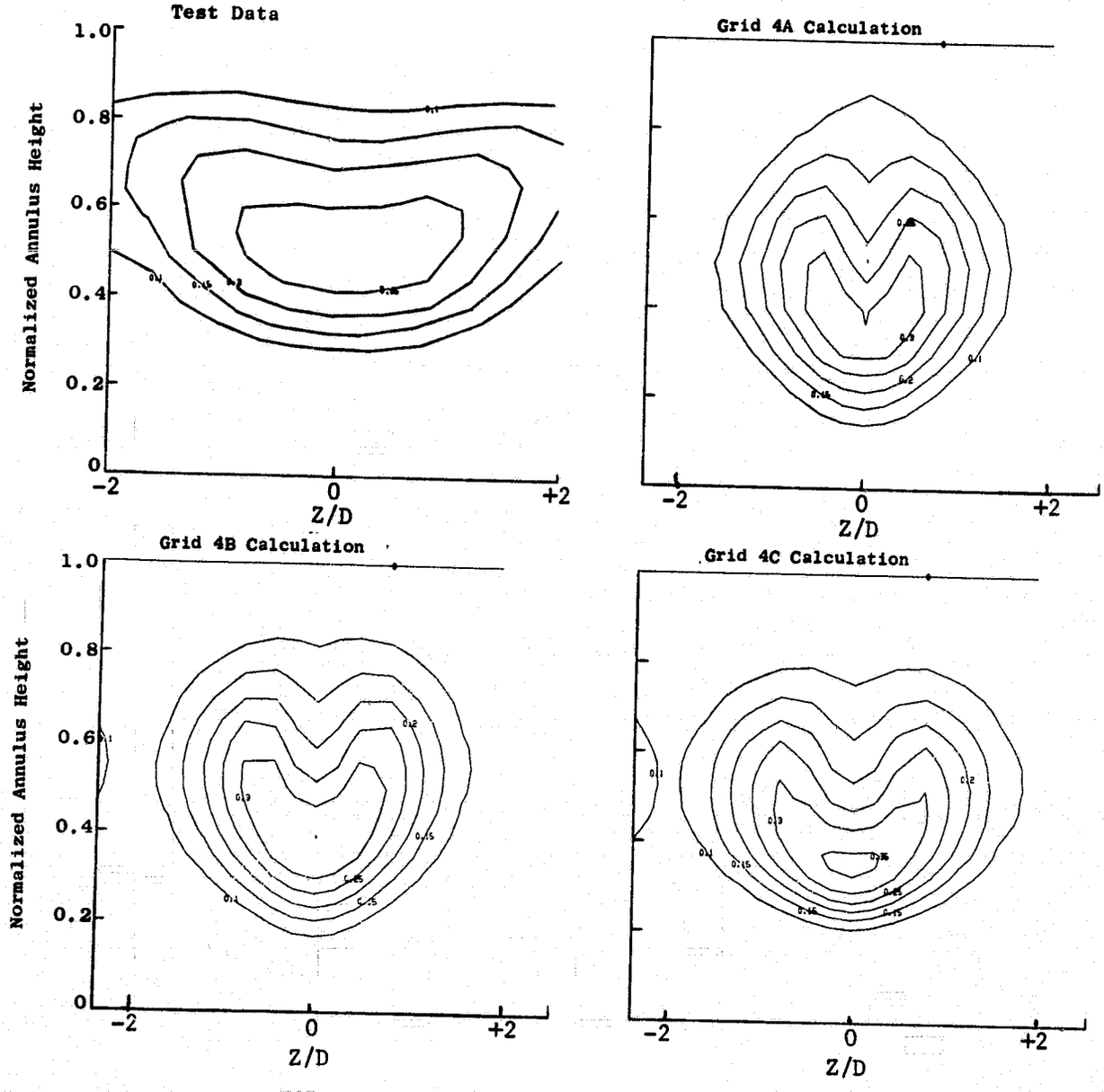


Figure 147. Calculated Results of Grid Sensitivity Investigation for Walker and Kors Experiment 69, X/D = 4.
Contours of $\frac{T_{Inlet} - T_{Local}}{T_{Inlet} - T_{Jet}}$

ORIGINAL PAGE IS
OF POOR QUALITY

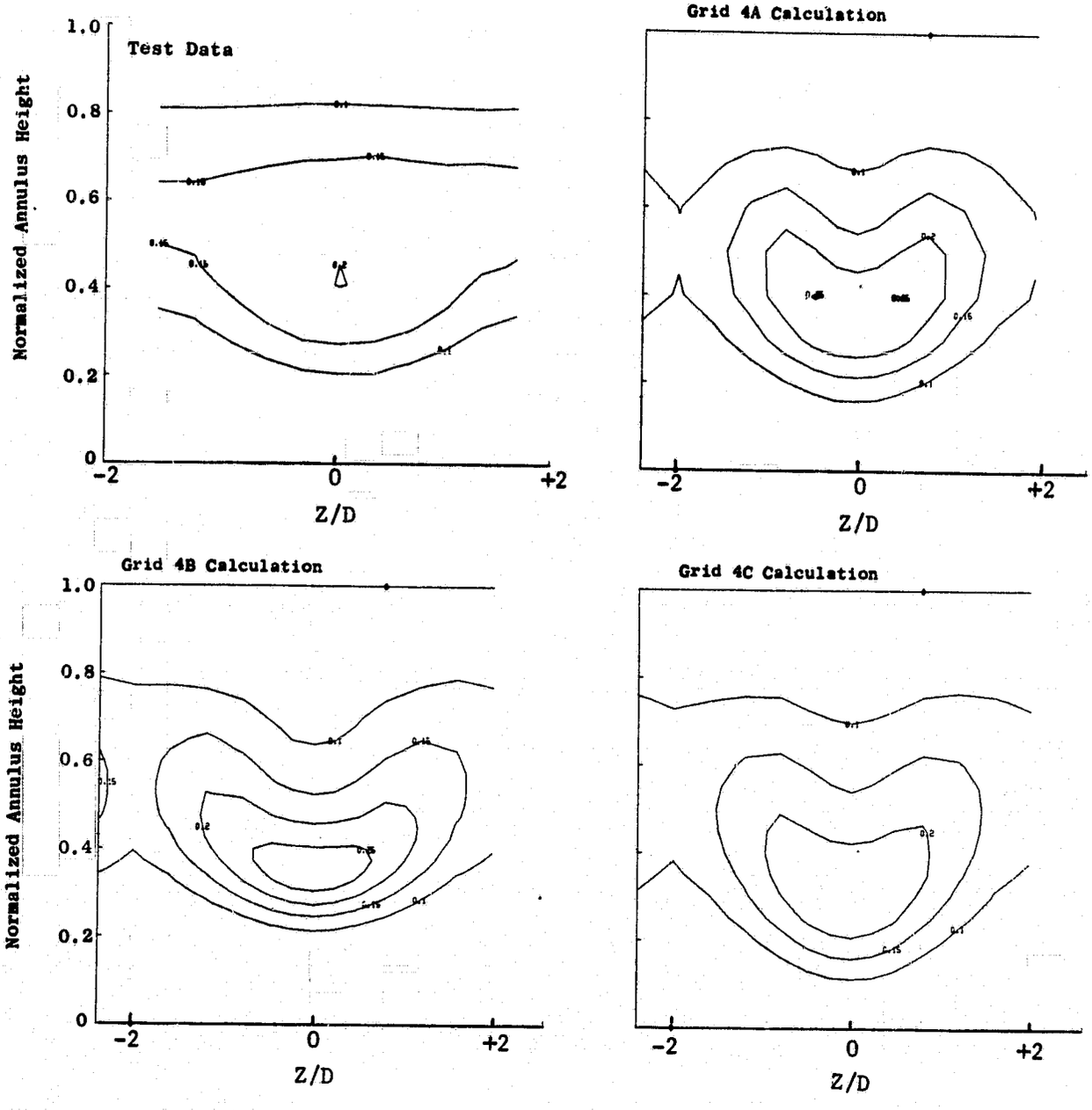


Figure 148. Calculated Results of Grid Sensitivity Investigation for Walker and Kors Experiment 69, X/D = 8.

Contours of $\frac{T_{Inlet} - T_{Local}}{T_{Inlet} - T_{Jet}}$

ORIGINAL PAGE IS
OF POOR QUALITY

Figure 149. Grid 4D Used to Investigate Sensitivity of Calculated Jet Penetration to Grid Detail Used.

results obtained using the (B) grid in Figures 150 and 151. It is observed from these figures that the more detailed Z grid did result in some increase in the calculated tangential spreading of the jet. The change was not significant. However, there was no change in the calculated jet penetration. These results suggest the overall penetration problem is not strongly grid dependent.

Up to this point in the dilution jet studies, the one parameter that had not been varied was the jet turbulence length scale. As previously mentioned, this parameter is not an input to the Northern Research code, but is derived internally. To provide greater flexibility, the Northern Research code was modified so that the jet turbulent kinetic energy and length scale could be input independently of the inlet. At the same time calculations were set up with the code prepared by the Garrett Turbine Company which had already provided direct turbulence energy and scale input capability for the dilution jets. Additional calculations were run using the modified Northern Research code and the medium grid of 21,000 nodes. The inlet turbulence kinetic energy and length scale inputs used were the same as used in the previous calculations. The jet turbulent kinetic energy input parameter was selected as 14 percent of the square of the injection velocity while the jet length scale parameter was varied from 1.5 to 100 percent of the effective jet diameter, (not individual node effective diameter). This represented a significant increase in the jet turbulent length scale. In summary the turbulence inputs were:

Inlet:

Turbulent kinetic energy/V^2 (AKFAC) = 6E-3

Turbulent length scale/duct height (ALFAL) = 2E-1

Jet:

Turbulent kinetic energy/V^2 (AKFACJ) = 1.43E-2
Turbulent length scale/jet diameter (ALFACJ) = 1.52E-2 to 1.0

The calculations were run for 200 iterations. The exact same calculations were then run using the Garrett code. Because of the similarities between the two models, the Garrett calculations served to provide a check of the modified Northern Research code as well as provide a back-to-back comparison between the two models. Within the range of jet length scale evaluated, a value of 15 percent of the effective jet diameter produced results closest to the measurements. The results of the calculations using this level of length scale for each of the two codes are compared to the measured test data in Figures 152 through 155. It is observed from these results that the two models indeed produce very similar solutions. More importantly, it is observed that the calculated jet penetration closely matches that observed from the measured test data. The change in the calculated penetration produced by the increased jet turbulent length scale is particularly noticeable when referring to the earlier calculations presented in Figures 141 through 144. It is also observed from the calculated results that the jet temperature dissipation closely matches

ORIGINAL PAGE IS
OF POOR QUALITY

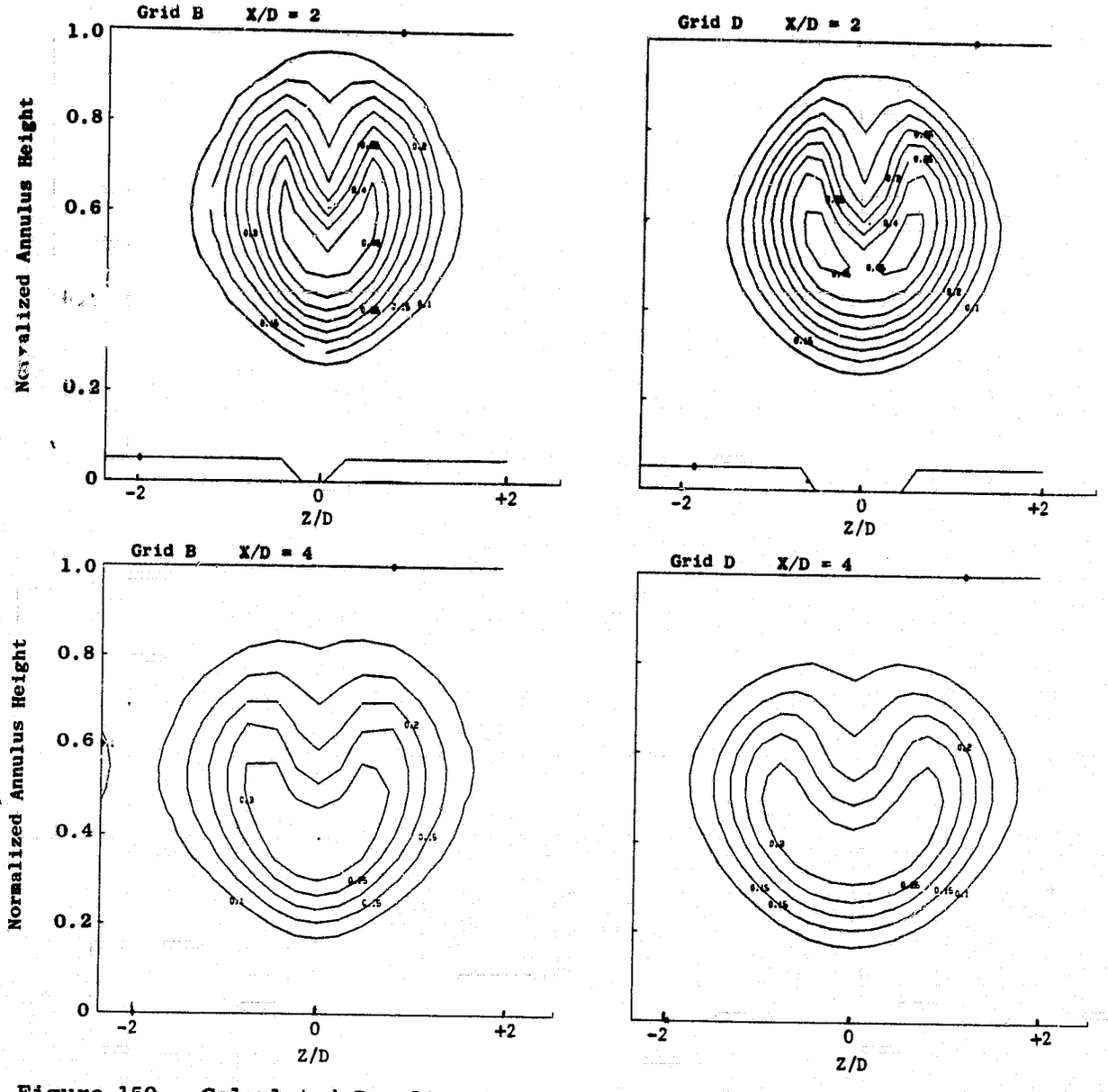


Figure 150. Calculated Results of Grid Sensitivity Investigation for Walker and Kors Experiment 69.

Contours of $\frac{T_{Inlet} - T_{Local}}{T_{Inlet} - T_{Jet}}$

ORIGINAL PAGE IS
OF POOR QUALITY

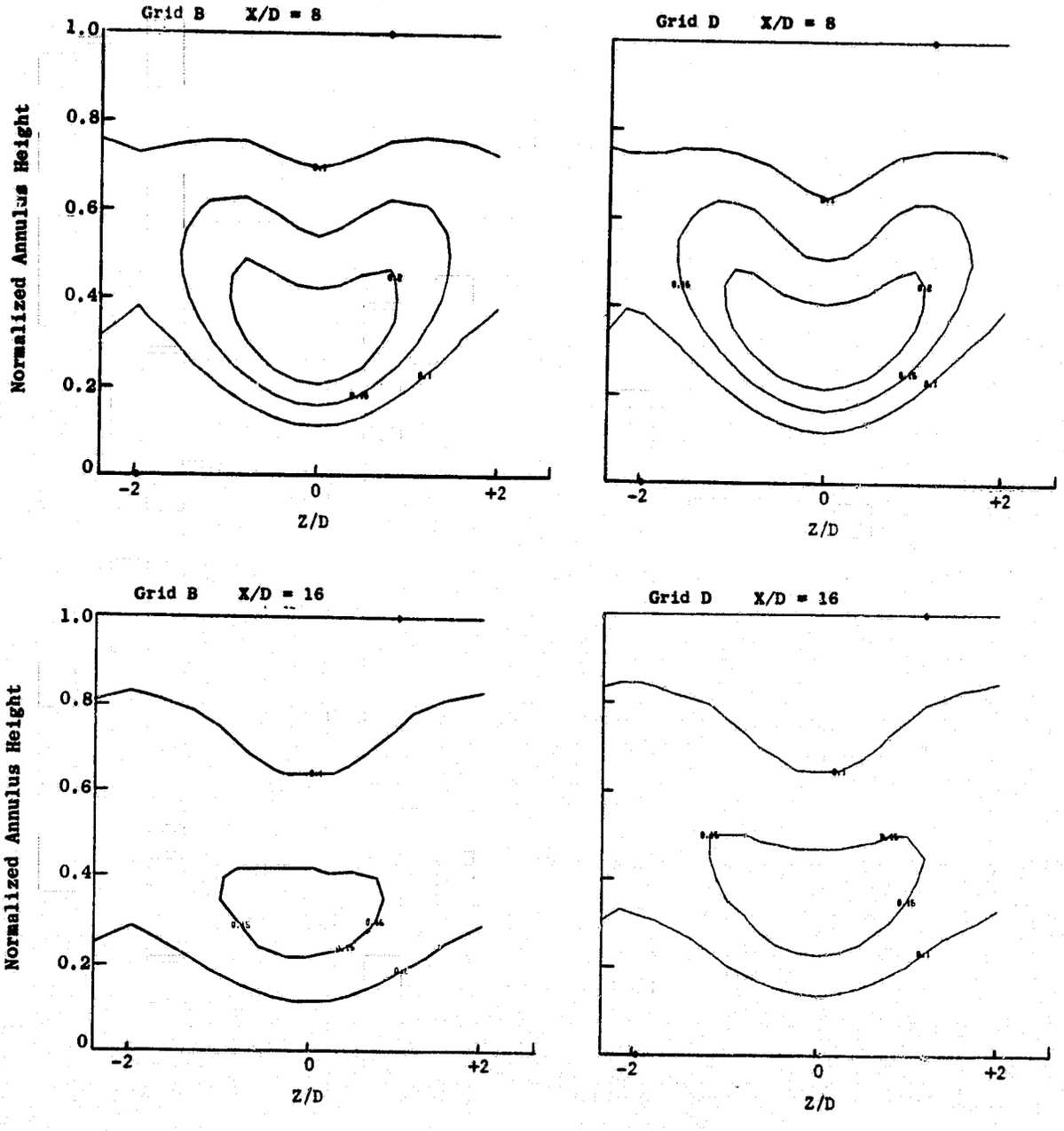


Figure 151. Calculated Results of Grid Sensitivity Investigation for Walker and Kors Experiment 69.
Contours of $\frac{T_{Inlet} - T_{Local}}{T_{Inlet} - T_{Jet}}$

ORIGINAL PAGE IS
OF POOR QUALITY

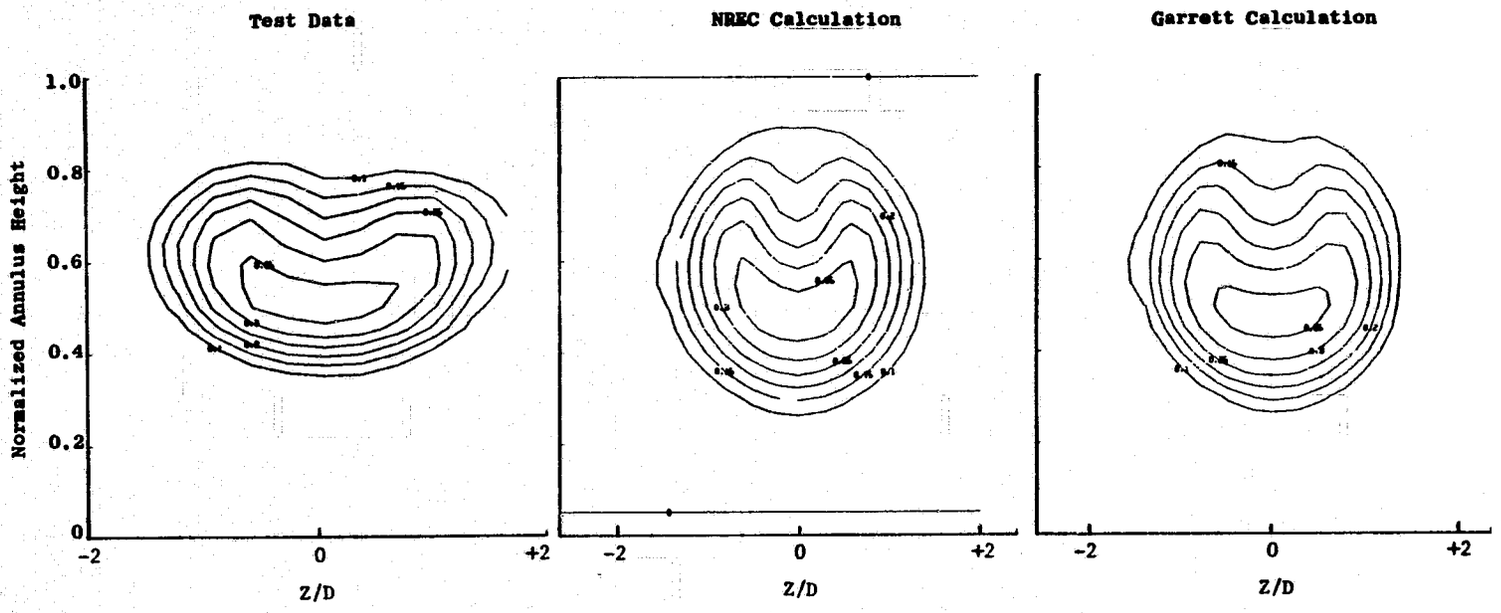


Figure 152. Comparison of Calculated Results of Walker and Kors Experiment 69 Obtained from the Northern Research and Garrett Codes, X/D = 2.
Contours of $\frac{T_{Inlet} - T_{Local}}{T_{Inlet} - T_{Jet}}$

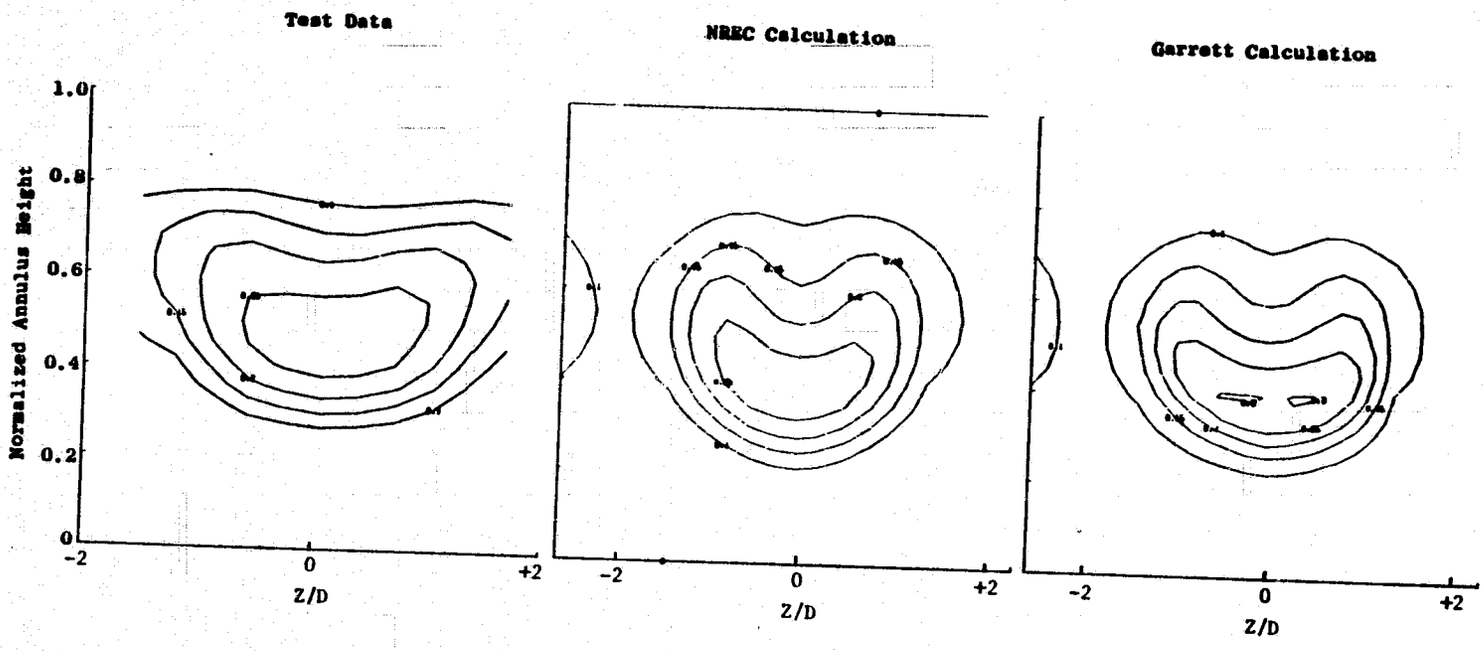
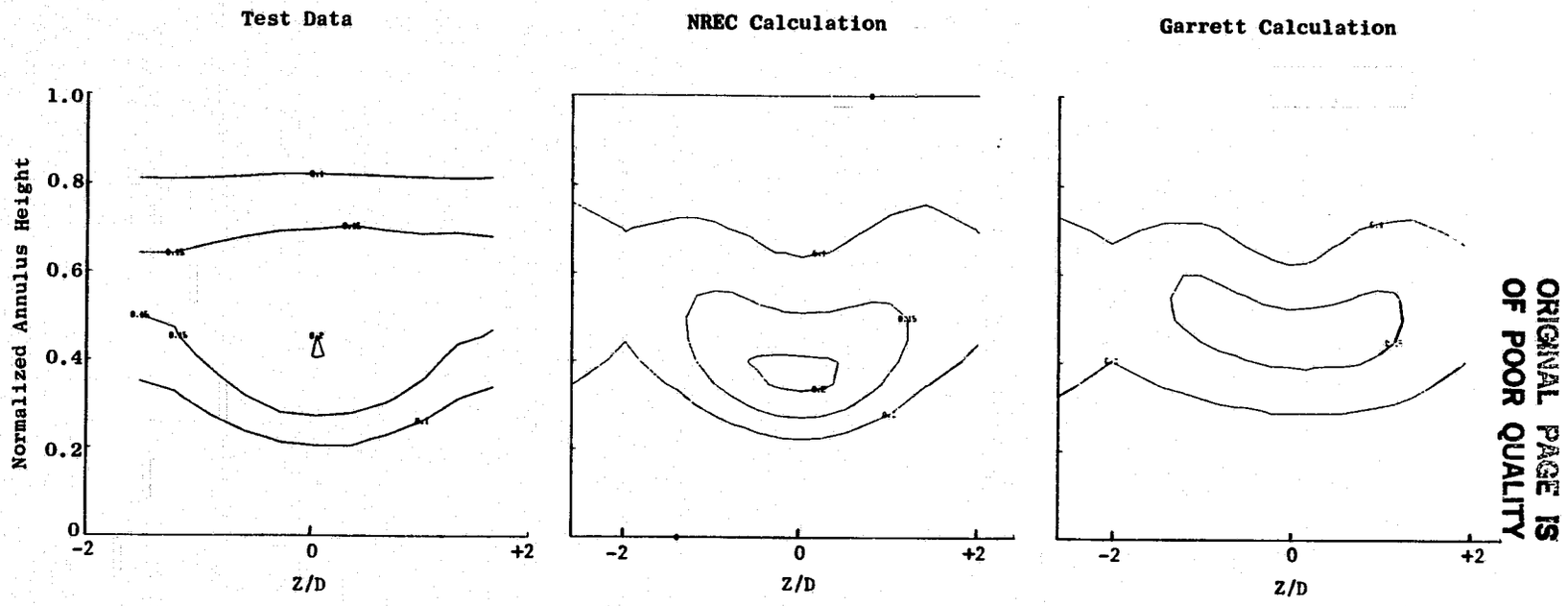


Figure 153. Comparison of Calculated Results of Walker and Kors Experiment 69 Obtained from the Northern Research and Garrett Codes, X/D = 4.

Contours of $\frac{T_{Inlet} - T_{Local}}{T_{Inlet} - T_{Jet}}$

ORIGINAL PAGE IS
OF POOR QUALITY



ORIGINAL PAGE IS
OF POOR QUALITY

Figure 154. Comparisons of Calculated Results of Walker and Kors Experiment 69 Obtained from the Northern Research and Garrett Codes, X/D = 8.
Contours of $\frac{T_{Inlet} - T_{Local}}{T_{Inlet} - T_{Jet}}$

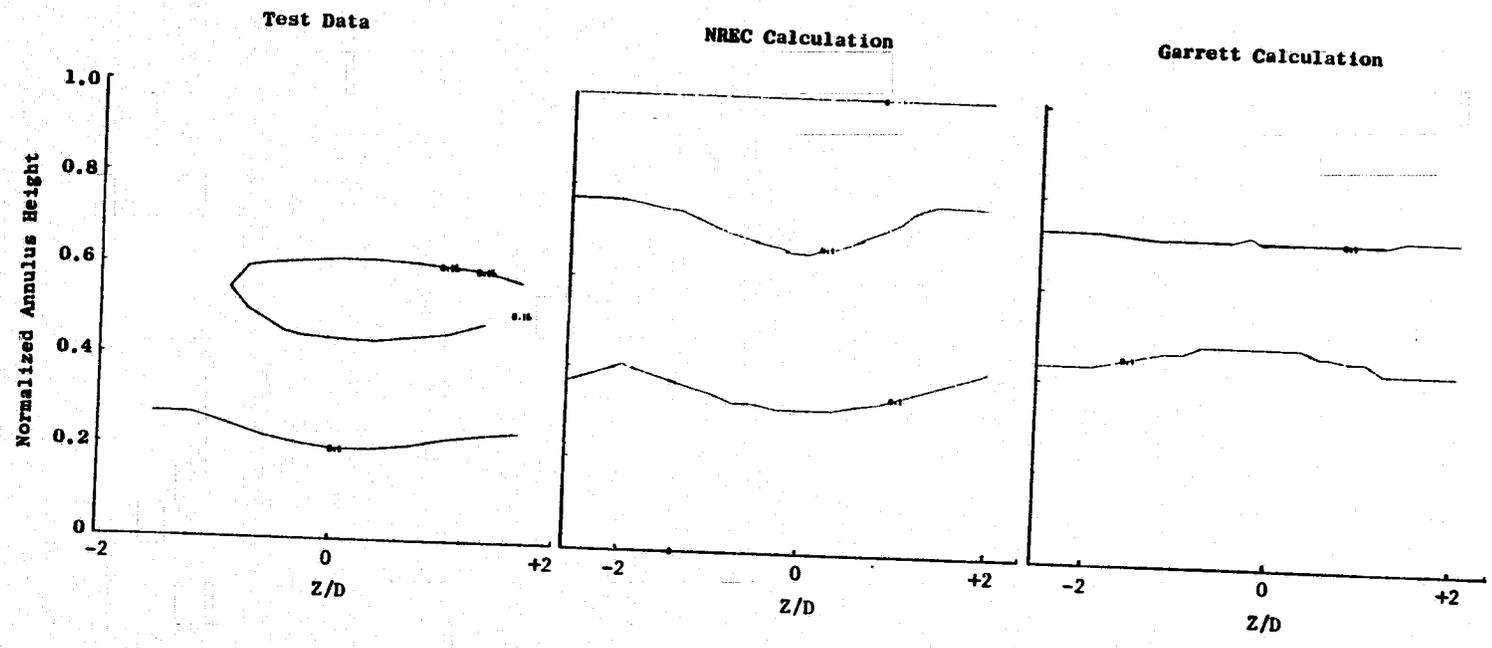
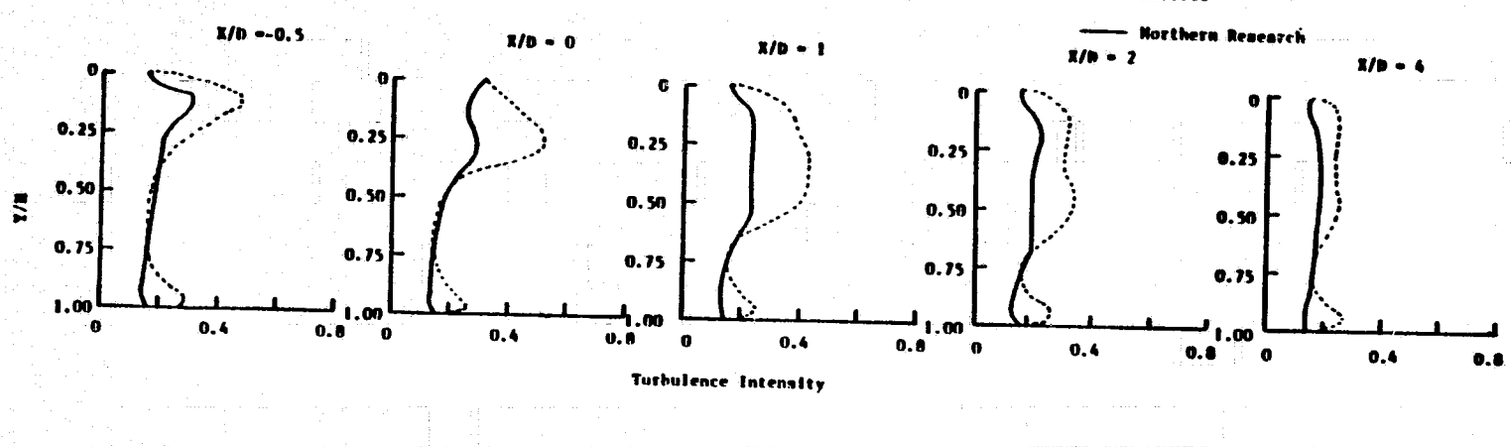


Figure 155. Comparisons of Calculated Results of Walker and Kors Experiment 69 Obtained from the Northern Research and Garrett Codes, X/D = 16.
Contours of $\frac{T_{Inlet} - T_{Local}}{T_{Inlet} - T_{Jet}}$

ORIGINAL PAGE IS
OF POOR QUALITY

the measured test data at all measurement planes downstream of the injection point. Earlier calculations had problems matching test results at measurement planes just downstream of the injection point. The one deficiency in the calculated results still shows a lack of early tangential spreading of the jet. The jet shape is too round just downstream of the injection point. The improvement observed in these calculations can be linked to the increased jet turbulent length scale, as it had been previously shown that the solution is insensitive to changes in the turbulent kinetic energy parameter. The results are consistent in that increasing the length scale reduces the turbulence dissipated allowing greater mixing. This reduces the jet penetration, and dissipates the jet core temperature more quickly. In Figures 156 and 157 plots of the turbulence intensities and length scales generated from these Northern Research and Garrett calculations of the experiment 69 test data are compared. From this comparison it is interesting to note that despite the identical turbulence inputs at the inlet and the jet, the two codes generate significantly different turbulence levels within the flow fields. Figure 157 also shows that the length scales predicted by the two programs within the flow field are also different from each other. However, using the modified Northern Research code and the medium grid, calculations of the Walker and Kors Experiment 67 test data were rerun. The larger jet length scale which had produced the satisfactory results in calculations of the Experiment 69 test data was used in this calculation. The calculated results are compared to the measured test data, and to the previous calculation of this experiment. This comparison is presented in Figures 158 through 161. Recall that the previous calculation used the unmodified Northern Research code in which the jet length scale was internally generated as approximately 3 percent of the effective diameter of the individual nodes comprising the jet. It is observed from this comparison that the rerun calculation using the larger jet length scale resulted in some reduction in penetration. While the results at X/D = 2.0 are reasonably close in penetration and temperature mixing to the measurements, at the further downstream locations, the calculated penetration is less than the measurements. The previous calculation using the small jet length scale is in good agreement with the jet penetration observed from the measured test data at all locations. It is also observed from this comparison that the larger jet length scale more quickly dissipates the jet core temperature. Calculated temperature levels are in agreement with the test data at $X/D \geq 2.0$. The previous calculation shows considerable error at this point. However, further downstream the rerun calculation shows the jet almost completely mixed out by X/D = 8.0, whereas the test data and the previous calcullations still show evidence of a jet core. These results provide evidence of too much mixing. Clearly, the results of the rerun calculations using the larger jet length scale are not as good as those from the previous calculations.

The inability of the calculation to produce results in good agreement with the experiment 67 and experiment 69 data sets while using a common set of turbulence inputs illustrates another deficiency in these codes. Since both experiments represented the same hole pattern with different injection velocities, one would expect the jet turbulent kinetic energy and length scale to adjust with the velocity increase in a manner maintaining relative turbulence intensity, and nondimensional length scale. In other words, the turbulence



ORIGINAL PAGE IS
OF POOR QUALITY

Figure 156. Comparisons of Calculated Results of Walker and Kors Experiment 69 Obtained from the Northern Research and Garrett Codes.

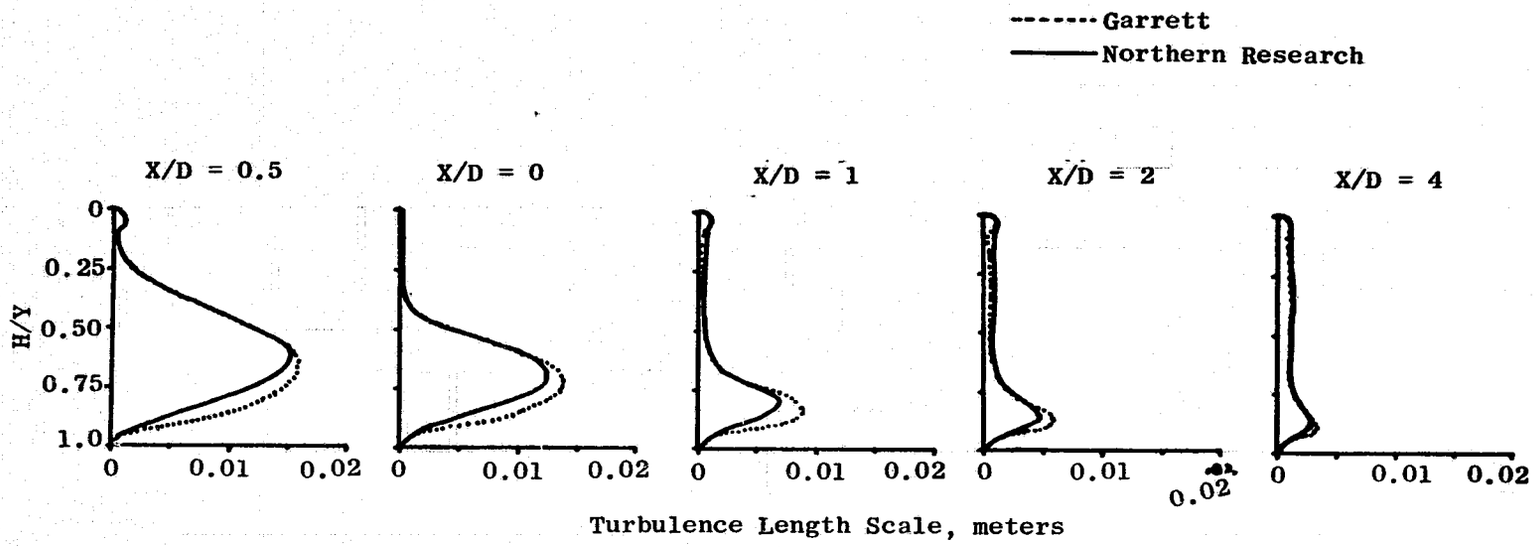


Figure 157. Calculated Turbulence Length Scales for Walker/Kors Experiment 69 AKFAC = 6E-3 ALFAC = 2E-1 AKFAC (JET) = 1.43E-2 ALFAC (JET) = 1.52E-2 Schmidt No. = 0.5.

ORIGINAL PAGE IS
OF POOR QUALITY

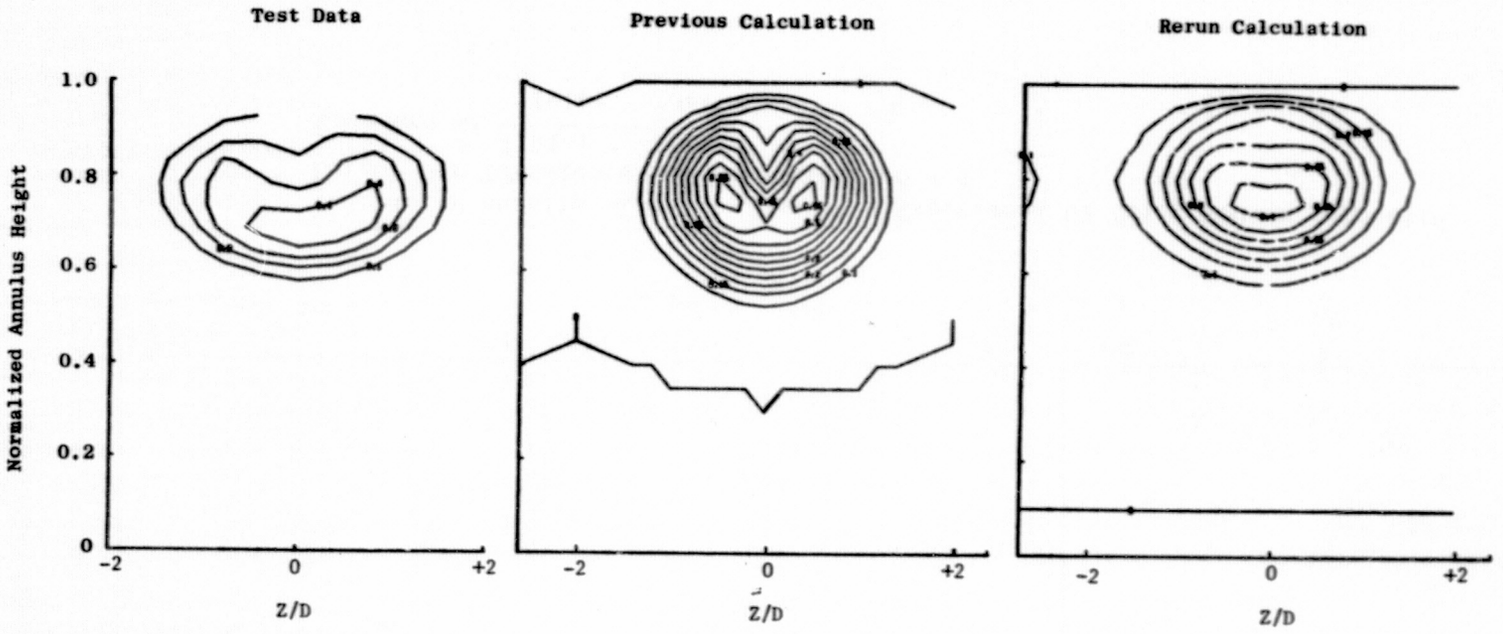


Figure 158. Calculated Results of Walker and Kors Experiment 67 Using Medium Grid with Larger Jet Turbulence Length Scale, X/D = 2.

Contours of $\frac{T_{Inlet} - T_{Local}}{T_{Inlet} - T_{Jet}}$

ORIGINAL PAGE IS
OF POOR QUALITY

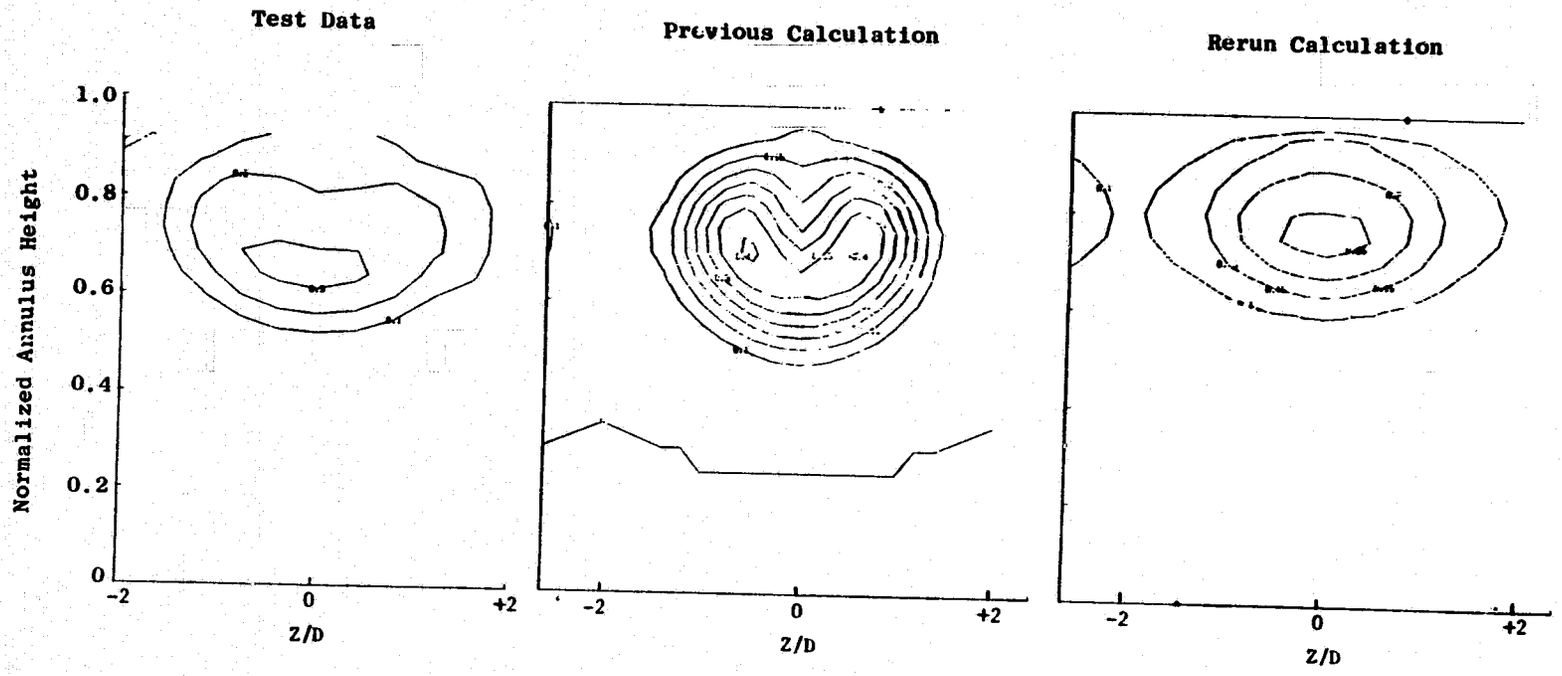


Figure 159. Calculated Results of Walker and Kors Experiment 67 Using Medium Grid with Larger Jet Turbulence Length Scale, X/D = 4.
Contours of $\frac{T_{Inlet} - T_{Local}}{T_{Inlet} - T_{Jet}}$

ORIGINAL PAGE IS
OF POOR QUALITY

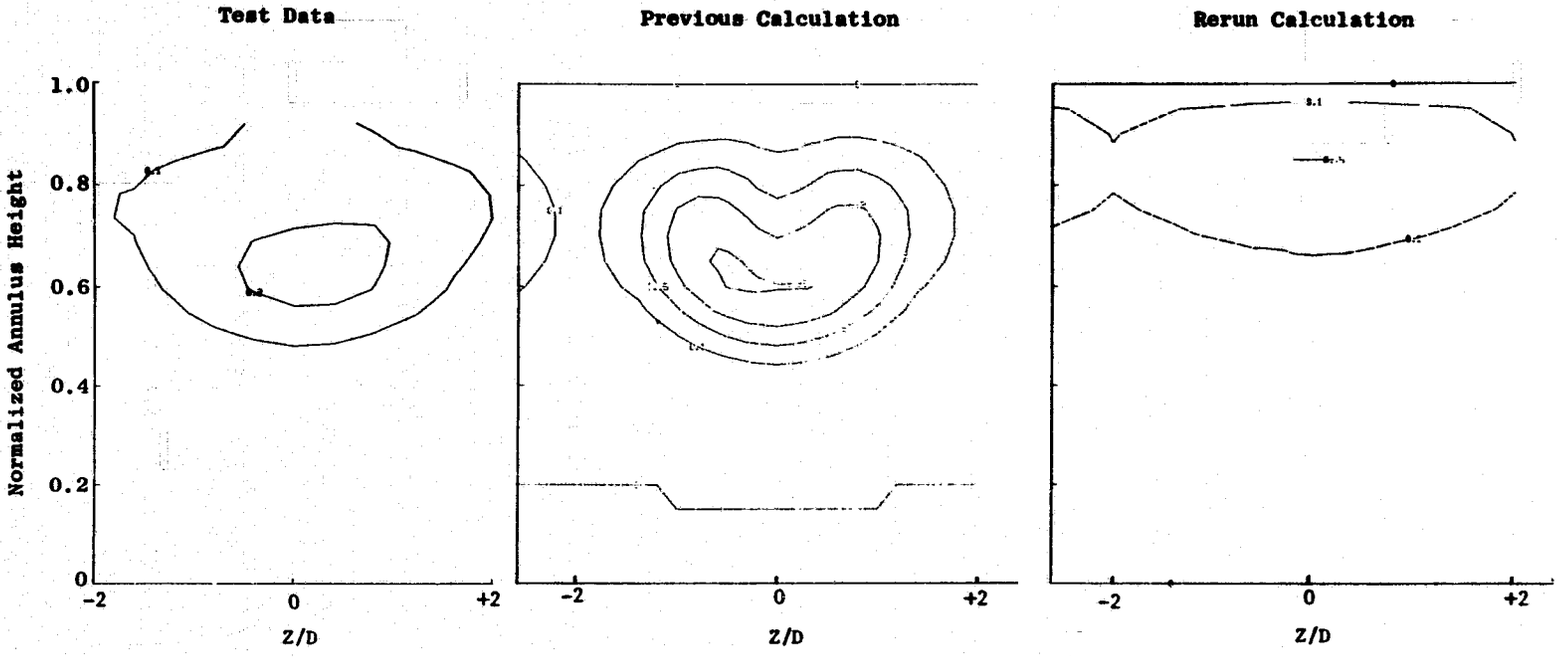


Figure 160. Calculated Results of Walker and Kors Experiment 67 Using Medium Grid with Larger Jet Turbulence Length Scale, X/D = 8.

Contours of $\frac{T_{Inlet} - T_{Local}}{T_{Inlet} - T_{Jet}}$

ORIGINAL PAGE IS
OF POOR QUALITY

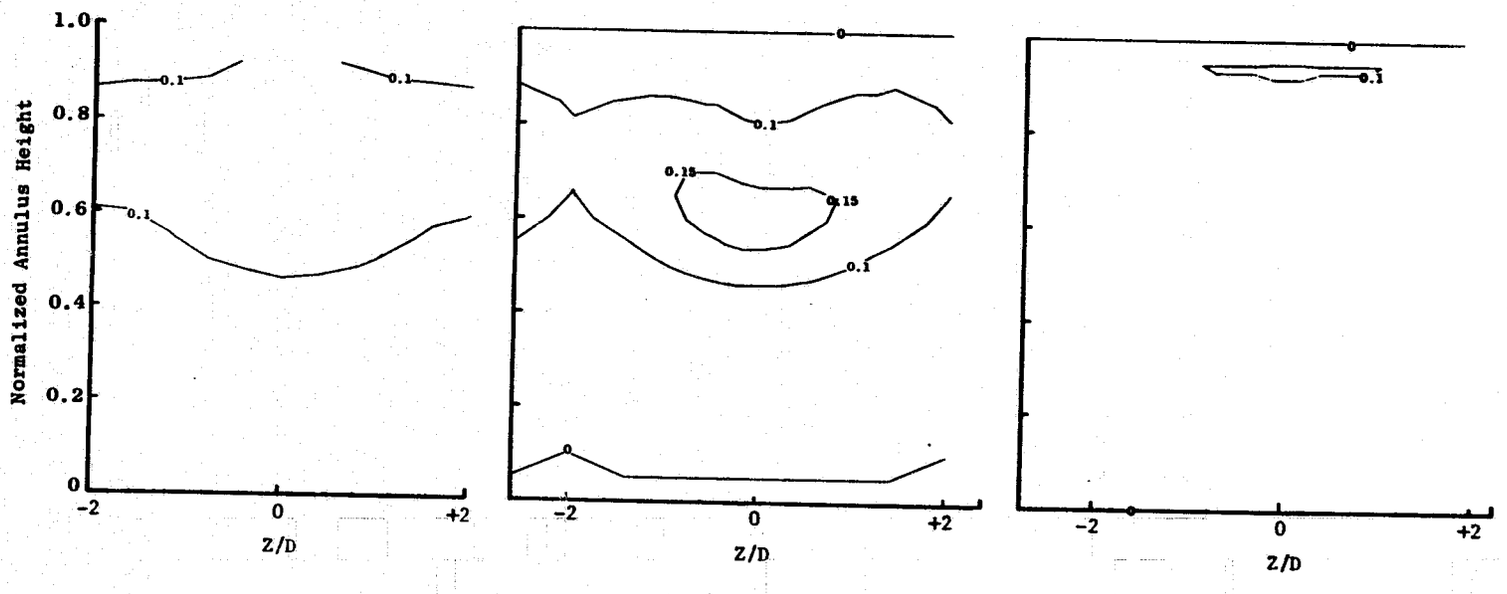


Figure 161. Calculated Results of Walker and Kors Experiment 67 Using Medium Grid with Larger Jet Turbulence Length Scale, X/D = 16.

Contours of $\frac{T_{Inlet} - T_{Local}}{T_{Inlet} - T_{Jet}}$

ORIGINAL PAGE IS
OF POOR QUALITY

energy and length scale inputs which produced satisfactory results for the calculations of Experiment 69 test data should also have produced satisfactory results for the Experiment 67 test data. This situation is awkward in that a combustor designer must have beforehand knowledge of what turbulence inputs to use in these codes in order to produce accurate results for the flow cases to be modified.

In addition to the calculations of the Walker and Kors test data, 3-D elliptic internal flow calculations of some of the experimental test configurations tested under this program were initiated. These calculations involved seven experimental test configurations (4, 5, 6, 7, 8, 13, and 17C), subjecting the model to progressively more complex internal flow fields. One of these (17C) involved fueled injection with heat release. For details into the experimental test configurations, refer to Volume II. These calculations provided assessment of the capabilities of the 3-D codes with more complex experiments. A coarse grid network was selected to use in most of these calculations because of the excessive run times and costs associated with more detailed grids. This relatively coarse grid was selected after the study illustrated by Figures 146 through 152 indicated that the calculated penetration of a dilution jet in crossflow was not strongly grid dependent. A detailed grid was developed for use in modeling the test configuration with fuel injection and heat release. Because of the reduced storage requirements in the Garrett 3-D code, it was selected to run calculations of the experimental test configurations. Calculations of the Walker and Kors data had demonstrated the close similarities in the results obtained from both the Garrett and Northern Research codes.

The coarse grid selected contained 13,365 total nodes. An illustration of this grid network is presented in Figure 162. The grid represented a single cup (18°) section of the 90° parallel wall annular experimental test rig. With this grid, multiple dilution holes could be modeled in two directly opposed rows on the outer and inner wall boundaries. This permitted modeling the two holes per cup primary row arrangement, and the three holes per cup secondary row arrangement featured in the experimental test rig. All dilution holes were modeled using nine nodes each, arranged in a square pattern. Because of the lack of detail in this grid, especially in the vicinity of the dilution holes, the geometric area of all dilution holes on the outer wall boundary are the same, as are all dilution holes on the inner wall boundary. Therefore, different hole sizes in the dilution rows featured in some of the experimental test configurations are not geometrically accommodated. Because of the annular geometry, the contraction effect on the inner wall boundary grid, and the resulting impact on the geometrical sizes of the inner wall dilution holes is not accommodated with this coarse grid. Directly opposed dilution holes intended to have the same area are larger on the outer wall boundary than on the inner wall boundary by an amount equal to the annulus radius ratio. Within the codes, checks on hole flow continuity result in adjustments to the injection density for holes suffering from these problems. The total injection momentum of the dilution jet is thus conserved.

The turbulence energy, length scale, and turbulent Schmidt number input values used in all 3-D calculations of the experimental test configurations are listed on the following page.

ORIGINAL PAGE IS
OF POOR QUALITY

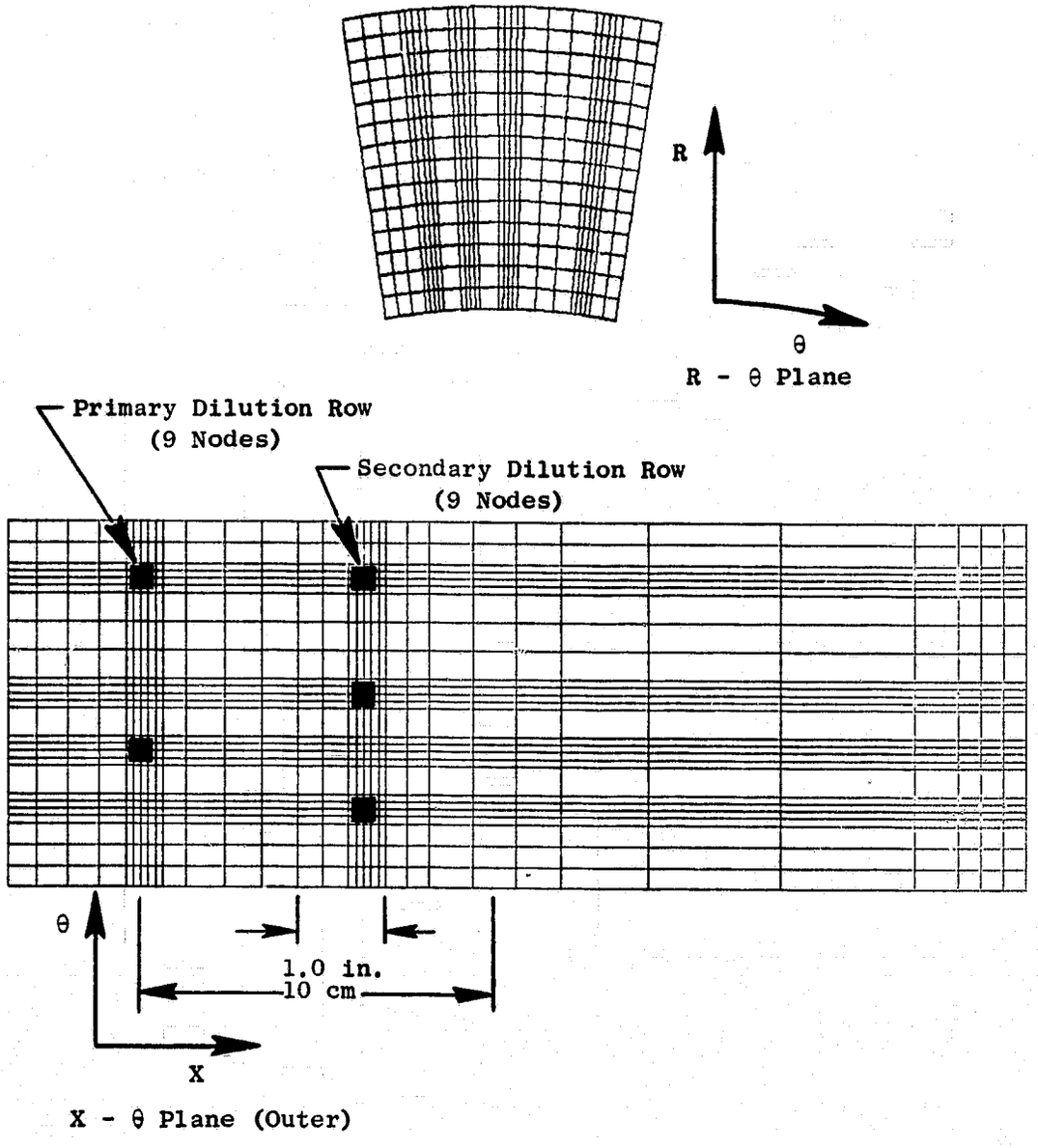


Figure 162. Coarse Grid Selected for Calculations of Experimental Test Configurations.

Inlet turbulent energy parameter (AKFAC) = 6×10^{-3}

Inlet turbulent length scale parameter (ALFAC) = 2×10^{-1}

Jet turbulent kinetic energy intensity = 10%

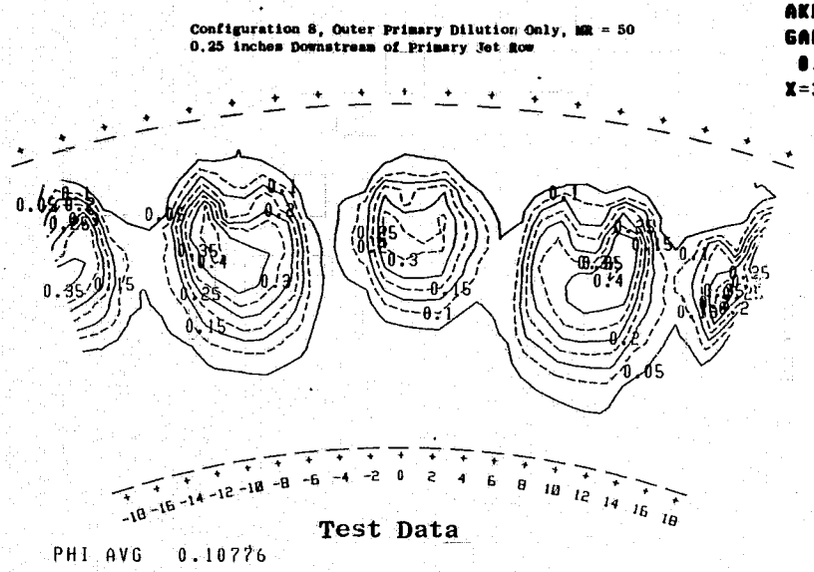
Jet turbulent length scale = 5×10^{-3} ft

Turbulent Schmidt Number = 0.5

Calculations using the coarse grid were generally run for 300 iterations. This number of iterations provided a reasonably converged solution without excessive costs. The calculated results were transformed into plots of temperature difference ratio contours for direct comparison with the plotted results from the experimental test data.

Calculated results for experimental test Configuration 8 are compared to the test data in Figures 163 through 166. This configuration represented the least complex flow field of the seven configurations modeled. The dilution pattern featured a single outer wall row of jets penetrating into a uniform cross flow at a momentum ratio of 50. The holes in this row featured alternating hole sizes simulating the GE/F101 primary dilution pattern. From comparison with test data, it is observed that the calculation predicts a severe overpenetration of the larger jet. This problem is particularly obvious in Figure 164 where the calculation predicts the larger jet to impinge on the opposite wall. This is reminiscent of earlier calculated results of the Walker and Kors experiment 69 test data (momentum ratio of 26) using very small jet turbulent length scale inputs. However, the turbulence inputs used in this calculation had produced a satisfactory result for the Walker and Kors test case. The difference in grid density may be a contributor, but further investigative calculations with grids were beyond the scope of the planned efforts. It is also observed from the comparison that calculated results close to the jet injection point show considerable discrepance in jet temperature levels. However, further downstream temperature levels show much better agreement. With the exception of the overpenetration of the larger jet, the calculated result at the aft measurement plane shows many similarities with the measured test data. Of particular note is the calculated depression of the 0.10 contour line at 0° also seen in the measured test data. The solution was run an additional 1,000 iterations to see if any improvement could be obtained. As anticipated, these results (not shown) showed almost no change over results obtained after 300 iterations.

Calculated results for experimental test Configurations 4 and 5 are compared to the test data in Figures 167 through 174. These configurations differed only in the jet injection momentum ratio. The dilution pattern in these configurations featured two directly opposed rows of jets penetrating into a uniform cross flow at a momentum ratio of 10 in Configuration 4 and 50 in Configuration 5. Both rows of holes featured the same pattern of alternating hole sizes simulating the GE/F101 combustor primary dilution pattern. Once again evidence of overpenetration from the calculation is seen in both sets of comparisons. The degree of overpenetration is more severe in the higher momentum ratio case. What is particularly disturbing is that similar turbulence inputs had resulted in a calculated underpenetration of the low momentum



Test Data

Calculation

Figure 163. Comparison of Measured and Calculated Results for Experimental Test Configuration 8.

ORIGINAL PAGE IS
OF POOR QUALITY

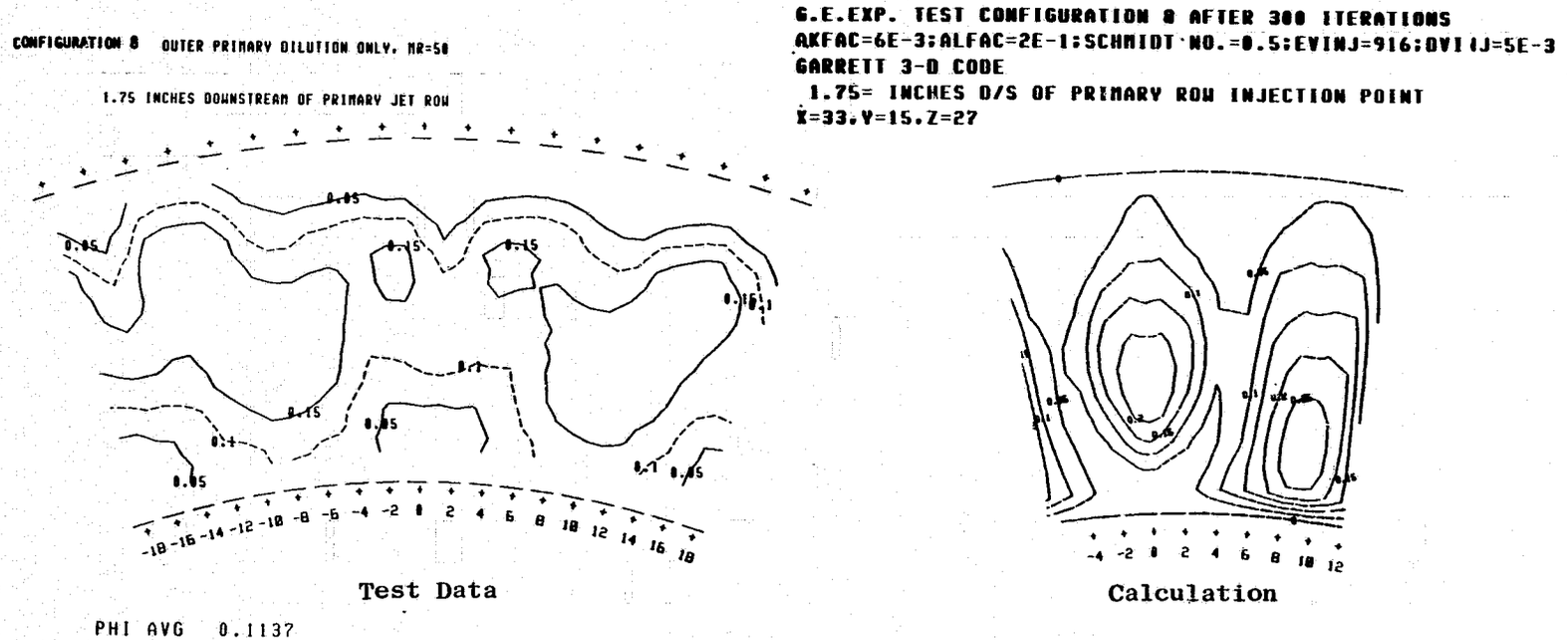
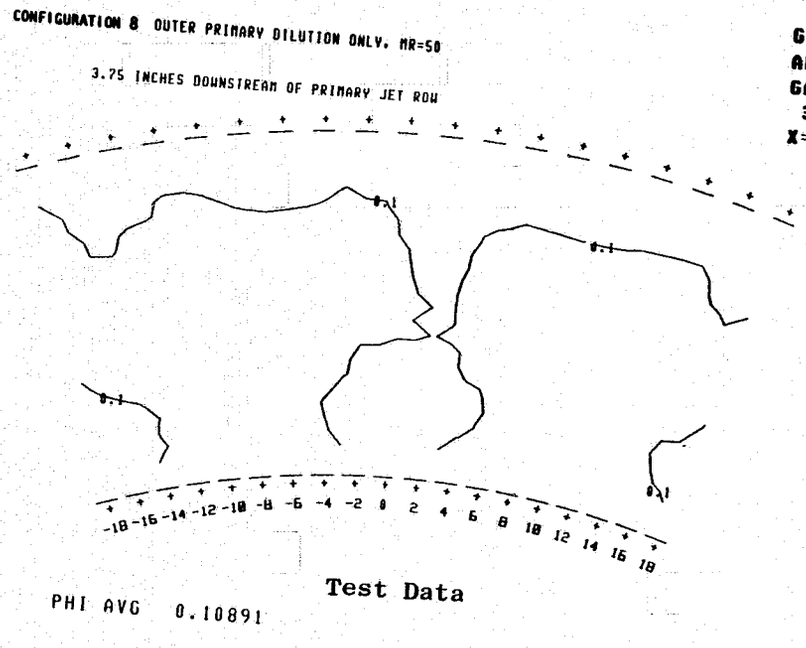


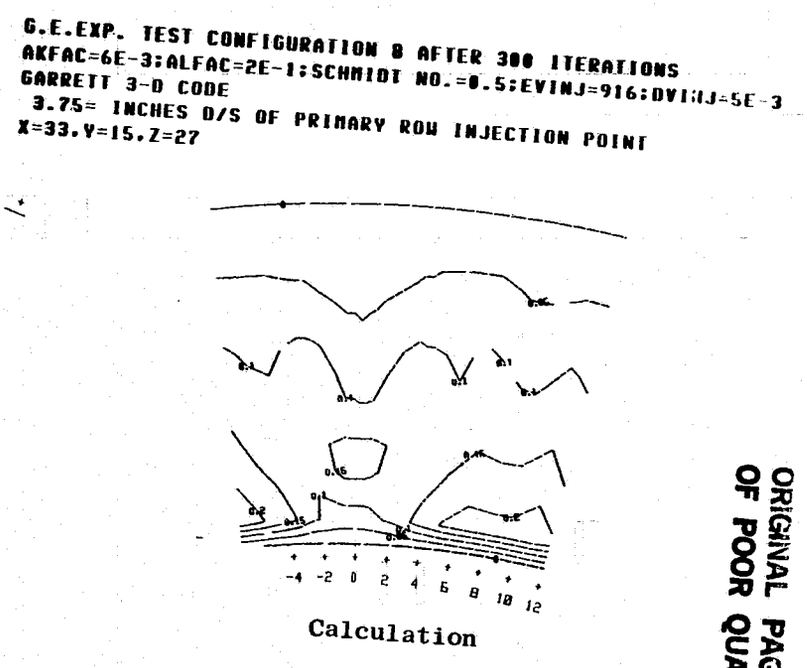
Figure 164. Comparison of Measured and Calculated Results for Experimental Test Configuration 8.

Contours of $\frac{T_{Inlet} - T_{Local}}{T_{Inlet} - T_{Jet}}$

ORIGINAL PAGE IS
OF POOR QUALITY



Test Data

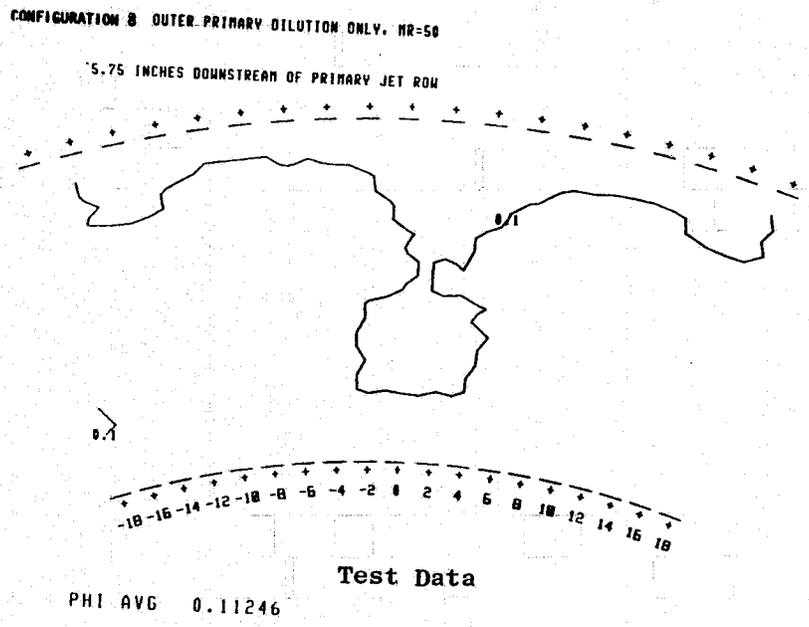


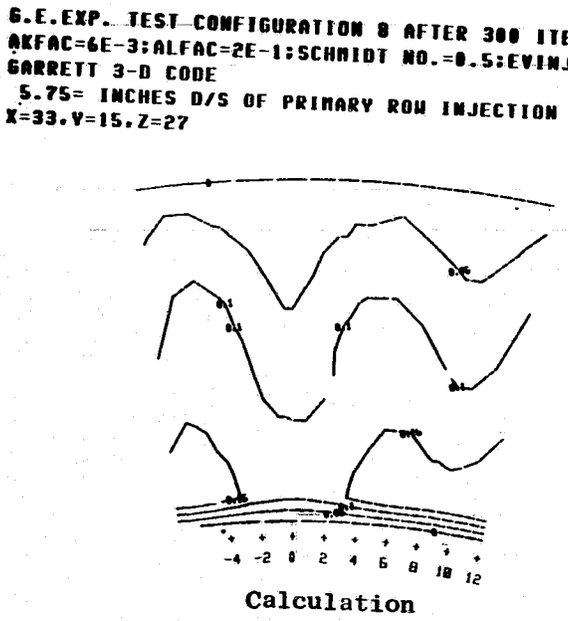
Calculation

Figure 165. Comparison of Measured and Calculated Results for Experimental Test Configuration 8.

Contours of $\frac{T_{Inlet} - T_{Local}}{T_{Inlet} - T_{Jet}}$

ORIGINAL PAGE IS
OF POOR QUALITY

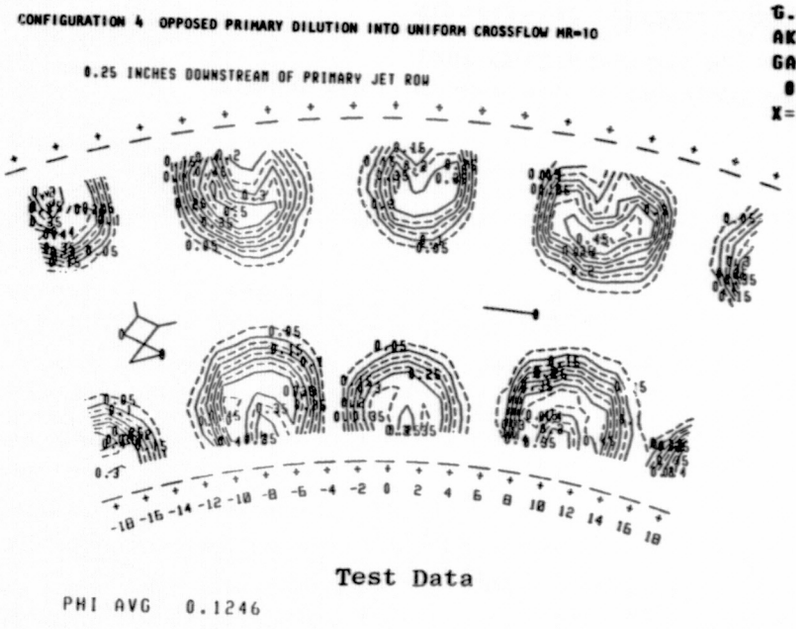




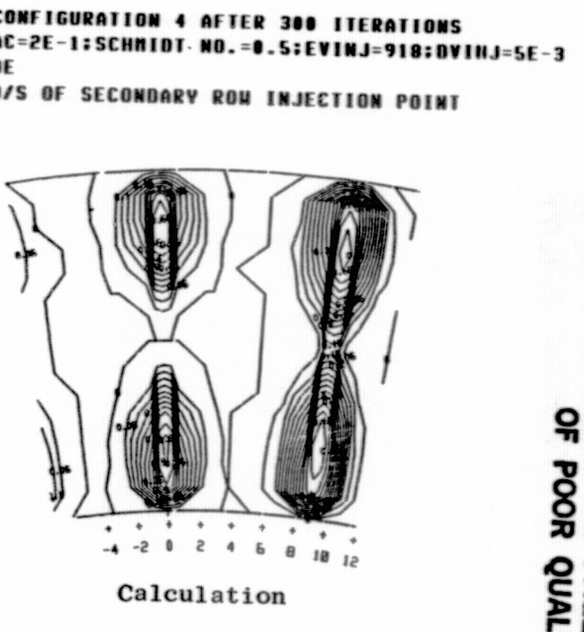
ORIGINAL PAGE IS
OF POOR QUALITY

Figure 166. Comparison of Measured and Calculated Results for Experimental Test Configuration 8.

Contours of $\frac{T_{Inlet} - T_{Local}}{T_{Inlet} - T_{Jet}}$



Test Data

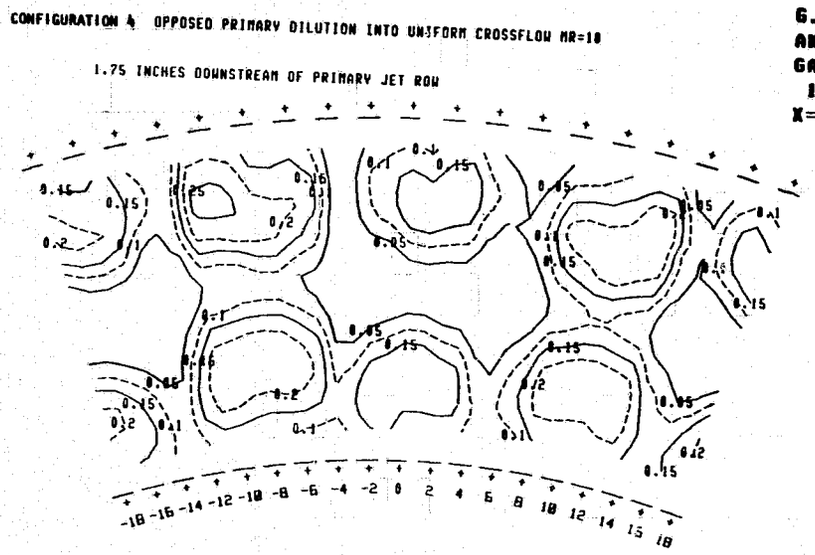


Calculation

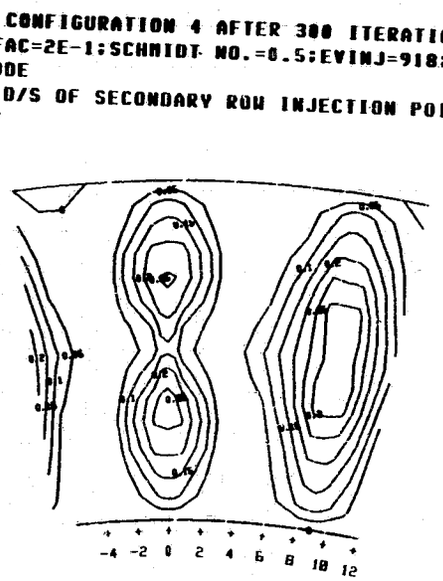
ORIGINAL PAGE IS
OF POOR QUALITY

Figure 167. Comparison of Measured and Calculated Results for Experimental Test Configuration 4.

Contours of $\frac{T_{Inlet} - T_{Local}}{T_{Inlet} - T_{Jet}}$



Test Data

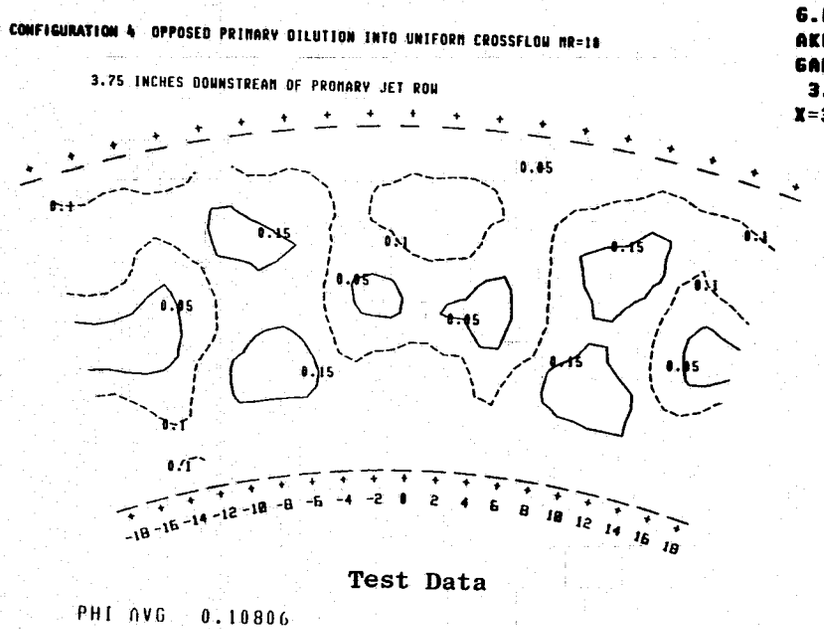


Calculation

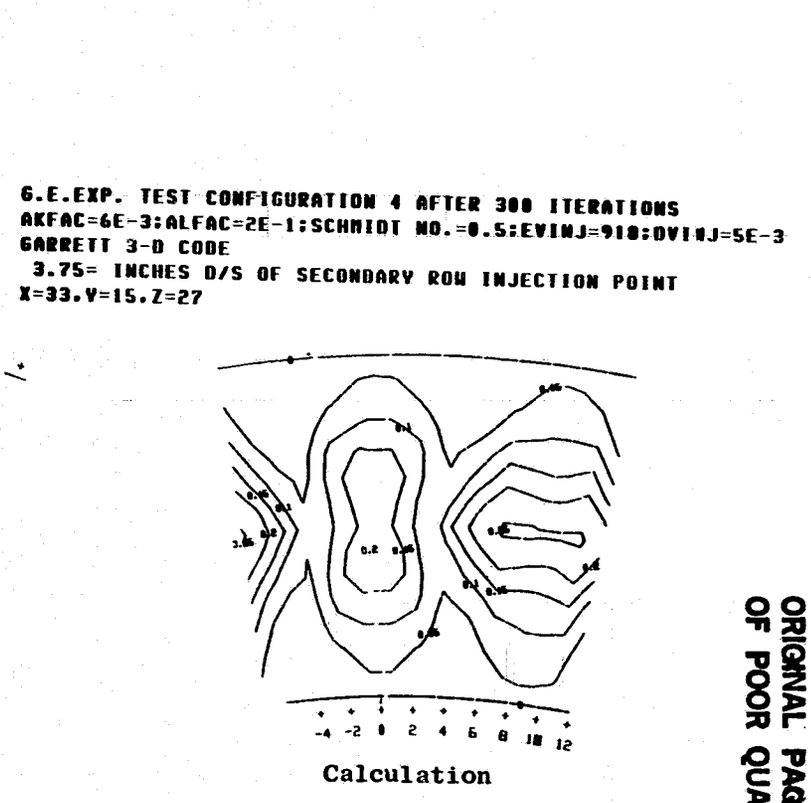
Figure 168. Comparison of Measured and Calculated Results for Experimental Test Configuration 4.

Contours of $\frac{T_{Inlet} - T_{Local}}{T_{Inlet} - T_{Jet}}$

ORIGINAL PAGE IS
OF POOR QUALITY



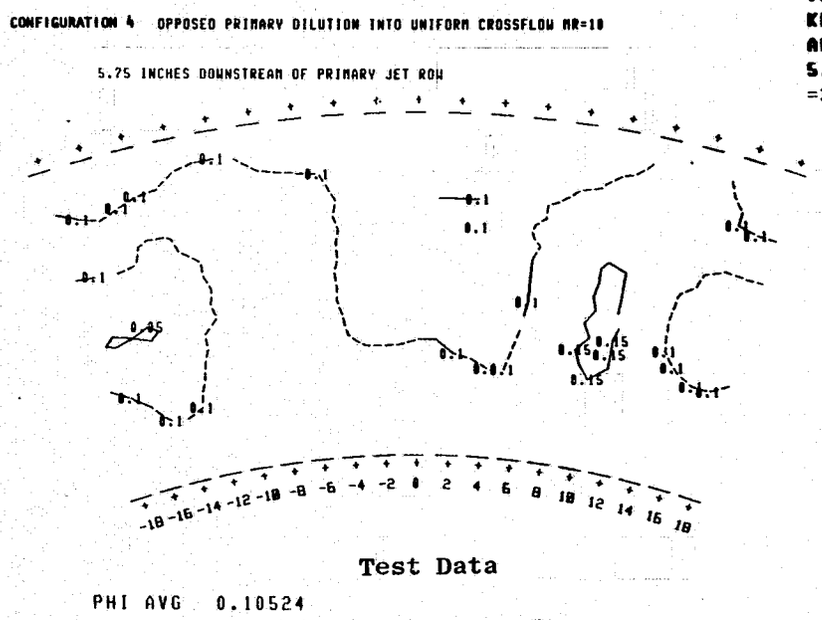
Test Data



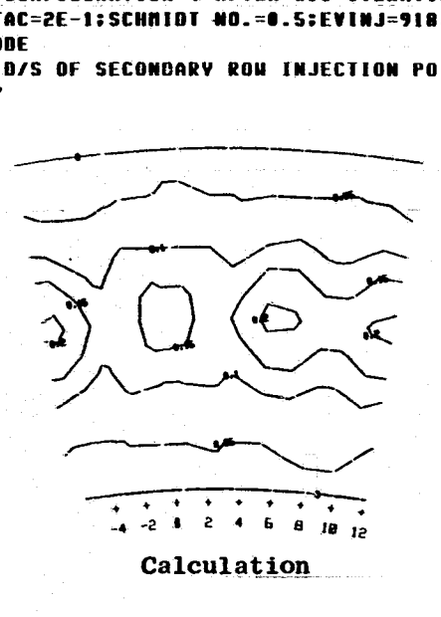
Calculation

ORIGINAL PAGE IS
OF POOR QUALITY

Figure 169. Comparison of Measured and Calculated Results for Experimental Test Configuration 4.
Contours of $\frac{T_{Inlet} - T_{Local}}{T_{Inlet} - T_{Jet}}$



Test Data

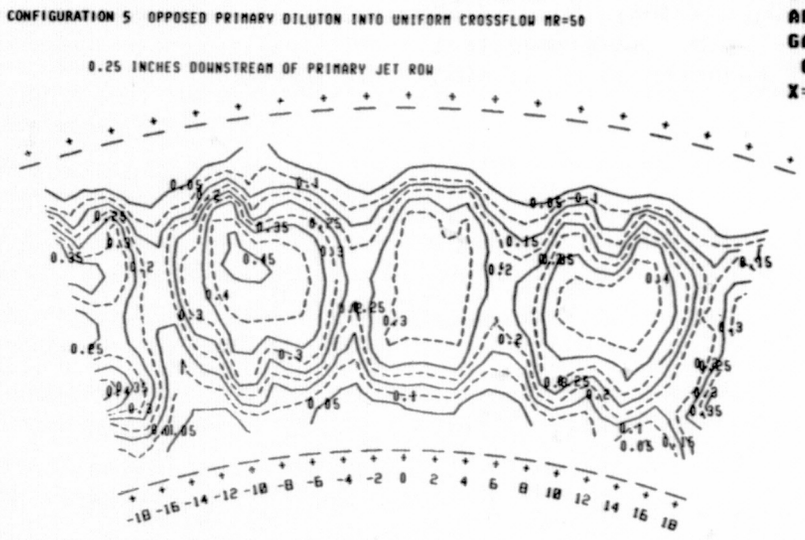


Calculation

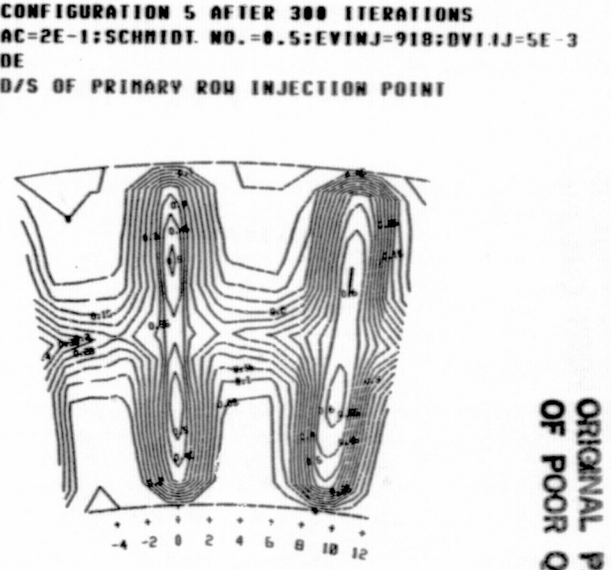
ORIGINAL PAGE IS
OF POOR QUALITY

Figure 170. Comparison of Measured and Calculated Results for Experimental Test Configuration 4.

Contours of $\frac{T_{Inlet} - T_{Local}}{T_{Inlet} - T_{Jet}}$



Test Data

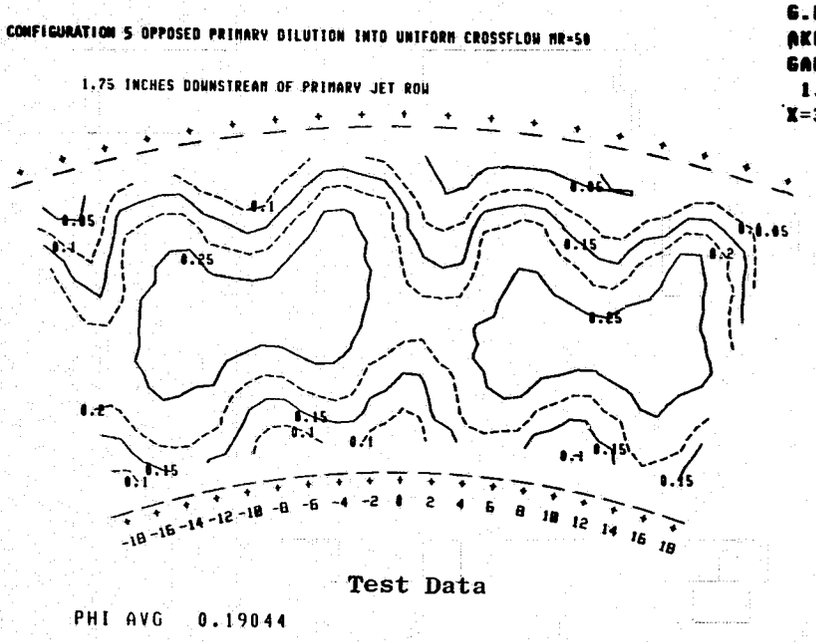


Calculation

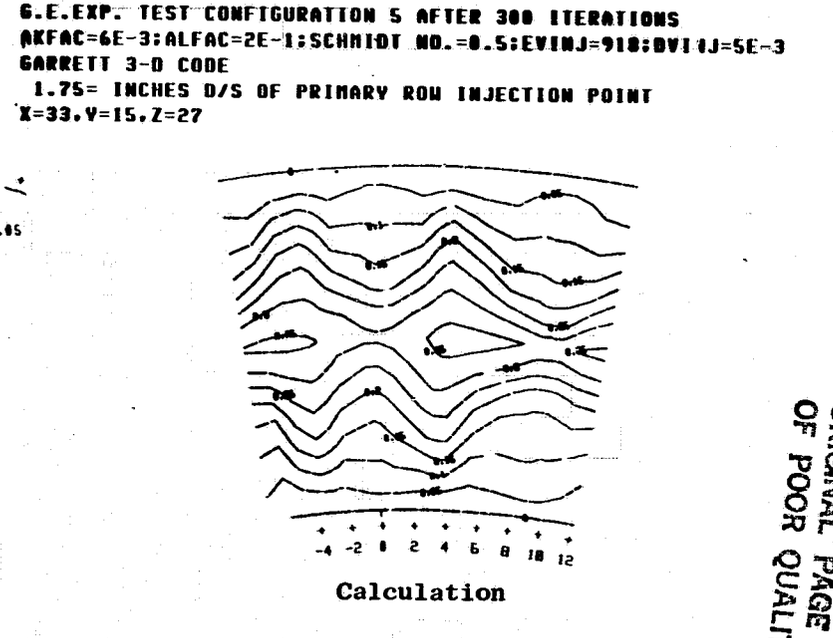
ORIGINAL PAGE IS
OF POOR QUALITY

Figure 171 Comparison of Measured and Calculated Results for Experimental Test Configuration 5.

Contours of $\frac{T_{Inlet} - T_{Local}}{T_{Inlet} - T_{Jet}}$



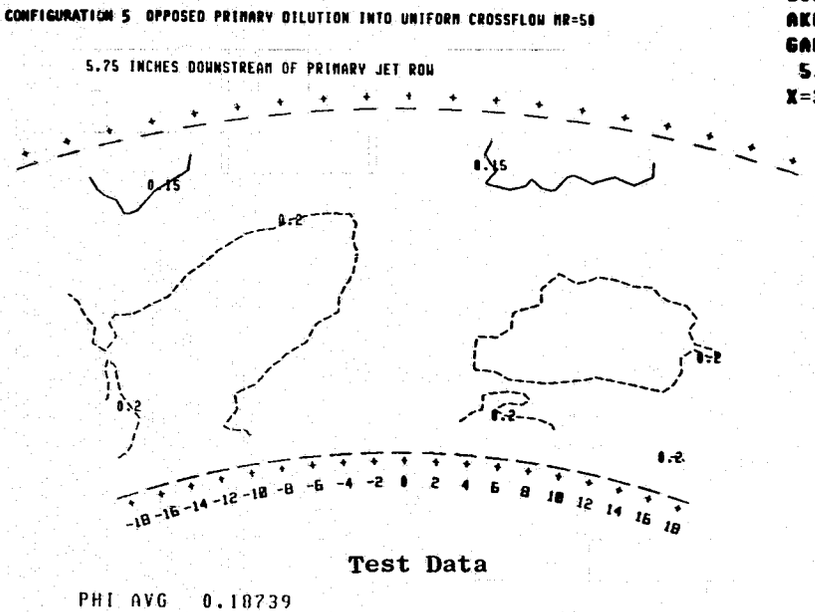
Test Data



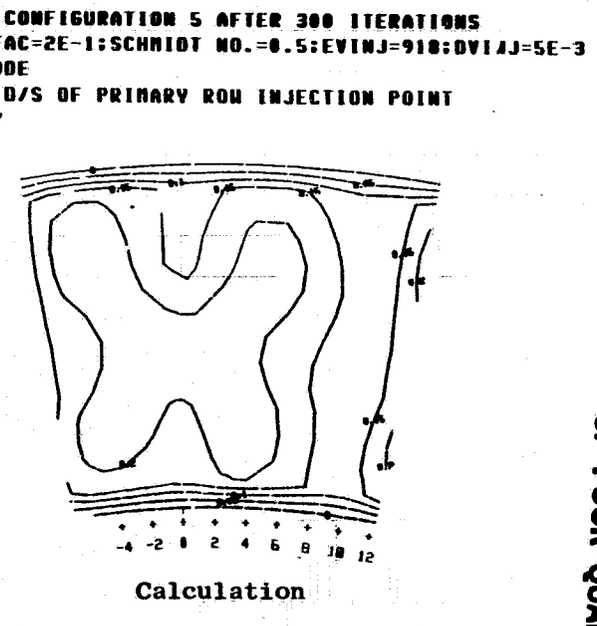
Calculation

ORIGINAL PAGE IS
OF POOR QUALITY

Figure 172. Comparison of Measured and Calculated Results for Experimental Test Configuration 5.
Contours of $\frac{T_{Inlet} - T_{Local}}{T_{Inlet} - T_{Jet}}$



Test Data

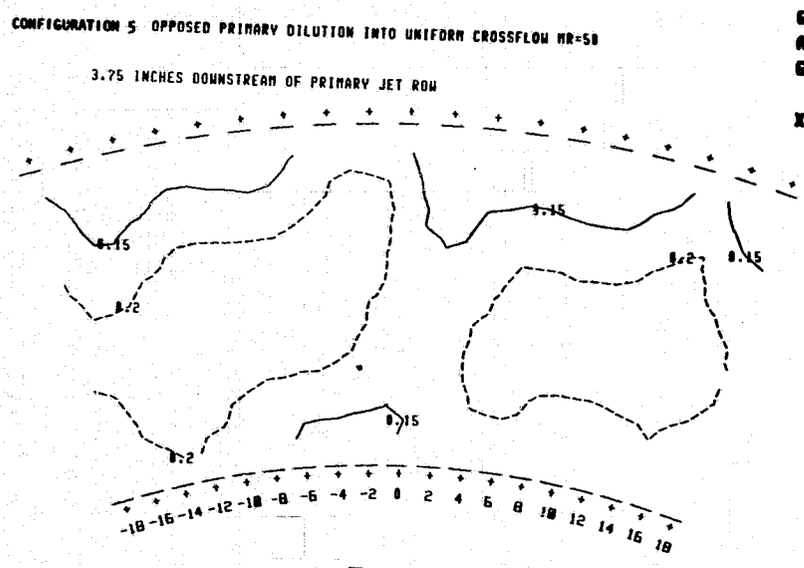


Calculation

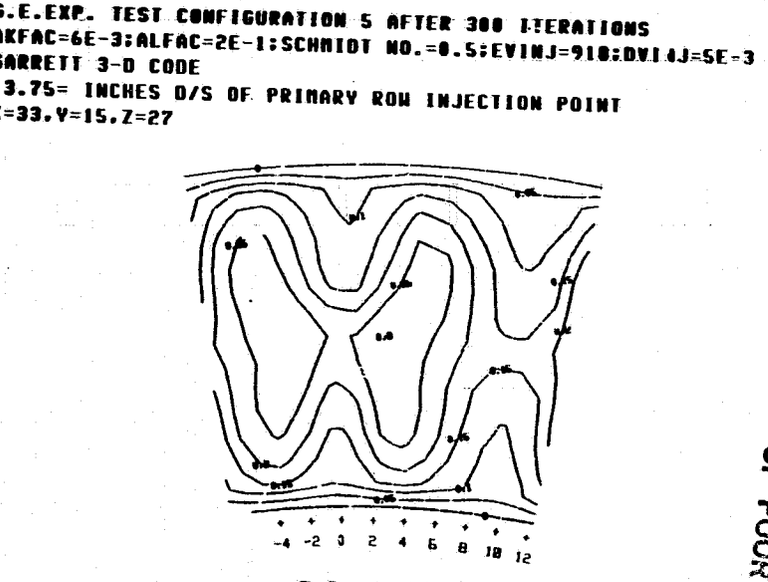
ORIGINAL PAGE IS
OF POOR QUALITY

Figure 173. Comparison of Measured and Calculated Results for Experimental Test Configuration 5.

Contours of $\frac{T_{Inlet} - T_{Local}}{T_{Inlet} - T_{Jet}}$



Test Data



Calculation

Figure 174. Comparison of Measured and Calculated Results for Experimental Test Configuration 5.

Contours of $\frac{T_{Inlet} - T_{Local}}{T_{Inlet} - T_{Jet}}$

ORIGINAL PAGE IS
OF POOR QUALITY

ratio Walker and Kors experiment 67 test case. Some similarities between the calculated results and the test data can be observed. However, in general, the calculated results do not accurately predict the measured test results.

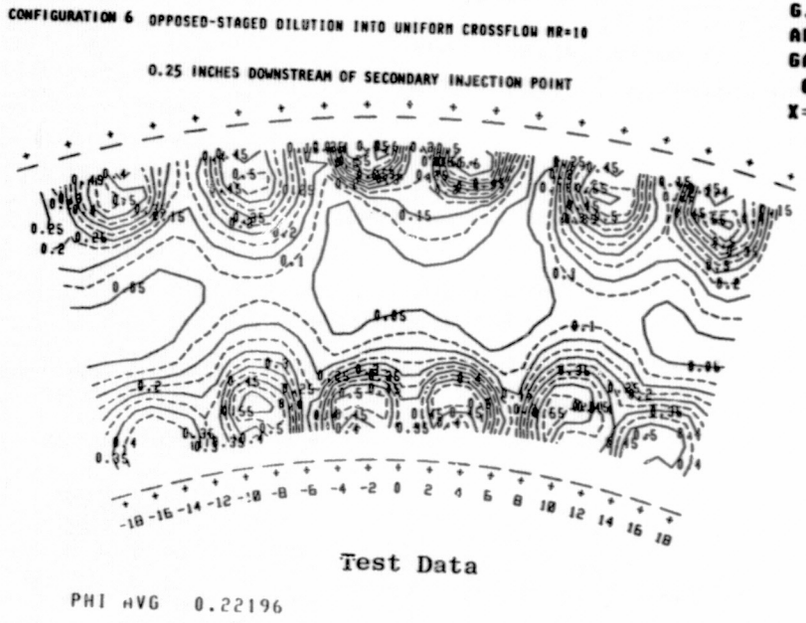
Calculated results for experimental test Configurations 6 and 7 are compared to the test data in Figures 175 through 182. These two configurations also differ only in the jet injection momentum ratio. The dilution hole pattern featured two pairs of directly opposed rows of jets penetrating into a uniform cross flow at an injection momentum ratio of 10 in Configuration 6 and 50 in Configuration 7. This overall hole pattern simulated the primary and secondary hole patterns of the GE/F101 combustor. Again these comparisons show evidence of calculated overpenetration especially in the region located at 9° clockwise from top center. However, some similarities are observed. The calculation reasonably predicted the hot spot centrally located within the annulus section in test Configuration 6 and also reasonably predicted the cold spot centrally located within the annulus section in Configuration 7. Predicted temperature levels in both cases are not in agreement with the data. As in calculations of Configurations 3, 4, and 5, this problem is much more acute near the jet injection point and improves considerably at the aft measurement plane. While the similarities between the calculations and test results are of note, in general, the calculated results for these configurations do not demonstrate the desired accuracy.

The next experimental test configuration modeled featured the same dilution hole pattern and injection momentum ratio featured in test Configuration 7. However, the uniform inlet configuration was replaced with a conventional combustor dome with counterrotating swirl cups. The swirler was modeled using the measured velocity data previously displayed in Figure 46 (Figure 183).

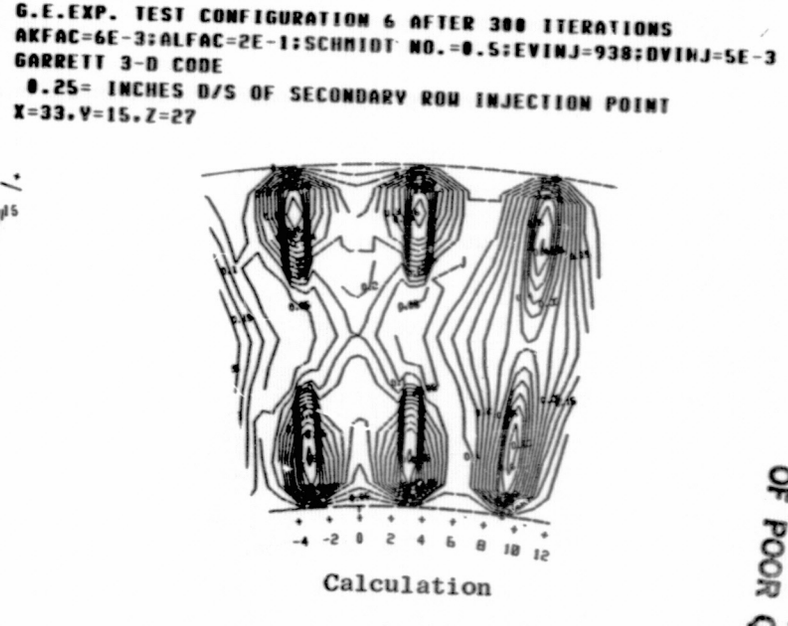
Calculated results for test Configuration 13 are compared to the measured test data in Figures 184 through 187. From these comparisons it is observed that the calculated results indicate slower mixing than is observed from the test data. However, at the aft measurement plane, the calculation shows the flow field well mixed and appearing similar to the test results, although a slight discrepancy in the temperature levels is observed.

The final experimental test configuration modeled represented a section of an actual GE/F101 combustor. For simplicity, all dome and liner cooling features were blocked off. Thus, only swirler and dilution airflow were present. Test Configuration 17C also featured the injection of JP5 fuel with heat release. The overall fuel-to-air ratio was 0.016. To model this more complex flow problem, a model that could treat contoured walls would be desirable.

The ability to utilize a noncylindrical combustor wall with the stairstep technique was briefly explored. While the technique was described in the available user's manuals and some of the framework was in the programming, it was not fully implemented, at least not for the aft end of the combustor. Figures 188 and 189 show grid and calculated results with a 3-D code for an F101-combustor shape with the stairstep technique introduced. Some difficulties remain in achieving convergence that prevented the use of this technique



Test Data

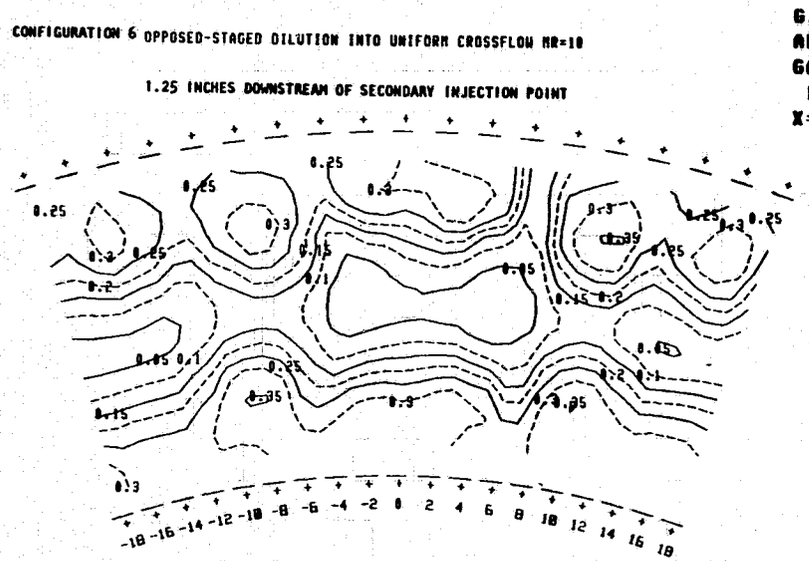


Calculation

Figure 175. Comparison of Measured and Calculated Results for Experimental Test Configuration 6.

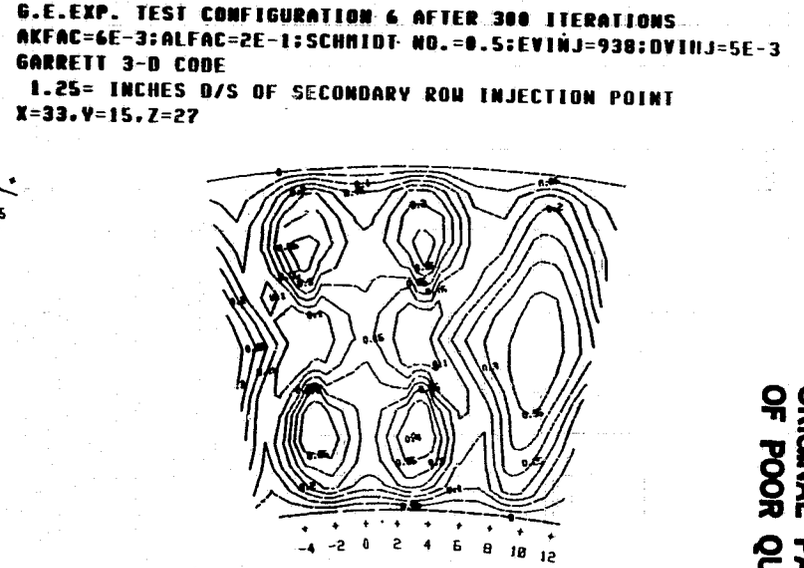
Contours of $\frac{T_{Inlet} - T_{Local}}{T_{Inlet} - T_{Jet}}$

ORIGINAL PAGE IS
OF POOR QUALITY



Test Data

PHI AVG 0.20426

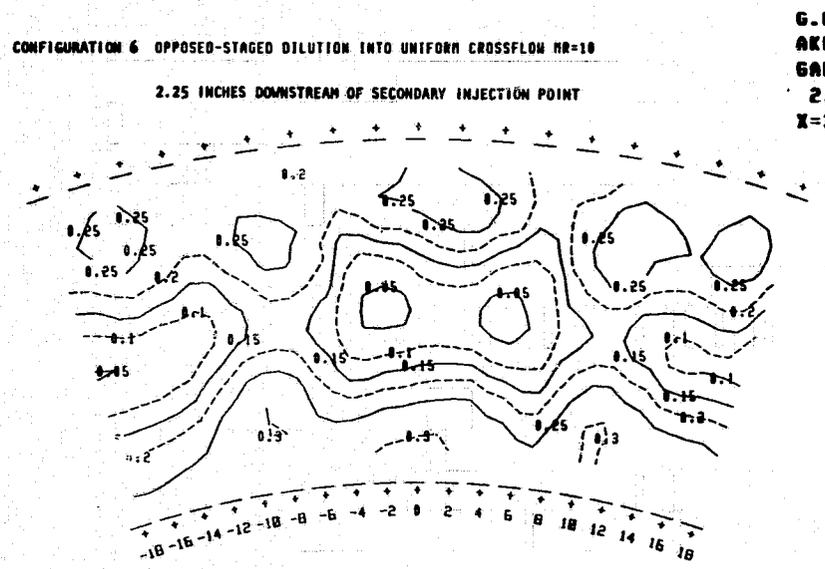


Calculation

ORIGINAL PAGE IS
OF POOR QUALITY

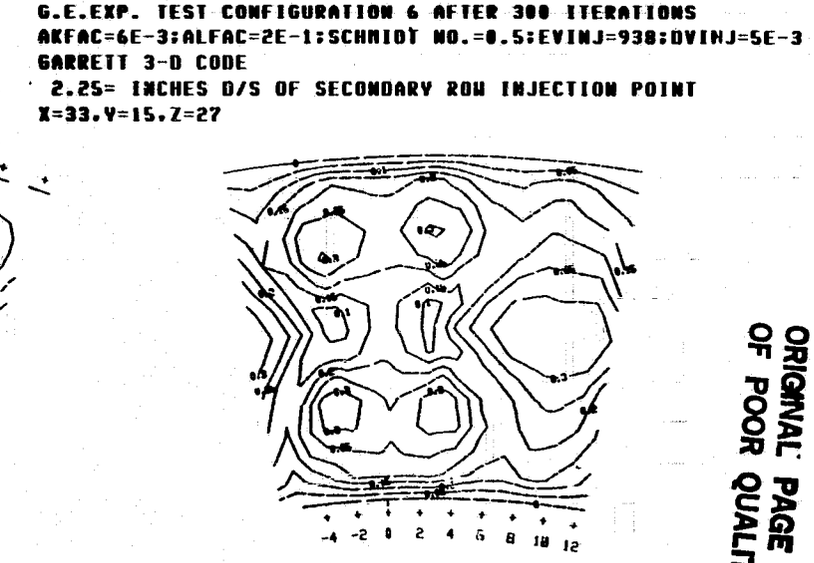
Figure 176. Comparison of Measured and Calculated Results for Experimental Test Configuration 6.

Contours of $\frac{T_{Inlet} - T_{Local}}{T_{Inlet} - T_{Jet}}$



Test Data

PHI AVG 0.19365

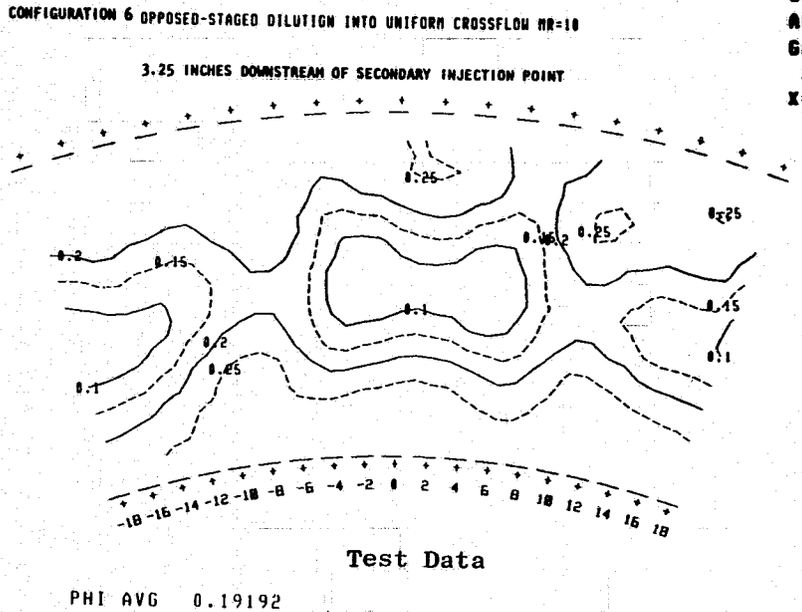


Calculation

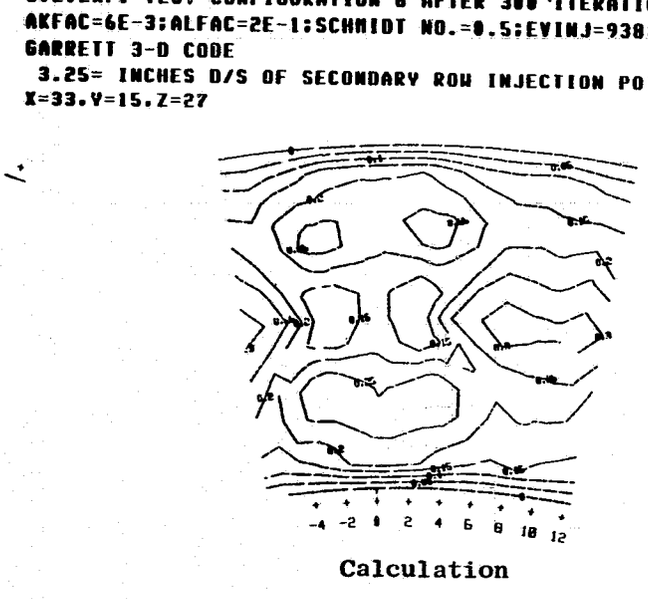
ORIGINAL PAGE IS
OF POOR QUALITY

Figure 177. Comparison of Measured and Calculated Results for Experimental Configuration 6.

Contours of $\frac{T_{Inlet} - T_{Local}}{T_{Inlet} - T_{Jet}}$



Test Data

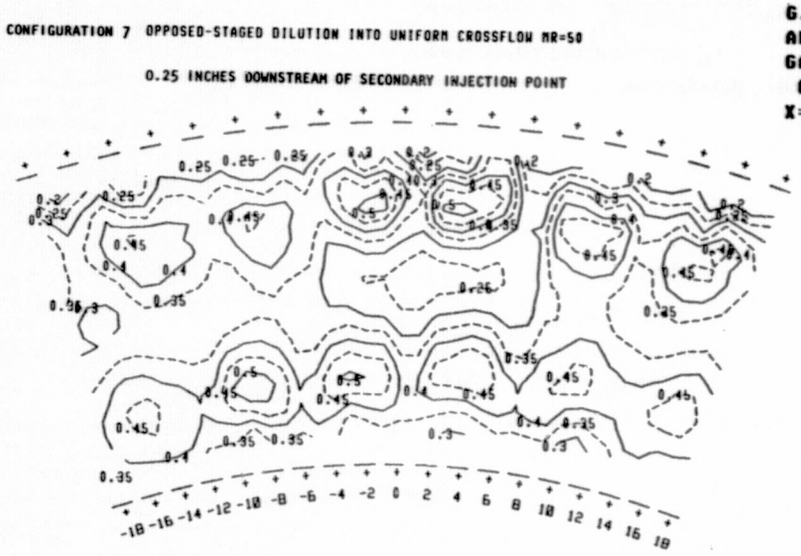


Calculation

ORIGINAL PAGE IS
OF POOR QUALITY

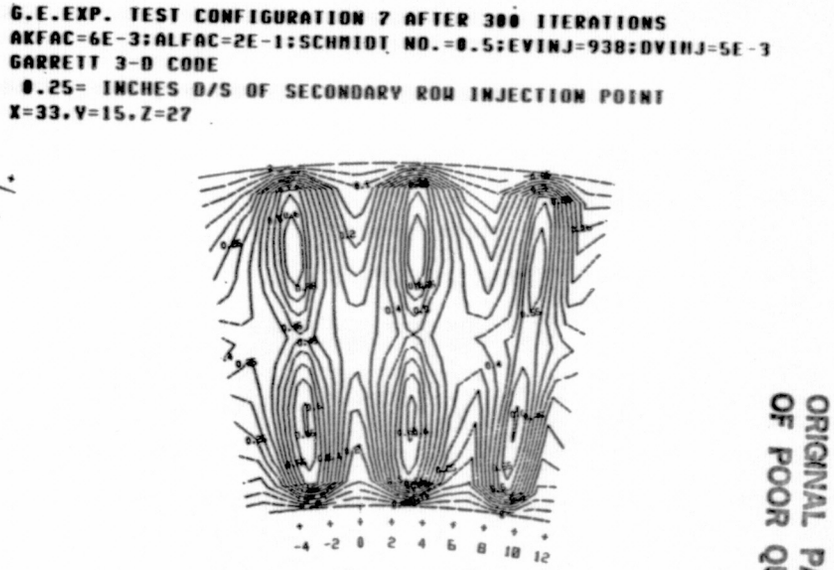
Figure 178. Comparison of Measured and Calculated Results for Experimental Test Configuration 6.

Contours of $\frac{T_{Inlet} - T_{Local}}{T_{Inlet} - T_{Jet}}$



Test Data

PHI AVG 0.36225

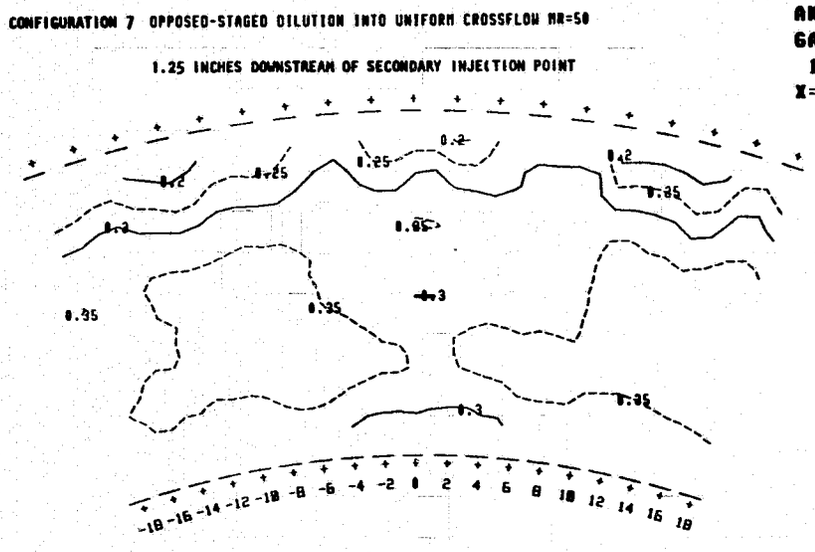


Calculation

ORIGINAL PAGE IS
OF POOR QUALITY

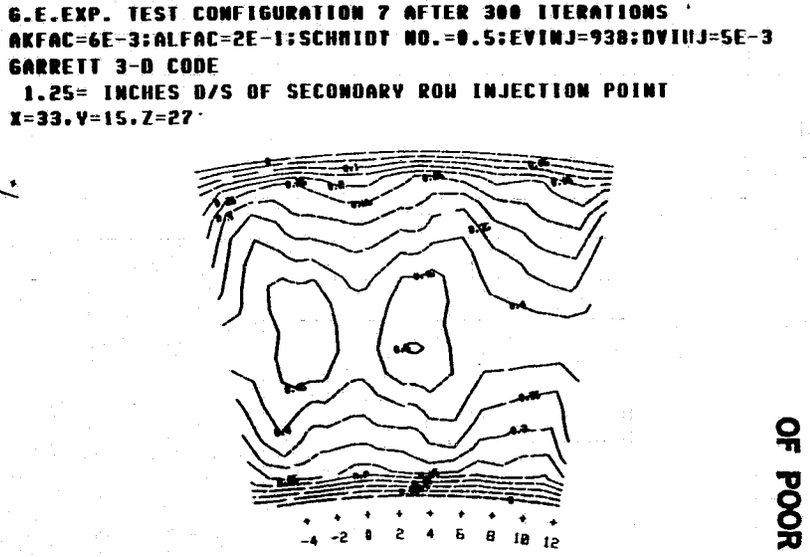
Figure 179. Comparison of Measured and Calculated Results for Experimental Test Configuration 7.

Contours of $\frac{T_{Inlet} - T_{Local}}{T_{Inlet} - T_{Jet}}$



Test Data

PHI AVG 0.32615

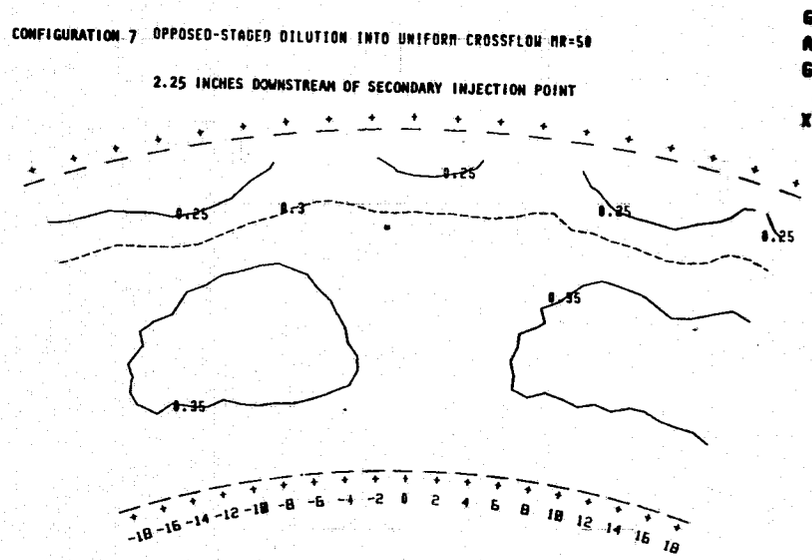


Calculation

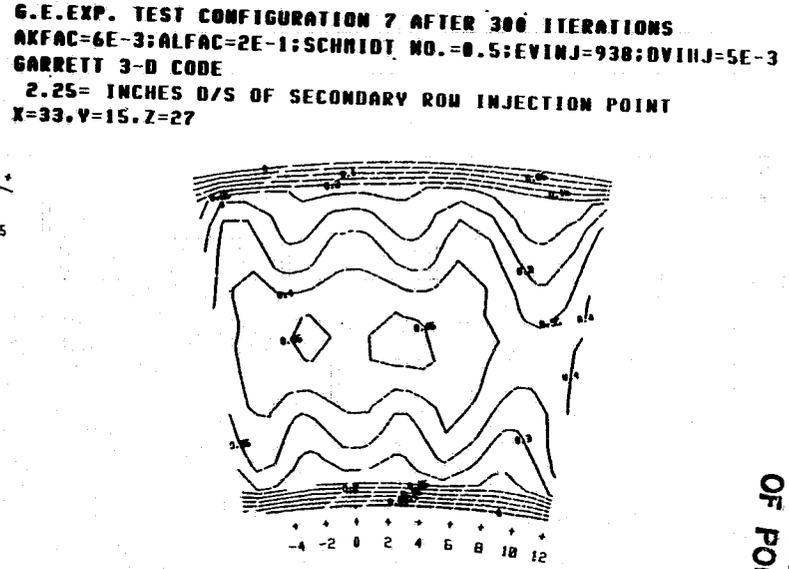
ORIGINAL PAGE IS
OF POOR QUALITY

Figure 180. Comparison of Measured and Calculated Results for Experimental Test Configuration 7.

Contours of $\frac{T_{Inlet} - T_{Local}}{T_{Inlet} - T_{Jet}}$



Test Data

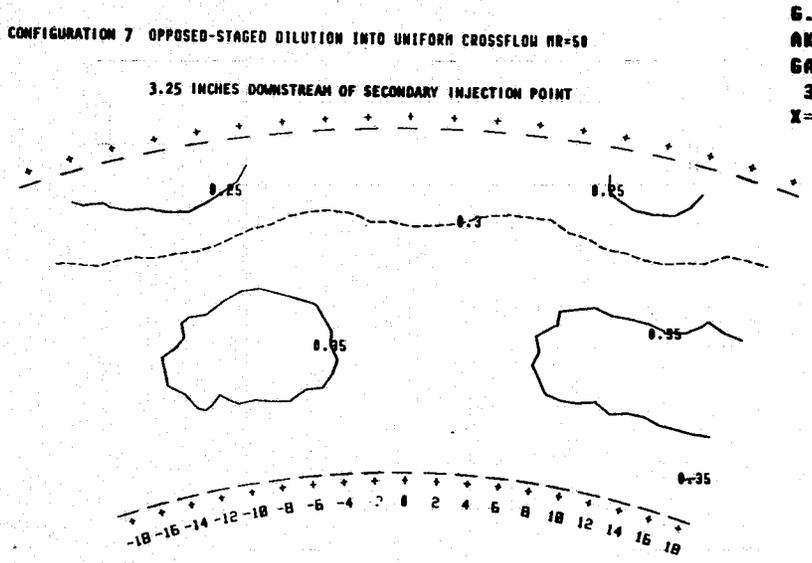


Calculation

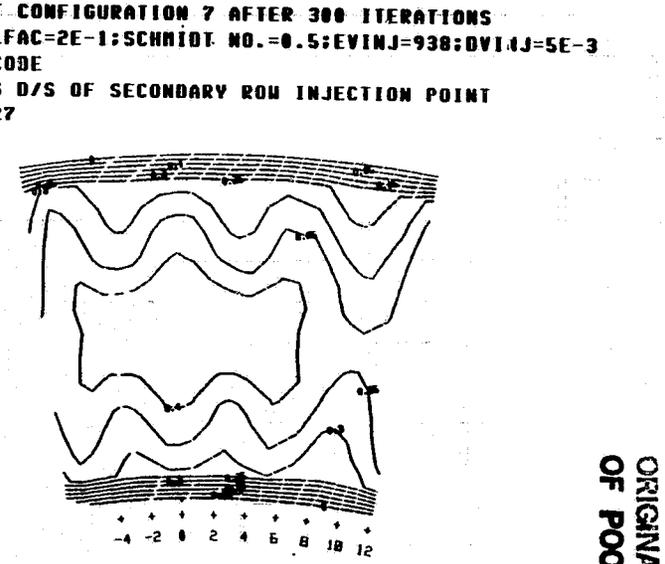
Figure 181. Comparison of Measured and Calculated Results for Experimental Test Configuration 7.

Contours of $\frac{T_{Inlet} - T_{Local}}{T_{Inlet} - T_{Jet}}$

ORIGINAL PAGE IS OF POOR QUALITY



Test Data



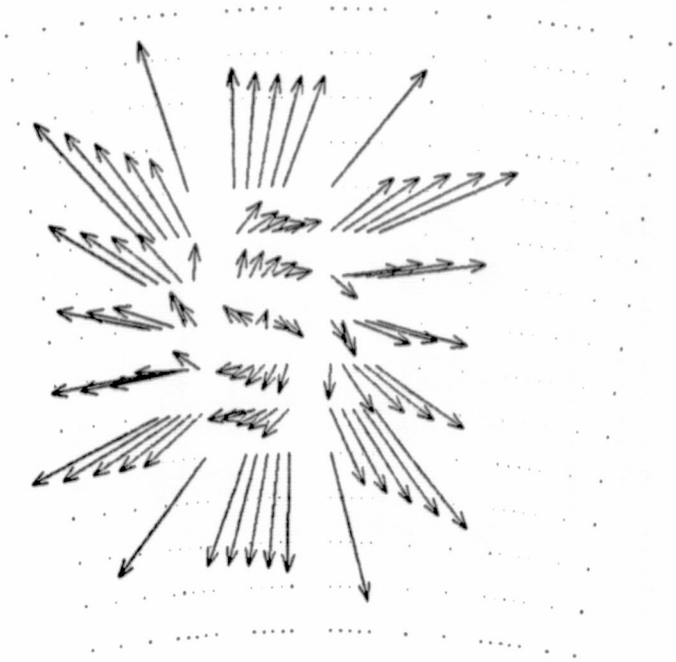
Calculation

ORIGINAL PAGE IS
OF POOR QUALITY

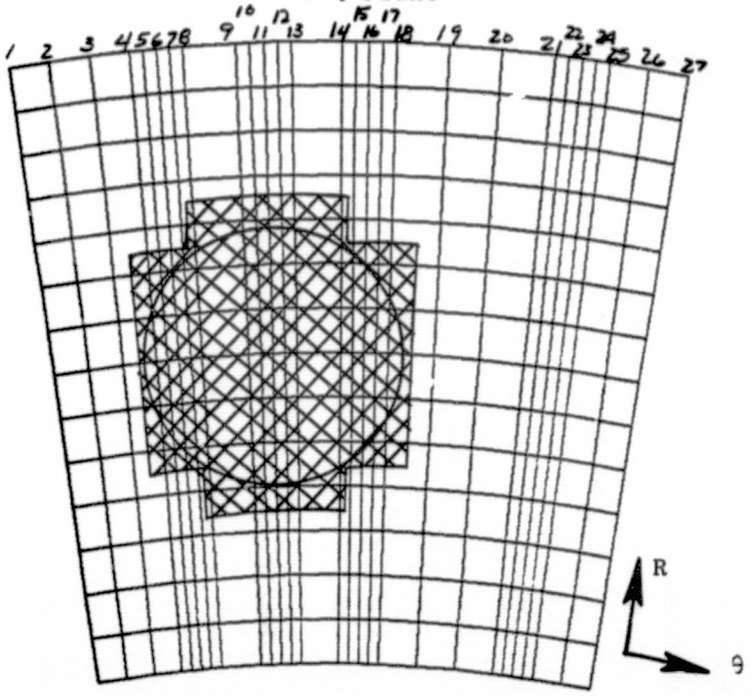
Figure 182. Comparison of Measured and Calculated Results for Experimental Test Configuration 7.

Contours of $\frac{T_{Inlet} - T_{Local}}{T_{Inlet} - T_{Jet}}$

ORIGINAL PAGE IS
OF POOR QUALITY

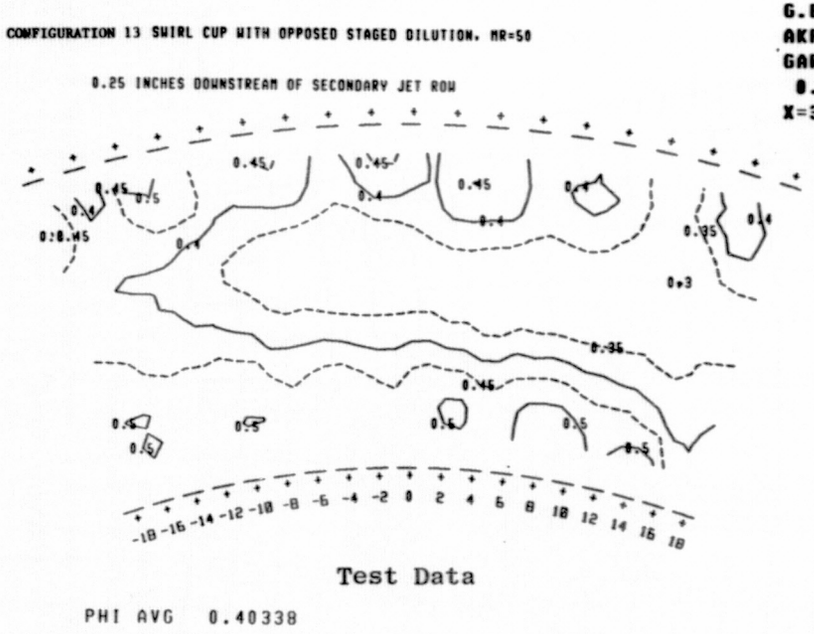


Swirler Velocity Pattern
R-θ Plane

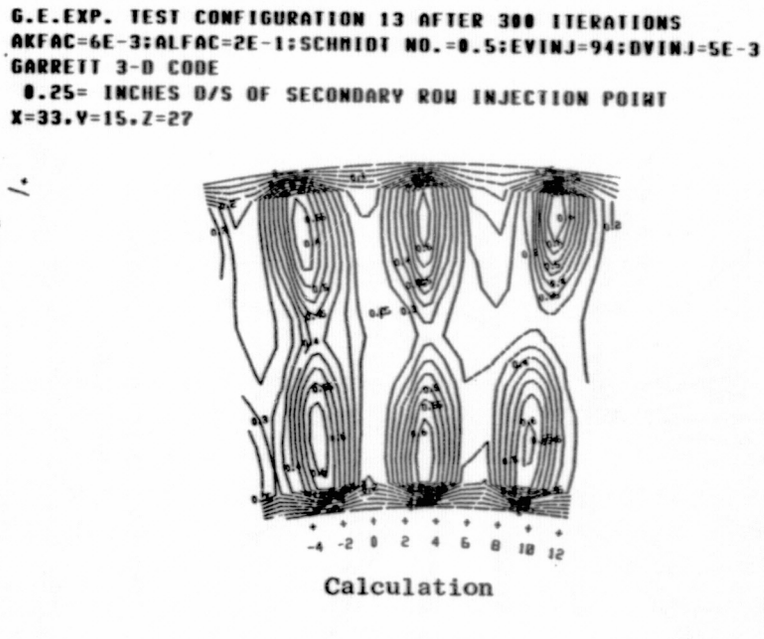


Shaded Area of Grid Represents
the Inlet Swirler

Figure 183. Swirler Input for Test Configuration 13 (Coarse Grid).



Test Data

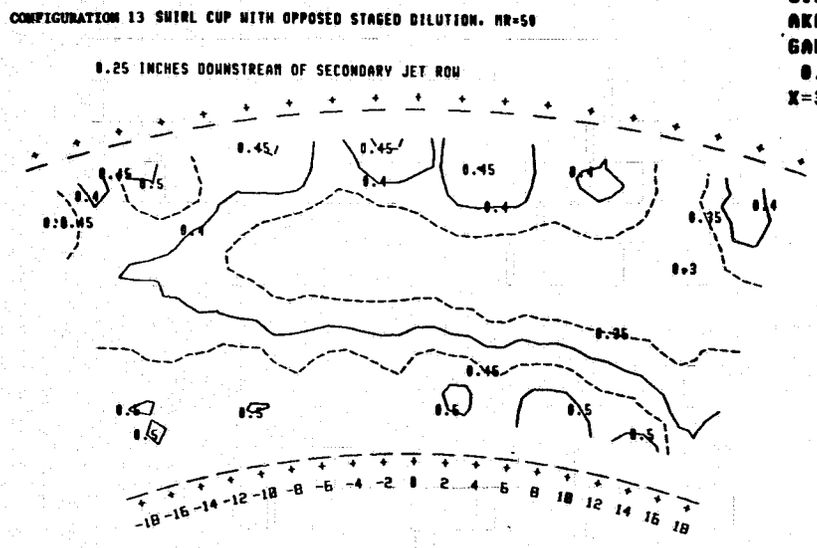


Calculation

Figure 184. Comparison of Measured and Calculated Results for Experimental Test Configuration 13.

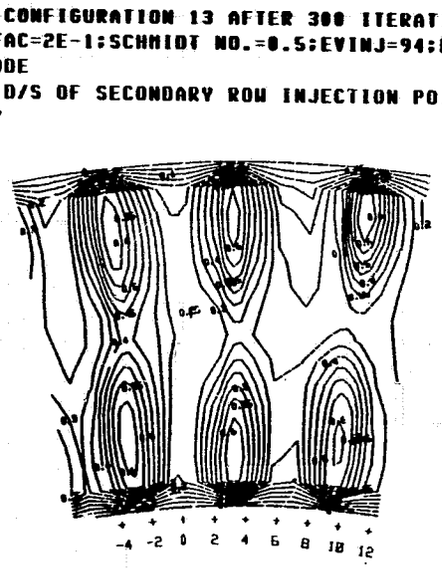
Contours of $\frac{T_{Inlet} - T_{Local}}{T_{Inlet} - T_{Jet}}$

ORIGINAL PAGE IS
OF POOR QUALITY



Test Data

PHI AVG 0.40338

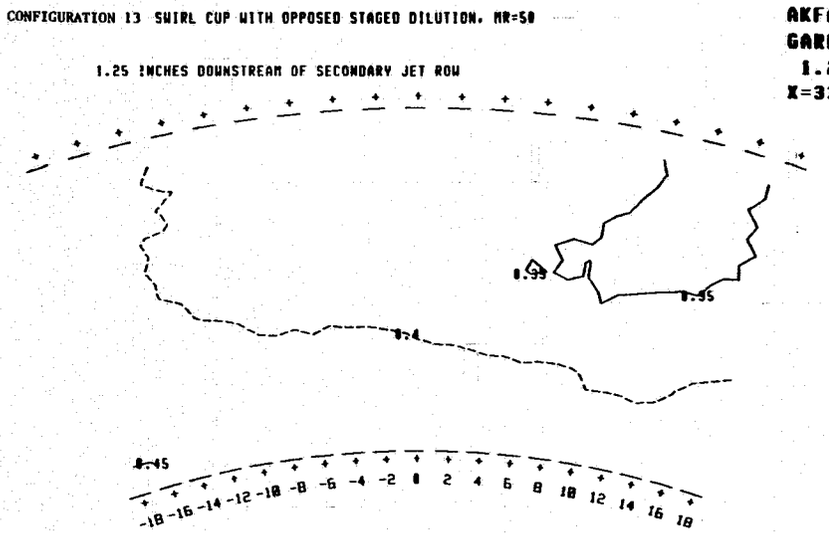


Calculation

ORIGINAL PAGE IS
OF POOR QUALITY

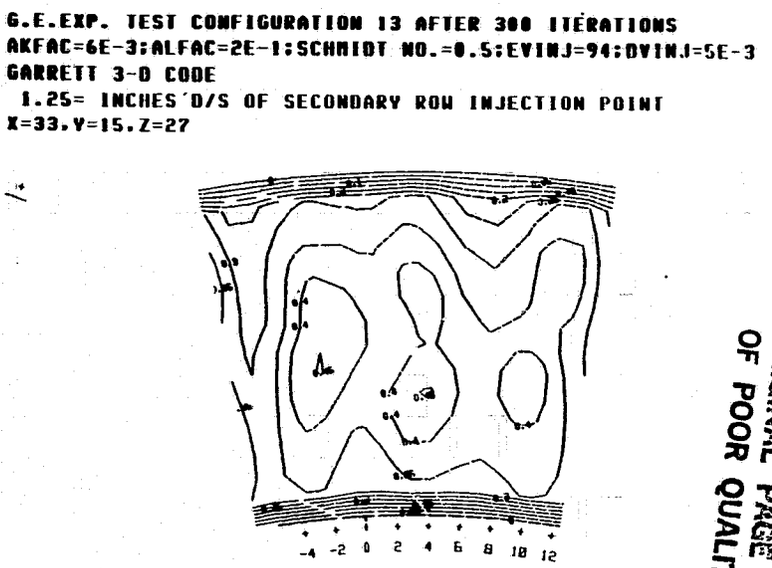
Figure 184. Comparison of Measured and Calculated Results for Experimental Test Configuration 13.

Contours of $\frac{T_{Inlet} - T_{Local}}{T_{Inlet} - T_{Jet}}$



Test Data

PHI AVG 0.38796

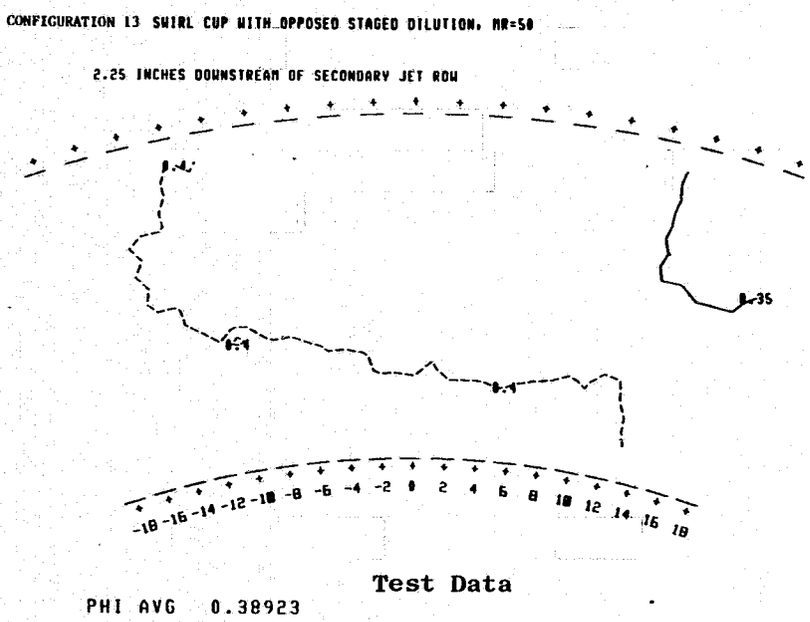


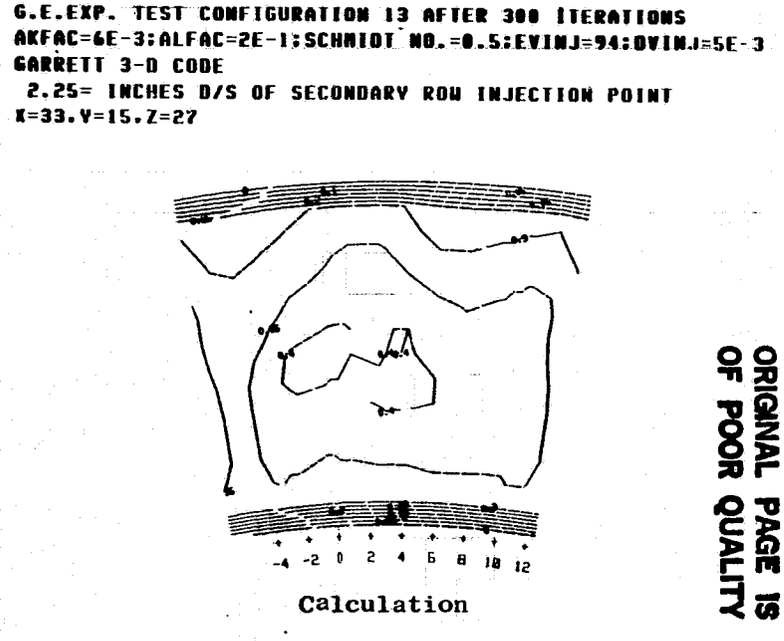
Calculation

ORIGINAL PAGE IS
OF POOR QUALITY

Figure 185. Comparison of Measured and Calculated Results for Experimental Test Configuration 13.

Contours of $\frac{T_{Inlet} - T_{Local}}{T_{Inlet} - T_{Jet}}$

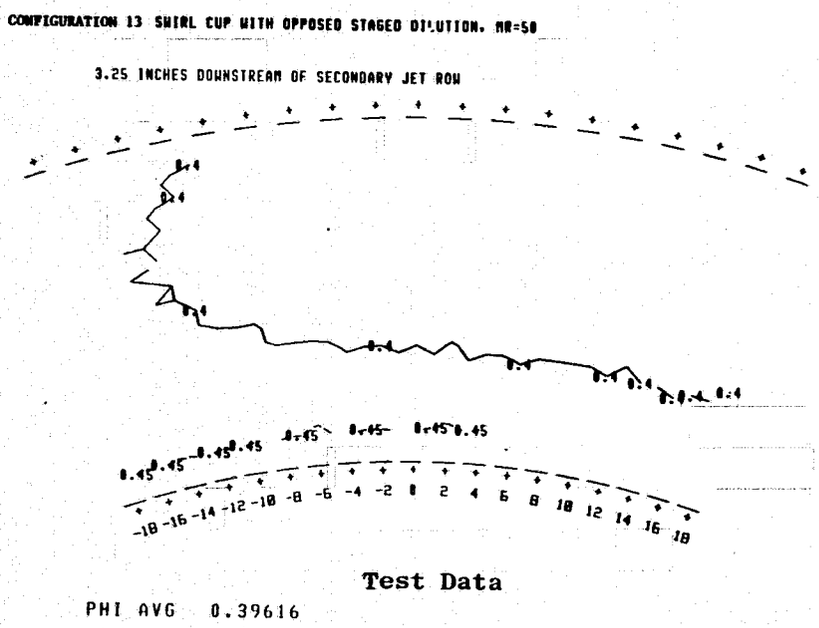




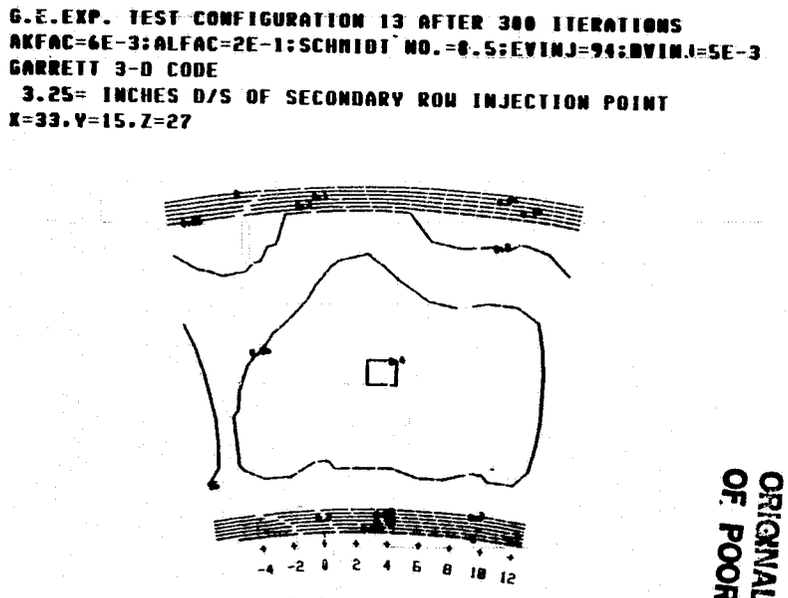
ORIGINAL PAGE IS
OF POOR QUALITY

Figure 186. Comparison of Measured and Calculated Results for Experimental Test Configuration 13.

Contours of $\frac{T_{Inlet} - T_{Local}}{T_{Inlet} \quad T_{Jet}}$



Test Data



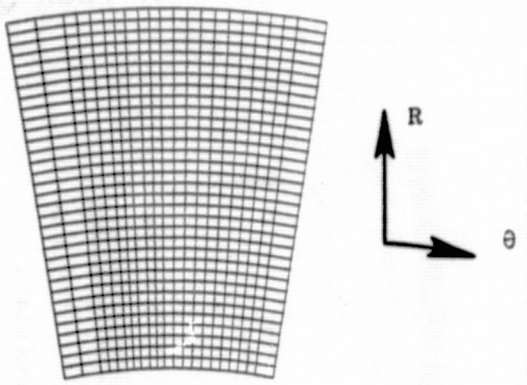
Calculation

ORIGINAL PAGE IS
OF POOR QUALITY

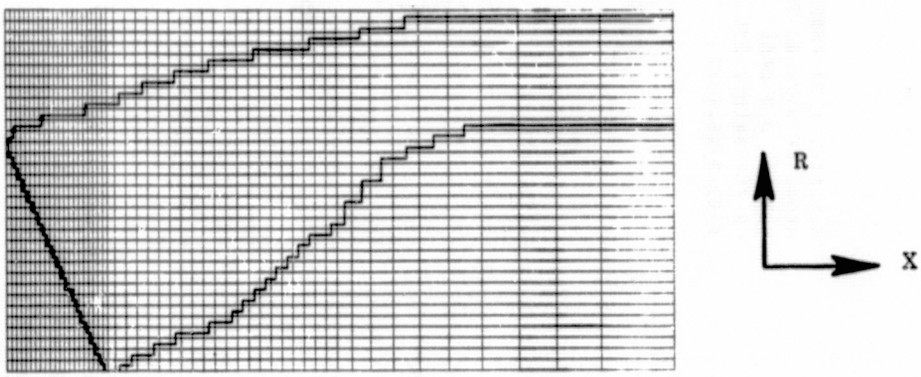
Figure 187. Comparison of Measured and Calculated Results for Experimental Test Configuration 13.

Contours of $\frac{T_{Inlet} - T_{Local}}{T_{Inlet} - T_{Jet}}$

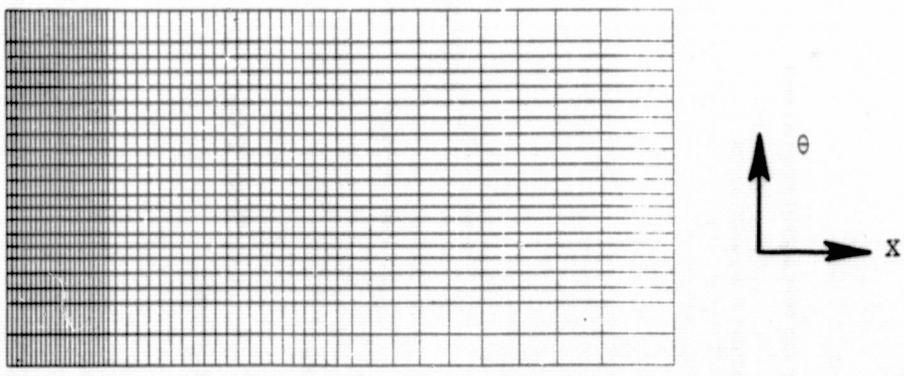
ORIGINAL PAGE IS
OF POOR QUALITY



R-Theta Plane



X-R Plane



X-Theta Plane (Outer)

Figure 188. F101 Contoured Wall Grid (53X 34Y 23Z).

ORIGINAL PAGE IS
OF POOR QUALITY

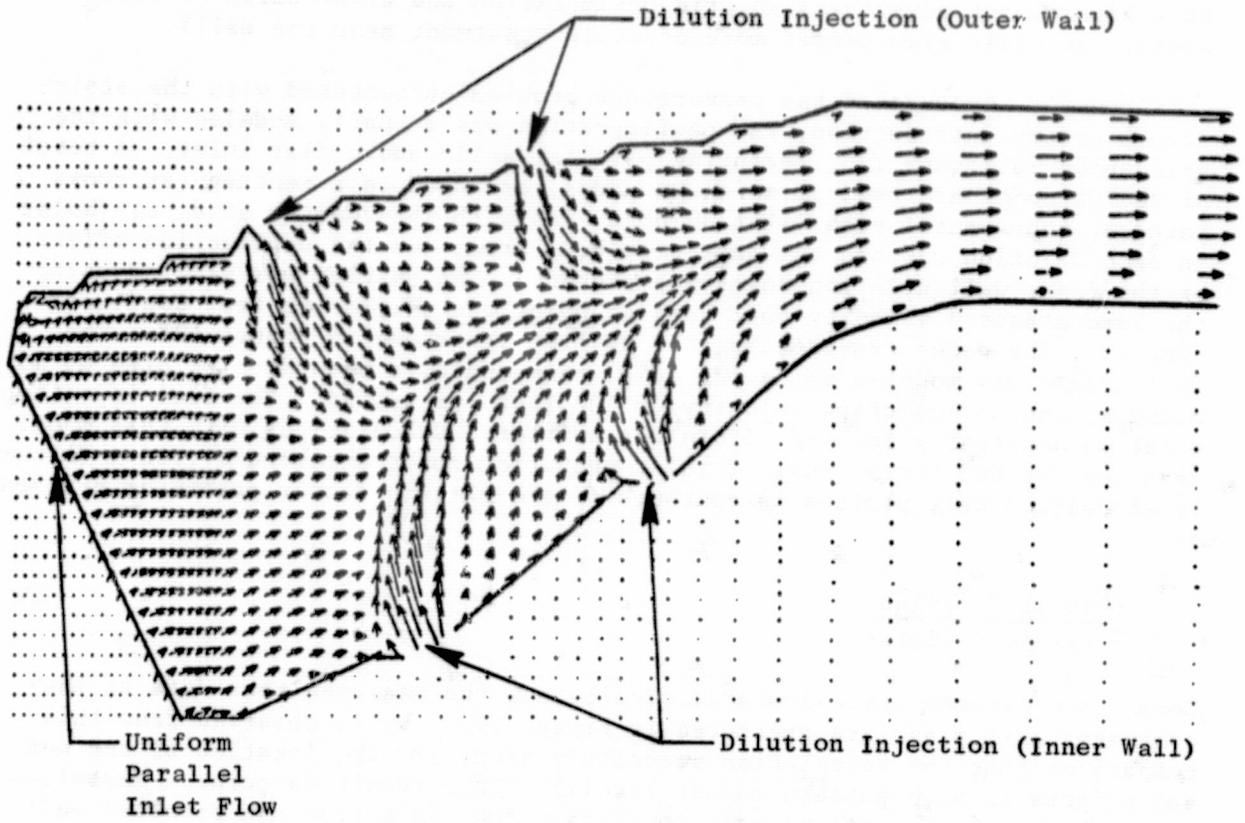


Figure 189. Combustor Calculation with Uniform Inlet (No Fuel).

in the assessment comparisons. However, the figures illustrate some of the major limitations of this method. First, more than half of the nodes are outside of the flowpath requiring storage but not providing detail in the flowpath. Grid concentration is introduced in regions within the flowpath where it is not necessarily needed. Achieving grid concentration next to the walls is awkward. Thus it is apparent that a body-fitted coordinate system would have significant advantages in grid optimization and elimination of unused nodes. It would also permit more accurate treatment near the wall.

However, because of the convergence problem encountered with the stair-step boundary introduction, the configuration was actually modeled with the grid shown in Figure 190, featuring parallel walls and a flat inlet. A total of 36,708 nodes are used of which 21 nodes, arranged in a rectangular cross pattern, represented each dilution hole. As with the coarser grid, all holes in each dilution row had the same geometric area, and the contraction effect on the inner wall dilution holes was present. The swirler was modeled using the same measured velocity data used to model the swirler in test Configuration 13. The nodes representing the swirler are shown in Figure 191. The fuel nozzle was modeled as having a 90° cone angle, a mean droplet size of 30 microns, and an injection velocity of 100 feet per second. The fuel injection point was centrally located within the swirler. Calculations with this model were run for 800 iterations. Total computation costs exceeded $7,000. Calculated results were plotted as contours of the pattern factor parameter defined as:

$$\frac{T_{local} - T_{inlet}}{T_{average} - T_{inlet}}$$

Comparison between the calculated results and the measured test data at the combustor exit plane are presented in Figure 192. It is observed from this comparison that the calculation accurately predicted the location of the hot spots (area of high pattern factor levels). This result is perhaps fortuitous since the model assumptions made concerning fuel injection and parallel wall boundaries represent gross approximations to the actual test case.

The presence of numerical diffusion errors was of concern for all 3-D calculations performed. Numerical diffusion error is the second order truncation error incurred when first order upwind numerics are used. Codes which use the so called hybrid scheme use central differencing (second order accurate) for cells where Peclet numbers are two or less. When Peclet numbers are above two, central differencing becomes unstable, and the hybrid numeric scheme reverts to pure first order upwind differencing. Thus, numerical diffusion errror is introduced everywhere the cell Peclet numbers exceed two, and the calculated mixing has little relationship to the calculated turbulence levels. Numerical diffusion error can be reduced through the use of detailed grids for codes using the hybrid differencing scheme. If enough storage is available, grids with sufficient detail could be used which would completely eliminate this error. The question is, how much grid is needed to accomplish this? In Figure 5 a grid network is shown which was used to obtain calculations of the Peclet numbers for a parallel wall model of a combustor with

ORIGINAL PAGE IS
OF POOR QUALITY

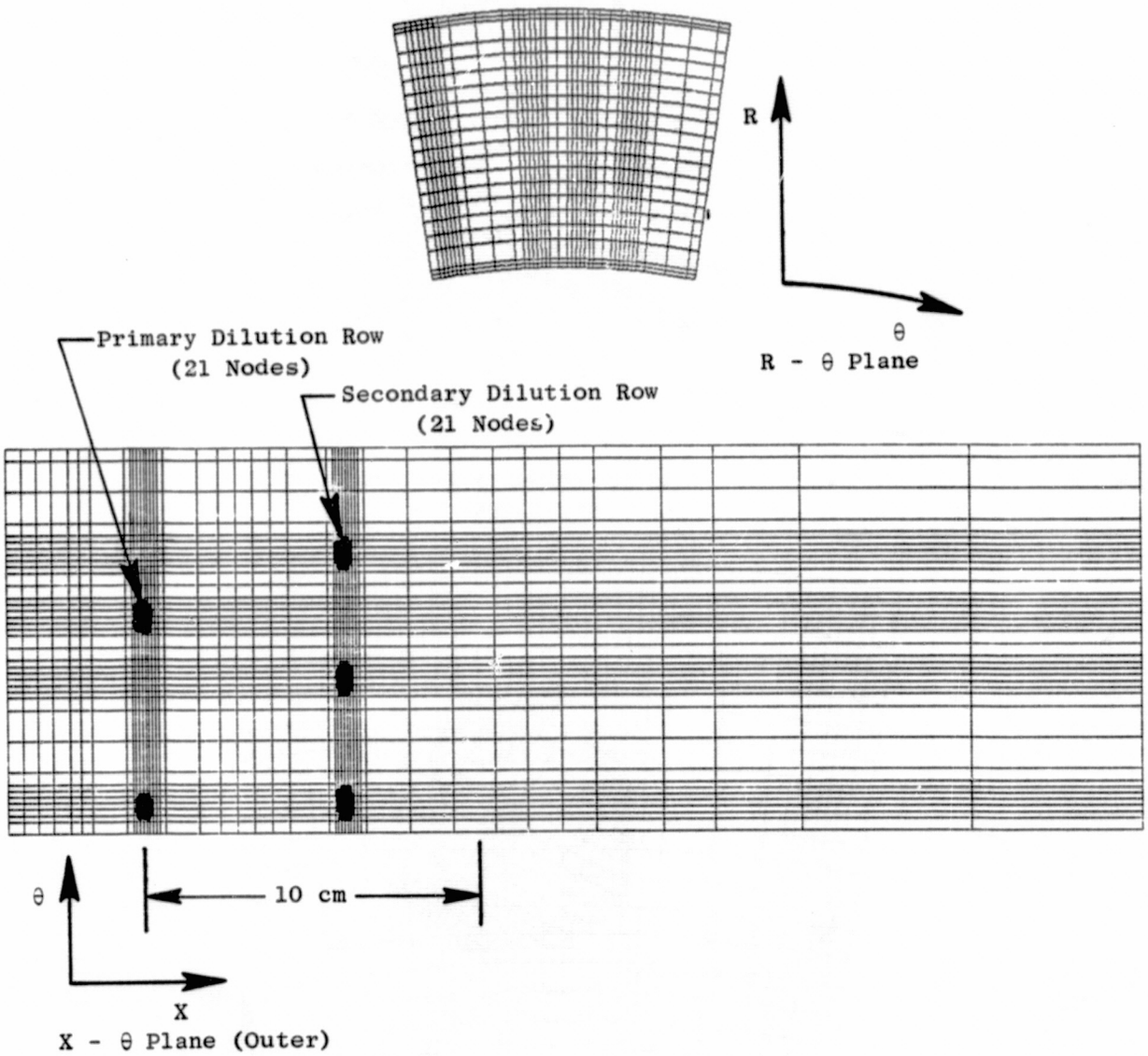
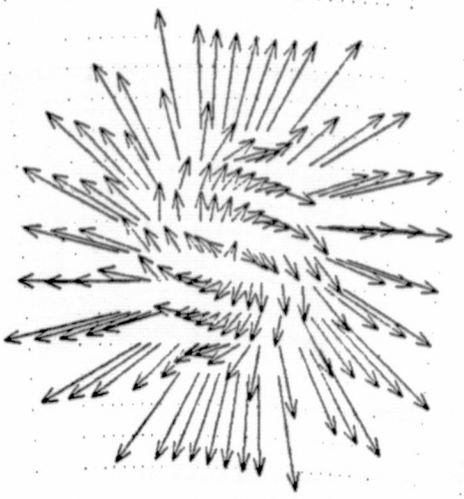
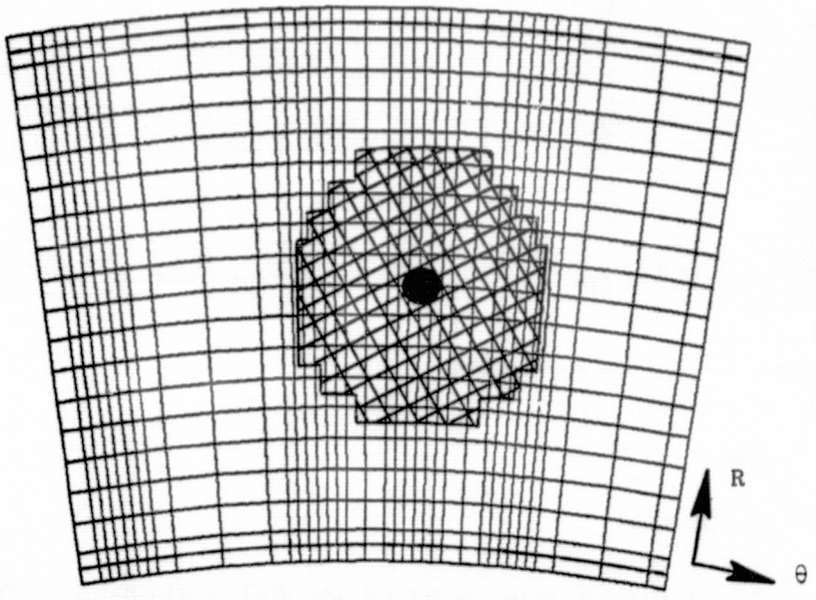


Figure 190. Detailed Grid Selected for Calculations of Experimental Test Configuration 17C.

ORIGINAL PAGE IS
OF POOR QUALITY



Swirler Velocity Pattern
R-θ Plane



Shaded Area of Grid Represents the Inlet
Swirler Fuel Nozzle Shown As Solid Circle

Figure 191. Swirler Input for Test Configuration 17C (Detailed Grid).

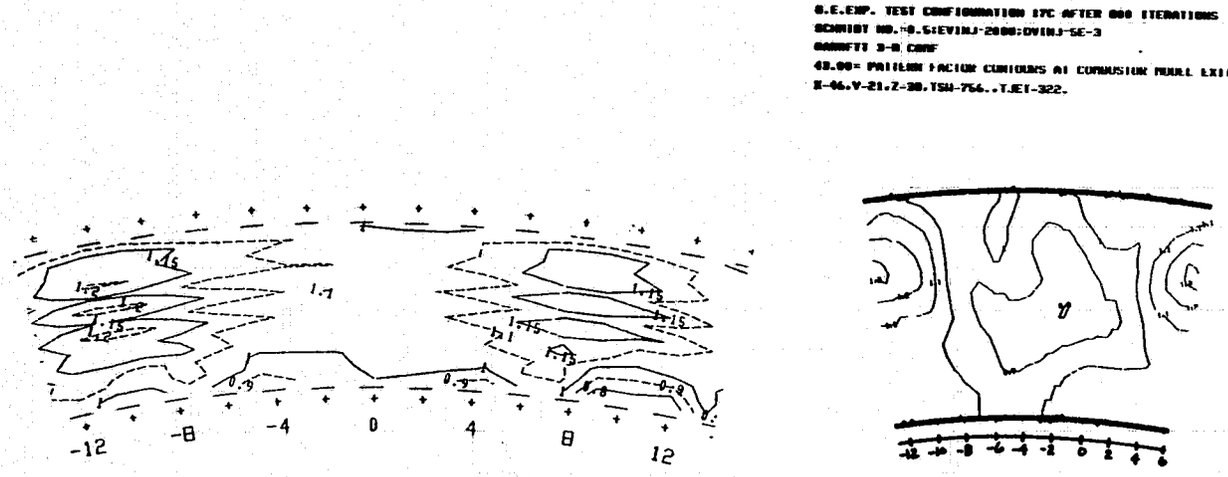


Figure 192. Detailed Grid Selected for Calculations of Experimental Test Configuration 17C. Contours of the Pattern Factor Parameter.

ORIGINAL PAGE IS
OF POOR QUALITY

inlet swirl, and fuel injection and heat release. In this grid a total of 38,640 nodes are used requiring approximately 90% of the available storage capacity. These calculations were run using the Garrett code which uses the hybrid differencing scheme. Plots of the calculated Peclet numbers are presented in Figure 6 for the (X) direction while Figures 193 and 194 show calculated Peclet numbers in the (Y) direction. In these figures the shaded regions represent areas within the flowfield where the Peclet number is less than two, or where numerical diffusion error is not introduced into the calculations. These results demonstrate that with a grid of this detail, in most of the flowfield, numerical error is introduced. As seen from these figures the amount of error can be substantial, as evidenced by the large regions where the Peclet numbers are considerably greater than two. Therefore, with the current grid limitations imposed as a result of available storage capacity, one cannot hope to eliminate the problem of numerical diffusion error with the "hybrid" scheme.

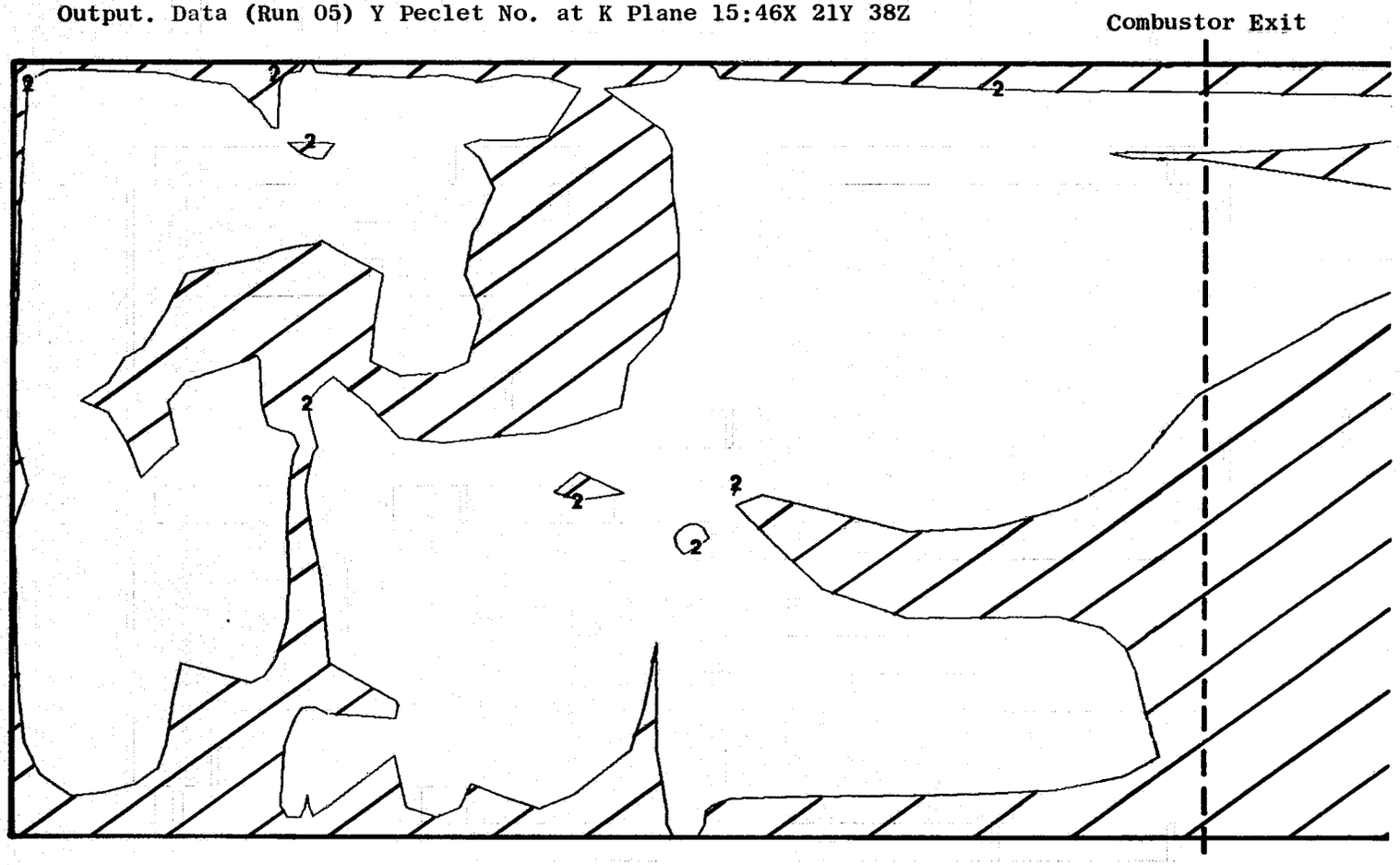
In reviewing the calculations performed as part of the assessment of the 3-D elliptic internal flow codes, several outstanding deficiencies were exposed. The following discussion addresses these deficiencies individually.

- While axisymmetric studies described in the previous section showed that grid independent results with accurate numerics could be accomplished, for 3-D treatment of a combustor, numerical diffusion is prominent in the calculations even with the maximum storage capacity available. While greater storage may become available, the running time costs would be excessive. It would seem that the most appropriate method of avoiding the numerical diffusion problem is to provide improved numerics rather than by increasing the grid density.

- The treatment of contoured walls by the stairstep technique wastes grid in regions external to the flowpath, and in unneeded regions within the flowpath, while grid optimization near the walls is very awkward. The use of a body-fitted coordinate system would greatly improve the ability to optimize grid for a given storage or computer cost limitation.

- The over penetration of dilution jets of high momentum ratios encountered in the initial studies resulted in considerable computer analysis investigation. Calculations of the Walker and Kors data suggested that the problem was not sensitive to grid or inlet turbulence boundary conditions. However, it was shown that great sensitivity existed to changes in the jet turbulent length scale boundary condition. Increasing the jet turbulent length scale produced significant increases in turbulent kinetic energy within the penetrating jet flowfield resulting in faster mixing, and improved agreement with the high momentum ratio jet data. Calculations of the experimental configurations tested in this program using the inlet and jet turbulence boundary conditions which had produced accurate solutions of the Walker and Kors data were performed. The grid selected for these calculations was coarse. The results from these calculations again showed jet over penetration. Additionally disturbing was the slight

F101 Combustion Model After 520 Iterations from Output File Garrett. Combmod1.
Output. Data (Run 05) Y Peclet No. at K Plane 15:46X 21Y 38Z



- Shaded Regions Represent (Y) Peclet Numbers Less Than 2

Figure 193. Calculated Peclet Number in the Y Direction from 3-D Combustor Calculation.

ORIGINAL PAGE IS
OF POOR QUALITY

F101 Combustion Model After 520 Iterations from Output File Garrett.
Combmodl. Output. Data (Run 05) Y Peclet No. at K Plane 15:46X
21Y 38Z



ORIGINAL PAGE IS
OF POOR QUALITY

Figure 194. Calculated Peclet Number in the Y Direction from 3-D Combustor Calculation.

under penetration observed in the calculations of experimental configurations featuring low momentum ratio jets. If improved numerics become available a reevaluation of the ability to accurately calculate dilution jets in crossflow would be appropriate. Perhaps then an absolute, but practical, grid requirement for satisfactory accuracy could be determined.

7.3 ASSESSMENT OF AEROTHERMAL MODULES IN GENERAL USE

An analysis of the GE/F101 combustor system was performed using the combustor analytical model currently in general use at General Electric. As recalled, the key elements of this model include the combustor inlet diffuser module (DIFLO), the combustor airflow distribution module (COBRA), and the combustor liner heat transfer module. The purpose of this investigation was to assess the predictive capability of the model against the measured test data. The F101 combustor system was selected to model because of the large amount of measured pressure and liner metal temperature data available from component and engine testing.

For assessing the diffuser and airflow distribution modules, component test data from F101 combustor S/N 0001 were selected from the data base. The operating conditions selected were:

P_3 = 16.5 atmospheres

T_3 = 834 K

W_3 = 30.5 kg/sec

For the diffuser performance analysis, the geometric features of the F101 inlet diffuser system along with the selected test conditions were input to the DIFLO module. Total pressure losses as a function of flow were generated for the outer stream, the dome stream, and the inner stream. The airflow distribution analysis was performed using the model shown in Figure 195. The flow areas of all the combustor airflow features were known from precise measurements made on a calibrated flow stand prior to component evaluation. This data, along with other geometrical aspects of the combustion system, plus the selected operating conditions were input to the COBRA model. The diffuser performance curves, generated from the DIFLO analysis, were used to establish the combustor inlet pressures.

Calculated results from the DIFLO and COBRA analyses are presented in Table XVIII and Figures 196 and 197. For comparison purposes measured test data and/or experience levels are included in these figures. In general, the agreement in calculated versus measured levels of diffuser performance, airflow distribution, and combustor pressure is very good. Past experience has shown that even when profile effects are simulated, the diffuser performance levels measured in a component test rig are not identical to levels measured in an engine. This appears to be related to higher turbulence levels in the engine flow discharging from the compressor turbomachinery and higher Reynolds number. This also accounts for a part of the small observed differences between the calculated results versus measured levels of diffuser performance, airflow distribution, and pressures.

ORIGINAL PAGE IS
OF POOR QUALITY

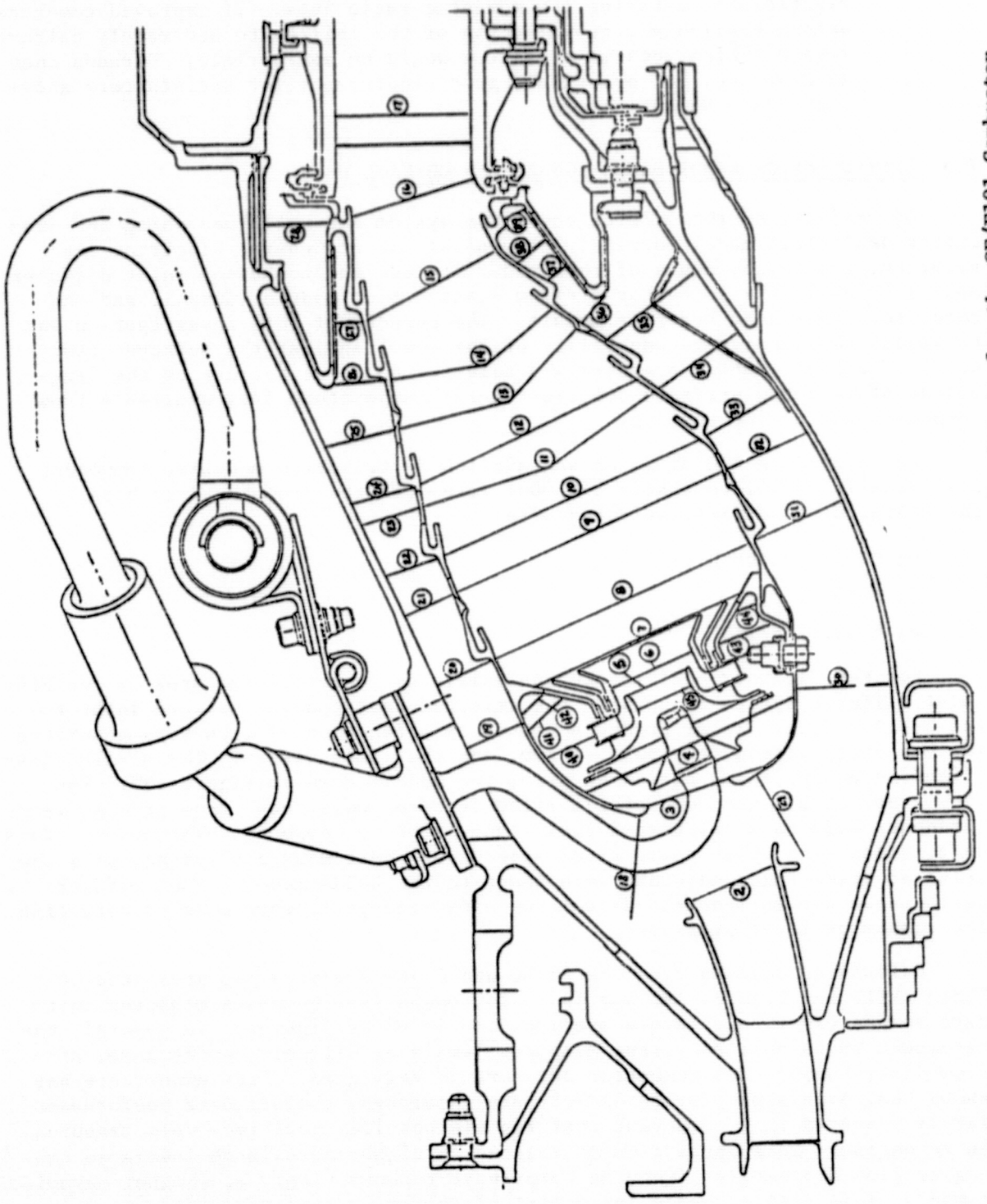


Figure 195. Airflow Distribution Module (COBRA) Station Layout for the GE/F101 Combustor.

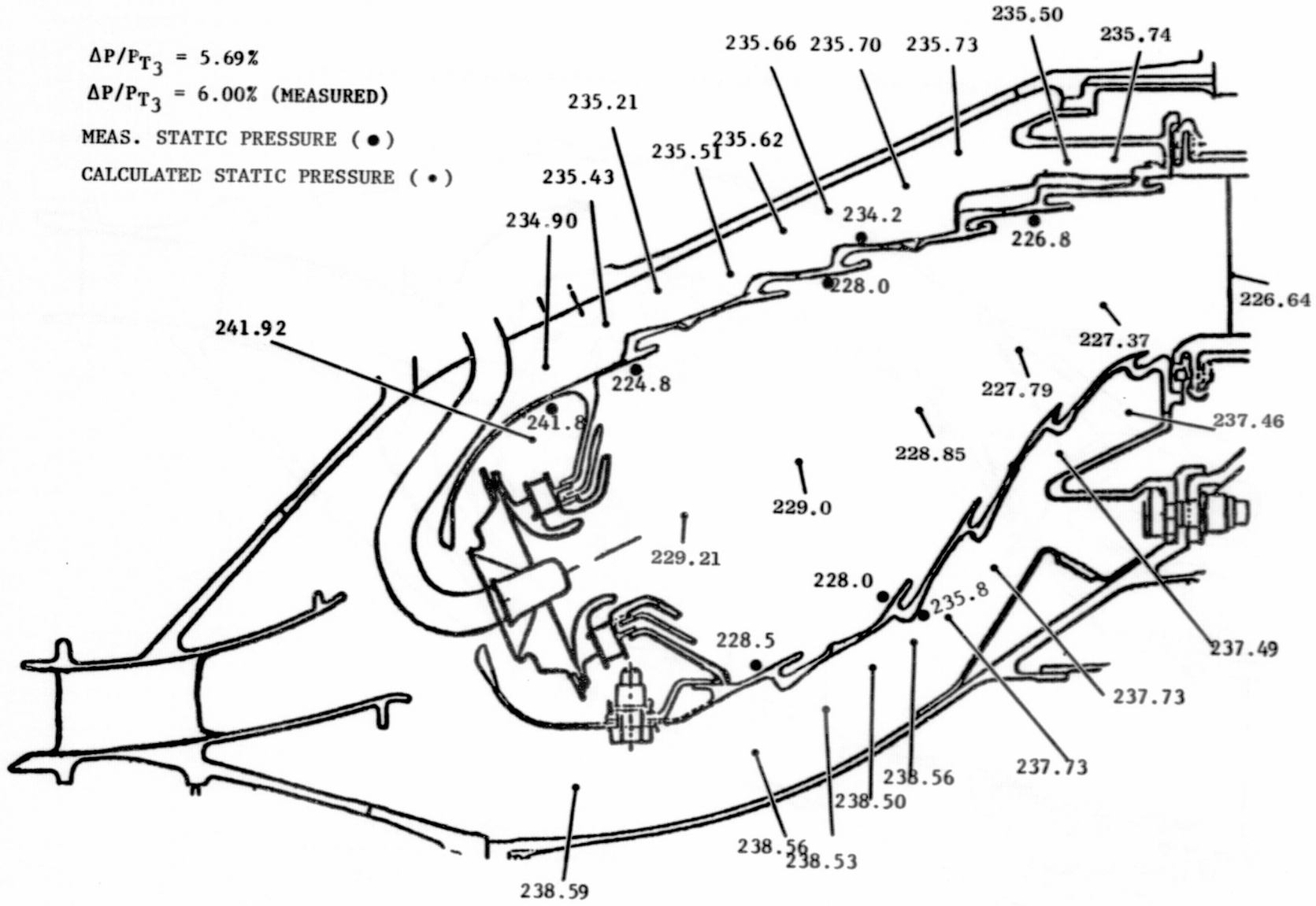


Figure 196. Comparison of Measured to Calculated Pressures and Airflow Distribution.

ORIGINAL PAGE IS
OF POOR QUALITY

ORIGINAL PAGE IS
OF POOR QUALITY

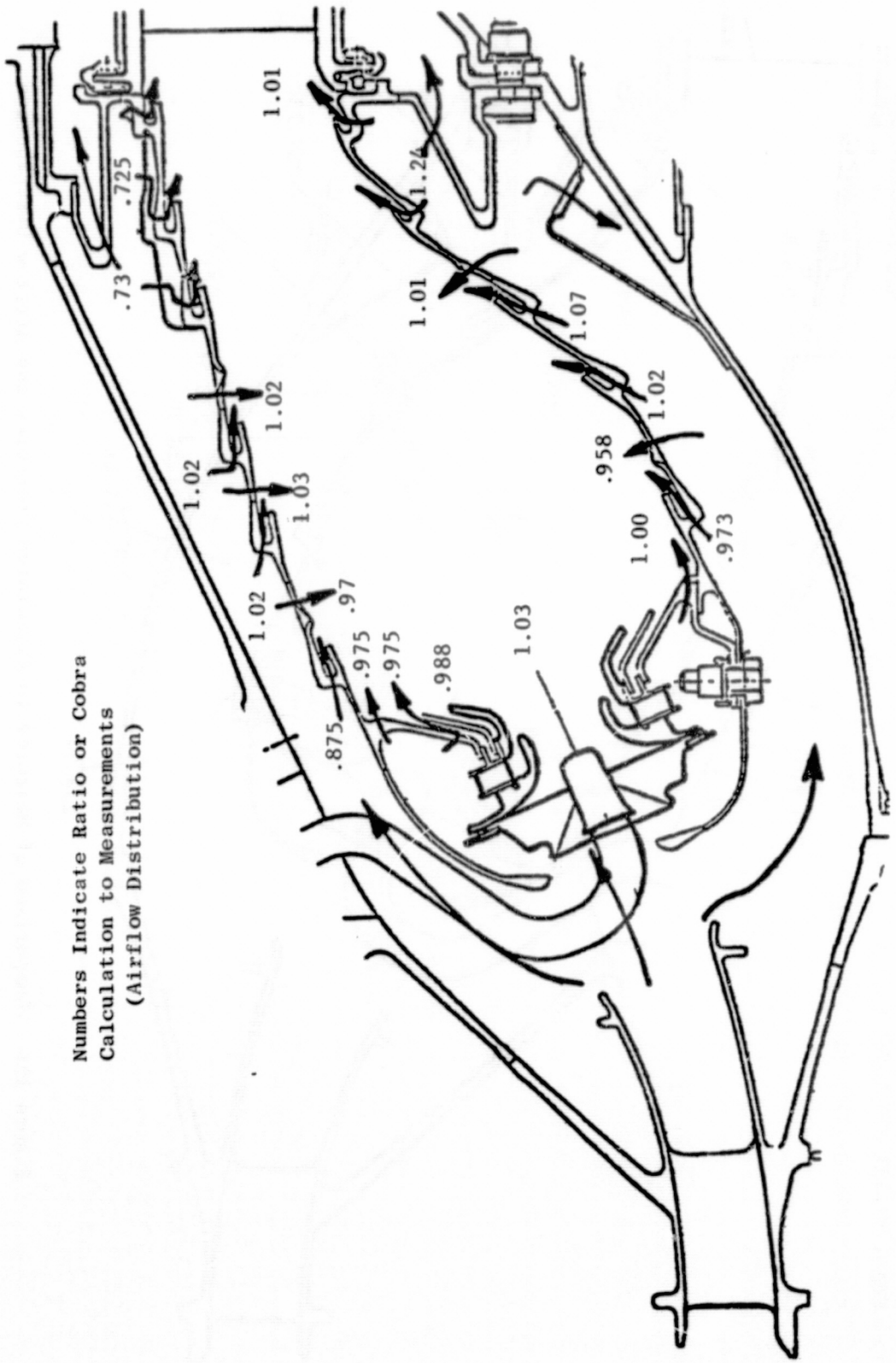


Figure 197. Ratio of Measured to Calculated Airflow Distribution.

The data base for the heat transfer module comparison consists of several sets of test data obtained with the F101 combustor. Two sets of data were obtained at simulated takeoff conditions in reduced pressure component tests and two sets of data were obtained in actual engine tests. The data from these four tests were used to make comparisons between measured and predicted temperatures. The predictions were made using the standard design practice correlations which have been utilized at the General Electric Company for a number of years. The combustor flow and temperature distributions were obtained from COBRA analysis and served as input to calculate the heat transfer input quantities such as boundary temperatures, heat transfer coefficients, and flame radiation.

Table XVIII. Summary of Analysis.

Diffuser Performance (DIFLO Analysis)		Experience
Outer Stream		
Flow	29.37% $\dot{W}_3$	
Prediffuser P_T Loss	1.17%	
Total Passage P_T Loss	2.88%	1.5-2.1%
Static Pressure Rise Coefficient	0.315	
Dome Stream		
Flow	30.55% $\dot{W}_3$	
Total P_T Loss	0.43%	0.5%
Static Pressure Rise Coefficient	0.905	
Inner Stream		
Flow	40.08% $\dot{W}_3$	
Prediffuser P_T Loss	0.73%	
Total Passage P_T Loss	1.82%	1.5-2.1%
Static Pressure Rise Coefficient	0.460	
Mass Weighted Diffuser P_T Loss	1.71%	

The first set of data selected was obtained as a part of a fuels effects program, Reference 115. Only one panel on each of the inner and outer liners were instrumented in that test. Calculated results from the General Electric

heat transfer module for the instrumented panels were made for the simulated takeoff condition using these data. The selected test conditions were defined as:

P_3 = 12.4 atmospheres

T_3 = 811 K

$W_{comb.}$ = 19.65 kg/sec

f/a = 0.0289

Comparison of the measured and predicted values are shown in Figures 198 and 199. Both maximum (hot streak) and average temperature distributions are shown in the figures. The agreement between the calculated and measured values is good. Shown also in these two figures and subsequent figures is the node network used in the heat transfer program.

A comparison for the second set of data, using all of the indentical assumptions on heat transfer correlations, is shown in Figures 200 and 201 for the simulated takeoff conditions which is defined as:

P_3 = 16.5 atmospheres

T_3 = 844 K

$W_{comb.}$ = 26.4 kg/sec

f/a = 0.0288

In this configuration, the aft two panels of the outer liner were impingement cooled while all other panels were convection cooled by the flow of air between the liner and the combustor casing. All of the panels in the configuration used in the previous comparison were convection cooled. As seen in these figures, the predicted temperatures for most of the panels are higher than the measured values, while as noted above, the agreement was good for the fuels effects data. An investigation of the data was made to determine the difference in the two sets of data. Two differences were found: first, the circumferential instrumented locations were different, and second, the method of installing the thermocouple to the liner surface was different between the two sets of data. The measured temperature variation around the circumference can be as much as 111 K (200° F) as shown in Figures 198 and 199 in which the measurements are for many circumferential locations. It is possible that higher temperatures existed on the liners than were recorded in this test. The thermocouples were installed with thermocouple sheath parallel to coolant flow in the fuels effects program, while in this test, the sheath was installed perpendicular to the coolant flow. Figure 202 compares these two installations. Installing the thermocouple sheath perpendicular to the coolant flow results in a boundary layer trip causing higher convection locally near the thermocouple junction. This effect can be introduced into the General Electric heat transfer module input. Figure 203 shows the comparison between the two calculated temperature distributions for a typical panel at sea level static conditions showing a calculated temperature difference of 70 K (125° F) at the thermocouple location.

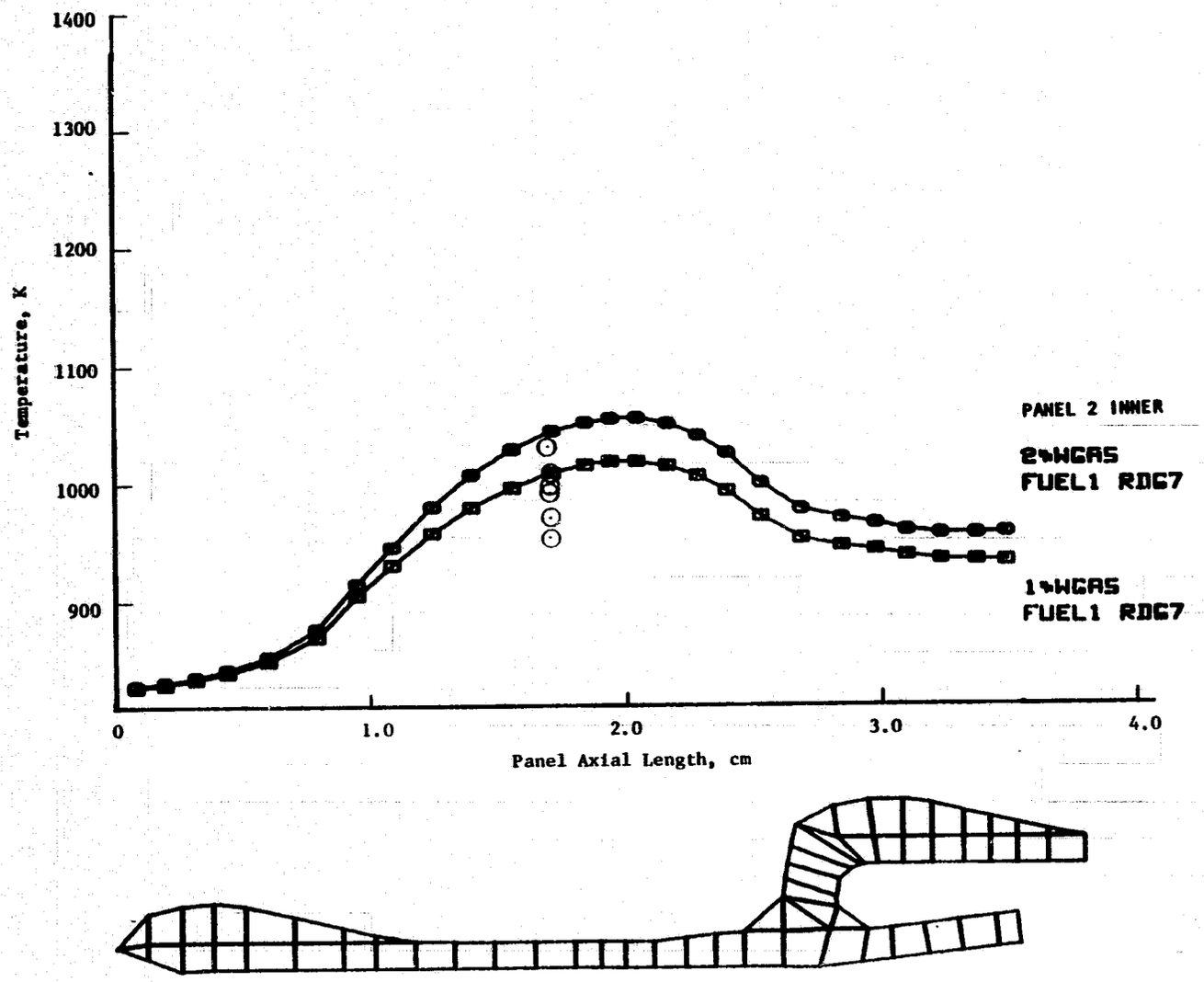


Figure 198. Comparison of Measured to Calculated Liner Metal Temperatures Using Data from Reference 115.

ORIGINAL PAGE IS
OF POOR QUALITY

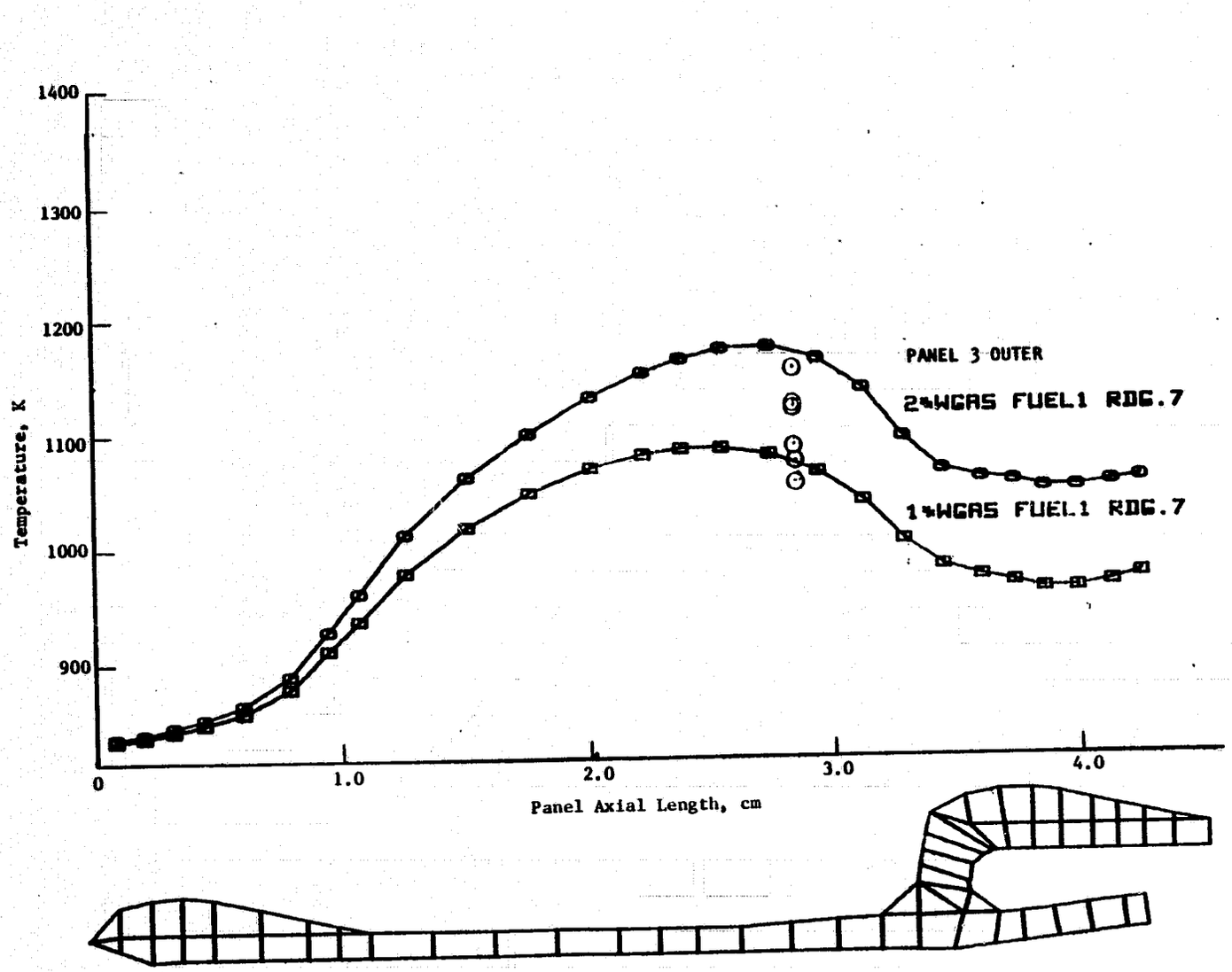


Figure 199. Comparison of Measured to Calculated Liner Metal Temperatures Using Data from Reference 115.

ORIGINAL PAGE IS
OF POOR QUALITY

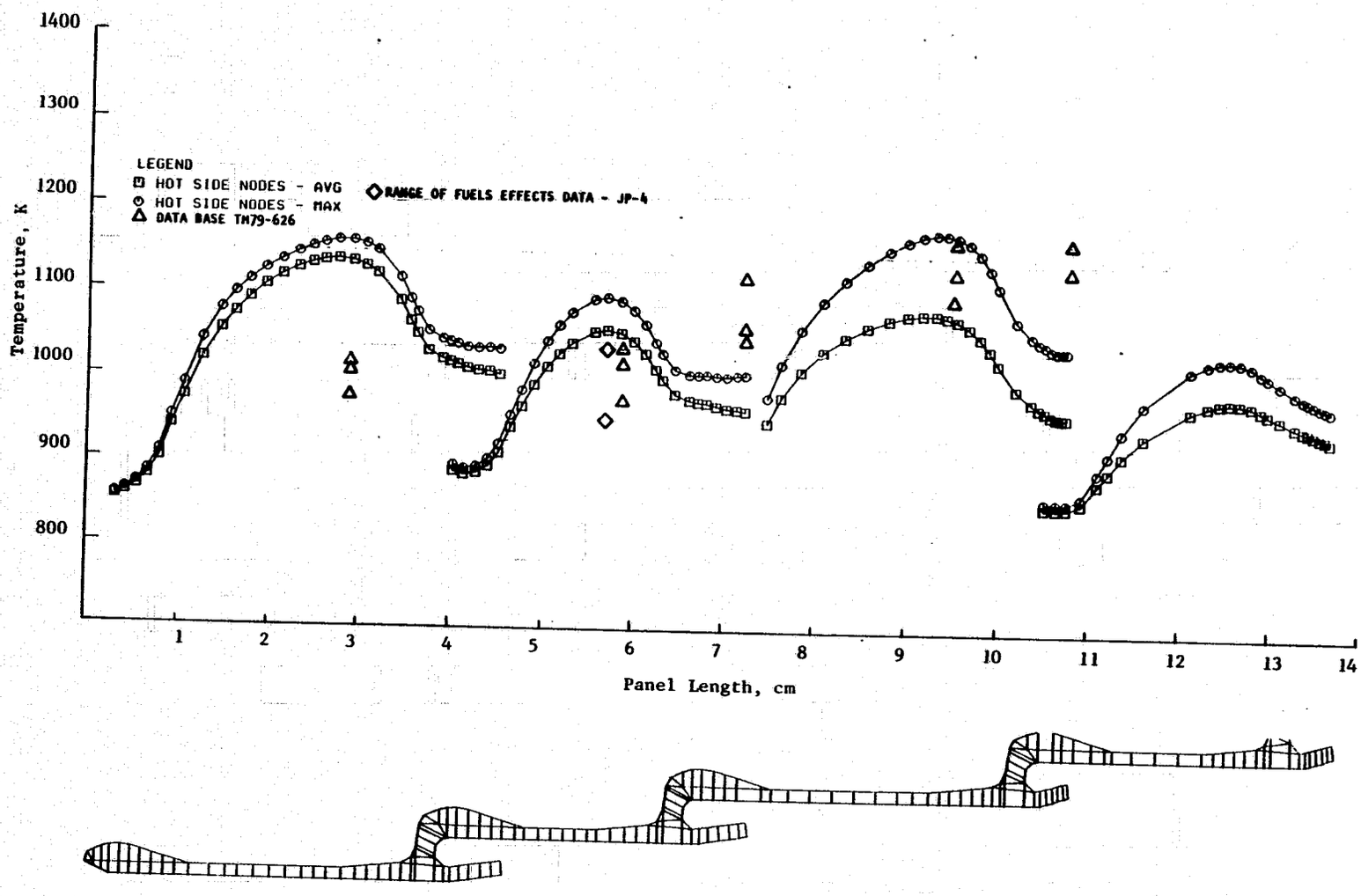


Figure 200. Comparison of Measured to Calculated Liner Metal Temperatures.

ORIGINAL PAGE IS
OF POOR QUALITY

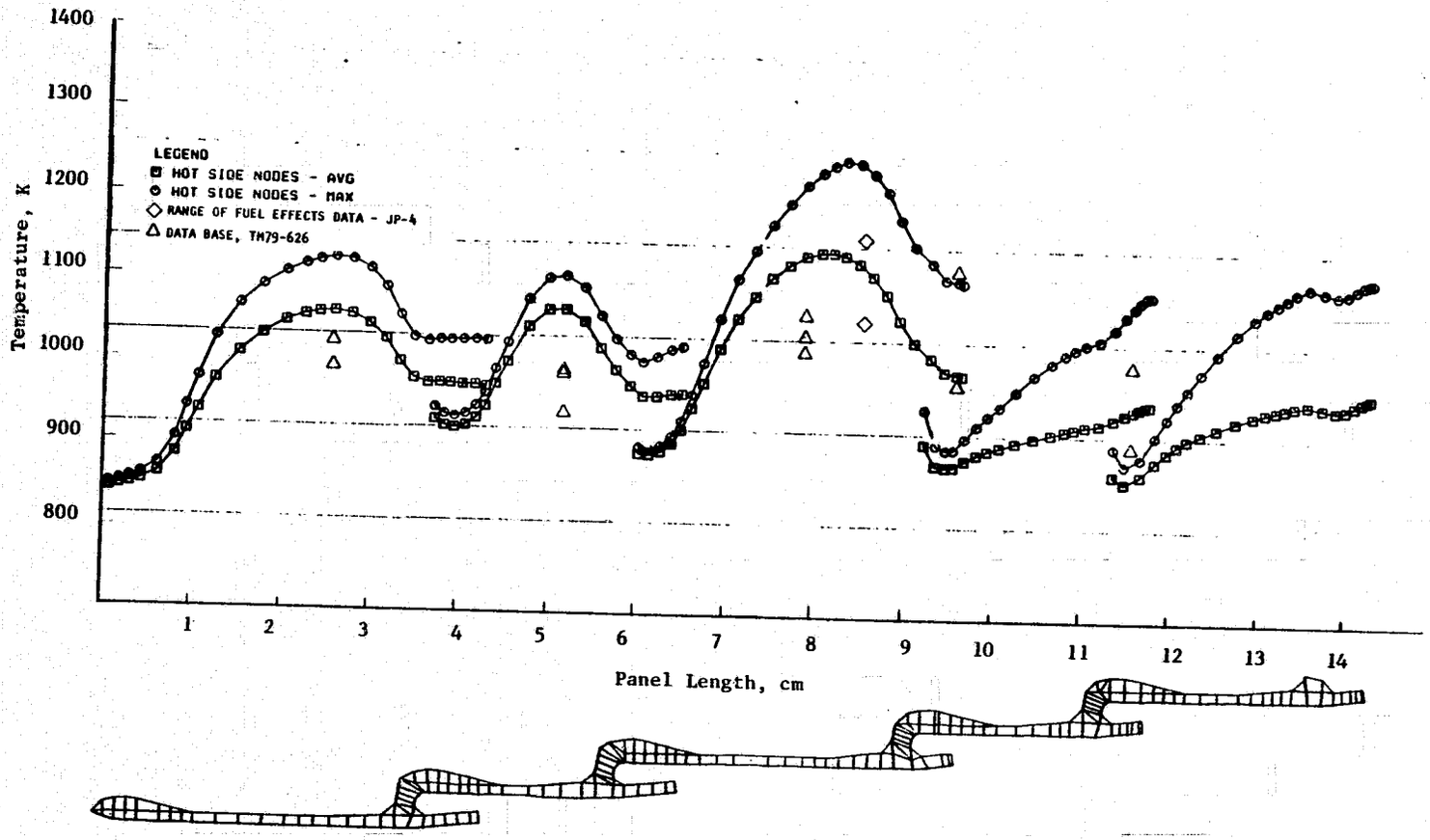


Figure 201. Comparison of Measured to Calculated Liner Metal Temperatures.

ORIGINAL PAGE IS
OF POOR QUALITY

ORIGINAL PAGE IS
OF POOR QUALITY

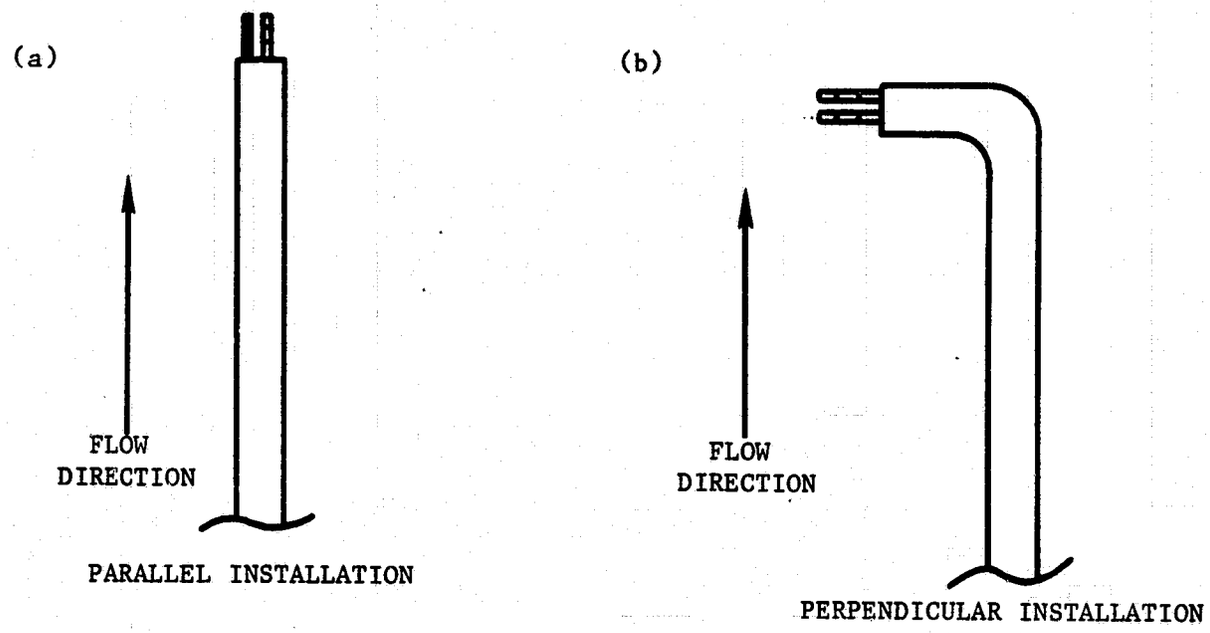


Figure 202. Parallel Versus Perpendicular Thermocouple Installation.

ORIGINAL PAGE IS
OF POOR QUALITY

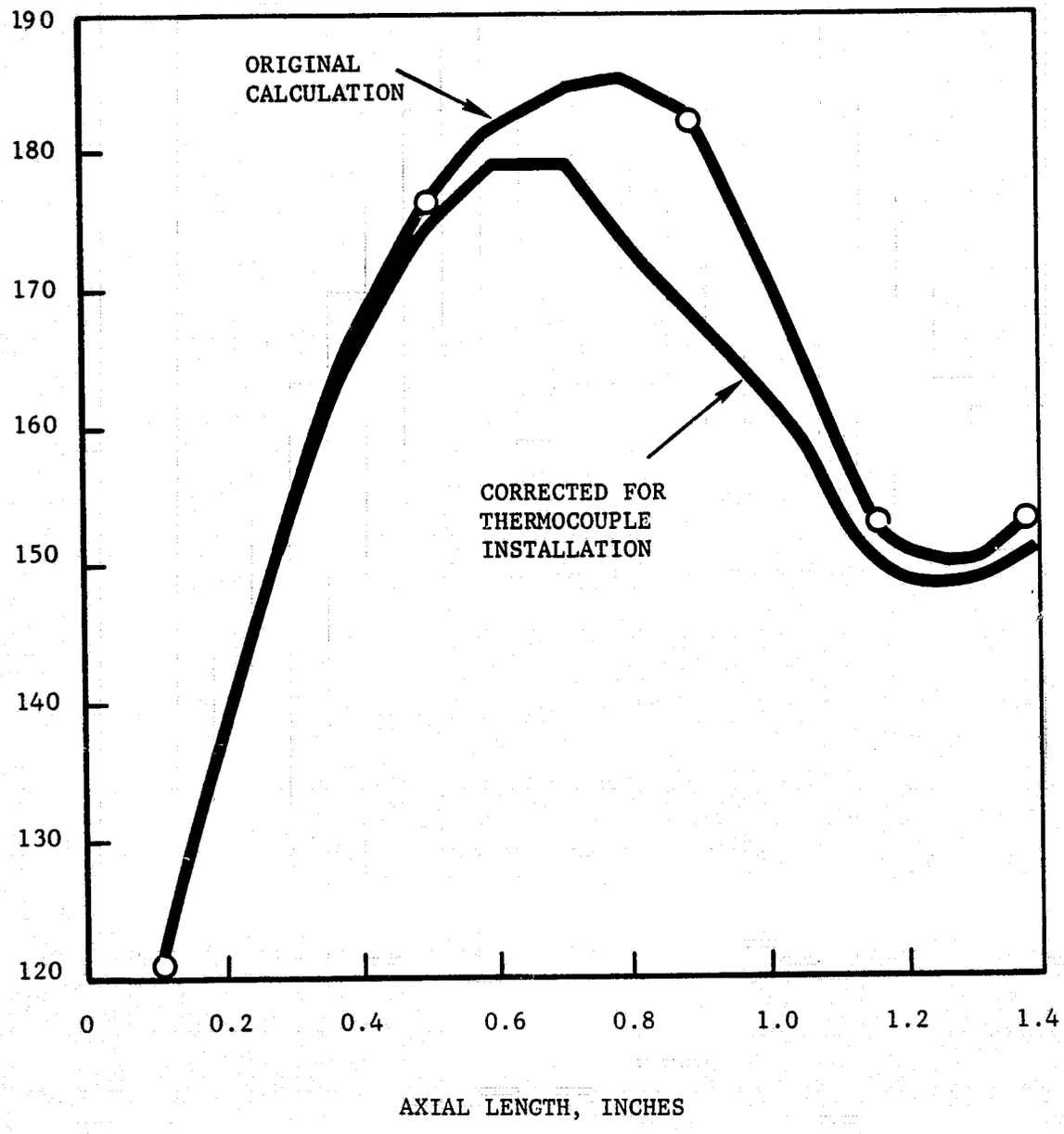


Figure 203. Comparison Between Measured Linear Temperature Using Parallel Versus Perpendicular Thermocouple Installation.

Thus, when the thermocouple installation feature is included in the General Electric heat transfer module, agreement between the calculated and measured data is significantly improved. However, the thermocouple still seems to be located in a cool region on the liner surface.

The predictions for the overhangs agree reasonably well with the measurements on the outer liner, Figure 201. The measurements, however, are much greater than the predictions on the inner liner. The thermocouple installations were different than for the panels and involved embedding the thermocouples on the hot side of the overhang. Thermocouple installation effects for this type of installation have sometimes allowed the thermocouple to read hotter than the surrounding metal. Differences in the inner and outer flow paths could contribute to the hotter overhang temperatures on the inner liner. The flow along the outer liner is nearly straight and at 90° to the dome region, while the flow along the inner liner must turn and accelerate as the passage converges. This could result in a decrement in film effectiveness which is not accounted for in the present analysis. An additional factor is that the inner liner has a view of the dome region and possibly receives a higher flame radiation than the corresponding point on the outer liner. These two factors could result in higher heat loads than assumed in the calculation.

Comparisons of the calculated and measured data for the engine test are shown in Figure 204. In this test, only the forward three panels and coolant injection slots of the outer liner were instrumented. The comparison is shown for the takeoff condition defined as:

P_3 = 25.3 atmospheres

T_3 = 799 K

W_{comb} = 45.26 kg/sec

f/a = 0.0287

In general, the agreement is good with the exception of panel 2 in which the only reading thermocouple was lower than the predicted values.

Another set of engine data was selected from the data base. In this test, the aft panels of both the inner and outer liners were instrumented. The comparisons of the calculated and measured values are shown in Figures 205 and 206. The comparison is for the test condition defined as:

P_3 = 25.2 atmospheres

T_3 = 800 K

W_{comb} = 88.75 pps

f/a = 0.032

As seen in Figure 205, the agreement for panel 5 of the outer liner is very good while the predicted temperatures are much higher than the measured values on panel 4. Their measured temperatures are very low, being only about 122 K (220° F) over the coolant temperature while experience has shown that this panel, at times, does suffer from higher temperature problems. The agreement

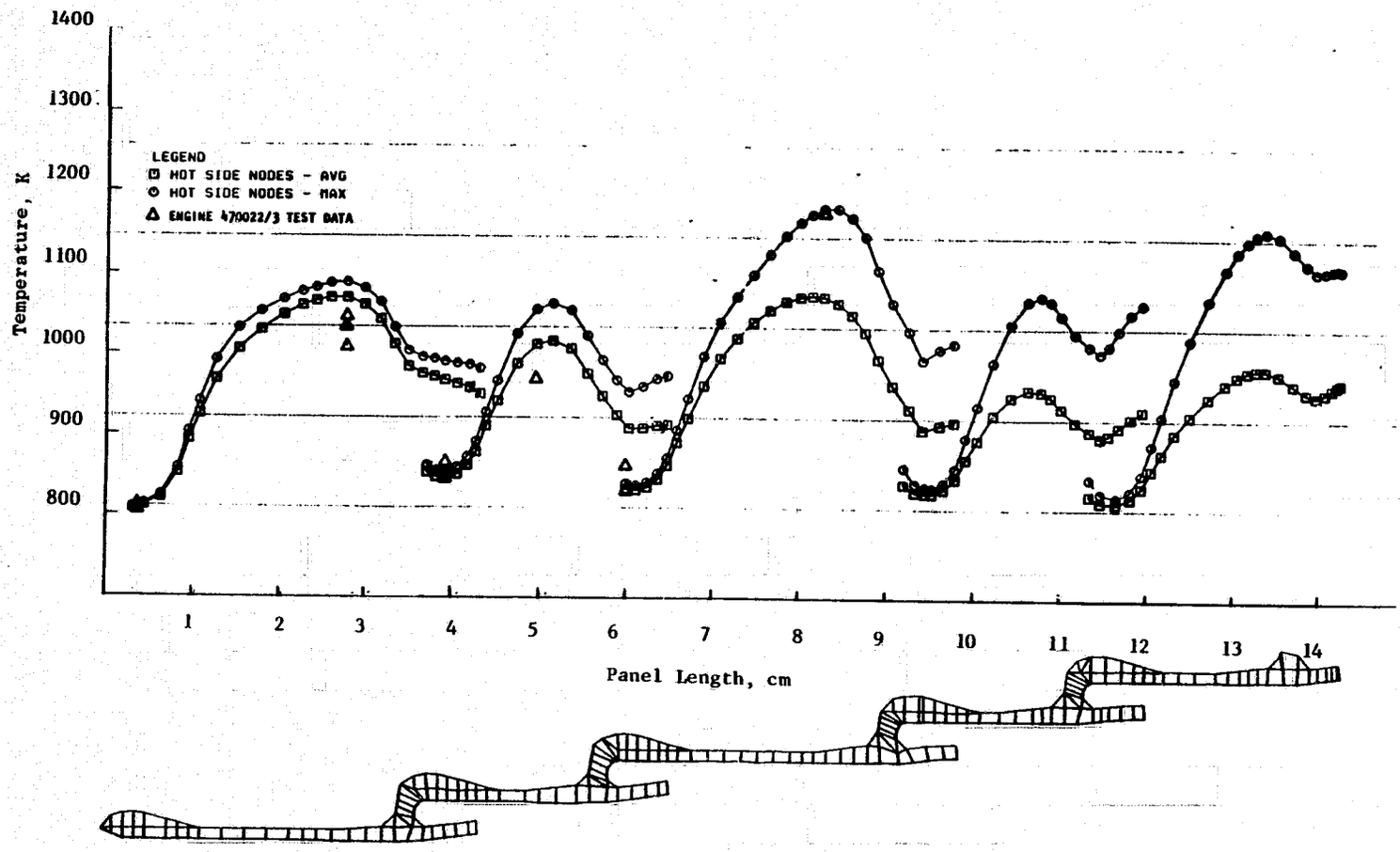


Figure 204. Comparison of Measured to Calculated Liner Metal Temperatures.

ORIGINAL PAGE IS
OF POOR QUALITY

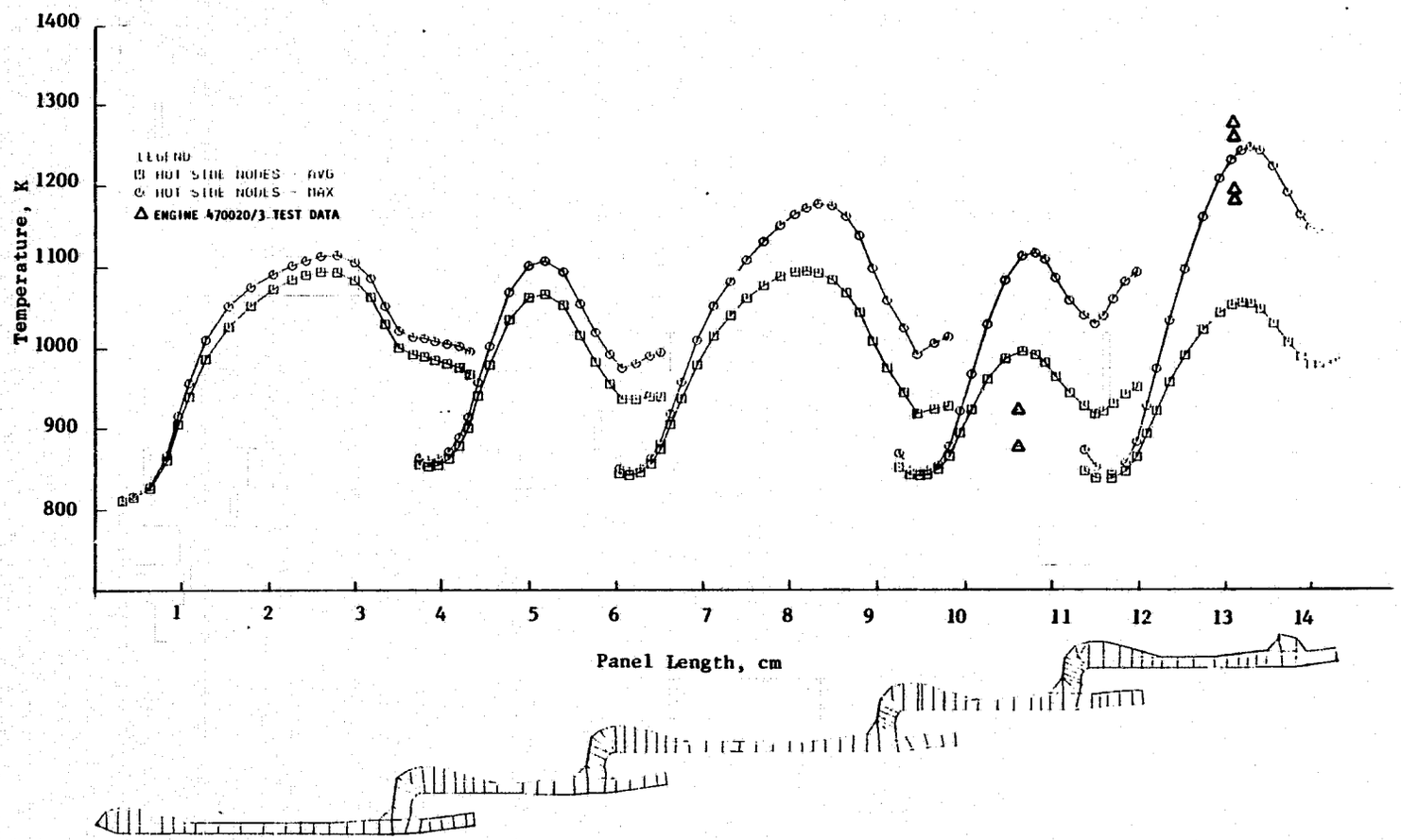


Figure 205. Comparison of Measured to Calculated Liner Metal Temperatures.

ORIGINAL PAGE IS
OF POOR QUALITY

between predicted value and the maximum measured temperature on panel 4 of the inner liner is good as shown in Figure 206. The predicted values for the other panels are much larger than the measured values. Two of the measurements were only about 111 K (200° F) over the coolant temperature and again as with the outer liner experience has shown that higher temperature levels exist on these panels.

The analyses to date have shown that, in general, reasonable agreement can be achieved between measured and calculated temperatures using the current heat transfer module. However, in certain regions of the combustor such as where the flow path converges and the flow must accelerate, improvements in the analysis could be made with better estimates of the velocity and gas temperature near the liners. Improved predictions of velocity and gas temperature as expected to be provided by the 3-D elliptic program could improve the present heat transfer analysis. It has also been shown that care must be taken to examine thermocouple locations and installation methods when selecting measured data sets.

The possibility of extracting information from the INTFLOW 3-D internal flow model for use as input to the Heat Transfer Module was examined. This examination included calculations from two different grids, shown in Figure 128, and the much finer grid shown in Figure 207.

Pertinent results from the coarse grid model are shown in Figures 208 and 209. In Figure 208, the temperature of the outermost node is plotted versus the distance from the film slot. If this temperature is to be used as a film or adiabatic wall temperature, it should gradually increase downstream of the film slot as the mainstream gas mixes with the injected air. As seen in the figure, the temperature at the first grid point downstream of the slot is already near the mainstream temperature and then decreases further downstream. The calculated temperature behaves more closely to a hot gas side boundary temperature outside of the protective cooling layer. However, inspection of the temperature profiles across the height of the combustor shown in Figure 209 show a difficulty with this postulated use. The radial temperature gradients near the wall are large and change with axial and circumferential locations, thus illustrating that even the concept of a hot side temperature just outside of the protective layer is faulty. A more detailed interpretation or utilization of the gradients seems to be required.

Calculations were made for the fine grid model shown in Figure 207 to compare directly with wind tunnel measured film protection data. The calculated temperatures using the outer node were converted to film effectiveness (T mainstream - T calculated/Tmainstream - T coolant) and are plotted in Figure 210 for several M ratios. The M ratio is the ratio of film slot mass velocity to the mainstream mass velocity. Also shown in the figure are curves for wind tunnel test data obtained at two M ratios. At first glance it appears that there is reasonable agreement between the calculated values and the measured data. Further examination shows that the trends for the M ratios are reversed. The wind tunnel test data show that the effectiveness decreases as the M ratio increases, a trend which is typical of a wide range of film slot designs, while the reverse trend is true for the calculated values.

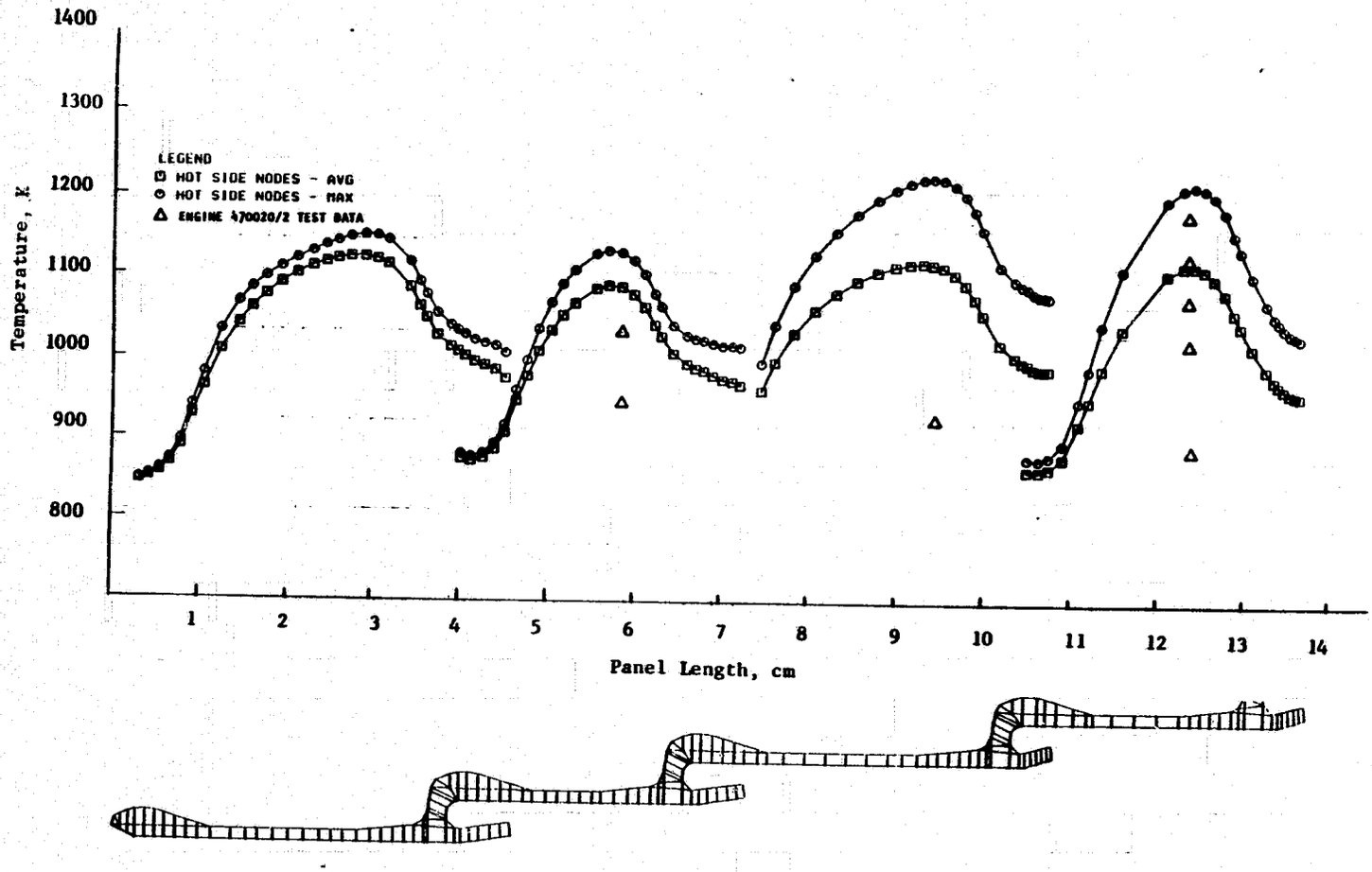


Figure 206. Comparison of Measured to Calculated Liner Metal Temperatures.

ORIGINAL PAGE IS
OF POOR QUALITY

ORIGINAL PAGE IS
OF POOR QUALITY

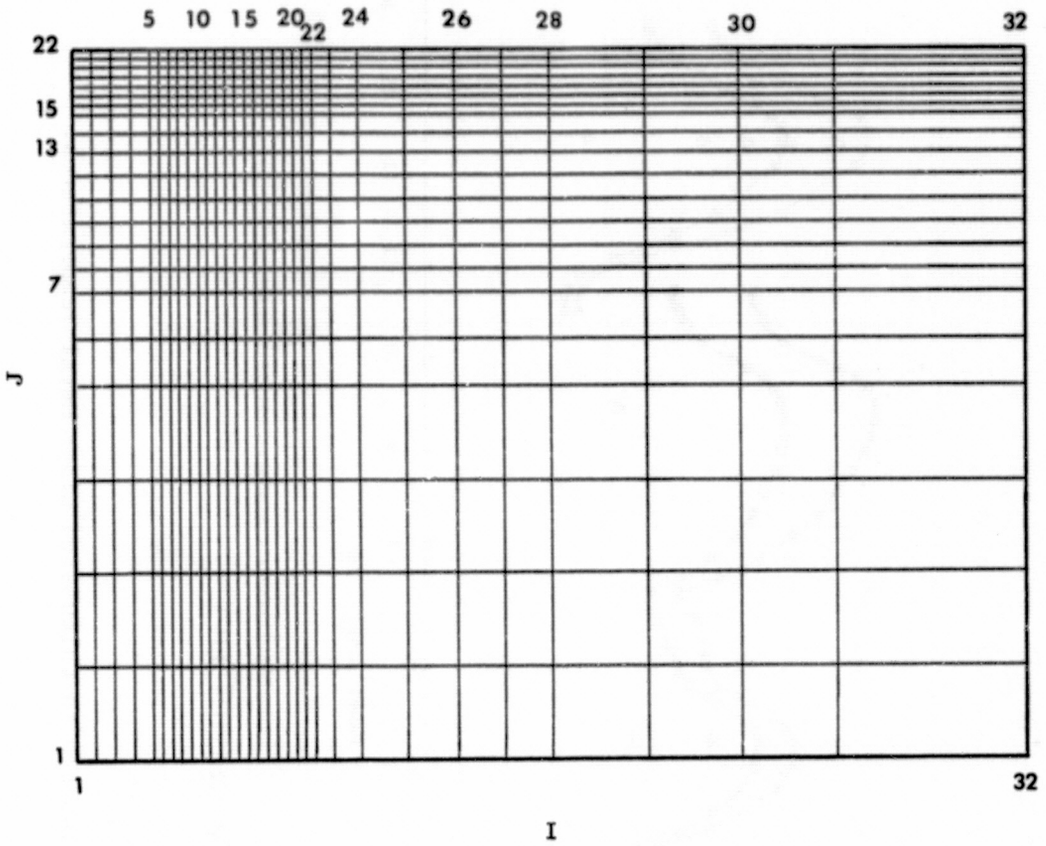


Figure 207. Detailed Grid Selected to Study Film Slot Treatment in the 3-D Elliptic Codes.

ORIGINAL PAGE IS
OF POOR QUALITY

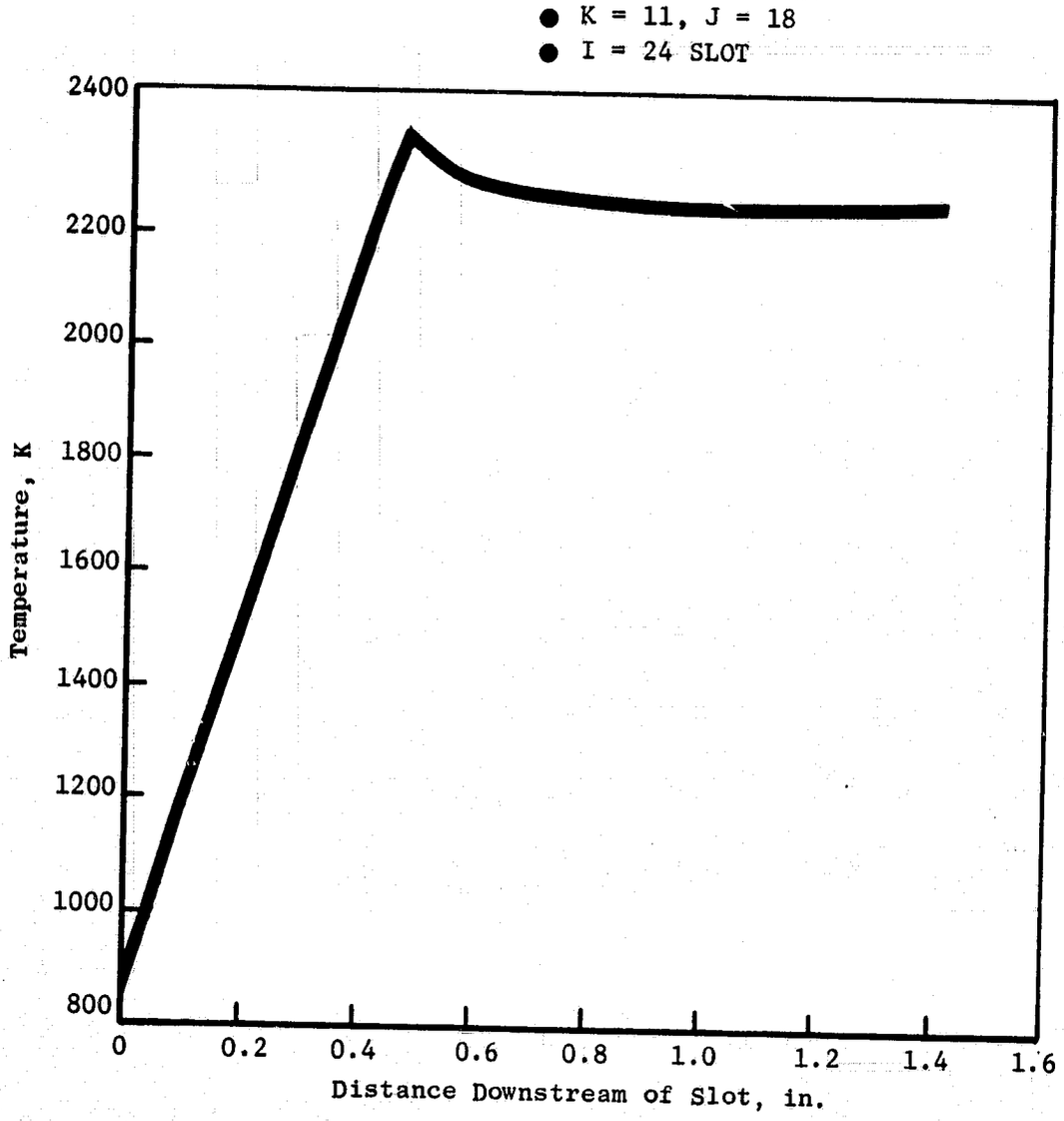


Figure 208. Calculated Temperature Profiles from 3-D Calculations Using Coarser Grid.

ORIGINAL PAGE IS
OF POOR QUALITY

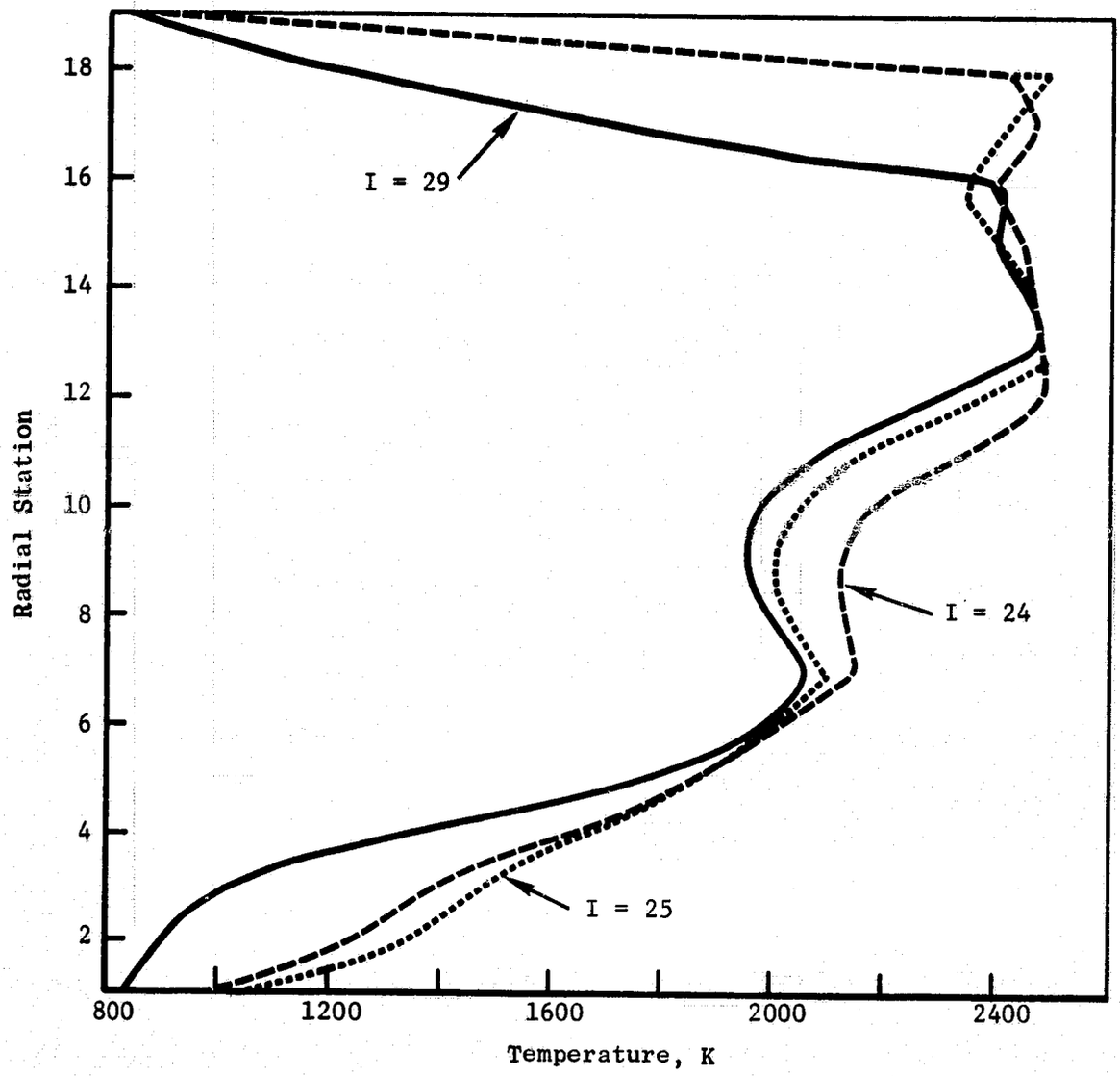


Figure 209. Calculated Temperature Profiles from 3-D Calculations Using Coarser Grid.

ORIGINAL PAGE IS
OF POOR QUALITY

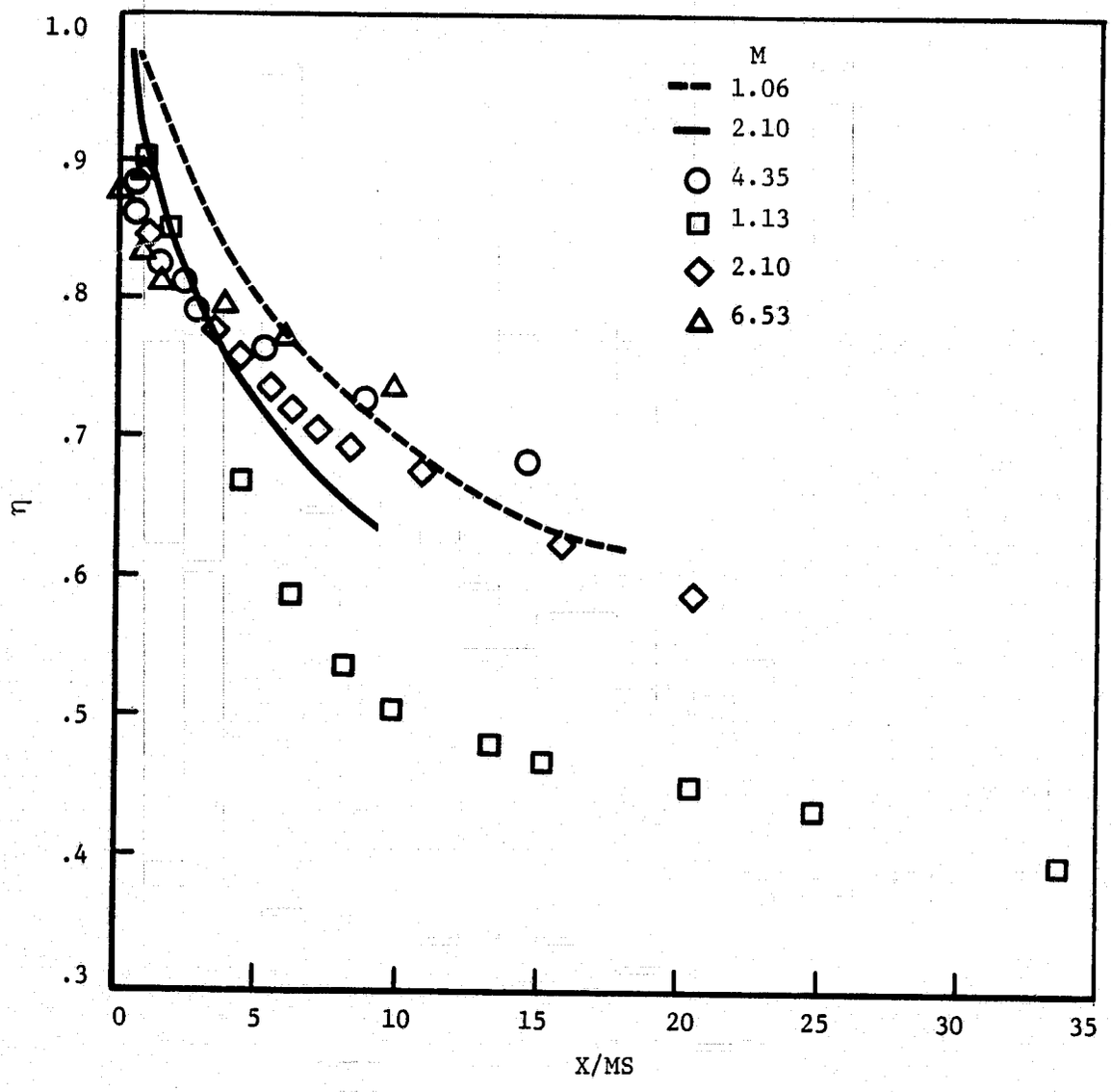


Figure 210. Calculated Film Effectiveness from 3-D Calculations Using More Detailed Grid.

Furthermore, it is known that significantly different film effectiveness is found for film slot geometry changes that cannot be identified by a grid such as that shown in Figure 207. There is a wealth of film effectiveness data available at General Electric and any new film slot configuration is wind tunnel tested before use. What is needed and not available is a method to define an effective temperature and velocity just outside the film protection layer from the gradients such as shown in Figure 209, that can be coupled with definitive wind tunnel data of film effectivenes

7.4 SUMMARIZED ASSESSMENT

7.4.1 Diffuser Module

Comparison of the diffuser module calculation with measured results showed reasonable agreement. This calculation provides early in the design process a valuable estimate of the average pressure level in the three streams that feed the combustor, the dome region, outer annulus, and inner annulus passages. However, early in the development process these pressures are measured in special diffuser tests. Diffuser development modifications are made early and frequently remain unchanged through subsequent combustor development efforts. Thus the basic inputs to the Flow Distribution Module during combustor development are available from measurements and the Diffuser Module is not a basic source of error. If, however, significant three-dimensional effects were present in these flows, such as wakes from fuel nozzles or structural struts, they may not be adequately documented by the measurements or by the computer programs currently used. Three-dimensional analytical treatments could provide more detailed information than available from measurements. However, while some older combustor designs exhibited effects within the combustor and in the exit gas temperature patterns that were attributable to upstream wakes, all current General Electric combustor/diffuser designs show no evidence of wakes affecting the flow through the combustor apertures. Thus, a refined three-dimensional treatment is not required at this time to improve the accuracy of analysis for combustor durability. However, it is expected that work on improved diffuser analysis methods including three-dimensional treatment will continue at General Electric.

7.4.2 Flow Distribution Module

Figure 196 shows comparisons of measurements with the calculations including specifically the overall check of pressure drop. There is some evidence of Reynolds number or approach turbulence levels affecting measured results because engine test results at high pressure with compressor discharge flow turbulence levels frequently show lower overall combustor pressure loss than combustor component test rigs. The flow coefficient correlations for individual apertures were derived generally from one atmosphere laboratory scale data in which turbulence levels in the approach flow are lower than expected

engine levels. In general, the effects of two-dimensional passage flow including approach boundary layer flows have been adequately treated in the experiments that generated the flow coefficient data. Three-dimensional elliptic computer programs could be used/developed to calculate flow coefficients, flow angles, and flow distribution within individual apertures and used as input to the Internal Flow Program. Figure 87 showed a two-dimensional case where the external flow passage and internal flow were, in fact, more than coupled - they were a single solution. However, the large collection of flow coefficient and angle data and correlations for individual apertures available at General Electric allow accurate calculations without the aid of detailed flow analyses. Whenever new aperture shapes with unknown flow characteristics are introduced into designs or test hardware, additional laboratory tests of the individual aperture are routinely conducted for inputs into the Flow Distribution Module. Thus, these same flow facts are available for input into the Internal Flow Module. At this time, more accurate methods of determining flow coefficient and angle information for the Flow Distribution Module are not significantly limiting the accuracy of General Electric's overall Aerothermal Model.

7.4.3 Heat Transfer Module

Figures 205 and 206 compare calculations of the Heat Transfer Module with measured metal temperature data along a General Electric combustor liner. Within the module, heat transfer conduction within the metal structure is calculated by routines that have long been in use at General Electric with well established accuracy. The convective heat transfer calculations are based on well established correlations in general use as modified by data and specific flow features that might be expected to alter the correlations. Wind tunnel data on special local heat transfer coefficients are measured and correlated where appropriate and introduced into the Heat Transfer Module calculation method. Film slots introduce cooling air along the hot side of the combustor wall which helps protect the surface from the hot combustor gases. Wind tunnel data on the effectiveness of cooling air to protect the surface are available at General Electric from a large variety of cooling slot designs, and for substantially new slot designs new wind tunnel data is obtained. These data/correlations are utilized in the Heat Transfer Module. The hot gas side inputs of velocity, temperature, and flame radiation are estimated from previous experience guided by forcing the heat transfer calculations to agree with metal temperature measurements in adjusting these values. The selection of these input values is the greatest source of error in the Heat Transfer Module. It is planned that the Internal Flow Module will in the future be able to supply more accurate values and a more detailed distribution of values than is available at present. The accuracy would be improved if hot gas side velocities and temperatures were available from a sophisticated Internal Flow Module even if the radiation still had to be estimated from calculations beginning with measured metal temperatures. It is expected that this temperature and velocity capability will become available well before reliable flame radiation calculations are available from the same three-dimensional calculated internal flow field.

7.4.4 Internal Flow Module

The background understanding of the Internal Flow Module, and the mathematical and physical sources of error within the module at General Electric came mostly from experience with the two-dimensional code GETREF. The two specific three-dimensional elliptic codes assessed in this effort came from sources outside of General Electric. In-house knowledge of the programming details was very limited. Some of the sources of the mathematical and physical errors encountered were reasonably well understood because of the experience with the two-dimensional code. The total effort was organized and structured based on this limited knowledge, and because of the time constraints of the program efficient restructuring of the effort consistent with new findings was not possible. The most significant finding that might have resulted in some restructuring was the high cost of obtaining reasonably converged solutions with the detailed grids thought to be appropriate for treating combustors with reasonable accuracy. The discovery of special difficulties with high momentum ratio jet penetration calculations involved more exp ɔration than originally planned and resulted in less exploration of full combustor analyses and comparison with gas exit temperature measurements.

In discussing the sources of error, a list of features in the order in which they are encountered in conducting an analysis is followed below (see Table XIX). In the next section the most important possible future efforts are discussed with respect to priority of need.

Table XIX. Sources of Error in 3-D Elliptic Model.

- Input-Output Capabilities
- Input Information Detail
- Fuel/Swirl-Cup-Air Insertion Angles and Velocities
- Numerics
- Turbulence Model
- Compositional Fluctuation Treatment/"Unmixedness"
- Chemical Reaction/Kinetics
- Flame Radiation Model
- Convection to Wall
- Film Slot Treatment
- Boundary Shape
- Computer Storage/Cost Effects of Framework, Convergence and Grid Detail
- Misimplementation of the Modeling Concepts

The input and output capabilities of the three-dimensional computer codes are somewhat inflexible. The inflexibility is the result of trying to make the program easy to use for the simpler combustor calculations. One example is the dome input provisions. Neither code permits the introduction of a swirler airflow around a fuel nozzle in an annular dome. This provision was, however, introduced at General Electric before this present program started. Changes in number of grid points require changes in the array descriptions that were simplified at General Electric. The boundary description for non-cylindrical walls at the aft end involving the stairstep approach while conceptually described was not implemented in the original coding. Many other desirable flexibility features in the input remain uncoded. The output has been coupled with General Electric plotting programs.

The importance of using the correct input details of flow, angle, and turbulence levels has been emphasized frequently in the literature. However, the knowledge of these details is often very limited. In swirl cups, for example, it is known that substantial changes in flow direction result from minor changes in the aperture shape that would not change the model geometry inputs at all. If this flow feature is not known for input to the calculation, gross errors in the resulting flowfield and fuel distribution result. The resulting early fuel spray distribution, even if known, is difficult to input properly since the individual rays, as the program is presently coded, must all originate from a point in the same axial plane as the swirler flow. The correct coupling of the spray with the swirler airflow is difficult using this input approach.

The fuel spray treatment is limited in input detail and is not completely coupled with the flowfield calculations. The special problems of large drops penetrating into low density air, which can be important for idle pressure levels and below, is largely eliminated at the high pressure levels where durability is evaluated. Even though the present fuel trajectory capability in the model may not permit appropriate input, it is possible to postulate an input technique where the fuel is input in the appropriate regions of the swirler air consistent with measurements, assuming fuel that follows the air streamlines from the input point on. By utilizing this type of treatment, the detailed sources of error in the present fuel injection treatment are largely circumvented.

Artificial or numerical diffusion is a major source of error. In a combustor calculation, this effect can be so great that the calculated mixing becomes almost independent of the turbulence model prescribing the turbulence. Calculated results look plausible because the general flowfield characteristics are controlled heavily by the pressure forces rather than the exact level of turbulent mixing. With the "hybrid" scheme, the accuracy of the numerics is increased by increasing the number of nodes in the calculation until central differencing is possible (cell Peclet number below 2). For two-dimensional flows, increasing the node density is possible and results in second order accurate results which allow accurate assessment of the physical model. However, for the three-dimensional combustors, the grid could not be refined to the extent needed to permit central differencing in the critical areas.

The number of node points was limited by the present computer storage capacity. While future storage capabilities will presumably increase, the cost of running such a program becomes nearly prohibitive. The appropriate solution would seem, to be to introduce improved numerics. Schemes that are more accurate than first order upwinding, perhaps second order, but that can be applied at high cell Peclet numbers (greater than 2) are needed. The artificial diffusion introduced by upwind differencing would then be eliminated. It should be noted that since the diffusion term is approximated by (second order) central differencing it is inconsistent and unnecessary to use schemes of higher orders for the convection term.

Simulation of the Air Force's bluff-body combustion experiments, Section 7.1.4, was performed by selective grid refinement until the cell Peclet numbers are below 2.0 for the critical regions. Everywhere else, analysis indicated that numerical truncation error was dominated by the other terms. This endorses the importance of automatic error assessment in the a posteriori spirit of McGuirk, et al., 1981[58].

The k-ε turbulence model itself is known to be limited in its ability to handle certain types of flow. The constants in the model were established from simple shear flows. Other flows are known to require other constants for accurate results. As mentioned in Section 7.1.4, even round (parabolic) jets require different constants while swirling flows require still other adjustments. Near and downstream of stagnation points, unusually high turbulence levels are measured that are not predicted by the model. Briefly, several difficulties are introduced in simplifying the Reynolds stress equations to the k-ε model; e.g., dropping convection of shear stress and adopting an eddy viscosity concept. Furthermore, this eddy viscosity is generally taken to be isotropic (though not in the algrebraic stress model). The dissipation rate equation remains another major source of error; and experimental data is not readily available for this quantity.

Other two-equation turbulence models have been considered, Section 6.4, but it is not established that any of these are in fact better than the present k-ε model. Further refinements have been postulated that take into account the multiplicity of scales that are really present. Solving the full Reynolds stress equations leads to higher order closure assumptions and in practice can be excessively expensive in computer time. The errors from the numerics treatment at present overwhelm the importance of the exact turbulence model. Hence, the numerics need to be improved before the turbulence model refinements are needed. The Algebraic Stress Model (ASM), Section 7.1.3, that was found to work well in swirling flows, has general characteristics in its equations. It deserves to be included as a refinement to the present model. Other possible modifications to the turbulence model are not established as reliable improvements and are, therefore, not recommended at this time. With improved numerics and the present k-ε model, calculated flows with useful accuracy should be possible. Of course, future developments in turbulence modeling are a valuable direction for longer term research.

A special aspect of the turbulence is the treatment of the random compositional fluctuations called "unmixedness." The usual velocity, temperature, and fuel/air concentration measurements are time averaged values of a level that is actually fluctuating rapidly with time. The calculated flow fields also represent time average values. As discussed in Section 6.6, a probability density function, pdf, can be used to describe the variation in values that constitute the mean or average value. This is especially important in considering kinetic or thermochemical phenomena such as the heat release. If the time average fuel/air ratio at a point in the flow field is stoichiometric, the time average temperature will be significantly lower than stoichiometric values even with fast kinetics (equilibrium reaction). This is because there will be significant over and under stoichiometric mixtures constituting the fluctuating levels. The pdf treats this phenomena with much better fundamental physics and rigor than the eddy break-up model currently in use in the available three-dimensional models. The pdf method has been compared with instantaneous measurements in a reacting jet, Section 7.1.1, and excellent agreement has been demonstrated. This approach has been implemented in the 2-D code GETREF. It is planned to adopt the pdf method for treating time fluctuations at General Electric in future three-dimensional elliptic codes.

The available programs use only very crude chemical kinetics. Detailed kinetics coupled with the flow field calculations result in excessive computer time, particularly when time fluctuations are simultaneously treated. However, for durability considerations, the combustor is operating at high pressure and the chemical kinetics proceeds very rapidly. Detailed kinetics is needed only if emissions or low pressure phenomena are involved. Since emissions are not within the scope of this effort concentrated on durability, no improved treatment is needed at this time.

Flame radiation involves radiation from the CO_2 and H_2O that are calculated by the model and from soot for which accurate calculation methods are not yet established. The flow field itself is practically unaffected by the inclusion of flame radiation in the model. The lack of an adequate flame radiation model in the codes available at General Electric resulted in excluding the evaluation of flame radiation from these present efforts. It is planned to postpone at General Electric efforts to provide a flame radiation model coupled with the three-dimensional Internal Flow Model until improvements are accomplished on other aspects of the model.

The calculation of the convection to the walls does not provide a good calculation of metal temperature but the method is adequate for defining the internal flow field away from the walls. The cooling film treatment even with a fine grid near the film does not produce the same wall protection characteristics that are found from measurement. The current coding does not permit the slot itself to be divided into a fine grid; the first grid point is intended to be at a specific fraction of a slot height outside of the slot. With a separate program, perhaps two-dimensional grid refinement would be possible. However, detailed differences within the slot itself are known to effect the protective ability of the cooling air, but this finer grid by itself cannot resolve these differences. The extraction of flow conditions

at the boundary between the film protection layer and the hot combustor gases would permit the use of existing correlations of film protection characteristics. However, as discussed in Section 7.3, this boundary is complex, involving temperature, velocity, and turbulence gradients. It is planned to develop a technique at General Electric for identifying "effective" boundary conditions for input to the Heat Transfer Module.

The ability to utilize nonclylindrical combustor walls with the stairstep technique has difficulties as discussed in Section 7.2. Grid line concentrations can exist in regions where they don't benefit the calculation. Also, many node points are outside of the flow field. This causes a given number of nodes to produce a less accurate answer than for a combustor with cylindrical walls and is, therefore, a significant source of error. A body-fitted coordinate system would eliminate this problem while simultaneously permitting a useful concentration of grid next to the wall.

Computing time costs as a source of error are a major consideration. Errors due to inadequate grid cannot be simply corrected by adding more grid. The storage limits of available computers are easily saturated, and detailed grids result in excessive computing time and costs. Looking back in history, the storage capacity of computers has increased at a rapid rate and computation costs have come down. It is expected that these trends will continue. However, the desires for increased grid are extreme. For example, an increase in grid by a factor of three in each direction would seem to be a moderate refinement, but this involves a factor of three cubed or 27 in storage requirement. Furthermore, the number of iterations required to achieve a converged solution increases for larger node arrays. With the present costs of a converged solution for detailed node distributions utilized in this program exceeding $5000 per case, significant increases in nodes are not practical with the present codes. Efforts are needed to provide more accurate answers with the same number of nodes as well as to provide significantly faster algorithms or other faster techniques for achieving converged solutions.

In addition to errors inherent in the mathematical and physical modeling concepts as discussed above, errors can enter the calculations due to misimplementation of the concepts. This can occur because of mistakes or poor judgment in the actual program coding, and can also occur when the user incorrectly inputs to the programs. This later possibility is increased when the user is not the writer of the program, perhaps even working in a different company, resulting in misunderstanding of parameters and input needs. More complete users-manuals, more like programmers manuals, can help. Careful checking of output details and features against physical expectations and previous calculation including those done by others and with other computer programs are also valuable guidance.

Needs for Benchmark Quality Data

The sources of error in future models will require further comparisons with benchmark quality data. Additional new experiments are appropriate. In

addition to more experiments similar to those that have been conducted in the past, some experiments should give special attention to obtaining as complete a documentation of the flow field under study as possible. The existing data, including the data selected and generated in this program, frequently do not include as much information as the modeler generally desires for his comparisons. For example, in addition to velocity, temperature, and turbulence intensity measurements in detail, the modeler who is trying to develop improved physical submodels would also benefit from measurement on the turbulence scale and the nature of the fluctuations, which are seldom obtained. Also, the inlet conditions to the experiment need to be correctly documented. In real combustors, little data exists on the internal flow details of any kind. However, the use of models in design will require inlet flow conditions. Experiments to provide detailed information should include noninterfering techniques to document those features of the flow that are expected to be affected by intrusive techniques. In the comparisons conducted in this work, calculations of turbulence intensity and scale were not always available and more complete data on the measured turbulence would have assisted in identifying the sources of error.

One specific area where additional data are critically needed in order to obtain reasonably accurate documentation for flow fields is in the region of the fuel injector and swirl cup. The flows emerging from this region are not properly defined at present by the model from simple representations of the geometry. This region can be experimentally explored to a considerable extent without the presence of the downstream portion of the combustor and also without reaction. This can simplify the experiment while still supplying valuable data on the character of the fuel and airflow in this region.

8.0 CONCLUDING REMARKS

8.1 SUMMARY

For comparison with the aerothermal model, data were selected from General Electric's data base and from the literature and new experimental data were obtained. The new experimental data involved temperature distribution data from a series of combustor-like flows of progressively increasing flow complexity. Comparisons of modules within General Electric's overall aerothermal model were conducted.

The comparison showed that the modules already in use are resonably accurate. The principal weakness in the Heat Transfer Module is in the accuracy of the hot gas side input. Also, the currently used methods do not include a module for accurate analytical estimation of the combustor exit gas temperature.

The mathematical and physical principles of the internal flow model were investigated in one- and two-dimensional studies of various flows for which "benchmark" quality data were available. These studies addressed the "numerical diffusion" error due to the use of first-order accurate discretization schemes as well as turbulence and turbulence-chemistry interaction phenomena.

The one-dimensional prescribed uniform velocity convection-diffusion equation was studied with and without source terms to ascertain the performance of various difference operators applied to the convection term; diffusivity was taken as a known constant. As is well known, differencing of the odd derivative can lead to instability if central differencing is used when the grid is coarse (local Peclet number less than two). One-sided upwind differencing provides an unconditionally stable finite difference representative of the convection term but is accurate only to first order in the grid spacing. This is one order less accurate than the centrally-differenced diffusion term (which, being an even derivative does not have the stability problem) and leads to artificial diffusion. Thus, the convection term differencing operator must compromise between formal accuracy and stability. One-dimensional prescribed nonuniform velocity flows and two-dimensional uniform velocity flows were also modelled. All these studies indicated the need for a second-order scheme (e.g., second-order upwinding or QUICK), rather than a first-order scheme (e.g., skew first-order upwinding which recognizes grid to streamline skewness but is still overly diffusive). Direct central-differencing of the convection term in three-dimensional flows is precluded by the excessive grid needed to ensure local Peclet numbers below two.

In the assessment of the physical submodels in two-dimensional recirculating flows, however, the grid density was increased until local Peclet numbers allowed central differencing. Such numerical error as existed was quantified. With this sound numerical basis the model was applied to three recirculating flows. A parabolic formulation - for which the numerical issue is not relevant - was also used to simulate a non-premixed jet flame for which high quality optical data were available. These studies indicated that the

suggested advanced physical models are necessary. Specifically, a probabilistic treatment for the random compositional fluctuations which lead to nonlinear turbulence-chemistry interaction is required. Furthermore, the isotropic eddy viscosity k-ε model was shown to be inadequate for flows with strong swirl components; an algebraic simplification of the full Reynolds stress equations which retains the two-equation format was suggested and validated.

In utilizing the 3-D calculations in INTFLOW difficulties were encountered in obtaining good comparisons with measurements of dilution jet penetration and mixing data. Variations of grid detail and input quantities to the calculations were examined to determine their effect on the solution. It was found that the higher momentum ratio jets were more sensitive to these inputs than lower momentum ratio jets which are less affected in their turning by the jet shape development from turbulence and more by the pressure field effect on the early jet. Calculations done with one set of parameters, but with both of the 3-D codes within INTFLOW, showed that similar penetration and mixing were calculated, even though the local calculated turbulence levels were different. The comparison of calculations for the dilution jet experiments conducted at General Electric are close in character to the measurements but not good enough to be a useful design tool at this time.

This effort did not establish the grid density needed to adequately treat dilution jets. To stay within reasonable computing time and storage demands, it is not possible to calculate combustor dilution patterns accurately with the available codes. The grid requirements for future 3-D codes with improved numerics could not be determined in this work; studies conducted with a 3-D code having the desired numerics improvements will be required to make this determination.

Comparison of calculations with an experiment that included fuel injection and heat release and a combustor dilution pattern, showed that the calculated gross temperature pattern in the gas of the combustor exit had considerable similarity to the measured values. Further analytical and experimental study is still needed, however, to define an adequate method for defining the input for the initial fuel and air distribution.

The computer running time costs of obtaining reasonably converged solutions was very high; thus future modeling improvements should strive for faster convergence techniques to increase the size of the maximum affordable grid along with alternate numeric schemes to provide greater accuracy for whatever grid is adopted. For inputting the dome air and fuel injection details, more experimental knowledge of the early flow development is needed.

8.2 PRIORITIZED RECOMMENDATIONS

Table XX presents a prioritized list of the main recommendations for treating the sources of error in the current 3-D elliptic internal flow code INTFLOW. The list includes two paths: needed basic capability and application to durability. The efforts in the second category should begin whenever it is decided that the needed basic capability is progressing fast enough to

Table XX. Prioritized Recommendations.

Needed Basic Capability

1. Improved 3-D Code Framework
   - Body-Fitted Coordinate System
   - Improved Numerical Scheme
   - Faster Convergence Speed
2. Improved Turbulence and Turbulence/Chemistry Treatment
   - ASM (Algebraic Stress Model)
   - One Scalar PDF
   - Alternate to Two-Equation Turbulence Model
3. Develop Treatment of Inlet Boundary Conditions: Dilution, Fuel, and Swirlers
   - Based on Empirical Data Including Extensive GE Data Base and New Experiments
4. Improved Chemical Kinetics Treatment Including Turbulent Compositional Fluctuations

Application to Durability

1. Liner Heat Transfer Inputs
   - Fuel and Swirler Air Insertion Treatment
   - Hot Gas Mixing With Film Cooling Air to Couple with Heat Transfer Model
   - Radiation Effects, to be Developed Later
2. Pattern Factor 3-D Design Tool
   - Perturbation Approach Recommended

justify work on features to permit the application to the design/development guidance process. These recommendations are based on a methodical study of 2-D flows and model problems and also on a more pragmatic application of the available 3-D code.

The first substantial improvement in capability can come from revisions in the basic code framework. A body-fitted coordinate system would permit needed improvements in the accurate treatment of the boundary, allow desired grid concentration near the walls, permit more flexible treatment of film slot heights, eliminate grid points outside of the flow field with their computer storage demands, and increase accuracy for all varying grid sizes throughout the flow field. Methods of accomplishing a body-fitted coordinate system can include a basic nonothogonal coordinate framework without any transformation, or a basic coordinate transformation technique. The latter seems most attractive at present.

Improved numerics should be incorporated, particularly a technique that will improve first order upwind differencing by extending regimes in which second-order accurate schemes can be applied. Several methods have been discussed, but further study and evaluation would be recommended before selecting the most appropriate technique.

Since running costs are a serious limitation, improved convergence speed is also needed. Convergence speed is affected somewhat by the numerics adopted, but solution algorithms should be adopted to give reduced running costs and, when larger computer storage becomes available, to permit increased grids. The present pressure-correction equation approach to handling continuity is another serious drawback in that it requires a staggered grid (with attendant increase in storage requirements) and also can slow down the convergence rate.

The second item in the needed basic capability list is improved turbulence and turbulence/chemistry interaction treatment. This may be of less overall impact than the first item, but at least the first two improvements recommended in this second item have already been implemented in 2-D at General Electric. The algebraic stress model for dealing with the turbulence anisotropy in swirling flows has been demonstrated and deserves to be included as an algebraic correction to the turbulence model.

The pdf, probability density function, treatment of random compositional fluctuations has been thoroughly evaluated. It is far superior in the character of its fundamental physics to the eddy break-up model in the current 3-D programs. This change is a very worthwhile improvement.

An appropriate change to the basic two-equation turbulence model to handle all flow regimes has not been identified. Reynolds stress transport equations and improved dissipation rate equations may be the only option. Timewise, such a solution may be a long way into the future.

The third item calls for improvement in the boundary flow input treatments. Inputs based on the physical geometry are not adequate. The flows leave the entry regions on angles and with turbulence levels that are affected

by small geometry features that are not directly treated by the models. Accurate inputs for these features must come from empirical data. An extensive data base exists at General Electric, but additional data will ultimately be needed, and methods of translating this empirical information into inputs to the model need to be developed. Detailed analysis with a 3-D model of the flow through a specific aperture has been considered as a technique for generating the inputs for the larger solution, but the basic need would still involve a significant new data base.

The last item in the list of needed basic capabilities is an improved chemical kinetics treatment. This will become particularly important if the same model is to be used for emissions or blowout calculations. For durability alone its impact is small and, therefore, has been placed far down the list. Expanded joint pdf methods have, however, been given considerable attention at General Electric, development concepts are available.

On the application to durability the two durability design needs of liner heat transfer inputs and pattern factor calculations are listed. For both, a method for fuel and swirler air insertion is needed. As in the third item above, this involves accumulation of new data as well as an accompanying analytical study on how to use the data.

The boundary between the film cooling protection and the hot gas side flows is not distinct. Temperature, velocity, and turbulence gradients are all present. However, similar techniques that would be used to introduce finer grid near the wall to calculate through the film can also be used to define "effective" hot gas side conditions at the film protection boundary. This will permit the use of existing wind tunnel data on the effect of film protection slots of different designs. This technique needs to be defined and programmed.

Methods of treating flame radiation can be developed at a later time. New data is being accumulated on flame radiation in ongoing programs and this data could be used in calibrating any future calculation methods. The final flame radiation calculations are expected to be a hybrid calculation not integrated with the INTFLOW iterations but utilizing the final flow field.

The exit gas temperature pattern factor design tool is conceived as a perturbation calculation at this time. While the absolute temperature pattern may not be accurate, much greater accuracy would be expected for the perturbaation effect due to a change in dilution hole pattern. This tool would be developed initially along this principle.

REFERENCES

1. Mongia, H.C. et al, "Combustor Design Criteria Validation," UATL-TR-78-55A, 55B, 55C, February 1979.

2. "The Design and Development of Gas Turbine Combustors - Phase II Basic Computing System," Volume Report No. 1420- . Northern Research and Engineering Corporation.

3. Claus, R.W., "Analytical Calculation of a Single Jet in Crossflow and Comparison with Experiment," National Aeronautics and Space Administration, Technical Memorandum 83027, 1983.

4. Lapp, M., Drake, M.C., Penney, C.M., Pitz, R.W., and Correa, S.M., "Turbulent $CO/H_2/N_2$ Jet Diffusion Flame in Coflowing Air," DoE Contract Report DE-AC04-78 ET 13146, 1983.

5. Green, A. and Whitelaw, J.H., "Measurements and Calculations of the Isothermal Flow in Axisymmetric Models of Combustor Geometries," J. Mech. Eng. Sci, 22, 119, 1980.

6. Vu, B.T. and Gouldin, F.C., "Flow Measurements in a Model Swirl Combustor," AIAA Paper No. 80-007, 1980.

7. Lightman, A.J., Richmond, R.D., Magill, P.D., Krishnamurthy, L., Roquemore, W.M., Bradley, R.P., Strutrud, J.S. and Reeves, C.M., "Velocity Measurements in a Bluff-Body Diffusion Flame," AIAA Fifteenth Thermophysics Conference, Snowmass, Colorado, AIAA-80-1544, 1980.

8. Walker, R.E., Kors, D.L., "Multiple Jet Study Final Report," NASA CR 121217, June 1973.

9. Holdeman, J.D., and Walker, R.E, "Mixing of a Row of Jets with a Confined Crossflow," AIAA J. 15, 243, 1977.

10. Ferguson, D.R. and Keith, J.S., "Modifications to the Streamline Curvature Program," NAS CR-132705.

11. Pai, B.R., Richter, W. and Lowes, T.M., "Flow and Mixing in Confined Coaxial Flows," J. Int. Fuel, 48, 185, 1975.

12. Owen, F.K., "Measurements and Observations of Turbulent Recirculating Jet Flows," AIAA J.. 14, 1556, 1976.

13. Habib, M A. and Whitelaw, J.H., "Velocity Characteristics of Confined Coaxial Jets With and Without Swirl," J. Fluids Eng., 102, 47, 1980.

14. Jones, W.P. and Launder, B.E., "The Prediction of Laminatization with a Two-Equation Turbulence Model," Int. J. Heat and Mass Transfer, 15, 301, 1972.

15. Saffman, P.G., "Model Equations for Turbulent Shear Flow," Stud. Appl. Math., 53, 17, 1974.

16. Patankar, S.V., Basu, D.K., and Albay, S.A., "Prediction of the Three-Dimensional Velocity Field of a Deflected Turbulent Jet," J. Fluids Eng., 99, 785, 1973.

17. Jones, W.P. and McGuirk, J.J., "Computation of a Round Turbulent Jet Discharging into a Confined Crossflow," Proc. 2nd Int. Symp. of Turbulent Shear Flows, 1979.

18. Crabb, D., "Jets in Crossflow," Ph.D. Thesis, University of London, 1979.

19. Crabb, D., Durao, D.F.G., and Whitelaw, J.H., "A Jet Normal to a Crossflow," J. Fluids Eng., 103,142, 1981.

20. White, A J., ASME Paper 80-WA/HT-26, 1980.

21. Claus, R.W., "Analytical Calculation of a Single Jet in Crossflow and Comparison with Experiment," National Aeronautics and Space Administration, Technical Memorandum 83027, 1983.

22. Kamotani, Y. and Greber, I., "Experiments on a Turbulent Jet in Cross Flow," AIAA J., 10, 1425, 1972.

23. Khan, Z.A. and Whitelaw, J.H., "Vector and Scalar Characteristics of Opposing Jets Discharging Normally into a Cross-Stream," Int. J. Heat and Mass Transfer, 23, 1673, 1980.

24. Khan, Z.A , McGuirk, J.J., and Whitelaw, J.H., " A Row of Jets Discharging in Crossflow," Fluid Dynamics of Jets with Applications to V/STOL, AGARD CP-308, 1982.

25. Kamotani, Y. and Greber, I., "Experiments on Confined Turbulent Jets in Cross Flow," NASA CR-2392, 1974.

26. Atkinson, K.N., Khan, Z.A., and Whitelaw, J.H., "Experimental Investigation of Opposed Jets Discharging Normally into a Cross-Stream," J. Fluid Mech., 115, 493, 1982.

27. Norgren, C T. and Humenik, F.M., "Dilution Jet Mixing Study for Gas-Turbine Combustors," NASA TN D-4675, 1968.

28. Jones, W.P., "Prediction Method for Turbulent Flows," VKI Lecture Series, 14, 1979-2, 1979.

29. Kent, J.H. and Bilger, R.W., "Turbulent Diffusion Flames," Fourteenth Symposium (International) on Combustion, The Combustion Institute, Pittsburgh, Pa., 1973.

30. Elliman, D.G., "Experimental and Numerical Study of an Axisymmetric Combustor," PhD Thesis, University of Nottingham, 1977.

31. Elliman, D.G., Fussey, D.E., and Hay, N., "Predictions and Measurements of a Turbulent, Axisymmetric Ducted Diffusion Flame," Int. J. Heat Mass Transfer, 21, 1978.

32. Toral, H. and Whitelaw, J.H., "Velocity and Scalar Characteristics of the Isothermal and Combusting Flows in a Combustor Sector Rig," Combustion and Flame, 45, 251, 1981.

33. Tuttle, J.H., Altenbrich, R.A., and Mellor, A.M., "Emission from and Within an Allison J-33 Combustor - II: The Effect of Inlet Air Temperature," Combustion Science and Technology, 7, 125, 1976.

34. Vranos, A. and Tabakk, E.F., "Combustion Product Distributions in the Primary Zone of a Gas Turbine Combustor, Combustion and Flame, 26, 129, 1976.

35. Noyce, J.R., Sheppard, C.G.W., and Yamba, F.D. "Measurements of Mixing and Species Concentrations Within a Gas Turbine Type Combustor," Comb. Sci. and Tech., 25, 209, 1981.

36. Crowe, C.T. "Gas-Droplet Flow Field in the Vicinity of an Atomizer," 11th JANNAF Comb. Meeting, 1974.

37. Crowe, C.T., Sharma, M.P., and Stock, D.E., "The Particle-Source-in-Cell (PSI-Cell) Model for Gas Droplet Flows," Dept. of Mech. Eng., Washington State University, 1977.

38. El-Banhawy, Y., Melling, A., and Whitelaw, J.H., "Combustion-Driven Oscillations in a Small Tube," Combustion and Flame, 33, 281, 1978.

39. El-Banhawy, Y. and Whitelaw, J.H., "An Assessment of an Approach to the Calculation of the Flow Properties of Spray Flames," AGARD, CP 275 Paper 12, 1980.

40. Botros, P., Law, C.K., and Siringano, W.A., "Droplet Combustion in a Reactive Environment," Comb. Sci. and Tech., 21, 123, 1980.

41. Driscoll, J.F. and Pelaccio, D.G., "Turbulence Eddy Viscosity and Mean Eddy Life Time measured in Spray Combustion," Comb. Sci. and Tech., 21, 205, 1980.

42. Nicholls, J.A., Kauffman, C.W., Pelaccio, D.G., Glass, D.R., and Driscoll, J.F., "The Effect of Fuel Sprays on Emission from a Research Gas Turbine Combustor," Comb. Sci. & Tech., 23, 203, 1980.

43. Libby, P.A. and Williams, F.A. (eds.), Turbulent Reacting Time, Topics in Applied Physics Volume 44, Springer-Verlag, Berlin, 1980.

44. Hinze, J.O., Turbulence, An Introduction to Its Mechanism and Theory, McGraw-Hill, 1959.

45. Jones, W.P. and Whitelaw, J.H., "Calculation Methods for Reacting Turbulent Flows, A Review," Combustor Flame, 48, 1, 1982.

46. Libby, P..A. and Bray, K.A., "Variable Density Effects in Premixed Turbulent Flames," AIAA Journal, 15, 1186, 1977.

47. Gosman, A.D. and Pun, W.M., Lecture Notes for Course Entitled, "Calculation of Recirculating Flows," Imperial College, HTS/74/72, 1974.

48. Syed, S.A. and Sturgess, G.J. "Validation Studies of Turbulence and Combustion Models, for Aircraft Gas Turbine Combustors," Momentum and Heat Transfer Processes in Recirculation Flows, ASME HTD, Vol. 13, 1980.

49. Bozsan, F., Ayers, W.H., Swithenbank, J., and Pan, Z., "Three-Dimensional Model of Spray Combustion in Gas Turbine Combustors," AIAA-81-0324, AIAA Nineteenth Aerospace Science Meeting, January 1981.

50. Lilley, D.G. "Flow Field Modeling in Practical Combustors: A Review," J. Energy, 3, 197, 1979.

51. Patankar, S., Numerical Heat Transfer and Fluid Flow, Hemisphere Publishing, 1980.

52. Launder, B.E. and Spalding, D.G, "The Numerical Computation of Turbulent Flows," Computer Methods in Applied Mechanics and Engineering, 3, 269, 1974.

53. Allen, D. and Southwell, R., "Relaxation Methods Applied to Determine the Motion in Two Dimensions, of a Viscous Fluid Past a Fixed Cylinder," Quart. J. Mech. and Appl. Math., 8, 129, 1955.

54. de Vahl Davis, G. and Mallinson, G.D., "An Evaluation of Upwind and Central Difference Approximations by a Study of Recirculating Flow," Computers and Fluids, 4, 29, 1976.

55. Castro, I.P., "Numerical Difficulties in the Calculation of Complex Turbulent Flows," Turbulent Shear Flows I. p 220, Springer-Verlag, Berlin, 1979.

56. Raithby, G.D., "A Critical Evaluation of Upstream Differencing Applied to Problems Involving Fluid Flow," Comp. Meths. Appl. Mech. Eng., 9, 75, 1976.

57. Leonard, B.P., "A Stable and Accurate Convective Modelling Procedure Based on Quadratic Upstream Interpolation," Comp. Meths. Appl. Mech. Eng. 19, 59, 1979.

58. McGuirk, J.J., Taylor, A.M.K.P., and Whitelaw, J.H. "The Assessment of Numerical Diffusion in Upwind-Difference Calculations of Turbulent Recirculating Flows," Third Symposium on Turbulent Shear Flows, September 1981.

59. Green, A., "Isothermal Models of Combustion Chamber Flows," PhD Thesis, University of London, 1981.

60. Cheng, S.I. and Shubin, G. "Computational Accuracy and Mesh Reynolds Number," J. Comp. Phys., 28, 315, 1978.

61. Stubley, G.D., Raithby, G.D. and Strong, A.B., "Proposal for a New Discrete Method Based on an Assessment of Discretization Errors," Numer. Heat Transfer, 3, 411, 1980.

62. Shyy, W., "Study of Finite Difference Approximations to Steady-State, Convection-Dominated Flow Problems," General Electric TIS Report, 1983.

63. Raithby, G.D., "Skew-Upstream Differencing Schemes for Problems Involving Fluid Flow," Comp. Meths. Appl. Mech. Eng., 9, 151, 1975.

64. Leschzinger, M A., "Practical Evaluation of Three Finite Difference Schemes for the Computation of Steady-State Recirculating Flows," Comp. Meths. Appl. Mech. Eng., 23, 293, 1980.

65. Leschzinger, M.A. and Rodi, W , "Calculation of Annular and Twin Parallel Jets Using Various Discretization Schemes and Turbulence Model Variations," Tras. ASME, J. Fluids Eng., 103, 352, 1981.

66. Han, T., Humphrey, J.A.C., Launder, B.E., "A Comparison of Hybrid and Quadratic-Upstream Differencing in High Reynolds Number Elliptic Flows," Comp. Meths. Appl. Mech. Eng., 29, 81, 1981.

67. Atias, M , Wolfsshtein, M. and Israeil, M., "Efficiency of Navier-Stokes Solver," AIAA J., 15, 263, 1977.

68. Gupta, M.M. and Manohar, R.P., " A Critique of a Second-Order Upwind Scheme for Viscous Flow Problems," AIAA J. 16, 759, 1978.

69. Richtmyer, R.D. and Morton, K.W., "Difference Methods for Initial-Value Problems," Second Edition, Interscience, New York, 1967.

70. Chu, C.K., "Numerical Methods in Fluid Dynamics," in Advances in Applied Mechanics, 18, p 286, Academic Press, New York, 1978.

71. MacCormack, R.W and Lomax, H., "Numerical Solution of Compressible Viscous Flows," Annual Review of Fluid Mechanics, p 289, Annual Review, Inc., Palo Alto, CA, 1979.

72. Dahlquist, G. and Bjorck, A., Numerical Methods, Prentice-Hall, Englewood Cliffs, NJ, 1974.

73. Gresho, P.M. and Lee, R.L., "Don't Suppress the Wiggles - They're Telling You Something!," in Finite Element Methods for Convection Dominated Flows, T.J.R. Hughes (Ed.), 37, The American Society of Mechanical Engineers, New York, 1979.

74. Varga, R.S., Matrix Iterative Analysis, Prentice-Hall, Englewood Cliffs, NJ, 1962.

75. Young, D.M. Iterative Solution of Large Linear Systems, Academic Press, New York, 1971.

76. Botta, E.F.F. and Velman, A.E.P. "On Local Relaxation Methods and Their Appplication to Convection-Diffusion Equations," J. Comp. Phys. 48, 127, 1982.

77. Libby, P.A. and Williams, F.A., " Some Implications of Recent Theoretical Studies in Turbulent Combustion," AIAA Journal, 19, 261, 1981.

78. Tennekes, H. and Lumley, J.L., "A First Course in Turbulence," MIT Press, 1972.

79. Durao, D.F.G. and Whitelaw, J.H., "Velocity Characteristics of the Flow in the Near Wake of a Disk," J. Fluid Mech., 85, 369, 1978.

80. Bilger, R.W., "Turbulent Flow with Nonpremixed Reactants," Turbulent Reacting Flows," Topics in Applied Physics, Vol. 44, Springer-Verglag, Berlin, 1980.

81. Borghi, R. and Dutoya, D., "On the Scale of the Fluctuations in Turbulent Combustion," Seventeenth (International) Symposium on Combustion, The Combustion Institute, Pittsburgh, PA, p 235, 1979.

82. Schefer, R.W., Dibble, R.W., and Driscoll, J.F., "Mass Fluxes $\rho'\mu'$ and $\rho'v'$ Measured in a Turbulent Nonpressurized Flame," Sandia Laboratories Report, SAND 82-8622, 1982.

83. Bray, K.A., "The Interaction Between Turbulence and Combustion," Seventeenth Symposium (International) on Combustion, 1979.

84. Pope, S.B. and Whitelaw, J.H., "The Calculation of Near-Wake Flows," J. Fluid Mech., 73, 1, 1976.

85. Taylor, A.M.K.P., "Isothermal and Combusting flows Behind Axisymmetric Baffles," PhD Thesis, University of London, 1981.

86. Durst, F. and Rastogi, A.K. "Turbulent Flow Over Two-Dimensionsal Fences," in Turbulent Shear Flows, 2, p 218, Springer-Verlag, Berlin, 1980.

87. Hah, C. and Lakshminarayana, B., "Prediction of Two- and Three-Dimensional Asymmetric Turblent Wakes, Including Curvature and Rotation Effects," AIAA Journal, Vol. 18, 1196, 1980.

88. Wolters, H.R., "Experimental onderzoek narr het verbrandingsverloop in een gasturbine verbandingrkramer en de invloed van water injectie op de volumna van stikstofoxiden," Technische Hogeschool, Delft, Mach 1973.

89. Pratt, D.T. and Wormeck, J.J. "CREK: A Computer Program for Calculation of Combustion Reaction Equilibrium and Kinetics in Laminar or Turbulent Flow," Washington State University, Report WSU-ME-TEL-761, March 1976.

90. Roquemore, W.M., Bradley, R P. Stutred, J.S., Reeves, C M, and Krishnamurthy, L., "Preliminary Evaluation of a Combustor for Use in modeling and Diagnostics Development," ASME Paper No. 80-GT-93, 1980.

91. Bilger, R.W., "The Structure of Diffusion Flames," Combustion Science and Technology, 13, 155, 1976.

92. Bilger, R.W. "The Structure of Diffusion Flames," Combustion Science and Technology, 13, 155, 1976.

93. Spalding, D.B., "Mixing and Chemical Reaction in Steady Confined Turbulent Flames," Thirteenth Symposium (International) on Combustion, The Combustion Institute, Pittsburg, PA, p 649, 1971.

94. Rhodes, R.P., "A Probability Distribution Function for Turbulent Flows," in Turbulent Mixing in Nonreactive and Reactive Flows, Plenum Press, 1975.

95. Pope, S.B. (1981), "Transport Equation for the Joint Probability Density Function of Velocity and Scalers in Turbulent Flows," Physics of Fluids, 24, 4, 588.

96. Curl, R.L., "Dispersed Phase Mixing I: Theory and Effects in Simple Reactors," AIChE Journal, 9, 175, 1963.

97. Pratt, D.T., Tenth Material Research Symposium, National Bureau of Standards, 1979.

98. Birch, A D., Brown, D.R., Dodson, M.G. and Thomas, J.R., "The Turbulent Concentration Field of a Methane Jet," J. Fluid Mech., 88, 431, 1978.

99. Roshko, A , "Structure of Turbulent Shear Flows: A New Look," AIAA Journal, 14, 1349, 1976.

100. Spalding, D.B., "A General Theory of Turbulent Combustion," J. Energy, 2, 16, 1978.

101. Howe, N.M. Jr., Shipman, C.W , and Vranos, A., "Turbulent Mass Transfer and Rates of Combustion in Confined Turbulent Flames," 9th Symposium (International) on Combustion, Organized by the Combustion Institute, Academic Press, New York, 1963.

102. Spalding, D.B., "Development of the Eddy-Break-up Model of Turbulent Combustion," Sixteenth Symposium (International) on Combustion, The Combustion Institute, Pittsburg, PA, p. 1657, 1976.

103. Pope, S.B., "The Implications of the Probability Equations for Turbulent Combustion Models," Comb. and Flame, 29, p 235, 1977.

104. Drake, M.C., Bilger, R.W., and Starner, S.H. "Raman Measurements and Conserved Scalar Modelling in Turbulent Diffusion Flames," Nineteenth Symposium (International) on Combusiton, 1983.

105. Becker, H.A., Hottel, H.C., and Williams, G.C. "The Nozzle-Fluid Concentration Field of the Round Turbulent, Free Jet," J. Fluid Mech., 30, 285, 1967.

106. Antonia, R.A. and Bilger, R.W., "The Heated Round Jet in a Coflowing Stream," AIAA J., 14, 1541, 1976.

107. Kennedy, I.M. and Kent, J.H., "Scalar Measurements in a Co-Flowing Turbulent Diffusion Flame," Comb. Sci. and Tech., 25, 109, 1981.

108. Sorinivasan, R., and Mongia, H.C., "Numerical Computations of Swirling Recirculating Flow," NASA CR-21-3517.

109. Sturgess, G.J., Syed, S.A., and McManur, K.R., " Importance of Inlet Boundary Conditions for Numerical Simulation of Combustor Flows," AIAA-83-1263, 1983.

110. Pope, S.B., "An Explanation of the Turbulent Round-Jet/Plane-Jet Anomaly," AIAA J., 16, 279, 1978.

111. Sturgess, G.J. and Syed, S.A. "Widely-Spaced Coaxial Jet, Diffusion Flame Combustor: Isothermal Flow Calculations Using the Two-Equation Turbulence Model," AIAA Twentieth Aerospace Sciences Meeting, Orlando, Florida, 1982.

112. Roquemore, W.M Britton, R.L. and Sandhu, S.S., "Investigation of the Dynanic Behavior of a Bluff Body Diffusion Flame Using Flame Emission," AIAA 20th Aerospace Sciences Meeting, Orlando, Florida, 1982.

113. Magill, P.D., Lightman, A.J., Orr, C.E., Bradley, R.P. and Roquemore, W.M., "Flowfield and Emission Studies in a Bluff Body Combustor," AIAA/ASME 3rd Joint Thermophysics, Fluids, Plasma and Heat Transfer Conference, St. Louis, Missouri, 1982.

114. Correa, S.M., and Pitz, R.W., "The Influence of Large-Scale Structures on Eulerian Models of Turbulent Reacting Flows," C.S. Yih (Ed.) Eastern States Section of the Combustion Institute, Fall Technical Meeting, Atlantic City, New Jersey, 1982.

115. Gleason, C.C., Oller, T.L. Shaysn, M.W., and Bahr, D.W., "Evaluation of Fuel Character Effects on the F101 Engine Combustion System," AFAPL-TR-79-2018, April 1979.

APPENDIX

NOMENCLATURE

a, b	- Exponents in β depending on ξ and ξ^{-2}
Ae	- Flow area
B	- Arrhenius preexponential factor
C_1, C_2, C_μ, C_{ε_1}, C_{ε_2}, C_{ϕ_1}	- Constants in turbulence model
C_p	- Specific heat at constant pressure
d	- Drop diameter
D	- Mass species diffusion coefficient
η_D	- Diffuser efficiency
f	- Friction factor
γ	- Ratio of specific heats
g	- Gravitational constant
g_i	- Gravitational acceleration vector
G_j	- Jacobi iterative matrix
G_w	- SOR iterative matrix
h	- Specific mixture enthalpy
h_i	- Specific enthalpy of species i (including heat of formation)
h_i^0	- Heat of formation of species i
I	- Identity matrix
k	- Wave number
k	- Turbulence kinetic energy
$k_{f(b)}$	- Forward (backward) chemical rate constant
k_{f_j}	- Forward Arrhenius rate of reaction j

L	- Lower triangular matrix
L/D	- Length to hydraulic diameter ratio
Mi	- Molecular weight of species i
N	- Number of species
N	- Number of nodes
Nu	- Nusselt number
p	- Static pressure
$P(\xi, \vec{x})$	- Density weighted probability density function
P_e	- Peclet number
$P_{e\Delta x}$	- Cell Peclet number
Pr	- Prandtl number
P_S	- Static pressure
P_T	- Total pressure
Q	- Dynamic pressure
R	- Universal gas constant
R_c	- Streamline radius of curvature
Re	- Reynolds number
S_ϕ	- Generalized source term in transport equation for the variable ϕ
Sc	- Schmidt number
s, n, r	- Streamwise, normal, and radial coordinates
t	- Time
T	- Temperature
T_c	- Truncation error in approximating convection term
T_d	- Truncation error in approximating diffusion term
T_S	- Static temperature

T_T	- Total temperature
u_i	- Velocity vector
U_s, U_n, U_r	- Streamwise, normal, and radial velocity components
U	- Radial velocity component
x_i	- Coordinate in i direction (i = 1, 2, 3)
Δx, Δy	- Cell dimensions in finite difference forumulation
Y_i	- Mass fraction of species i
$\dot{w}_i$	- Chemical production rate of species i per unit mass
α_j	- Exponent of temperature in expression for k_{f_j}
δ_{ij}	- Kronecker delta
ϵ	- Turbulent kinetic energy dissipation rate
$\epsilon_{i,j}$	- Viscous dissipation correlation in Reynolds stress transport equation
λ	- Eignevalue of G_w
μ	- Molecular viscosity
μ	- Eigenvalue of G_J
μ_t	- Turbulent eddy viscosity
μ_{eff}	- $\mu + \mu_t$, effective eddy viscosity
ν'_{ij}, ν''_{ij}	- Stoichiometric reactant and product coefficients for species i and reaction j
ξ	- Mixture fraction (conserved scaler)
ξ, ξ''^2	- Mean and variance of the pdf $P(\xi, \vec{x})$
ρ	- Mixture density
σ_ϕ, σ_k, σ_ϵ, σ_t	- Turbulent Prandtl/Schmidt numbers
$\bar{\tau}_D$	- Drop lifetime
τ_{ij}	- Viscous stress tensor
ϕ	- Generalized scalar variable
w	- Relaxation factor in iterative process

Overbars

$\bar{}$	- Conventionally (time) averaged quantity
$\tilde{}$	- Density weighted (time) averaged quantity
$()'$	- Conventional fluctuation
$()''$	- Density-weighted fluctuation

HT Nomenclature

ϵ_g	= Flame emissivity
$\frac{f}{a}$	= Local average fuel-air ratio
ρ_b	= Mean beam length, 1.8 times the dome height, feet
p_g	= Combustor pressure, atmosphere
T_{gas}	= Gas Temperature, ° R
K	= Luminosity factor, for nonluminous emissivity K = 1.0
η	= Film effectiveness
T_{film}	= Film Temperature ° F
T coolant	= Coolant Temperature ° F
Q/A	= Radiation (flame or liner to casing) Btu/hr-ft^2
$h_{backside}$	= Cold side heat transfer coefficient Btu/hr-ft^2-° F
hg	= Hot side heat transfer coefficient Btu/hr-ft^2-° F